



ACTA DE EVALUACIÓN DE LA TESIS DOCTORAL (FOR EVALUATION OF THE ACT DOCTORAL THESIS)

Año académico (academic year): 2016/17

DOCTORANDO (candidate PHD): MOLINA JURADO, ANTONIO

PROGRAMA DE DOCTORADO (Academic Committee of the Programme): D336 DOCTORADO EN HIDROLOGÍA Y GESTIÓN DE LOS RECURSOS HÍDRICOS

DEPARTAMENTO DE (Department): Geología, Geografía y Medio Ambiente

TITULACIÓN DE DOCTOR EN (Phd title): DOCTOR/A POR LA UNIVERSIDAD DE ALCALÁ

En el día de hoy 21/07/17, reunido el tribunal de evaluación, constituido por los miembros que suscriben el presente Acta, el aspirante defendió su Tesis Doctoral con Mención Internacional (In today assessment met the court, consisting of the members who signed this Act, the candidate defended his doctoral thesis with mention as International Doctorate), elaborada bajo la dirección de (prepared under the direction of) DAVID CARLOS FERNÁNDEZ REMOLAR // MIGUEL ÁNGEL DE PABLO HERNÁNDEZ.

Sobre el siguiente tema (Title of the doctoral thesis): ESTUDIO DE LAS CONDICIONES PALEOAMBIENTALES DURANTE LA TRANSICIÓN NOÉICO - HESPÉRICO EN MARTE: ARIADNES Y COOGOON. (PALEONVIROMENTAL CHARACTERIZATION OF THE NOACHIAN - HESPERIAN TRANSITION ON MARS. ARIADNES AND COOGOON)

Finalizada la defensa y discusión de la tesis, el tribunal acordó otorgar la CALIFICACIÓN GLOBAL¹ de (no apto, aprobado, notable y sobresaliente) (After the defense and defense of the thesis, the court agreed to grant the GLOBAL RATING (fail, pass, good and excellent): — EXCELLENT / SOBRESALIENTE —

Alcalá de Henares, a 21 de July de 2017

[Signature]

Fdo. (Signed): [Name]

[Signature]

Fdo. (Signed): [Name]

[Signature]

Fdo. (Signed): [Name]

FIRMA DEL ALUMNO (candidate's signature),

[Signature]

Fdo. (Signed): [Name]

Con fecha 4 de octubre de 2017 la Comisión Delegada de la Comisión de Estudios Oficiales de Posgrado, a la vista de los votos emitidos de manera anónima por el tribunal que ha juzgado la tesis, resuelve:

- Conceder la Mención de "Cum Laude"
No conceder la Mención de "Cum Laude"

La Secretaria de la Comisión Delegada

[Signature]

1 La calificación podrá ser "no apto" "aprobado" "notable" y "sobresaliente". El tribunal podrá otorgar la mención de "cum laude" si la calificación global es de sobresaliente y se emite en tal sentido el voto secreto positivo por unanimidad. (The grade may be "fail" "pass" "good" or "excellent". The panel may confer the distinction of "cum laude" if the overall grade is "Excellent" and has been awarded unanimously as such after secret voting.)

UNIVERSIDAD DE ALCALÁ. PATRIMONIO DE LA HUMANIDAD

INCIDENCIAS / OBSERVACIONES:  
(Incidents

/

Comments)





Universidad  
de Alcalá

COMISIÓN DE ESTUDIOS OFICIALES  
DE POSGRADO Y DOCTORADO

En aplicación del art. 14.7 del RD. 99/2011 y el art. 14 del Reglamento de Elaboración, Autorización y Defensa de la Tesis Doctoral, la Comisión Delegada de la Comisión de Estudios Oficiales de Posgrado y Doctorado, en sesión pública de fecha 4 de octubre, procedió al escrutinio de los votos emitidos por los miembros del tribunal de la tesis defendida por *MOLINA JURADO, ANTONIO*, el día 21 de julio de 2017, titulada *ESTUDIO DE LAS CONDICIONES PALEOAMBIENTALES DURANTE LA TRANSICIÓN NOÉICO - HESPÉRICO EN MARTE: ARIADNES Y COOGOON. (PALEONVIROMENTAL CHARACTERIZATION OF THE NOACHIAN - HESPERIAN TRANSITION ON MARS. ARIADNES AND COOGOON)*, para determinar, si a la misma, se le concede la mención "cum laude", arrojando como resultado el voto favorable de todos los miembros del tribunal.

Por lo tanto, la Comisión de Estudios Oficiales de Posgrado **resuelve otorgar** a dicha tesis la

**MENCIÓN "CUM LAUDE"**

Alcalá de Henares, 10 de octubre de 2017  
EL PRESIDENTE DE LA COMISIÓN DE ESTUDIOS  
OFICIALES DE POSGRADO Y DOCTORADO



  
Juan Ramón Velasco Pérez

**Copia por e-mail a:**

Doctorando: MOLINA JURADO, ANTONIO

Secretario del Tribunal: OLGA PRIETO BALLESTEROS.

Directores de Tesis: DAVID CARLOS FERNÁNDEZ REMOLAR // MIGUEL ÁNGEL DE PABLO HERNÁNDEZ



Universidad  
de Alcalá

ESCUELA DE DOCTORADO  
Servicio de Estudios Oficiales de  
Posgrado

DILIGENCIA DE DEPÓSITO DE TESIS.

Comprobado que el expediente académico de D./D<sup>a</sup> \_\_\_\_\_  
reúne los requisitos exigidos para la presentación de la Tesis, de acuerdo a la normativa vigente, y habiendo  
presentado la misma en formato:  soporte electrónico  impreso en papel, para el depósito de la  
misma, en el Servicio de Estudios Oficiales de Posgrado, con el nº de páginas: \_\_\_\_\_ se procede, con  
fecha de hoy a registrar el depósito de la tesis.

Alcalá de Henares a \_\_\_\_\_ de \_\_\_\_\_ de 20 \_\_\_\_\_



Fdo. El Funcionario



**DISSERTATION**

**TESIS DOCTORAL**



Universidad  
de Alcalá

Programa de Doctorado en Hidrología y  
Gestión de los Recursos Hídricos

**PALEOENVIRONMENTAL CHARACTERIZATION OF  
THE NOACHIAN-HESPERIAN TRANSITION ON MARS:  
ARIADNES AND COOGOON**

ESTUDIO DE LAS CONDICIONES PALEOAMBIENTALES  
DURANTE LA TRANSICIÓN NOÉICO-HESPÉRICO EN MARTE:

ARIADNES Y COOGOON

Antonio Molina Jurado

Advisors /  
Directores:

David Carlos Fernández Remolar  
Miguel Ángel de Pablo Hernández



CENTRO DE ASTROBIOLOGÍA  
ASOCIADO AL NASA ASTROBIOLOGY INSTITUTE



2017



Cover original design by © Starline / Freepik.  
Artist's impression of Mars 4 Ga ago by ESO/M. Kornmesser.  
Background HiRISE images from NASA/JPL/University of Arizona  
and HRSC perspective view from ESA/DLR/FU Berlin.



Universidad  
de Alcalá

Programa de Doctorado en Hidrología y  
Gestión de los Recursos Hídricos

**PALEOENVIRONMENTAL CHARACTERIZATION OF THE  
NOACHIAN-HESPERIAN TRANSITION ON MARS:  
Ariadnes and Coogoon**

ESTUDIO DE LAS CONDICIONES PALEOAMBIENTALES  
DURANTE LA TRANSICIÓN NOÉICO-HESPÉRICO EN MARTE:  
Ariadnes y Coogoon

Disertación presentada por

**ANTONIO MOLINA JURADO**

Directores:

**David Carlos Fernández Remolar  
Miguel Ángel de Pablo Hernández**

Alcalá de Henares, 2017

This page intentionally left blank.





Universidad  
de Alcalá

DEPARTAMENTO DE GEOLOGÍA, GEOGRAFÍA Y  
MEDIO AMBIENTE

C/ Colegios, 2  
28801 Alcalá de Henares (Madrid)  
Teléfonos: 91 885 44 29  
Fax: 91 885 44 39  
e-mail: [dep419@uah.es](mailto:dep419@uah.es)

**Francisco Javier Salas Rey**, Director del Departamento de Geología, Geografía y Medio Ambiente de la Universidad de Alcalá, en representación de su Consejo de Departamento,

### HACE CONSTAR

Que la Tesis Doctoral titulada “Palaeoenvironmental characterization of the Noachian-Hesperian transition on Mars: Ariadnes and Coogoon”, realizada por D. **Antonio Molina Jurado**, reúne las características adecuadas para su exposición y defensa pública: rigor científico, aportaciones novedosas y aplicación adecuada de la metodología. Por tales motivos doy mi conformidad para que se proceda al depósito y registro de esta Tesis Doctoral.

Alcalá de Henares, 21 de abril de 2017



Francisco Javier Salas Rey  
Director del Departamento de Geología, Geografía y Medio Ambiente

## INFORME FAVORABLE DE DIRECTORES DE TESIS

Esta memoria de Tesis Doctoral es presentada por Antonio Molina Jurado para optar al título de Doctor por la Universidad de Alcalá de Henares. La presente Tesis ha sido realizada en el Departamento de Planetología y Habitabilidad del Centro de Astrobiología (CSIC-INTA) y el Departamento de Geología, Geografía y Medio Ambiente de la Universidad de Alcalá, y pertenece al Programa de Doctorado de Hidrología y Gestión de los Recursos Hídricos (D336) de la Universidad de Alcalá, regulado por el R.D. 1393/2007. La investigación ha sido financiada mediante una beca JAE-Predoc 2010 (Junta de Ampliación de Estudios) del Consejo Superior de Investigaciones Científicas (CSIC) perteneciente al Ministerio de Economía, Industria y Competitividad de España.

Como directores de la Tesis Doctoral confirmamos que el trabajo ha sido realizado por el doctorando bajo nuestra dirección, respetándose los derechos de los autores citados. Así mismo, certificamos que el trabajo reúne las condiciones necesarias de contenido, teóricas y metodológicas para ser admitido a trámite ante la correspondiente comisión con el fin de obtener el referido Título de Doctor, y por lo tanto se autoriza la presentación de la Tesis Doctoral titulada "Estudio de las condiciones paleoambientales durante la transición Noéico-Hespérico En Marte: Ariadnes y Coogoon" para su defensa. Para que así conste, firman bajo estas líneas:

Dr. David C. Fernández Remolar

Co-director Tesis Doctoral




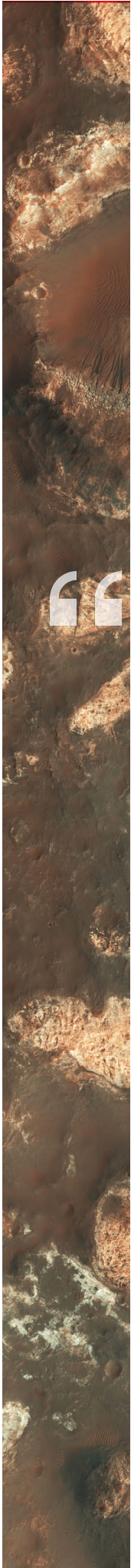
Dr. Miguel Ángel de Pablo Hernandez

Co-director y tutor Tesis Doctoral

Mr. Antonio Molina Jurado

Doctorando





## THE BEAUTY OF MARS EXISTS IN THE HUMAN MIND,

*Without the human presence, it is just a collection of atoms,  
no different than any other random speck of matter in the universe.*

*It's we who understand it,  
and we who give it meaning.*

*All our centuries of looking up at the night sky and watching it  
wander through the stars.*

*All those nights of watching it through the telescopes,  
looking at a tiny disk trying to see canals in the albedo changes.*

*All those dumb sci-fi novels with their monsters  
and maidens and dying civilizations.*

*And all the scientists who studied the data, or got us here.*

***THAT'S WHAT MAKES MARS BEAUTIFUL***”

— ***Sax Russell***  
**in Kim Stanley Robinson's, Red Mars**

This page intentionally left blank.

## ABSTRACT

This Ph.D. thesis is based on the stratigraphic and geomorphologic recognition and mapping of the Ariadnes (Eridania) and Coogoon (Arabia Terra) areas on Mars, which have extensive records from the Noachian-Hesperian transition (3.71 Ga ago). The ultimate goal is to characterize the paleohabitats arising during a global change occurred at the end of the Noachian, which transformed the planet conditions from wet and neutral to much dryer and acidic.

Several available satellite data sets were included in a Geographic Information System (GIS) to obtain the required information. The data is provided from the sensors onboard MEx (Mars Express), MRO (Mars Reconnaissance Orbiter) and Mars Odyssey orbiters. These datasets consider different types of data, such as 1) topography (MOLA and HRSC), 2) images from the visible spectrum (HRSC, CTX, and HiRISE), 3) hyperspectral data cubes with wider spectral resolution (THEMIS and CRISM), and even 4) thermal data (from THEMIS) to analyze thermal inertia and surface temperatures. This work includes different approaches that go from automatic topography delineation to hyper-spectral analysis for composition. They make possible to obtain geologic maps with a proposed stratigraphy for the studied areas supported by surface dating through crater-counting.

Comparing the results with the analysis of terrestrial analogs and the literature, we discuss different genetic hypotheses for the geologic features of particular interest and their relation to the environment during the Noachian-Hesperian transition. Our results coming from almost antipodal locations of the planet shows an apparently similar environmental evolution during the earliest times that diverts with time. However, they are in concordance with a Noachian epoch where wet episodes were more frequent and long-lived, becoming more scarce and acidic. Materials and landforms could have been formed in a succession of sustained aqueous events, but continuous warmer conditions were not necessary for leading to the described geologic settings.

## RESUMEN

Esta tesis doctoral se basa en el reconocimiento y la cartografía estratigráfica y geomorfológica de las zonas de Ariadnes (Eridania) y Coogoon (Arabia Terra) en Marte, con el fin último de caracterizar los paleohabitats que se dieron en el planeta durante la transición entre el Noéico y el Hespérico (hace 3.71 Ga). Ambas áreas de estudio contienen registros de este cambio global que tuvo lugar al final del Noéico y que transformó las condiciones ambientales del planeta, de húmedas y con pH neutro a mucho más secas y ácidas.

Los datos planetarios, que han sido incluidos en un Sistema de Información Geográfica (SIG) para obtener la información necesaria, provienen de sensores a bordo de los orbitadores MEx (Mars Express), MRO (Mars Reconnaissance Orbiter) y Mars Odyssey. Se trata de datos son muy diversos que abarcan 1) topografía (MOLA y HRSC), 2) imágenes en el espectro visible (HRSC, CTX y HiRISE), 3) cubos hiperespectrales con imágenes de amplio rango espectral (THEMIS y CRISM), e incluso 4) datos térmicos (provenientes de THEMIS), que permiten analizar tanto la inercia térmica como la temperatura superficial. Este trabajo incluye diferentes enfoques que van, desde la delineación automática de rasgos topográficos al análisis composicional. Esto ha permitido realizar mapas geológicos y proponer una secuencia estratigráfica para las zonas estudiadas, apoyándose con dataciones de la superficie a partir de conteo de cráteres.

Mediante el análisis de análogos terrestres y la literatura previa, discutimos los resultados planteando hipótesis genéticas de diferentes elementos geológicos de interés. Ambas zonas antípodas muestran una evolución ambiental similar durante los tiempos más pretéritos, que diverge a partir del Hespérico. Nuestros hallazgos concuerdan con un Noéico con episodios húmedos frecuentes y duraderos, que se van volviendo más ácidos y escasos con el paso del tiempo. Tanto los materiales como las formas del terreno observadas, sin embargo, podrían haberse dado en condiciones que no hubieran sido permanentemente templadas, aunque se requiere de eventos húmedos sostenidos para dar lugar a la configuración geológica descrita.



## EPILOGUE

Esta tesis es el fruto de una gran cantidad de trabajo, mucho del cual no se ve reflejado en el documento aquí presentado. Pero cabe preguntarse, ¿en que consiste una tesis doctoral? Esta definición ya de por sí puede requerir de un estudio tan complejo como el que pretenda explicar. En este caso, el doctorado se ha considerado esencial y fundamentalmente un proceso de aprendizaje. Quien escribe estas líneas, el doctorando, ha dedicado muchos años no solo a argumentar una posible hipótesis, sino a formarse, intentando siempre ponerse a prueba y yendo más allá de lo que sería simplemente “hacer el trabajo”.

Muestra de ello es que este documento se encuentre casi al completo escrito en lengua inglesa, a pesar de no ser el estudiante ni mucho menos bilingüe ni contar con un supervisor nativo. También, que sin tener una financiación más allá de la manutención, haya intentado acudir a trabajar a algunos de los recónditos lugares en la Tierra que muestran semejanza con los exóticos y alejados paisajes del planeta sujeto de estudio: los famosos análogos marcianos. La única manera de conocer íntimamente los procesos que suceden (o sucedieron) en Marte es realizando trabajo de campo en campañas que habitualmente no han tenido relación directa con el objetivo de este trabajo, pero que han resultado imprescindibles para una correcta comprensión e interpretación de los resultados. Estos proyectos paralelos, sin embargo, han supuesto más de un año de inversión de tiempo sin contar los preparativos que suponen tales empresas.

Del mismo modo, la implicación con las propias misiones que proveen de estos datos parece algo crucial cuando no es posible seleccionar tus propios muestreos. El doctorando no se ha limitado a pasar gran parte de estos años aprendiendo nuevas técnicas de tratamiento de datos y poniéndose al día de los últimos avances provenientes del planeta vecino, sino que ha participado activamente en las operaciones del rover Curiosity, de la misión MSL de la NASA (siendo operador del instrumento REMS), así como de la selección de sitios de aterrizaje de la próxima misión ExoMars de la ESA (donde prestó apoyo a la candidatura de Coogoon y

Mawrth). A pesar de verse los trabajos derivados de esta actividad escasamente reflejados aquí, si han supuesto de nuevo un importante hito profesional.

Durante la mayor parte del desarrollo de esta tesis también se ha vivido un proceso de recesión económica con la subsiguiente repercusión en la financiación de estancias de investigación. Esto no ha sido sin embargo un impedimento para que, tras una estancia breve de tres meses en Alemania, financiada por el CSIC, que mediante la beca JAE-predoc ha hecho posible esta investigación, y donde gracias a la ayuda de los doctores E. Hauber, L. Le Deit y S. Adeli se encaminó en gran medida este trabajo, se realizaron otras dos estancias financiadas por mi propio bolsillo. Durante el tramo final del trabajo también me he visto en la necesidad de compaginar estos estudios con contratos de investigación, de los cuales me siento muy orgulloso.

Y el cambio que hago de impersonal a utilizar este estilo más directo no es casual. No todo han sido complicaciones. Si al “Antonio pasado”, aquel que en los primeros años de universidad aún no sabía que le apasionaba y tan solo acababa de leer la magnífica trilogía de Kim Stanley Robinson titulada “Marte”, le dijeran que acabaría trabajando para la NASA en un proyecto del Centro de Astrobiología no lo habría creído. Tampoco que habría estado trabajando en la Antártida, cruzando el peor mar del mundo y sin embargo acompañado de las mejores personas. Y si al querer recorrer camino atrás las huellas ya las ha borrado la nieve del tiempo, aún se divisa esos primeros años de facultad en que con jornadas intensivas no solo de trabajo me iba enamorando de mi profesión y de mis compañeros, con muchos de los cuales aún tengo la suerte de compartir alegrías y complicaciones, tantos años después.

Un profesor en concreto, J.M. Campanario, llenaba algunas de las horas que quedaban entre teoría y prácticas, en una asignatura sobre introducción a los trabajos científicos. Puede que mi colaboración con él fuera esa pequeña semilla que comenzó a germinar con el proyecto final de carrera, un intensivo trabajo sobre la caracterización de Marte al que dedique prácticamente un año. Aprendí lo inimaginable para aquel aún estudiante de licenciatura de Miguel Ángel de Pablo y

Miguel Ramos, que pasaron de ser profesores a ser compañeros y amigos. Tras realizar el master en Hidrología y Recursos Hídricos en que presenté un proyecto final sobre los canales de marte, parecía claro hacia dónde me llevaba la corriente. Y sin embargo de esos cauces secos consiguió brotar este doctorado gracias al inestimable apoyo de David Fernández-Remolar.

Este trabajo trata de cambio, de evolución y de indagar en el pasado, y eso es todo eso lo que tratan de reflejar en estas líneas. Y al igual que en este trabajo, hay mucho que ha sido y que aquí quedara sin reflejarse. Pero aún hay cosas que, en ese cambio constante, han permanecido casi imperturbables durante estos años. Así son los amigos de verdad, que por suerte puedo contar con más dedos que los de una mano, y que a pesar de este doctorado siguen estando ahí. Al igual que la familia, mi padre, mi hermana y mi madre, y sus constantes esfuerzos por mantenerme a flote en esta corriente que no siempre lleva agua dulce. Y a los compañeros que forman parte de ese “et al.” sin el que el trabajo que es la vida no estaría nunca completo.

Para finalizar este breve epílogo hay algo que debo aclarar, y este lugar es tan bueno como cualquier otro. ¿“*Martian*” o “*martian*”? Pues como en tantas otras cosas, y al igual que a la hora de definir en que consiste un doctorado, hay diversidad de opiniones. Y aquí, como siempre, he intentado no ir a por lo más común, ni lo más fácil o ni lo establecido; sino a tomar una decisión lógica y ser consecuente con ella. Dejemos “*Martian*” para las formas de vida marciana cuando la encontremos, y que “*martian*” sea ese adjetivo cercano que se refiere a eso que parece tan importante como para “capitalizarlo” pero que resulta cada vez más familiar. Equiparemos lo “*martian*” con lo “*terrestrial*”. Al fin y al cabo, no son tan diferentes.

Rivas-Vaciamadrid, 15 de abril de 2017,

A handwritten signature in black ink, appearing to read 'Antonio Molina Jurado', with a stylized flourish above the name.

Fdo. Antonio Molina Jurado

This page intentionally left blank.

## 0 INDEXES

### 0.1 TABLE OF CONTENTS

#### PALEOENVIRONMENTAL CHARACTERIZATION OF THE NOACHIAN-HESPERIAN TRANSITION ON MARS: ARIADNES AND COOGOON

<b>ABSTRACT .....</b>	<b>9</b>
<b>RESUMEN .....</b>	<b>10</b>
<b>EPILOGUE .....</b>	<b>11</b>
<b>0 INDEXES.....</b>	<b>15</b>
<b>0.1 TABLE OF CONTENTS .....</b>	<b>15</b>
<b>0.2 LIST OF FIGURES .....</b>	<b>19</b>
<b>0.3 LIST OF TABLES .....</b>	<b>27</b>
<b>0.4 LIST OF ABBREVIATIONS .....</b>	<b>29</b>
<b>1 INTRODUCTION .....</b>	<b>31</b>
<b>1.1 THE PRESENT AND FUTURE RESEARCH ON MARS.....</b>	<b>31</b>
<i>1.1.1 Movement, change and evolution .....</i>	<i>31</i>
<i>1.1.2 Introduction to Mars.....</i>	<i>32</i>
<i>1.1.3 Geology history of Mars.....</i>	<i>35</i>
<b>1.2 AIM AND OBJECTIVES .....</b>	<b>39</b>
<b>1.3 THESIS STRUCTURE .....</b>	<b>42</b>
<b>2 METHODOLOGY .....</b>	<b>45</b>
<b>2.1 DATA .....</b>	<b>45</b>
<i>2.1.1 Data sources.....</i>	<i>45</i>
<i>2.1.2 Instruments and datasets .....</i>	<i>47</i>
<i>2.1.3 Databases.....</i>	<i>53</i>
<b>2.2 METHODS .....</b>	<b>55</b>
<i>2.2.1 Data management.....</i>	<i>55</i>
<i>2.2.2 Software and scripts .....</i>	<i>57</i>
<i>2.2.3 Data input and editing.....</i>	<i>58</i>
<i>2.2.4 Data analysis .....</i>	<i>64</i>
<i>2.2.5 Outputs .....</i>	<i>67</i>

<b>3</b>	<b>ARIADNES .....</b>	<b>69</b>
3.1	INTRODUCTION.....	69
3.1.1	<i>Regional settings.....</i>	69
3.1.2	<i>Research objectives .....</i>	73
3.2	CARTOGRAPHY.....	75
3.2.1	<i>Geologic map.....</i>	75
3.2.2	<i>Units.....</i>	78
3.2.3	<i>Geologic and geomorphic features.....</i>	92
3.3	DATING .....	99
3.3.1	<i>Selected areas.....</i>	99
3.3.2	<i>Results of crater counting.....</i>	102
3.3.3	<i>Chronostratigraphic constraints.....</i>	106
3.4	SPECTRAL ANALYSIS .....	108
3.4.1	<i>Visible near infrared CRISM data.....</i>	108
3.4.2	<i>Infrared THEMIS data and derived thermal inertia .....</i>	116
3.4.3	<i>THEMIS decorrelation stretched color infrared images .....</i>	123
3.5	PHYSICAL ANALYSIS.....	127
3.5.1	<i>Temperature.....</i>	127
3.5.2	<i>Morphometric analysis.....</i>	129
3.6	GEOLOGICAL HISTORY OF ARIADNES.....	134
<b>4</b>	<b>COOGOON.....</b>	<b>141</b>
4.1	INTRODUCTION.....	141
4.1.1	<i>Regional settings.....</i>	141
4.1.2	<i>Research objectives .....</i>	145
4.2	CARTOGRAPHY.....	147
4.2.1	<i>Geologic map.....</i>	147
4.2.2	<i>Units.....</i>	150
4.2.3	<i>Geologic and geomorphic features.....</i>	164
4.3	DATING .....	175
4.3.1	<i>Selected areas.....</i>	175
4.3.2	<i>Results of crater counting.....</i>	178



<b>4.4</b>	<b>SPECTRAL ANALYSIS</b> .....	<b>182</b>
4.4.1	<i>Visible near infrared CRISM data</i> .....	182
4.4.2	<i>Infrared THEMIS data and derived thermal inertia</i> .....	187
<b>4.5</b>	<b>PHYSICAL ANALYSIS</b> .....	<b>191</b>
4.5.1	<i>Temperature</i> .....	191
<b>4.6</b>	<b>GEOLOGICAL HISTORY OF COOGOON</b> .....	<b>193</b>
<b>5</b>	<b>DISCUSSION</b> .....	<b>199</b>
<b>5.1</b>	<b>TERRESTRIAL ANALOGS</b> .....	<b>199</b>
5.1.1	<i>Understanding the Earth to understand Mars</i> .....	199
5.1.2	<i>Deception Island, an unusual antarctic analog</i> .....	201
5.1.3	<i>Iceland, the ice-lava interaction hot spot</i> .....	204
5.1.4	<i>Rio Tinto, a martian river in Spain</i> .....	207
<b>5.2</b>	<b>GENETIC HYPOTHESIS</b> .....	<b>210</b>
5.2.1	<i>Eridania System</i> .....	210
5.2.2	<i>Ariadnes and Caralis light-toned deposits</i> .....	217
5.2.3	<i>Ariadnes and Caralis knob fields</i> .....	224
5.2.4	<i>Western Arabia Terra</i> .....	230
5.2.5	<i>Coogoon phyllosilicate-bearing deposits</i> .....	236
5.2.6	<i>Coogoon main channel</i> .....	241
<b>5.3</b>	<b>NOACHIAN-HESPERIAN GLOBAL PROCESSES</b> .....	<b>246</b>
<b>5.4</b>	<b>ARIADNES AND COOGOON AS LANDING SITES</b> .....	<b>251</b>
5.4.1	<i>Landing missions</i> .....	251
5.4.2	<i>Technical constraints</i> .....	251
5.4.3	<i>Scientific relevance</i> .....	256
<b>6</b>	<b>CONCLUSIONS</b> .....	<b>259</b>
<b>7</b>	<b>REFERENCES</b> .....	<b>261</b>
<b>8</b>	<b>APPENDICES</b> .....	<b>281</b>
8.1	<b>CSFD PLOTS FOR ARIADNES AREAS</b> .....	<b>281</b>
8.2	<b>CSFD PLOTS FOR COOGOON AREAS</b> .....	<b>289</b>
8.3	<b>MEASURED DIMENSIONS OF THE UNCERTAIN ORIGIN DEPRESSIONS</b> .....	<b>293</b>
8.4	<b>SPECTRAL SAMPLES</b> .....	<b>294</b>

<b>8.5</b>	<b>ACADEMIC ACTIVITY DURING THE PH.D.</b>	<b>295</b>
8.5.1	<i>Courses</i>	295
8.5.2	<i>Teaching experience</i>	295
8.5.3	<i>Participation in R &amp; D Projects Funded in Public Calls</i>	295
8.5.4	<i>Publications and other scientific-technical documents</i>	296
8.5.5	<i>Stays in foreign centers</i>	298
8.5.6	<i>Grants and scholarships obtained</i>	298
8.5.7	<i>Contributions to conferences</i>	299

## 0.2 LIST OF FIGURES

<b>Figure 1.1.a</b>	Diagram comparing the Earth's (inner) and Mars' (outer) orbits around the Sun and their seasons [Source: Carr, 2007].	33
<b>Figure 1.1.b</b>	The evolution of the obliquity (a), eccentricity (b) and insolation (c) at the north pole surface at the summer equinox (Ls 90°) over 10 Ma [Source: Laskar et al., 2002].	34
<b>Figure 1.1.c</b>	Geologic processes and various features evolution on Mars, compared to similar major time subdivisions in Earth history [Source: Carr and Head, 2010].	37
<b>Figure 2.2.a</b>	Diagram of the five components that comprises the GIS used on this Ph.D. thesis.	55
<b>Figure 2.2.b</b>	MOLA MEGDR data for the (A) Ariadnes and (B) Coogoon study areas. The topographic colored dataset overlaps the greyscale hillshade with a 50% transparency.	58
<b>Figure 2.2.c</b>	MOLA PEDR data that shows the real coverage of the topographic records for the (A) Ariadnes and (B) Coogoon study areas.	59
<b>Figure 2.2.d</b>	CTX mosaics created for the (A) Ariadnes and (B) Coogoon study areas.	60
<b>Figure 2.2.e</b>	HiRISE mosaics created for the (A) Ariadnes and (B) Coogoon study areas.	61
<b>Figure 2.2.f</b>	HRSC image and DEMs mosaics for the (A) Ariadnes and (B) Coogoon study areas.	62
<b>Figure 2.2.g</b>	Schematic representation of the processes to derive the different outputs shown in this dissertation from the raw data.	68
<b>Figure 3.1.a</b>	Shaded relief derived from altimetry and colorized by elevation of the Eridania System, a group of depressions located between Terra Sirenum and Terra Cimmeria.	70
<b>Figure 3.1.b</b>	Crater larger than 10 km in diameter [Salamunićcar et al., 2012] and main valleys [Hynek et al., 2010] in the region of Eridania System overlapping a shaded relief derived from MOLA altimetry. 1 km a.m.d. contour line showed as an approximation to the paleolake coastline.	71
<b>Figure 3.1.c</b>	Tanaka et al. [2014] geologic map of Mars where a white square marks the study area.	72
<b>Figure 3.2.a</b>	Ariadnes Basin geologic map.	75
<b>Figure 3.2.b</b>	Several fluvial morphologies carving <i>eNhp</i> observed in CTX images, which are colorized with MOLA topography. A2 and B2 show differently interpreted features.	79
<b>Figure 3.2.c</b>	Ariadnes (A) and southeastern (B) knob fields in HiRISE images showing up the typical surfaces of the <i>HNkf</i> unit. Colorized topography (A2) and MOLA PEDR (B2) topography overlapping HRSC include some interpreted morphologies. C to E and F to H boxes are magnified locations in A and B.	80
<b>Figure 3.2.d</b>	(A) CTX image mosaic of <i>eHed</i> unit occurrences, identified as mesas (B) which laterally changes to a mantling. A2 and B2 show colorized overlapping MOLA topography and interpreted features. Magnified views in HiRISE images showed in C to E.	83

<b>Figure 3.2.e</b>	(A) CTX image mosaic that show the <i>AHrp</i> unit occurring as smooth plains and low cratered surfaces affected by tectonic features. (B) Light-toned knobs can be observed, though an impact ejecta blanket from the NE has locally disturbed the surface. <b>A2</b> and <b>B2</b> show colorized overlapping MOLA topography with some distinctive morphologies. <b>C</b> to <b>E</b> are magnified images of the main features. .... 85
<b>Figure 3.2.f</b>	(A) Mosaic of CTX images showing outcrops of the <i>eAsp</i> unit. <b>A2</b> displays a colorized overlapping MOLA topography and tracing the most distinctive structures in the area. <b>B</b> to <b>D</b> are magnified views that provide a greater detail of the <i>eAsp</i> unit. <b>B</b> and <b>C</b> show the relation between <i>eAsp</i> and the adjacent <i>AHrp</i> unit and <b>B</b> displays some tracks of dust devils crossing the surface of this dark smooth unit. .... 87
<b>Figure 3.2.g</b>	Mosaic of different CTX images showing two sets of the <i>eAed</i> unit outcrops ( <b>A</b> and <b>B</b> ). <b>A2</b> and <b>B2</b> show a colorized MOLA topography overlapping the CTX images and includes the outline of some landscape morphologies and geological units. <b>C</b> to <b>E</b> images show a magnified view of the unit. .... 89
<b>Figure 3.2.h</b>	CTX image mosaic of two of the <i>eAed</i> unit occurrences ( <b>A</b> and <b>B</b> ). <b>A2</b> and <b>B2</b> show colorized overlapping MOLA topography and interpreted features. Magnified views showed in <b>C</b> to <b>H</b> . .... 90
<b>Figure 3.2.i</b>	Rose diagrams of the azimuthal directions followed by the ( <b>A</b> ) ridge crests, ( <b>B</b> ) wrinkle ridges, and ( <b>C</b> ) linear depressions or channels mapped for the Ariadnes basin. .... 93
<b>Figure 3.2.j</b>	Examples of craters and associated morphologies in Ariadnes. ( <b>A</b> ) A single-layer rampart ejecta crater; ( <b>B</b> ) Two single-layered ejecta pancakes (SLEPs); ( <b>C</b> ) External area of a double-layered ejecta crater overlapping the outer layer of a multiple-layered ejecta, and ( <b>D</b> ) Rim and SLEP of an older impact crater affecting a crater field. Images are HRSC ( <b>A</b> , <b>C</b> ) and CTX ( <b>B</b> , <b>D</b> ). .... 97
<b>Figure 3.3.a</b>	Map of the selected areas to apply crater counting. ( <b>A</b> ) Original (blue polygons) and reduced (red and yellow polygons) areas for the region. ( <b>B</b> and <b>C</b> ) Shows the areas of the knobs and matrix for <i>HNk<sub>f1</sub></i> and <i>HNk<sub>f2</sub></i> occurrences, respectively. .... 99
<b>Figure 3.3.b</b>	Differential ( <b>left</b> ) and cumulative ( <b>right</b> ) crater size-frequency distributions (CSFD) for the complete Ariadnes region and calculated ages. .... 103
<b>Figure 3.3.c</b>	CSFD ages obtained in the different sectors and units excluding <i>HNkp</i> . .... 104
<b>Figure 3.3.d</b>	CSFD formation and resurfacing ages for the <i>HNkp</i> unit obtained after using the Hartmann (blue) and Neukum-Ivanov (orange) chronology systems. .... 105
<b>Figure 3.3.e</b>	Average ages for the Ariadnes units resulting from the crater size-frequency distribution. .... 107
<b>Figure 3.4.a</b>	CRISM cubes footprints. The background is a combination of a MOLA shaded relief and a geological map. .... 109
<b>Figure 3.4.b</b>	Ariadnes mineralogy characterized trough the phyllosilicate index displayed above the CRISM cubes footprints. The background image is a MOLA shaded relief. .... 110
<b>Figure 3.4.c</b>	CRISM ( <b>color</b> ) and lab ( <b>gray</b> ) spectra of ( <b>A</b> ) Mg- and Fe-smectite, ( <b>B</b> ) Al-smectite plus halides, and ( <b>C</b> ) sulfate bearing materials in the Ariadnes study area. .... 112
<b>Figure 3.4.d</b>	Phyllosilicate index overlapping false color data from projected CRISM cubes. .... 112

**Figure 3.4.e** CTX visible images (numbers 1) and THEMIS derived thermal inertia image (numbers 2) [Christensen *et al.*, 2013] mosaics, for some regions of interest in the Ariadnes study area. .... 118

**Figure 3.4.f** Qualitative (A) and quantitative (B) THEMIS IR derived thermal inertia image mosaics [Christensen *et al.*, 2013] for the Ariadnes study area that overlaps a MOLA shaded relief. .... 120

**Figure 3.4.g** CTX visible images (number 1, left) and mosaics of THEMIS thermal inertia image (number 2, right) [Christensen *et al.*, 2013] for several regions of interest in Ariadnes. The images centered in (A) North, (B) Northeast, (C) East, and (D) West trace the evaporite deposits (with polygons) for each sector. .... 122

**Figure 3.4.h** Results of the THEMIS thermal inertia data (tiu, J·m<sup>-2</sup>·K<sup>-1</sup>·s<sup>-1/2</sup>) for each sample (white background) and control (gray background) areas. .... 123

**Figure 3.4.i** False color decorrelation stretch (DCS) images of THEMIS IR radiance data. .... 124

**Figure 3.4.j** (A) Orange polygons showing the location of the THEMIS DCS images in the study area. Images in B to F show different morphological features of the putative chloride-bearing deposits. .... 126

**Figure 3.5.a** Daytime (**orange circles**, 14 to 16 h) and nighttime (**blue circles**, 4 to 6 h) mean surface temperatures for each image shown in Earth time. .... 128

**Figure 3.5.b** Daytime (**orange circles**, 14 to 16 h) and nighttime (**blue circles**, 4 to 6 h) mean surface temperatures for each image, versus their acquisition time (in Martian solar longitude, ° Ls), as they were at the same type year. .... 129

**Figure 3.5.c** (Left) Histogram showing the area (km<sup>2</sup>) distribution of Ariadnes knobs. (Upper right) Histogram of average (blue) and median (orange) inner altitude (from MOLA) for each knob polygon larger than 0.5 km<sup>2</sup> (limited to MOLA horizontal precision). (Lower right) Histogram of knob thickness that was obtained as a range of altitudes (from MOLA) inside each polygon larger than 0.5 km<sup>2</sup>. .... 130

**Figure 3.5.d** Ariadnes knob field map showing each knob colorized by their (A) size; (B) thickness; and (C) median and (D) maximum altitude. .... 132

**Figure 3.5.e** Scatterplot of thickness versus area for knobs larger than 0.5 km<sup>2</sup> (**blue**) and smaller than 10 km<sup>2</sup> (**orange**), which follow a linear regression (**dark blue** and **red**, respectively). .... 133

**Figure 3.5.f** Rose diagrams of the azimuthal directions followed by the segments composing the outlines for the knobs in Ariadnes area (Figure 3.2.a), weighted by their length. .... 133

**Figure 3.6.a** Interpretative geological cross-sections (A' - A'' and B' - B'') showing relations between different units achieved by the contact relationships between units and the ages obtained by crater counting (Subchapter 3.3). .... 134

**Figure 3.6.b** (Left) Age determination (dots) and error ranges (lines) obtained from different units of the area of study. (Right) Stratigraphic sequence of Ariadnes inferred from age determinations and spatial relations between units determined in the cartography. .... 135

**Figure 4.1.a** Context map showing main regional features around Coogoon Valles in Arabia Terra. The map is a MOLA shaded relief on a stretched color elevation scale (meters relative to Mars datum). .... 142

<b>Figure 4.1.b</b>	Craters larger than 10 km in diameter [ <i>Salamunićcar et al., 2012</i> ] and main valleys [ <i>Hynek et al., 2010</i> ] in the region of Western Arabia Terra, that is overlapped to a shaded relief derived from MOLA altimetry. It is showing the -3 km a.m.d. contour line, which is very approximate to the Arabia shoreline height in the region.....	143
<b>Figure 4.1.c</b>	Geologic map of Mars [ <i>Tanaka et al., 2014</i> ] adapted to the region. ....	145
<b>Figure 4.2.a</b>	Coogoon area geologic map. The legend includes type areas for all the units, and a MOLA colored hillshaded relief map (bottom left corner).....	147
<b>Figure 4.2.b</b>	Images are showing the <i>eNhp</i> unit in CTX images and colored with MOLA topography, where geological features are included (right column; <b>A2</b> and <b>B2</b> ). ( <b>A</b> ) Gullies carving the north rim of a crater. ( <b>B</b> ) A remnant occurrence of <i>eNhp</i> unit between an old rimless crater and the Coogoon channel.....	151
<b>Figure 4.2.c</b>	Outcrops of the <i>eNcb</i> in a CTX image mosaic ( <b>A1</b> ) colored with MOLA topography and including some interpreted geological features ( <b>A2</b> ). The denuded surfaces ( <b>B</b> to <b>D</b> ) are shown in the CTX images, where <i>Member C</i> was eroded exposing the clay-rich materials of the <i>Member A</i> and <i>B</i> . The hi-resolution images allow to appreciate the texture, layering, and structures in the deposits ( <b>E</b> to <b>G</b> ). ....	154
<b>Figure 4.2.d</b>	CTX image mosaics ( <b>A1</b> and <b>B1</b> ) colored with MOLA topography that shows the main geological units ( <b>B1</b> and <b>B2</b> ) associated to <i>INcb</i> . The better resolution in HiRISE images from some locations shows the textures in the light-toned materials ( <b>C</b> to <b>H</b> ). ....	155
<b>Figure 4.2.e</b>	Some examples of the <i>INtt</i> unit surfaces in CTX image mosaics ( <b>A1</b> and <b>B1</b> ) colored with MOLA topography showing the main geological features ( <b>B1</b> and <b>B2</b> ). ....	158
<b>Figure 4.2.f</b>	CTX image mosaic ( <b>A1</b> ) colored with MOLA topography showing the main geological units ( <b>A2</b> ) including <i>IHlp</i> . At the bottom, HiRISE images showing fabric and texture of morphologies and topological relations with other units in two zoom levels ( <b>B</b> to <b>D</b> , up; and <b>E</b> to <b>G</b> , down).....	159
<b>Figure 4.2.g</b>	Some examples of <i>NACd</i> outcrops in the main channel. Images are CTX mosaics ( <b>A1</b> ) combined to colored MOLA topography where the different geological units are shown ( <b>A2</b> ). In CTX images, textural zonation and relation among the surfaces are clearly observable ( <b>B</b> to <b>D</b> ). The texture of clay-bearing deposits in hi-resolution images ( <b>E</b> to <b>G</b> ).....	162
<b>Figure 4.2.h</b>	CTX image mosaics showing ridges in the <i>INtt</i> unit ( <b>A1</b> ), which is colored ( <b>B1</b> ) with MOLA topography. A cross-section (red line) shows the asymmetrical elevation profile of ridges. ....	165
<b>Figure 4.2.i</b>	Rose diagrams of the azimuthal directions followed by the ( <b>A</b> ) ridge crests and channels, both ( <b>B</b> ) observed and ( <b>C</b> ) inferred, mapped for the Coogoon area. ....	166
<b>Figure 4.2.j</b>	Impact crater with a multiple layered ejecta (MLE) in the terminus of Coogoon Valles displayed in CTX image mosaics ( <b>A1</b> ) colored with HRSC topography showing the main geological features ( <b>A2</b> ). Detail of the location where the fluidized ejecta and the channel are contacting ( <b>B</b> and <b>C</b> ) and central pit colored with HRSC topography ( <b>D</b> ).....	167
<b>Figure 4.2.k</b>	CTX image mosaics showing some examples of uncertain origin depressions identified in Coogoon Valles area.....	169



<b>Figure 4.2.l</b>	Projection of the uncertain depressions found in Coogoon in the scatterplot that show the differences between terrestrial thermokarst and supervolcanoes, and the proposed for Mars [Source: Modified from <i>Michalski and Bleacher, 2013</i> ]	170
<b>Figure 4.3.a</b>	Map of the selected areas to apply crater counting	175
<b>Figure 4.3.b</b>	Differential ( <b>left</b> ) and cumulative ( <b>right</b> ) CSFD for the full study area in Coogoon ( <b>Figure 4.3.b</b> ), obtained as explained in Subpart 2.2.4ii	178
<b>Figure 4.3.c</b>	Adjusted ages for the different crater counting areas of Coogoon, obtained with the Hartmann ( <b>blue</b> ) and Neukum-Ivanov ( <b>orange</b> ) chronology systems (Subpart 2.2.4ii)	179
<b>Figure 4.3.d</b>	Average ages for each studied unit, resulting of crater size-frequency distribution that were calculated for some specific sampling areas	180
<b>Figure 4.4.a</b>	CRISM cube footprints and identification number (#ID)	183
<b>Figure 4.4.b</b>	ROIs (hollow crosses) where spectra profiles were extracted from the CRISM FRT0008438 cube to calculate the ratioed spectra. The background ( <b>A1</b> ) is a CTX image mosaic and ( <b>A2</b> ) the result of calculating the phyllosilicate index that overlaps an enhanced visible color image from CRISM. High resolution images of some specific outcrops (C to D) are also displayed to correlate texture and composition of the geological units in the area	184
<b>Figure 4.4.c</b>	CRISM (color) and lab (grays) spectra of ( <b>A</b> ) Mg-smectite, ( <b>B</b> ) Al-smectite and halides, and ( <b>C</b> ) sulfate-bearing materials in Coogoon. The spectra are obtained as the average of a 3 x 3 pixel ROIs ratioed by a nearby spectrally neutral region of the same size	185
<b>Figure 4.4.d</b>	<b>A to E</b> CTX visible images (labeled as number 1) and its correlative THEMIS thermal inertia mosaics (labeled as 2) as shown by Christensen et al. [2013] in selected locations of interest in the Coogoon Valles. The fan/delta deposits ( <b>A</b> and <b>B</b> ) show the lowest values, while the interior of the craters ( <b>C</b> and <b>E</b> ) and the main channel ( <b>D</b> ) show the highest thermal inertia	188
<b>Figure 4.4.e</b>	Qualitative ( <b>A</b> ) and quantitative ( <b>B</b> ) THEMIS IR derived thermal inertia image mosaics [Christensen et al., 2013] for Coogoon overlapping a MOLA shaded relief	190
<b>Figure 4.5.a</b>	Daytime ( <b>orange circles</b> , 14 to 16 h) and nighttime ( <b>blue circles</b> , 4 to 6 h) mean surface temperatures for each image against acquisition time (in Earth dates)	192
<b>Figure 4.5.b</b>	Daytime mean surface temperature ( <b>orange circles</b> each 14 to 16 h, and nighttime mean surface temperature ( <b>blue circles</b> ) recorded each 4 to 6 h against acquisition time (in Martian solar longitude, ° Ls) for all available image	192
<b>Figure 4.6.a</b>	Two block diagrams resulting from the combination of the geological map of the area and interpretative geological cross section sections in Coogoon Valles	193
<b>Figure 4.6.b</b>	( <b>Left</b> ) Age determination (blue squares) and error ranges (blue lines) obtained from the different units of the study area of Coogoon. ( <b>Right</b> ) Stratigraphic sequence of Coogoon inferred from age determinations and spatial relations between units determined by geological mapping	195
<b>Figure 5.1.a</b>	( <b>A</b> ) Location map of the terrestrial analog sites described in this chapter: ( <b>B</b> ) Iceland, ( <b>C</b> ) South Shetland Islands in Antarctica, and ( <b>D</b> ) Río Tinto in Spain	200

<b>Figure 5.1.b</b>	(A) Plateau close to Whalers Bay in Deception Island [Source: A. Molina], compared with (B) a true color image of Gale Crater as photographed by the NASA MSL Curiosity rover [Source: NASA/JPL-Caltech/MSSS].	202
<b>Figure 5.1.c</b>	Photographs from (A) Mekón Valley and (B) a rim close to Telefon Bay in Deception Island [Source: A. Molina and M.A de Pablo]. Image satellite from different types of fluvial features in Deception Island (C to E) and Coogoon (F) and Ariadnes (G and H).	203
<b>Figure 5.1.d</b>	(A) Patterned ground in Byers Peninsula, Livingston Island (Source: A. Molina) and (B) similar morphologies found in the NASA Phoenix landing site [Source: <a href="#">NASA/JPL-Caltech/University of Arizona/Texas A&amp;M University</a> ].	204
<b>Figure 5.1.e</b>	Geothermal springs and fumaroles in (A) Krýsuvík, Reykjanes peninsula, and (B) Landmannalaugar, Iceland. [Source: A. Molina].	206
<b>Figure 5.1.f</b>	Images of (A) origin and (B) downstream Río Tinto during a dry period, when sulfate salts precipitate on the river shores [Source: A. Molina].	207
<b>Figure 5.2.a</b>	Reclassified elevation of the Eridania System region, showing height ranges of the Eridania rims and the different levels of the hypothesized paleolake, where black dashed line shows the 1 km a.m.d. paleoshoreline [Irwin <i>et al.</i> , 2002, 2004b]. Pink-outlined polygons indicate the extension of the knob aggregations found in the region.	210
<b>Figure 5.2.b</b>	Radargrams in the north of Ariadnes area, displaying the variety of echoes seen with MARSIS from orbits 2676 (A) and 4808 (B) [Source: Adapted from White <i>et al.</i> , 2009].	212
<b>Figure 5.2.c</b>	(A) Regional map of crustal thickness [Zuber <i>et al.</i> , 2000]. (B) Surface topography (average as dotted lines and Ariadnes cross-cutting section as straight line) and crustal profile.	214
<b>Figure 5.2.d</b>	CTX imagery showing the diversity of the knob fields in the Eridania System outside of the study area in two different scales. See <a href="#">Figure 5.2.a</a> for A to C images context. Images A to C show the extension of D to F images. The scale in the upper position corresponds to A to C, whereas the scale below corresponds to D to F.	217
<b>Figure 5.2.e</b>	(A) Plot that shows the relation between the backscattering fraction and the asymmetry parameter, which is related to internal heterogeneity and the surface roughness, as experimental studies on artificial ( <b>black symbols</b> ) and natural samples ( <b>red symbols</b> ) having varied physical properties as grain shape, roughness, internal structure [Fernando <i>et al.</i> , 2016; and references therein]. Those results are compared to the obtained with two CRISM images in (B) Eridania Basin (FRT000951C), and (C) Mawrth Vallis (FRT000117BB). Purple stars are the mean Mars values. [Adapted from: Fernando <i>et al.</i> , 2016].	223
<b>Figure 5.2.f</b>	Ice-wedge polygon fields in Northern Alaska displaying (A) an active state with raised margins, and (B) a degraded state with elevated centers [Source: Permafrost Laboratory of the University of Alaska Fairbanks].	228
<b>Figure 5.2.g</b>	Reclassified elevation of Western Arabia Terra region showing the mean elevation of some of the hypothesized paleoshorelines [Head <i>et al.</i> , 1999; Webb, 2004]. The -3,000 m a.m.d. contour line is very approximate to the Arabia shoreline height in the region. The red dash outlined polygons to the NE indicate	

- the possible plain-style caldera found in the region [*Michalski and Bleacher, 2013*] and in light blue the channels of [*Hynek et al., 2010*]. The white square displays the Coogoon study area (Chapter 4). ..... 230
- Figure 5.2.h** Observed topography for (A) the Tharsis and (B) anti-Tharsis hemispheres compared with the modeled topography for the same hemispheres (C and D, respectively), all of them overlapping a shaded relief. [*Source: Phillips et al., 2001*]..... 231
- Figure 5.2.i** (A) Regional map of crustal thickness [*Zuber et al., 2000*].(B) Surface topography (average as dotted lines and Coogoon cross-cutting section as a straight line) and crustal profile (not at the same vertical scale). Arrows denote approximate locations of compressional and extensional regions. .... 233
- Figure 5.2.j** Mg/Fe phyllosilicate detections (**red colors**) to the west of Coogoon study area, obtained with 3.2  $\mu\text{m}$  band from OMEGA and CRISM MultiSpectral Polar (MSP) images, overlapping a THEMIS daytime IR mosaic. The red outlined circle points to the delta-like structure in the outlet of Coogoon Valles. [*Source: Westall et al., 2014*]..... 237
- Figure 5.3.a** Ariadnes and Coogoon antipodal locations over an artist's impression which shows how Mars may have looked about 4 Ga ago. .... 237
- Figure 5.3.b** Timeline of the main geological events identified globally on Mars (center) and Eridania and Arabia regions (both sides). The end of formation date range for the different units defined in the studied areas (Ariadnes and Coogoon) is also displayed. Horizontal lines show the epoch (straight) and periods (stripped) boundaries. .... 249
- Figure 5.4.a** Latitude (A) and Elevation (B) constraints for the ExoMars (**grey**) and Mars2020 (**black**) missions. Ariadnes and Coogoon regions (**orange**) and study areas and proposed landing sites (**red**) extensions.... 253
- Figure 5.4.b** Slopes ( $^{\circ}$ ) obtained from MOLA data (at about 330-m length scale) in Ariadnes (A) and Coogoon (B) regions.... 254
- Figure 5.4.c** Rock abundance (%) from Viking Infrared Thermal Mapper (IRTM) in Ariadnes (A) and Coogoon (B) regions. .... 255
- Figure 5.4.d** Thermal Inertia (A) and Albedo (B) constraints for the ExoMars and Mars2020 missions. The green color is within the acceptable range, and red and dark blue are outside the permitted range (**Table 5.4.a**). Ariadnes and Coogoon regions (**black box**) and study areas and proposed landing sites (**white lined**) extensions. .... 256

This page intentionally left blank.

### 0.3 LIST OF TABLES

<b>Table 1.1.a</b>	Martian epoch boundary ages calculated with Hartmann 2004 iteration chronology system [Hartmann, 2005] and the Neukum chronology system [Hartmann and Neukum, 2001a; Ivanov, 2001] based on a cumulative chronology function. [Source: Michael, 2013].....	36
<b>Table 1.3.a</b>	Schematic summary table of the structure of this dissertation, showing the divisions, chapters and main subchapters. For a complete index (excluding the subparts), see the Table of Contents on page 9...	42
<b>Table 2.1.a</b>	List of internet addresses used as the source of data, information and tools employed in this research. Central column indicates the hosting organizations. ....	46
<b>Table 2.1.b</b>	Remote-sensing space-borne imaging and altimetry data instruments used in this dissertation (A = Altimeter, MC = Multi-spectral camera, HC = Hyper-spectral camera) and their main characteristics. ...	52
<b>Table 2.2.a</b>	Coordinate and projection system properties of this Ph.D. thesis GIS.....	56
<b>Table 3.3.a</b>	Crater counting data of the different polygons obtained from the MOLA DTM dataset. In blue the original area polygons.....	101
<b>Table 3.4.a</b>	List of CRISM cubes analyzed for the Ariadnes study area named as FRT000XXXX, where XXXX is the label. The table includes acquisition information, center coordinates and the number of ROIs couples for each cube (spectra of interest and nearby neutral spectra used for ratio). The highlighted rows mark the cubes shown in <a href="#">Figure 3.4.d</a> . ....	108
<b>Table 3.4.b</b>	Relation of the martian surface materials thermal inertia and their particle size and/or degree of the consolidation range reproduced from [Jones et al., 2014] * Grain size classified according to the Wentworth scale [Wentworth, 1922]. ....	116
<b>Table 3.4.c</b>	THEMIS decorrelation stretch (DCS) information, as band characteristics, and false color that corresponds to chloride-bearing material for each DCS image combination [Osterloo et al., 2010]. ....	124
<b>Table 3.5.a</b>	Temperature data recovered from the THEMIS BTR images of Ariadnes.....	127
<b>Table 3.5.b</b>	Area and altitude statistics (obtained from MOLA data) for the polygons of the Ariadnes knob field. Knobs with an area larger than 0.5 km <sup>2</sup> analyzed separately (limited to MOLA horizontal precision), as for polygons which area is among 0.5 and 10 km <sup>2</sup> .....	130
<b>Table 4.3.a</b>	Statistics of crater counting polygon including altitude obtained from the MOLA DTM. ....	177
<b>Table 4.4.a</b>	List of CRISM cubes in the Coogoon study area. The table includes acquisition information, center coordinates and the number of ROIs couples (spectra of interest and nearby neutral spectra, used for spectral ratios).....	182
<b>Table 4.5.a</b>	Statistics of the THEMIS BTR images obtained and processed for the area.....	191
<b>Table 5.2.a</b>	Potential emplacement origins and whether they could potentially satisfy observed characteristics of the Eridania System depression.....	216
<b>Table 5.2.b</b>	Potential emplacement origins and whether they could potentially satisfy observed characteristics of the light-toned deposits in Eridania System.....	224

<b>Table 5.2.c</b>	Potential origins of Ariadnes and Carolis knob fields and whether they could potentially satisfy observed morphologic characteristics.....	229
<b>Table 5.2.d</b>	Hypotheses on the possible origin of the Western Arabia Terra terrains and whether they could potentially satisfy the observed characteristics. ....	235
<b>Table 5.2.e</b>	Potential emplacement origins and whether they could potentially satisfy observed characteristics of the <i>INcd</i> phyllosilicate-bearing deposits in Coogoon Valles area. ....	240
<b>Table 5.2.f</b>	Comparative of how the observed characteristic in Coogoon main channel (i.e., central section) fits the types of channels on Mars. ....	245
<b>Table 5.4.a</b>	Basic technical constraints for ExoMars and Mars2020 missions and the approximate value of those variables (range or average $\pm$ SD) in Ariadnes and Coogoon study areas and the proposed landing sites close to them. ....	252

## 0.4 LIST OF ABBREVIATIONS

AU	Astronomical Units (adim)
a.m.d.	Above Martian datum
BTR	THEMIS' Brightness Temperature Record
CAT	CRISM Analysis Toolkit
CCD	Charge coupled device
CDAs	Crater detection algorithms
CRISM	Compact Reconnaissance Imaging Spectrometer for Mars
CSFD	(Impact) crater size–frequency distribution
CTX	Context Camera
DCS	THEMIS' DeCorrelation Stretch product
DEM	Digital elevation model
DLE	Double-layered ejecta
ESA	European Space Agency
FRT	CRISM's Full Resolution Targeted products
Ga	Gigaannum, one billion (1,000,000,000) years
GCS	Guidance Control Software
GIS	Geographic Information System
HiRISE	High Resolution Imaging Science Experiment
HRL	CRISM's Half Resolution Long Targeted products
HRSC	High Resolution Stereo Camera
IAU	International Astronomical Union
IR	Infrared
ISIS	Integrated Software for Imaging Spectrometers
LHB	Late Heavy Bombardment
Ls	Areocentric longitude (in degrees)
Ma	Megaannum, one million (1,000,000) years
MEGDR	MOLA's Mission Experiment Gridded Data Records
MEx	Mars Express
MGS	Mars Global Surveyor
MLE	Multiple-layered ejecta
MOLA	Mars Orbiter Laser Altimeter
MRO	Mars Reconnaissance Orbiter
MY	Mars Year
NASA	National Aeronautics and Space Administration
ODY	Mars Odyssey
PEDR	MOLA's Precision Experiment Data Records
PIGWAD	Planetary Interactive G.I.S.-on-the-Web Analyzable Database
QCD	Quasi Circular Depression
RGB	Color model in which Red, Green and Blue are added together
ROI	Regions of interest
SLEP	Single-layered ejecta pancake
THEMIS	THERmal EMission Imaging System
THMPROC	THEMIS Processing Web Interface
TI	Thermal inertia
USGS	United States Geological Survey
VNIR	Visible/near-infrared

This page intentionally left blank.



# 1 INTRODUCTION

## 1.1 THE PRESENT AND FUTURE RESEARCH ON MARS

### 1.1.1 MOVEMENT, CHANGE AND EVOLUTION

One of the most difficult scientific challenges has been to reach the understanding that everything in our universe is constantly changing. Everything moves in the space. Not only the Earth and the other planets revolve around the Sun, but millions of asteroids also do. Moreover, the planet's gravity forces keep hundreds of those cold rocks and larger bodies orbiting them, what we call moons. Every single body rotates around its axis, but the Solar System also travels around the Milky Way while it moves across the universe. However, this apparently fixed configuration is only the picture that we see today; over the years, planets have rearranged their positions as electrons in an atom, asteroids diverted paths and collide over other bodies' surfaces, and even our galaxy is on a collision course with Andromeda, the closest one in the Local Group.

Returning to Earth, the celestial movements are the source of several phenomena that occur on the surface. Years, seasons and days are caused by them, but also the tides, and all the atmospheric and oceanic circulation. An asteroid caused the dinosaurs' extinction, but another might well either originate the life on Earth or even transport what became the first being on the planet. The same life that changed the planet forever, the continuously evolving biosphere (and we are its most 'dynamic' component).

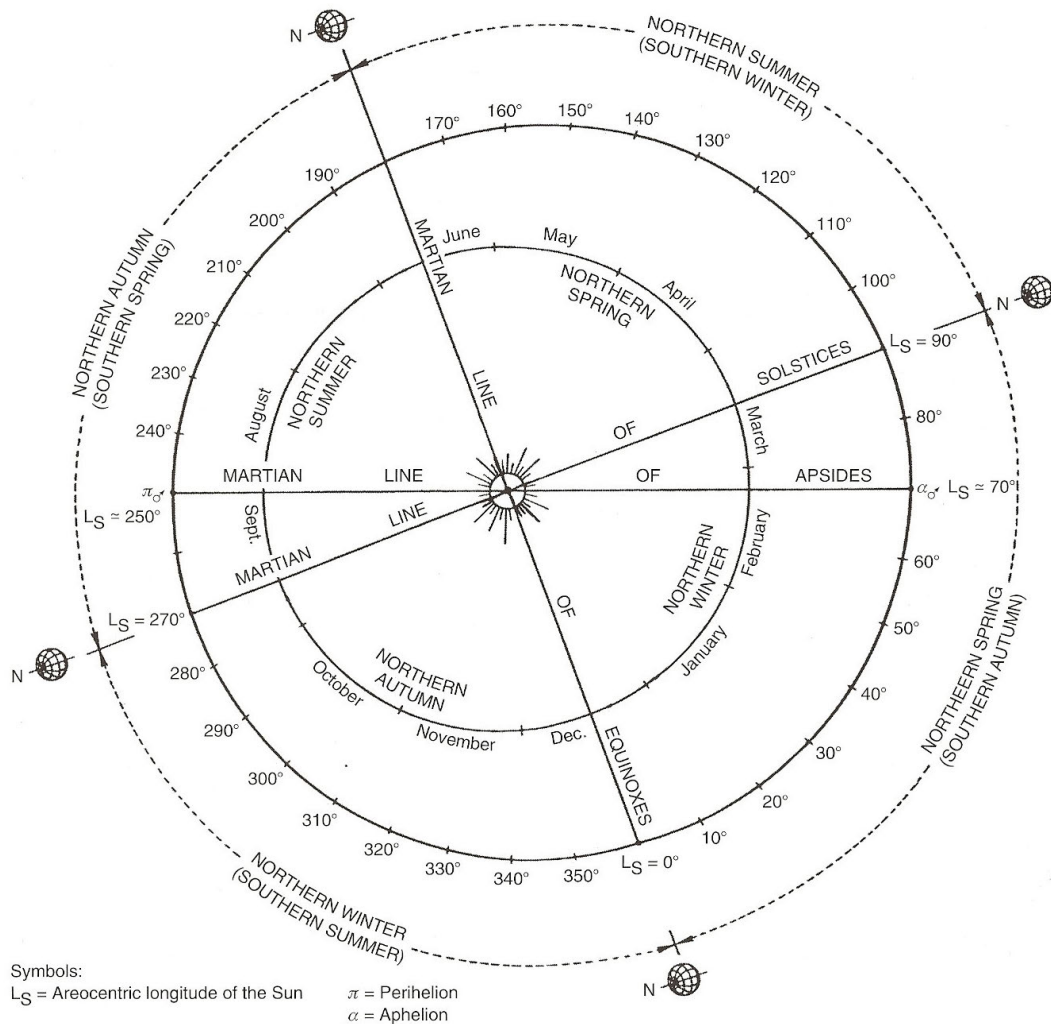
The planet surfaces are constantly changing through those global dynamics, that also include the interior activity as volcanism and tectonism as a reminder of the hot and chaotic formation times. However, the Earth surface constant evolution has not left much from those early ages. Mars, much cooler and quiet, still holds the key to unveil that past. So, despite the fact that it is much what we have learned from our neighbor in the last decades, it remains much to study in its yet elusive geologic evolution.

### 1.1.2 INTRODUCTION TO MARS

When studying Mars, it is important to be aware of the general picture. The neighbor planet holds several similarities with the Earth but also some crucial differences that determine its past and current environment. Starting with the basics, Mars is the fourth planet from the Sun and the outermost of the rocky, terrestrial planets that comprise the inner Solar System. A larger distance from our star implies a longer year (686.98 Earth days), but also a lower solar radiation income and, therefore, Mars has always been colder than Earth. However, the way the radiation reaches the planet is also important.

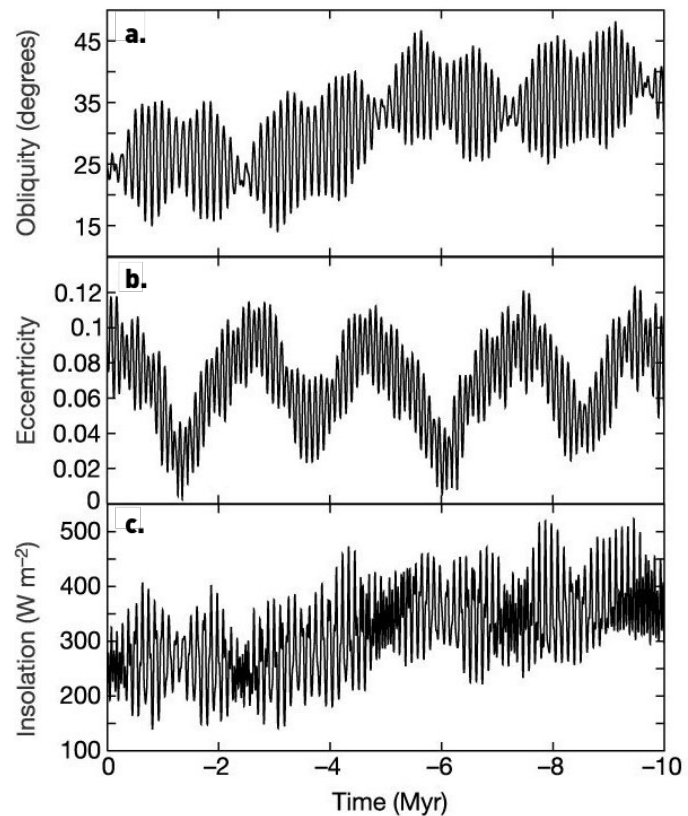
Mars has a highly eccentric orbit around the Sun ([Figure 1.1.a](#)), with an eccentricity a few times larger than Earth's (0.093 compared to 0.017). This causes a large difference between the aphelion and perihelion distances (1.67 and 1.38 AU, respectively [e.g., *Greeley*, 2013]; where Astronomical Unit is the mean distance between the Earth and the Sun). Mars rotates about 40 minutes slower than Earth; therefore, a Mars day (also referred as 'sol') lasts 24 hours, 39 minutes, and 35 seconds [e.g., *Carr*, 2007]. The neighbor planet also has a spin axis inclined slightly more than ours ( $25.19^\circ$ ), which leads to distinctive seasons. The seasons are defined by Mars' position in orbit and described by areocentric longitudes (Ls) of the Sun in degrees ([Figure 1.1.a](#)).

Martian seasons are more extreme than their terrestrial analogs due to greater and less stable eccentricity and spin axis inclination ([Figure 1.1.a](#)). Today, the hemispheres receive a substantially different amount of sunlight since Mars eccentric orbit makes the planet's southern winters long and extreme, while the northern winters are short and relatively warmer. However, this has varied chaotically in a significant amount in the past ([Figure 1.1.b](#)). Besides, Mars' tilt has more variation than Earth's, with an oscillation of tens of degrees over a 100,000-year cycle. That changed the radiation distribution in the surface dramatically, producing short ice ages during Mars history ([Figure 1.1.b](#)).



**Figure 1.1.a** Diagram comparing the Earth's (inner) and Mars' (outer) orbits around the Sun and their seasons. The martian days are referred as  $L_S$ , the angle of the planet current position compared to during the equinoxes [Source: Carr, 2007].

Mars is also smaller than Earth. Its radius is about a half of our planet's (about 3,400 km compared to 6,400 km), and thereby the total surface area of Mars is just about equal to the land surface on Earth above sea level. The average density of Mars is also lower than of the Earth (3,93 versus 5,52 g/cm<sup>3</sup>). As a consequence, the martian gravity is only 0.37 g [e.g., Carr, 2007]. This characteristic is tied to the inability of Mars to retain a dense atmosphere, which currently is thin in comparison with the Earth's, with only 6.5 mbar (101 kPa). The current martian atmosphere is composed mostly of carbon dioxide (95 %), with minor amounts of nitrogen, argon, oxygen, carbon monoxide, and water vapor [e.g., Greeley, 2013].



**Figure 1.1.b** The evolution of the obliquity (a), eccentricity (b) and insolation (c) at the north pole surface at the summer equinox ( $L_s 90^\circ$ ) over 10 Ma [Source: Laskar et al., 2002].

The faint atmosphere of Mars varies not only along the planet surface due to the topographic differences, but seasonally. The amount of carbon dioxide and water vapor oscillates, with a variation in pressure of 25 % during the year. The asymmetrical radiation income previously mentioned caused that the summertime sublimation of the martian poles to be unequal. In the northern pole the temperatures rise enough to sublimate not only the  $\text{CO}_2$  ice, but also the  $\text{H}_2\text{O}$  ice; while in the southern pole, the radiation is not sufficient to reach the water ice. Different axis tilt would reconfigure this cycles and the  $\text{CO}_2$  and  $\text{H}_2\text{O}$  distribution, relocating the ice caps around the Equator in the lower planet inclinations [e.g., Levrard et al., 2004; Forget et al., 2006].

In spite of all the differences, Mars is still the most Earth-like of all the objects in the Solar System. It not only has similar celestial dynamics, Mars' core and mantle are also iron rich, but the latter has the double as iron oxide [Halliday et al., 2001]. Mars' surface also shows evidence of processes related to running water, glaciers, wind, volcanism, and tectonic deformation. The current cold and dry climate

prevents the presence of extensive liquid water on the surface, but Mars preserves ancient geologic record that shows a much wetter past. To unveil this past, the study of this ancient geologic signatures becomes fundamental.

### 1.1.3 GEOLOGY HISTORY OF MARS

Geologic time can be considered as absolute or relative time. If absolute time determines a specific age for a rock or a geologic event expressed in years, relative geologic time simply states it they are older or younger than other rocks or events. To provide an absolute age of rock is necessary to use isotopes (i.e., unstable radioactive elements) that convert to more stable isotopes at a known rate. If we are aware of this rate and can measure the amounts of unstable and stable isotopes in a sample, it is possible to determine the age of the rock from its formation. But not every rock contains such isotopes, either not automated dating systems for robotic spacecraft have not yet been developed. Consequently, absolute dates from outside the Earth have been obtained only for rock samples from the Moon and for meteorites, some of which are from Mars. Since no direct samples are available from other planets yet, only relative ages can be assigned with confidence. The principles of superposition, embayment, and cross-cutting relations are routinely applied for this purpose [Greeley, 2013].

Additionally, the relative ages of planetary surfaces can be established based on the impact craters size-frequency distribution (CSFD). Old surfaces should contain statistically more impact craters than the younger surfaces, since they have been exposed to the impact environment for a longer time. Then, by counting the number of craters over a planetary surface, their relative age can be determined. Crater counts can also be used to derive absolute ages for planetary surfaces. This concept was developed for the Moon and later verified with returned rock samples analysis and radiogenic dating. Crater counts for other planetary surfaces, as Mars', can also be used to derive absolute ages, from extrapolation of those calibrated lunar crater counts [Hartmann and Neukum, 2001; and references therein].

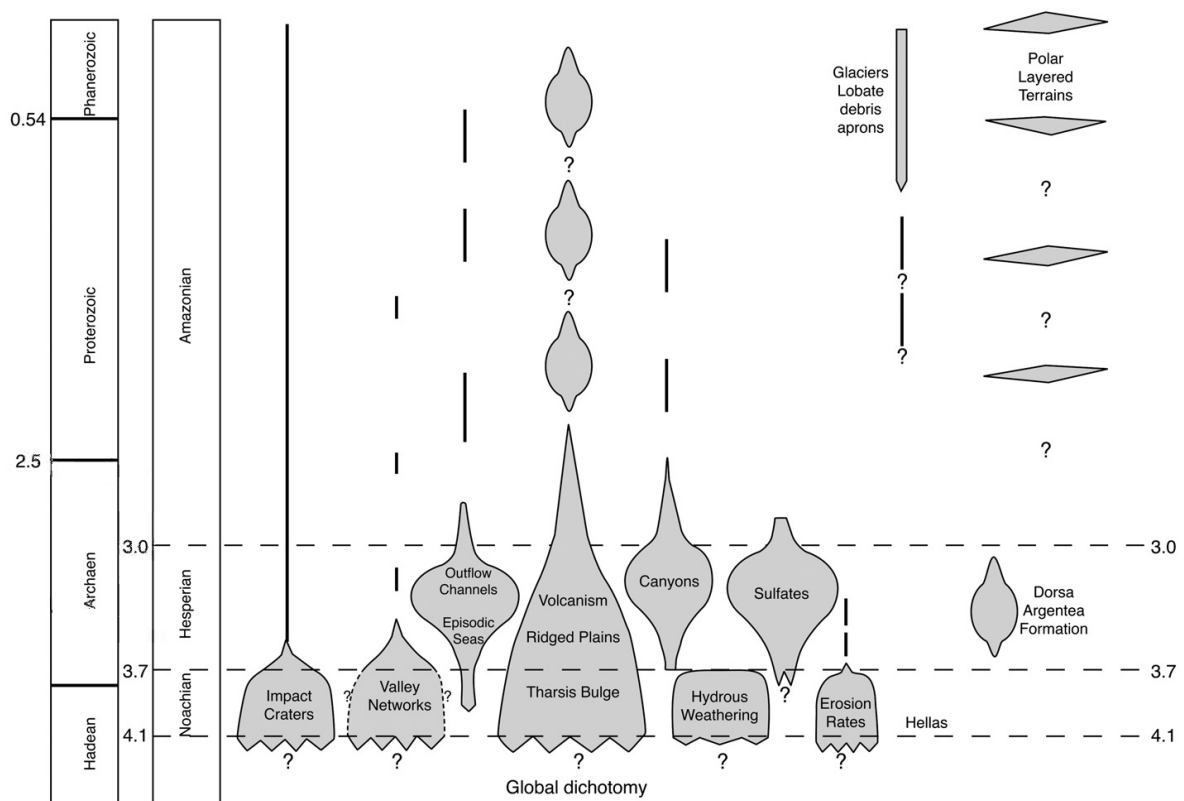
Unlike the Moon, Mars’ surface is not only shaped by planetary external factors, as impact cratering processes. The martian surface displays its interaction with the atmosphere (e.g., aeolian, polar), the hydrosphere (e.g., fluvial, lacustrine), the cryosphere (e.g., glacial and periglacial), and the planet interior (e.g., tectonism and volcanism). Also, those geological processes vary significantly in relative importance in space and time. The cratering flux in the terrestrial planets was larger during the beginning of the Solar System history, with a peak occurred 4.1 to 3.8 Ga ago, known as the Late Heavy Bombardment (LHB). The volcanic activity reflects the thermal evolution of the planet. And other features, as the layered ice caps, record different atmospheric cycles.

The stratigraphic record of a planet represents the products or deposits of these geological processes and how they are arranged relative to one another. Accordingly, the geological history of a planet can be reconstructed from understanding the details of its stratigraphic records studied from orbit observations since the late 1990s [Tanaka *et al.*, 2014]. Delineation of time periods by surface crater density statistics establishes a temporal framework for determining surface age and time-ordering Mars history into Noachian, Hesperian, and Amazonian epochs [Michael, 2013].

**Table 1.1.a** Martian epoch boundary ages calculated with Hartmann 2004 iteration chronology system [Hartmann, 2005] and the Neukum chronology system [Hartmann and Neukum, 2001a; Ivanov, 2001] based on a cumulative chronology function [Source: Michael, 2013].

EPOCH	BOUNDARIES (Ga)	
	Hartmann	Neukum
Early	3.94	3.96
Middle		
Late		
	<b>Noachian</b>	
Early	3.71	3.56
Middle		
Late		
	<b>Hesperian</b>	
Early	3.37	3.24
Middle		
Late		
	<b>Amazonian</b>	
Early	1.23	1.03
Middle		
Late		
Early	0.33	0.27
Middle		
Late		

Mars differentiated into crust, mantle, and core within a few tens of millions of years of the Solar System formation. By 4 Ga ago, more than 70 % of the crust would have accumulated. Most of the geologic record before then has been erased by subsequent erosion and high impact rates, with basin-forming impact events [Carr and Head, 2010]. The formation of Hellas, a > 2,000 km circular impact basin in the southern hemisphere, is then considered as the base of the Noachian [Frey, 2003]. However, older pre-Noachian geologic events are still recorded on the martian surface, as those evident depressions which have no structural representation in visual imagery, named as Quasi-Circular Depressions (QCDs) [Frey et al., 2002]. Also, the formation of the global dichotomy is believed to have occurred before the Noachian (Figure 1.1.c), in the earliest stages of the planet evolution [e.g., Frey, 2004; Andrews-Hanna et al., 2008]. Presumably warmer, surface conditions between large impact events are all unknown.



**Figure 1.1.c** Geologic processes and various features evolution on Mars, compared to similar major time subdivisions in Earth history [Source: Carr and Head, 2010].

The Noachian period is characterized by high rates of cratering, erosion, and valley formation (Figure 1.1.c). The impacts caused hydrothermal and mechanical alteration of the materials around the impact sites and their ejecta, increasing their porosity, and thereby affecting groundwater dynamics and facilitating their aeolian and fluvial erosion [e.g., Carr and Head, 2010]. Moreover, most of the volcanic activity that led to the Tharsis rise take place during this period [Phillips et al., 2001], enabling the formation of channels and a widespread production of weathering products, such as phyllosilicates [Ehlmann et al., 2011].

Almost at the same time than the transition between the Hadean and Archean on Earth, a major change occurred on Mars that marked the beginning of the Hesperian period (Figure 1.1.c). The volcanic activity continued, but episodically, forming extensive lava plains that characterize most of the Hesperian surfaces. The records also indicate lower valley formation rates compared with the Noachian, becoming the large outflow channels and their terminal lakes prevalent. That is intimately related to the lower rock alteration rates found, and weathering caused by saline and acidic surface and near-surface waters conditions formed sulfate-rich local deposits [e.g., Bibring et al., 2006].

The pace of geologic activity slowed, and the impact, volcanic, and weathering rates decreased through the years until the current Mars cold, dry, and oxidizing environment, characteristic from the Amazonian epoch (Figure 1.1.c). The surficial processes involving ice and wind are more evident than for earlier eras, as obliquity variations driven processes (see Part 1.1.2). Gullies are by far the most common fluvial-like features, and there is evidence of episodic wetter climatic conditions that allowed for intermittent ice and water processes [Rodriguez et al., 2015; and references therein]. However, a recent study claims that those morphologies may not even be carved by water-driven processes [Núñez et al., 2016]. The lack of unanimous scientific understanding in processes occurring today on the martian surface highlight the difficulty of unveiling the geological record and reaching a full and unequivocal comprehension on ancient environmental activity.



## 1.2 AIM AND OBJECTIVES

The main aspiration of this doctoral dissertation is to constrain the potential environmental conditions on Mars during the Hesperian-Noachian transition, which took place 3.71 Ga ago (or 3.56 Ga, depending on the chronology system considered; see Part 1.1.3). A major change occurred at the end of the Noachian, which transformed the planet conditions from wet and neutral to much dryer and acidic. Mars is the most Earth-like object in the Solar System and holds a balance between active ancient global dynamics, which could be similar to the Earth' by the time, and the recent stable conditions, which allows the conservation of much older geologic records than on our planet. In addition, understanding the paleoclimate of Mars and the nature and extent of the interaction of water with crustal materials is of great importance for understanding if the planet was once habitable and supported life.

Results of this research can be used to evaluate potential future landing sites for the robotic and human exploration of Mars, but also as an opportunity for a greater understanding of climate change on Earth. There have been major climatic changes on Mars similar to those on Earth, such as variation in the hydrosphere acidification, greenhouse gasses, glacier coverage, and the ozone layer protecting against the solar radiation. Research on the environmental evolution of Mars can thus shed light on the processes that are driving short-term global changes in the geologic and atmospheric cycles of Earth.

In order achieve the previously mentioned goal the investigation focusses in two different regions of Mars **1)** that shows, by orbital data, sufficient geologic records from both the Hesperian and Noachian epoch. The ultimate goal is to understand the environments that enabled the formation of such surfaces, and ultimately identify what happened in between. The two selected areas were also chosen according to two additional criteria: **2)** the lack of previous exhaustive research, and **3)** the abundant presence of water-related signatures. The relevance of water on Mars is evident but is even more important since this document is orientated to support the candidature for a Ph.D. in Hydrology and Water Resources Management. Moreover, the candidate

was granted to conduct this research in the ‘Centro de Astrobiología’ by the Spanish National Research Council (CSIC), and the ancient aqueous systems that could have supported microbial activity are of particular interest in Astrobiology. The selected areas are therefore Ariadnes Colles and Coogoon Valles, two of the few places on Mars that show extensive Noachian and Hesperian records overlapped and evident signatures of water-related activity.

A multidisciplinary approach is necessary to achieve the main aim of this dissertation. The research requires gathering a significant diversity and volume of data available from orbital instruments provided by NASA and ESA agencies. The datasets need to be integrated into a geographic information system (GIS) that would allow interpreting the different geologic material and formations. Additionally, the surfaces must be dated, and the physical characteristic of the surface studied, to obtain a compositional and mechanical characterization of the different materials. Finally, the resulting information would require composing the most solid geologic history, to evaluate the possible factors and environments that are in agreements with the geologic records. The comparison between the two almost antipodal areas will allow differentiating global tendencies from those with local and regional extent ultimately. Accordingly, the main objectives of this research of this Ph.D. thesis are:

- 1. Review the literature:** Do a preliminary examination of the bibliography on the knowledge of the Noachian-Hesperian transition that would allow selecting the best study areas, and if those candidates have been studied before. Also, a continuous update on the new discoveries in the regions and eras is required. It also includes a methodologic review.
- 2. Create a geographic information system:** Collect all the necessary data available for both study areas to achieve the other objectives. All the records need to be selected and processed, to be overlapped validly. This information includes topography, images from different spatial and spectral resolution, previous databases, among others. The GIS software needs to include all the tools to perform the right analyses.
- 3. Develop geologic maps:** Delimitate the different geologic units and features according to the planetary science standards using the developed GIS. The result must be a clear layout and the equivalent to a map pamphlet, with the description of the different type areas and features.

4. **Date the study areas:** Provide a general CSFD for both study areas, and, when possible, the different geologic units and features. It requires to select the most suitable surfaces (enough size, representative, uniform) and to draw the observable impact crater rims for the results to be solid enough, differentiating them from other similar features and secondary impact craters. Analyze the CSFD, providing approximate formation ages and distinguishing the major resurfacing events.
5. **Perform remote sensing analyses:** Analyze the hyper- and multi-spectral images to obtain additional information of the surface materials. Get the spatial extension of the outcrops and their spectral signature, which will be compared with spectral library samples.
6. **Study the surface temperatures:** Process the infrared records to obtain surface temperatures and thermal inertia, and their temporal and spatial distribution. Interpret the observed thermal inertia values, both qualitative and quantitative, and their geologic implication.
7. **Analyze the Ariadnes knob field morphologically:** Delimitate the knobs extension in Ariadnes (and Caralis) to improve the cartography and to allow a better constraint of their possible origin by morphometric and topographic distribution studies.
8. **Evaluate the geology history of both study areas:** Analyze superposition, embayment, and cross-cutting relations and perform cross sections of the areas. Develop the possible stratigraphic sequence comparing the dating results and the previous analyses. Propose a reasonable timeline that could have led into the observed characteristics.
9. **Do field work in known martian analogs:** Visit some martian analogs to understand better the landforms, processes, and morphologies in situ. Compare the observed characteristic in the field with their signal from orbital data. Apply the observations to the orbital data obtained from Mars.
10. **Discuss different genetic hypotheses for geologic features of particular interest:** Review of the previous formation possibilities that have been published about those features and similar ones. Evaluate the implication of the different alternatives and how they fit the observed characteristics.
11. **Discuss the possible environment during the Noachian-Hesperian transition:** Use all the previous results to assess the environmental characteristics before and after the epoch boundary. Compare both regions to infer possible global environmental conditions.
12. **Assess the study areas as possible future landing sites:** Compare the engineering constraints of present and future missions with the characteristics found in the survey areas. Discuss their scientific interest as potential landing sites.

### 1.3 THESIS STRUCTURE

This document is organized into three main divisions (**Table 1.3.a**). A (I) presentation that comprehends a brief review on the topic and explains the dissertation scope, structure, and methodology (Chapters 1 and 4); the (II) results obtained for the two different study, including their independent geologic interpretation (Chapters 3 and 4); and the (III) analysis of the obtained results, comparing both results among them and with the current knowledge, that will ultimately allow reaching the final conclusions (Chapters 5 and 6). Each chapter is divided into subchapters (e.g., 1.1), and each subchapter may include different parts (e.g., 1.1.1), and subparts (e.g., 1.1.1.i). Figures and tables are listed separately, using a letter and referring to their respective subchapters (e.g., Figure 1.1.a and Table 1.1.a).

**Table 1.3.a** Schematic summary table of the structure of this dissertation, showing the divisions, chapters, and main subchapters. For a complete index (excluding the subparts), see the Table of Contents on page 15.

DIVISION	CHAPTER	SUBCHAPTER	PART	SUBPART	
<b>I. Presentation</b>	1. Introduction	1.1. Mars research	1.1.1. Evol.		
			1.1.2. Mars		
			...		
			1.2. Geologic history		
			...		
	2. Methodology	2.1. Data	2.1.1. Sources		
			2.1.2. Dataset		i. MOLA ii. CTX ...
			...		
			2.2. Methods		
			2.2.1. Procc.		...
		2.2.2. Cartog.		...	
		...			
<b>II. Results</b>	3. Ariadnes	3.1. Introduction			
		3.2. Cartography			
		...			
	4. Coogoon	4.1. Introduction			
		4.2. Cartography			
		...			
<b>III. Analysis</b>	5. Discussion	5.1. Analogs			
		5.2. Genetic hypothesis			
		...			
	6. Conclusions				
<b>Appendices</b>					

The results are divided by location into two different chapters. Each of them is equally divided in six subchapters (Table 1.3.a). The first include an introduction to the previous knowledge of each region (geological and geographical) introducing the study area location and summarizing the objectives of the research in the area. The second subchapter describes the developed geologic map, explaining the different units and features represented on it. The third subchapter includes the dating results from crater counting, going from the selection of the dating areas to the age assignation for each unit and resurfacing events. The subchapter number three shows the remote sensing results obtained from different datasets, and their interpretation, while the number five include the performed physical surveys. The sixth subchapter of the results involves the integration of all the information for each area.

The discussion chapter begins with a brief introduction to the different terrestrial analogs studied, necessary to interpret the orbital data. The second subchapter includes the evaluation of the possible origin of the most interesting geological characteristics found in both areas, comparing the results with the bibliography and between areas. The subchapter number three assess the implication of the geologic record found to the Noachian-Hesperian epoch transition, both regionally and globally. A final subchapter of the discussion, the number four, include the potential of the studied areas as possible candidates for future missions to Mars, both from an engineering and scientific perspective. The last chapter summarizes the conclusions of this Ph.D. dissertation.



## 2 METHODOLOGY

### 2.1 DATA

#### 2.1.1 DATA SOURCES

During the last 10 – 15 years, the amount of data recovered from the martian surface has exponentially increased. The earliest images of Mars were obtained by the NASA Mariner-4 in 1965 and the latter Mariner-6 and Mariner-7 in fly-by missions [Carr, 2007; and references therein]. The first successful Mars orbiter (so the first operative artificial device orbiting another planet than the Earth) was the Mariner-9, launched in 1971. It provided about 6,000 images, compared to the less than 300 obtained in previous missions. This milestone was broadly overcome through the over 50,000 images acquired by the 1975 twin Viking orbiters. The post-Viking datasets have displayed an exponential increase in quality and diversity [Bibring *et al.*, 2005; Jaumann *et al.*, 2007; Malin *et al.*, 2007; McEwen *et al.*, 2007; Murchie *et al.*, 2009], and today the amount of available public data is more than ever, increasing continuously, as I write these lines.

The information from the Mars surface and atmosphere is collected from numerous instruments onboard orbiters (spacecraft or satellites orbiting the planet), landers (motionless platforms), and rovers (vehicles). Their development is paid with public funds, so National Aeronautics and Space Administration's (NASA) and European Space Agency's (ESA) policies obliged to make the space instruments data public and accessible. So, it is digitally stored and available from dedicated servers in standard formats in order to ensure the data integrity for future years. Thanks to the work of data producers, data providers, and independent data users, the acquisition and processing of those records by the scientific community are becoming easier each day, enabling to transform the data into valuable information on Mars surface. A compilation of the main data sources of Mars data can be found in [Table 2.1.a](#).

**Table 2.1.a** List of internet addresses used as the source of data, information and tools employed in this research. Central column indicates the hosting organizations.

DATABASES		
Planetary Data System (PDS)	NASA	<a href="https://pds.jpl.nasa.gov/">https://pds.jpl.nasa.gov/</a>
Planetary Science Archive	ESA	<a href="https://www.cosmos.esa.int/web/psa/">https://www.cosmos.esa.int/web/psa/</a>
PDS Mars Orbital Data Explorer	NASA	<a href="http://ode.rsl.wustl.edu/mars/">http://ode.rsl.wustl.edu/mars/</a>
MISSIONS AND INSTRUMENTS		
Mars Exploration Program	NASA	<a href="http://marsprogram.jpl.nasa.gov/">http://marsprogram.jpl.nasa.gov/</a>
Robotic exploration of Mars	ESA	<a href="http://exploration.esa.int/mars/">http://exploration.esa.int/mars/</a>
MOLA <i>MEGDRs</i>	NASA	<a href="http://pds-geosciences.wustl.edu/missions/mgs/megdr.html">http://pds-geosciences.wustl.edu/missions/mgs/megdr.html</a>
HiRISE	Lunar and Planetary Laboratory	<a href="http://hirise.lpl.arizona.edu/">http://hirise.lpl.arizona.edu/</a>
HRSC	Free University of Berlin	<a href="http://hrscview.fu-berlin.de/">http://hrscview.fu-berlin.de/</a>
THEMIS	Arizona State University	<a href="http://themis.asu.edu/">http://themis.asu.edu/</a>
CRISM	NASA	<a href="http://crism.jhuapl.edu/">http://crism.jhuapl.edu/</a>
OTHERS		
<i>Isis</i> Support	NASA	<a href="https://isis.astrogeology.usgs.gov/IsisSupport/">https://isis.astrogeology.usgs.gov/IsisSupport/</a>
Astrogeology Science Center	USGS	<a href="https://astrogeology.usgs.gov/">https://astrogeology.usgs.gov/</a>
PIGWAD	USGS	<a href="https://webgis.wr.usgs.gov/pigwad/download/mars_dl.htm">https://webgis.wr.usgs.gov/pigwad/download/mars_dl.htm</a>
PDS Geosciences Spectral Library	NASA	<a href="http://speclib.rsl.wustl.edu/">http://speclib.rsl.wustl.edu/</a>
Reflectance Experiment Laboratory (RELAB)	Keck Observatory / NASA	<a href="http://www.planetary.brown.edu/relab/">http://www.planetary.brown.edu/relab/</a>
BIBLIOGRAPHY		
The Astrophysics Data System	NASA	<a href="http://adsabs.harvard.edu/">http://adsabs.harvard.edu/</a>
Lunar and Planetary Institute	USRA	<a href="http://www.lpi.usra.edu/resources/">http://www.lpi.usra.edu/resources/</a>
TOOLS		
THEMIS Processing Web Interface	Arizona State University	<a href="http://thmproc.mars.asu.edu/">http://thmproc.mars.asu.edu/</a>
<i>Craterstats</i> and <i>CraterTools</i>	Free University of Berlin	<a href="http://www.geo.fu-berlin.de/en/geol/fachrichtungen/planet/software/">http://www.geo.fu-berlin.de/en/geol/fachrichtungen/planet/software/</a>
<i>CRISM Analysis Tool</i> (CAT)	Brown University	<a href="http://www.planetary.brown.edu/html_pages/software_crism.htm">http://www.planetary.brown.edu/html_pages/software_crism.htm</a>



## 2.1.2 INSTRUMENTS AND DATASETS

### i. *Mars Orbiter Laser Altimeter (MOLA)*

The Mars Orbiter Laser Altimeter (MOLA) [Zuber *et al.*, 1992; Smith *et al.*, 2001] was an instrument onboard NASA's Mars Global Surveyor (MGS) spacecraft [Albee *et al.*, 2001] that acquired data from 1997 to 2006. The MOLA consisted of an altimeter that transmitted infrared laser pulses at a frequency of 10 Hz toward Mars' surface to recover a topographic dataset. This data has been used to generate topographic maps of the whole planet. Topography on Mars is described as the planetary radius minus the areoid radius at a given longitude and latitude.

The MOLA data products used in this research are individual altimetry readings organized along the spacecraft orbit track (*Precision Experiment Data Records*, PEDR) and GIS-ready digital elevation models (*Mission Experiment Gridded Data Records*, MEGDR) of 128 pixels per degree [Smith *et al.*, 2003], which is equivalent to a maximum of 463 meters per pixel at the martian equator (Table 2.1.b).

The MEGDR are created and provided by the USGS by binning altimetry values from the PEDR products acquired over the entire MGS mission, adjusted for consistency [Neumann *et al.*, 2001; Neumann, 2003] and converted to the planetary radius. The vertical precision of individual elevations approaches 37 cm, and the average accuracy of each point is originally ~100 meters in horizontal position and ~1 meter in radius [Neumann *et al.*, 2001] (Table 2.1.b). However, the total elevation uncertainty is at least  $\pm 3$  meters due to the global error in the areoid and regional uncertainties in its shape ( $\pm 1.8$  meter according to Lemoine *et al.* [2001]). The data is very sparse near the two poles because these areas were sampled by only a few off-nadir altimetry tracks. Gaps between tracks of 1 – 2 km are common, and some gaps of up to 12 km occur near the equator. The digital elevation model (DEM) points located in these gaps in MOLA data were filled by interpolation. None of the studied areas in this thesis is near the poles, therefore, to obtain more accurate results we used PEDR products to perform cross sections or determine punctual elevations, since those are the most accurate elevation values available.

ii. *Context Camera (CTX)*

The Context Camera (CTX) [Malin *et al.*, 2007] is an instrument onboard NASA's Mars Reconnaissance Orbiter (MRO) spacecraft that has been in a nearly circular and polar orbit of Mars since 2006. The CTX consists of a digital camera designed to provide the spatial context for the other MRO instruments, using a charge coupled device (CCD) with a band pass of 0.5 – 0.7  $\mu\text{m}$  (Table 2.1.b). The camera obtains panchromatic images of the surface of Mars with a resolution of about 6 meters per pixel and a swath width of about 30 to 40 kilometers from an altitude of about 290 kilometers [Malin *et al.*, 2007]. Since its orbit insertion, the CTX has obtained images that cover over 90 % of the Mars' surface by the end of the year 2015. Some of the images repeat coverage with roll angles up to  $\pm 30^\circ$ , and can be considered 'valid' stereo pairs (Table 2.1.b) and usable to obtain DEMs through photogrammetric processing [Shean *et al.*, 2011].

This extensive coverage of CTX products in combination with their medium to high spatial resolution makes this dataset highly suitable for regional studies. However, not general mosaics are available and generate seamless mosaics with CTX can be tricky. For large areas, illumination conditions and calibration differences between images usually results in hard edges between images. There is not a public release of derived DEMs or an official list of possible stereo pairs, which anyhow will cover a relatively small area for regional studies.

iii. *High Resolution Imaging Science Experiment (HiRISE)*

The High Resolution Imaging Science Experiment (HiRISE) [McEwen *et al.*, 2007] is the high-resolution camera onboard the MRO spacecraft designed to complement the CTX images. The HiRISE camera contains a total of 14 CCD arrays, each of which operates as a 2048-pixel-wide line detector and produces images in the red part of the spectrum (0.55 – 0.85  $\mu\text{m}$ ) in a swath 6 kilometers wide, and in the blue-green region (0.40 – 0.60  $\mu\text{m}$ ) and the infrared region (0.80 – 1.00  $\mu\text{m}$ ) in a 1.2 km wide nested center image. The result are the most detailed images acquired from Mars orbit to date (and from other planetary body than the Earth), with 0.25 to 1.3 meters per pixel in ground resolution [McEwen *et al.*, 2007] (Table 2.1.b). Due to

overlapping (tilted) orbits, stereo pair images can be obtained and generate geodetically controlled DEMs (Table 2.1.b).

Despite the high spatial resolution of the HiRISE images, the coverage is very limited, especially for the stereo pairs. The images usually only record the most promising targets, as water-related features and impact craters than can provide information from the materials underneath. The high-resolution also allows the gathering of valuable information, as unit textures, studying features in detail and mapping at large scale (i.e., localized exhumation). Only a small fraction of the studied areas was covered by the time of this dissertation elaboration, and there was not any available derived DEMs.

#### iv. *High Resolution Stereo Camera (HRSC)*

The ESA's mission Mars Express (MEx), orbiting Mars since December 2003, is equipped with the High Resolution Stereo Camera (HRSC) [Neukum *et al.*, 2004; Jaumann *et al.*, 2007]. This stereo camera provides up to 5 panchromatic (0.59 – 0.77  $\mu\text{m}$ ) multi-angle ( $\pm 18.9^\circ$ ) observations during a single orbital pass. Additionally, by the use of 4 CCD lines equipped with spectral filters, it acquires visible/near-infrared (VNIR) images (centered from 0.44 to 0.95  $\mu\text{m}$ ) at the same time (Table 2.1.b). The HRSC is hereafter a multi-sensor that allows near-simultaneous color and high-resolution stereo imaging data during a single overpass [Gwinner *et al.*, 2016; and references therein].

The total coverage of available images exceeds today the 90 % of the global surface. But, despite the large size of the images, HRSC is influenced by the special highly elliptical MEx's orbit. Due to that, the images have a continually changing illumination angle and low repetition rate. Additionally, the images' surface width (and resolution) is strongly dependent on the spacecraft's variable altitude. As a consequence, the image strips still show varying brightness even after radiometric calibration, which is caused by differing illumination and atmospheric conditions and a systematically applicable procedure remains elusive [Michael *et al.*, 2016].

The topographic coverage is more limited than for panchromatic products, but the capability to obtain a DEM linked to an image and their accurate match, allow an exceptional image-topography dataset set to work in regional studies. The swath width of a typical HRSC image is ~60 km, and the average spatial resolution of HRSC images is commonly between 10 and 20 meters per pixel for the panchromatic nadir channel at the nominal periapsis altitude of 250 km (Table 2.1.b). However, the highly elliptical orbit of MEx induces changes in the ground resolution and swath width. The sub-pixel accuracy of the three-dimensional point determination allows the derivation of DEMs with a typical grid cell size of 50 to 100 m and height (vertical) accuracy of ~10 m in each pixel [Scholten *et al.*, 2005; Jaumann *et al.*, 2007].

v. *Thermal Emission Spectrometer (THEMIS)*

THEMIS sensor (Thermal Emission Imaging System) is an instrument onboard of the Mars Odyssey (ODY) spacecraft, which arrived at Mars in 2001. The THEMIS camera acquires multi-spectral thermal-infrared images in nine wavelengths (centered from 6.8 to 14.9  $\mu\text{m}$ ) and visible/near-infrared images in five bands (centered from 0.42 to 0.86  $\mu\text{m}$ ) [Christensen *et al.*, 2004] (Table 2.1.b). These wavelengths were especially selected to study surface mineralogy and physical properties of Mars since infrared imagery allows distinguishing physical surface characteristics better than images taken at visible light wavelengths. THEMIS also has an extensive coverage of the Mars surface (about 90 %).

With 100 m/pixel sampling and an image width of approximately 32 km, THEMIS day and night multi-spectral infrared images have 100 meters per pixel, and one-band visible images have 18 meters per pixel [Christensen *et al.*, 2004] (Table 2.1.b). For this research, we used three different types of data products. Two GIS-ready IR mosaics (day and nighttime) [Edwards *et al.*, 2011] and two other THEMIS-derived global thermal inertia (TI) mosaics (qualitative and quantitative) provided support for the geologic mapping. Thermophysical variations often correspond to features identified in high-resolution images, and the integration of these data sets allows more robust scientific conclusions to be reached. Moreover, *Brightness Temperature Records* (BTR), an especially calibrated product derived from the Band

9 (12.57  $\mu\text{m}$ ), were processed to obtain derived surface temperatures [Ferguson *et al.*, 2006a]. Finally, the *DeCorrelation Stretch images* (DCS) processing maximizes the differences between bands to highlight the compositional information [e.g., Hamilton *et al.*, 2007; Osterloo *et al.*, 2008], supplying additional remote sensing information on the studied surfaces.

In the quantitative TI mosaic, the apparent values are unmodified during the mosaicking process. However, despite the fact that TI is independent of season and local time, substantial differences can still be prominent in this derived product due to many factors affecting the measured surface temperatures. The main factors are calibration uncertainties in the instrument (random error standard deviation between images of  $\sim 4$  K at 180 K [Christensen *et al.*, 2004], which corresponds to errors of  $50 - 120 \text{ J}\cdot\text{m}^{-2}\cdot\text{K}^{-1}\cdot\text{s}^{-1/2}$ ), transient atmospheric phenomena (such uncorrected water-ice clouds), surface slopes not taken into account, and the presence of ice in the shallow subsurface [Putzig and Mellon, 2007; Bandfield and Feldman, 2008]. All these uncertainties led to an absolute accuracy for the THEMIS thermal inertia of  $\sim 20$  %, that doubles when the measures are within the same image ( $\sim 10$  %) [Ferguson *et al.*, 2006b]. As the warmer the temperatures, the highest the data quality (highest signal to noise ratio), the warmest season available is always on top in these mosaics.

The individual images and tiles have been stretched and blended in the IR mosaics and normalized in the qualitative global TI mosaic. This qualitative product is particularly useful in geologic mapping, where a seamless product is needed to differentiate unit boundaries, textures, and morphologic features.

#### vi. *Compact Reconnaissance Imaging Spectrometer for Mars (CRISM)*

The Compact Reconnaissance Imaging Spectrometer for Mars (CRISM) is a visible/near-infrared imager on the MRO spacecraft. It acquires  $10 \text{ km} \times 10 \text{ km}$  images that cover the wavelength range between  $0.36 - 3.92 \mu\text{m}$  in 544 spectral channels at a spectral resolution of  $6.5 \cdot 10^{-4} \mu\text{m}$  per channel. The data is recorded by two distinct detectors, the S-detector in the range of  $0.39 - 1.02 \mu\text{m}$ , and the L detector in the range of  $1.02 - 3.92 \mu\text{m}$  wavelength (Table 2.1.b). Those bands were selected with the

objective of characterize crustal mineralogy, map the mineralogy of key areas at high spectral and spatial resolution, and measure spatial and seasonal variations in the atmosphere. This high-resolution hyperspectral mapping allows searching for evidence of aqueous and/or hydrothermal activity, and to map and characterize the mineralogy, geology, and stratigraphy of surface deposits.

The CRISM hyperspectral data is acquired in several modes, and the spatial resolution varies with them. For example, *Full Resolution Targeted* (FRT) data products have 18 meters per pixel and *Half Resolution Long Targeted* (HRL) data products only 36 meters per pixel [Murchie et al., 2007] (Table 2.1.b). We only used FRT the data, and in the range of 1.0 – 2.6  $\mu\text{m}$ , as it is the range where absorption bands of the material of interest usually occur. The CRISM data is available as hyperspectral data cubes, that comprises the different spectral bands combined to form a three-dimensional [x, y,  $\lambda$ ] product, where x and y represent two spatial dimensions and  $\lambda$  represents the spectral dimension.

**Table 2.1.b** Remote-sensing space-borne imaging and altimetry data instruments used in this dissertation and their main characteristics (A = Altimeter, MC = Multi-spectral camera, HC = Hyper-spectral camera).

INSTRUMENT MISSION	TYPE	SPECTRAL RANGE ( $\mu\text{m}$ )	RESOLUTION		DEM		
			Spatial ( $\text{m}/\text{pixel}$ )	Radiom. ( $\text{bit}$ )	AQCUISITION	PRECISION ( $\text{m}$ )	
<b>MOLA</b>	MGS	A	-	<b>Equator:</b> 463 <b>Polar:</b> 116	-	LIDAR	<b>H:</b> ~100 <b>V:</b> $\pm 1.8$
<b>CTX</b>	MRO	MC*	0.5 – 0.8	5.0 – 6.5 <b>DEM:</b> 12 – 18	12 – 13	Stereo	Uncertain
<b>HiRISE</b>	MRO	MC	0.4 – 1.0	0.25 – 1.30 <b>DEM:</b> ~1.5	12 – 13	Stereo	<b>H:</b> ~100 <b>V:</b> ~0.2
<b>HRSC</b>	MEx	MC	<b>Pan:</b> 0.59 – 0.77 <b>VNIR:</b> 0.44 – 0.95	2.3 – 10.0 <b>DEM:</b> >50	8	Stereo	<b>H:</b> 50 – 200 <b>V:</b> 50 – 200
<b>THEMIS</b>	ODY	MC	<b>VIS:</b> 0.425 – 0.860 <b>IR:</b> 6.78 – 14.88	<b>VIS:</b> 18.0 <b>IR:</b> ~100	8	-	-
<b>CRISM</b>	MRO	HC	<b>S:</b> 0.39 – 1.02; <b>L:</b> 1.02 – 3.92	<b>FRT:</b> 18 <b>HRL:</b> 36	-	-	-

\* Only one panchromatic band.

### 2.1.3 DATABASES

#### i. *Global geologic maps*

A decade after the successful Viking missions, the USGS released two geologic maps of the western and eastern equatorial region of Mars [Scott and Tanaka, 1986; Greeley and Guest, 1987] summarizing the knowledge of the martian surface gained by the time. These two products complement each other in the first global geological map ever made from another planet than the Earth in such detail, and were used as a framework for most of the subsequent works on the geology of Mars. Over the years, the increase in the amount and quality of data allowed the elaboration of more detailed maps of restricted areas of the planet [e.g., Kuzmin *et al.*, 2000; Tanaka *et al.*, 2005; de Pablo and Carrillo, 2012]. During the elaboration of this dissertation, the USGS released a new global geologic map of Mars, in only one map sheet this time [Tanaka *et al.*, 2014]. This cartography records the distribution of geologic units and landforms on Mars' surface through time, updating the previous findings following a similar procedure that it is followed in this thesis.

Although the regional geologic framework for this dissertation was provided initially from the early version(s) of this geologic map [Molina *et al.*, 2012, 2013b]; the current research uses this recent geologic map instead [e.g., Molina *et al.*, 2017]. The map layers are public available online (<https://pubs.usgs.gov/sim/3292/>) and were integrated into the GIS, allowing to produce two specially adapted figures, one for each study region (Figure 3.1.c and Figure 4.1.c).

#### ii. *Crater and channel databases*

For regional scale visualization and analysis of channels and impact craters, we have used the features that were previously cataloged by other authors and included into global databases. Those are compiled and made GIS-ready for the planetary community, becoming a very valuable input for any martian spatial-related research.

Two impact crater databases for Mars were used in this dissertation. The *Robbins Crater Database* [Robbins and Hynek, 2012] is available through the USGS's *Planetary Interactive G.I.S.-on-the-Web Analyzable Database* (PIGWAD, Table 2.1.a).



It contains 384,343 craters with diameters up to one kilometer with detailed information about their position, modification state, and interior and ejecta morphologies. The craters were mapped manually using THEMIS Daytime IR planet-wide mosaics and MOLA topographic maps (Part 2.1.2) to identify craters that may have a distinct visual signature. Most basins (such as Hellas or Utopia) or quasi-circular depressions (QCDs) were not included due to their ambiguous rims.

We also considered the *MA132843GT impact crater catalog* that includes the 57,633 craters from previous manually assembled catalogs [Salamunićcar and Lončarić, 2008] and 72,668 additional craters identified using several crater detection algorithms (CDAs) with MOLA and optical images [Salamunićcar et al., 2012]. This dataset is available from the Astrogeology Science Center web page (Table 2.1.a) ([https://astrogeology.usgs.gov/search/map/Mars/Research/Craters/GoranSalamuniccar\\_MarsCraters](https://astrogeology.usgs.gov/search/map/Mars/Research/Craters/GoranSalamuniccar_MarsCraters)). While this database was used in the regional maps Figure 3.1.b and Figure 4.1.b, the *Robbins Crater Database* [Robbins and Hynek, 2012] was used for the CSFD in the full area of Coogoon Valles (Subchapter 4.3). The other CSFDs included in this dissertation use craters that were mapped manually by the author as described in Subpart 2.2.4ii.

For channels in the regional maps (Figure 3.1.b and Figure 4.1.b), we used the database described in Hynek et al. [2010], where the features were manually mapped as vector-based polylines identified using THEMIS daytime IR, MOC wide angle, and Viking images, and the topographic data from MOLA. This dataset includes the topographic troughs that had a visual indication of valleys formed by fluvial processes.

### iii. *Spectral Libraries*

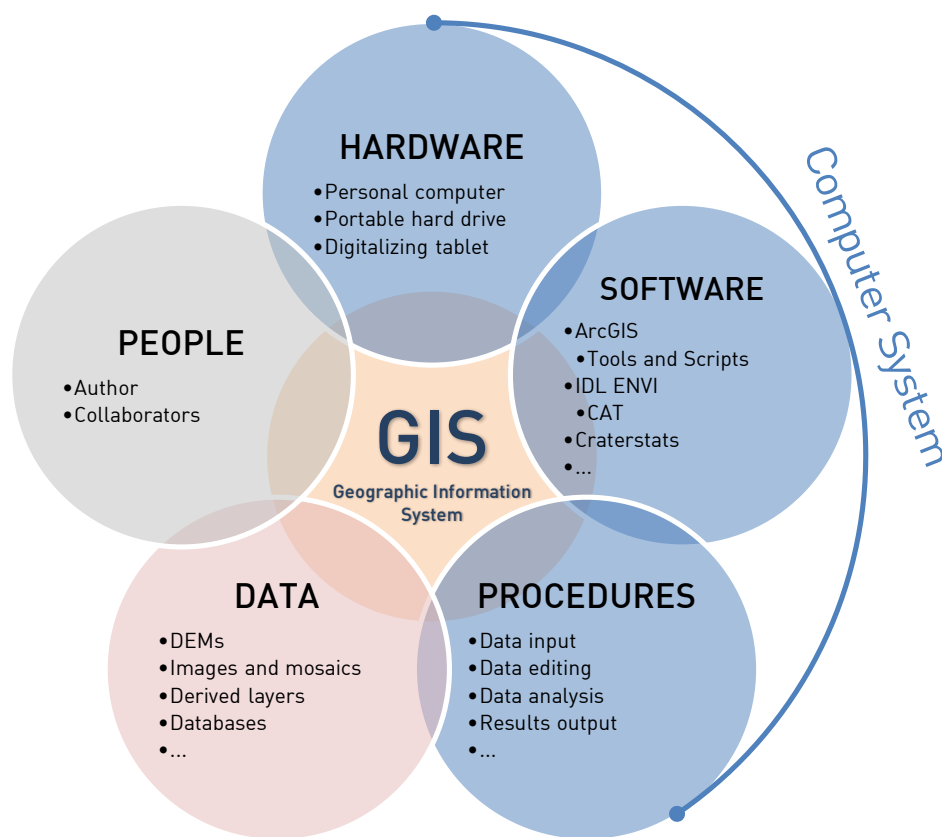
The comparison of spectral signatures obtained from hyperspectral remote sensing (see Subpart 2.2.4iii) with the obtained from laboratory samples allows to distinguishing different minerals and materials [e.g., Gaffey, 1985] and even their relative elemental abundance. In this dissertation, we used the samples from the Reflectance Experiment Laboratory (RELAB) (Table 2.1.a) library and other publications (see Appendix 8.1).



## 2.2 METHODS

### 2.2.1 DATA MANAGEMENT

The geographic component is substantially predominant in this research since to achieve most of its objectives (see Subchapter 1.2) is required to identify patterns, relationships, and trends in spatial data (or that have a spatial context). The use of a GIS allows data from different sources to be integrated into the same computer platform, in other words, a GIS is a tool for manage and analysis of spatial data [e.g., Heywood *et al.*, 2006] (Figure 2.2.a).



**Figure 2.2.a** Diagram of the five components that comprises the GIS used on this dissertation.

Hence, the data was managed by a complete GIS) (Figure 2.2.a) that enable the people involved in the research organize and visualize data efficiently by integration with other data into a computer system, and in the analysis and creation of new data that can be operated on in turn [Heywood *et al.*, 2006]. In this fashion, the data (see Part 2.1.2) was selected, acquired and integrated into a GIS software. We employed *ArcGIS* (version 10 *Desktop*, by *ESRI*) to compile and merge all available data sets into

the same geographical reference, as well as to perform an integrative analysis to produce the geological mapping of the area of study. *ArcGIS* was also used to visualize and consult the data, complete some analyses, and obtain final layouts. Other software was also used, as the *IDL ENVI* (version 4.7, by *ITT Visual Information Solutions*) to perform for reading, displaying, and analyzing hyperspectral data complemented with the *CRISM Analysis Toolkit (CAT)* version 7.3.1). The software and procedures ([Figure 2.2.a](#)) have been running mainly on a personal computer (laptop *MacBook Pro*, with both *MacOS* and *WindowsOS* partitions). The hardware meets the essential requirements for running a GIS [*Burrough et al.*, 2015], with a processor with sufficient power to run the software, enough memory for the storage of large volumes of data (2 Tb external hard drive, *Lacie*), a good quality high-resolution color graphics screen, and other data input and output devices (a digitizing tablet together with the standard mouse and keyboard).

For all the layouts, the geographic coordinate system used was the standard Mars 2000 spheroid ([Table 2.2.a](#)). As projection system, the equidistant cylindrical (a.k.a., equiarectangular) with a central meridian at 180° was selected, since the Ariadnes area is between the two sides of that meridian. This projection system shows a regular grid of parallels and meridians (North is always up), that cause larger distortions the closer to the poles. Both study areas are near enough to the Equator (standard parallel) to minimize this effect and still using a unified system for both locations, but features (as craters) are still deformed. As an exception, different coordinate and projection systems from the [Table 2.2.a](#) were used for the [Figure 5.1.a](#).

**Table 2.2.a** Coordinate and projection system properties of this dissertation GIS.

<b>Geographic Coordinate System</b>	GCS Mars 2000 Sphere
<b>Datum</b>	D_Mars_2000_Sphere
<b>Prime Meridian</b>	Reference Longitude (0.0°)
<b>Central Meridian</b>	180.0°
<b>Semi-major and Semi-minor Axes</b>	3,396; 190.0
<b>Projection</b>	Equidistant Cylindrical
<b>Angular Unit</b>	Degree (0.0174532925199433)
<b>Linear unit</b>	Meter

## 2.2.2 SOFTWARE AND SCRIPTS

### i. *ArcGIS Desktop*

'ArcGIS' (from Esri, <http://desktop.arcgis.com/>) is the most popular commercial GIS, and many tools and scripts for planetary sciences are developed for it. This software was used to collect and manage the different data employed in this dissertation but also to perform spatial analysis, extract information, and create the included maps. Although the early work of this thesis was conducted with the version 9, most (if not all) the presented results in this dissertation has been obtained with the version 10 (released in 2010), which includes PDS support. Some extensions were implemented to this software to perform specific tasks, as the '*Crater Tool*' [Kneissl et al., 2015] or the '*Polar Plots and Circular Statistics*' ([http://www.jennessent.com/arcgis/Polar\\_Plots.htm](http://www.jennessent.com/arcgis/Polar_Plots.htm)).

### ii. *ENVI IDL*

The '*ENvironment for Visualizing Images*' (ENVI) software, from Exelis Visual Information Solutions, is an application used to process and analyze geospatial imagery in remote sensing. A collection of '*IDL/ENVI*' procedures, CRISM calibration data files, and miscellaneous reference data files, known as '*CRISM Analysis Toolkit*' (CAT) (available in the PDS <http://pds-geosciences.wustl.edu/missions/mro/crism.htm>) was developed by Brown University to open and display CRISM images, apply certain standard corrections, and produce summary parameters. This extension only works in old versions of '*ENVI*', so we used the 5.6 version to perform the spectral analysis included in this dissertation combined with the CAT 7.3.

### iii. *Others*

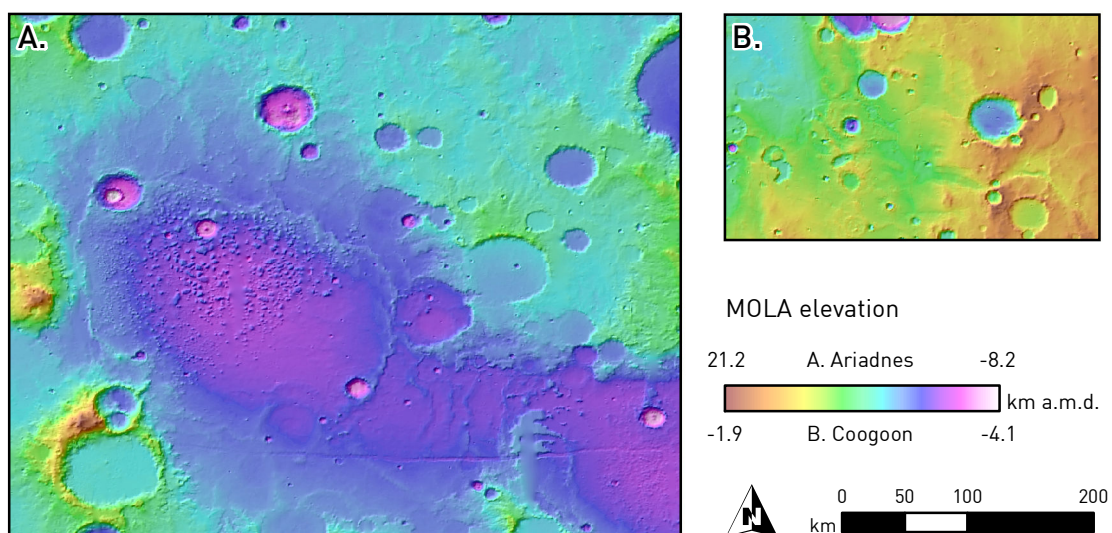
We used the '*Integrated Software for Imagers and Spectrometers*' (ISIS) software [Torson and Becker, 1997] distributed by the USGS for image processing (specially at the early stages) and '*Craterstats2*' (compiled with IDL) from the Free University of Berlin ([Table 2.1.a](#)) to perform the CSFD analyses. The delineation of the knobs was performed using '*Vextractor*', a professional software for converting raster images to vector that offers a coordinate binding system supporting ArcGIS Shapefiles (.shp). The Goldensoftware's '*Grapher*' was used as the main graphing tools, combined with Adobe '*Photoshop*' and '*Illustrator*', and the Microsoft '*Office*' productivity suite.

### 2.2.3 DATA INPUT AND EDITING

Since the beginning of this thesis research (late 2010), there have been several changes in the way to work with Mars' datasets. New data products have been available, and new software has been released during the last years. Therefore, the process to incorporate data to the GIS and to extract valuable information have become simpler and faster thanks to the work of data providers and users, who have improved public available datasets and methodologies. So, it is important to note that this part of the dissertation includes the most recent processing methods in most cases, but also outdated procedures in some others. In both instances, the described processes allow to obtain reproducible results.

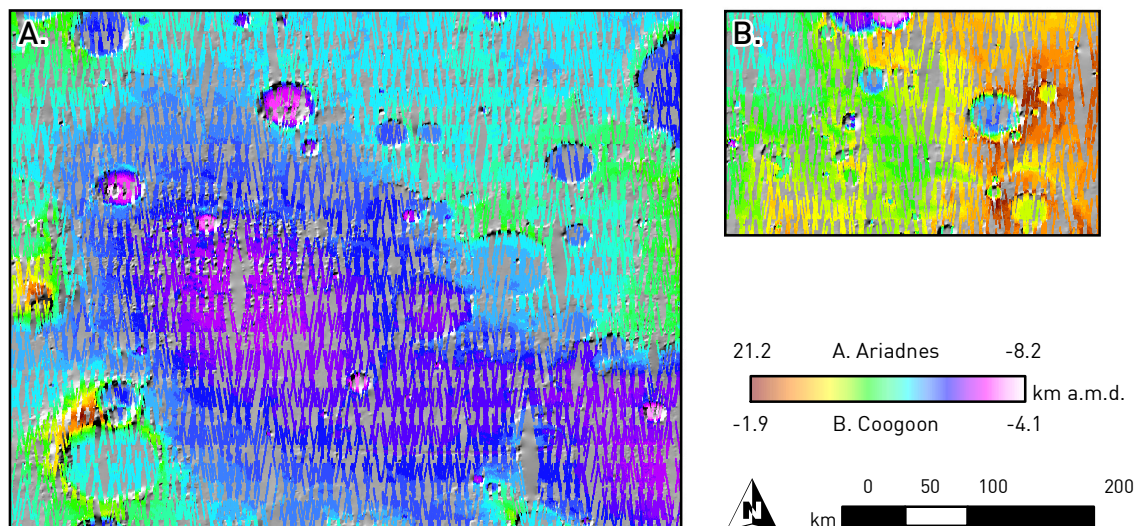
#### i. *Mars Orbiter Laser Altimeter (MOLA)*

The MOLA MEGDR topographic map of Mars (Subpart 2.1.2i, [Figure 2.2.b](#)) can be downloaded in GIS-ready format from the PDS (see Part 2.1.1) (<ftp://pdsimage2.wr.usgs.gov/pub/pigpen/mars/mola/>). Additionally, a greyscale hillshade layer is available from the Astrogeology Science Center, obtained using as input parameters 45° altitude and 315° azimuth in full resolution topographic data (see Part 2.1.1) ([https://astrogeology.usgs.gov/search/map/Mars/GlobalSurveyor/MOLA/Mars\\_MGS\\_MOLA\\_Shade\\_global\\_463m](https://astrogeology.usgs.gov/search/map/Mars/GlobalSurveyor/MOLA/Mars_MGS_MOLA_Shade_global_463m)).



**Figure 2.2.b** MOLA MEGDR data for the (A) Ariadnes and (B) Coogoon study areas. The topographic colored dataset overlaps the greyscale hillshade with a 50 % transparency.

To achieve an enhanced visualization, the stretched DEM was exported as a RGB image in 'ArcGIS' (Data > Export > Force RGB) and visualized together the hillshade as a phansharp image (Figure 3.1.a and Figure 4.1.a). Also, shapefiles with MOLA PEDR product for each area (Subpart 2.1.2i, Figure 2.2.c) were obtained from the MOLA PEDR query (<http://ode.rsl.wustl.edu/mars/dataPointSearch.aspx>).



**Figure 2.2.c** MOLA PEDR data that shows the real coverage of the topographic records for the (A) Ariadnes and (B) Coogoon study areas.

## ii. Context Camera (CTX)

By the time of Ariadnes Basin study, all the available images within that area were downloaded from the PDS (see Part 2.1.1) and processed with the 'ISIS' software. This specialized image processing package was used to perform noise removal and radiometric and geometrical corrections, as well as map projections, following the recommended procedures [USGS Astrogeology Team, 1999]. Today, there is an easier way to process this dataset, as it is explained in the ISIS support forum (<https://isis.astrogeology.usgs.gov/IsisSupport/index.php?topic=3860.0>). It is as easy as download the jpeg2000 images, the 'ISIS' headers from the Arizona State University (ASU) Data Explorer (<http://viewer.mars.asu.edu/viewer/ctx#T=0>), and run the 'ctx\_project' script, located in the same folder ([ftp://pdsimage2.wr.usgs.gov/pub/pigpen/Python/ctx\\_project.exe](ftp://pdsimage2.wr.usgs.gov/pub/pigpen/Python/ctx_project.exe)).



To include all the images in the GIS project and improve the visualization, a mosaic dataset was created for each location (Ariadnes\_CTX and Coogoon\_CTX, inside their geodatabases). After adding all the raster images, the footprints were built. To avoid the dirty edges, Minimum Data Value was set to 10 and Shrink distance to 200 meters. The boundary was delimited as the same extent as the study area (Figure 2.2.d). The coverage of this images was almost complete for both study areas.

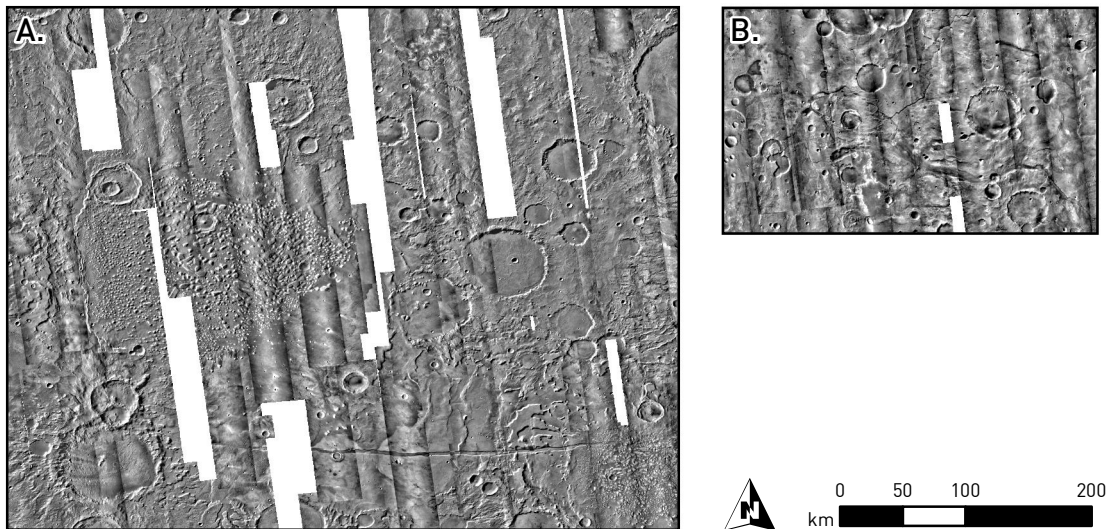


Figure 2.2.d CTX mosaics created for the (A) Ariadnes and (B) Coogoon study areas.

### iii. *High Resolution Imaging Science Experiment (HiRISE)*

HiRISE team provides these high-resolution images in jpeg2000 format with embedded projection labels. This GIS-ready product can be included directly into ArcGIS 10, but the projection in which they are georeferenced generates fitting issues (<https://isis.astrogeology.usgs.gov/IsisSupport/index.php/topic.2339.msg9393.html>). Those problems can be fixed with the use of a script that automatically generalize, clarify, and correct the images to the equirectangular projection used in this dissertation (Part 2.2.1) (<https://isis.astrogeology.usgs.gov/IsisSupport/index.php/topic.3440.msg13384.html>). No HiRISE DEM was available in any of the study areas by the time this research was performed.

In a similar way than with CTX, a mosaic dataset was created for each location (Ariadnes\_HiRISE and Coogoon\_HiRISE, inside their geodatabases). After adding all the raster images, the footprints were built. To avoid the dirty edges, Minimum Data Value was set to 10 and Shrink distance set to 200 meters. The HiRISE coverage is very

limited for both study areas (Figure 2.2.e), being available only close to the CRISM images or features of high interest, sometimes in clusters.

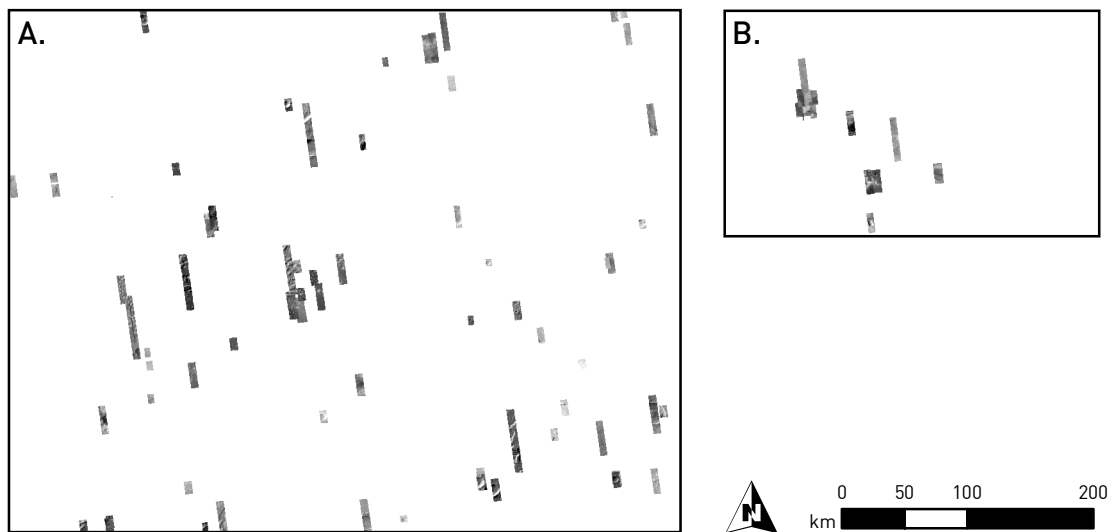


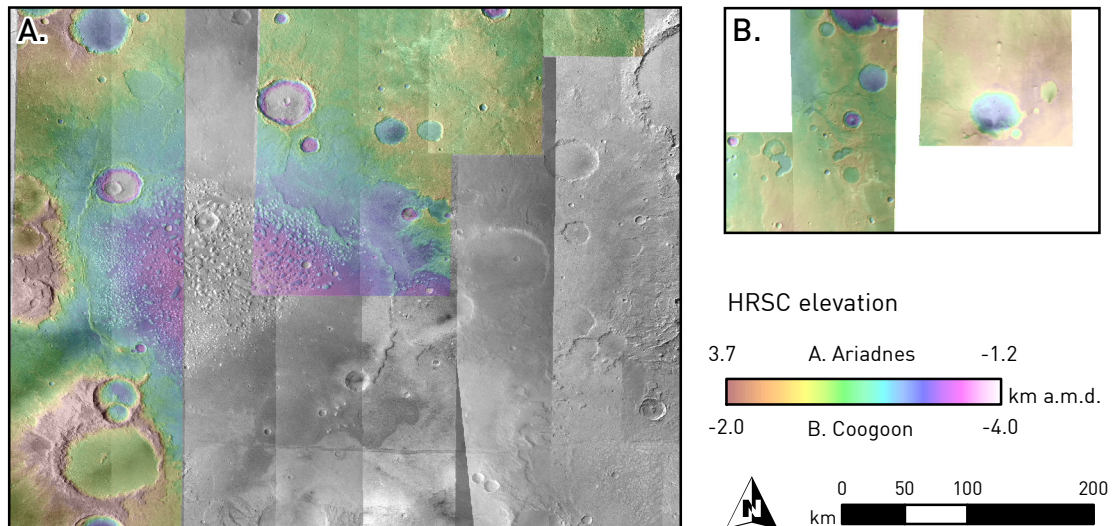
Figure 2.2.e HiRISE mosaics created for the (A) Ariadnes and (B) Coogoon study areas.

#### iv. *High Resolution Stereo Camera (HRSC)*

The georeferenced and corrected HRSC images and DEMs matching the study area were obtained from the HRSCview Free University of Berlin servers (<http://hrscview.fu-berlin.de>). The Level 4 processing include the georeferencing information that allows a direct inclusion into 'ArcGIS'. When the images were not available in that level (i.e., only in Level 3), they were processed with the ESA Mars Express HRSC data to GIS converter tool ('HRSC2GIS', <http://arcscripts.esri.com/details.asp?dbid=15566>), developed by J. Oosthoek from the Geological Survey of the Netherlands.

To include all the images into the GIS and improve the visualization, as with the previous datasets, a mosaic dataset was created for each location (Ariadnes\_HRSC and Coogoon\_HRSC, inside their geodatabases). After including all the raster images, the footprints were built. To avoid the dirty edges, Minimum Data Value was set to 10 and Shrink distance set to 200 meters. The boundary was delimited as the same extent as the study area (Figure 2.2.f). The coverage of this images was complete for Ariadnes but very lacking for Coogoon, with less than half of the study area covered. All the available images from Coogoon, however, had their correspondent DEM processed, while less than half of Ariadnes had HRSC DEM coverage.





**Figure 2.2.f** HRSC image and DEMs mosaics overlapped for the (A) Ariadnes and (B) Coogoon study areas.

v. *Thermal Emission Spectrometer (THEMIS)*

To obtain the surface temperature the highest brightness temperature value in THEMIS nighttime IR bands 3 – 9 for each pixel was used. To achieve that the images available for the study areas were selected from the PDS Mars Orbital Data Explorer and processed using the THMPROC (Table 2.1.a). The ‘*THEMIS Processing Web Interface*’, known as THMPROC, is a web-based interactive tool used for THEMIS data processing developed by the Arizona State University. For each image, we applied Signal Drift Corrections, Rectify, Correlated Noise Removal, Automated Radiance Correction, and Return to Projected Image processing. The selected projection was Simple Cylindrical, using as central meridian the 0, Planetocentric latitude, and the -180 to 180 longitude configurations. The Perl (programming language) routine ‘*ISIS2world.pl*’ (available in the PIGWAD, Table 2.1.a) extract the projection information that allow a correct integration into the GIS.

Similar processing was performed in the earliest stages of the thesis for THEMIS nighttime IR and thermal inertia data. However, for the final version, processed mosaics available from the USGS’ Astrogeology Science Center web page (Table 2.1.a) and released in 2014 were used. While there is a global THEMIS-IR Night mosaic ([https://astrogeology.usgs.gov/search/map/Mars/Odyssey/THEMIS-IR-Mosaic-ASU/Mars\\_MO\\_THEMIS-IR-](https://astrogeology.usgs.gov/search/map/Mars/Odyssey/THEMIS-IR-Mosaic-ASU/Mars_MO_THEMIS-IR-)

[Night mosaic 60N60S 100m v14](#)), the thermal inertia mosaics (qualitative and quantitative) are only available divided into tiles (<https://astrogeology.usgs.gov/maps/mars-themis-derived-global-thermal-inertia-mosaic>). The DCS images, as they were only used as a visual approximation, were obtained from the THEMIS web page ([Table 2.1.a](#)), provided as derived products. The THEMIS DCS used in this dissertation are showed in [Figure 3.4.j](#).

vi. *Compact Reconnaissance Imaging Spectrometer for Mars (CRISM)*

The CRISM raw data cubes were selected and downloaded from the PDS Mars Orbital Data Explorer ([Table 2.1.a](#)). The available cubes for each area are showed in [Figure 3.4.a](#) and [Figure 4.4.a](#). For each image, we downloaded the raw data cube files (*Experiment Data Record*, EDR) and auxiliary data (*Derived Data Record*, DDR; and *Ancillary Data Records*, ADR). Using the CAT ENVI software (Subpart 2.2.2ii), we perform photometric and atmospheric corrections, among others. This software was also used to obtain the summary parameters [*Viviano-Beck et al., 2014*; and references therein] that allow to identify the absorption bands distribution along the surface, and project them for their inclusion into the GIS. Spectra were also extracted and ratioed using ENVI, as described in Subpart 2.1.2vi.

In late 2016, new data products were released: *Targeted Empirical Records* (TER) and *Map-projected Targeted Reduced Data Records* (MTRDR). Those data sets contain fully corrected data (from the instrument perspective) and the corresponding map projected products, respectively [*Murchie et al., 2016*]. However, by their release time, all the spectral analyses were already performed and this data is not considered for this dissertation.

## 2.2.4 DATA ANALYSIS

### i. *Cartography*

The geologic mapping in this thesis follows the cartographic criteria common in planetary geology based on texture and relief of the planetary surface. We had to differentiate geologic (material) units and geomorphic features [Wilhelms, 1990; Hansen, 2000]. Geomorphological unit boundaries were determined using a digitizing table and following the differential morphological and topological patterns as identified in the image and topographic datasets. The symbolization is based on the USGS guidance for planetary geology features [FGDC, 2006].

The study area was divided into eight units whose boundaries were differentiated depending on whether the contacts between units were clearly observed or only inferred by geomorphic changes. Such units were mapped following their characterization in previous publications. They were named beginning with one or two capital letters indicating its estimated age (Noachian, Hesperian, Amazonian, or two periods combined in age; Part 1.1.3), followed by one or two lower-case letters (initial/s of unit names). This rule is not applied to the impact craters and ejecta unit (cr), which comprise all the impact crater-derived features without an assigned age.

We mapped the impact crater rims, using different symbols when they are smaller or larger than 5 km in diameter. Craters smaller than 1 kilometer were not mapped to improve map clarity, although craters as small as 15 meters in diameter were used for crater counts in selected areas. Rimless, buried, or degraded craters were identified with a specific symbol, different from the one used for well-preserved structures. Other structural elements, such as tectonic features (e.g., fractures and faults, wrinkle ridges, and ridge crests), have also special symbols assigned. Ridge crests were identified mainly as linear features with positive topography with a cross-sectional profile that is much sharper than that of wrinkle ridges. Furthermore, shallow depressions, which apparently are the geomorphological record of valleys carved by water, were mapped as linear features following the most topographically depressed points of the 'stream bed.'

The delineation (i.e., vectorization) of the knob fields in Ariadnes area was performed using a semi-automated boundary detection method. For this purpose, we prepared squares of around  $50 \times 50$  km in the HRSC images and exported them to 'Vextractor' software (Part 2.2.2). In this software, we used a brightness threshold after applying a blur effect and image segmentation to differentiate light-toned knob materials from the surroundings. Subsequently, we applied a de-speckle filter and an algorithm to remove the isolated spots, followed by edge detection, vectorization, and export to a shapefile. Finally, we revised the knobs one by one, correcting delimitation flaws and combining them in a unified layer. This method is based on the detection of the image edge, and the delimitation corresponds to the knob outcrop and not to the actual elevation of the mounds. Consequently, in this case, we give preference to compositional mapping criteria against morphological. MOLA topography does not have enough resolution to provide good results for smaller knobs (Table 2.1.b), and HRSC-derived DEMs do not cover the complete extension of the knob field by the time the analysis was performed (Figure 2.2.f).

ii. *Surface dating*

We used statistical analyses of crater size-frequency distribution (CSFD) with the objective of constraining the formation ages and resurfacing events that have affected the different surfaces in both study areas. The counting areas were selected from the most relevant geological units and key features, and their selection is justified in each respective chapter (Part 3.3.1 and Part 4.3.1). Also, the complete extent of the study area was considered a counting area to obtain the regional ages. Craters larger than 5 kilometers were counted for regional ages, and those down to 15 meters were used for selected areas; using always fractions of all intersecting craters. When a representative area was selected, uniform and with an adequate size, the inner craters were mapped manually using CTX images (Subpart 2.1.2ii). The craters that could be secondary or produced by other process than impact, were mapped marked as uncertain. The ages were calculated with and without those unclear features, discarding them when they appear as anomalous data. The randomness analysis reveals the possible clustering or trend to order in the crater population [Michael *et al.*, 2012].

For crater mapping and counting we used the ‘*Crater Tool*’ ‘*ArcGIS*’ extension [Kneissl *et al.*, 2015]. The resulting crater size-frequency curves were analyzed with the software ‘*Craterstats2*’ [Michael and Neukum, 2010; and references therein] that has been designed to obtain ages for the studied areas. The ages were calculated using the chronology function and production function described in Hartmann [2005]. Also, the results using the production function of Ivanov [2001] was calculated and showed in all the CSFD results plots.

The unit surface age was considered as the age range for the end of the creation for each unit that was obtained from simple cumulative fits (Appendices 8.1 and 8.2). Erosional or mantling processes change the crater population by removing the low-diameter edge of the size distribution. We applied the resurfacing correction to the younger ages [Michael and Neukum, 2010] and obtained the end ages of the resurfacing events. Those events were identified using the differential crater frequency, where they are clearer, but the ages considered were those calculated by the cumulative crater frequency using the previously defined intervals (Appendices 8.1 and 8.2). For areas that overlap the same unit, the average formation and resurfacing ages are also plotted.

### iii. *Spectral analysis*

The use of spectral reflectance date back from the 1970s, when mineral groups were identified through the characteristic absorption bands found in their reflected spectra. The application to data obtained from sensors onboard satellites, the hyperspectral remote sensing [Goetting and Lyon, 1986], required of the application of ‘rationing’ due to topographic and atmospheric distortion. The difference between the values in a pixel in a wavelength with the same pixel in another wavelength highlight those differences in reflectance caused by the absorptions of the minerals, reducing other unrelated variations. A record of the evolution of Mars is preserved in the rocks and sediments exposed at its surface. Minerals can fingerprint many processes that build the martian rock record. The high spatial and spectral resolution of modern orbital instruments allow determining the nature of the outcropping materials in the surface, providing a tool to infer surficial mineral composition.

One of the most common remote sensing techniques to highlight the spectral differences is the ‘decorrelation stretch,’ an image enhancement process firstly used on aerial photos. To generate the THEMIS IR-DCS images, noise filters are applied to all available bands before applying the DCS algorithm. The result is later saved as a simple image (.png). These filters are useful for reducing the anomalous noise in the qualitative DCS image, but are not appropriate for the application to a quantitative radiance product. Next, three bands of the radiance image are selected for decorrelation and displayed in color as variations of red, green, and blue. The THEMIS IR-DCS images are executed on three standard RGB band combinations: bands 6, 4, and 2; bands 8, 7, and 5; and bands 9, 6, and 4 (Figure 3.4.i).

On the other side, CRISM L-channel data ( $\lambda = 1.0 - 3.9 \mu\text{m}$ ) was analyzed using the standard data pipeline, which corrects for instrument effects, calibrates the data to I/F, and performs a first-order atmospheric correction using the volcano-scan method (Subpart 2.2.3vi). All spectral analyses were performed on unprojected data to avoid un-certainties due to resampling. We used ratioed spectra obtained using the averaged values for geological regions of interest (ROIs formed by a  $3 \times 3$  pixel window) against the values of similar ROI from a spectrally unremarkable surface of comparable albedo in the same column. The ROIs were selected guided by the summary parameters [Viviano-Beck *et al.*, 2014; and references therein] where the signal was most strong. Those ratioed spectra were compared to library spectra (Appendix 8.4) to identify their mineralogical match (Subpart 2.1.3iii).

## 2.2.5 OUTPUTS

### i. *Plots*

Most of the plots included in this dissertation have been represented using the ‘*Grapher*’ software (Subpart 2.2.2iii) after extracting the represented data from the GIS as a spreadsheet. Some other plots were drawn using ‘*Craterstats2*’ software (Subpart 2.2.2iii), adapted from previous publications, and sometimes plotted directly using ‘*ArcGIS*’ (Figure 2.2.g). The interpretative profiles were obtained from real data from the GIS, plotted in ‘*Grapher*’ and later modified using ‘*Photoshop*’ (Figure 2.2.g). The rose diagrams have been achieved from the ‘*ArcGIS*’ extension cited in Subpart 2.2.2i.

The compositional information was processed using a specific image analysis software (Subpart 2.2.2ii), obtaining the absorption band depth maps that were later included into the GIS for visualization (Subpart 2.2.4iii) and the spectral signatures that were plotted using ‘*Grapher*’ (Figure 2.2.g)

ii. *Maps*

All the maps included in this dissertation are designed using the layout tools included in ‘*ArcGIS*’ (Figure 2.2.g). They are intended to be self-explanatory, including legends and indicators of their extension in a broader context (study areas, region). The symbolization is based on USGS guidance for planetary geology features [FGDC, 2006]. All the maps include a visual scale and north arrow. In some maps, we used as an alternative to overlaying tints on hillshades the pan-sharpening function, using a hillshade created from a DEM as the panchromatic raster and a DEM with a color ramp that has been converted to a multispectral raster. The output from the pan-sharpening function is then used as input for the contrast and gamma stretching functions.

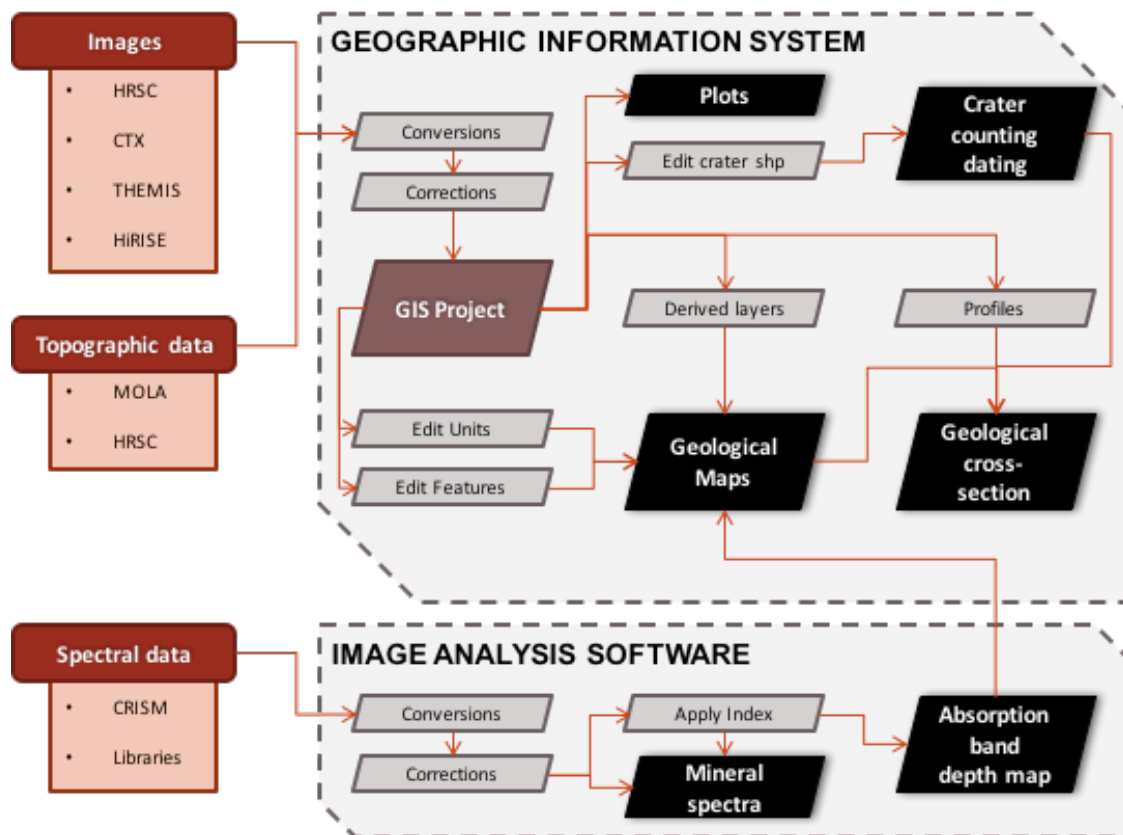


Figure 2.2.g Schematic representation of the processes to derive the different outputs shown in this dissertation from the raw data.



## 3 ARIADNES

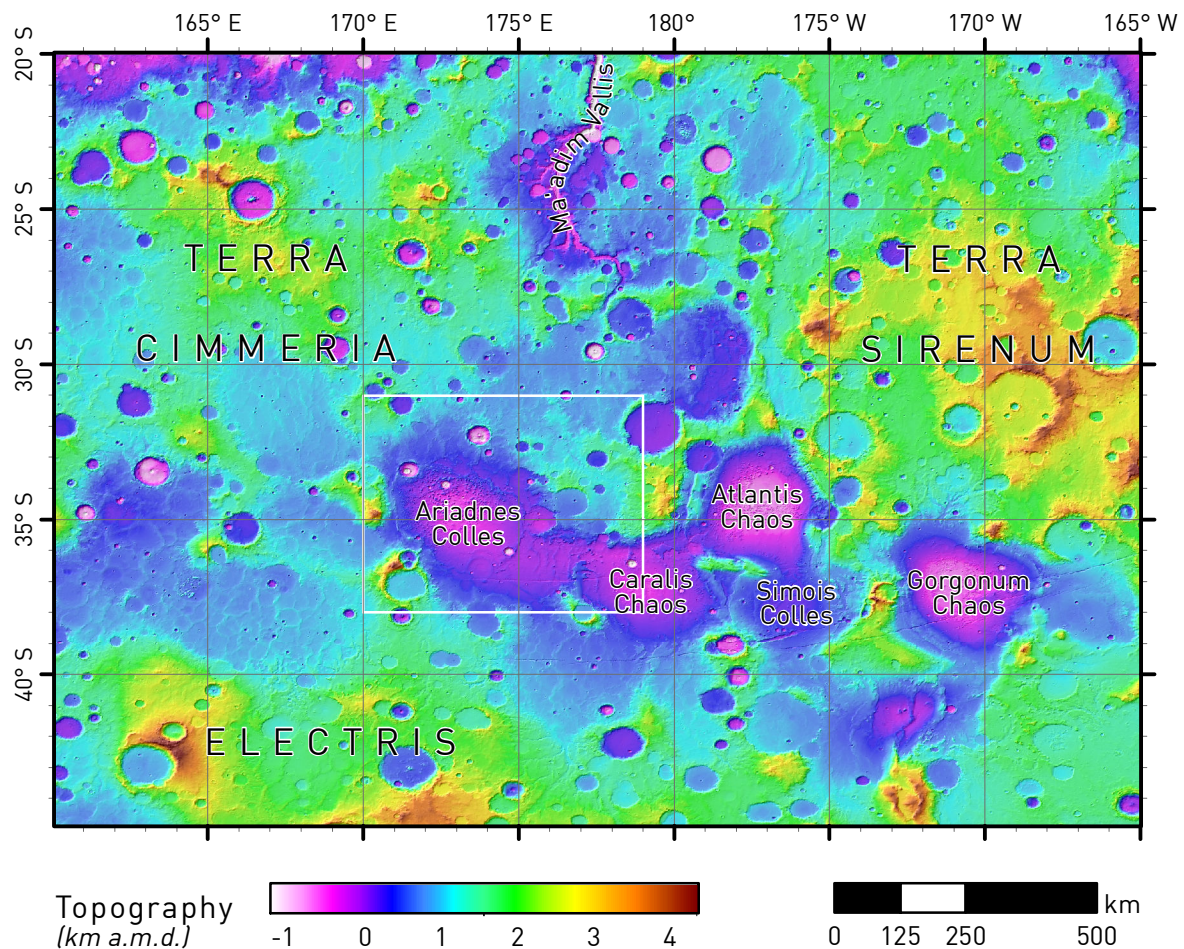
### 3.1 INTRODUCTION

#### 3.1.1 REGIONAL SETTINGS

Ariadnes area consists of an intriguing group of depressions that occur between Terra Sirenum and Terra Cimmeria ([Figure 3.1.a](#)). As supported by several lines of evidence, such depressions likely were covered by a million square kilometer paleolake, Eridania Lake, hereinafter-called Eridania system [*Irwin et al.*, 2002, 2004a; *Baker and Head*, 2012b]. The Eridania System includes five basins that are, from west to east, Ariadnes [e.g., *Molina et al.*, 2012; *Adeli et al.*, 2015], Caralis, Atlantis [e.g., *de Pablo and Fairén*, 2004; *Adeli et al.*, 2012, 2015], Simois and Gorgonum [e.g., *Oyarzun et al.*, 2003; *Marquez et al.*, 2005; *Howard and Moore*, 2011]. In addition, other depressions appear to the N and to the SW, and Copernicus and Newton Crater lie to the SE and E. These other features does not meet the same characteristics but might be related with this system.

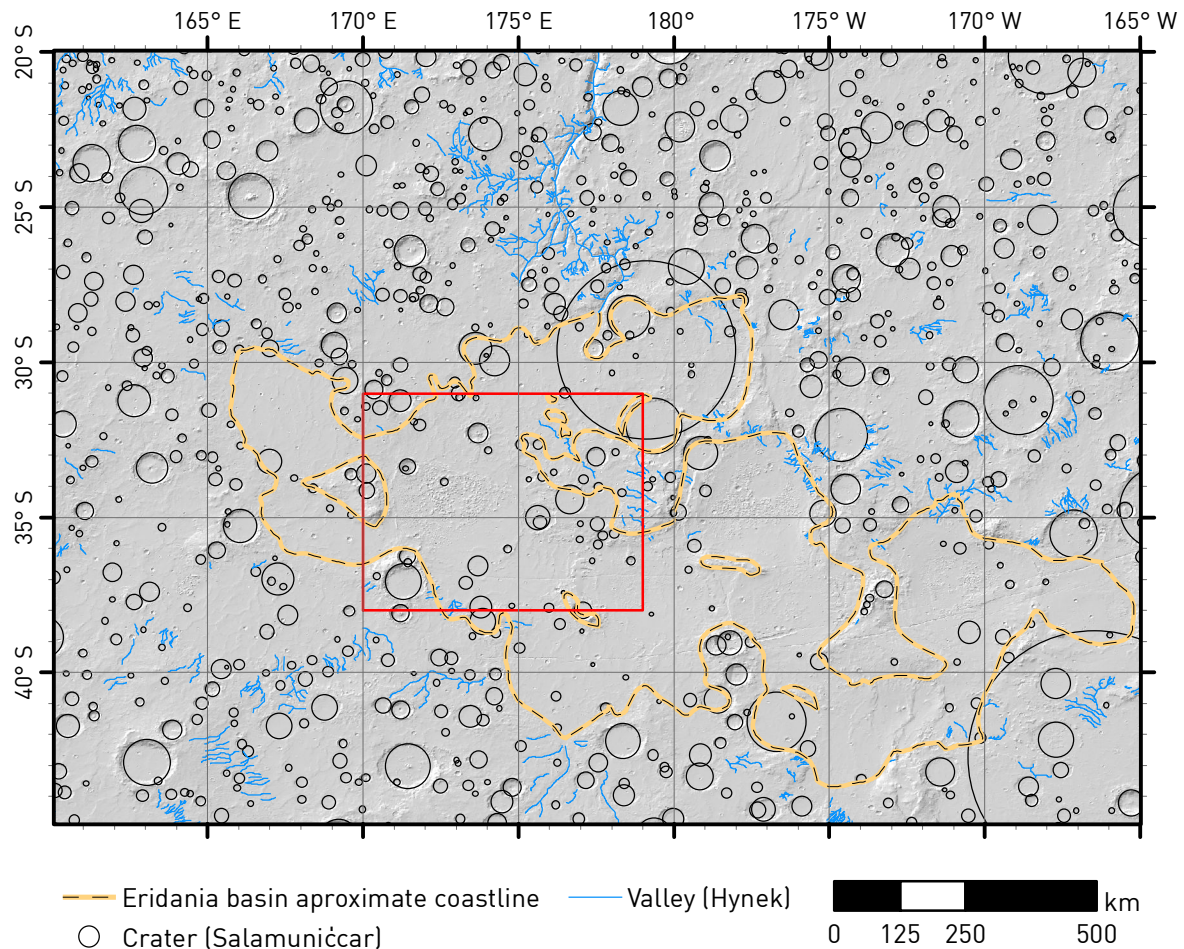
The approximate coastline of this so-called paleolake is hypothetically around one kilometer above the mean Martian datum ([Figure 3.1.b](#), *Irwin et al.*, 2002). The valleys disposition shows common features as flowing to the basin interior, similar height for the lowest part of the channel, as well as sourced at the head of Ma'adim Vallis ([Figure 3.1.a](#) and [Figure 3.1.b](#)). This evidence the existence of a stable water table in the Ariadne system. Besides, the modelization of the water table in the area also predicts that the groundwater has reached the surface [*Andrews-Hanna et al.*, 2010]. Furthermore, Ma'adim Vallis is an outflow channel sourced in the Ariadnes basin and flowing to the northern plains [*Baker et al.*, 1991]. It was originated by the catastrophic overflow of the Eridania paleolake during the Late Noachian (3.71 – 3.83 Ga) [*Kuzmin et al.*, 2000; *Irwin et al.*, 2004a]. The low crater density inside this depression, which is easily recognizable at [Figure 3.1.b](#), strongly suggest that it was a lacustrine basin. As a consequence, the different erosional features within and around Ariadnes basin contour indicates that the Eridania System temporarily hosted a water body likely produced by a groundwater source, which lasted long enough to promote the formation of the different fluvial features [*Fassett and Head*, 2008].





**Figure 3.1.a** Shaded relief derived from altimetry and colored by elevation of the Eridania System, a group of depressions located between Terra Sirenum and Terra Cimmeria. White square displays the study area, including Ariadnes and part of Caralis basins.

The infilling deposits of Eridania System depressions show an internal structure forming small hills or knobs. They are referred to as *colles* (plural of *collis*, which is Latin for ‘hill’) or *chaos* (chaotic terrains formed by jumbled and mixed lithological units) in the martian cartographic nomenclature [see *Greeley and Guest, 1987; Gazetteer, 2015*]. Recent data have revealed that these colles or chaos fields do not display the typical morphologic characteristics of chaotic terrains located east of the Valles Marineris, which were interpreted as likely formed by the catastrophic drainage of pressurized groundwater aquifers [e.g., *Lucchitta et al., 1994; Schultz, 1998*]. However, the Terra Sirenum chaos or chaotic terrains consist of groups of round and light-toned mounds distributed in a chaotic terrain-like pattern [*Adeli et al., 2012a; Molina et al., 2012; Wendt et al., 2013*].

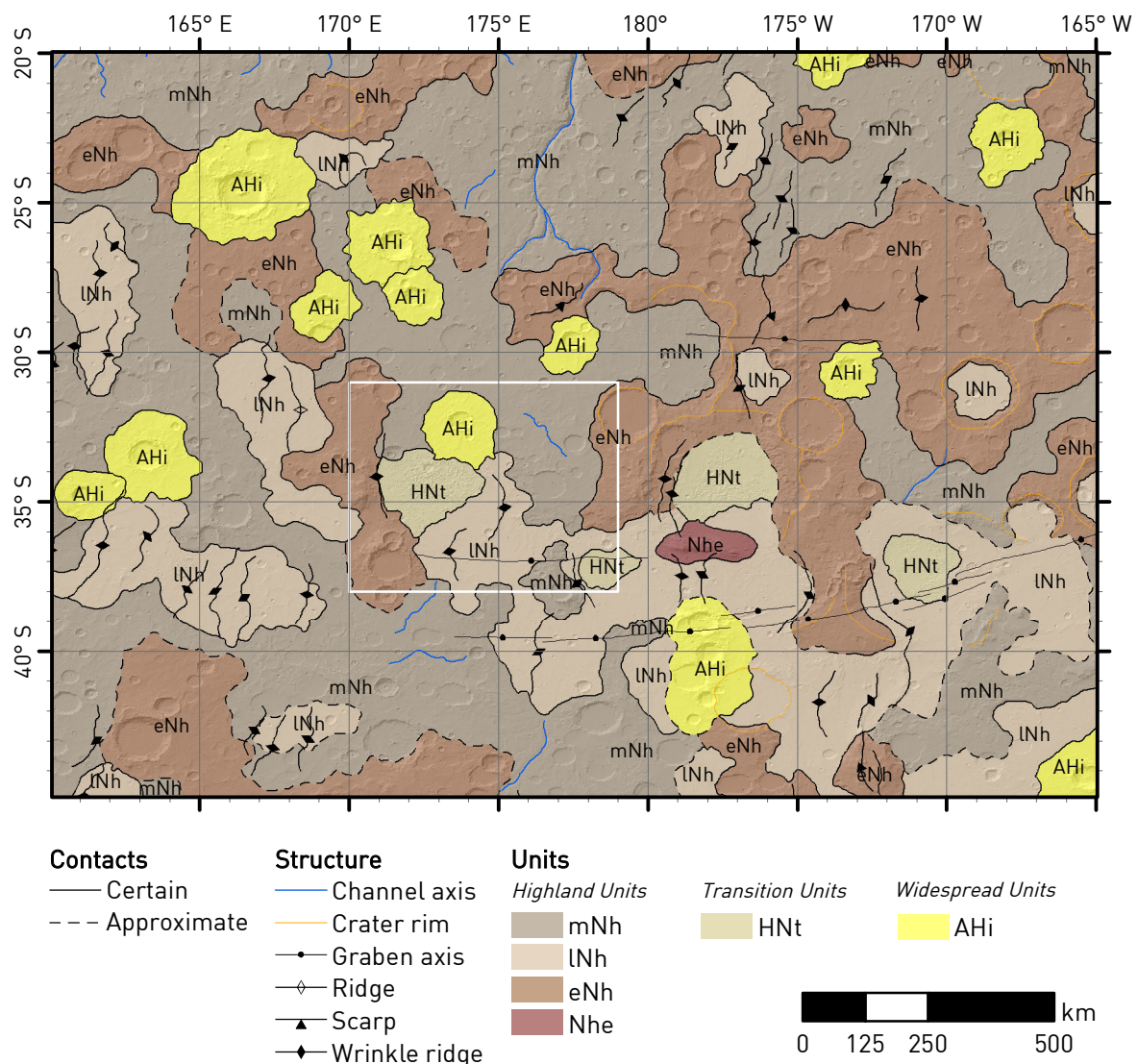


**Figure 3.1.b** Crater larger than 10 km in diameter [Salamunićcar *et al.*, 2012] and main valleys [Hynek *et al.*, 2010] in the region of Eridania System overlapping a shaded relief derived from MOLA altimetry. The 1-km a.m.d. contour line is showed as an approximation to the paleolake coastline. The red box displays the Ariadnes study area.

The Eridania System area extends from Terra Cimmeria to Terra Sirenum regions. Due to its location and complex geologic history, it is considered one of the key regions to understand the Early history of Mars [Anderson and Dohm, 2011b]. It consists of large Noachian outcrops older than 3.71 Ga [Hartmann and Neukum, 2001a; Michael, 2013], which are among the oldest stratigraphic units of the western hemisphere [Anderson *et al.*, 2012]. Such materials are followed by volcanogenic deposits that formed from 3.7 Ga to 3.4 Ga [Hartmann and Neukum, 2001b] and which infilled the deeper areas of the Ariadnes system (Figure 3.1.c) [Tanaka *et al.*, 2014]. The region shows a high density of faults and ridge crests that have been associated with the Tharsis volcano-tectonic province, located 4,000 km away [Phillips *et al.*, 2001; Anderson and Dohm, 2011b, 2011a]. Tharsis is a broad elevated (up to 10 km)



region extending over 30 million square kilometers, formed by large-scale extrusive and intrusive volcanism mostly active during the Noachian Period (>3.71 Ga ago; [Phillips et al., 2001]. Furthermore, Terra Sirenum is cross-cut by the Sirenum Fossae fault system that displays several stages of faulting [Anderson and Dohm, 2011b]. It was hypothesized that were created by the emplacement of regional-scale dike swarms [Wilson and Head, 2002]. Such structures were extensively modified by younger fractures as well as by fluvial activity or collapse structures as grabens [Anderson and Dohm, 2011b]. This tectonic system can be observed as the chain of successive grabens that appear in the Sirenum region from East to West (Figure 3.1.c).



**Figure 3.1.c** Tanaka et al. [2014] geologic map of Mars where a white square marks the study area.

Fe/Mg-rich smectite clays and other phyllosilicate deposits have been detected in the knob fields of Atlantis, Coralis and Gorgonum Chaos and Ariadnes Colles [Adeli *et al.*, 2012b; Molina *et al.*, 2012; Wendt *et al.*, 2013; Michalski *et al.*, 2015]. In this regard, the Ariadnes basin shows some of the best-preserved outcrops. Smectite clays could be authigenic minerals formed in a standing body of water, evaporation of solutions fed on groundwater or by alteration processes [Ehlmann *et al.*, 2011; Berger *et al.*, 2014]. However, they may also be detrital minerals that formed elsewhere and were transported to and deposited in the basin. In addition, deposits of chloride-bearing salts have been identified in the region, which occurrence suggests evaporative processes [Osterloo *et al.*, 2008a; Glotch *et al.*, 2010; Osterloo *et al.*, 2010].

### 3.1.2 RESEARCH OBJECTIVES

In earlier studies, the research of Ariadnes region was based on regional and local maps of the Eridania System [De Hon, 1977; Greeley and Guest, 1987; Irwin *et al.*, 2004a, 2004a; Tanaka *et al.*, 2014], as well characterization of different geological units that have been partially mapped [Grant *et al.*, 2010; Osterloo *et al.*, 2010; Baker and Head, 2012b]. However, these maps have been produced using images with lower resolution than currently available, and they not provide a detailed stratigraphic framework.

To this regard, in this dissertation we aim to determine the stratigraphical relationships between the geological units to constrain the evolution of paleoenvironmental and climatic conditions during the Late Noachian-Early Hesperian period. In our approach, we have produced a 1:1 Million geological map of the western Eridania System (NE of Eridania quadrangle), which extends from 31°S to 38°S and from 170°E to 179°E (Figure 3.1.a to Figure 3.1.c). The study area includes the entire Ariadnes basin and part of the Caralis basin. In addition, we conducted an integrative research in the area which will help to understand the complex geological evolution of the region, including: 1) the statistical analysis of crater size-frequency distributions to estimate absolute model ages, 2) the analysis of hyperspectral data

and infrared images, and **3)** the morphometric study of the knobs located inside both basins.

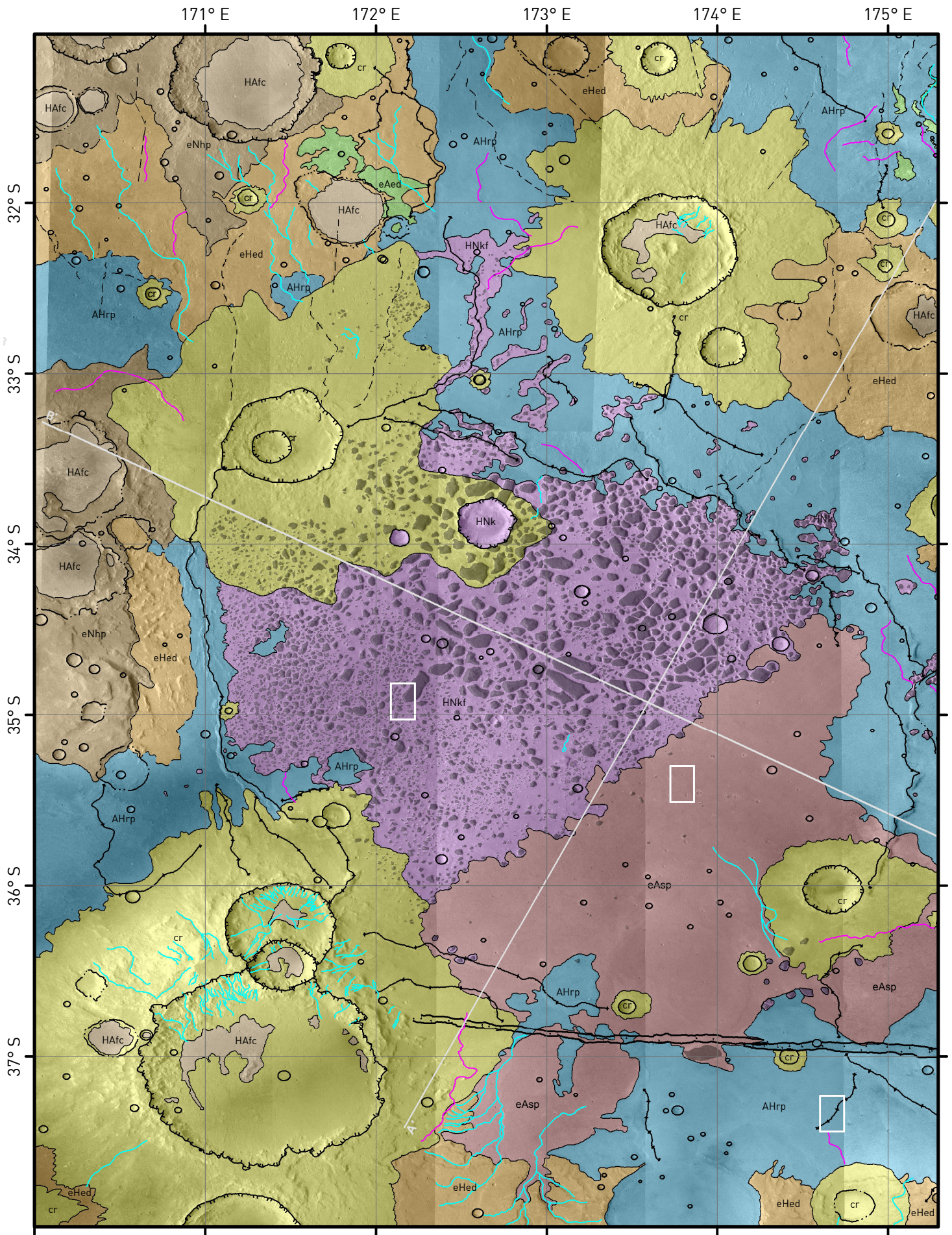
## 3.2 CARTOGRAPHY

### 3.2.1 GEOLOGIC MAP

The study area (31 – 38°S; 170 – 179°E; [Figure 3.1.a](#) to [Figure 3.1.c](#)) was divided into eight units which boundaries were differentiated depending on whether the contacts were clearly observed or merely inferred by geomorphic changes ([Figure 3.2.a](#)). Such units were mapped following a characterization that was described in previous publications (see Part 3.1.1). The 1:1 Million map also includes the delineation of the main geomorphological features, such as crater rims, faults, ridges, and linear depressions or channels. Individual knobs in the fields were delineated and marked as polygons. Earlier versions of this map have been published [*Molina et al.*, 2013b, 2014b].

**Figure 3.2.a** (Next two pages) Ariadnes Basin geologic map (regional location in [Figure 3.1.a](#) to [Figure 3.1.c](#)). The cross-section transects (A' – A'' and B' – B''); [Figure 3.6.a](#)) displayed as straight white lines.

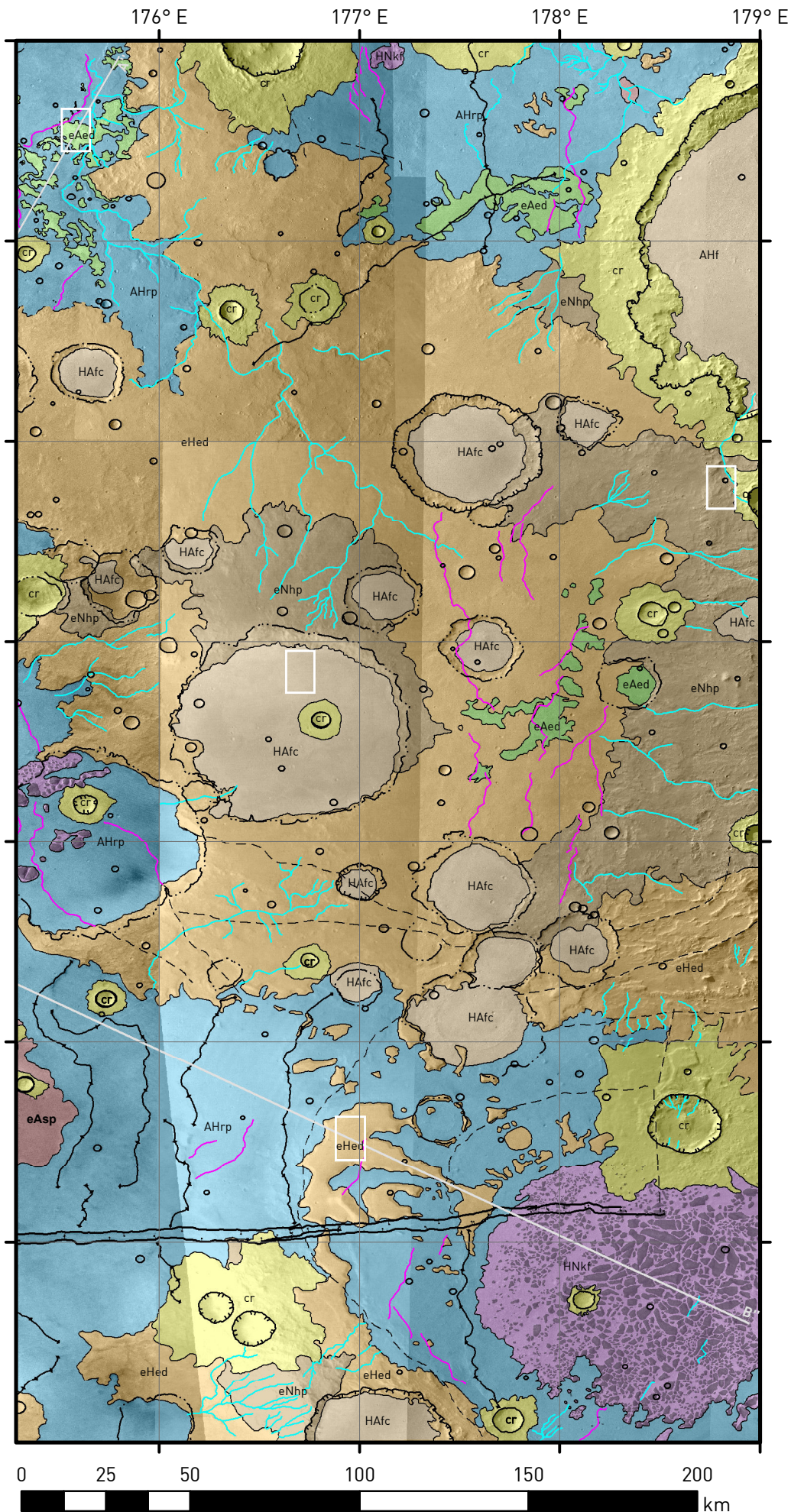




Geographic Coordinate System: Mars 2000 spheroid (Semi-major axis: 3,396,190.0 m;  
 Semi-minor axis: 3,376,200.0 m; Inverse flattening: 0.0058860)  
 Projection System: Equidistant Cylindrical (Central meridian: 180°)

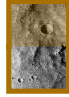
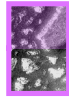
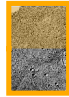
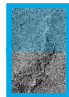
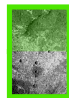
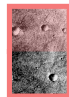

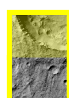






## MAP LEGEND

### MAP UNITS

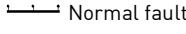
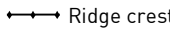
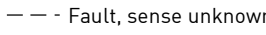
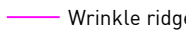
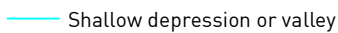
-  eNhp  
EARLY NOACHIAN HIGHLAND PLAINS
-  HNKf  
HESPERIAN NOACHIAN KNOB FIELDS
-  eHed  
EARLY HESPERIAN ELECTRIS DEPOSITS
-  AHrp  
AMAZONIAN HESPERIAN RIDGED PLAINS
-  eAed  
EARLY AMAZONIAN EVAPORITE DEPOSITS
-  eAsp  
EARLY AMAZONIAN SMOOTH PLAINS
-  HAfc  
HESPERIAN AMAZONIAN FLAT-FLOOR CRATER INFILLING
-  cr  
IMPACT CRATERS AND EJECTA


### MAP SYMBOLS

#### Contacts

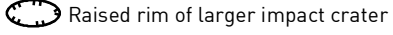
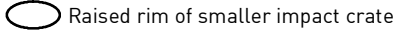
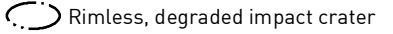
- Contact—Location accurate
- - Contact—Location approximate

#### Tectonic and topographic features

-  Normal fault
-  Ridge crest
-  Fault, sense unknown
-  Wrinkle ridge
-  Shallow depression or valley

-  Knob outcrop

#### Impact craters features

-  Raised rim of larger impact crater
-  Raised rim of smaller impact crater
-  Rimless, degraded impact crater

Scale 1:1,700,000 (at publication scale)

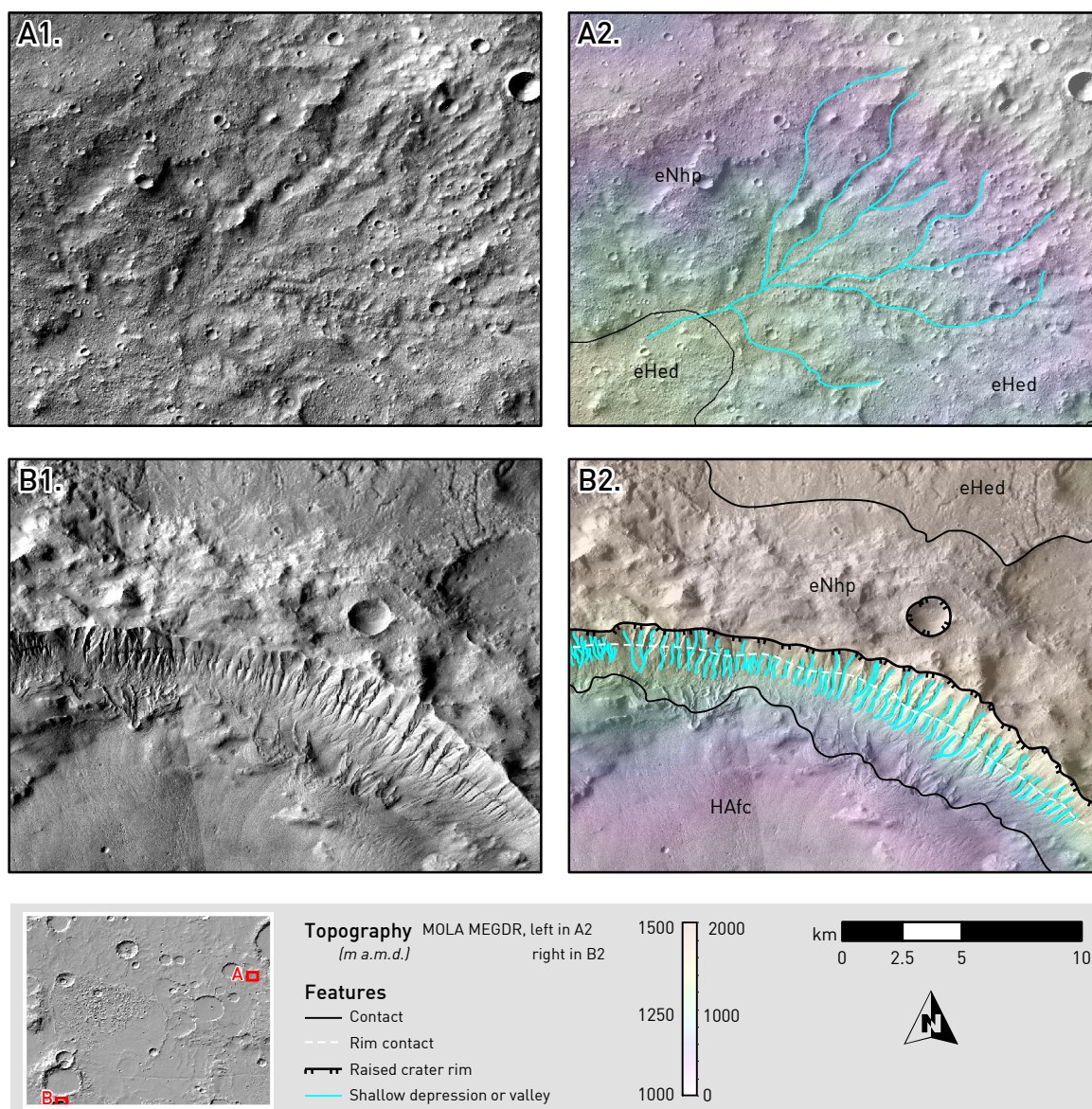


### 3.2.2 UNITS

We have defined eight distinct geologic units in the study area. The description of their general morphology, texture, and possible origin is provided here. Other geological characteristics, as formation ages and mineral composition, are described in higher detail in Subchapters 3.3 and 3.4, respectively.

#### i. *eNhp*, EARLY NOACHIAN HIGHLAND PLAINS

The early Noachian highlands plains (*eNhp*) are mapped as the Noachian cratered plains (*Npl*) in [Greeley and Guest, 1987], as well as the Early Noachian highland unit (*eNh*) in Tanaka et al. [2014]. Such unit is considered the basement and the oldest surface in our mapping area as it shows a highly-cratered surface. In this regard, its rugged, uneven, and heavily degraded surface shows relict relief forms. Those are morphologically expressed as few patches in the margins of the basin, which match the highest locations in the study area. The *eNhp* unit is commonly carved by several dendritic fluvial valley networks (Figure 3.2.b-A), though they are currently eroded and buried with younger sediments. The larger crater rims –mapped as the *cr* unit for clarity, but considered as part of this the *eNhp* unit for interpretation– are affected by a set of much denser and younger gully systems. The Figure 3.2.b-B shows a set of regular gullies that are characterized as straight and steep-sided channels carving the older materials, sourced in a wider head and ending in terminal alluvial fans [Carr, 1996]. The fans are deposited above a sedimentary infilling of the crater topped with a flat surface (flat-floor crater infilling; *HAfc*), which shows ice-related structures as glaciers and glacial tongues from an intermediate event (Figure 3.2.b-B).



**Figure 3.2.b** Several fluvial morphologies carving *eNhp* observed in CTX images, which are colorized with MOLA topography. To the right, **A2** and **B2** show differently interpreted features. **(A)** Eroded dendritic fluvial valley network at the NE of the study area. **(B)** Various gullies carving a crater rim that show minimal alteration, suggesting a younger age than the main fluvial network.

## ii. *HNkf*, HESPERIAN NOACHIAN KNOB FIELDS

The Hesperian Noachian knob fields unit (*HNkf*) appears in the topographically lower parts of the Ariadnes and Caralis basins. Also, some isolated *HNkf* patches and knobs can be found in the *AHrp* (Amazonian Hesperian ridged plains). This surface was mapped as Chaotic material (*Hcht*) in *Greeley and Guest [1987]* and identified as the fourth type of Electris deposit in *Grant and Schultz [1990]*, where it is described as “positive-relief chaotic terrain [...] found in degraded large craters”. *Lucchitta et al.*

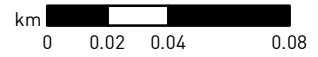
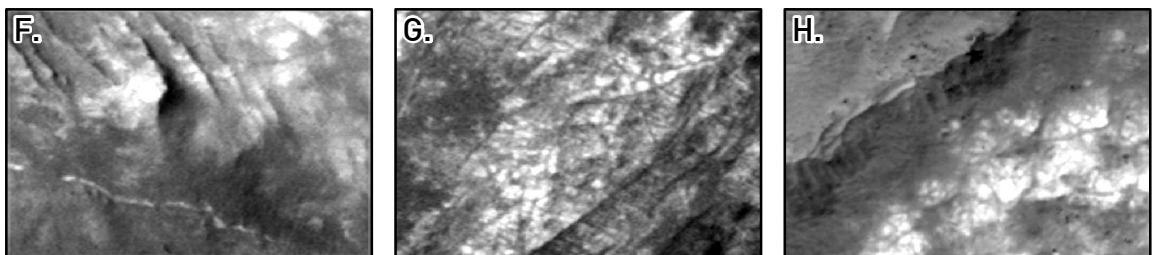
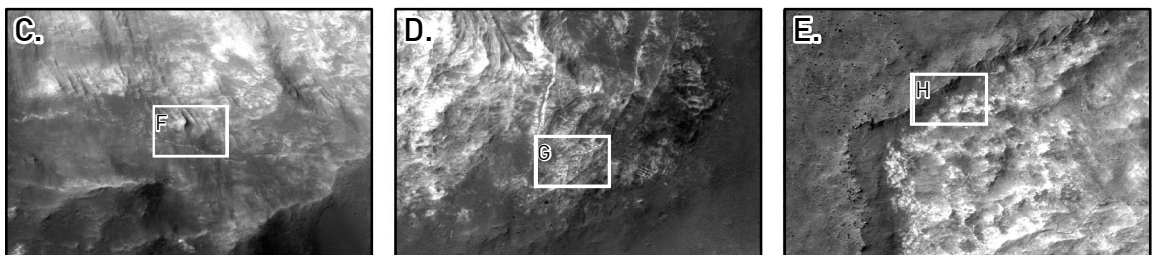
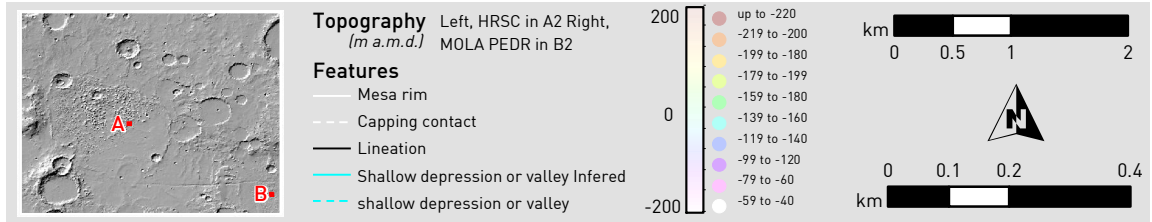
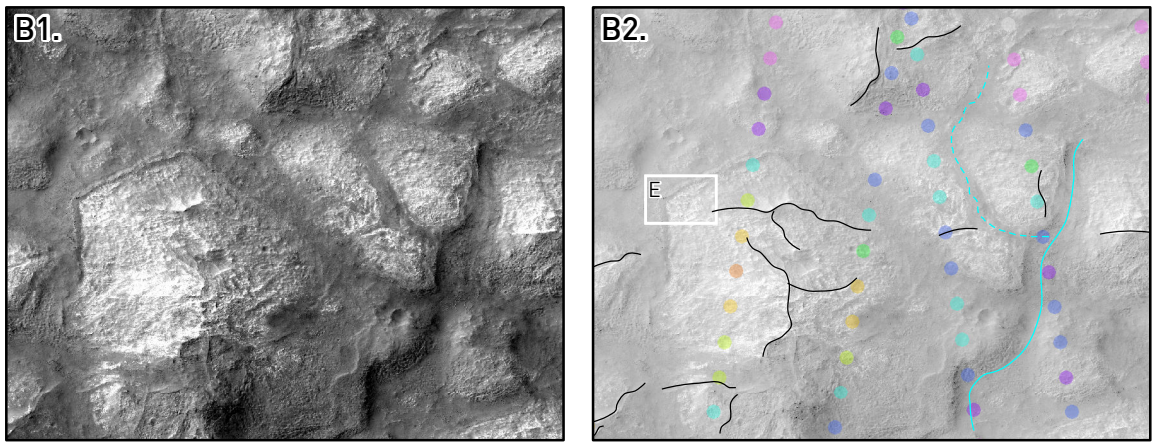
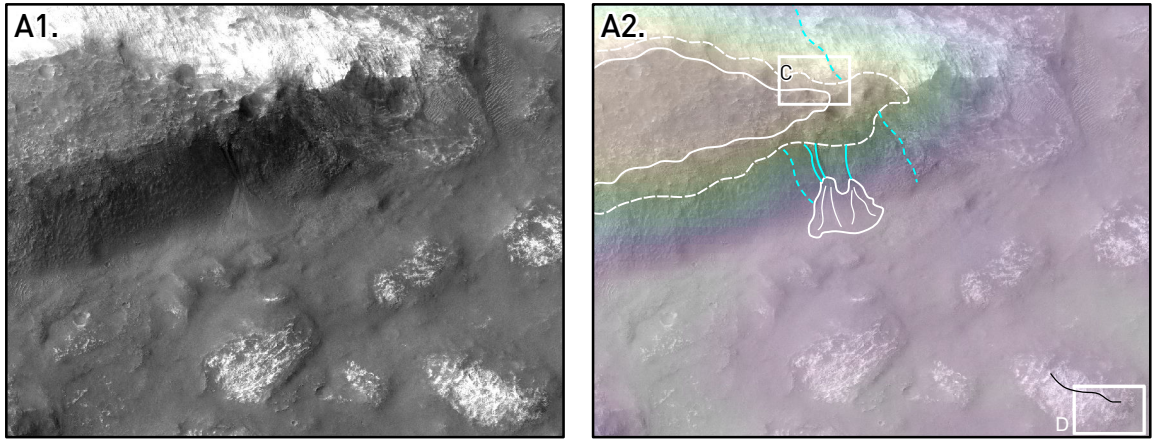
[1986] were the first on referring to this area as ‘chaotic’. High-resolution data has shown that this unit displays light-toned knobs separated by a dark smooth material that fills the space between them (Figure 3.2.c). These characteristics are quite different from the typical chaotic terrains that consist of irregular groups of large blocks, tilted, and flat [Sharp, 1973]. In the recent map of Tanaka *et al.* [2014], the unit is called Hesperian and Noachian transition unit (*HNt*) and is referred as “Knobs, mesas, and intervening aprons and plains” (Figure 3.1.c).

The *HNkf* unit is located at the bottom of the two major depressions and presents remnants of a mesa-like surface in their center, surrounded by smaller and irregular light colored knobs (Figure 3.2.b-A) and some isolated minor fields (Figure 3.1.c). We have identified more than 5,000 light-toned knobs, but only 337 are larger than 5 km<sup>2</sup>. Most of the knobs are located at absolute elevations between -200 and 500 m relative to the martian datum and have an altitude ranging between 50 and 300 m (see the extensive morphometric study in Part 3.5.2). The higher elevations follow the E – W general topographic alignment of the area and fit well the ridge crest systems on *AHrp*. A dark material, which is similar to *AHrp* and *eAsp* (Early Amazonian smooth plains unit), infills the depressions that are placed between knobs. In some locations to the southeast, such material disappears and is replaced by a surface that has channel-like grooves (Figure 3.2.b-B).

A darker capping layer is emplaced at the top of the mesa-like knobs (Figure 3.2.b-A). The capping has a thickness of ~100 m and could be a duricrust or some resistant material that shows flat and large outcrops, which may have protected this formation against degradation. Small channels and gullies carve the knobs flanks (Figure 3.2.b-A). Few fluvial morphologies are also placed between the knobs (Figure 3.2.b-B).

**Figure 3.2.c** (Next page) Ariadnes (A) and southeastern (B) knob fields in HiRISE images showing up the typical surfaces of the *HNkf* unit. Colorized topography (A2) and MOLA PEDR (B2) topography overlapping HRSC include some interpreted morphologies. C to E and F to H boxes are magnified locations in A and B. Scale in the upper position corresponds to A and B, whereas the scale below corresponds to C to E and the one in the bottom to the F to H images.





The light-toned deposits show bedding morphologies that suggest an internal layering (Figure 3.2.c-C and F). If so, the dark capping level is resting over the light-toned layers by an angular unconformity, which suggests a tilting phase followed by an erosive episode. The dark material between the knobs overlay them in a gradational contact following an uneven pattern, when covering the knobs rims and its inner depressions (Figure 3.2.c-D and G). In some locations, the contact shows a step, with the layer of dark material covering the knobs against slope (Figure 3.2.c-E and H).

We interpret the occurrence of cross-cutting lineaments along the surface of the knob fields as a consequence of tectonic activity (faults). This process may have combined with volcanism or hydrothermal activity that produced some related structures as dikes (Figure 3.2.c-D and E). In a closer look at the surface, the light-toned materials show a meter-sized polygonal texture that is broadly distributed in most of the outcrops (Figure 3.2.c-F to H). Such a pattern, which is usually the product of desiccation or thermal contrast, commonly appear in phyllosilicate and salt-bearing deposits [McKeown *et al.*, 2013].

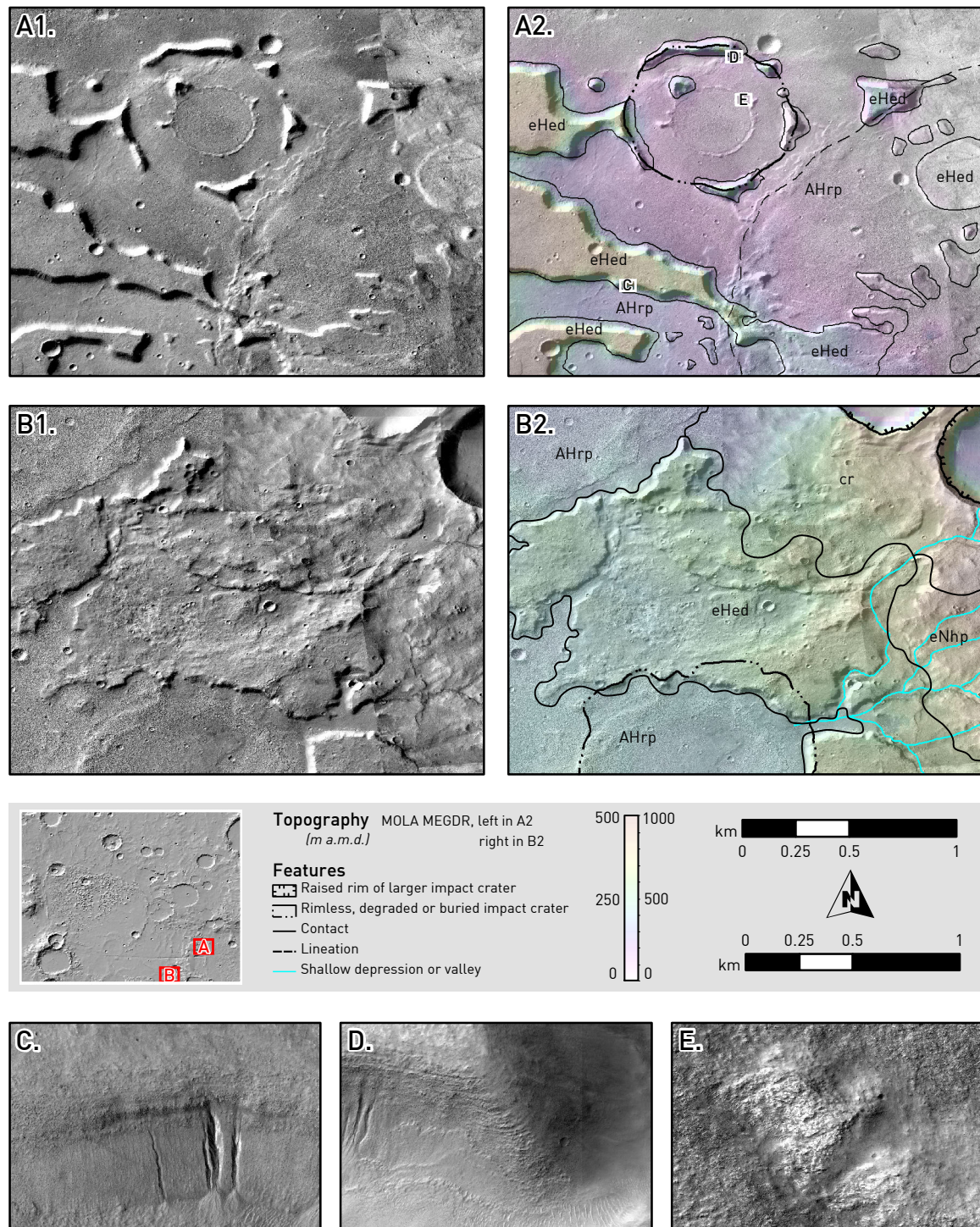
### iii. *eHed*, EARLY HESPERIAN ELECTRIS DEPOSITS

The early Hesperian Electris deposits (*eHed*) occur unevenly along the margins of the basins, as a mantling blanket that tapers out towards the higher reliefs (Figure 3.2.d-B). It roughly matches the Etched unit (*Nple*) described in Greeley and Guest [1987], as well as the middle Noachian highland unit (*mNh*) on Tanaka *et al.* [2014] (Figure 3.1.c). Furthermore, Grant and Schultz [1990] provide a more detailed characterization of the deposits, after recognizing three different types that describe as: 1) gradational deposits in mantled and unmantled regions, 2) gullied cuestas, and 3) irregular promontories and mesas.

The *eHed* unit usually occurs in the S and SW of Ariadnes as high-standing mesas with steep margins and a flat upper surface (Figure 3.2.d-A). It laterally varies to a thin mantling deposit with poorly defined contacts (Figure 3.2.d-B) which is covering *eNhp*. In addition, the mesas rims display horizontal layering (Figure 3.2.d-



C and D). In some cases, mesas outlines adapt to the crater morphologies (Figure 3.2.d-A) adopting circular patterns. In addition, when co-occurring, it seems that *eNhp* underlays the *AHrp* unit (Figure 3.2.d-C to E).



**Figure 3.2.d** (A) CTX image mosaic of *eHed* unit occurrences, identified as mesas (B) which laterally changes to a mantling. A2 and B2 show colorized overlapping MOLA topography and interpreted features. Magnified views in HiRISE images showed in C to E. Scale in the upper position corresponds to A and B, whereas the scale below corresponds to C to E.

The *eHed* materials show a thickness of 300 – 500 m and cratered upland surfaces [Grant and Schultz, 1990; Grant et al., 2010]. In some locations, the light-toned outcrops are similar to the knob-bearing material in the *HNkf* unit, and the polygonal pattern seems more irregular, as well as lesser sharp and pristine though (Figure 3.2.d-D). There was discrepancy on the emplacement of this deposits in previous works. The early Mars global maps described them as eolian, volcanic, fluvial, and impact related [Scott and Tanaka, 1986; Greeley and Guest, 1987]. Later, they were hypothesized as relict polar [Schultz and Lutz, 1988], lacustrine [Moore and Howard, 2005], or loess [Grant and Schultz, 1990; Moore and Howard, 2005; Grant et al., 2010] deposits.

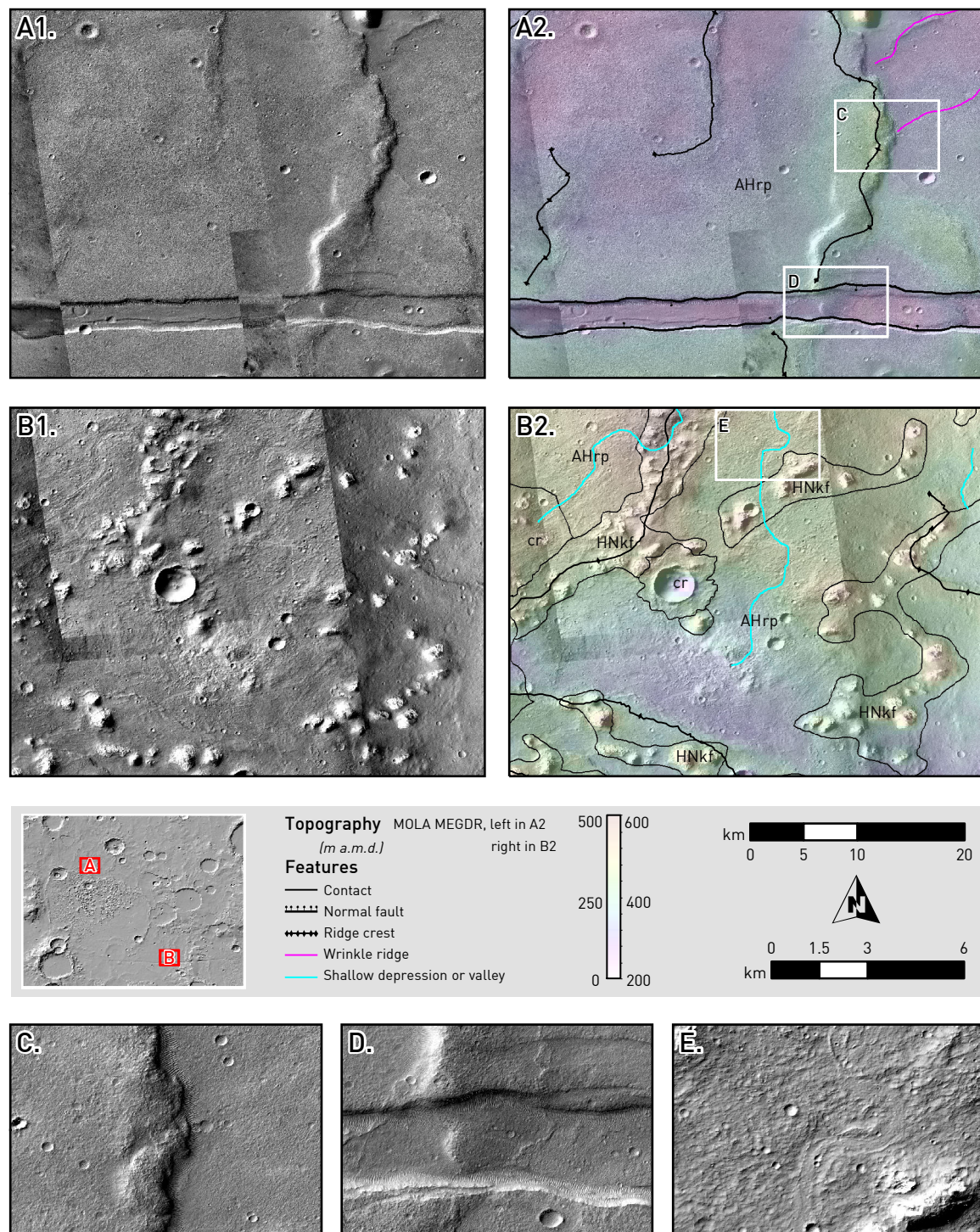
As observed in the *HNkf* mesas (see Figure 3.2.c), the *eHed* is carved by fresh gullies, most frequently on slopes (Figure 3.2.d-C and D). It is also heavily eroded by abundant branched and sinuous channels, which are deeply entrenched on the deposits. Some exceptional examples of channels are found in the NE and S side of Ariadnes area (Figure 3.2.d-B). In addition, in the easternmost side, the *eHed* unit is affected by several wrinkle ridges (Figure 3.2.a).

#### iv. *AHrp*, AMAZONIAN HESPERIAN RIDGED PLAINS

The Amazonian Hesperian ridged plains (*AHrp*) consist of a flat, smooth, and relatively crater-free unit that occurs inside the deepest topographic depressions in the study area. Such unit is named as the Hesperian Ridged Plains deposits (*Hr*) by Greeley and Guest [1987], whereas Tanaka et al. [2014] (Figure 3.1.c) defined it as the late Noachian highland unit (*LNh*). The *AHrp* unit is affected by several tectonic structures along its surface including sinuous grabens, ridge crests, and wrinkle ridges (Figure 3.2.e-A). It displays a smooth texture, which turns into a distinctive rough surface at higher detail (Figure 3.2.e). *AHrp* is usually interpreted as volcanic deposits [Greeley and Guest, 1987; Tanaka et al., 1988], which numerous crests interpreted as exhumed dikes [Head et al., 2006] are evidence of regional dike-emplacement events. The contacts of the *AHrp* outcrops usually postdates *eHed* (Figure 3.2.d) and *HNkf*, which can be considered as the matrix of *eHed* (see Figure 3.2.e-B, where it is partially covered by the ejecta of a closer impact as well). Although the Early Amazonian



smooth plains unit (*eAsp*) is similar to *AHrp*, it results from a later resurfacing episode caused by volcanism or hydrological activity.



**Figure 3.2.e** (A) CTX image mosaic that show the *AHrp* unit occurring as smooth plains and low cratered surfaces affected by tectonic features. (B) Light-toned knobs can be observed, though an impact ejecta blanket from the NE has locally disturbed the surface. A2 and B2 show colorized overlapping MOLA topography with some distinctive morphologies. C to E are magnified images of the main features. The upper scale corresponds to A and B, the one below to C to E.



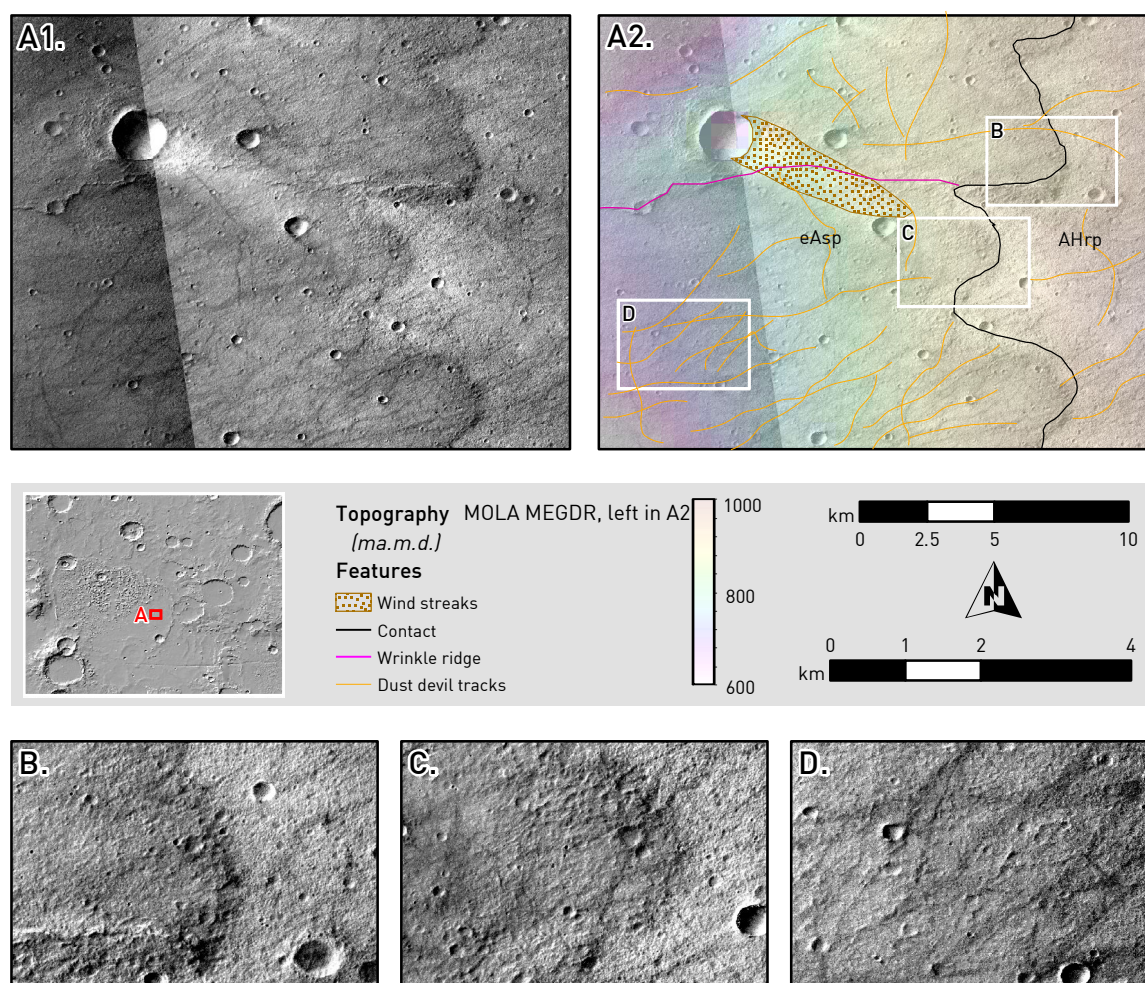
The ridge crests that affect the unit have a prominent relief, reaching dozens of meters high, and usually show significant width changes, being around 5 km wide. The crests display wrinkled surface at its lower flanks and they present an alignment around the basin margins (see [Figure 3.2.a](#)). The crests are also affected by tectonic structures, wrinkle ridges ([Figure 3.2.e-C](#)), and by the graben systems of the Sirenum Fossae ([Figure 3.2.e-D](#)). The deformation of the *AHpr* unit by such tectonic structure, which was related to the Tharsis bulge rise, strongly suggest that its formation predates the planetary event involved in the formation of the Tharsis complex. On the other hand, although the fluvial activity markers are not very abundant in this unit, some examples of inverted channels can be observed affecting its surface ([Figure 3.2.e-E](#)).

v. *eAsp*, EARLY AMAZONIAN SMOOTH PLAINS

The early Amazonian smooth plains (*eAsp*) unit consists of a thin deposit that is restricted to the SE of the Ariadnes basin ([Figure 3.2.a](#)). It is characterized by a smooth texture, a planar topography, and dark surface ([Figure 3.2.f](#)), which contrasts with a more abrupt topography of the overlaid *HNkf* and *AHrp* units. The overlaying contact varies going from a sharp cliff ([Figure 3.2.f-C](#)), which laterally disappear becoming a less clear border ([Figure 3.2.f-D](#)). Furthermore, the unit appears as a single outcrop of about 18,200 km<sup>2</sup> to the SE of the main knob field around the Ariadnes basin.

The matrix material of the *HNkf* unit, which is characterized by the knob field, has a very similar appearance as the *eAsp* unit, though occurring at a lower topographic position than *AHrp*. Interestingly, different morphologies affecting *AHrp* as channel-like and flow marks, as well as wrinkle ridges, wind streaks, and dust devil tracks ([Figure 3.2.f-F](#)), provides useful hints to evaluate its texture, inner structure, and composition. Although the *eAsp* material may have flowed in a recent event as mud, glacier, or lava flow, the wrinkle ridges might postdate its formation, providing an older age for this unit. On the surface, such material is affected by wind-driven structures that suggest it could be easily friable. In addition, the *eAsp* unit presents a

unique spectral signature, with high IR reflectance and low albedo. A detailed study of this results and their implication can be found in Part 3.4.2.



**Figure 3.2.f** (A) Mosaic of CTX images showing outcrops of the *eAsp* unit. **A2** displays a colorized overlapping MOLA topography and tracing the most distinctive structures in the area. **B** to **D** are magnified views that provide a greater detail of the *eAsp* unit. **B** and **C** show the relation between *eAsp* and the adjacent *AHrp* unit and **B** displays some tracks of dust devils crossing the surface of this dark smooth unit. Scale in the upper position corresponds to **A** and **B**, whereas the scale below corresponds to **C** to **E**.

vi. *eAed*, EARLY AMAZONIAN EVAPORITE DEPOSITS

Several deposits that occur marginally along the perimeter of the basin have some water-related features, and which have been identified previously in local studies [Osterloo *et al.*, 2008a, 2010]. It occurs in four different groups of outcrops that have been defined as a unique unit defined as the early Amazonian evaporite deposits (*eAed*). Such unit occurs in the form of patches to the north and the east of the study area. They do not appear as continuous either well-exposed outcrops,

because of dust, impact, and water-related features that erode and over impose them. Consequently, it impedes to delimitate its exact extension, age, and nature. In some sites, the unit is limited to an exposed cliff (Figure 3.2.g-A).

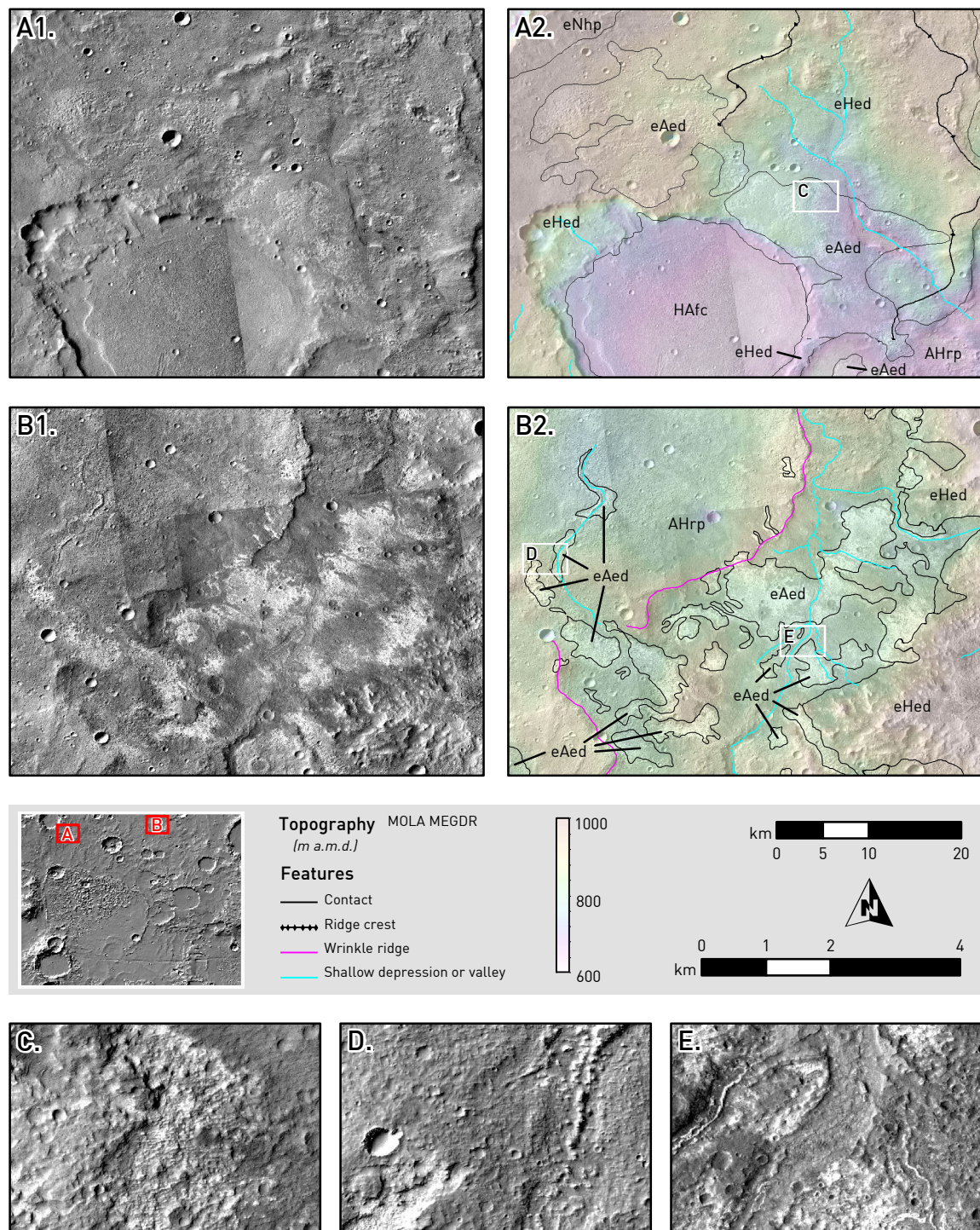
The *eAed* unit has a high albedo and a polygonal texture at a higher detail that usually fills depressions enclosed by a marginal and discontinuous belt of channels. Interesting enough, they are located between 0.8 and 1.0 km a.m.d.; that is an elevation close to the proposed Eridania Lake shoreline (Figure 3.1.b). All features are consistent with salt-bearing deposits formed under a strong evaporation as have been described in the chloride deposits on Mars [Osterloo *et al.*, 2008a, 2010]. In addition, such unit also displays low IR reflectance and high albedo (see Part 3.4.2). Although CRISM data does not provide a conclusive spectral signature for the presence of chlorides (Part 3.4.1), the THEMIS DCS data show the spectral evidence of the existence of chlorine-bearing salts in the area (Part 3.4.3).

The occurrence of the *eAed* unit in the area can be grouped into four areas of exposure. According to their location, the first set of *eAed* outcrops (Figure 3.2.g-A) extends around 500 km<sup>2</sup> in the NW of Ariadnes area. It occurs as a platform enclosing an impact crater that is excavating the *eHed* unit, above a scarp which altitude ranges from 600 to 900 m a.m.d. In this site, a branched channel entrenches on the eastern side of the platform forming a flat-floor section where the channel is widened. As there is not high-resolution coverage for this deposit, it is not possible to have a greater detail of the outcrop (Figure 3.2.g-C). Although it does not offer a sharp view of the surface texture, a polygonal pattern can be slightly appreciated.

The second group of *eAed* bright materials crop out to the north of the study area (Figure 3.2.g-B) as a broad alluvial plain associated with the termination of a fluvial channel sourced at the *eHed* mesas and flowing to the south of the location. The *eAed* deposits are widely distributed inside the lowermost margin of the area between the slopes and ridges, and with an altitude which ranges from 800 to 900 m a.m.d. The *eAed* unit is currently associated with inverted structures that are fossilizing branched channels and craters as well (Figure 3.2.g-D and E). In addition,



the texture has a polygonal pattern even though the surface of the unit is affected by sand dunes and overlapped with a dark capping material (Figure 3.2.g-E).



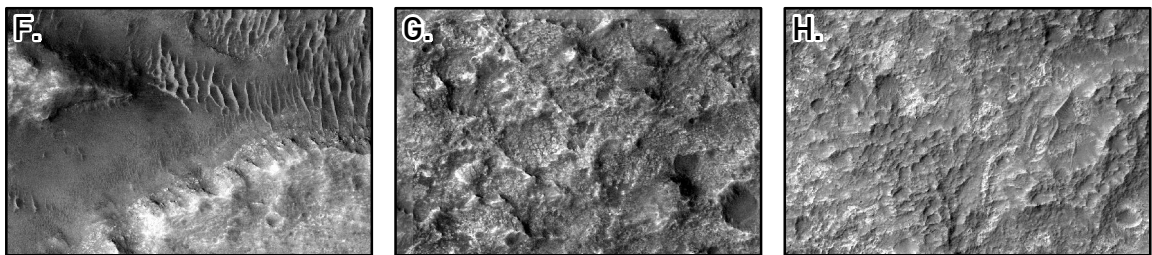
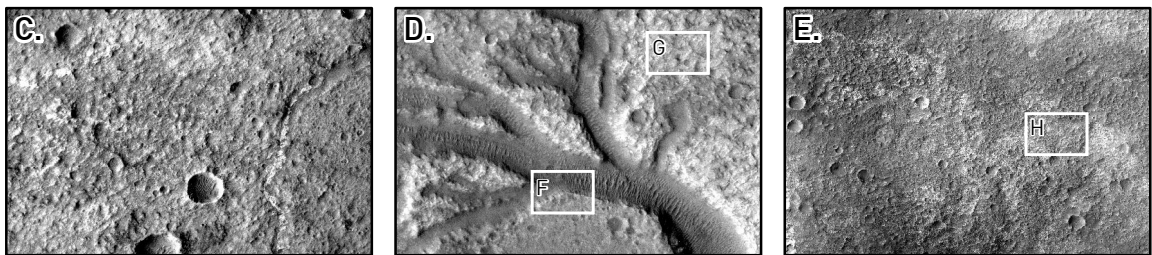
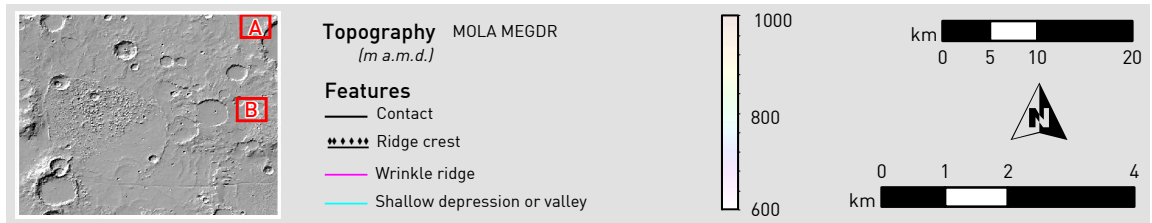
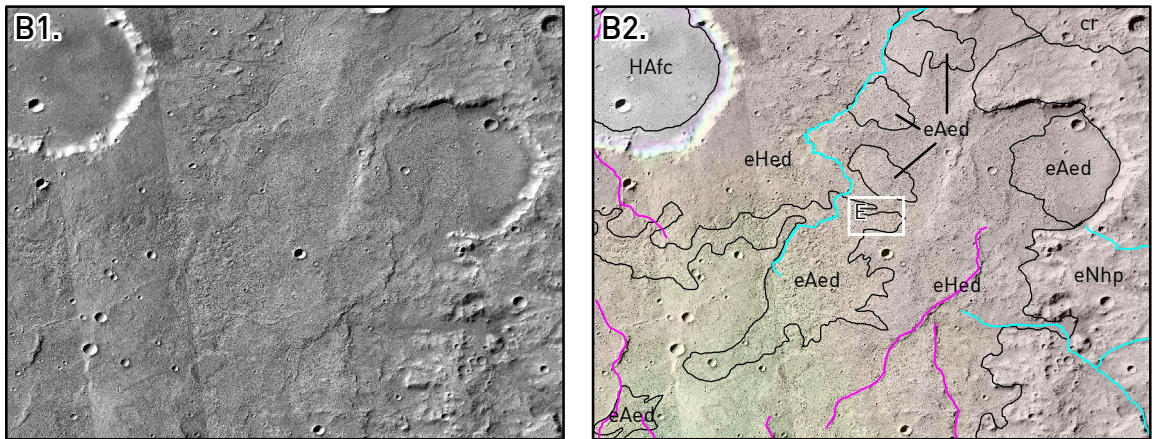
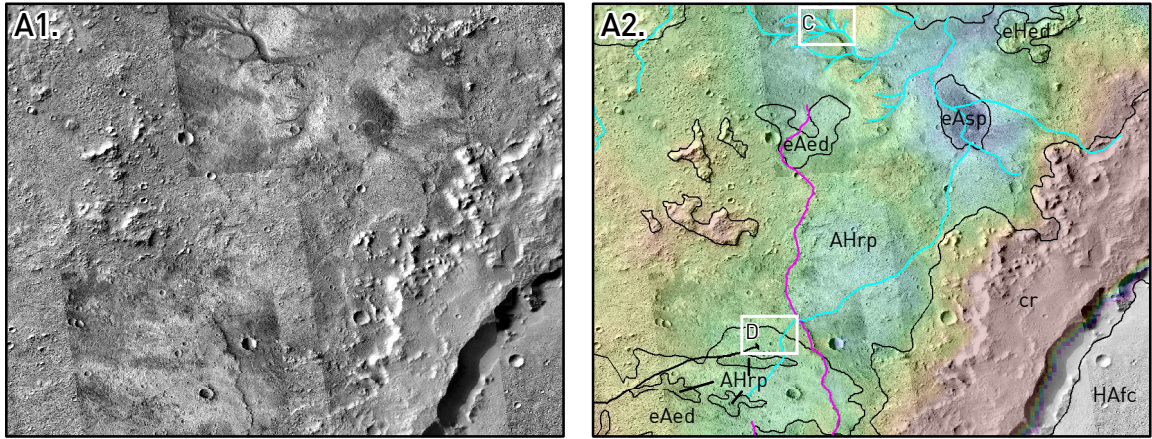
**Figure 3.2.g** Mosaic of different CTX images showing two sets of the *eAed* unit outcrops (A and B). A2 and B2 show a colored MOLA topography overlapping the CTX images and includes the outline of some landscape morphologies and geological units. C to E images show a magnified view of the unit in some locations. Scale in the upper position corresponds to A and B, whereas the scale below corresponds to C to E.

The third set of *eAed* occurs at the Northeastern side of the study area ([Figure 3.2.h-A](#)). As the second set of outcrops, it is located at an altitude ranging from 800 to 900 m a.m.d. along the *AHrp* plains, which are surrounded by channels and ridge crests ([Figure 3.2.h-C](#)). Although this set was mapped in those locations where the spectral signal had the enough quality to determine the mineral composition as likely chlorides (e.g., high albedo, low IR, and specific combination of colors in DCS; Part 3.4.3), the set has a larger extension towards the east as can be inferred from the images ([Figure 3.2.h-D](#)). The high-resolution imaging data provide additional and valuable information, which includes the branched channel carving those deposits, showing even some outcrops below the dark eolian deposits forming dunes in places ([Figure 3.2.h-D](#)). The polygonal pattern can also be observed in clean surfaces ([Figure 3.2.h-E](#)).

The fourth and last set of the *eAed* unit occurs on the Eastern side of the study area ([Figure 3.2.h-B](#)), with a range of altitudes going from 850 to 1,050 m a.m.d. It lies above the *eHed* unit filling a depression that seems to be related to the terminal part of a channel flowing from the north, as well as to a proximal segment of another channel, which courses north until reaching the second occurrence area ([Figure 3.2.g-B](#)). Although a dark capping covers the deposits in some places ([Figure 3.2.h-E](#)), the texture underneath shows the characteristic polygonal pattern under higher resolution ([Figure 3.2.h-H](#)).

**Figure 3.2.h** (Next page) CTX image mosaic of two of the *eAed* unit occurrences (**A** and **B**). The other two are showed in [Figure 3.2.g](#). **A2** and **B2** show colorized overlapping MOLA topography and interpreted features. Magnified views showed in **C** to **H** in two different scales. **C** and **D** are CTX images and **E** to **H** are HiRISE. Scale in the upper position corresponds to **A** and **B**, whereas the scale below corresponds to **C** to **E** and the one in the bottom to the **F** to **H** images.





vii. *HAfc, HESPERIAN AMAZONIAN FLAT-FLOOR CRATER INFILLING*

In this work, those heterogeneous deposits infilling the crater depressions have been defined as the Hesperian-Amazonian ‘flat-floor crater infilling’ unit (*HAfc*). It includes slope-derived debris, resedimented volcanic air-fall, lacustrine sediments, as well as fan deposits. As the crater deposits usually have a limited extension that prevents to establish reliable stratigraphic relations with other deposits without a detailed survey (that is outside of the scope of this work), their specific age cannot be determined, and, therefore, they cannot be integrated into the chronological framework of Ariadnes. Thus they are defined and categorized as this generical unit.

viii. *cr, IMPACT CRATERS AND EJECTA*

Those deposits that are excavated from a crater cavity during an impact and which are sedimented around the crater cavity in the form of detrital materials are defined as ejecta. The ejecta mainly consists of impact breccias containing a combination of the fragmented and melted materials [e.g., Barlow *et al.*, 2014]. In this regard, the impact process usually produces a mantling deposit which composition shows a high heterogeneity in composition and nature. Such deposit that occur around the crater rim and other related surfaces is classified here as the impact crater and ejecta unit (*cr*). Diverse impact crater morphologies are present in the area that will be discussed at higher detail in Subpart 3.2.3ii.

### 3.2.3 GEOLOGIC AND GEOMORPHIC FEATURES

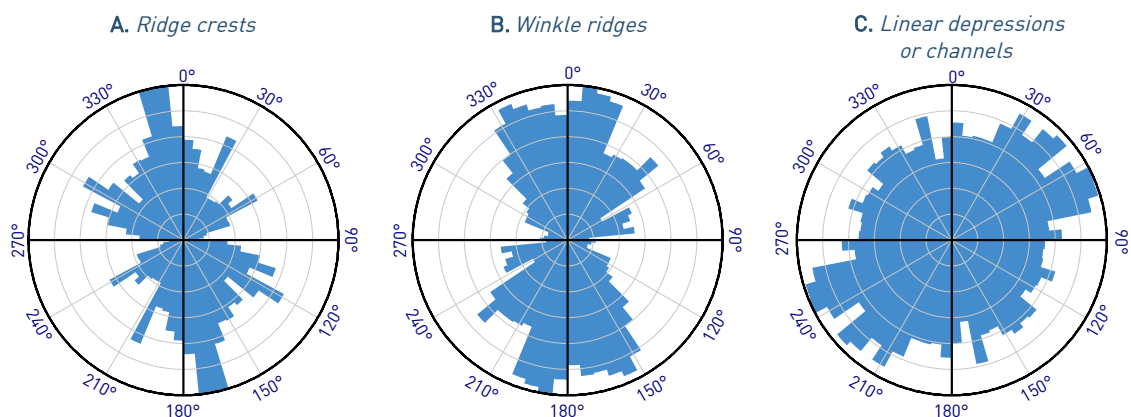
i. *Tectonic features*

The tectonic activity is a factor that has played an essential role in the geological evolution of the region. In this regard, different structures as faults and ridges are arranged following a set of conjugate faults, known as the distal Sirenum Fossae fault system (terminates at about 187.8°E, approximately 200 km south of Ariadnes Colles) [Wilson and Head, 2002; Kneissl *et al.*, 2015]. The formation of complex systems of faults radial and concentric to Tharsis occurred in several stages throughout its volcanic evolution. They are attributed to faulting due to isostatic, dynamic, or thermal uplift, radial dike emplacement and the subsequent surface faulting and fracturing or a combination of both (see Kneissl *et al.*, 2015; and references therein).



The tectonic activity of the Sirenum Fossae fault system has been dated back throughout the Early Hesperian Epoch [Anderson *et al.*, 2001], although a recent work suggests that it took place around 3.5 Ga ago, in the Late Hesperian [Kneissl *et al.*, 2015]. Both ages must be considered with caution since this last work focusses only in the NE part of the Eridania System, and these calculated ages only represent the age of the end of the formation or reactivation of a tectonic fault. Besides, Sirenum Fossae fault system may represent two or more separate episodes of tectonism [Lias *et al.*, 1999].

In the Ariadnes region, such a conjugate system results from the combination of two main directions for the wrinkle ridges: NW – SE ( $120^\circ - 300^\circ$ ) and NE – SW ( $30^\circ - 210^\circ$ ), which are perpendicular between them (Figure 3.2.a). Azimuthal analysis (Figure 3.2.i-A) reveals that the predominant direction of this ridges is NNW – SSE ( $170^\circ - 350^\circ$ ), as the result of the influence of both conjugate systems. Those northwest-trending ridges are consistently with possible radial dikes emplaced during the formation of the Tharsis rise (5,000 km to the ENE,  $\sim 80^\circ$ ) and other local stress centers as Hadriaca (4,000 km to the WSW,  $\sim 248^\circ$ ) and Tyrrhena (3,500 km to the W,  $\sim 260^\circ$ ) Paterae [Lias *et al.*, 1999]. Northeast-trending features are not consistent with Tharsis-related or basin-centered stresses (Hellas, Isidis). They might be related to Elysium volcano-tectonic activity, local thermal centers, regional volcanoes, or global isotropic stresses as the result of compressional forces [Watters, 1993; Schultz and Tanaka, 1994].



**Figure 3.2.i** Rose diagrams of the azimuthal directions followed by the (A) ridge crests, (B) wrinkle ridges, and (C) linear depressions or channels mapped for the Ariadnes basin (Figure 3.2.a). Directions were weighted by the segment lengths.



The most relevant feature of this complex inside the study area is a large graben that goes through the basin floor crossing the southern area from east to west. The tectonic structures are clearly present in the Caralis knob field and affect the materials of the *AHrp* unit. Also, a large parallel graben can be found 150 km to the south, outside of the study area (Figure 3.1.c). Such tectonic structures have around 2 to 4 km wide and 100 to 200 m in deep. Images reveal that the graben cross-cut *eAsp*, *AHrp*, *eHed* and *HNkf* materials (e.g., Figure 3.2.e) indicating that their formation post-dates both units' development.

In addition, several faults and ridges have been found affecting mainly the *AHrp* and *eHed* units (Figure 3.2.a), and where there is a clear tectonic and structural control of fluvial morphologies in locations. The tectonic control is not generalized, in any case. Azimuthal analysis (Figure 3.2.i-C) shows not a predominant direction for channels, but an NE – SW direction trend, which is almost perpendicular to the main trend for ridge crest. Interestingly enough, some alignments can be easily observed at the NW and SE of the study area, although the dust cover on Mars complicates the characterization of most of the faults in Ariadnes.

The ridge crests are mostly restricted to the Amazonian Hesperian ridged plains (*AHrp*). The structure of ridge crests are characterized by linear features with positive topography and a distinct cross-sectional profile, which is sharp and vertical on one side and more oblique on the other (Figure 3.6.a). The ridge origin is not clear, as they can result from different geological processes that may have co-occurred over time. The formation hypothesis include tectonic and impact deformation, degradation by fluvial and glacial activity, mass-wasting erosion, and volcanism [Anderson and Anderson, 2010]. As a result, it is not easy to establish a clear formation process for the ridge crests in Ariadnes. However, as they have a circular outline that is centered in both the Ariadnes and Caralis basins, it might represent structural rings associated with basins formation (Figure 3.2.a). On the contrary, they might also the result of mud or lava flows, which could have resulted from one or more thermal events [de Pablo and Fairén, 2004] or the sediment compaction under the Eridania Lake water

table [Irwin *et al.*, 2002]. The origin of structure and the ridge crests of Ariadnes will be further discussed in the Part 5.2.1 of this work.

The wrinkle ridges are linear arc-shaped or sinuous topographic highs, preferentially found in plains areas that have been interpreted as the result of the tectonic contraction that is sourced in deep-seated thrust faulting [Korteniemi *et al.*, 2014]. They have been compared to the terrestrial foreland basement uplifts [Golombek *et al.*, 2001], which vary in orientation and follow a circular outline that is similar to impact structures [Watters, 1993]. The wrinkle ridges are located mostly the central part and margin of the study area. In this regard, a cluster of wrinkle ridges was found on the east side following and fitting to the 177.5° E meridian. The predominant direction of this features according to the performed azimuthal analysis (Figure 3.2.i-B) reveals an N – S direction trend, with similarities to the NW – SE direction found for the ridge crests.

## ii. *Impact features*

The study area includes several old impact craters, which rim have been degraded and/or buried (Figure 3.1.a). Most of them are related to the *eNhp* and *eHed* units, as these old materials have been exposed to a long-term degradation over billions of years. Other craters were covered by deposits of the *HArp* unit leaving a reduced positive relief either in the rims and/or the central peak, as can be observed in Figure 3.2.d-A2, where there is also an example of an inverted crater. In addition, there are also many examples of fresh craters in the area (Figure 3.2.j), which most frequently occur on the western side of the study area. Some of them are so vast that the ejecta blankets have totally covered the units around. In this case, they have been considered as an independent unit, named as ‘impact crater and ejecta’ unit (*cr*) that was already described in the unit definition (Subpart 3.2.2viii).

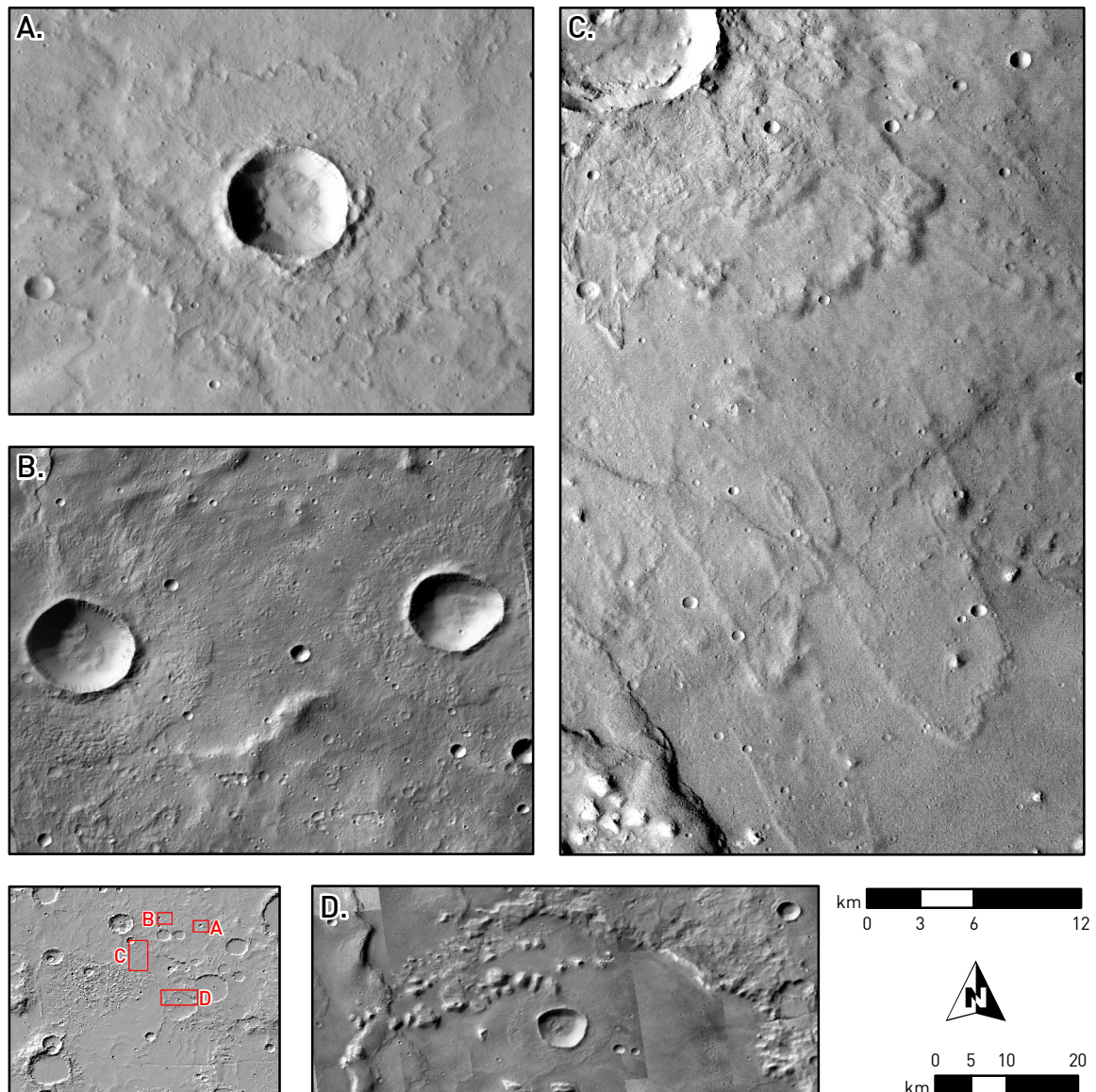
Impact craters offer a valuable information of the materials that they exhume. In this regard, they expose the underground materials to the exterior, and also provide evidence of the constitution of the impacted materials through the shape and texture of their ejecta. Some ejecta in the area show fluidized layered deposits, which

could have been formed when the ejected material at the time of the impact interact with the volatiles present in the subsurface or the atmosphere [Barlow and Robbins, 2014].

Interestingly, the study area shows a high diversity of morphologies and degradation stages of this sort of ejecta. In this regard, such kind of ejecta appears in [Figure 3.2.j-A](#), that is displayed as a single-layered ejecta (SLE) with a distal radial ridge with lobate or rampart morphology. If this deposit is nearly continuous and circular with a convex scarp, it is defined as single-layered ejecta pancake (SLEP), which some examples can be found affecting the *AHrp* unit ([Figure 3.2.j-B](#) and [D](#)). Such morphology represents the inner layer of a double-layered ejecta (DLE), which have lost the thin and outer layer by erosion [Barlow, 2006]. A DLE is shown in [Figure 3.2.j-C](#) that is overlapping a much larger multiple-layered ejecta (MLE) to the NW, which can be observed at regional scale (e.g., [Figure 3.2.a](#)).

As discussed in the Subpart 3.2.2vii, the crater infillings (*HAfc*) usually consists of a smooth and flat mixture of materials, including impact breccia and volcanic-derived materials as well as fluvial, glacial and gravitational deposits. The large and eroded crater in [Figure 3.2.j-C](#) is filled with materials of the *AHrp* unit, which show the presence of a small knob field on the upper right part of the image.

Indeed, the formation of the Ariadnes and Caralis basins has been associated with large impacts [e.g., Irwin *et al.*, 2004a]. However, they have a bowl-shaped morphology, lack of evident ejecta, and show different tectonic features around them (Section 3.2.3i), suggesting that they may result from a large mass-wasting or subsidence episode [e.g., Wilson and Head, 2002]. Nevertheless, both depressions show crater-like analogies, as the following: **1)** they may have hosted a lake [e.g., El-Maarry *et al.*, 2014a], **2)** the occurrence of the interior knob fields could be a remnant of central mound exposed to long-term degradation [Bennett and Bell III, 2016], **3)** the crater floors use to have chaotic [Korteniemi and Hargitai, 2014] or polygonal terrains [El-Maarry *et al.*, 2014b]. In any case, the interpretation of the origin of the Ariadnes and Caralis basins will further discussed in Part 5.2.1.



**Figure 3.2.j** Examples of craters and associated morphologies in Ariadnes. (A) A single-layer rampart ejecta crater; (B) Two single-layered ejecta pancakes (SLEPs); (C) External area of a double-layered ejecta crater overlapping the outer layer of a multiple-layered ejecta, and (D) Rim and SLEP of an older impact crater affecting a crater field. Images are HRSC (A, C) and CTX (B, D). Scale in the upper position corresponds to A to C, whereas the scale below corresponds to D.

### iii. *Erosional features*

In this work, only channels and the delineation of the knobs outcrop are mapped as erosional features. Channels consist of shallow and linear depression that have been likely modeled by water (or ice). The channel morphologies are usually found carving the *eNhp* and *eHed* units, and some traces of channelized structures are easily recognized in *eAsp*. In addition, the rims of large craters are usually carved

by abundant and dense linear gullies, which flow in both directions, from the upper side of the rim to inside and outside the crater.

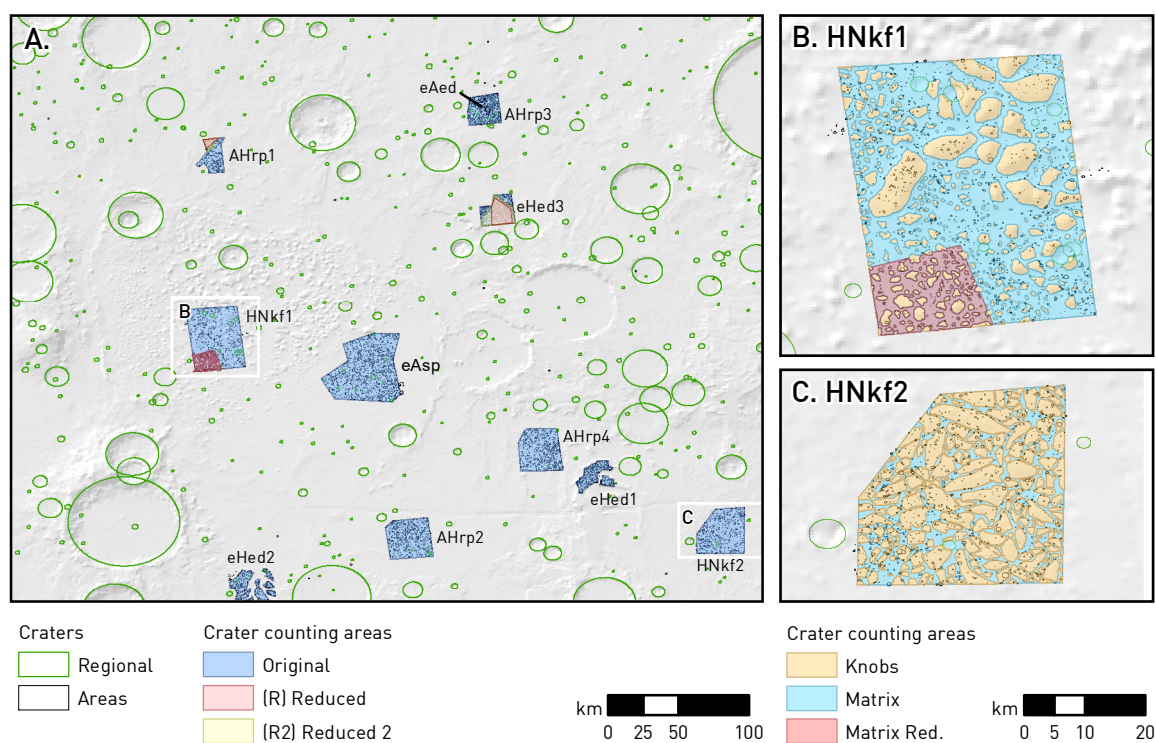
On the other hand, the knob clusters currently appear following a chaotic pattern at the bottom of the basins, where are embedded by a darker material surround the bright rounded and eroded, light-toned reluctant materials forming the knobs. Some of them are covered with a dark and resistant capping layer, which protect the lower deposits promoting its preservation in form of a mesa-like structures (see Subpart 3.2.2ii). The processes involved in the formation, deposition and preservation will be discussed below in Parts 5.2.2 and 5.2.3.



### 3.3 DATING

#### 3.3.1 SELECTED AREAS

Age is a critical variable to unlock the chronostratigraphic framework, which is indeed essential to understand the geological evolution of a given area. In this regard, the chronostratigraphy of Ariadnes area has been obtained through the CSFD analysis (Subpart 2.2.4ii) of the areas including the most relevant geological units of the region. Well-exposed deposits, which are covered by CTX images (Subpart 2.2.3ii), has been selected as the crater counting locations. In addition, HRSC imagery (Subpart 2.2.3iv) has been used to obtain regional ages through the statistical calculations of the impact craters for the area covering the whole study area (Figure 3.2.a).



**Figure 3.3.a** Map of the selected areas to apply crater counting resumed in the Table 3.3.a. (A) Original (blue polygons) and reduced (red and yellow polygons) areas for the region, which results are showed in the Figure 3.3.c. (B and C) Shows the areas of the knobs and matrix for *HNkf1* and *HNkf2* occurrences, respectively. These results are showed at Figure 3.3.d. The background image is a MOLA shadow relief map.

The Amazonian Hesperian ridged plains (*AHrp*) and the early Hesperian Electris deposits (*eHed*) units expose considerable and uniform surfaces with enough image coverage to apply the crater counting. In this regard, four polygons were



selected around the *AHrp* unit, which were named as *AHrp*<sub>1</sub> to *AHrp*<sub>4</sub>. The *AHrp*<sub>2</sub> and *AHrp*<sub>4</sub> consist of 800 km<sup>2</sup> parallelograms in Southwestern Ariadnes that are characterized by the occurrence of some structures, as ridges (Figure 3.3.a). Although the *AHrp*<sub>1</sub> and *AHrp*<sub>3</sub> polygons are located in complex surfaces which are not unequivocally categorized inside this unit, they were selected to obtain additional information and improve the final results in age. On this subject, *HArp*<sub>1</sub> varies gradually to the Hesperian Noachian knob fields (*HNkf*) unit that make difficult to distinguish among them. The selected area is mostly lacking knobs, although a large sector is affected by impact ejecta, what lead us to performing the analysis in two alternative smaller or reduced areas (*AHrp*<sub>1R</sub> and *AHrp*<sub>1R2</sub>; Table 3.3.a). In particular, *AHrp*<sub>3</sub> was selected to age the unit and recognize resurfacing events that have occurred in the region. *AHrp*<sub>3</sub> is located in the northeast part of the study area where includes some *eAed* unit outcrops and outlines a complex terrain that is affected by ridges and channels.

The Amazonian deposits are also wide enough to apply the crater-counting technique. In this particular, a large sector (~2,000 km<sup>2</sup>, Table 3.3.a) with a uniform exposition of sediments was selected for characterizing the age of the early Amazonian smooth plains (*eAsp*). The sector covering the early Amazonian evaporites deposits (*eAed*), however, show an uneven distribution and preservation of outcrops, and has been split in several polygons which analysis has to address the border effect.

The early Hesperian Electris deposits (*eHed*) is a quite controversial unit which definition and origin have been highly discussed in the literature (Section 3.2.2.iii). Therefore, some sectors containing Electris have been selected for the purpose of corroborating (or contradicting) its homogeneity and consistency. The *eHed*<sub>1</sub> sector is defined inside the continuous extension of the mesa on the southwestern side, which exposes the unit outcrops so continuously than is enough to perform a good estimation of the age through crater counting. To same extent, the *eHed*<sub>2</sub> sector is emplaced on the remaining surface of a degraded mesa in the southern margin, that is carved by several channels. This sector defines a fragmented surface which age

analysis can produce more uncertain results. The eHed<sub>3</sub> area was selected corresponding to the diversity of the ‘coating’ variety of the unit. As the eHed<sub>3</sub> surface is interrupted by a scarp, two alternative polygonal subsets named as eHed<sub>3</sub>R and eHed<sub>3</sub>R<sub>2</sub> (Table 3.3.a, note the height statistics) have been defined to obtain ages through crater counting.

**Table 3.3.a** Crater counting data of the different polygons obtained from the MOLA DTM dataset. In blue the original area polygons.

NAME	AREA ( <i>km</i> <sup>2</sup> )	Heights from MOLA DTM ( <i>m</i> )					
		MIN	MAX	RANGE	MEAN	STD	MEDIAN
AHrp1	320	468	704	236	543	48	535
AHrp1R	36	529	628	99	557	20	552
AHrp1R2	50	525	628	103	552	19	548
AHrp2	826	219	513	294	344	54	334
AHrp3	454	759	977	218	893	31	890
AHrp4	842	-33	211	244	82	39	73
eAsp	1930	-318	102	420	-47	64	-57
eAed	35	851	913	62	879	11	878
eHed1	293	249	640	391	488	61	487
eHed2	331	671	987	316	820	49	813
eHed3	420	938	1243	305	1070	59	1073
eHed3R	207	1022	1220	198	1103	37	1099
eHed3R2	323	975	1220	245	1086	45	209
HNkf1	1582	-465	482	947	-74	111	-87
HNkf1_knb	569	-305	482	787	-4	125	-16
HNkf1_knb2	39	-3	252	255	166	54	183
HNkf1_mx	1014	-465	212	677	-114	79	-115
HNkf1R	215	-177	286	463	-30	66	-38
HNkf1R_knb	80	-155	286	441	-11	75	-17
HNkf1R_mx	147	-177	212	389	-40	58	-46
HNkf2	955	-279	70	349	-155	43	-159
HNkf2_knb	598	-260	70	330	-151	41	-154
HNkf2_mx	355	-279	-16	263	-163	46	-169

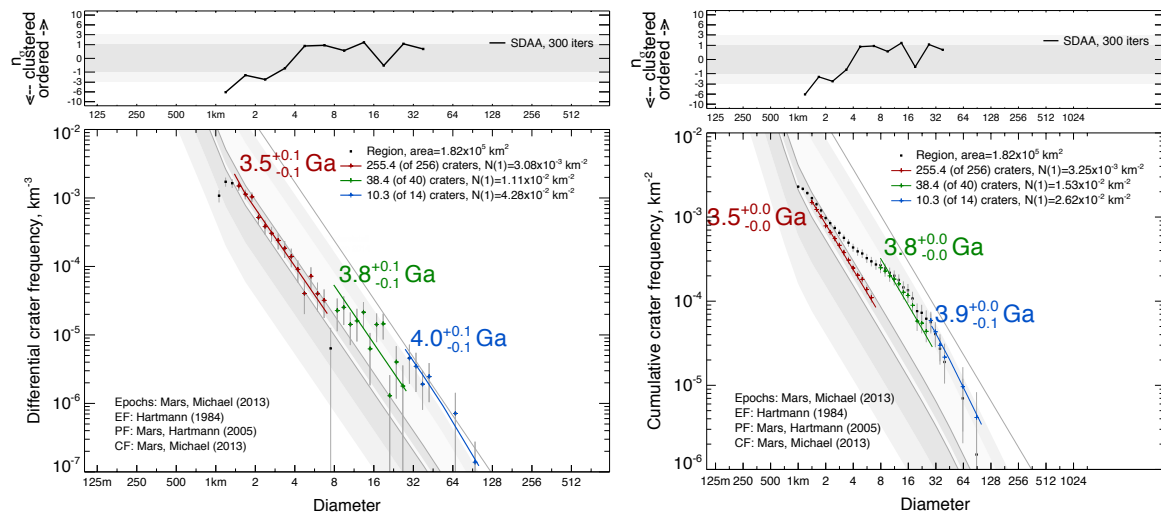
The Hesperian Noachian knob field unit (*HNkf*) is one of the essential units in this study. However, since it captures the transition between the Noachian and Hesperian ages, its dating is greatly challenging. The outcrop distribution of the unit is quite complex and shows two well-differentiated subunits as the knob fields and the knob-aggregating matrix (delineation procedure is described in Subpart 2.2.4i).

In this unit, two large sectors, HNkfi and HNkf2 (Table 3.3.a), were outlined to date the central and southeast fields, respectively. As HNkfi sector has a highly heterogeneous surface, it was resized to a smaller polygon in its southwest fraction (HNkfiR; Table 3.3.a). Despite there is no evidence of mesas on that side, it has a relatively uniform pattern of knobs, which can be enough to obtain a reliable age. In this regard, those new sectors that only cover either the knobs or the matrix fraction are named adding ‘\_knb’ and ‘\_mx’ (Table 3.3.a) in an attempt to distinguish both materials. Therefore, HNkfi\_knb2 (Table 3.3.a) is restricted to the top of the two largest mesas in the HNkfi sector (Figure 3.3.a).

### 3.3.2 RESULTS OF CRATER COUNTING

Through the CSFD analyses for the entire area (Figure 3.3.b), we obtained three very distinctive range of ages. Interestingly enough, the results are very similar when using different methods as the differential and cumulative crater frequency. On this respect, an age of formation of about  $3.9 \pm 0.1$  Ga, as well as two main resurfacing ages of 3.8 and 3.5 Ga, have been obtained (Figure 3.3.b) after the analysis using the *Hartmann* [2005] chronology function. Furthermore, the randomness analysis reveals a possible clustering in the smallest craters (from 1 to 3 km; Figure 3.3.b). Most of the others randomness analysis points to a trend to order but inside the reliability range (Appendix 8.1).

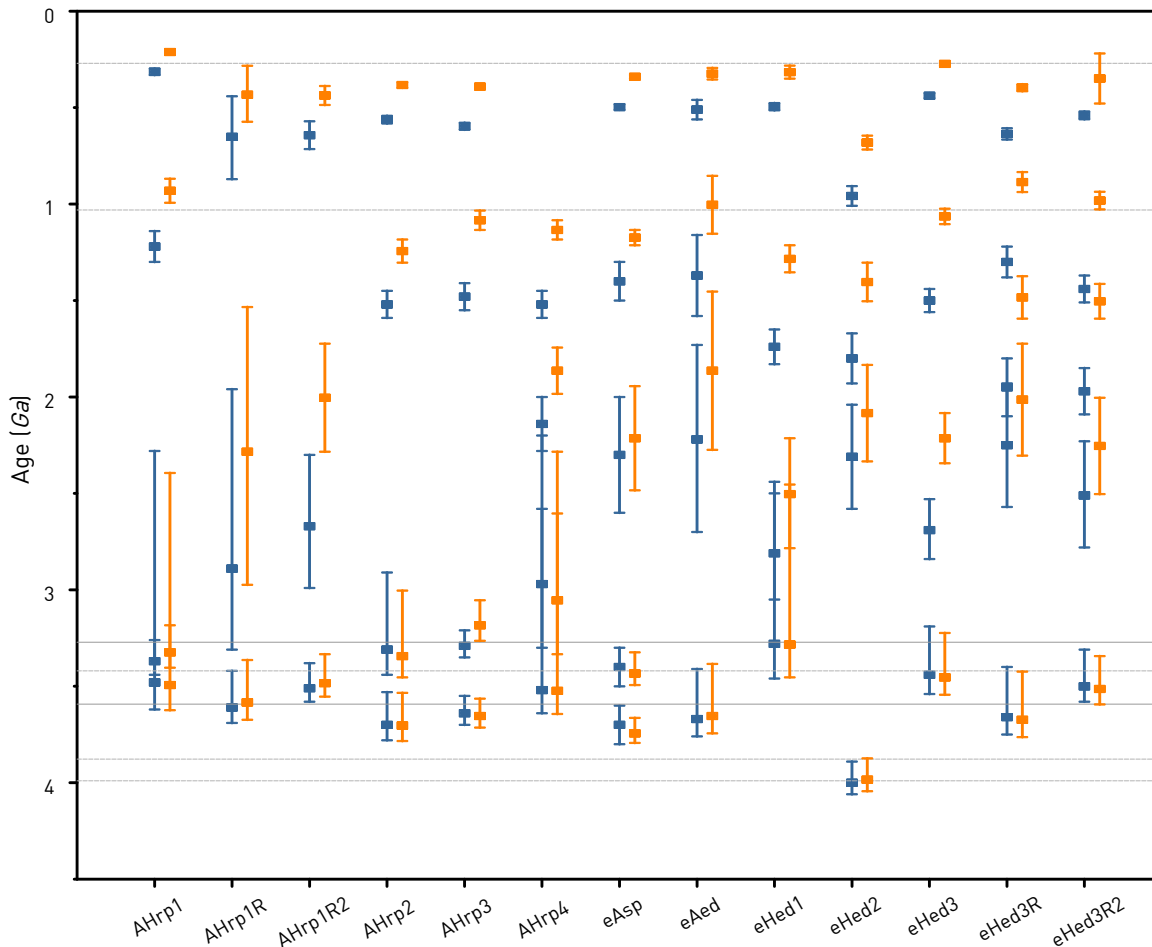
The same CSFD analyses were performed for the sectors defined above that outline representative areas for the different geological units in the Ariadnes region (Table 3.3.a and Figure 3.3.a). All these results are summarized in Figure 3.3.c and Figure 3.3.d, which provide the results for the geological units in Ariadnes, as well as specific ages for the Hesperian Noachian knob field (*HNkf*) unit, respectively. Although the two most used chronology functions [*Neukum and Ivanov*, 1994; *Hartmann*, 2005] were used in each case (see Part 2.2.4ii), only the *Hartmann* [2005] function will be considered in this analysis. The complete set of CSFD and calculated age plots for each area can be found in Appendix 8.1.



**Figure 3.3.b** Differential (left) and cumulative (right) crater size-frequency distributions (CSFD) for the complete Ariadnes region and calculated ages (obtained as explained in Subpart 2.2.4ii). The upper scatterplot shows the results of the randomness analysis.

Starting with the *AHrp* unit associated crater counting areas, some ages can be interrelated among the different CSFD calculated ages. The randomness analysis suggests that *AHrp*<sub>1</sub>R<sub>2</sub> is the more solid polygon derived from *AHrp* unit (Appendix 8.1). The average of formation (oldest) ages for this unit is  $3.6 \pm 0.2$  Ga, actually the same age than the calculated for *AHrp*<sub>1</sub>R area (Figure 3.3.c). Some other recurrent age is  $1.5 \pm 0.1$  Ga, which is found in any sector excepting in *AHrp*<sub>1</sub> providing an age of  $1.2 \pm 0.1$  Ga instead (and not observable for the reduced polygons *AHrp*<sub>1</sub>R and *AHrp*<sub>1</sub>R<sub>2</sub>). Furthermore, the youngest resurfacing age found in this region is  $\sim 0.6$  Ga, which is in every *AHrp* polygon excepting *AHrp*<sub>4</sub> (Figure 3.3.c). In few cases, an age of  $3.2 \pm 0.2$  Ga was obtained, whereas between 2 and 3 Ga there is a not well-defined resurfacing age (Figure 3.3.c).

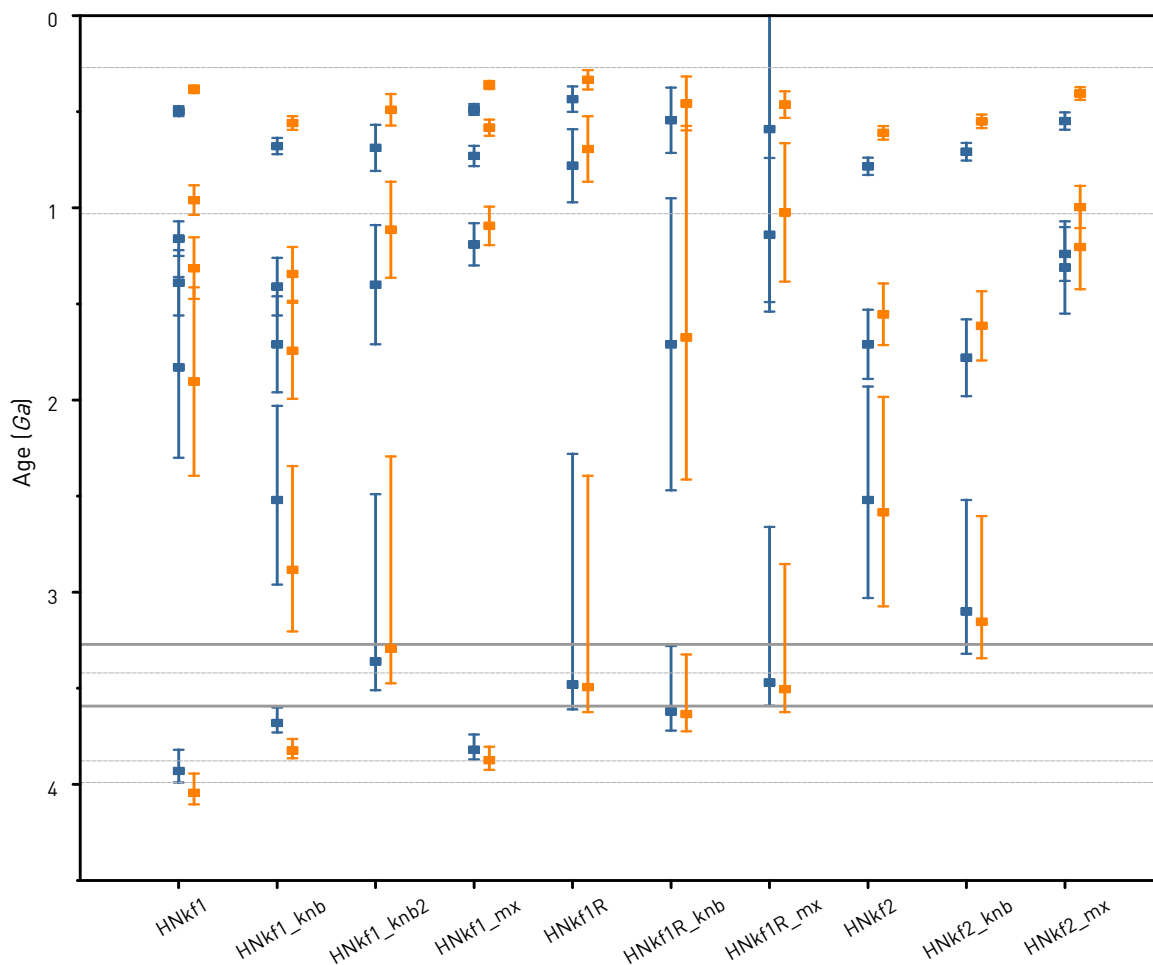
The different ages obtained in the *eHed* unit polygons does not match among them as well as the ages recorded for the areas within the previous unit (Figure 3.3.c). In *eHed*, the average formation age is around  $3.5 \pm 0.3$  Ga, but providing a much older date as  $4.0 \pm 0.1$  Ga in the *eHed*<sub>2</sub> polygon, that currently records ages older than the other areas for this unit (Figure 3.3.c). In addition, ages ranging around 0.6 Ga,  $1.8 \pm 0.1$  Ga and  $2.5 \pm 0.3$  Ga were obtained as resurfacing ages, which are similar to the recorded in the *AHrp* unit (Figure 3.3.c).



**Figure 3.3.c** CSFD ages obtained in the different sectors and units excluding *HNkp*. They have been calculated using the Hartmann (blue) and Neukum-Ivanov (orange) chronology systems (Subpart 2.2.4ii). The derived transition ages of Hartmann [Michael, 2013] are displayed as horizontal lines. The CSFD plots can be found in Appendix 8.1.

The CSFD ages calculated for in the *eAed* unit does not show significant differences with the *AHrp3* polygon (Figure 3.3.c). Consequently, either the *eAed* unit is nearly synchronous or its formation did not affect the crater distribution. The most remarkable difference between them is the resurfacing age of  $2.2 \pm 0.5$  Ga recorded in *eAed* against the  $3.3 \pm 0.1$  Ga that is obtained in *AHrp3* (Figure 3.3.c). The younger age in *eAed* could be related with the  $2.5 \pm 0.3$  Ga date found in *eHed* unit areas that suggests it could be the result of the same resurfacing event. The *eAsp* unit also shows ages with the same age ranges as *AHrp*, though whereas the  $3.4 \pm 0.1$  Ga age is lacking and also the  $2.3 \pm 0.3$  Ga event correspondent to the ones in *eHed* and *eAed* (Figure 3.3.c).





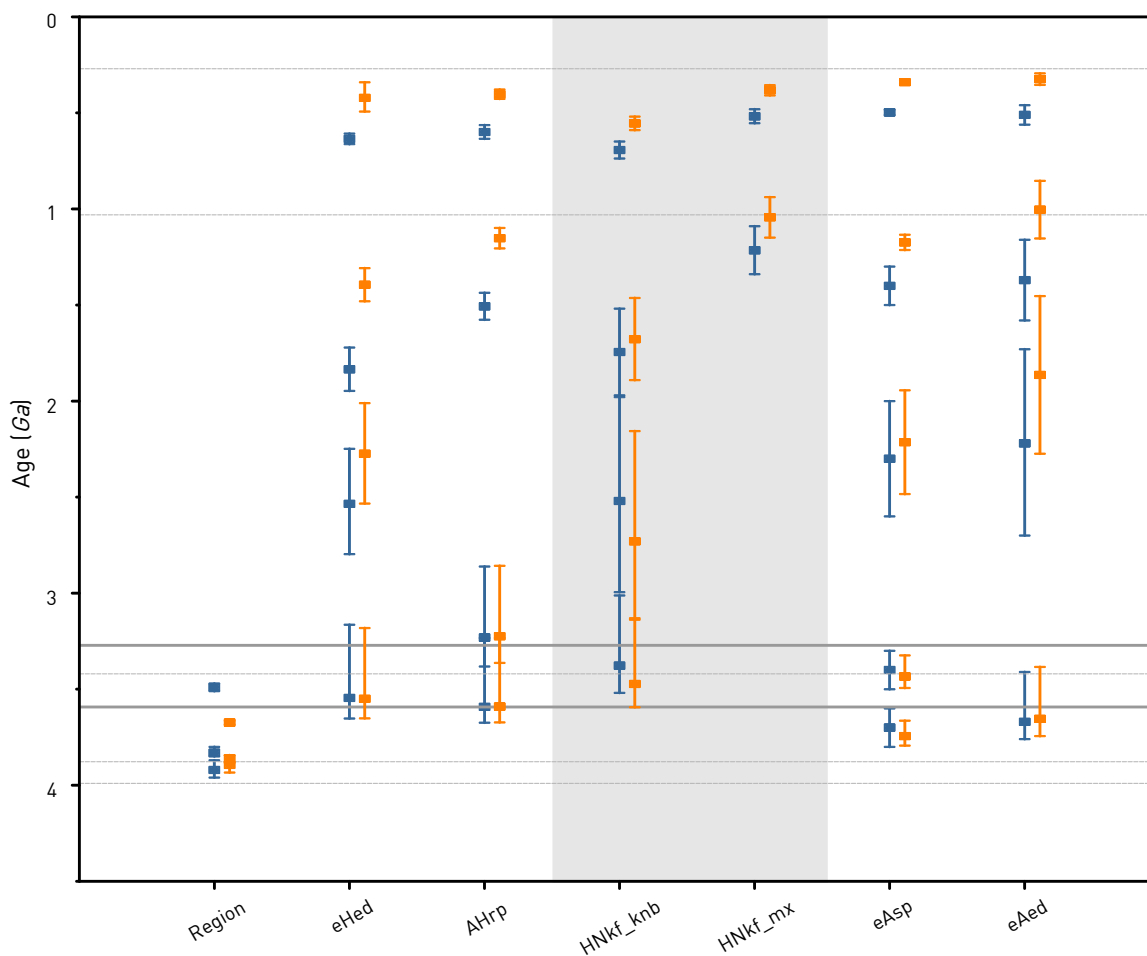
**Figure 3.3.d** CSFD formation and resurfacing ages for the *HNkp* unit obtained after using the Hartmann (blue) and Neukum-Ivanov (orange) chronology systems (Subpart 2.2.4ii). The derived transition ages of Hartmann [Michael, 2013] are displayed as horizontal lines. The CSFD plots can be found in Appendix 8.1

The interpretation of results in the polygons including the *HNkp* unit are uncertain since distinguishing among craters affecting knobs versus craters impacted on the matrix is not simple. In addition, as pointed out in the Part 3.3.1, a cautious interpretation to the crater counting analysis must be done in this unit as is affected by the border effect (border craters were included in the analysis) and their surfaces are heterogeneous, since knob fields are indeed a complex topography. Interestingly, when no differentiation between knobs and matrix is made, the result of CSFD analysis (Figure 3.3.d) is a remarkable difference in ages between the *HNkp1* and *NHkp1R* polygons. On the other hand, two different trends in ages are obtained when the crater counting analysis is separately applied in matrix and knobs. In this regard, the knobs areas show resurfacing ages that are older than for the polygons analyzed

for the matrix. The average ages for the two knob fields are  $3.4 \pm 0.3$  Ga and  $1.7 \pm 0.2$  Ga (Figure 3.3.d). It is noteworthy that the older ages recorded in the matrix have been achieved with the few craters which are also emplaced at the boundary the knob fields, and they should not be representative for the crater-counting of the *NHkp* matrix. While in both matrix and knobs areas a  $1.2 \pm 0.1$  Ga age is obtained, two younger resurfacing ages as 0.5 and 0.7 Ga for matrix and knobs can be found, respectively, which might date the same resurfacing event (Figure 3.3.d).

### 3.3.3 CHRONOSTRATIGRAPHIC CONSTRAINTS

The range of ages obtained by analyzing of the CSFD provide some results that can be used to infer the main events that affected Ariadnes surface, but are not very conclusive. However, when the age results are combined with the cartographic and stratigraphic relations between units (Subchapter 3.2), it is possible to obtain a valuable information with regard to the chronostratigraphic framework of the region (Figure 3.3.e) when the average age is calculated (see Part 3.3.2). Although such dates are not strictly the formation ages of the geological units, they can be used to estimate the age of units with unidentified ages. As a result, the older ages in the region (ranging ~4 to 3.8 Ga) are consistent with the age of the early Noachian highland plains (*eNhp*). Furthermore, the age at ~3.5 Ga is recorded in most of the units sampling areas (Figure 3.3.e), displaying a common age for the whole region of Ariadnes. On this respect, as the early Hesperia Electris deposits (*eHed*) unit underlay the Amazonian-Hesperian ridge plains unit (*AHrp*) and directly overlies *eNhp* unit, it is reasonable to assume that the event at ~3.5 Ga may represent the formation an age of *eHed*. In this context, the formation of *AHrp*, could have taken place along the Hesperian-Amazonian transition (~3.2 Ga). The *eAsp* materials lie over *AHrp* in a thin layer that may reflect the surface underneath and no formation age could be addressed from CSFD analysis. Consequently, the formation of the matrix, after considering its morphological and stratigraphic relations with the units above, likely meets the date for the origin of the *AHrp* unit. This suggests a common origin for them as the crater counting shows no difference in the result. This could be the case for *eAed* and *AHrp* units as well (Figure 3.3.e).



**Figure 3.3.e** Average ages for the Ariadnes units resulting from the crater size-frequency distribution (Figure 3.3.c and d). They were calculated in different sampling areas (Figure 3.3.a), obtained with the Hartmann (blue) and Neukum-Ivanov (orange) chronology systems (Subpart 2.2.4ii). Hartmann derived transition ages [Michael, 2013] displayed as horizontal lines.

Different successive events of resurfacing can be inferred from the chronostratigraphic results of the Ariadnes units (Figure 3.3.e). At around 2.4 Ga, one or several resurfacing events might have affected *eHed*, the knob fields (*HNkf*), and the Amazonian deposits (*eAsp* and *eAed*). From 2.0 to 1.0 Ga, there are successive resurfacing events that unequally affect the Ariadnes basin surface. The first one could have affected to *eHed* and the knob fields at ~1.8 Ga, which could be followed by a set of events affecting the *AHrp* unit, the knobs field matrix (*HNkf\_mx*), and the Amazonian deposits (*eAsp* and *eAed*) at about 1.4 Ga. At around 0.6 Ga, a last resurfacing event could have likely affected entirely to the study area surface. Interestingly enough, such a later event has not been detected by the regional analysis, very likely as a consequence of disregard the smaller craters.

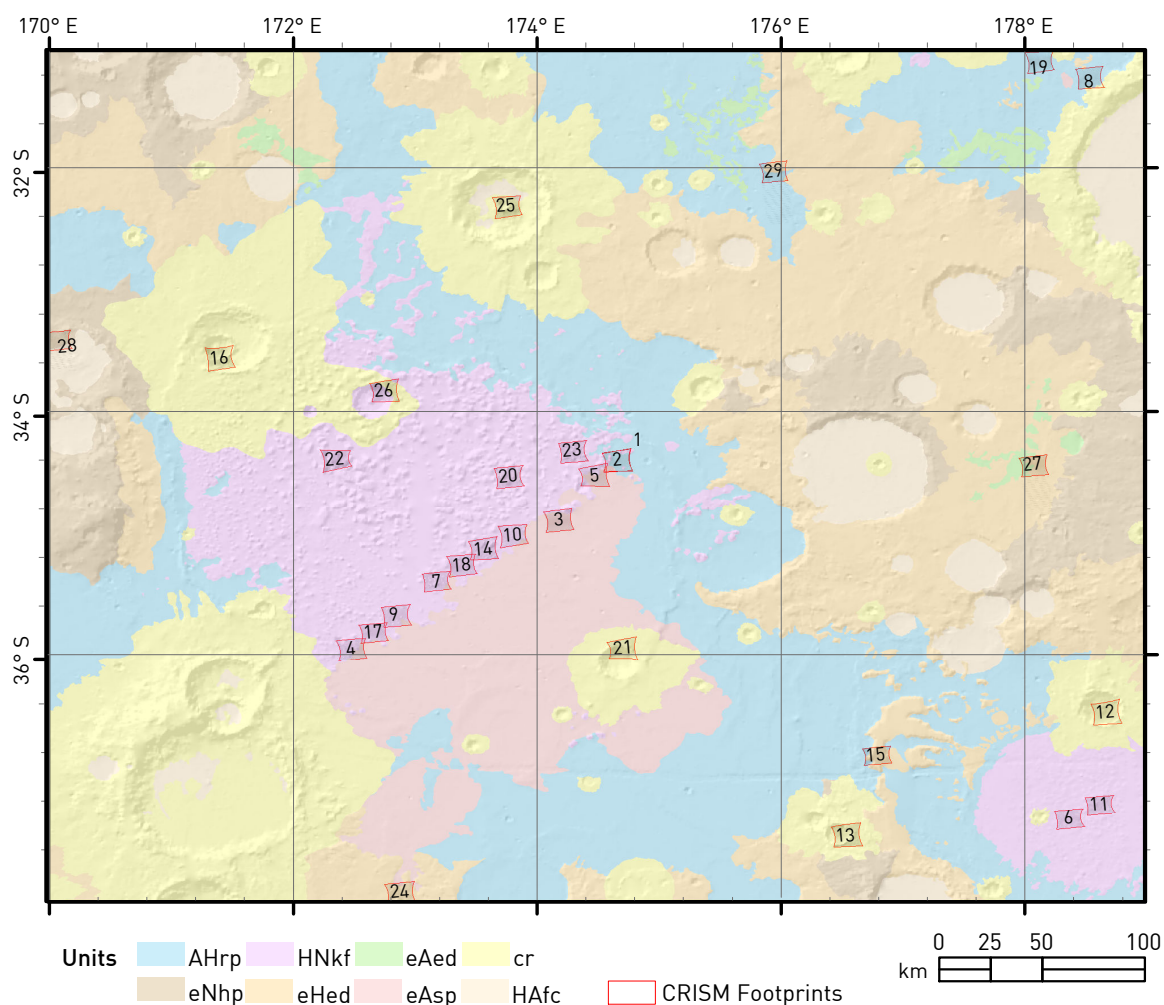
### 3.4 SPECTRAL ANALYSIS

#### 3.4.1 VISIBLE NEAR INFRARED CRISM DATA

Any CRISM cube available for the region at the time of the study (29 in total; [Table 3.4.a](#) and [Figure 3.4.a](#)) were analyzed as described in Subpart 2.2.4iii. Attending to their distribution ([Figure 3.4.a](#)), most of them cover the boundary between the Ariadnes central knob field (*HNkf*) and the *eAsp* unit. On the other hand, the coverage for other units is limited and providing limited information on the mineral composition of the surface.

**Table 3.4.a** List of CRISM cubes analyzed for the Ariadnes study area named as FRT000XXXX, where XXXX is the label. The table includes acquisition information, center coordinates and the number of ROIs couples for each cube (spectra of interest and nearby neutral spectra used for ratio). The highlighted rows mark the cubes shown in [Figure 3.4.d](#).

#ID	LABEL	ACQUISITION		COORDINATES		ROIs PAIRS
		DATE	TIME	LAT	LON	
1	<b>06458</b>	17/06/07	21:59	-34.31	174.65	3
2	067fe	04/07/07	08:35	-34.29	174.65	0
3	<b>07c54</b>	19/09/07	10:08	-34.80	174.17	2
4	07dcd	24/09/07	13:33	-35.86	172.47	0
5	<b>07f7e</b>	30/09/07	17:19	-34.43	174.46	3
6	08612	23/10/07	07:38	-37.22	178.42	3
7	<b>08c90</b>	16/12/07	18:57	-35.29	173.23	7
8	090d8	29/12/07	02:29	-31.17	178.58	0
9	09dd2	10/02/08	06:37	-35.57	172.90	2
10	0a0d1	21/02/08	13:51	-34.90	173.80	12
11	0a106	22/02/08	14:14	-37.11	178.68	6
12	0a3ff	04/03/08	21:22	-36.41	178.66	7
13	0a57e	10/03/08	00:49	-37.39	176.53	1
14	0a923	23/04/08	05:23	-35.03	173.55	5
15	0b4a6	30/06/08	00:47	-36.70	176.77	0
16	<b>0caf3</b>	25/09/08	09:14	-33.51	171.46	3
17	0d0f4	23/10/08	02:59	-35.72	172.65	1
18	11d69	01/04/09	09:52	-35.16	173.37	0
19	11d8f	02/04/09	10:12	-31.01	178.11	0
20	1256d	29/04/09	03:38	-34.44	173.83	2
21	12955	10/05/09	10:47	-35.85	174.69	0
22	<b>13786</b>	03/07/09	22:01	-34.26	172.34	7
23	<b>1669b</b>	09/02/10	19:36	-34.23	174.35	2
24	16872	14/02/10	23:00	-37.85	172.87	0
25	17d97	11/04/10	10:34	-32.24	173.75	0
26	18fe7	25/05/10	14:56	-33.73	172.74	2
27	1b81a	22/10/10	14:56	-34.58	178.10	0
28	1c280	28/11/10	15:14	-33.46	170.08	0
29	1c5c1	10/12/10	22:44	-32.17	175.97	0

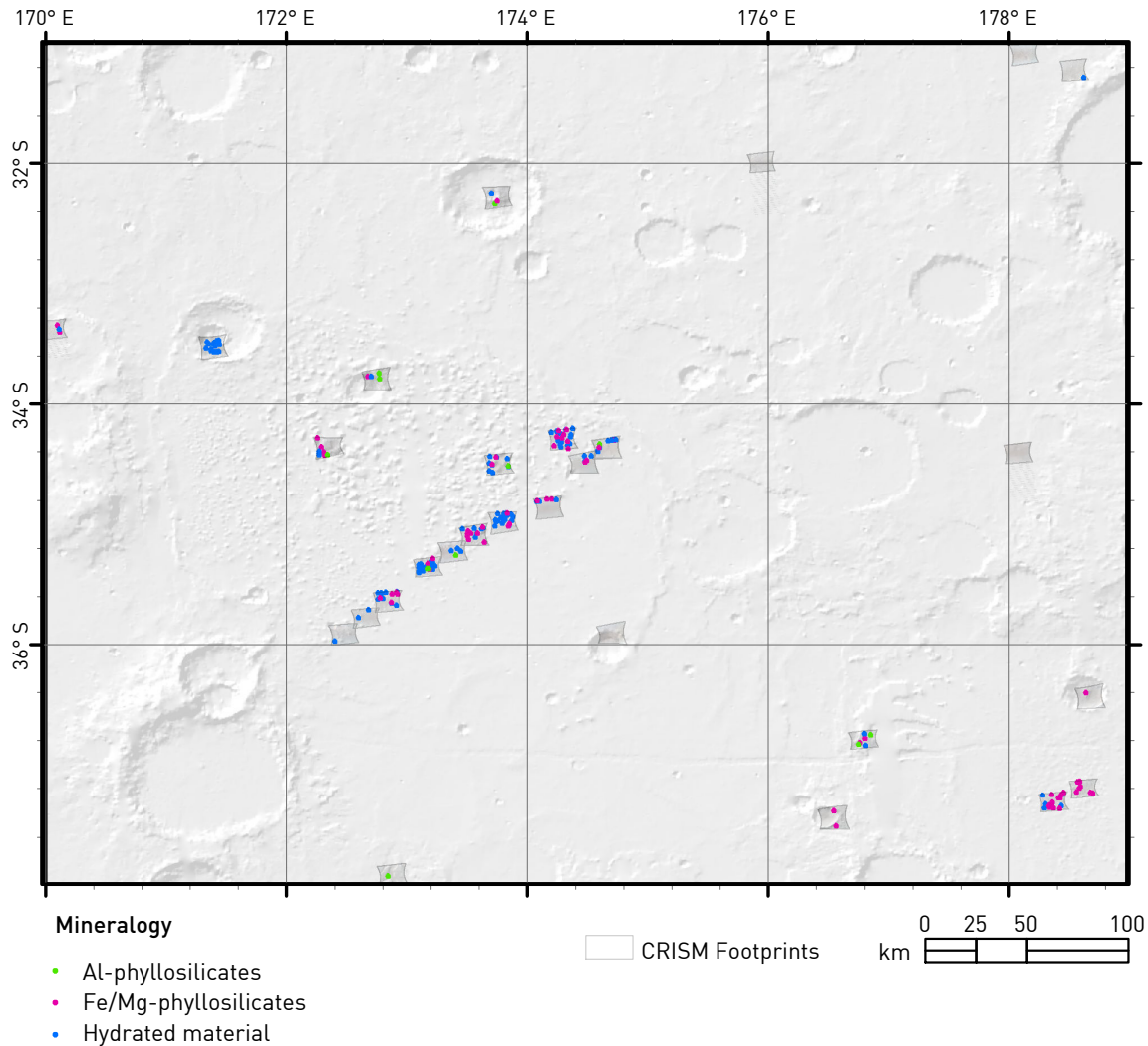


**Figure 3.4.a** CRISM cubes footprints (#ID) listed in the [Table 3.4.a](#) (1 and 2 are overlapped images). The background is a combination of a MOLA shaded relief and a geological map showing the units identified in Subchapter 3.2.

As explained in the Subpart 2.2.4iii, different indexes were applied to all the CRISM cubes to identify the mineral composition of the geological units in Ariadnes basin area. The application of the phyllosilicate index (PHY) [e.g., *Viviano-Beck et al.*, 2014], which characterizes the presence of hydroxylated minerals including phyllosilicates, has provided the clearest results ([Figure 3.4.b](#)). Using this algorithm, the hydrated Fe/Mg-OH bearing minerals (e.g., Fe/Mg-phyllosilicates) will appear red, whereas the hydrated Al/Si-OH bearing minerals (e.g., Al-phyllosilicates or hydrated silica) will alternatively appear green, or cyan. Blue color defines other hydrated minerals such as sulfates, hydrated silica, carbonates, or ice water content. In this regard, the hydroxylated minerals in the study area occur mostly in the *NHkf*

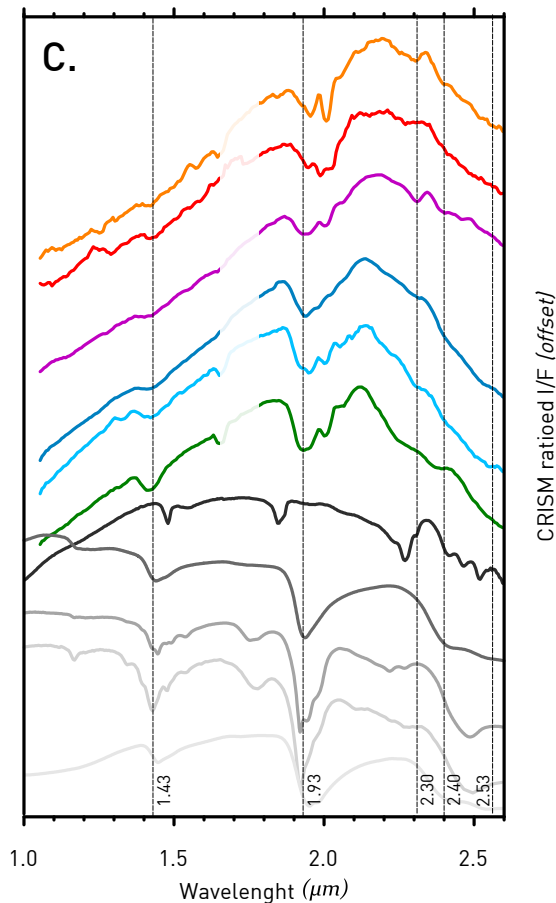
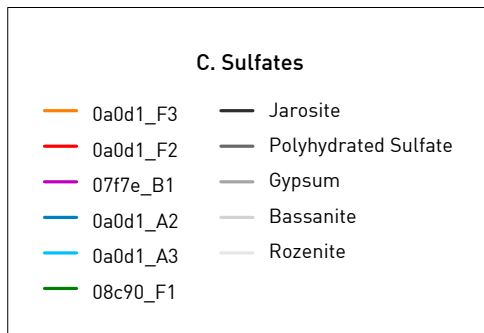
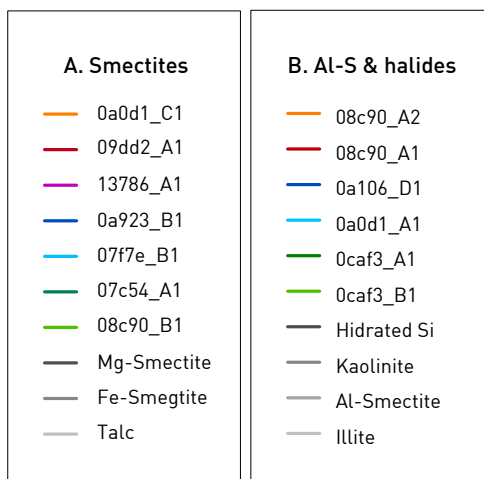
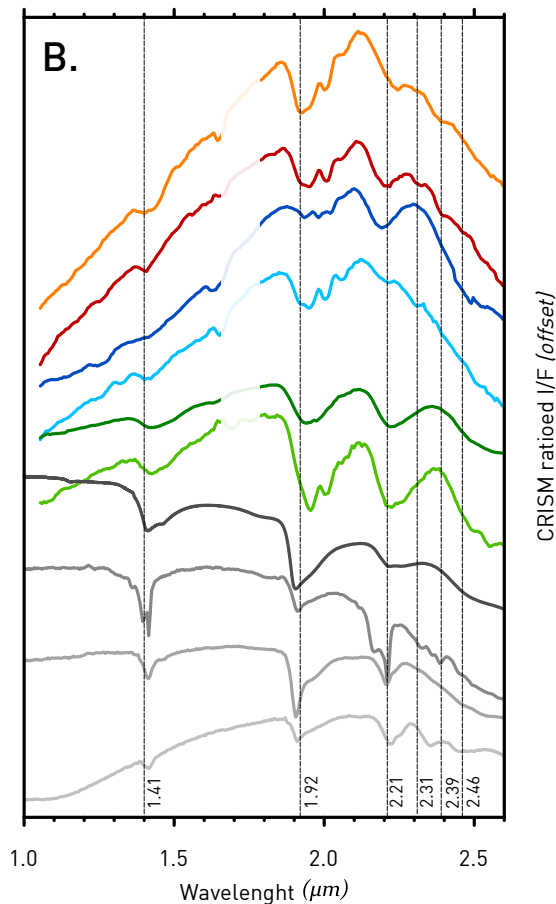
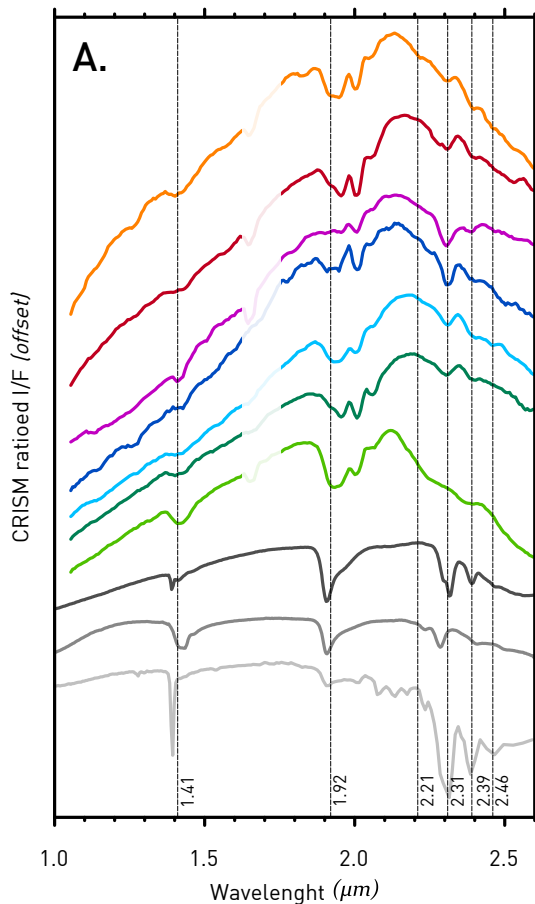


unit (Figure 3.4.b) having a strong signal in the layered light-toned knobs. Other units are spectrally neutral in the CRISM spectra.



**Figure 3.4.b** Ariadne mineralogy characterized through the phyllosilicate index (D2300; BD2200; BD1900R) [Viviano-Beck *et al.*, 2014] displayed above the CRISM cubes footprints. The background image is a MOLA shaded relief.

As the other applied indexes provide undefined results, the phyllosilicate index was used to obtain traces of aqueous alteration. Several regions of interest (ROIs) were selected in the locations where the signal was the stronger. Each spectrum was ratioed with each corresponding neutral ROI located in the same data column, as described in Subpart 2.2.4iii. In this regard, 68 spectra profiles were obtained and then classified by their absorption bands and general shape. The best ratioed spectral signatures are shown in Figure 3.4.c compared to laboratory analysis of Terrestrial samples (Appendix 8.4).



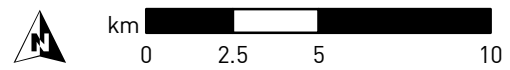
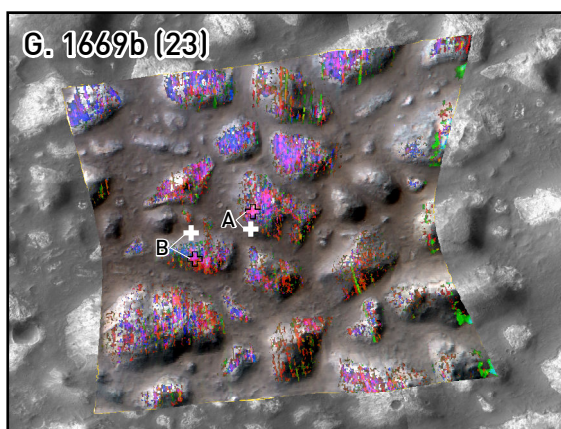
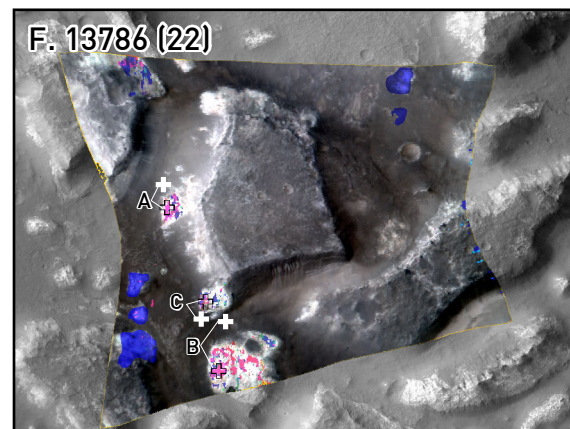
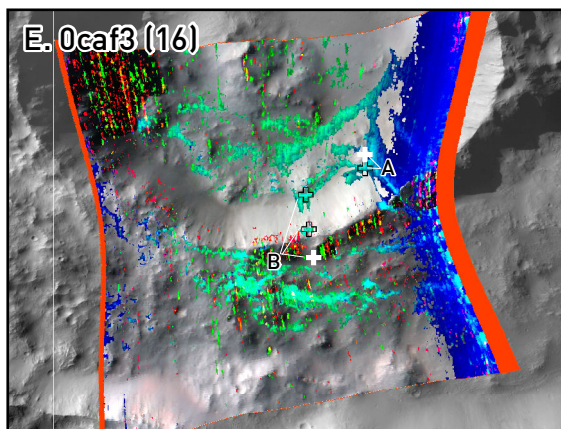
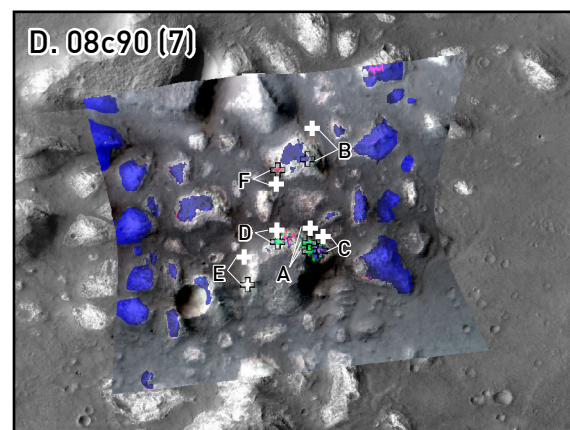
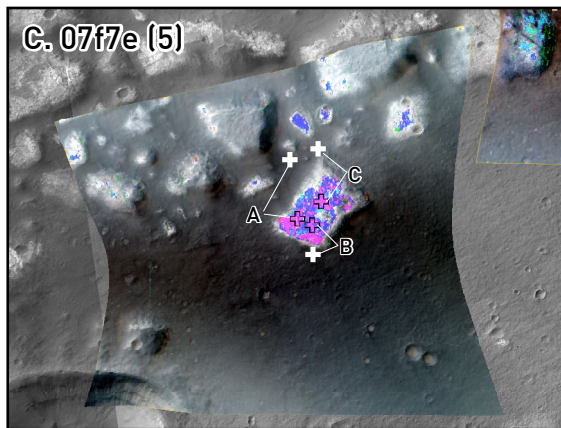
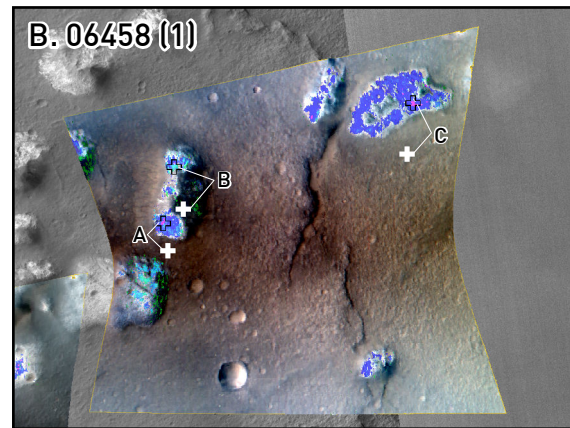
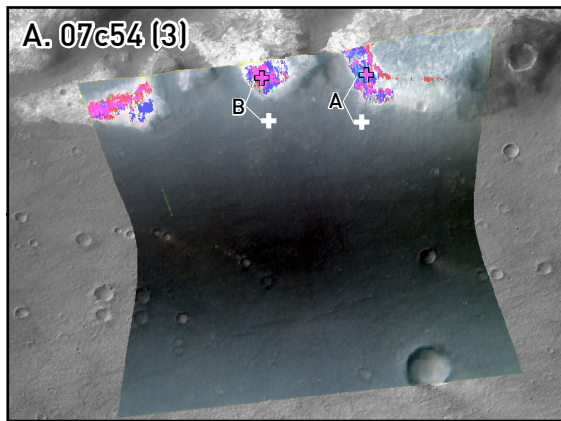
**Figure 3.4.c (Previous page)** CRISM (color) and lab (gray) spectra of (A) Mg- and Fe-smectite, (B) Al-smectite plus halides, and (C) sulfate bearing materials in the Ariadnes study area. The spectra are obtained as the average of a 3 x 3 pixel ROIs rated by a nearby spectrally neutral region of the same size. The major spectral absorptions are indicated as vertical lines and labels refer to the image id (FRT0000XXXX) followed by the ROI id. Lab spectra sources are described in Appendix 8.4.

Smectites are 2:1 phyllosilicate minerals detected in the 1.0 – 2.6  $\mu\text{m}$  spectral region by absorptions at  $\sim 1.9 \mu\text{m}$  and  $\sim 2.3 \mu\text{m}$  due to cations in the octahedral site; often accompanied by vibrational absorptions caused by overtones at  $\sim 1.4 \mu\text{m}$  related to OH, as well as at  $\sim 2.4 \mu\text{m}$  associated to the presence of cations [e.g., Clark *et al.*, 1990]. In this regard, the specific absorptions are a function of the cation composition. Mg-rich smectites, as saponite (which ideal formula is described as  $(\text{Ca}/2, \text{Na})_{0.3}(\text{Mg}, \text{Fe}^{2+})_3(\text{Si}, \text{Al})_4\text{O}_{10}(\text{OH})_2 \cdot 4(\text{H}_2\text{O})$ ), typically have absorptions at  $1.38 - 1.39 \mu\text{m}$  and  $2.31 - 2.32 \mu\text{m}$  (Figure 3.4.c-A), while Fe-smectites, as nontronite (ideal formula  $\text{Na}_{0.3}\text{Fe}_2^{3+}(\text{Si}, \text{Al})_4\text{O}_{10}(\text{OH})_2 \cdot n\text{H}_2\text{O}$ ), have band centers near  $1.43 \mu\text{m}$  and  $2.29 \mu\text{m}$  (Figure 3.4.c-A).

In the Ariadnes area, several spectra have strong absorptions at  $\sim 1.9 \mu\text{m}$  and  $\sim 2.31 \mu\text{m}$ , and weaker absorptions at  $\sim 1.4$  and  $\sim 2.39 \mu\text{m}$  (Figure 3.4.c-A). They are consistent with Mg-bearing smectites, as saponite. In the oaod1\_C1 and o9dd2\_A1 spectra (Figure 3.4.c-A), the absorption at  $\sim 2.31 \mu\text{m}$  is broader and reaches the  $2.29 \mu\text{m}$ , which may correspond to a Fe-smectite or a mineral mixing [McKeown *et al.*, 2009]. The mineral mixing is likely causing the  $\sim 1.9 \mu\text{m}$  absorption to be less clear [Ehlmann *et al.*, 2009]. However, the strong doublet at  $\sim 2.29$  and  $\sim 2.31 \mu\text{m}$ , which are observed in talc-rich samples, indicate that the Ariadnes deposits may include talc-saponite mixed-layer clays, which are common in seafloor sediments [Cuadros *et al.*, 2013]. Talc (ideal formula  $\text{Mg}_3\text{Si}_4\text{O}_{10}(\text{OH})_2$ ) is a hydrothermal alteration of non-aluminous magnesium silicates, with higher the Fe-content, more similar to saponite.

**Figure 3.4.d (Next page)** Phyllosilicate index (R: D2300; G: BD2200; B: BD1900R; see [Viviano-Beck *et al.*, 2014] overlapping false color data (R:  $2.53 \mu\text{m}$ ; G:  $1.51 \mu\text{m}$ ; B:  $1.08 \mu\text{m}$ ) from projected CRISM cubes. Cubes are identified with FRT0000xxxx (#ID in brackets in Table 3.4.a) which location is shown in Figure 3.4.a. Black crosses spot the ROIs from where spectra profiles were extracted, while white crosses mark the neutral spectra used to calculate the rationed spectra of Figure 3.4.c.





**Mineralogy**

- Al-phyllsilicates
- Fe/Mg-phyllsilicates
- Hydrated material

**ROI pairs**

- ⊕ Target
- ⊕ Neutral

Additional spectra in the Ariadnes area show strong absorptions at  $\sim 1.9 \mu\text{m}$  as well, but at  $\sim 2.21 \mu\text{m}$  instead  $\sim 2.31 \mu\text{m}$ . They also have weaker absorptions at  $\sim 1.4 \mu\text{m}$ , and less frequently at  $\sim 2.39 \mu\text{m}$  and  $\sim 2.46 \mu\text{m}$  (Figure 3.4.c-B). The group of Al-smectites, as montmorillonite (ideal formula  $(\text{Na,Ca})_{0.3}(\text{Al,Mg})_2\text{Si}_4\text{O}_{10}(\text{OH})_2 \cdot n(\text{H}_2\text{O})$ ), shows similar absorptions at  $\sim 1.9 \mu\text{m}$  and  $\sim 2.2 \mu\text{m}$  (Figure 3.4.c-B), though some other Al-phyllosilicates, included in the Kaolinite-group and Al-micas, has similar spectral signatures. Kaolinite (ideal formula  $\text{Al}_2\text{Si}_2\text{O}_5(\text{OH})_4$ ) has a prominent  $1.4 \mu\text{m}$  absorption feature related to vibrations of hydroxyl groups, as well as a doublet at  $2.16$  and  $2.21 \mu\text{m}$  (Figure 3.4.c-B) resulting from a combination of vibrations of Al-OH [Clark *et al.*, 1990]. The o8c9o\_A1 and oa1o6\_D1 ratioed spectra exhibit a broader absorption band at  $\sim 2.2 \mu\text{m}$ , which may correspond to the presence of Kaolinite. On the other hand, Al-micas as for instance illite (ideal formula  $(\text{K,H}_3\text{O})(\text{Al,Mg,Fe})_2(\text{Si,Al})_4\text{O}_{10}[(\text{OH})_2,(\text{H}_2\text{O})]$ ) exhibit a  $2.2 \mu\text{m}$  band, and can be characterized by additional bands at  $2.26 \mu\text{m}$ ,  $2.35 \mu\text{m}$ , and  $2.44 \mu\text{m}$  related to the stretch and bend combination of Al-OH bonds (Figure 3.4.c-B) [Clark *et al.*, 1990]. Such combination of absorptions cannot be observed in any of the spectra and should be discarded from the phyllosilicates in Ariadnes.

Hydrated silica (ideal formula  $\text{SiO}_2 \cdot n\text{H}_2\text{O}$ ) have absorptions at  $2.21 - 2.22 \mu\text{m}$  related to Si-OH combination tones as well as some other absorptions as at  $2.26 \mu\text{m}$  resulted from H-bound Si-OH,  $1.91 \mu\text{m}$  associated to structural  $\text{H}_2\text{O}$ , and  $1.4 \mu\text{m}$  from structural  $\text{H}_2\text{O}$  and OH [Stolper, 1982]. The  $\sim 1.4 \mu\text{m}$  band center shift to longer wavelengths when increasing the crystallinity of hydrated silica [Rice *et al.*, 2013]. Similar characteristics can be found in the ocaf3\_A1 and ocaf3\_B1 ratioed spectra (Figure 3.4.c-B). Hydrated silica can form through several abiotic pathways, and display a diverse degree of crystallinity as noncrystalline (hydrated glass), weakly crystalline (opal) and crystalline (quartz) [Smith *et al.*, 2013]. Interestingly, the  $1.4 \mu\text{m}$  band location on these ratioed spectra in Ariadnes matches with opal, and their location inside an impact crater suggests that it was either exhumed or, most likely, produced by the impact itself.



Finally, other spectra found to have absorptions at  $\sim 1.93 \mu\text{m}$  and  $\sim 1.4 \mu\text{m}$  but do show a strong band neither at  $\sim 2.2 \mu\text{m}$  nor  $\sim 2.3 \mu\text{m}$  (Figure 3.4.c-C). In this regard, OH- or H<sub>2</sub>O-bearing sulfates are characterized by absorptions at  $1.4 \mu\text{m}$  related to OH,  $\sim 1.9 \mu\text{m}$  associated to H<sub>2</sub>O, and a number of absorptions in the  $2.1 - 2.6 \mu\text{m}$  region that are attributed to OH or H<sub>2</sub>O combinations or overtones and/or S-O bending or stretching overtones [Cloutis *et al.*, 2006]. In any case, the identification of polyhydrated sulfates is challenging along the  $1.0 - 2.6 \mu\text{m}$  region and cannot be confirmed in the area. However, some examples with distinct and similar spectral characteristics that have been detected on Mars show jarosite (ideal formula  $(\text{Na,K,H}_3\text{O})\text{Fe}_3(\text{SO}_4)_2(\text{OH})_6$ ; [Farrand *et al.*, 2006], gypsum (ideally  $\text{CaSO}_4 \cdot 2(\text{H}_2\text{O})$ ) [Gendrin *et al.*, 2005], bassanite (ideally  $2\text{CaSO}_4 \cdot (\text{H}_2\text{O})$ ) [Wray *et al.*, 2010], and rozenite (ideally  $\text{Fe}^{2+}\text{SO}_4 \cdot 4\text{H}_2\text{O}$ ) [Gilmore *et al.*, 2011] as sulfate minerals with a similar absorption pattern (Figure 3.4.c-C). The oaod1\_F2, oaod1\_F3 and o7f7e\_B1 spectra show a similar pattern, as they have absorptions at  $\sim 2.30 \mu\text{m}$  and  $\sim 2.40 \mu\text{m}$ , which may result from a mixture of sulfate (as gypsum or bassanite) and smectite. In addition, as oaod1\_A2, oaod1\_A3 and o8c9o\_F1 have absorption bands at  $1.43 \mu\text{m}$ ,  $1.93 \mu\text{m}$ ,  $\sim 2.4 \mu\text{m}$  and  $\sim 2.5 \mu\text{m}$  as well, it suggests the occurrence of sulfates in the area.

Although chlorides lack diagnostic absorption features in the visible and near-infrared, it is possible to identify them using CRISM cubes [Glotch *et al.*, 2010]. However, as the CRISM coverage was limited, which prevented its identification, THEMIS TI (Part 3.4.2) and DCS (Part 3.4.3) was used to detect the Cl-bearing salts [Osterloo *et al.*, 2010].

### 3.4.2 INFRARED THEMIS DATA AND DERIVED THERMAL INERTIA

The thermal inertia (TI) is the ability of any material to conduct and store heat [e.g., *Kahle et al., 1976; Kieffer et al., 1977*]. Materials with low TI have low thermal conductivity, which implies that its surface heats during the day and cools during the night at a rate faster than another material with higher TI values. This effect is caused by a non-efficient distribution of the heat to the subsurface by conduction. In planetary surfaces, the TI is essentially independent of local time, latitude, and season, though is driven by the particle size, bedrock outcrop, rock abundance, and degree of cementation [*Mellon et al., 2000; Putzig and Mellon, 2007*]. As thermal inertia strongly correlates with apparent grain size [*Jakosky, 1986; Jakosky and Christensen, 1986*], the higher the TI, the larger the particle size, as well as the greater the degree of consolidation (see [Table 3.4.b](#)) [*Jones et al., 2014, and references therein*]. Therefore, while the Martian global dust is characterized by low TI and high albedo, high values of TI and low albedo are typical of rock and duricrust occurrence, displaying the least higher values of albedo [*Jones et al., 2014; and references therein*].

**Table 3.4.b** Relation of the martian surface materials thermal inertia and their particle size and/or degree of the consolidation range reproduced from [*Jones et al., 2014*]

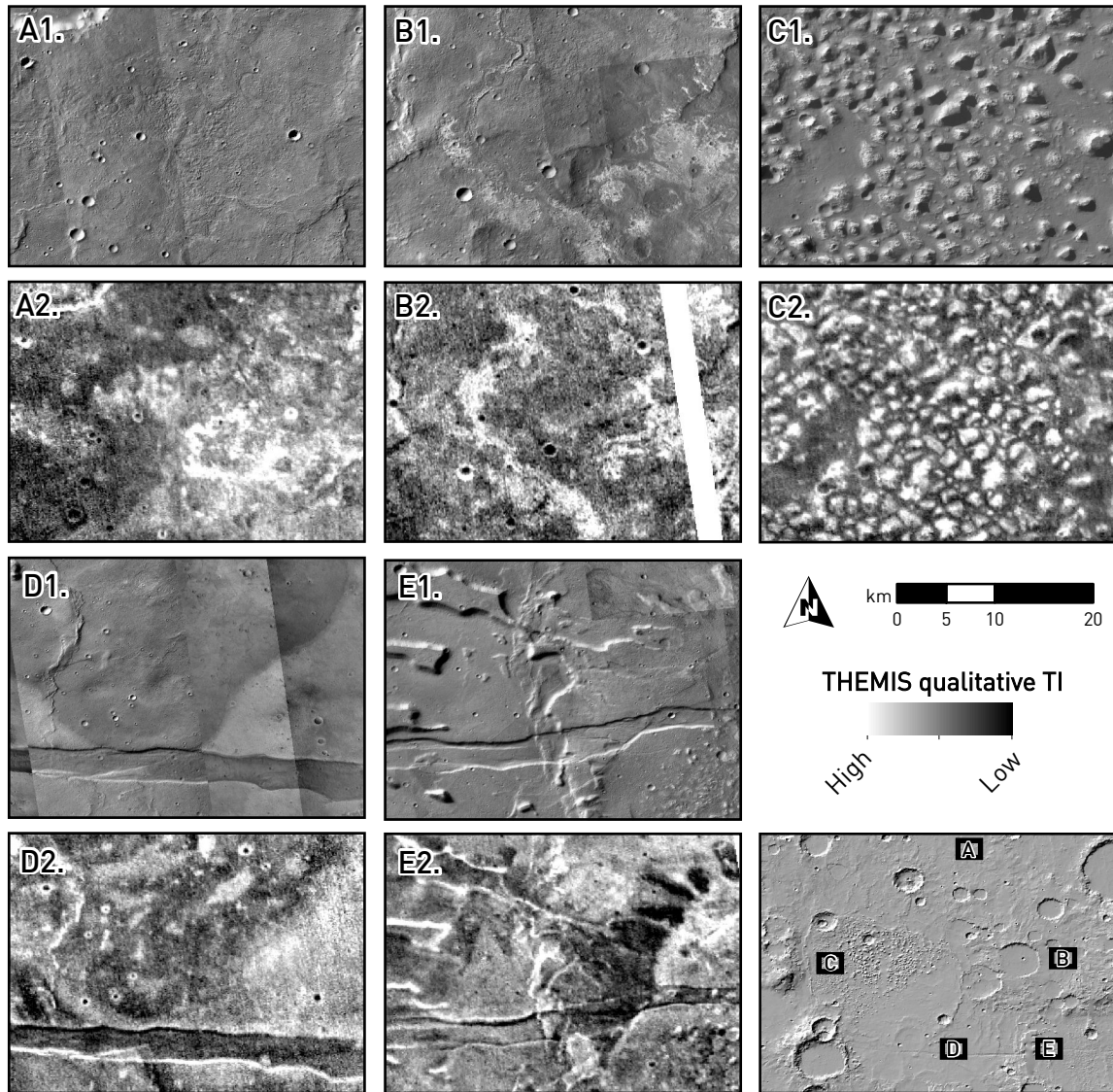
MATERIAL	DIMENSIONS ( <i>grain size</i> )*	THERMAL INERTIA ( <i>tiu</i> )	ALBEDO
<b>Dust</b>	2-6 $\mu\text{m}$	20-150	> 0.27
<b>Sand</b>	60-2000 $\mu\text{m}$	150-400	< 0.15
<b>Duricrust</b>	Grains 100-300 $\mu\text{m}$ Bulk 0.6-3 mm	350-600	< 0.15
<b>Granules / Coarse sand</b>	2-4 mm	400-800	< 0.15
<b>Pebbles / bedrock</b>	4-250 mm	800-2068	< 0.15
<b>Boulders / Ice-cemented soil</b>	> 250 mm	> 2068	< 0.1
<b>Ice</b>	-	> 2500	> 0.4

\* Grain size classified according to the Wentworth scale [*Wentworth, 1922*].

On Mars, TI provides information on the distribution of exposed surface materials, which have a diverse composition and are found in a wider range of states of consolidation. Soils, sediments, pebbles, and boulders, are globally distributed,

some of them distinguishable from high-resolution image textures. The global dust storms occur on Mars episodically, and cover the surface with a fine lamina of dust that forms part of the regolith. Fine dust particles ( $\sim 1 - 10 \mu\text{m}$ ) remain in suspension indefinitely [Toon *et al.*, 1977], but larger grains of dust and silt (around  $60 \mu\text{m}$ ) are lifted, transported through the atmosphere, and eventually fall covering the martian surface with a fine-grained layer of regolith. The heaviest and largest particles (up to  $\sim 0.1 \text{ mm}$ ) move by saltation [Almeida *et al.*, 2008] and may also be lifted and transported over mayor distances by the atmospheric currents. Coarse-grained sand (up to  $1 - 5 \text{ mm}$ ) may be winnowed along short distances and accumulated as aeolian lag deposits. As dusty surfaces hide the features and material outcrops and bedrocks by a fine layer, they can disturb the bedrock detection by remote sensing. TI provides a way of sensing the physical properties of shallow subsurface materials that may be obscured by thin coverings of dust, and revealing patterns and shapes indistinguishable on visible images. The [Figure 3.4.e](#) shows some examples for the identification of features and materials in the area of study by their appearance trough visible (directly related to albedo variation) and TI derived from THEMIS IR data.

In Ariadnes, chloride deposits were identified by their spectral signature in localized spots [Osterloo *et al.*, 2008b]. The extension of these salt deposits is difficult to observe on visible imagery ([Figure 3.4.e-A1](#) and [B1](#)), while are sharper in thermal images to display high values in thermal inertia than their surroundings ([Figure 3.4.e-A2](#) and [B2](#)). The combination of images shown in [Figure 3.4.e-A](#) allows to distinguish the aeolian Electris deposits (*eHed*) –with lower TI values and similar albedo– from the evaporites that underlay below dust deposits. In addition, it is also possible to differentiate a shoreline like morphology outlining the basin boundary in the SE of the image. In the [Figure 3.4.e-B](#), the effect is more evident, where some of the covered material is recognized by high albedo values. The high TI signal matches the inverted channel even when this is covered with other deposits.



**Figure 3.4.e** CTX visible images (numbers 1) and THEMIS derived thermal inertia image (numbers 2) [Christensen et al., 2013] mosaics, for some regions of interest in the Ariadnes study area. The evaporite deposits (*eAed*; A and B) and the knobs (*HNkf*; C and D) show the highest thermal inertia values. In other areas, it is possible to observe differences in texture and composition non-observables in the visible images (E).

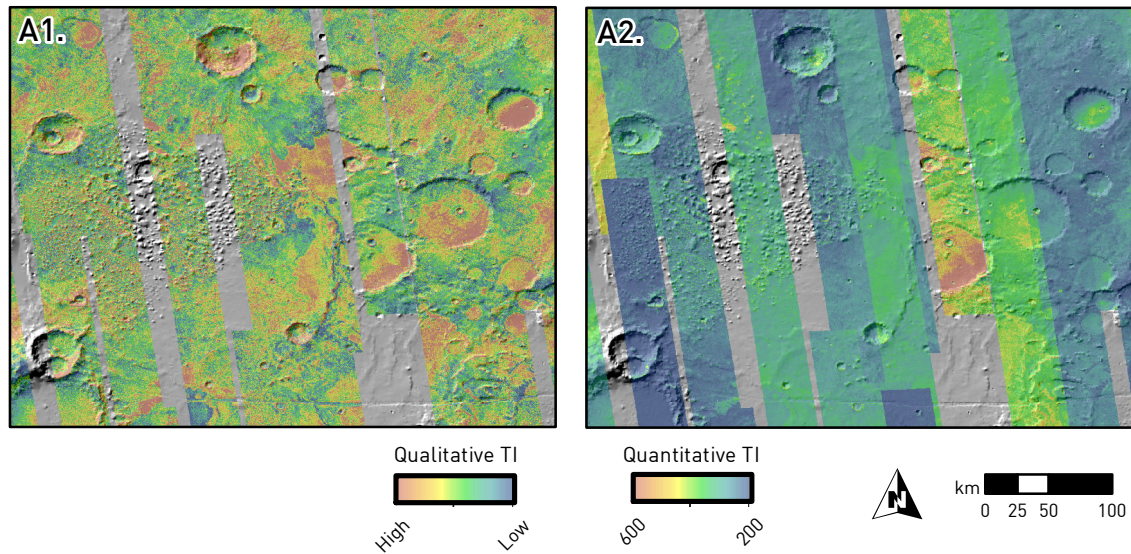
This revealing effect occurs in the knob fields as well (Figure 3.4.e-C1 versus C2), where the knobs materials are more visible in Figure 3.4.e-C2 by the thermal properties than in the visible images. In addition, the TI allows inferring the size and shape of knobs when the dark (low albedo) matrix between them is not thermally influent. This sensing is especially useful in the mapping process and permits to observe information otherwise hidden. In this case, it facilitates the observation of the real extension and pattern distribution of knobs.

The effect is especially dramatic in [Figure 3.4.e-D-1](#) and [D2](#), where some knobs in CTX visible images cannot be identified, but they are observable in the THEMIS derived TI. Indeed, in these images it is also possible to see tectonics lineaments. In this regard, ridge crest and graben rims are lighter (displays higher thermal inertia) as result of the topographic effect and the exposition of less degraded material. In addition, the sharp border between Amazonian Hesperian ridged plains (*AHrp*) and early Amazonian smooth plains (*eAsp*) is sharp in both albedo and TI, which suggests a textural and/or compositional difference.

The [Figure 3.4.e-E1](#) and [E2](#) show more complex cases, where sedimentary units and erosive structures are also affected by tectonics. In this case, several deposits with compositional and/or textural differences were formed before the graben formation. It should be noted that the boundary between the deposits that are surrounding the basin of this field is extraordinarily clear. It displays low TI and an albedo ranging from medium to high values, while the peripheral deposits have a higher TI and a slightly lower albedo. Based in these effect, we can interpret that the sedimentary deposits are either more consolidated/coarse-grained or have a different composition.

The [Figure 3.4.f](#) shows the qualitative and quantitative THEMIS IR thermal inertia mosaics for the entire Ariadnes basin area (Subpart 2.2.3v). Although the qualitative data do not provide quantitative thermophysical or compositional information about the surface, they are extremely useful as a survey tool, especially in areas with materials that exhibit a wide range of thermophysical properties. As can be observed in [Figure 3.4.f-A](#), the highest IT values concentrate into the largest impact crater basins, as part of the flat-floor crater infilling (*HAfc*), and in some crater rims (*cr*). There are also other high-TI patches matching the ridge plains (*AHrp*) and the evaporite deposits (*eAed*) ([Figure 3.4.e-A](#) and [B](#)). The knob fields (*HNkf*) unit also display a particular pattern showing a high TI in the knobs and a much lower TI in the embedding matrix ([Figure 3.4.e-C](#)). The lowest TI occurs in some impact crater rims and ejecta deposits, and also in shadow areas, resulting from a topography effect.



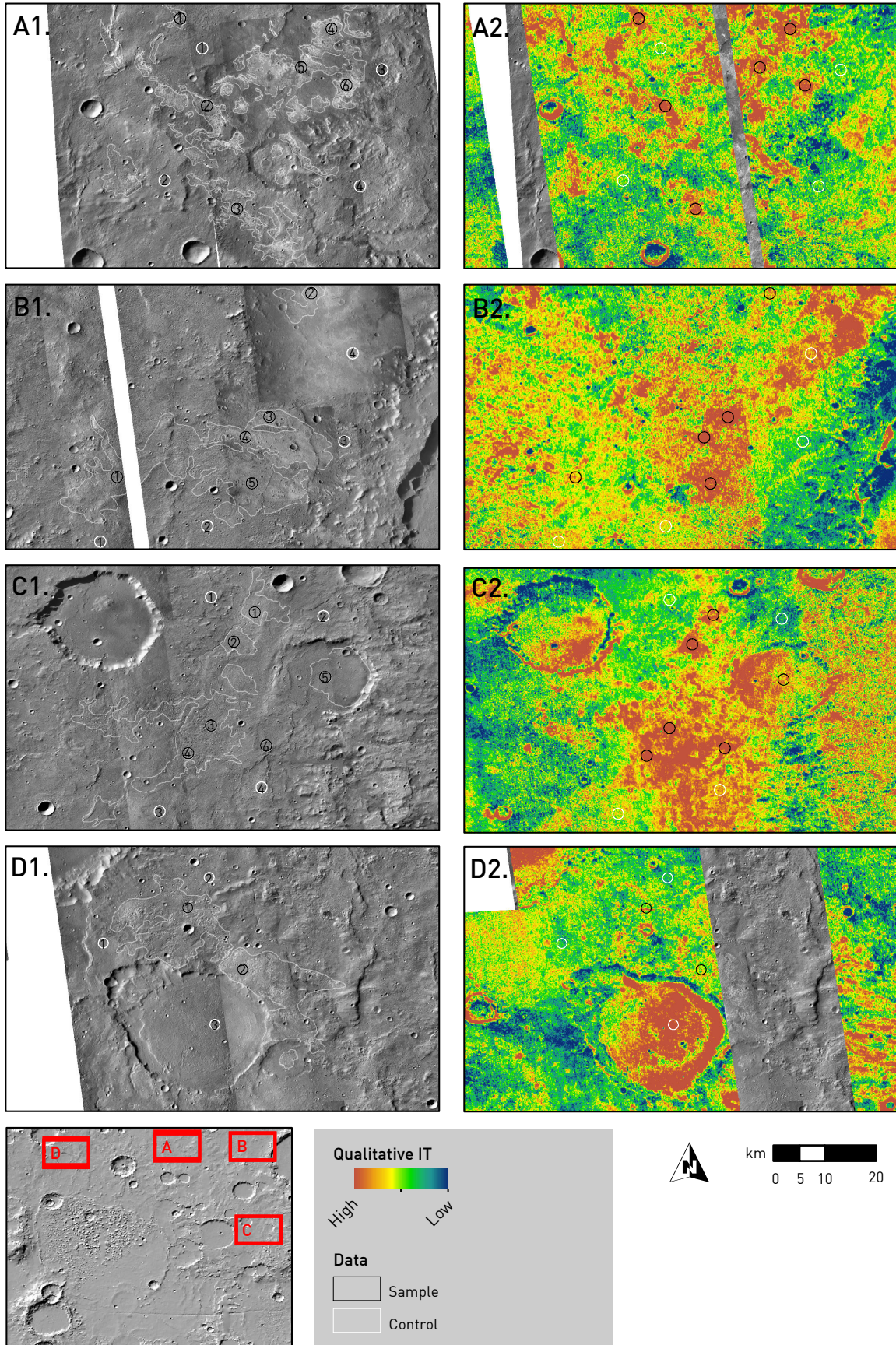


**Figure 3.4.f** Qualitative (A) and quantitative (B) THEMIS IR derived thermal inertia image mosaics [Christensen *et al.*, 2013] for the Ariadnes study area that overlaps a MOLA shaded relief. Thermal inertia expressed in tiu ( $\text{J}\cdot\text{m}^{-2}\cdot\text{K}^{-1}\cdot\text{s}^{-1/2}$ ).

Since the THEMIS IR images were acquired at different local times, seasons, and years (Subpart 2.1.2v), the calibration and calculation of the TI values are conditioned to a great uncertainty (Subpart 2.1.2v) that produces very heterogeneous results (Figure 3.4.f-B). To mitigate this effect, the evaporitic deposits (*eAed*) were sampled to obtain numeric results (Figure 3.4.g). Several one kilometer in radius circles were taken as sampling and control areas for each four outcrops. All of them display a higher TI than the surrounding materials, excepting for the Western deposit (Figure 3.4.g-D) where the absence of images make the evaluation of this deposit challenging.

The statistic results for quantitative TI in the sampling and control areas (Figure 3.4.g) are shown in Figure 3.4.h. The TI values varies greatly, even in the same deposits, which is resulting from calibration problems discussed above (Figure 3.4.f-B). Although some trends can still be observed. The westernmost image in the North deposit (Figure 3.4.g-A and Figure 3.4.h-A; 1 to 3 samples) have a TI of  $475 \pm 40$  tiu, while the controls (1 and 2) have about  $380 \pm 20$  tiu. The results for the image more to the east covering the same deposit shows  $380 \pm 20$  tiu (4 to 6) and  $330 \pm 10$  tiu for the controls (3 to 4). In both cases, the TI seems to be overestimated considering the results obtained for the rest of the samples (Figure 3.4.h), although highest values of TI are considered more accurate in this mosaic (Subpart 2.1.2v).



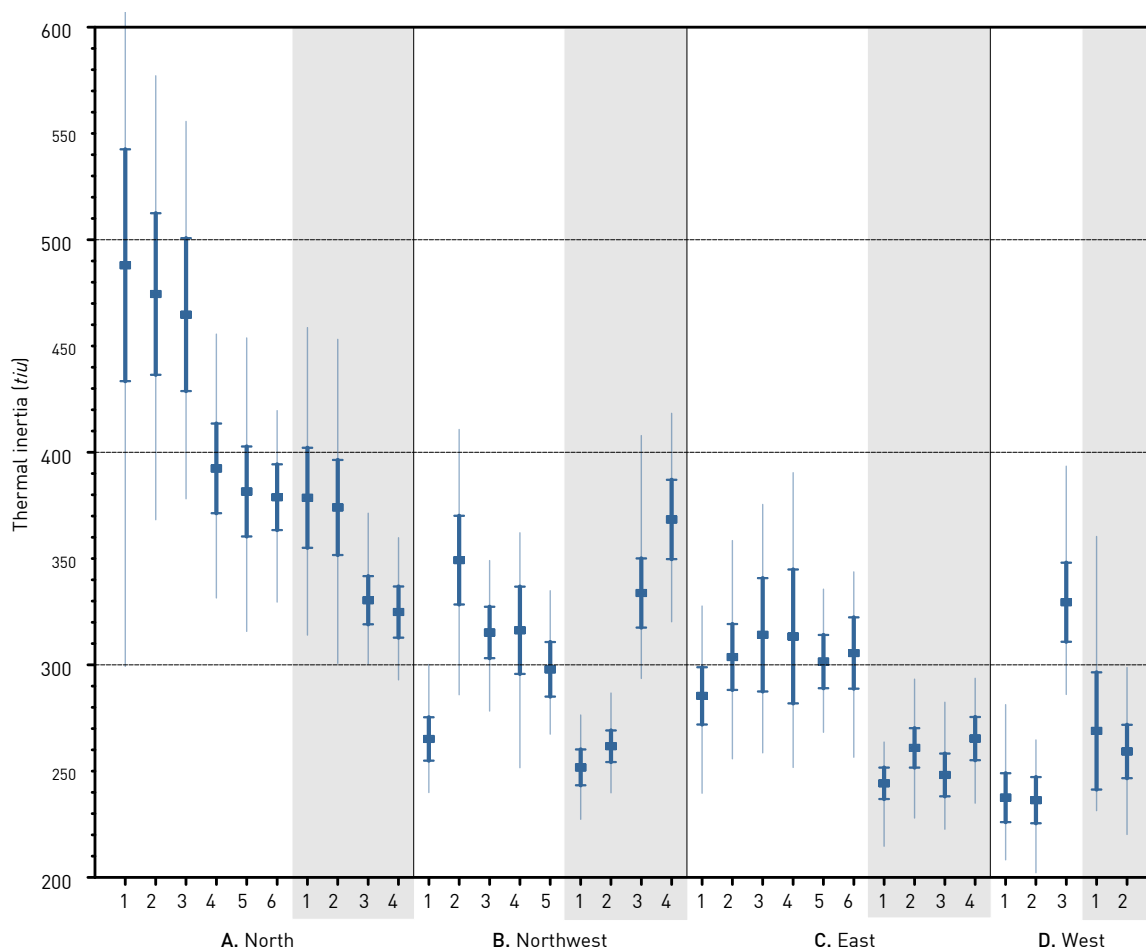


**Figure 3.4.g (Previous page)** CTX visible images (number 1, left) and mosaics of THEMIS thermal inertia image (number 2, right) [Christensen *et al.*, 2013] for several regions of interest in Ariadnes. The images centered in (A) North, (B) Northeast, (C) East, and (D) West trace the evaporite deposits (with polygons) for each sector. Circular areas with radius of one kilometer were taken as sample and control outside the unit area, and which results are showed in [Figure 3.4.h](#).

In the Northeast deposit ([Figure 3.4.g-B](#) and [Figure 3.4.h-B](#)), the external samples (1 and 2) come from different images, whereas the central part (3 to 5) shows  $320 \pm 20$  tiu, and which controls (1 and 2) display values about  $250 \pm 10$  tiu ([Figure 3.4.h](#)). Although the image averages higher values, the higher TI values in 3 and 4 control areas may be interpreted as the deposits extends to the east. The range of data is consistent with the TI record in the East deposit ([Figure 3.4.g-C](#) and [Figure 3.4.h-C](#)) with  $310 \pm 20$  tiu in samples 1 to 6, and  $250 \pm 20$  tiu in their control (1 to 4). As the deposit in the East area actually extends few additional kilometers eastward, the sample number 6 is actually outside the polygon outlining its boundaries. Finally, samples from the West deposit ([Figure 3.4.g-D](#) and [Figure 3.4.h-D](#)) are below 275, excepting at the sample number 3, which corresponds to the flat-floor crater infilling (*HAfc*). Despite the heterogeneity of the TI data for the West area, TI values of around 300 to 350 tiu for the deposits and about 250 tiu for the surroundings are obtained. This result is relatively low when compared to the data collected in the North deposits ([Figure 3.4.h](#)).

The results discussed above suggest that the materials in Ariadnes are generally fine-grained, with some coarse sand, that experienced cementation and duricrust formation in the evaporite deposits, which have a low dust coverage. In this regard, the grain size is around  $60 \mu\text{m}$  for sands and up to 3 mm for duricrust. This is consistent with the interpretation of materials obtained by the geological mapping of Ariadnes (Subchapter 3.2). In this context, the Electris deposits (*eHed*), which are proposed to be airfall deposits (Subpart 3.2.2iii), provided a TI consistent with sands and fine grains. Furthermore, the evaporite deposits (*eAed*) also meet higher TI values, given that they behave as a duricrust in semi-arid conditions formed by the accumulation of precipitates by evaporation pumping and capillarity [Jakosky and Christensen, 1986].





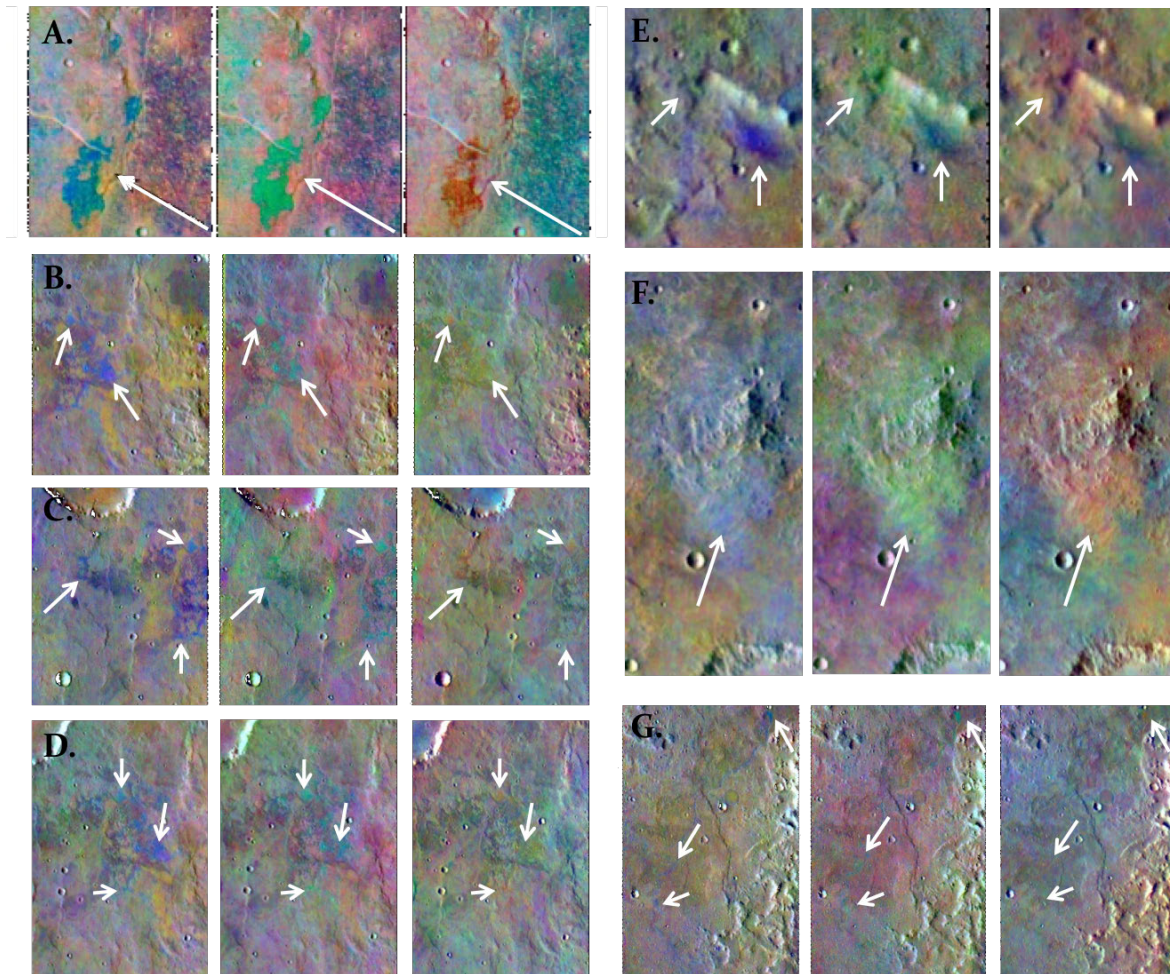
**Figure 3.4.h** Results of the THEMIS thermal inertia data ( $tiu$ ,  $J \cdot m^{-2} \cdot K^{-1} \cdot s^{-1/2}$ ) for each sample (white background) and control (gray background) areas displayed in [Figure 3.4.g](#). Where each box represents the average, the whiskers interval provides the Standard Typical Deviation (STD), and the light blue lines trace the data range of TI.

### 3.4.3 THEMIS DECORRELATION STRETCHED COLOR INFRARED IMAGES

THEMIS IR images can not only be used to obtain textural information derived from the thermal properties of the Mars surface [*Ferguson et al.*, 2006a]. Furthermore, some additional information with regard to mineral composition can be obtained as well [*Ferguson et al.*, 2006a]. *Osterloo et al.* [2010] proposed a method to identify potential chloride bearing deposits using THEMIS IR images. In this sense, the DCS IR images [*Hamilton et al.*, 2007] –which acquisition is described in Subpart 2.2.3v– consist of the combination of three images, processed with an image color enhancement technique that amplifies the contrast of uncorrelated multispectral information [*Gillespie et al.*, 1986]. DCS images display the selected bands in red, green, and blue (RGB) channels, respectively. The characteristics of the available variants of false color images are summarized in [Table 3.4.c](#).

**Table 3.4.c** THEMIS decorrelation stretch (DCS) information, as band characteristics, and false color that corresponds to chloride-bearing material for each DCS image combination [Osterloo et al., 2010].

Bands (RGB)	Decorrelation stretch (DCS) images				
	8/7/5		9/6/4		6/4/2
Center Wavelength ( $\mu\text{m}$ )	11.79/11.04/9.35		12.57/10.21/8.56		10.21/8.56/6.78
Chloride false color	Blue	Green	Teal	Orange	Yellow



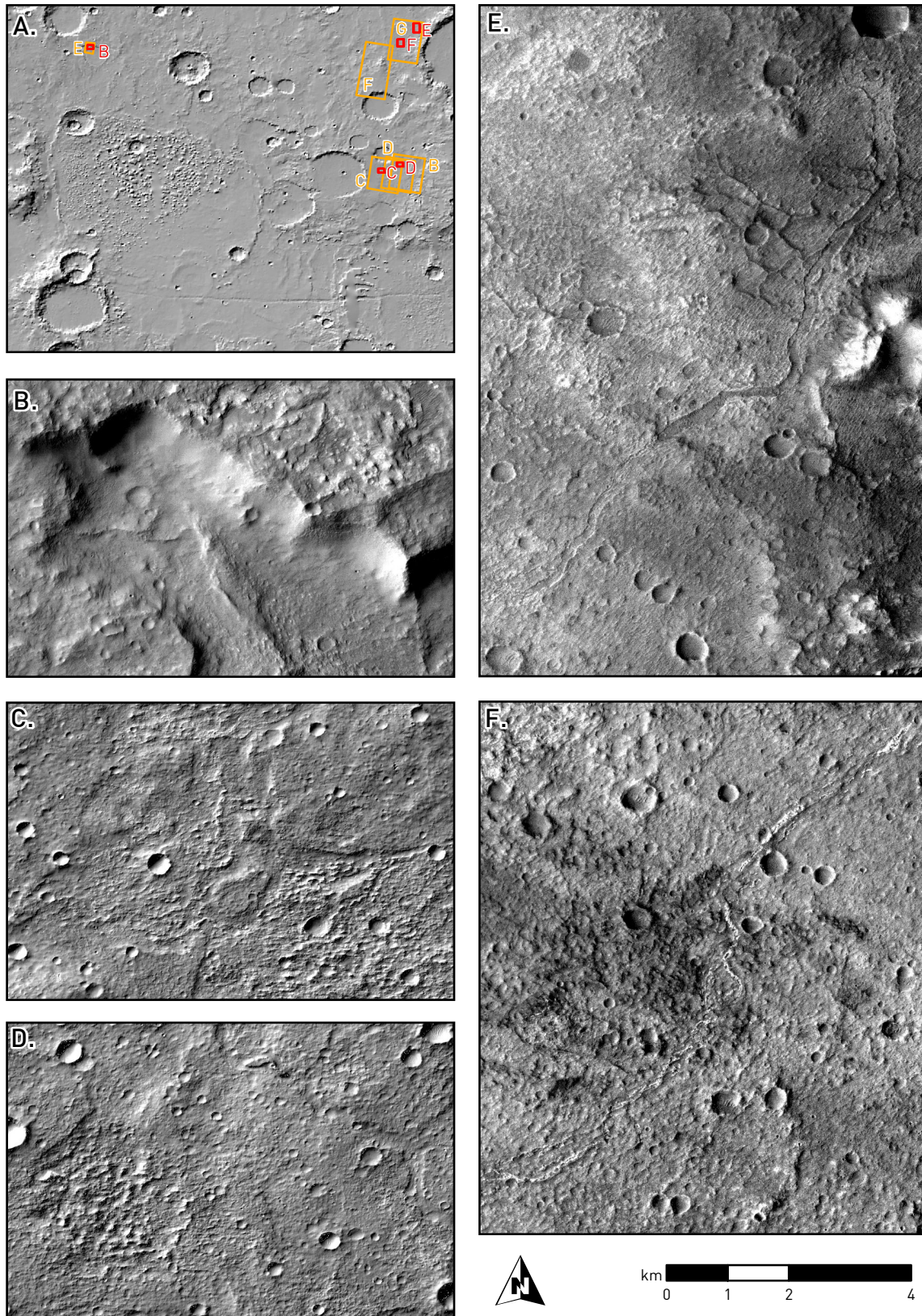
**Figure 3.4.i** False color decorrelation stretch (DCS) images of THEMIS IR radiance data. (A) I34346002 (~18.9°S, ~332.2°E) DCS image used as example of chloride bearing material that is shown in [Osterloo et al., 2010]. Several examples in Ariadnes are shown in the images (B) I24170003, (C) I08533003, (D) I07397002, (E) I17269002, (F) I15609005, and (G) I08533003, where the white arrows mark the chloride materials detected by DCS. The location for each image is shown in Figure 3.4.j.

The chloride-bearing materials are easily distinguishable in the DCS images, which appear [Osterloo et al., 2010] as blue, green/teal and orange/yellow in the 8/7/5, 9/6/4/ and 6/4/2 stretches images, respectively (Table 3.4.c). Such a pattern in the



DCS images was detected in several locations agreeing the occurrence of early Amazonian evaporites deposits (*eAed*). Some of those areas were already described by *Osterloo et al.* [2010], which occur in the eastern area of Ariadnes as saline patches with irregular boundaries, as well as forming linear to sinuous morphologies (Figure 3.4.i-B to D). Furthermore, in the upper right corner of the study area, the *eAed* unit shows rim-forming (Figure 3.4.i-F) and narrow channel-like morphologies associated to chlorides (Figure 3.4.i-G). Intriguingly, the northern outcrops of *eAed* do not show any similar pattern, while the western materials display features that enforces the visual identification (Figure 3.4.i-E).

The distribution and morphology of the deposits has been used as complementary information to understand the geological context for the chloride-bearing materials [*Osterloo et al.*, 2008a, 2010]. In this regard, the Figure 3.4.j shows the most relevant morphologies that have been identified in the DCS (Figure 3.4.i). The westernmost deposits in Ariadnes (Figure 3.4.i-E and Figure 3.4.j-B) does not display very distinctive morphologies. Indeed, in this location a deposit arranged with a regular slope is the only material that can be assigned to the chloride-bearing unit. The deposits located at the top of the slope though do display light toned and appearance similar to the typical evaporites. On the other hand, the Eastern deposits (Figure 3.4.i-B to D and Figure 3.4.j-C and D) occurring as patches with irregular boundaries when observed through the DCS images are agree with the described of chloride-bearing deposits. In addition, they are located in shallow depressions and display a rough morphology that clearly differentiates them from the surrounding terrain. However, as discussed above, the materials also occur as linear and sinuous morphologies as shown in Figure 3.4.i-G, where there are clear examples. Such materials match shows a channel-like morphology (Figure 3.4.j-E) that display inversion to the South (Figure 3.4.j-F). The deposit distribution and morphology, which are in close association to valley networks and topographic lows, strongly suggest that they are composed of salts precipitating from oversaturated solutions.



**Figure 3.4.j** (A) Orange polygons showing the location of the THEMIS DCS images in the study area (Figure 3.4.i). The red boxes trace the position of CTX image mosaics in the main chloride-bearing occurrences observable with DCS images. Images in B to F show different morphological features of the putative chloride-bearing deposits.



### 3.5 PHYSICAL ANALYSIS

#### 3.5.1 TEMPERATURE

A nearly full coverage for daytime (i.e., images that were taken from 14 to 16 hours in local time) and a complete coverage of nighttime images (i.e., obtained from 4 to 6 hours in local time) from THEMIS were obtained, which derived temperatures are summarized in [Table 3.5.a](#).

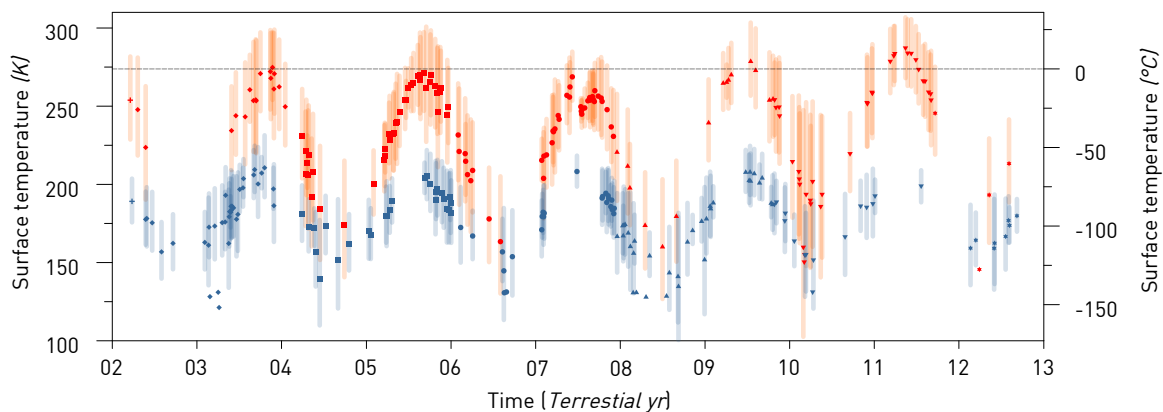
**Table 3.5.a** Temperature data recovered from the THEMIS BTR images of Ariadnes.

	Number of images	Surface temperature ( <i>K</i> )		
		Mean	Minimum	Maximum
<b>Daytime</b> (14 to 16 h)	144	237.5	91.4	306.8
<b>Nighttime</b> (4 to 6 h)	154	176.0	91.5	331.4

The mean surface temperature for each image versus acquisition time is shown in [Figure 3.5.a](#). In the case of a limited specific heat produced by a surface with a very thin atmosphere and negligible humidity, direct insolation is the main variation factor for surface temperatures. Although under these conditions, the daily temperature range larger is greater than 50 degrees, seasonal changes in the solar radiation are also recorded in the annual temperature cycle. As a martian year lasts 687 terrestrial days, which equals about two Earth's years, the winter solstice and summer solstice match with the minimum and maximum surface temperatures, respectively. Such a seasonal pattern can be easily observed when plotting the temperature data for each year ([Figure 3.5.b](#)).

Although the results displayed in [Figure 3.5.b](#) consist of the mean temperature of several images of a large area, the interannual variation is low. In this regard, the first half of the year shows a greater dispersion of data, which, however, show a lower scattering than the daily variation in temperature. The main variations between years are observed in daytime temperatures, while nighttime values remain much closer each other. By examining the temperature evolution in the last six martian years, it is

possible to recognize that the Mars Year (MY) 30 (last Mars year with data) was the warmest period, which has provided a daytime temperature of 20 degrees higher than the average temperature. In addition, MY 30 reached the lowest daytime temperatures during the winter solstice. Such seasonal evolution could be related to a clearer atmosphere with less suspended particles.

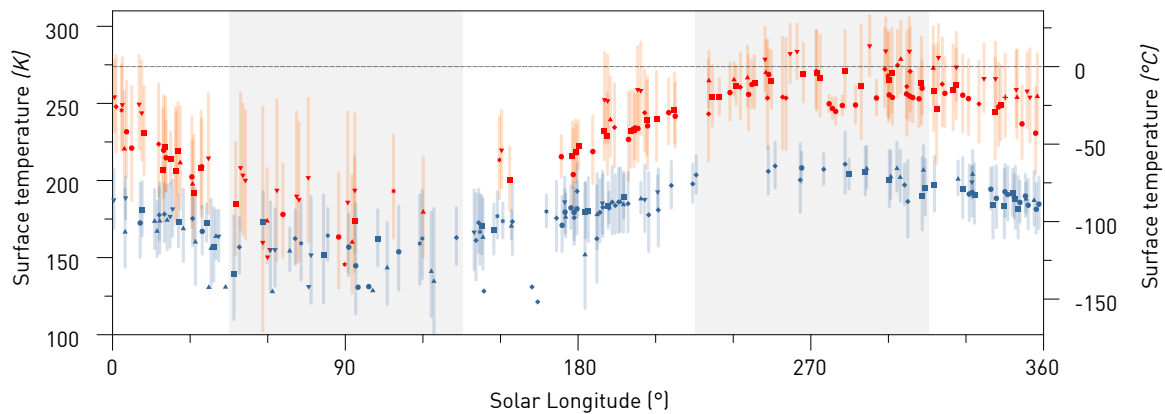


**Figure 3.5.a** Daytime (**orange circles**, 14 to 16 h) and nighttime (**blue circles**, 4 to 6 h) mean surface temperatures for each image shown in Earth time.

Even though [Figure 3.5.b](#) results are mean temperatures from a bunch of images in a wide area, interannual variability is sparse. The first half of the year shows greater dispersion in the data, with still lower differences than the daily variation in temperature. The main variations between years are observed in daytime temperatures since nighttime values remain closer to each other. Through them, we can say that the MY 30 was the warmest, with about 20-degree higher daytime year temperatures than the average. That year also reach the lowest daytime temperatures during the winter solstice. Than behaviors may be attributable to a year with clearer atmosphere with less suspended particles.

It is worth mentioning that during the summer solstice of MY 28, when temperatures were maximal in that year, there was a dramatic decrease in temperatures as well, which matches with an abnormal global dust storm [*Wang and Richardson, 2015*]. In MYs 24–30, storms were most frequently observed during Ls  $\sim 130 - 250^\circ$  and Ls  $\sim 305 - 350^\circ$ , but the 2007 global dust storm in MY 28 was the only one recorded during Ls  $\sim 250 - 300^\circ$ . During episodes of dust storms, the heat transfer to the surface significantly decreases as the suspended particles absorb most of the

radiation incident on the planet. By nighttime, these particles emit infrared radiation back and heating the Mars surface. Thus, greater the number of particles, more isothermal the temperature gradient. Under these conditions, the diurnal temperature variations are strongly decreased and become negligible [Carr, 2007].



**Figure 3.5.b** Daytime (**orange circles**, 14 to 16 h) and nighttime (**blue circles**, 4 to 6 h) mean surface temperatures for each image, versus their acquisition time (in Martian solar longitude, ° Ls), as they were at the same type year.

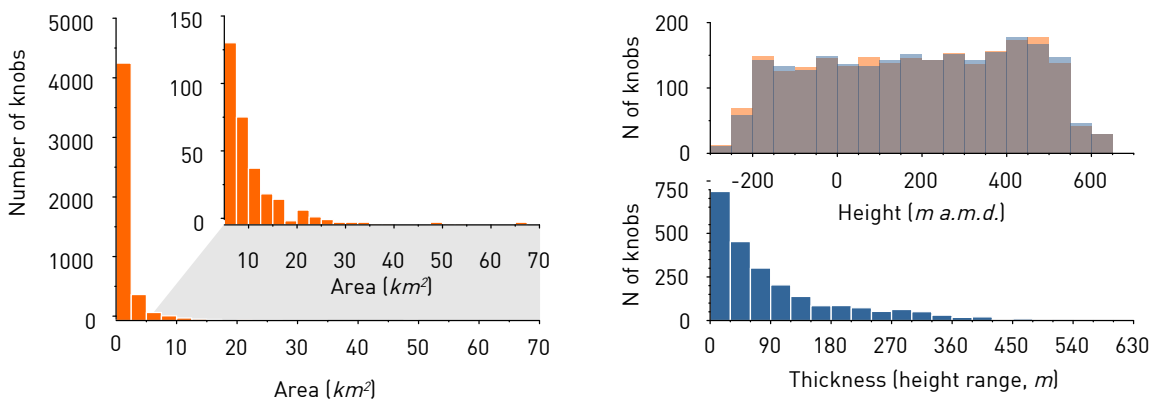
### 3.5.2 MORPHOMETRIC ANALYSIS

The morphometric analysis required the cartography of knobs, which shape was previously outlined as knob polygons (see [Figure 3.2.a](#) and Subpart 2.2.4i). As a result, we obtained a scatter diagram plotting the area versus thickness of around 5,000 knobs ([Figure 3.5.c](#)). In this regard, the extension varies between 65.86 to 0.01 km<sup>2</sup>, which was the lower recognizable size ([Table 3.5.b](#)). The size range is very diverse following a geometric distribution, with only 337 polygons larger than 5 km<sup>2</sup> and 122 larger than 10 km<sup>2</sup>, and where few areas were larger as 50 km<sup>2</sup> ([Figure 3.5.c](#)). It is worth mentioning that the size and detection of the smaller polygons are limited by the image resolution and the dust coverage, which is hiding the real extension of the smallest features. However, such data is an initial approach to understanding better the formation of knob fields. Having this in mind, a plain numerical analysis of the knob morphology shows that they have an average size of 1.87 km<sup>2</sup> with a standard deviation of 3.82 km<sup>2</sup> ([Table 3.5.b](#)).



**Table 3.5.b** Area and altitude statistics (obtained from MOLA data) for the polygons of the Ariadnes knob field. Knobs with an area larger than 0.5 km<sup>2</sup> analyzed separately (limited to MOLA horizontal precision), as for polygons which area is among 0.5 and 10 km<sup>2</sup>.

	Area (km <sup>2</sup> )	Altitude (m a.m.d)						
		MIN	MAX	Range	Average	Median	STD	
ALL	MIN	0.01	-308.00	-301.00	0.00	-301.00	-301.00	0.00
	MAX	65.86	701.00	785.00	653.00	709.00	701.00	164.44
	Range	65.85	1009.00	1086.00	653.00	1010.00	1002.00	164.44
	Average	1.87	146.55	204.11	57.56	173.61	170.72	17.29
	Median	0.71	137.00	207.00	18.00	164.58	162.00	7.00
	STD	3.82	246.37	251.32	89.55	245.11	245.17	24.00
	> 0.5 km <sup>2</sup>	MIN	0.55	-308.00	-272.00	0.00	-287.11	-289.00
	MAX	65.86	660.00	785.00	653.00	667.00	660.00	164.44
	Range	65.31	968.00	1057.00	653.00	954.11	949.00	164.44
	Average	3.06	143.50	239.58	96.07	188.58	185.05	28.14
	Median	1.57	146.50	257.00	59.00	193.29	192.50	19.45
	STD	4.70	237.33	239.57	101.70	233.74	234.17	26.41
> 0.5 km <sup>2</sup> and < 10 km <sup>2</sup>	MIN	0.55	-308.00	-272.00	0.00	-287.11	-289.00	0.00
	MAX	9.92	660.00	785.00	514.00	667.00	660.00	140.42
	Range	9.37	968.00	1057.00	514.00	954.11	949.00	140.42
	Average	2.22	153.51	236.86	83.36	192.03	188.45	25.18
	Median	1.47	162.50	254.00	53.00	204.58	201.50	18.07
	STD	1.93	236.87	242.40	84.53	236.55	236.95	22.77



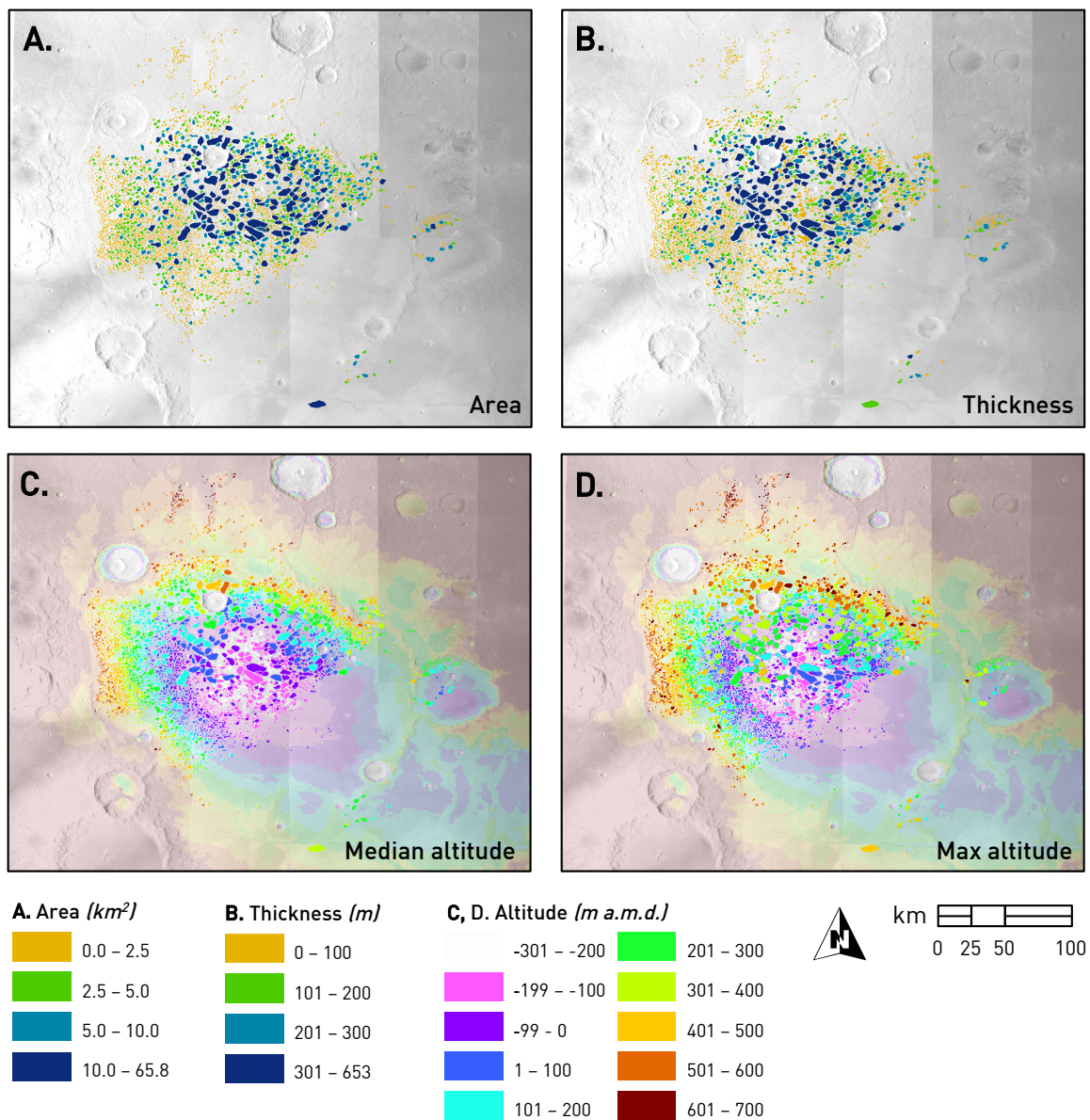
**Figure 3.5.c** (Left) Histogram showing the area (km<sup>2</sup>) distribution of Ariadnes knobs. (Upper right) Histogram of average (blue) and median (orange) inner altitude (from MOLA) for each knob polygon larger than 0.5 km<sup>2</sup> (limited to MOLA horizontal precision). (Lower right) Histogram of knob thickness that was obtained as a range of altitudes (from MOLA) inside each polygon larger than 0.5 km<sup>2</sup>.

Most of the larger polygons (between 5 and 10 km<sup>2</sup>) spread out in the center and the northeastern part of the Ariadnes field (Figure 3.5.d-A), whereas those knobs smaller than 5 km<sup>2</sup> stretch to marginal areas of the basin. In addition, the smaller knob polygons are more abundant to the SW and disappear when reaching the large ridge crest to the west of the basin. To the northeast area, the ridges act as a boundary for the knob field, though, particularly to the north, some small isolated polygons surpass the ridge chain. To the south, the knob boundary shows an SW-NE direction that is also visible in larger knobs and the northern isolated minor knobs. Furthermore, some isolated knobs larger than 5 km<sup>2</sup> are recognized in different locations that occur to the W and the SW part of the basin (Figure 3.5.d-A).

Whereas most of the knobs occur at an absolute elevation ranging from -200 to 500 m relative to the martian datum, the complete knob field ranges between -300 to 800 m a.m.d. (Figure 3.5.c) following a normal distribution. As the MOLA horizontal precision is 0.5 km per pixel (Subpart 2.1.2i) and at least a window of two pixels is recommended for accuracy, the numerical calculation was done with and without those polygons with area lower than 0.5 km<sup>2</sup> (Table 3.5.b). Although two W-E alignments can be spotted in the height distribution, the knobs follow the topography of the area (Figure 3.5.d-C). In regard to the morphology, the knobs do not show a clear relation between morphology and altitude. Besides, the knobs display a very diverse morphology (from irregular to mesa-like shape), but its median and average altitudes are similar (Figure 3.5.c).

Although the knobs occurring at the lowest altitude follow the general bowl-like morphology of the basin (Figure 3.5.d-C and D), some alignments can be observed when considering the maximum height (Figure 3.5.d-D). Knobs in the center of the field reach much higher altitudes about their surroundings than those located close to the margins. The range of altitudes (difference among maximum and minimum) inside a polygon provides the knob thickness or knob height (Figure 3.5.d-B). The knobs reach a maximum thickness of 653 meters, but most of them are much thinner (Figure 3.5.c), following a geometric distribution (Figure 3.5.d-B). The numerical analysis shows that knobs average about 100 meters high, with a deviation of ~100

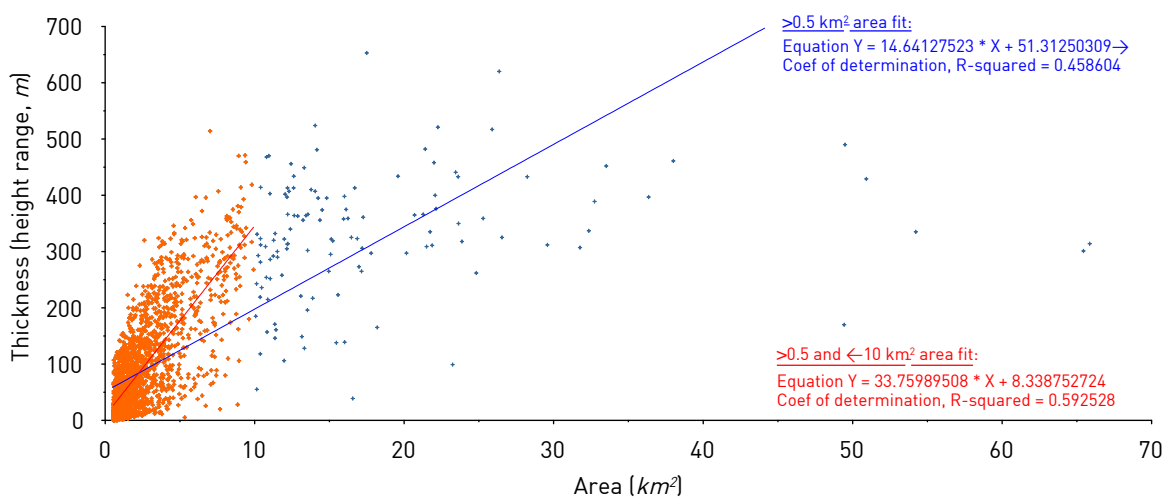
meters (Table 3.5.b). The spatial distribution of the thickness is quite similar to the occurrence of areas, where the larger, the thicker is the knob.



**Figure 3.5.d** Ariadnes knob field map showing each knob colored by their (A) size (polygon area in  $km^2$ ); (B) thickness (range of altitudes from MOLA); and (C) median and (D) maximum altitude (from MOLA). The background image is an HRSC image mosaic that, in frames C and D, is overlapped to a color classified MOLA topography.

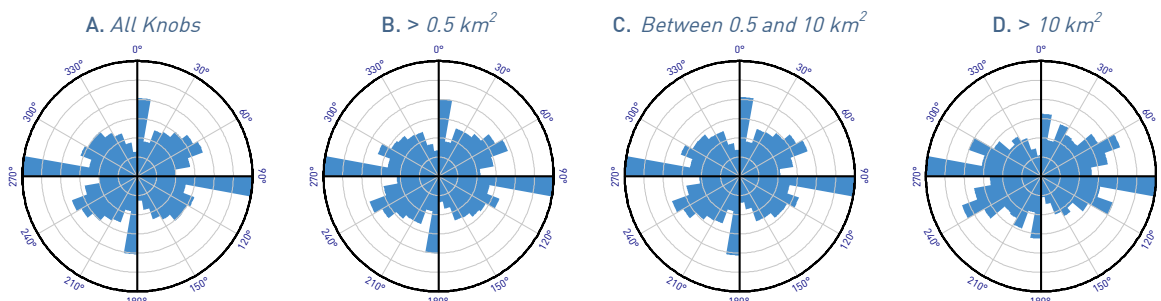
The thickness (height range in meters) versus area ( $km^2$ ) of knob polygons is showed in Figure 3.5.e. There is a clear relation between both parameters that fits relatively well to a linear regression. The regression fit is even stronger when the polygons are smaller than  $10 km^2$  (reaching a coefficient of determination of 0.59 when excluded, versus just 0.46 with them). An R-square of 1 may indicate that the

knobs have a horizontal extension perfectly related to their height. The deviation from this proportion may help to infer information about the knob field formation and evolution. However, this is only the expression of the outcropping heights, since there is a matrix of unknown thickness among the mounds. This matrix follows the topographic trends perfectly, indicating a uniform deposition.



**Figure 3.5.e** Scatterplot of thickness versus area for knobs larger than 0.5 km<sup>2</sup> (**blue**) and smaller than 10 km<sup>2</sup> (**orange**), which follow a linear regression (**dark blue** and **red**, respectively).

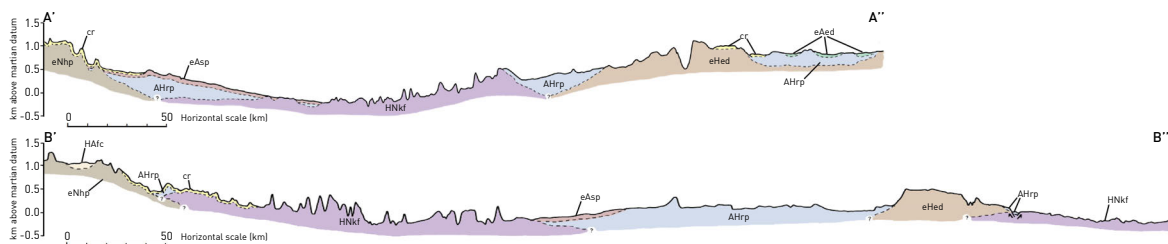
An azimuthal analysis of the knobs outline segments reveals two clear direction trends from east to west, and perpendicularly, from north to south. That directionality is evident in most of the knobs, although the NS is not observable for the largest knobs (> 10 km<sup>2</sup>, **Figure 3.5.f-D**). This trend may be related to structural influence (ridges in the area shows a strong NS trend, **Figure 3.2.i**).



**Figure 3.5.f** Rose diagrams of the azimuthal directions followed by the segments composing the outlines for the knobs in Ariadnes area (**Figure 3.2.a**), weighted by their length. There were considered (A) all the knobs, (B) only the larger than 0.5 km<sup>2</sup>, (C) the ones between 0.5 and 10 km<sup>2</sup>, and (D) the ones larger than 10 km<sup>2</sup> (**Table 3.5.b**).

### 3.6 GEOLOGICAL HISTORY OF ARIADNES

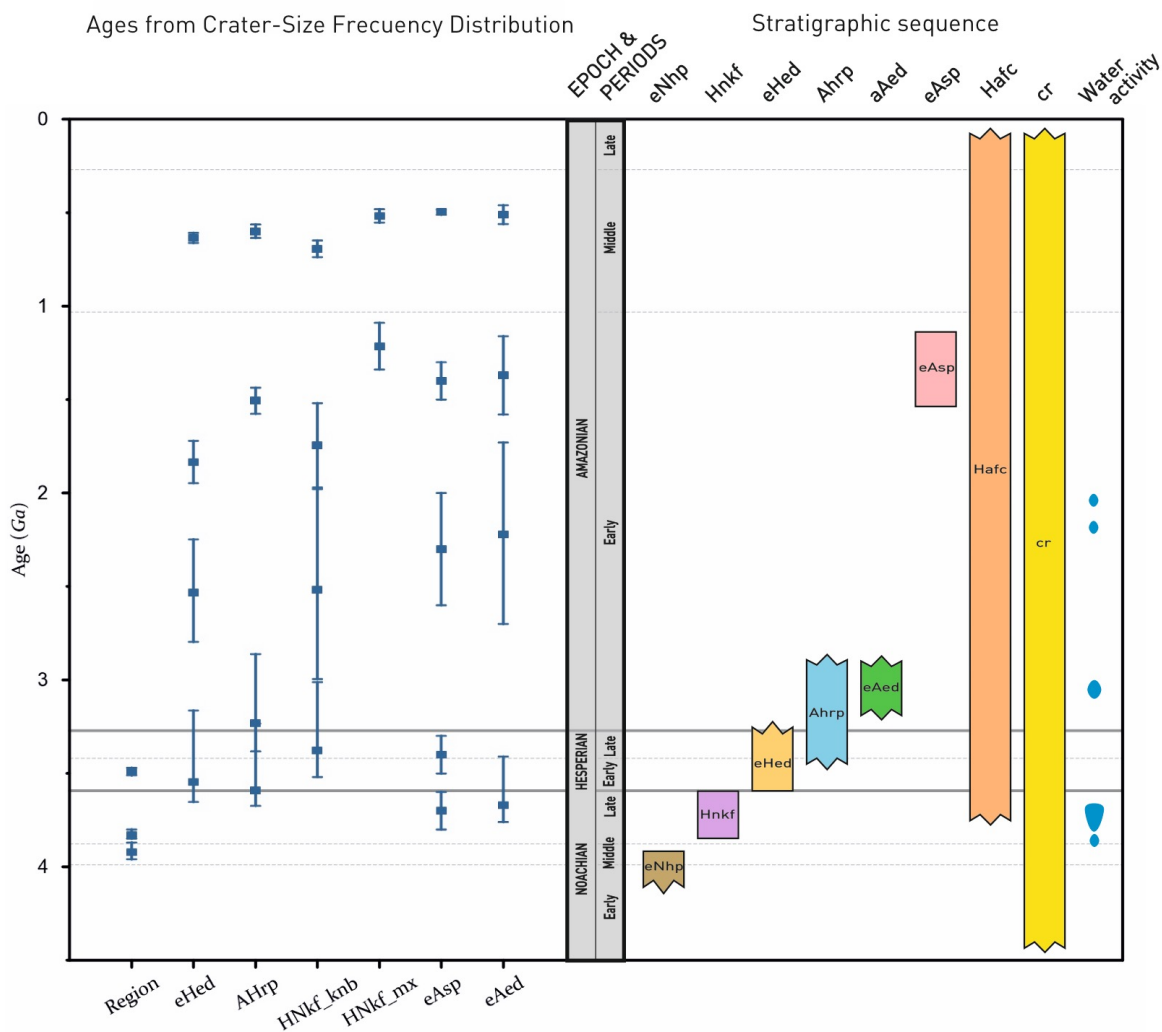
This subpart of the dissertation includes a geological data synthesis to understand the evolution of the Ariadnes basin. The interpretation comes from the integration of a detailed cartography (Subchapter 3.2) and the multi- and hyperspectral data analysis (Subchapter 3.4), which results from the combination of physical (e.g., unit size, boundaries, texture, color among others) and compositional data (e.g., mineral association) obtained in the region. This has to be integrated inside a temporal background that is supported by the crater counting on the most suitable surfaces (Subchapter 3.3) of the different mapped geological units. As a result, such data integration provide enough information to build a consistent chronostratigraphic framework and several cross-sections that are potentially limited by isochrones and provide the different infilling events of the Ariadnes Basin. In this regard, two hypothetical cross-sections show the temporal distribution and geometry of units in the Ariadnes study area (Figure 3.6.a).



**Figure 3.6.a** Interpretative geological cross-sections (A' – A'' and B' – B'') showing relations between different units achieved by the contact relationships between units and the ages obtained by crater counting (Subchapter 3.3). Cross-section transects are showed on the location map (Figure 3.2.a) as straight white lines.

In addition, when coming to the surface age results (see Figure 3.6.b in Subchapter 3.3), which are considered as the age range for latest forming age or resurfacing and the spatial distribution for each unit, it can be aged the resurfacing processes. The early Noachian highlands plains (*eNhp*) unit constitutes the basement and oldest surface in our mapping area, underlying all the other units. It dates from about 3.8 – 4.0 Ga, in agreement with the estimated in previous studies that the basement age is Middle Noachian [Greeley and Guest, 1987] or Middle Noachian to Early Hesperian [Kuzmin *et al.*, 2000]. As most of the highlands materials, it shows a relatively flat spectrum in VNIR CRISM data (Part 3.4.1) and their surfaces are eroded, formed mostly by large impact crater structures.





**Figure 3.6.b** (Left) Age determination (dots) and error ranges (lines) obtained from different units of the area of study. Horizontal straight lines represent boundaries between the geologic periods of Mars, whereas dashed lines mark boundaries between epochs [Michael, 2013]. (Right) Stratigraphic sequence of Ariadnes inferred from age determinations and spatial relations between units determined in the cartography. At the right, the blue ellipses show the duration of valley networks and the outflow channel activity on Mars [Tanaka, 1997; Fassett and Head, 2008].

During the Middle and Late Noachian, a long-standing hydrological episode affected the Eridania System, the interconnected system of depressions in the region (Part 3.1.1) that was originated by an unknown process (probably impact, groundwater sapping, or volcano-tectonic related). During the existence of the Eridania Lake, as which hosted one or several individual water bodies, fine-grained materials containing phyllosilicates (Part 3.4.1) deposited, forming the Hesperian Noachian knob fields (*HNkf*) unit. As the crater counting of *HNkf* surface was uncertain due to the limited extension of the unit, the results only provided some resurfacing dates.

However, simple stratigraphical correlations suggest that *HNkf* was deposited between *eNhp* and *AHrp* units formation, as *eNhp* is an ancient Noachian basement in the region and *AHrp* covers the light-toned mounds of the knob fields (Figure 3.6.a). The Hesperian-Noachian age for this unit is in agreement with other studies [e.g., Baker and Head, 2012a; Wendt et al., 2013]

The *HNkf* knob fields could have been formed by alteration plus transportation of marginal basin materials, or formed in-situ by the alteration of the interior basin substrate. Addressing this question is critical to understand the evolution of the hydrological evolution of Ariadnes area. The main source of water could have been very diverse including large outflow input, runoff originated from meteoric sources, underground reservoirs, or multiple combinations of them occurring in one or different episodes. In this regard, the thickness of the clay-bearing materials (about 100 m, Part 3.5.2) suggests that it has recorded the existence of a permanent water table for a relatively extended period of time. The continuous layering and uniform thickness variation in the basin (Figure 3.6.a), both following the altitude and morphology of the basin (Part 3.5.2) strongly support that the runoff and groundwater were the main sources of water in Ariadnes. As the Ma'adim Valles and Eridania Lake catchment basins are not extensive enough to explain the amount of material carved [Irwin et al., 2002, 2004a], it is most likely a combination of them, where groundwater must play a major role as lake water input [Irwin et al., 2005b; Baker and Head, 2012b].

The occurrence of phyllosilicates in the light-toned knobs provides an additional information of the sedimentary environment that produced the formation of the *HNkf* unit. As shown above (Part 3.4.1), such deposits are mostly composed of Mg-smectites and Talc mixtures, that are common as alteration products in seafloors and deep crustal areas and also suggesting a hydrothermal origin [e.g., Dekov et al., 2008; Cuadros et al., 2013; Yamanaka et al., 2013]. In addition, Fe-smectites were also found in some specific locations that suggest surface weathering as a possible secondary origin for the deposits [Bishop et al., 2008]. Furthermore, Al-smectites and hydrated silica were also observed (Part 3.4.1) in an eventual association with craters [Ehlmann et al., 2009; Michalski et al., 2015]. Both may be the product of the alteration

of silicates and impact melt followed by a post-impact hydrothermal activity [Osinski *et al.*, 2013], but also Al-smectite as the identified kaolinite are considered geomarkers of weathering in acidic conditions [e.g., Fernández-Remolar and Knoll, 2008; Baldrige *et al.*, 2009]. Finally, although it is very likely that sulfates are occurring in the area, its weak spectral signal suggests that they are a minor fraction of the materials composing the deposits that infilled Ariadnes.

The presence of knob fields is clear evidence that some regional event modified the layered phyllosilicate-rich deposits. Although the process that caused such chaotic surface is unclear, the geological context suggests that it was most likely associated with a combination of fluvial erosion or water discharge combined with a tectonic pulse, a catastrophic groundwater discharge or collapse of an ice wedge. Interesting enough, the resulting chaos-like surface displays knobs alignments that follow the preferential tectonic directions in the region. Whereas the knobs occupying the center of the basin show mesa-like morphologies, that are likely as a result of the protection of a topping resistant capping unit, as well as of the protective effect done by the external knobs against the water erosion (Part 3.5.2). The layering of this knobs tilt, and they present relict elongated features on their surface (Subpart 3.2.2ii). This observation can be explained by some hydrothermal or groundwater activity, which can bend the phyllosilicate-bearing deposits. The surface would shrink, what would divide up the layer by the weak points produced by tectonic stresses, as a possible origin for the knob field formation.

During the late Hesperian, and close to the transition to the Amazonian epoch, the *AHrp* and *eAsp* units were resurfaced in the North and Northwest of the study area. This activity is likely related to the deposition of the early Hesperian Electris deposits (*eHed*). It might have been associated with some volcanic event, as Elysium [e.g., Werner, 2009], that could have produced the airfall layer of Electris [Grant *et al.*, 2010]. This light-toned material presents a mesa-like surface with a thickness of 200 – 500 m. Although it extends along the region as an uneven mantling cover predating *AHrp*, it has an unclear relation with *HNkf*, which could suggest that both *AHrp* and *HNkf* units could be the same materials [Wendt *et al.*, 2013]. Furthermore,

while the spectrometric analyses (Subchapter 3.4) are inconclusive, some weak phyllosilicate signatures were identified in indexes supporting a common composition (Part 3.4.1). Although, it was not possible to obtain a quality spectrum to confirm unequivocally that.

The volcanisms that may be involved in the formation of *eHed* was probably derived from the same pulse of magmatic activity that was responsible for the formation of the Amazonian Hesperian ridged plains (*AHrp*). These lava flows, which are characterized by wrinkle ridges (i.e., contractional tectonic features formed by a combination of folding and thrust faulting), cover the floors of the most of the topographic depressions in the region (including the space between knobs), and that can be the result of the infilling of fissure vents that deposited materials on the lowest-standing areas. The crater-counting show that *AHrp* was formed in the Hesperian-Amazonian transition (~3.2 Ga, [Figure 3.6.b](#)), which is younger than the previous aging that estimated was formed in the Early Hesperian [*Greeley and Guest*, 1987; *Wendt et al.*, 2013] but more in agreement with other authors that found ages near the Late Noachian/Early Hesperian boundary (i.e., 3.55 Ga) [*Baker and Head*, 2012a]. Since no evidence of landforms produced by volcano-water interactions (e.g., pseudo-craters) are observed either the lake must be drained when the volcanic *AHrp* unit was emplaced or it was produced by a different process.

As *eHed* unit predates *AHrp*, *Electris* should have been deposited shortly before the formation of ridge plains, which would give an age of around 3.50 Ga ([Figure 3.6.b](#)). This age is close to the late Hesperian as estimated by *Grant and Schultz* [1990] and *Baker and Head* [2012a] (~3.43 Ga) but come in disagreement with the dating of 3.88 Ga proposed by *Wendt et al.* [2013].

The volcanic activity that formed the *Electris* deposits could also have greatly increased the hydrological activity in this period, and resulting in the formation of the early Amazonian evaporites (*eAed*). Since these evaporitic sediments overly the *AHrp* and *eHed* units ([Figure 3.6.a](#)), *eAed* should be younger than both units ([Figure 3.6.b](#)). Furthermore, the *eAed* evaporite-like material could have been formed by the

Hesperian-Amazonian boundary, which has likely recorded a climatic transition from wetter towards hyperarid conditions [Fassett and Head, 2008]. This would be in agreement with the age constraints proposed by Osterloo *et al.* [2010] that date the evaporite-rich materials to occur in the Middle to Late Noachian, as well as in the Late Hesperian. The occurrence of the salts-bearing material patches (Part 3.4.2) that are associated to the Eridania Lake shoreline (800 to 1,000 meters a.m.d.) suggests a new period of activity of the Ariadnes paleolake during the Hesperian to Amazonian transition.

The Electris deposits and the southern surface of *AHrp* were modified by a second resurfacing event at about 2.40 Ga (Figure 3.6.b), which is likely related to a younger fluvial event that eroded the older materials in the area [Fassett and Head, 2008; Ehlmann *et al.*, 2011]. Some previous studies differ arguing that the Electris deposits postdates the *AHrp* materials [Grant *et al.*, 2010; Baker and Head, 2012a], but more recent works [Wendt *et al.*, 2013; Pajola *et al.*, 2016] agree with our observation that they were covered or embayed by the ridged plains materials (*AHrp*).

Finally, during the Early to Late Amazonian transition, a renewed period of aqueous activity occurred on Mars [Tanaka, 1997; Fassett and Head, 2008]. It matches several regional resurfacing events that led to the formation of the early Amazonian smooth plains (*eAsp*) unit materials (Figure 3.6.b). This thin layer, which is aged at about 1.40 Ga (Figure 3.6.b), may correspond to lava flows and a secondary alteration of the *AHrp* related with this humid event. The resurfacing age was also obtained in the matrix deposits with a distinctive thermal behavior, which suggests a texture and/or composition contrasting with the *AHrp* unit.

In summary, the Ariadnes region has experienced a significant amount and diversity of geologic activity, especially close to the Noachian-Hesperian boundary (Figure 3.6.b). During the Late Hesperian, light-toned phyllosilicate-bearing deposits (*HNkf*) were formed inside the basin. It was followed by the Electris airfall material (*eHed*) deposition, which was likely formed promoted by Hesperian volcanism. Later on, during the Hesperian, both *HNkf* and *eHed* units were partially covered by lava



flows (*AHrp*) that formed the extensive ridged plains. However, in a preceding event, the chaotic-like knob fields were originated inside the basins that were accompanied by a second episode in the Amazonian of salty duricrust (*eAed*), which were created in ponding areas occurring peripherally around the coastline of the Ariadnes Basin. In this regard, water has played an important role shaping and altering the materials that have infilled the basin. The different volcanic episodes renewed the hydrological cycle that was dominated by groundwater supply. It is evidenced by a complex mixture of watery-derived structures that includes valley networks carving the Electris and Ridged Plains materials, gullies in the raised Noachian craters and knob slopes, evaporite deposits, and weathered lavas of *eAsp*. Consequently, such a long history of hydrological activity that has been recorded in form of sedimentary deposits or fluvial-related structures strongly suggests Ariadnes as a key area to understand the Noachian-Hesperian transition.

## 4 COOGOON

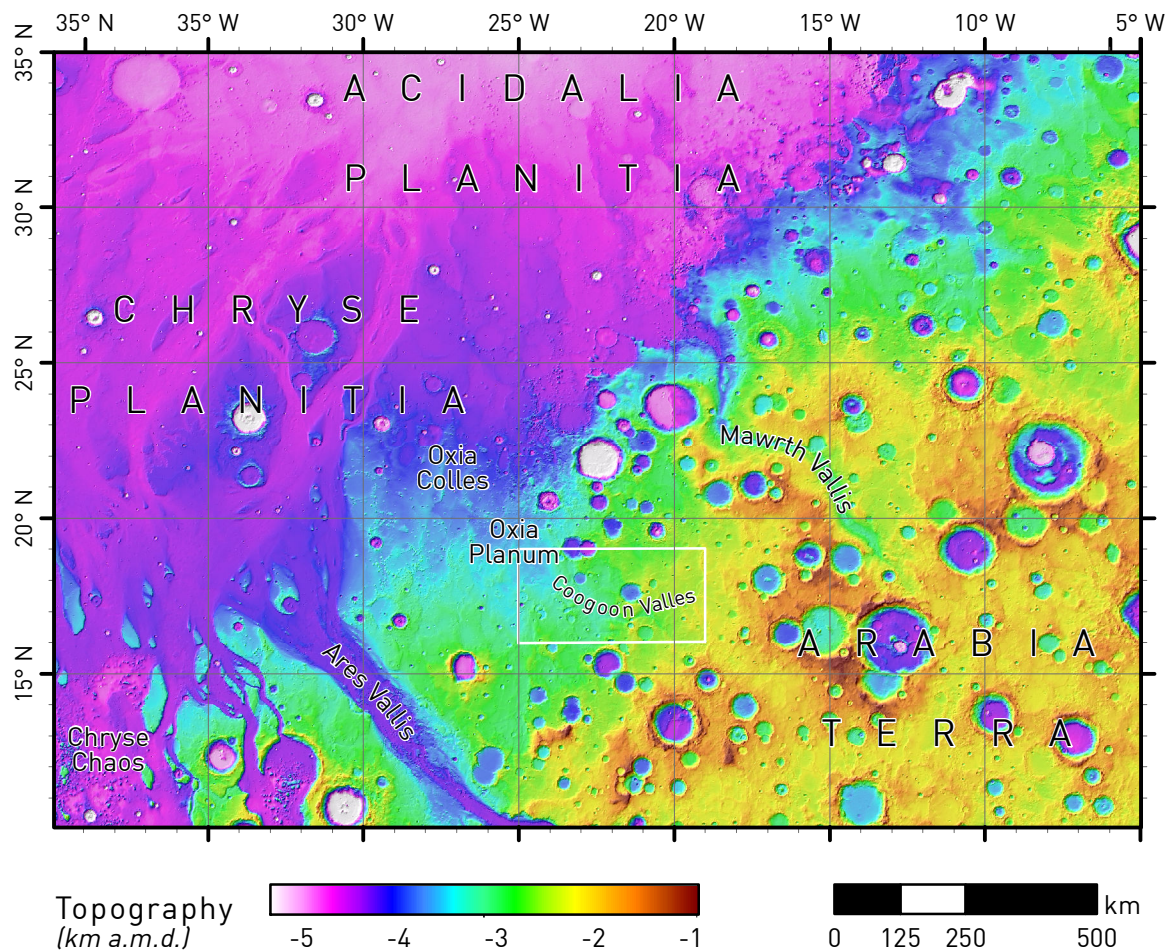
### 4.1 INTRODUCTION

#### 4.1.1 REGIONAL SETTINGS

Coogoon is located in the region of Arabia Terra, that represents a transition in the topography and crustal thickness from the highlands of the southern hemisphere to the northern lowlands [Neumann *et al.*, 2004; and references therein]. This transition is much more gradual when compared with other limiting regions and usually transverses 3 km below to 1 km above martian datum, while the rest of the highlands range from 1 to 4 km a.m.d. (see [Figure 4.1.a](#)) [Dohm *et al.*, 2007]. Furthermore, although the region of Arabia Terra displays an elevated crater density, equivalent to the southern highlands [Brugman *et al.*, 2015], it has typical attributes to characterize it from the rest of the martian highlands. It shows the lowest topography in the heavily cratered terrain on Mars (< 1 km a.m.d., [Figure 4.1.a](#)) [Smith *et al.*, 2001] and a crustal thickness that is more consistent with the northern plains [Zuber *et al.*, 2000]. Such features have aroused many questions about determining the origin of the region that has been proposed to be: **1**) an uplifted part of the northern lowlands [Zuber, 2001], **2**) an extensively denuded part of the southern highlands [Hynek and Phillips, 2001], **3**) the remains of an inundated impact basin [Dohm *et al.*, 2007], or **4**) the remnant of a enormous impact crater rim [Andrews-Hanna *et al.*, 2008]. The Coogoon study area includes a terrain closer to the southern plains, located between Mawrth and Ares Valles, which occurs on the western side of Arabia Terra ([Figure 4.1.a](#)).

The existence of a northern hemispheric ocean during the Noachian-Hesperian boundary (3.5 Ga) is as uncertain as the origin of Arabia Terra itself. Several authors have proposed the existence of the Oceanus Borealis [e.g., Clifford and Parker, 2001; Fairén *et al.*, 2003; Di Achille and Hynek, 2010], a sea which may have affected, surrounded or even covered the area until the Late Noachian. In this regard, Arabia Terra approximately outlines an equipotential line followed by a hypothetic coastline defined as the ~4-Ga Arabia shoreline (Contact 1 in Clifford and Parker [2001]). This shoreline, identified from geomorphologic and topographic analyses, varies in

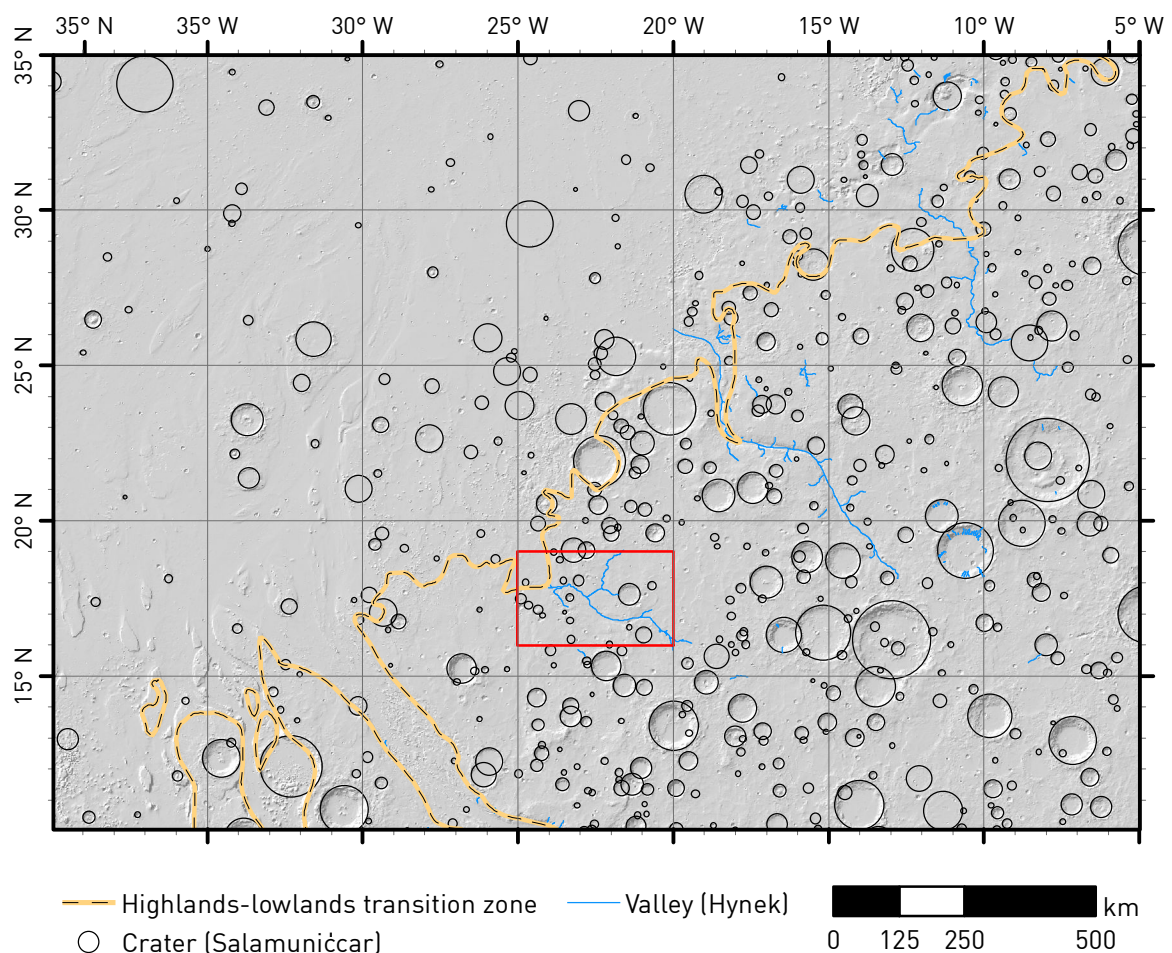
thousands of kilometers in high. In the [Figure 4.1.b](#), the shoreline is represented by the -3 km a.m.d. contour line, which is very approximate to the Arabia shoreline height in the region. This contour line is also close to the global equipotential surface obtained by the analysis of deltaic features and valley networks location ( $-2.5 \pm 0.2$  km a.m.d.) [*Di Achille and Hynek, 2010*], claimed to correspond the maximum extension of a putative ocean ( $1.24 \cdot 10^8$  km<sup>3</sup>) during the Late Hesperian. Among other characteristics, the lower crater density in the lowlands was claimed as evidence for the existence of such an Oceanus Borealis ([Figure 4.1.b](#)) [*Carr and Head, 2003*].



**Figure 4.1.a** Context map showing main regional features around Coogoon Valles in Arabia Terra. The map is a MOLA shaded relief on a stretched color elevation scale (meters relative to Mars datum). The white box indicates the study area.

Either way, water appears to have played a major role in the evolution of Arabia Terra. The heterogeneous topography and long geological evolution of the region have driven to a very complex hydrological activity in surface and subsurface water masses. Such activity, combined with the Noachian to Middle Hesperian climatic

transition, induced the alternation in relevance between erosion, transport, and sedimentation over time [Irwin *et al.*, 2005a; Dohm *et al.*, 2007; Fassett and Head, 2008; Andrews-Hanna *et al.*, 2010]. The combination of all those processes has produced the denuded surface that we can observe today (Figure 4.1.c) [Tanaka *et al.*, 2014]. The occurrence of isolated mesas [Malin and Edgett, 2000; Hynes and Phillips, 2001] and partially degraded craters [Craddock *et al.*, 1997] suggest that the region was exposed to a large erosional resurfacing. This erosion may be associated with the so-called warmer and wetter ancient Mars [Craddock and Maxwell, 1993; Golombek *et al.*, 2006]. Nevertheless, both the lacking of valley networks and the presence of inverted sedimentary structures in Arabia Terra (as channels and fan/delta systems) [Carr, 1996; Hynes *et al.*, 2010] evidence that some other long-lasting resurfacing processes operated in this region besides fluvial erosion [e.g., Malin and Edgett, 2003].



**Figure 4.1.b** Craters larger than 10 km in diameter [Salamunićcar *et al.*, 2012] and main valleys [Hynes *et al.*, 2010] in the region of Western Arabia Terra, that is overlapped to a shaded relief derived from MOLA altimetry. It is showing the -3 km a.m.d. contour line, which is very approximate to the Arabia shoreline height in the region. The white box displays the study area.

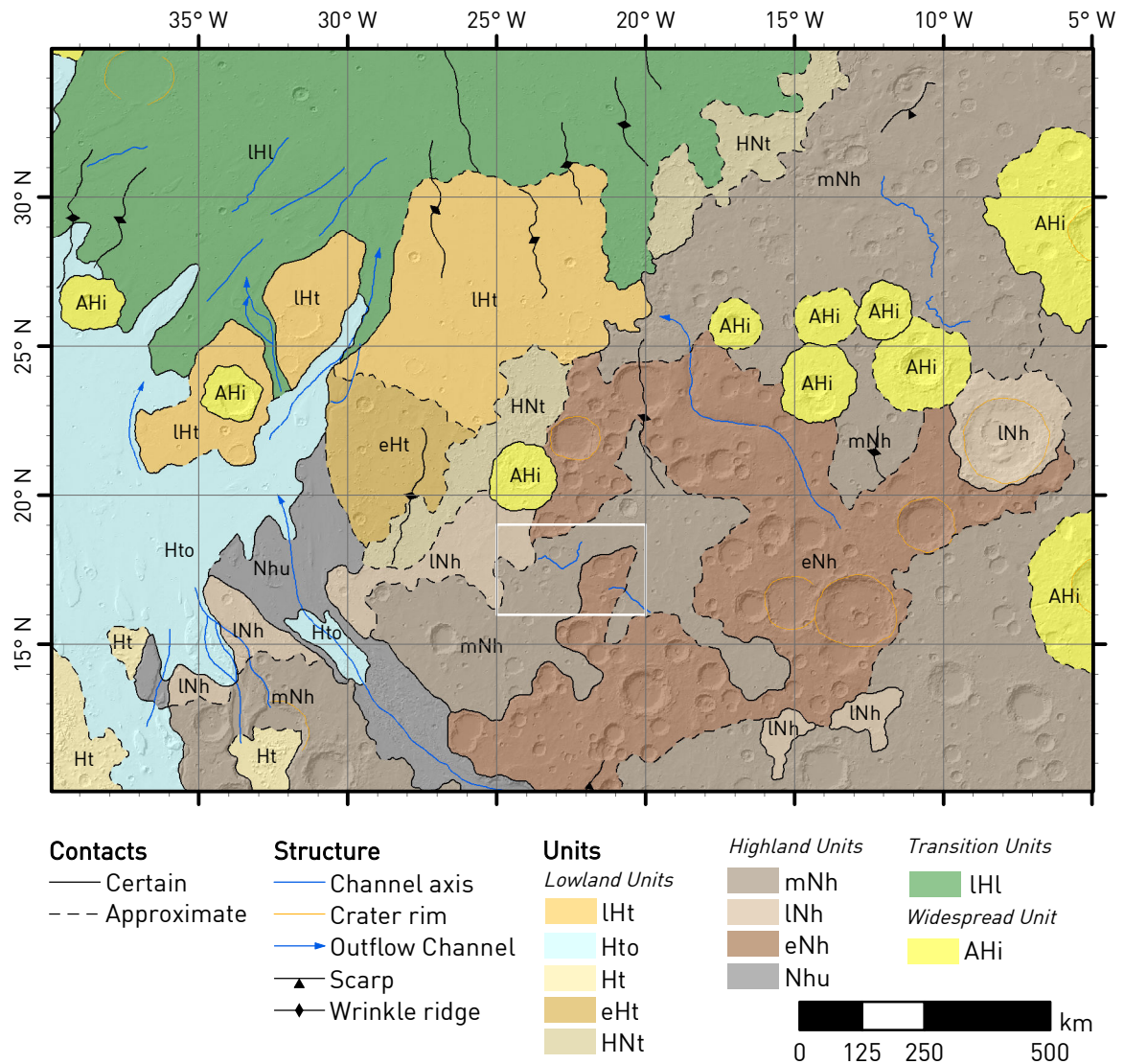


The presence of thick stacks of layered deposits in Arabia Terra has been interpreted as an evidence of deposition of sedimentary rocks in Early Mars [Malin and Edgett, 2000; Andrews-Hanna et al., 2010], though the origin of that layered fine-grained material is not entirely understood. Alternatively, based on their stratigraphy, morphology, and erosional characteristics, those deposits have been described as the result of prolonged volcanic processes [Moore, 1990]. The lack of identifiable volcanic sources that could have produced such deposits in the region is questioning the possible volcanogenic hypothesis for these sediments. However, Michalski and Bleacher [2013] recently detected some irregular craters in Arabia Terra, which have been interpreted to be large volcanic structures. The processes that lead the formation of such volcanic systems should be likely capable of producing explosive emissions of large quantities of pyroclastic tuff [Michalski and Bleacher, 2013] and, therefore, providing a likely source for that materials.

The west of Arabia Terra displays one of the largest phyllosilicate outcrops on Mars, which shows a homogeneous stratigraphy in the region in form of Fe/Mg-phyllosilicate overlain by an Al-phyllosilicate and hydrated silica assemblages [Noe Dobrea et al., 2010]. Indeed, such outcrops are larger than the successions of Noachian phyllosilicate beds described in Mawrth Vallis [Bibring et al., 2006]. The origin of these extensive phyllosilicate deposits is not completely clear, and several working hypotheses have been used to explain their formation that includes sedimentary origin, hydrothermal groundwater circulation, and bedrock weathering [Michalski and Noe Dobrea, 2007; Noe Dobrea et al., 2010; Ehlmann et al., 2011; Michalski et al., 2013b]. The adequate characterization of those deposits is essential to support or reject the water versus the volcanic origin in the geologic history of the region.

Previous studies provided large scale regional maps of the Coogoon Valles region [Scott and Tanaka, 1986; Tanaka et al., 2005, 2014]. Since then, the information about the area has increased exponentially that has ended in 2015 as the selection of Coogoon, Marth Vallis, and Oxia Planum as landing site candidates for the upcoming Exomars Mission.





**Figure 4.1.c** Geologic map of Mars [Tanaka et al., 2014] adapted to the region. The white box traces the study area.

#### 4.1.2 RESEARCH OBJECTIVES

As the aim of this work is to understand those events accompanying the Noachian-Hesperian transition, Coogoon Valles has been selected as an unexplored region to provide additional information to understand such transition and which might have been recorded in form of geomorphic and sedimentary records. In this regard, this area has a channel that had carved the Noachian materials of the Highlands, which has recorded evidence of erosion, transport, and deposition episodes dating back to the Early Noachian. In addition, an extensive erosion has exposed some of the oldest materials in Terra Arabia, which have been allowing the satellite survey.

In order to understand the geological processes that have shaped Coogoon over billions of years, we have produced a 1:1 Million geologic map of the Coogoon Valles channel system centered in the Oxia Palus quadrangle, which extends from 16° N to 19° N and from 335° E to 341° E, respectively (Figure 4.1.a to Figure 4.1.c). This cartography is used as a base for an extensive research about the geological features of the region, which has been conducted in a similar way in the Eridania System. Therefore, it includes the same statistical analyses of crater size-frequency distributions to estimate absolute model ages, as well as the analysis of hyperspectral and IR images.

## 4.2 CARTOGRAPHY

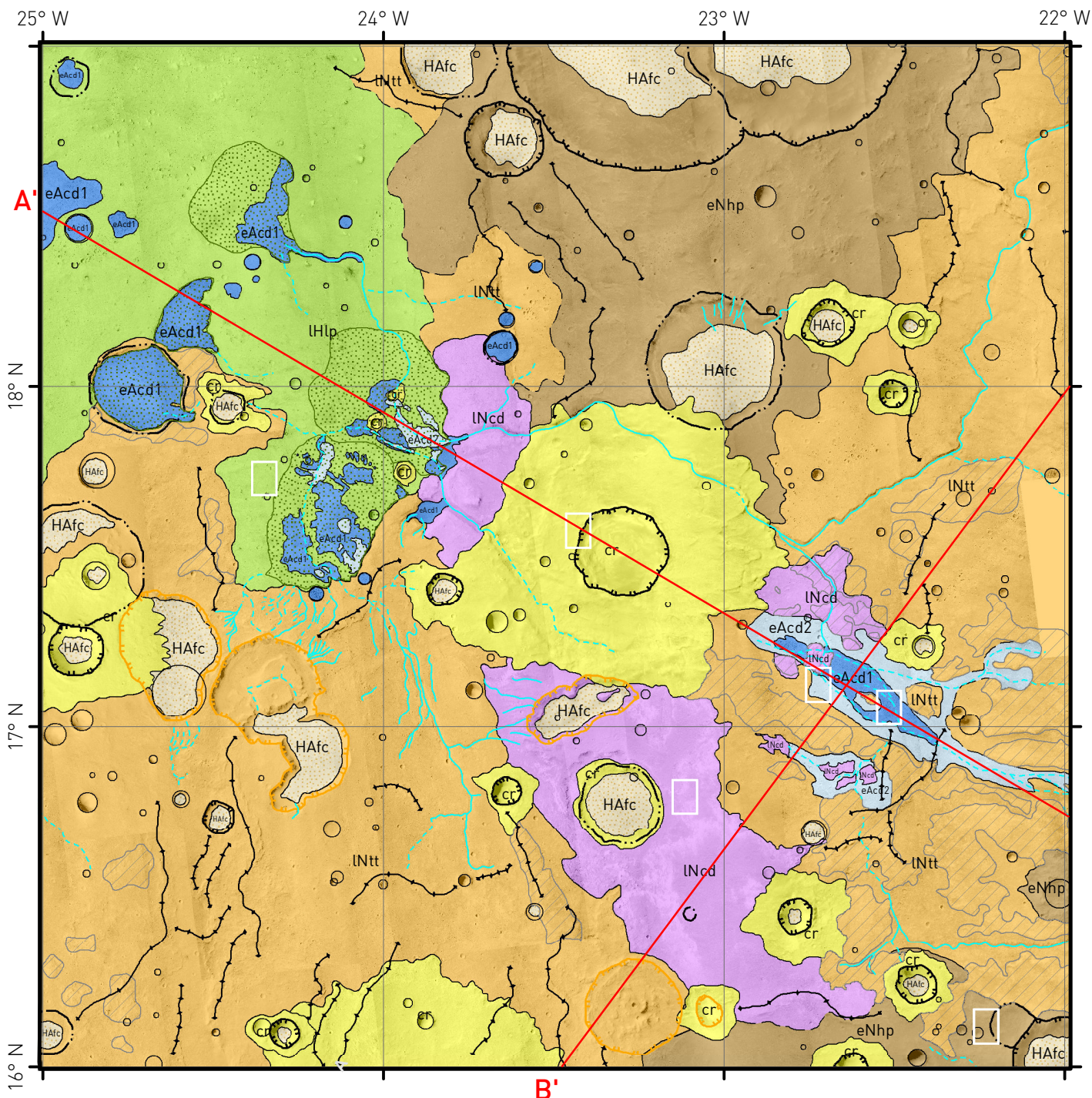
### 4.2.1 GEOLOGIC MAP

The study area ( $16^{\circ} - 19^{\circ}$  S;  $335^{\circ} - 341^{\circ}$  E; [Figure 4.1.a](#) to [Figure 4.1.c](#)) has been classified into eight geological units which boundaries were differentiated depending on whether observed or only inferred contacts by structural and textural changes in visible and IR images as described in Subpart 2.2.4i. In addition, this 1:1 Million geological map of Coogoon includes the delineation of the main geomorphic features affecting the different geological units. These results have been published in *Molina et al.* [2017].

The area includes almost the complete hydrology system of Coogoon Valles with other surrounding channels. In the area, the highest altitude corresponds to the eastern side to reach  $-2$  km a.m.d., from where the topography descends gradually to the W-NW up to an altitude of about  $-3$  km a.m.d. This gradual transition, that goes from the martian highlands to the lowlands, is disrupted by the Coogoon Valles carving.

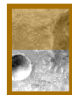
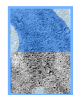
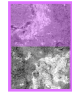

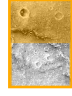
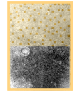
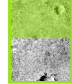
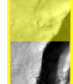
**Figure 4.2.a** (Next two pages) Coogoon area geologic map (regional location in [Figure 4.1.a](#) to [Figure 4.1.c](#)). The legend includes type areas for all the units, and a MOLA colorized hillshaded relief map (bottom left corner).






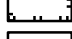
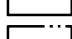
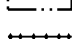


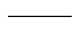
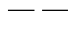



## MAP LEGEND

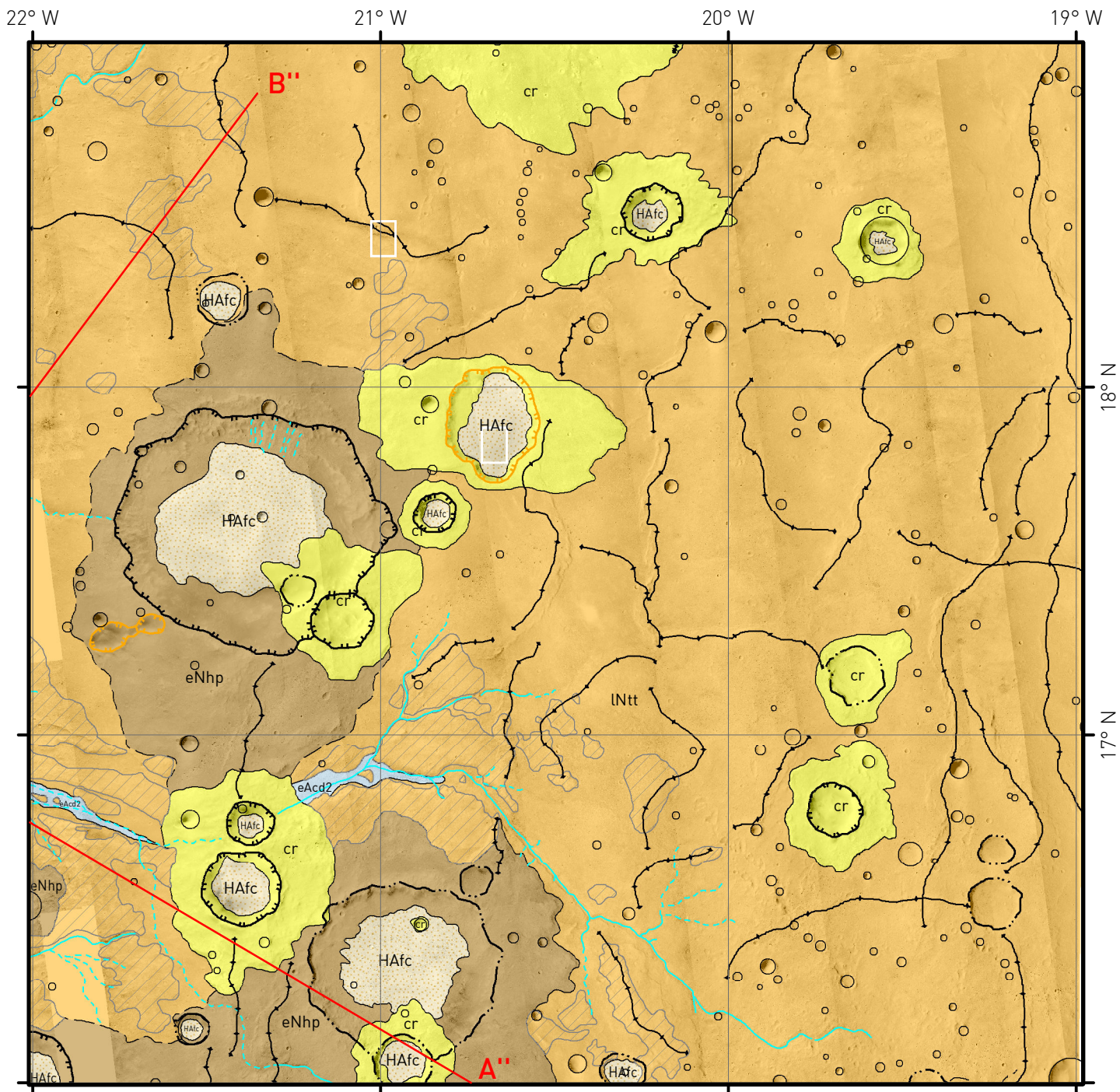
### MAP UNITS

 eNhp EARLY NOACHIAN HIGHLAND PLAINS	 NAcd1 NOACHIAN AMAZONIAN CHANNEL DEPOSITS - Member 1
 lNcd LATE NOACHIAN CLAY-BEARING DEPOSITS	 NAcd2 NOACHIAN AMAZONIAN CHANNEL DEPOSITS - Member 2
 lNtt LATE NOACHIAN TRITIONAL TERRAINS	 HAfc AMAZONIAN HESPERIAN FLAT- FLOOR CRATER INFILLING
 lHlp LATE HESPERIAN LOWLAND PLAINS	 cr IMPACT CRATERS AND EJECTA

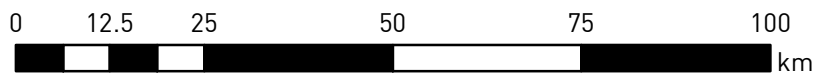
### MAP SYMBOLS

	Mesas, raised remnant terrain
	Fan or delta, fluvial deposits
	Raised rim of uncertain origin depressions
	Raised rim of larger impact crater
	Raised rim of smaller impact crater
	Rimless, degraded or buried impact crater
	Ridge crest
	Shallow depression or valley
	Inferred shallow depression or valley
	Contact - Location accurate
	Contact - Location approximate





Geographic Coordinate System: Mars 2000 spheroid (Semi-major axis: 3,396,190.0 m;  
Semi-minor axis: 3,376,200.0 m; Inverse flattening: 0.0058860)  
Projection System: Equidistant Cylindrical (Central meridian: 180°)



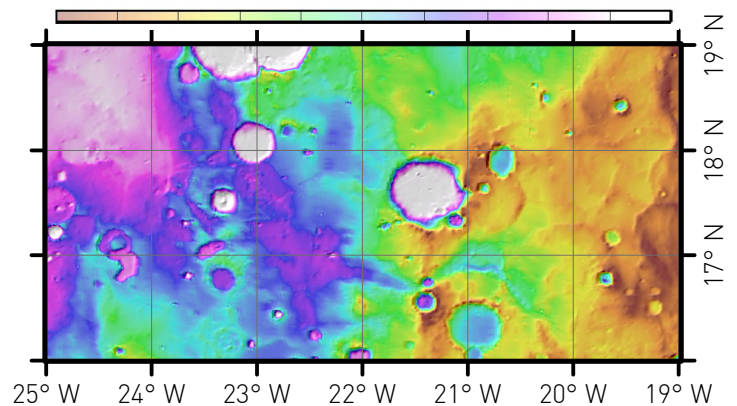
Scale 1:1,000,000 (at publication scale)



### Mars quadrants

	Mare Boreum				Mare Boreum			
	Diacria	Arcadia	Mare Aicalium	Isenius Lacus	Casius	Cebrenia		
90°	Amazonis	Tharsis	Lunae Palus	Chryse Palus	Arabia	Syrtis Major	Amenthes	Elysium
0°	Memnonia	Phoenicis Lacus	Coprates	Margaritifer Sinus	Sinus Sabaeus	Iapygia	Mare Tyrrhenum	Aeolis
	Phaethontis	Thaumasia	Argyre	Noachis	Hellas	Eridania		
	Mare Australe				Mare Australe			
	180°	90° W	0°	90° E				

### MOLA topography (km a.m.d.)





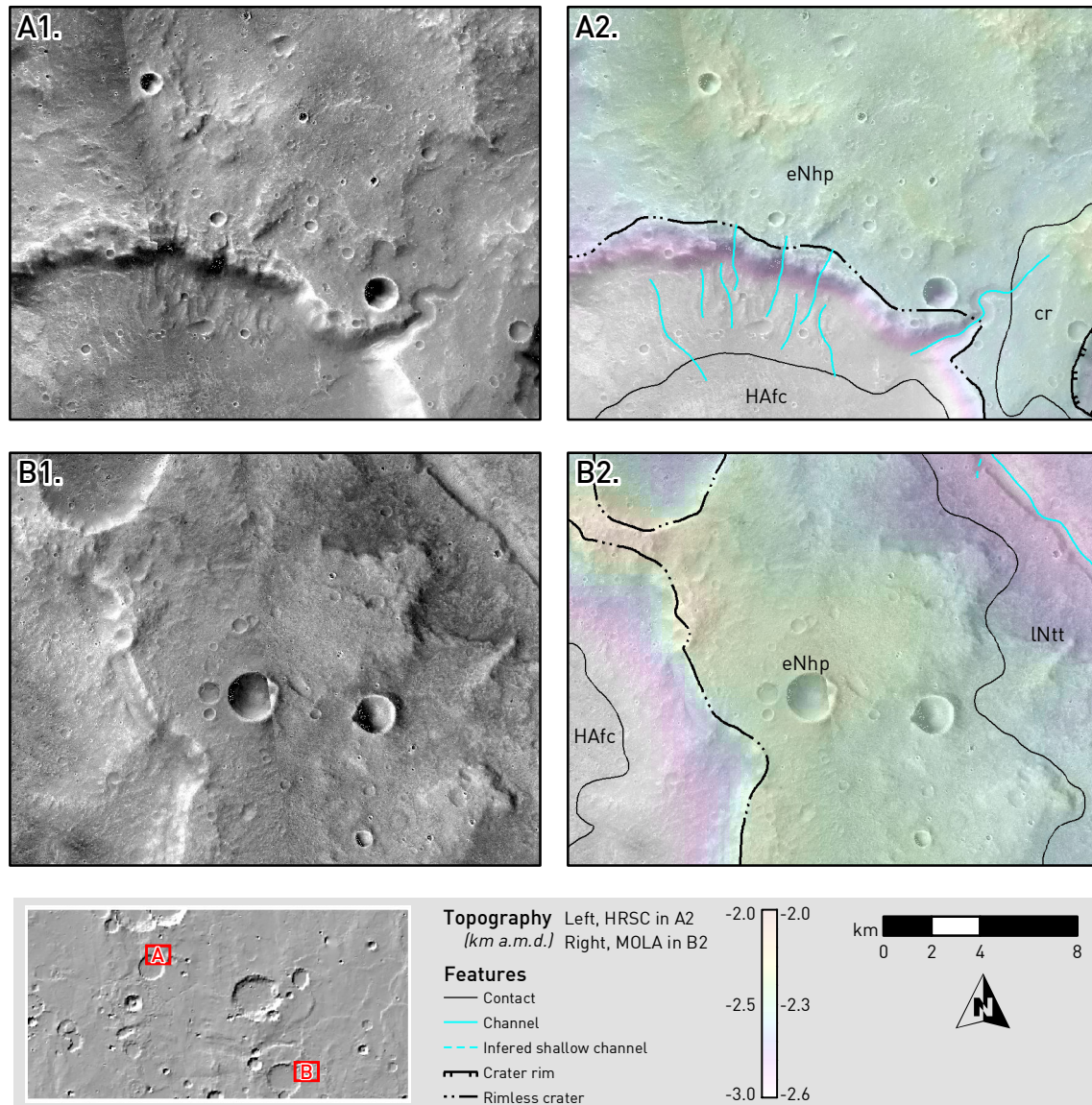
## 4.2.2 UNITS

In the area of study, we have identified eight distinct geologic units on the basis of general morphology, structure and texture, and the interpretation about its possible origin is also discussed. Note that some of the units herein defined coincide with those described in the global map of Tanaka et al. [2014] (Figure 4.1.c). Formation ages and mineral composition are described in Chapter 4.3 and Chapter 4.4, respectively.

### i. *eNhp*, EARLY NOACHIAN HIGHLAND PLAINS

The Early Noachian highland plains unit (*eNhp*, Figure 4.2.a) corresponds to the basement, which is the oldest unit in Coogoon Valles. It occurs in the highland terrains affected by the largest impact craters in the area and in a wide elevation range going from around -2 to -4 km a.m.d. (Figure 4.2.a). Interestingly, those craters display a dense gully systems carving the north rims (Figure 4.2.b-A). The *eNhp* unit is characterized by a rugged, uneven, and heavily degraded surface that displays a relict relief, and which outcrops in the center of the study area.

The surfaces identified here as *eNhp* were defined as Noachian cratered plains unit (Npl) in Scott and Tanaka [1986], Noachis Terra unit (Nn) in Tanaka et al. [2005] and the Early Noachian highland unit (eNh) in Tanaka et al. [2014] (Figure 4.1.c). Such unit has generally been interpreted to consist of ancient crater deposits mixed with mass wasting, aeolian, volcanic, and other materials deposits, that cannot be differentiated [Scott and Tanaka, 1986; Tanaka et al., 2005, 2014]. The most degraded materials in this unit have been identified as the Late Noachian transitional terrains unit (*LNtt*). In this regard, the *eNhp* unit corresponds to the occurrence of high-standing crater materials showing evidence of erosion and degradation. This is supported by the occurrence of sedimentary deposits that are sourced on the crater structures. The clear and consistent identification of *eNhp* is problematic, and sometimes can be perceptible by a slight elevation difference occurring as subtle scarps (Figure 4.2.b-B).



**Figure 4.2.b** Images are showing the *eNhp* unit in CTX images and colorized with MOLA topography, where geological features are included (right column; A2 and B2). (A) Gullies carving the north rim of a crater. (B) A remnant occurrence of *eNhp* unit between an old rimless crater and the Coogoon channel.

ii. *INcd*, LATE NOACHIAN CLAY-BEARING DEPOSITS

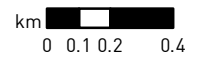
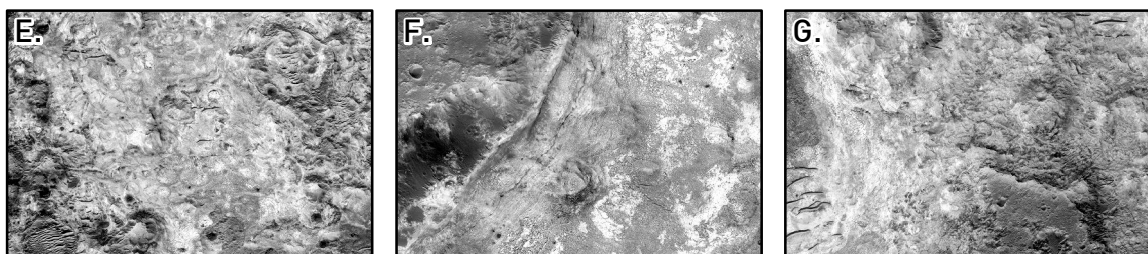
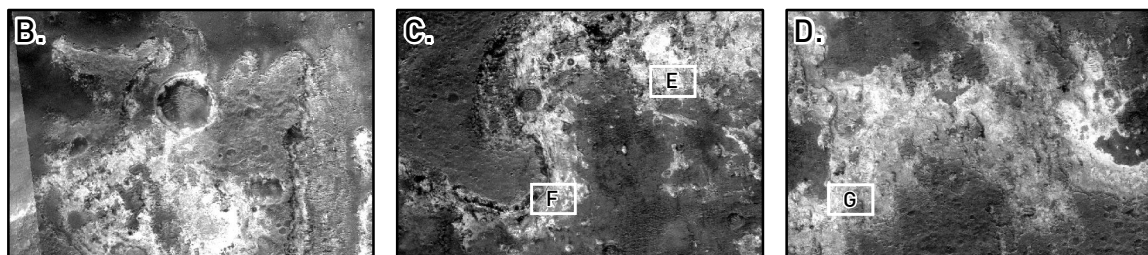
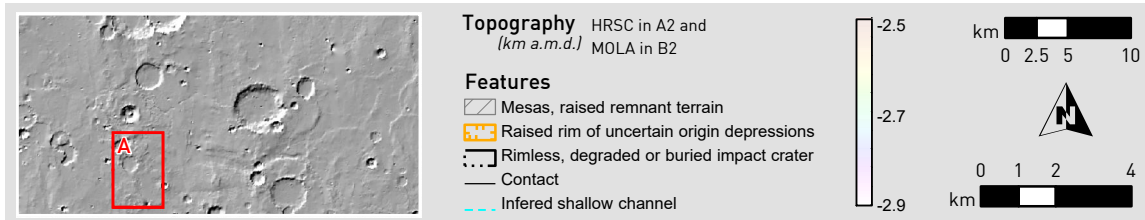
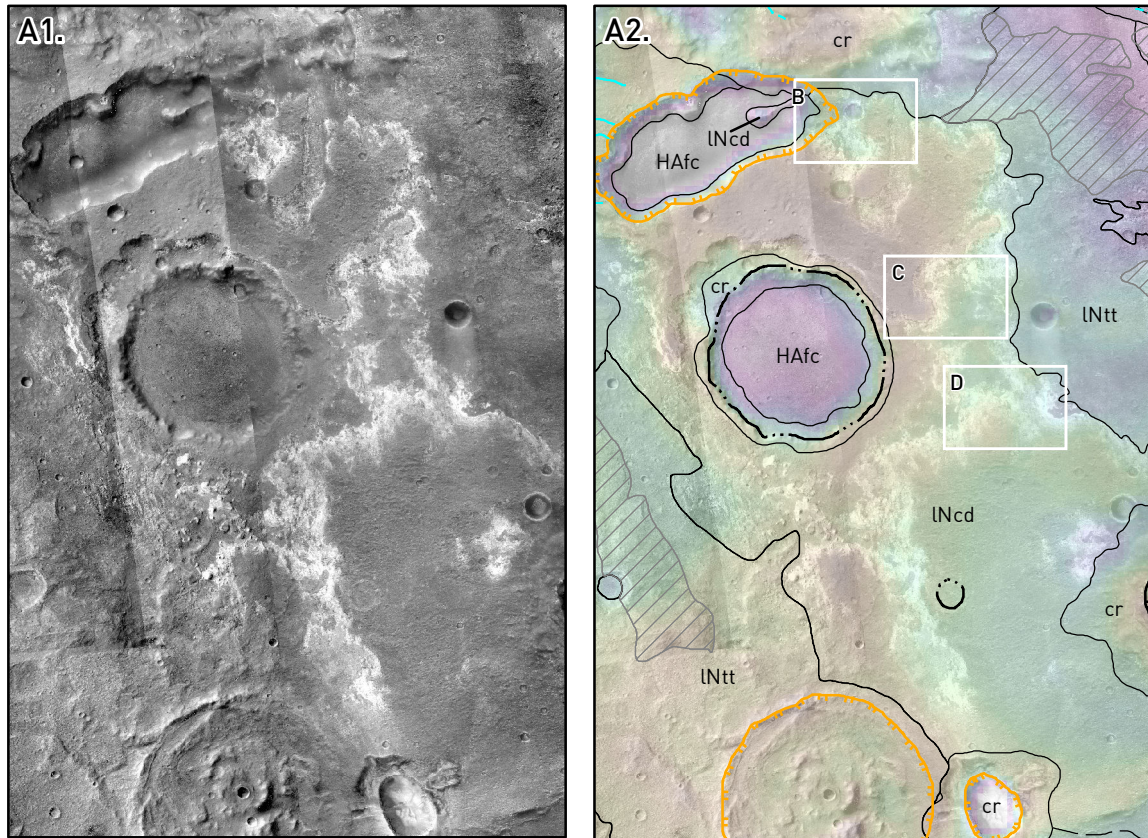
The unit designated as Late Noachian clay-bearing deposits (*INcd*, Figure 4.2.a) shows light-toned (high albedo) materials that are uncomfortably covered by different levels of a heavily cratered and indurated dark capping (or mantling) material [Michalski and Noe Dobrea, 2007; Noe Dobrea et al., 2010]. The clay-bearing deposits consist of layered and indurated deposits that have been exposed by erosion, according to the observed patterns (Figure 4.2.c). They are accompanied by an apparent signature of hydrated materials, which will be discussed later (Chapter 4.4).

While the unit is covered by the dark capping, it has been additionally blanketed by a large ejecta, and both hinder estimating its real extension in the area. From south to north, it seems to extend along a 50-km-wide strip located at the ending location of the Coogoon channel and around an elevation ranging from  $-2.5$  to  $-3.0$  km (Figure 4.2.a). Although the unit shows a bizarre morphology occurring as knobs and mounds around the fluvial structures, the global geologic maps have not differentiated it due to its limited dimension that is only relevant at larger scales.

The spectral (Chapter 4.4) and textural (Figure 4.2.c) characteristics observed in hyperspectral and hi-resolution images (Part 2.1.2) allow to differentiate four distinctive lithological sets that agree with the Noachian stratigraphy described in Mawrth Vallis [Bishop *et al.*, 2008; Wray *et al.*, 2008; Loizeau *et al.*, 2012] as the following: 1) the lowermost Fe/Mg-phyllsilicate-bearing materials (*Member A*), 2) the lower intermediate Al-phyllsilicate-bearing materials (*Member B*), 3) upper intermediate dark-toned capping materials lacking of clear spectral signature (*Member C*), and 4) dispersed hummocky deposits accumulating in topographic depressions and with a dark spectral signature that overlies the *Member A*, represented by the Fe/Mg smectitic deposits.

The *Member A* of the *INcd* unit has an internal layering and a maximum thickness of 400 – 500 meters [Noe Dobrea *et al.*, 2010]. It should be easily degraded as it is only found in low terrains and does not show abrupt landforms as mounds, cliffs, or boulders, resulting from erosion. It displays circular patterns that can be eroded crater remnants. Under the HiRISE image resolution (Table 2.1.b), the *Member A* displays a massive and smooth surface that splits up in angular and large blocks (up to 10 meters in diameter) to form a polygonal texture with sharp edges (Figure 4.2.c-F and G). In this regard, such a polygonal pattern is found to occur in other areas with Fe/Mg smectite-rich deposits. As the multilayered material is easily friable, the rock blocks are transported downslope and get to occur as an accumulation of more fractured sharp boulders at the bottom of the hills.





**Figure 4.2.c (Previous page)** Outcrops of the *eNcb* in a CTX image mosaic (A1) colorized with MOLA topography and including some interpreted geological features (A2). The denuded surfaces (B to D) are shown in the CTX images, where *Member C* was eroded exposing the clay-rich materials of the *Member A* and *B*. The hi-resolution images allow to appreciate the texture, layering, and structures in the deposits (E to G).

The *Member B* of the *INcd* unit usually occurs a 30 – 60 thick deposit forming cliffs in topographic highs above the materials of *Member A*, which suggests that is more resistant to erosion. However, there is no record of alluvial deposits at the bottom of the cliffs. As this unit is also light-toned, it is sometimes indistinguishable from the underlying *Member A*. The *Member B* has a massive to polygonal texture, which has a splitting pattern tighter than the polygonal cracks in the *Member A*. In this regard, it has rounder and more ordered polygons which size is lower than 2 meters (Figure 4.2.c-E and G). In some cases, the space between polygons is filled by a cementing material that locally forms lineaments and ridges. The occurrence of dunes showing a high albedo likely indicates that the fine light-tone materials are weakly lithified, and easily transported by the wind after erosion. Although the *Member B* is usually devoid of structures, it occurs in cliffs when covered by the cap unit and forms buttes in places where the cap unit has been completely removed. This effect suggests that *Member B* materials are competent, though their surfaces do not retain craters. In addition, it is obvious that the *Member B* is more easily erodible than the dark overlaying materials (*Member C*), as the impact craters are erased by erosion faster than the cratering rate.

A hardened layered material overlying the lower phyllosilicate-bearing units has been defined as the *Member C* of the *INcd* unit (Figure 4.2.c). It displays a low-albedo and, based on a spectrally neutral signature, has an anhydrous composition (see Subchapter 4.4). As the inner layering is relatively thin, it complicates to evaluate whether the cratering is affecting to older deposits after being draped by the capping unit, or, subsequently impacted and postdated the indurated deposits. In any case, the *Member C* is strongly affected by high crater density, which suggests a long-time exposition to the surface. As this unit is competent against erosion, show a frequent association with inverted structures including craters, valleys, and basins.

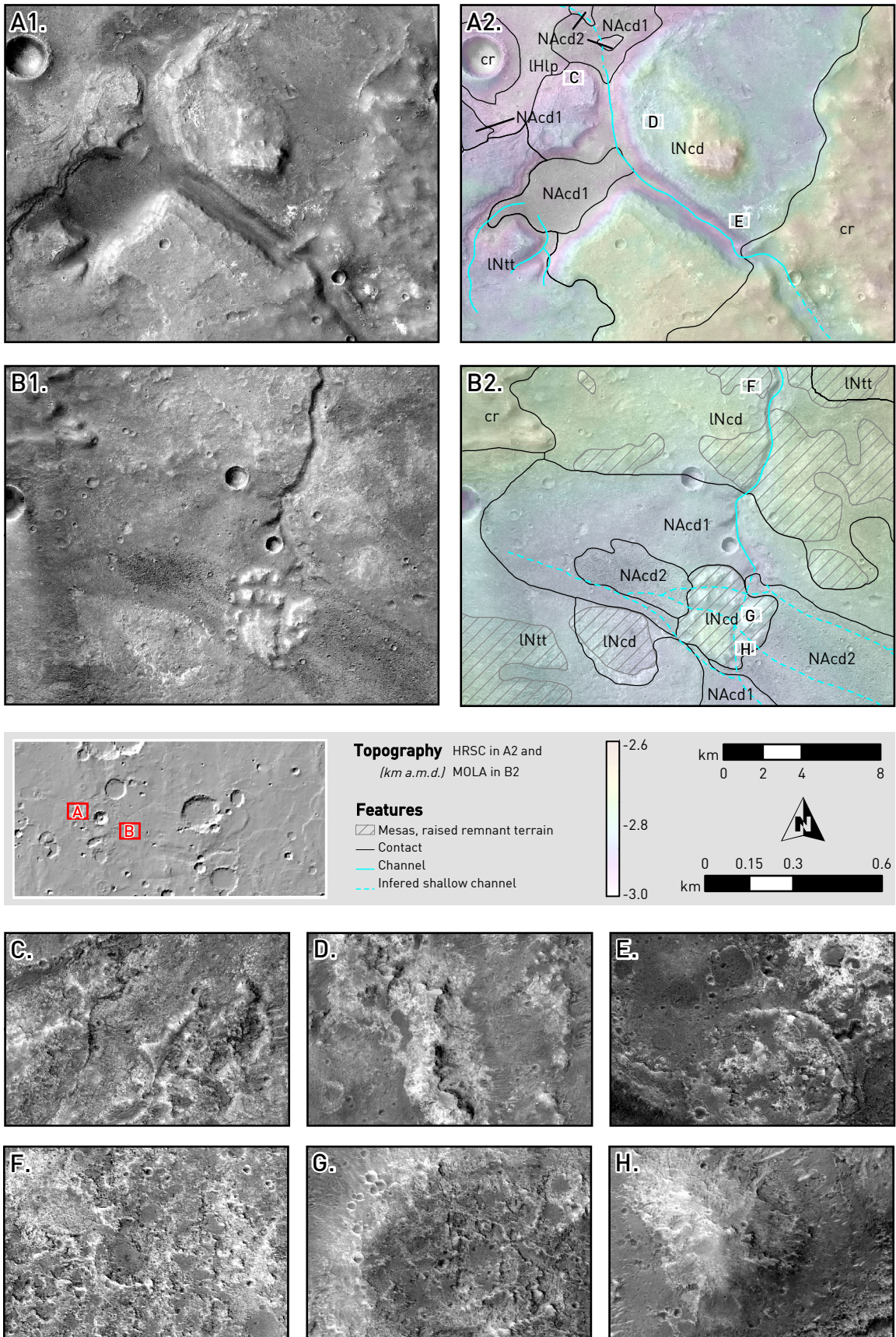


Finally, the *Member D* of the *INcd* unit usually accumulates in topographic depressions where overly the *Member A*. This material templates the polygonal textures of the lower phyllosilicate subunits, which suggests it is relatively thin. As it does show hummocks and boulders, this suggests that it has experienced some lithification degree.

The *INcd* unit includes several types of surfaces and it is composed of different lithological units that have a diverse set of structures and textures, which additionally are exposed to a varying degree of alteration. As a consequence, the delimitation of the real extension of *INcd* is challenging. In this regard, the [Figure 4.2.d](#) compile few examples of deposits in Coogoon that were categorized as *INcd*. Although the termination of the Coogoon channel is not as denuded as the outcrops shown in [Figure 4.2.c](#), it is possible to observe few occurrences of bright polygonal surfaces ([Figure 4.2.c-C to E](#)). It emplaces the real extension of the clay-rich strata to the terminal location of the channel.

The *INtt* unit occurs emplaced in mesas and highly eroded mounds ([Figure 4.2.c-F](#)). In this regard, the mesa surfaces currently show a 'flaked' or denuded surface revealing isolated bright outcrops with apparent polygonal texture, which suggests that those formations are *INcd* characteristic clay-rich materials. There are some small outcrops in the altered mesa that is embayed by channel deposits in the interior of the main channel, as an island. It is eroded to form a group of mounds that resembles a small knob field or chaotic terrain ([Figure 4.2.c-G and H](#)).

**Figure 4.2.d** (Next page) CTX image mosaics (A1 and B1) colorized with MOLA topography that shows the main geological units (B1 and B2) associated to *INcb*. The better resolution in HiRISE images from some locations shows the textures in the light-toned materials (C to H).

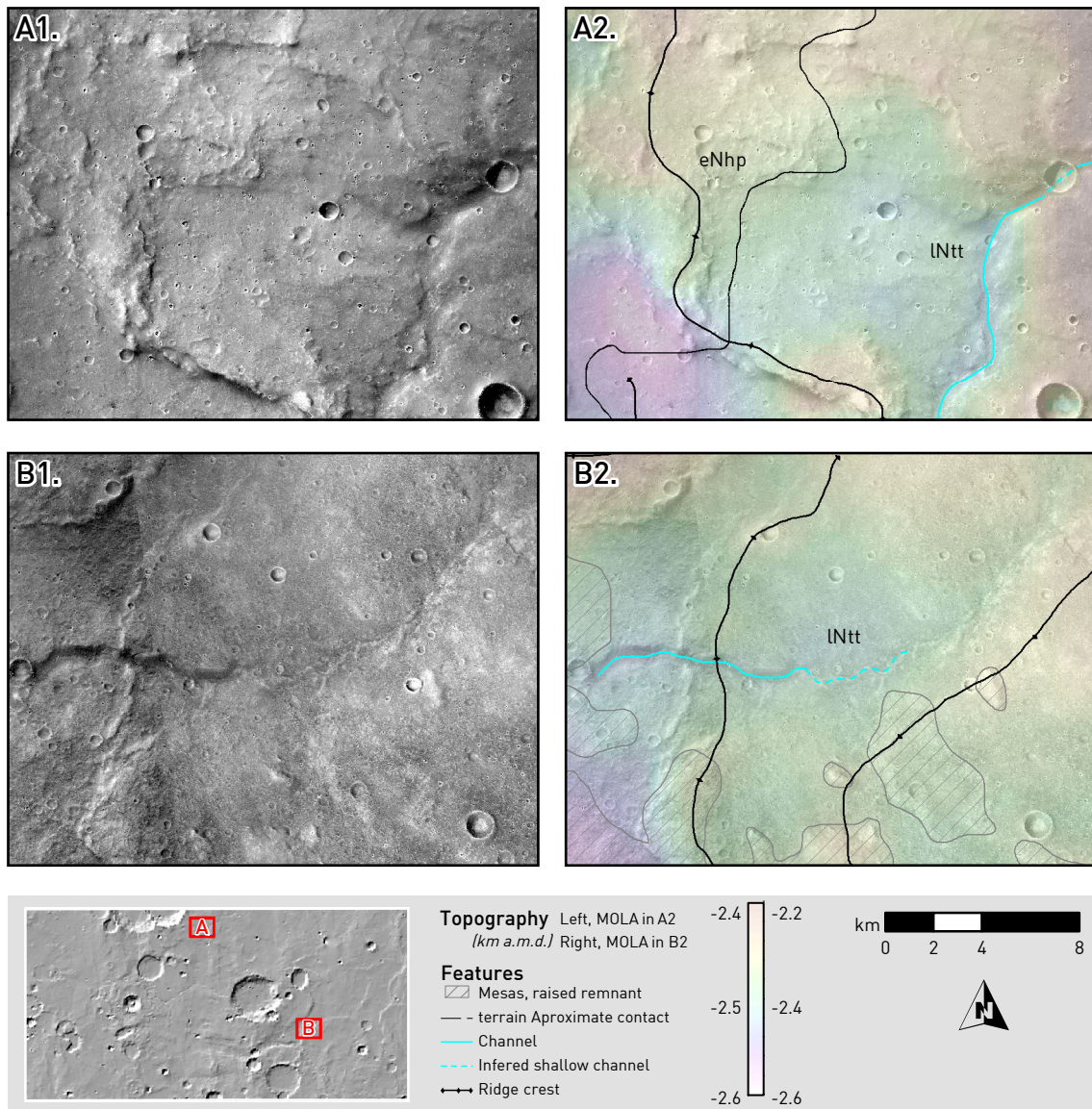


### iii. *INtt*, LATE NOACHIAN TRANSITIONAL TERRAINS

The Late Noachian transitional terrains unit (*INtt*, [Figure 4.2.a](#)) is an indeterminate mixture of materials that has subsequently experience a covering by dust and carving by channels, which have been deformed by several regional suites of ridges ([Figure 4.2.e](#)). It corresponds to the ridged plains material (*Hp*) in *Scott and Tanaka* [1986], was included in the Noachis Terra unit (*Nn*) in *Tanaka et al.* [2005] and nearly matches the Middle Noachian highland unit (*mNh*) of *Tanaka et al.* [2014] ([Figure 4.1.c](#)). Commonly, a sharp gradient separates *INtt* unit, which occurs in topographic lows, from more raised outcrops of *eNhp*. Although the *INtt* materials could have actually originated from physical or chemical sedimentation in topographic lows, they could have also resulted from a volcanic input. The contact of the *INtt* unit is mostly unclear ([Figure 4.2.e-A](#)) because it includes different transition stages.

In the study area, the *INtt* unit is also defined by mesa-like morphologies that are the remnant of an older denuded surface ([Figure 4.2.e-B](#)). Although the origin of the mesas material is unclear, they could have likely derived from the degradation of *INcd*. This possibility is only supported by their proximity to the *INcd* mesas, and by their high albedo, and internal layering. However, the limitation of CRISM coverage (Subpart 2.2.3vi) does not allow to confirm the occurrence of phyllosilicates in the exhumed light-toned materials. Whereas the mesas mostly occur to the south-central location of the study area, the system of complex ridges affecting to *INtt* are mainly limited to the east and west ([Figure 4.2.a](#)). The ridge system displays a preferred north-south orientation conjugated by a secondary SW-NE direction ([Figure 4.2.e-B](#)). Indeed, the secondary heading is consistent with the orientation of some channels, which can be related to tectonic control. A significant number of channels carved *INtt* materials and eroded the mesa-like formations. In the [Figure 4.2.e-B](#) can be observed as a channel erodes one of the ridges crests, which changes the orientation upstream to SW – NE, following the direction of another ridge.





**Figure 4.2.e** Some examples of the *INtt* unit surfaces in CTX image mosaics (A1 and B1) colorized with MOLA topography showing the main geological features (B1 and B2).

iv. *IHlp*, LATE HESPERIAN LOWLAND PLAINS

The Late Hesperian lowland plains (*IHlp*, Figure 4.2.a) form a low cratered smooth surface that occurs at the NW corner, which has the lowest topography in Coogoon (from -3.1 to -2.9 km a.m.d.). This unit surface was previously mapped as the Chryse Planitia 1 unit (HNCc1) in Tanaka *et al.* [2005], and as the Late Noachian highland unit (INh) in Tanaka *et al.* [2014] (Figure 4.1.c). As it can be observed in high-resolution imagery from the occurrence of erosive remnants (Figure 3.1.c-B), *IHlp* apparently has a friable and easy erodible response to geological agents. At those locations where it is exposed, varying polygonal textures are recognized on a large

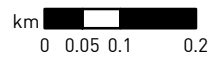
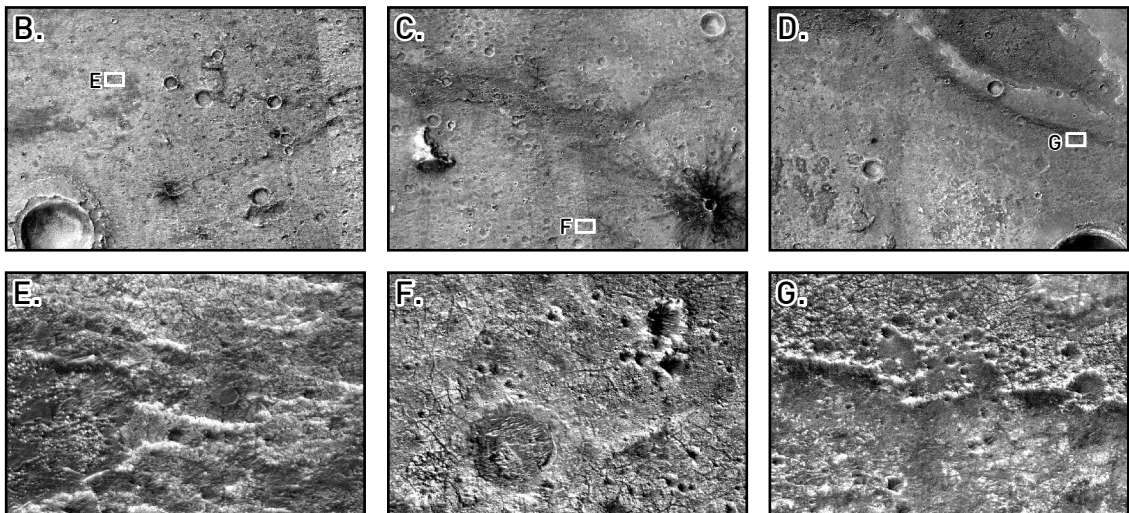
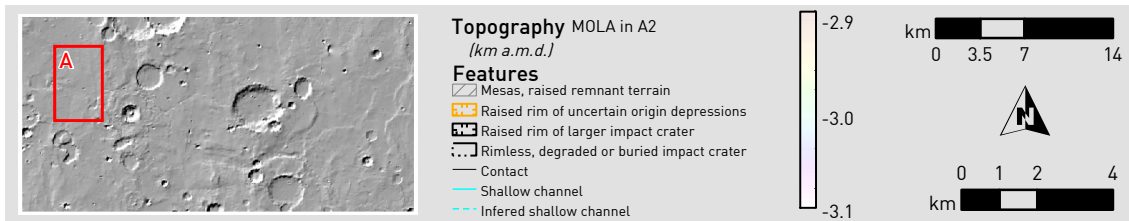
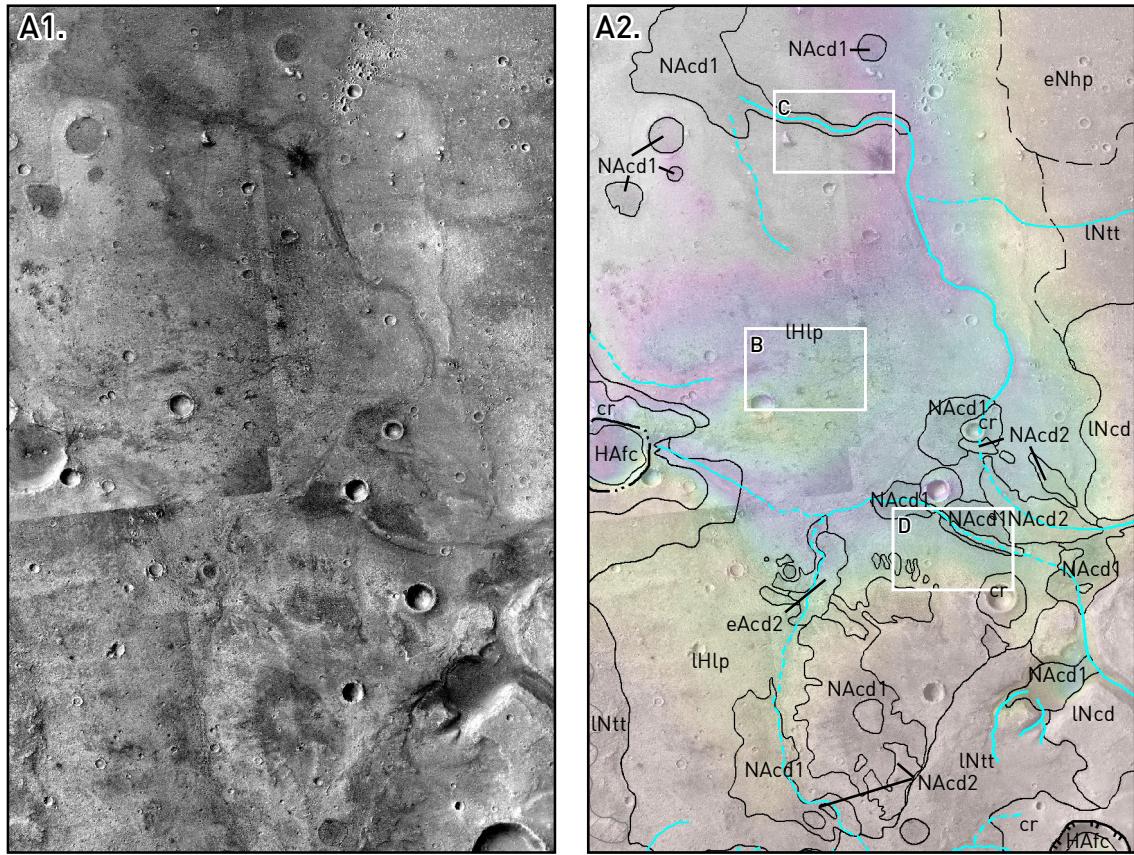


scale. In some locations, the unit shows a small-sized grain texture that co-occurs with other deposit that has a much greater grain size and sharper appearance (Figure 4.2.f-E). The different materials seem to overlay each other and are topped by a darker capping unit. Although some surfaces display a more uniform texture, as angular-shaped polygons (Figure 4.2.f-F); some other locations show dramatic changes in the surface textures (Figure 4.2.f-G), displaying strong analogies with the channel deposits included in the *NACd* unit (Figure 4.2.f).

A complex system of fan/deltaic deposit is emplaced in front of a sharp step slope that limits the *IHlp* unit to the northwest (Figure 4.2.f). These features are situated on the terminal mouth of the Coogoon channel, disturbed by the impact structures and debris. Younger fluvial activity has subsequently carved *IHlp* and produced new fluvial deposits, which can eventually show positive inversion. Small and isolated knobs of light-toned and massive material are also observed in this unit surface (Figure 3.1.c-C).

The interpretation of the geology, synthesizing all the morphological data, suggest that the *IHlp* unit has resulted from the accumulation of phyllosilicate-bearing material that was eroded and transported from the highland terrains. Subsequent events may have modified the uneven layers of material more friable or produce a secondary texture. Alternatively, the materials may also have been generated by the deposition occurred in a long-standing body of water, which could be suggested by the location of a possible shoreline close to the border of the unit [e.g., Fairén et al., 2003]. Such a lacustrine sedimentation would be lately (or alternately) shaped and modified by fluvial activity. As these materials barely retain craters, making difficult to obtain an age and origin (Part 4.3). Further evaluation of the formation hypotheses is included later in this Ph.D. thesis (Part 5.2.5).

**Figure 4.2.f** (Next page) CTX image mosaic (A1) colorized with MOLA topography showing the main geological units (A2) including *IHlp*. At the bottom, HiRISE images showing fabric and texture of morphologies and topological relations with other units in two zoom levels (B to D, up; and E to G, down).



v. *NACd1, NOACHIAN AMAZONIAN CHANNEL DEPOSITS – Member 1*

Both main and tributary channels are filled with materials that show varying textures. The deposits that are filling the main channel show a diverse appearance going from the center to the channel banks that can be observed in the northwest section, where the channel infilling is well preserved (Figure 4.2.g-C). In this regard, the textural differences are also confirmed by thermal inertia (Part 4.4.2). In the center of the channel, a dark pitted material has been named as Noachian Amazonian channel deposits – Member 1 (*NACd1*). Those materials are embayed and overlaid by a smooth flacked material (Figure 4.2.g-F) assigned to the Noachian Amazonian channel deposits – Member 2 (*NACd1*). The *NACd1* materials display a low albedo (dark-toned) and pitted texture. In hi-resolution images, they show bright-toned patches with blocky to fractured pattern only preserved in some locations (Figure 4.2.g-E). In other areas, the collapse and erosion of the overlying deposits of *NACd2* allow observing the real extension of the layer (Figure 4.2.g-D and G). These alluvial sediments locally exhibit irregular polygonal fracturing in large scale (Figure 4.2.g-E to G).

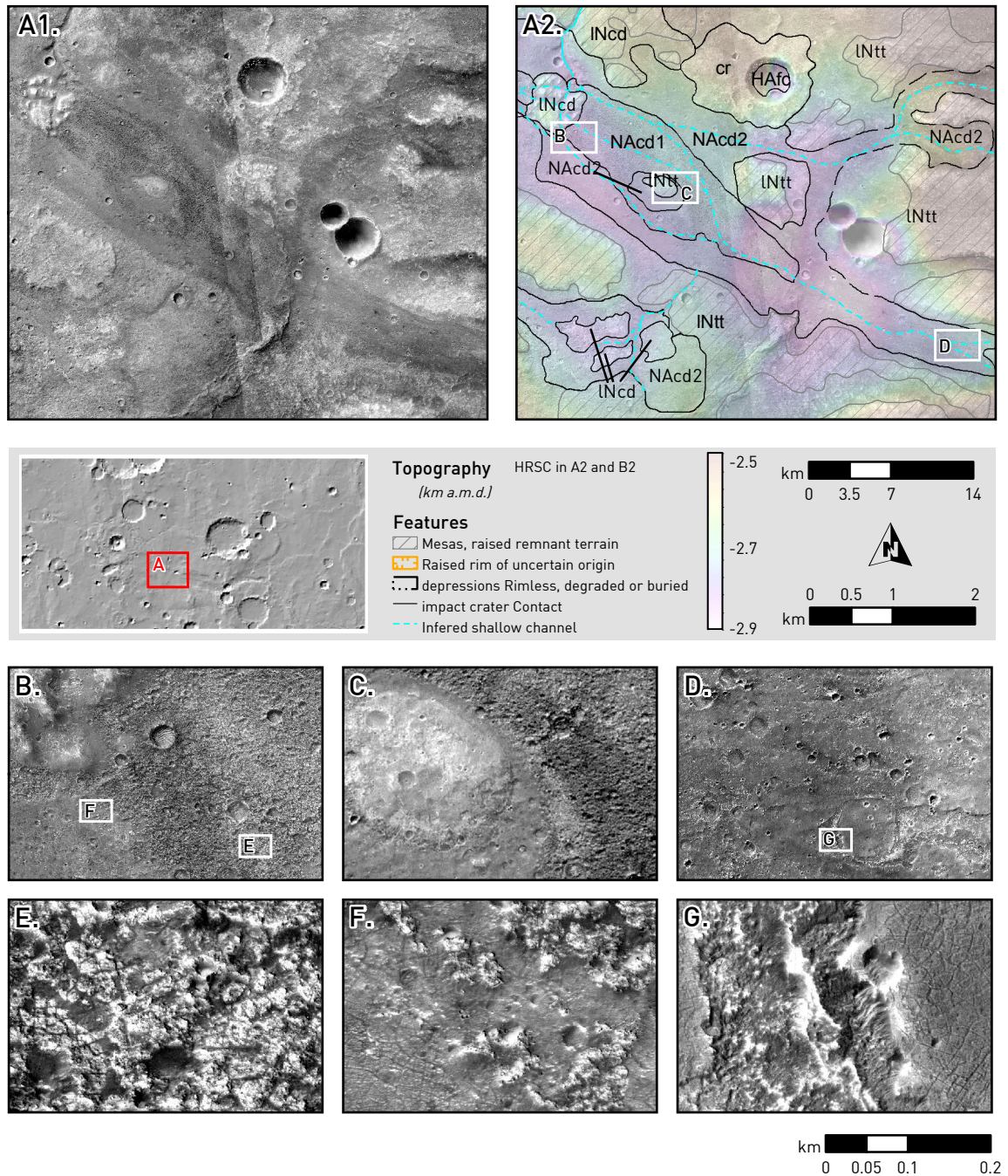
The contact between the fluvial infillings (*NACd1* and *NACd2*) and the older terrains that occur as relict islands (*INcd* and *INtt*) in Coogoon channel is sharp (e.g. Figure 4.2.g-C). In addition, the contact between the smooth *NACd2* unit and the pitted materials of the *NACd1* unit in hi-resolution images suggests that *NACd2* occurs as a thin layer that partially overlay *NACd1* (Figure 4.2.g-F, D, and G). In other locations, *NACd1* can be found in the terminal area of the channel occurring as an inverted fan/delta system and different infillings of craters (Figure 4.2.a and Figure 4.2.f). The higher elevation of the unit in the main channel is about -2.8 km a.m.d., meanwhile at the fan/delta it occurs at an altitude ranging from -2.9 to -3.1 to km a.m.d.

vi. *NACd2, NOACHIAN AMAZONIAN CHANNEL DEPOSITS – Member 2*

The Noachian Amazonian channel deposits – Member 2 (*NACd2*, Figure 4.2.a) occurs in some channel beds and depressions of Coogoon. Where the channel bed is free of the light-toned dunes, it covers the bottom of the channel showing a ‘flacked’



texture. The *NACd2* materials display a smooth texture and are associated with lower values of thermal inertia, which is characteristic of fine-grained dark deposits (Part 4.4.2). The *NACd2* unit occurs along the main Coogoon channel has an elevation range between -2.6 to -2.9 km a.m.d.



**Figure 4.2.g** Some examples of *NACd* outcrops in the main channel. Images are CTX mosaics (A1) combined to colored MOLA topography where the different geological units are shown (A2). In CTX images, textural zonation and relation among the surfaces are clearly observable (B to D). The texture of clay-bearing deposits in hi-resolution images (E to G).



The smooth materials of the *NACd2* unit display a reticulated texture composed of multiscale polygonal fractures that extend over the whole channel bedrock (Figure 4.2.g-F and G). This pattern shows a better preservation than in the *NACd1* unit. Indeed, it is not clear whether this fracturing is original to the upper deposits or, alternatively, the *NACd2* materials template and enhance the underlying textural and structural patterns. The extension of the same structures into both *NACd1* and *NACd2* units suggests that the upper member occurs as a thin layer. Consequently, the *NACd1* materials are visible in those places where *NACd2* materials were not emplaced or have been removed occurring as a ‘flacked’ relict. In this regard, Figure 4.2.g-D and G shows at different scale how the *NACd1* underlies *NACd2* in a crater rim outcrop. In some locations, *NACd2* is replaced by depressions with a round to elliptic shape that expose the underlying materials. Such morphologies resemble the structures resulting from collapse and/or erosion, which adopt a characteristic flacked fabric. As some materials of the fluvial deposits occurring to the NW resemble in appearance, they were mapped as the same unit (Figure 4.2.a and Figure 4.2.g).

vii. *HAfc, HESPERIAN AMAZONIAN FLAT-FLOOR CRATER INFILLING*

Bolide impactors formed craters throughout all the region, which rims and ejecta, including rampart margins and secondary craters, remain relatively well preserved. Such craters postdate the Noachian, when erosion rates across the entire planet may have been significantly higher (see Part 1.1.3). Therefore, the impactor structures do not belong to the Noachian units and are mapped as the impact craters and ejecta unit (*cr*), which will be described in higher detail in the next section. They range in age from Early Hesperian to Late Amazonian and mostly overlie adjacent units. In this regard, many degraded craters were infilled by plains-forming material mapped as the Hesperian-Amazonian flat-floor crater infilling unit (*AHcf*). It includes slope-derived debris, aeolian dust and sand, relocated volcanic air-fall, lacustrine sediments, and fluvial deposits. High-resolution images indicate that the crater floor unit is currently composed of finely layered and friable materials. They cannot be easily put into a chronological context, due to its limited extension that difficulties in establishing stratigraphic relations with other units. However, they were mapped,

when it was possible to characterize them regarding its stratigraphic context (e.g., occurrences of *NACd1*).

#### viii. *cr*, IMPACT CRATERS AND EJECTA

The *cr* unit corresponds to the material excavated from the crater cavity after an impact, which forms a deposit of debris defined as ejecta. It consists primarily of breccias containing a combination of the fragmented and melted materials that have been produced after the impact on the geological substrate [e.g., Barlow et al., 2014]. Since this process introduces new deposits showing abrupt changes in composition and nature with regard to the underlying material, we have defined them as the impact crater and ejecta unit (*cr*), which includes the crater rim, ejecta, and other similar surfaces. The diverse impact crater morphologies that are present in the area will be studied at higher detail in Subpart 4.2.3ii.

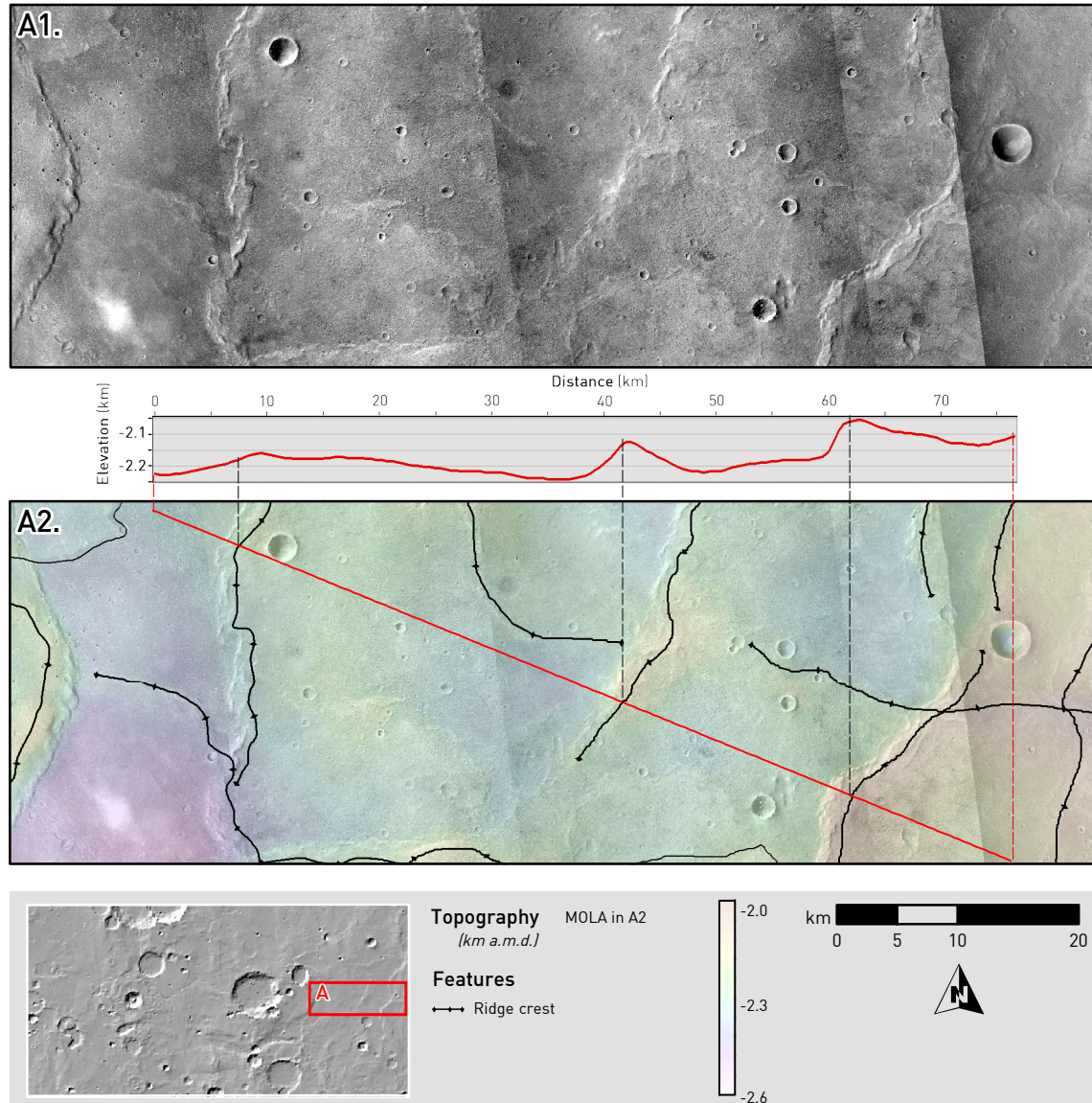
### 4.2.3 GEOLOGIC AND GEOMORPHIC FEATURES

#### i. *Tectonic features*

Different sets of ridges, troughs, and fractures occur in the region of Coogoon. The ubiquitous sets of ridges are characterized by a positive topography, and a sharp side defines cross-section profile traced through a parallel wrinkle, which is followed by a second side with a more gradational gradient (Figure 4.2.h). The most dominant ridge direction system is developing an N-S orientation (Figure 4.2.i). The mapping of several ridge crests (Figure 4.2.a and Figure 4.2.h) has shown that they mainly occur on the surfaces classified as *INtt* and *eNhp* units. It could be the result of the Noachian basement weakening as the consequence of the impact-related fracturing and grind, and comminution of the ancient target material [MacKinnon and Tanaka, 1989].

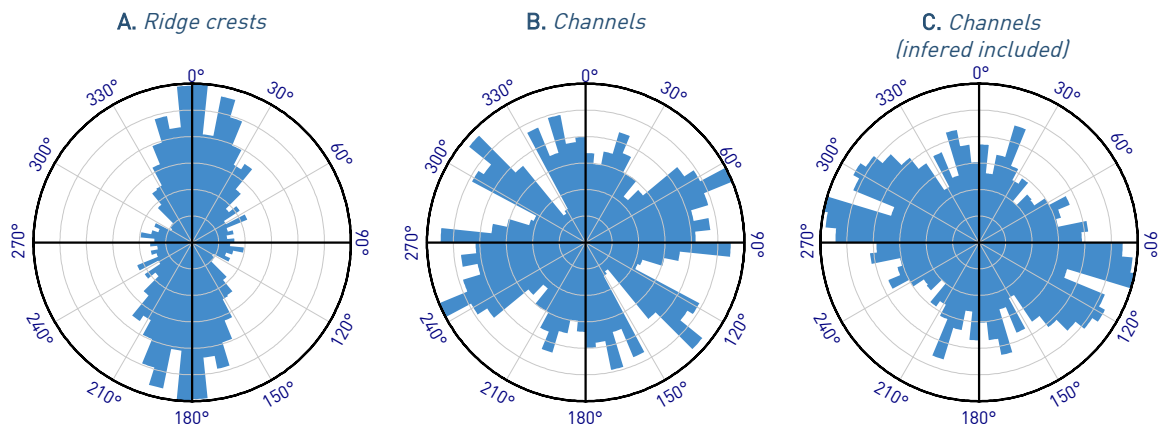
The origin of the ridge sets is not clear, as they can result from a variety and combination of geologic processes that could be related to the early Tharsis deformation, the lowland-highland topographic transition or, on the other hand, some other geological processes including a different tectonic origin, impact deformation, fluvial, glacial, or mass-wasting erosion, and volcanism [Anderson and Anderson, 2010]. In our study area, the morphology of the ridge section suggests that

most of the ridges could be associated with contraction features. Also, the wrinkles are visible following the ridge pattern in the stepped side, though they can secondarily occur as standalone structures.



**Figure 4.2.h** CTX image mosaics showing ridges in the *INtt* unit (A1), which is colorized (B1) with MOLA topography. A cross-section (red line) shows the asymmetrical elevation profile of ridges.

Although faults are not clearly observed in CTX images (Subpart 2.1.2ii), some alignments can be locally recognized, mostly to the NW and SE of the study area. Interestingly, the tectonic structures exert a strong control in the evolution of the fluvial morphologies (Figure 4.2.i), displaying a clear NW and SE alignment, but only if the inferred channels are included (most inside of the channel beds, Figure 4.2.a).



**Figure 4.2.i** Rose diagrams of the azimuthal directions followed by the (A) ridge crests and channels, both (B) observed and (C) inferred, mapped for the Coogoon area (Figure 3.2.a). Directions were weighted by the segment lengths.

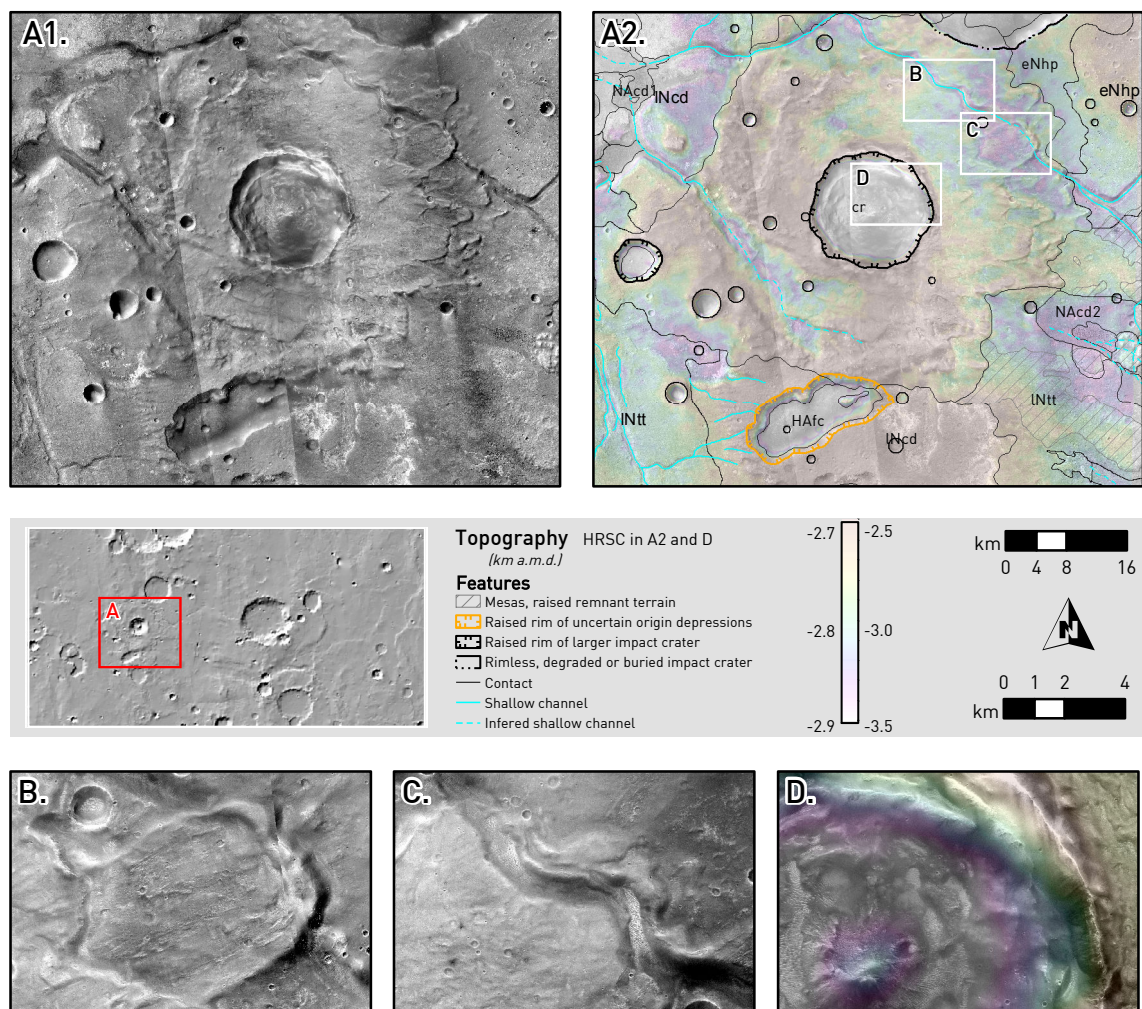
## ii. Impact features

The study area includes some old impact craters that are rimless or have a degraded and/or buried rim (Figure 4.2.a). Most of them are related to the unit *eNhp*, that corresponds to the basement and oldest unit in the study area, which presumably dates from the Noachian epoch. There are also many examples of fresh craters, some of them are so large that their ejecta blankets have covered the older units affecting them. In this context, they are included inside an independent unit that has been defined as impact crater and ejecta unit (*cr*, Figure 4.2.a). Some impact craters display fluidized layer ejecta deposits that were likely formed when the ejected material interacted with a substrate enriched in volatiles or a thicker atmosphere at the time of impact [Barlow and Robbins, 2014]. The study area shows a high diversity of morphologies and degradation stages of this type of ejecta, and of the most noteworthy examples is an impact crater associated to multiple layered ejecta (MLE) occurring centered at 17.5° N and 336.7° E (Figure 4.2.j, that receives the id of S002858B07957R10512K23849T70961Y2005S in Salamunićcar *et al.* [2012]; and 11-000573 in Robbins and Hynek [2012] (see Subpart 2.1.3ii).

The MLE craters have been suggested as an evidence of the existence of liquid reservoirs [Barlow and Bradley, 1990] or volatile-rich substrates in a planetary surface. They are the result of an impactor affecting multiple ice layers or an aquifer [Barlow and Perez, 2003]. Indeed, the central pits, as the one found on the crater discussed in Coogoon (Figure 4.2.j-D), have also been proposed to be formed by degassing of a



volatile-rich substrate during the crater formation [Barlow and Bradley, 1990]. The morphology, thickness, and extension of the ejecta blanket are unequally distributed around the crater. The ejecta lobes are observed more clearly in the eastern side of the crater, where 2 – 3 different ejecta layers can be recognized (Figure 4.2.j-B and C). Conversely, in the western area of the crater, the ejecta layer is less complex, and the multi-layering structure is unclear. Although the impact postdates the fluvial events that carved the encircling ejecta, it is unclear whether the ejecta is covering them (Figure 4.2.j-B) or is in the other way around (Figure 4.2.j-C). An additional scenario is that after the deposition of the ejecta blanket, a reactivation of the channel took place and subsequently eroded the layered material.



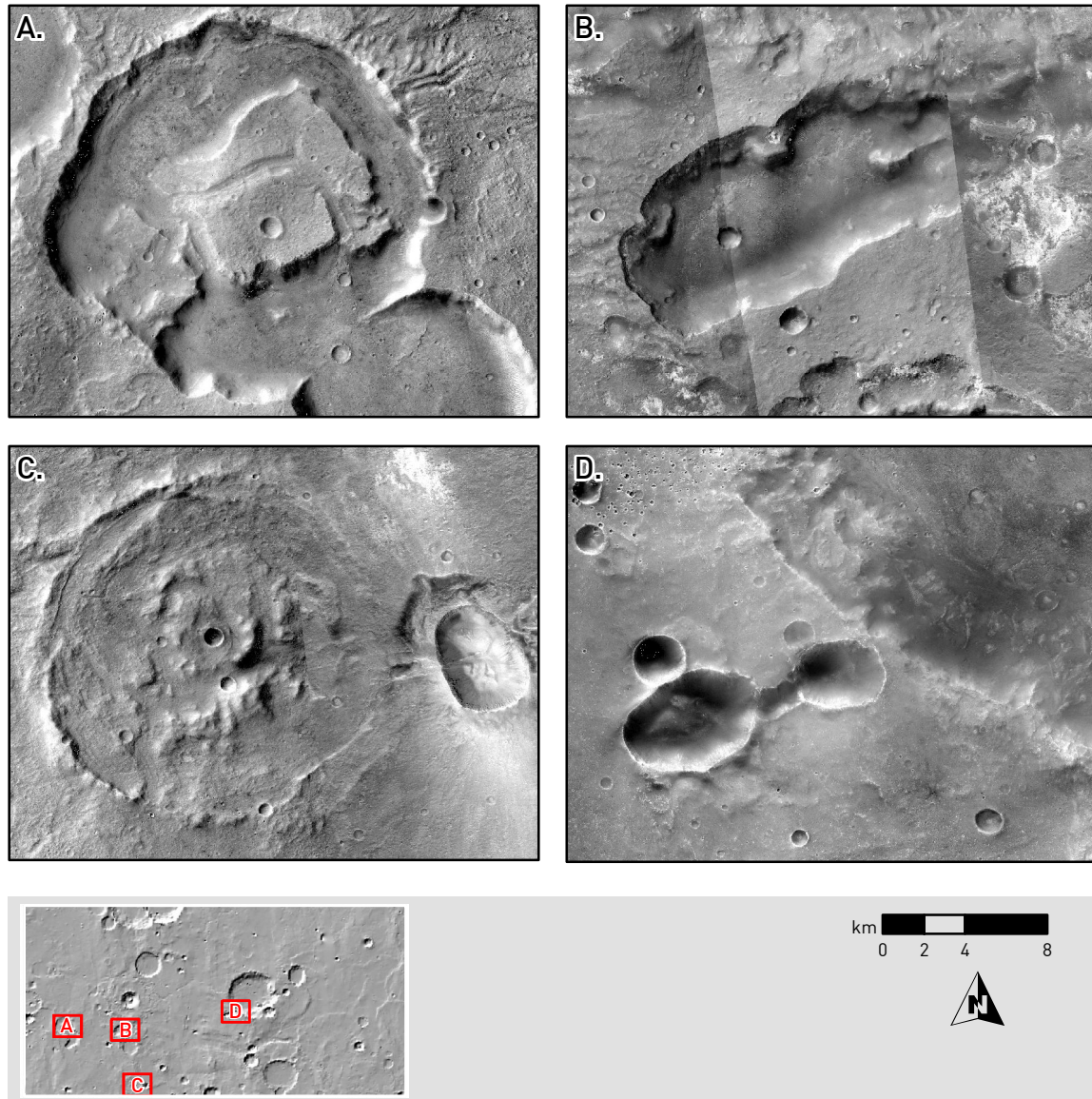
**Figure 4.2.j** Impact crater with a multiple layered ejecta (MLE) in the terminus of Coogoon Valles displayed in CTX image mosaics (A1) colorized with HRSC topography showing the main geological features (A2). Detail of the location where the fluidized ejecta and the channel are contacting (B and C) and central pit colorized with HRSC topography (D).

The crater infillings (*HAfc*) are usually composed of a smooth and flat mixture of materials that includes impact breccia, fluvial, glacial, gravitational, and volcanic-related deposits. In Coogoon, some of the craters are additionally filled with a dark pitted material that resemble the *NACdl* material. These deposits could have been placed by the deposition under a stable water table held by the crater bowl that, in some cases, might have caused the formation of a delta/fan deposit in the crater interior.

Finally, it is worth to mention a group of intriguing topographic depressions that does not fit well with the characteristic impact crater, shown in [Figure 4.2.k](#). They are marked on the geologic map as depressions of uncertain origin ([Figure 4.2.a](#)) and they present either a nearly circular ([Figure 4.2.k-A](#) and [C](#)), or extremely elongated ([Figure 4.2.k-B](#)) to irregular ([Figure 4.2.k-D](#)) geometry (Appendix 8.3). Some of them are also lacking ejecta, uplifted rim, and central peak, showing unusual interior morphologies ([Figure 4.2.k-A](#) and [C](#)).

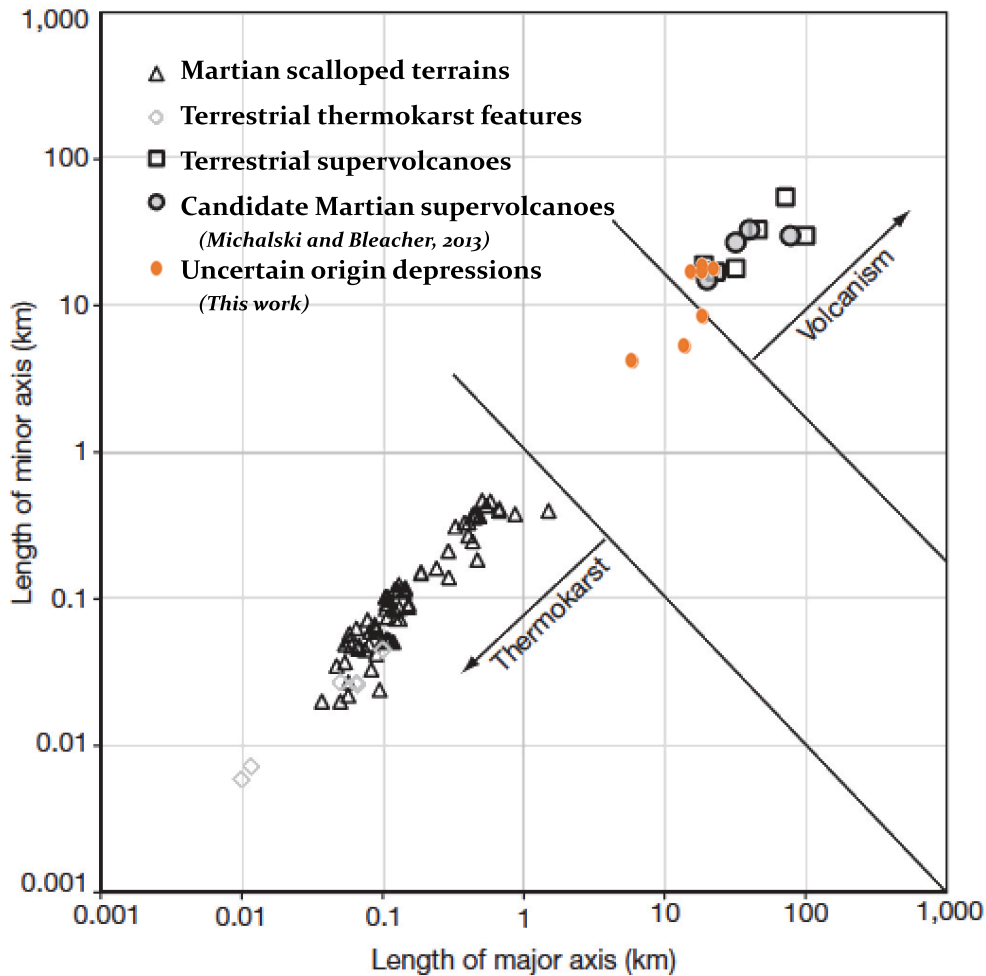
Some of these unusual features may be caused by an impactor that came in at a very low angle or split into different fragments [*Herrick and Hessen, 2006; Herrick, 2014b*]. That is the case of a couple of depressions centered at  $338.27^\circ$  E,  $17.30^\circ$  N ([Figure 4.2.k-D](#)) and  $336.95^\circ$  E,  $16.17^\circ$  N ([Figure 4.2.k-C](#)). The first depression shows an NW-SE major axis of 14 km and an SW-NE minor axis of 5 km (Appendix 8.3). The second depression, much smaller, has a major axis of 5.5 km and a minor of 4.0 km (Appendix 8.3). Both structures show raised rims and degraded ejecta. In addition, the smaller depression exhibits an ejecta blanket with bilateral symmetry that could be the relict of a butterfly ejecta, where the blanket dominantly expands sideways [*Herrick, 2014a*]. Attending to the shape of the ejecta blanket, a new depression located at  $339.32^\circ$  E,  $17.90^\circ$  N ([Figure 4.2.a](#)) can be a degraded version of this kind of impact-related features.





**Figure 4.2.k** CTX image mosaics showing some examples of uncertain origin depressions identified in Coogoon Valles area.

Finally, there is a group of structures that are much harder to classify as they lack the features found in craters and current sedimentary depressions (Figure 4.2.k-A). They correspond to circular structures that are located at  $335.65^{\circ}$  E,  $17.10^{\circ}$  N (Figure 4.2.k-C), and  $336.73^{\circ}$  E,  $16.17^{\circ}$  N (Figure 4.2.k-B) showing a diameter of 19 km and 16 km, respectively (Appendix 8.3). It also includes an elongated and flat-floored depression found at  $336.57^{\circ}$  E,  $16.05^{\circ}$  N that has 19 km in its major axis and 8 km in its minor axis. They lack most of the geological features of an impact origin, and could be caused by a ground collapse instead. This sinking may have produced by several factors, as tectonics, groundwater, thermokarst, volcanism, or a combination of them.



**Figure 4.2.l** Projection of the uncertain depressions found in Coogoon in the scatterplot that show the differences between terrestrial thermokarst and supervolcanoes, and the proposed for Mars. Dimensions for the depressions in this work can be found in Appendix 8.1 [Source: Modified from *Michalski and Bleacher, 2013*].

Indeed, these depressions are similar to those depressions proposed in *Michalski and Bleacher* [2013] as plains-style caldera complexes. In this context, the scatter plot shown in [Figure 4.2.l](#) shows the morphological classification of typical terrestrial and martian thermokarst structures and terrestrial supervolcanoes with regard to the structures in Arabia Terra that have been interpreted as calderas [*Michalski and Bleacher, 2013*]. The scatterplot shows that the volcanic calderas are orders of magnitude larger than the thermokarst structures; and when the uncertain Coogoon depressions ([Figure 4.2.k-A to C](#)) are plotted in the diagram ([Figure 4.2.l](#)), they lay in the range of martian volcanic edifices. The implications and analysis in this regard will be further discussed later (Part 5.2.4).



### iii. *Erosional features*

The Coogoon Valles landscape results from an interplay of channels with an unclear source, which differs in morphology, preservation stage, and relative age [Molina *et al.*, 2017]. The eastern zone is formed by an NW-SE steep-sided channel, carving the Late Noachian transition terrains (*INtt*). In this area, the channel has a V-shaped valley with a straight morphology that fairly keeps a constant width of 600 to 800 meters. At the channel termination, the section is gradually increased to a width of more than 3 kilometers. However, the channel is disrupted locally by younger impact craters and their fluidized ejecta, what prevent to estimate the original dimensions of the channel in the zone. In the eastern area, the Coogoon channel system has an NW-SE direction, which is common to other channels in Arabia Terra as the result of a structural control produced by the basement. The channel is devoid of a well-developed tributary system that is a common feature in the surface runoff channel systems. In some locations, there are short-length (up 5 km) branched tributaries that meet the main channel at nearly right angles, which roughly define a rectangular drainage pattern.

The central zone of Coogoon Valles shows fluvial structures with very distinctive morphologic features that are entirely different from those described in the eastern side of the channel. The main channel in this area is a relict part (~100 km long) of a broad channel with significant variations in section (~4 – 12 km in width). In this location, the channel is morphologically similar to the oldest martian outflow channels ending at the northern lowlands [e.g. Mawrth Vallis; Carr and Head, 2010]. On Mars, the large outflow channels of Noachian age are scarce (See Part 1.1.3), and only a few examples were identified in the highland plains. This wide channel in Coogoon presents similarities in morphology to some sections of Mawrth Vallis (Figure 4.1.a).

The main channel meets a tributary coming from the NE, to form a single channel (i.e., without tributaries) that arrives at the northwestern part of the Coogoon study area. This tributary channel shows similar features to the Eastern Coogoon Valles including constant width, steep-sided banks, V-shaped section, and

few secondary tributaries. The channel resulting from the meeting of the main channel and the tributary postdates the impact crater and the MLE that disrupts the channel termination. In the center of the study area, south to the wider channel section, there is some evidence of another tributary channel showing a discontinuous outline that is flowing from a small depression associated with *INcd* deposits. In this location, there is a second stream displaying a more continuous trace that runs from SE. In this context, the discontinuous trace of channels is consistent with several fluvial reactivation events.

In addition, there is an independent channel system that flows from the NW of the study area to the lowlands, adopting a parallel drainage pattern when is flowing on the *IHlp* unit. It terminates in a delta/fan that is disrupted by a crest, which impedes to evaluate whether or not the sedimentary fan-like structure is connected to the channel system, to another channel occurring west, or caused by groundwater discharge. In the area, we also mapped as erosional features some raised materials that reassembling to relict mesas, which mostly concentrate around the *INtt* and *INcd* units in the central region of the area of study. They occur as scattered structures of elevated topography rising about one hundred meters, which show a rough surface and light-toned patches. They are interpreted as preserved Late Noachian deposits, which alteration by fluvial and mass wasting processes that produced the sedimentary deposits enclosing the relict structures.

#### iv. *Depositional features*

To the west of Coogoon area, the channel is terminated by alluvial fan/delta deposits. In this location, the channel system ends into three different sedimentary structures interpreted as alluvial fan/delta deposits, which show different morphology and degree of preservation (Figure 4.2.f).

The first depositional structure is located centered at 17.6° N, 335.9° E and an altitude of -2.9 km a.m.d. (Figure 4.2.f). Lobes of dark material comprise this complex sedimentary feature with NW direction. As it is not clearly associated with channels in the area, the origin of the sediment source can be hardly recognized. However, the

direction of the deposition indicates that was likely related to the course of the channel system to the NW or the main broader channel. A later deformation of the fluvial network (impact or tectonic related) might have altered the channel course that has previously formed the fan. The occurrence of another lobe appearing south of the main fan/delta-like sedimentary structure is the channel migration southward of the main fluvial system. It would include at least two different stages of formation that suggest a sedimentary evolution, which is compatible with an episodic and long-lasting hydrological activity in the area. In addition, the outer part of the sedimentary fan lobes is fringed by positive structures with a stretch, and sinuous outline, which can be interpreted as a small inverted channel that formed during the generation and growth of the alluvial fan/delta. The area shows high values of TI measured in THEMIS images (Part 4.4.2), which suggests the presence of materials with a coarse texture or the formation of a surface crust (i.e. induration).

A second structure (17.9° N / 336.1° E, -2.9 km a.m.d., [Figure 4.2.f](#)) occurs from a certain distance of the end of the channel system, which suggests that was formed by groundwater / sapping activity. It shows multiple overlying lobes with similar texture and stratigraphy as shown by the *NACd1* and *NACd2* materials ([Figure 4.2.f-D](#)). The surface that underlies the fan lobes is formed by phyllosilicate-bearing materials of the *IHlp* and *INcd* units. However, the eroded margins of the underlying phyllosilicate-bearing rocks do not show of layering. Although the origin of the underlying deposits is unclear, the presence of the same succession of materials observed in the outflow channel (*NACd, Member 1 and 2*), besides they have the same E to W direction as the channel postdated by the MLE crater, could indicate that both structures are related.

It is hard to determine whether such large sedimentary structures are alluvial or deltaic, as we were not able to found certain evidence for an ancient body of standing water (e.g., terraces, shorelines). Also, there is no geomorphological evidence as a crater or topographic low that could suggest the existence of a closed basin. In this regard, although the shoreline found in Arabia Terra dated as 4 Ga [*Clifford and Parker, 2001*] does show no compelling geomorphological evidence of its existence in

Coogoon, the suggested altitude matches quite well with the location of the sedimentary structures.

To the north, we found some structures showing different morphology as the fan-like sedimentary structures described above. The clearest example is a structure centered at coordinates 18.4° N, 335.7° E and occurring at an altitude of -3 km a.m.d. (Figure 4.2.f). This feature resembles an alluvial fan that occurs at the end of a single channel running out from the south and entering into the plains of Oxia Planum (Figure 4.2.f-C). Such a large sedimentary structure is composed of dark deposits with a similar appearance as the materials of *NACd1*. The fan is located at the end of a sinuous inverted channel, which shows a discontinuous outline due to infilling and degradation by erosion and the same texture than the *NACd1* found in the other structures.

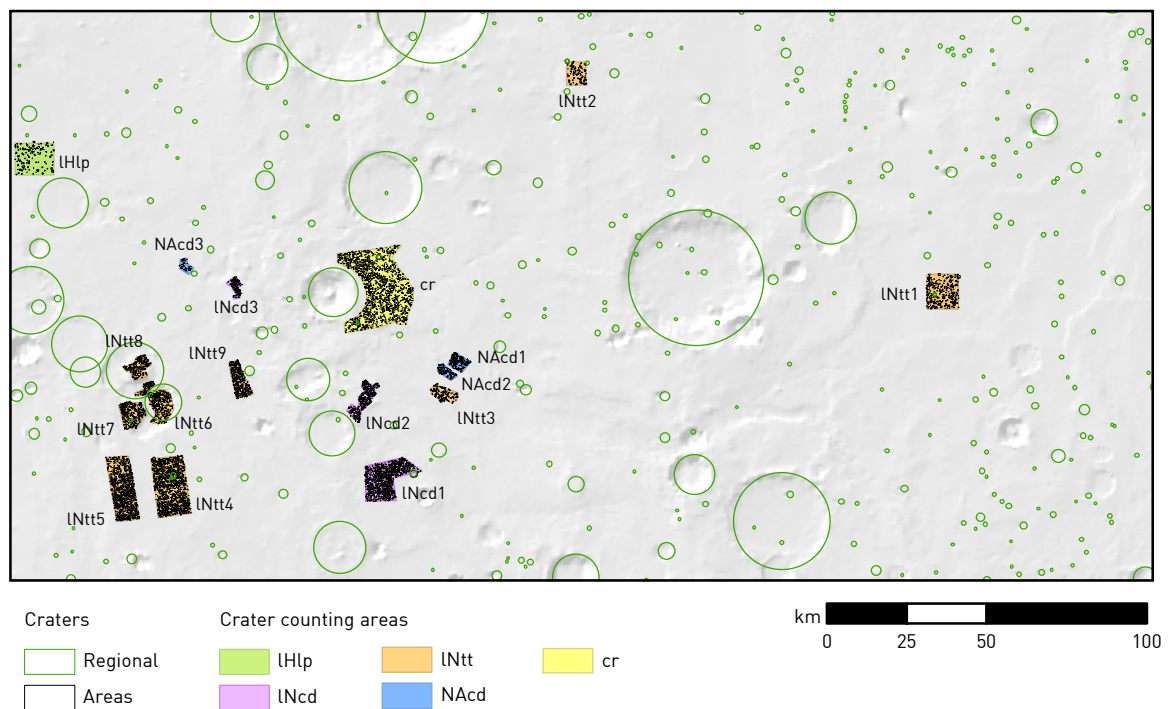
At a very close position to the alluvial fan, there are a couple of fan-shaped structures, also with similar textures, occurring to the west and southwest, respectively. One of them seems to fill old and degraded craters, obscuring the fan-like shape. Attending the topography and morphologies observed in the high-resolution images (Figure 4.2.f-A, B, and E), there could be a channel network connected to the deposits. The channels have been exposed to an episode of erosion and burial that left inverted channels and patches of phyllosilicate-bearing material.



## 4.3 DATING

### 4.3.1 SELECTED AREAS

The ages assigned to each of the previously described mapped units were based on the analysis of the CSFD in the area of Coogoon Valles. In this way, the formation ages and resurfacing events that have affected the surface of the area were constrained. To achieve that, we have selected sample areas from the most relevant geological units and geomorphological landmarks (Table 4.3.a, Figure 4.3.a). The areas were chosen based on representativeness and availability in the coverage in CTX images (Subpart 2.2.3ii). The craters inventoried in the database of *Robbins and Hynek* [2012] (Subpart 2.1.3ii), where the area matches the extension of the study area in Coogoon Valles ( $16^{\circ} - 19^{\circ} \text{ N}$ ;  $335^{\circ} - 341^{\circ} \text{ E}$ ; Subchapter 4.1), were used for regional ages.



**Figure 4.3.a** Map of the selected areas to apply crater counting resumed in the Table 4.3.a. The polygons were symbolized after the same color pattern as the units shown in the geological map of Subchapter 4.2. Craters used in the discrete areas are differentiated of the crater analysis in the region. The background image is a MOLA shadow relief map.

As denudation and tectonic stress dominate the surface of the region, it is challenging to obtain a reliable estimation of the surface age. Consequently, the

selection of the dating areas becomes crucial. At this scale, the age of the basement, the Early Noachian highland plains (*eNhp*), needs to be inferred from the regional age, as their outcrops are limited and quite degraded. However, the surfaces that have been formed from the alteration of the *eNhp* unit, the Late Noachian transitional terrains (*INtt*), shows larger and well-preserved outcrops in the area. In order to characterize the surfaces of *INtt*, two uniform samples including the ridged highland plains were selected, as INtt1 to the east and INtt2 to the north of the study area (Figure 4.3.a). While the first unit represents a uniform surface between the conjugated ridges of the *INtt* surface, the INtt2 dating area is located right next to a channel. In addition, we have distinguished an area named INtt3 that is also alongside a fluvial feature that occurs south the central zone of Coogoon main channel (Figure 4.3.a). As some of those surfaces were modified by fluvial events, the areas were selected to elucidate the resurfacing effect of the channel along the surface of *INtt*. In the same way, the INtt3 and INtt4 areas were chosen to test the ages in the SW sector, where there is another channel system (Figure 4.3.a). To the west, INtt3 has a crest, while INtt4 to the east, includes the free of tectonic features surface nearby.

The estimation of the formation and resurfacing age of a unit surface provide not only information about the constitutive materials, but also the processes that have shaped and altered them. In this regard, three different areas as INtt6, INtt7, and INtt8, were selected southwest of the study area, inside, outside, and on a central mound of the depression of uncertain origin (Figure 4.3.a), respectively. Finally, INtt9 is located in the transition between *INtt*, the Late Noachian clay-bearing deposits (*INcd*), and the channel previously mentioned (Figure 4.3.a).

The *INcd* materials are difficult to date as the unit is easily eroded, and shows denuded surfaces when the protective capping is removed. Those materials also present inverted impact craters and other intriguing circular features on their surface, which difficult the right identification of the craters. Some of the circular structures may correspond either to an underlying layer, being a relict part of an overlying deposit or, on the other hand, it may correspond to some circular morphology unrelated to impacts. Consequently, we have only estimated the ages related to the

upper capping layer, but not of the clay-bearing deposits outcrops. These results provide the youngest estimation of the stratigraphic sequence with sufficient confidence. The INcd1 area includes a significant extension of the capping unit that occurs to the south (Figure 4.3.a), whereas the INcd2 is a remnant closer to the Coogoon channel and next to an old impact crater (Figure 4.3.a). Besides, the INcd3 area, emplaced on a mound in the termination of Coogoon main channel (Figure 4.3.a), is more limited and uncertain as it may not be formed by the same hard capping materials. However, the age determination of this area can provide additional information to build the chronostratigraphic framework of Coogoon.

**Table 4.3.a** Statistics of crater counting polygon including altitude that was obtained from the MOLA DTM.

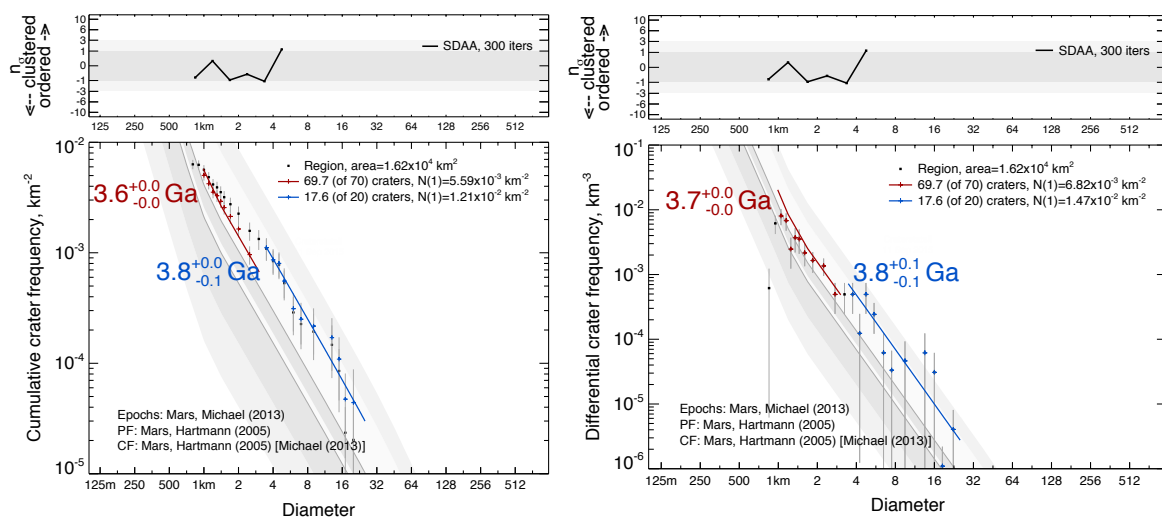
NAME	AREA ( $km^2$ )	Altitude (m)					
		MIN	MAX	RANGE	MEAN	STD	MEDIAN
INcd1	139	-2712	-2630	82	-2676	15	-2674
INcd2	46	-2629	-2463	166	-2558	48	-2568
INcd3	16	-2800	-2704	96	-2746	20	-2750
INtt1	104	-2223	-2150	73	-2179	14	-2178
INtt2	42	-2477	-2367	110	-2390	17	-2388
INtt3	32	-2813	-2749	64	-2774	13	-2775
INtt4	183	-2632	-2506	126	-2570	30	-2568
INtt5	144	-2626	-2413	213	-2504	42	-2507
INtt6	75	-3035	-2921	114	-3007	19	-3014
INtt7	51	-2667	-2552	115	-2618	28	-2616
INtt8	36	-2817	-2581	236	-2688	59	-2678
INtt9	47	-2816	-2774	42	-2802	7	-2803
cr	181	-2943	-2657	286	-2811	47	-2814
LHlp	118	-3109	-3049	60	-3077	14	-3076
NAcd1	23	-2855	-2807	48	-2830	13	-2830
NAcd2	15	-2869	-2844	25	-2861	5	-2862
NAcd3	12	-2925	-2895	30	-2909	8	-2909

The eastern side of the MLE in the termination of Coogoon Valles was considered as one crater counting area (Figure 4.3.a), which has been named as cr, in an attempt to estimate when this was produced. Since the ejecta blanket is somewhat thin, it is expected that the underlying surface age can distort the age estimation of the crater.

Finally, the Noachian Amazonian channel deposits (*NACd*) were also considered for CSFD. However, those materials may have been buried and subsequently exposed and the impact bombardment may have been discontinuous, affecting to the age results. In addition, the *NACd* materials, like the *INcd* ones, are thin and weak and could be mimicking the underlying strata and preserving the impact craters. In this context, the interpretation of the resulting ages for the *INcd* surface needs to be cautious. The *NACd*<sub>1</sub> and *NACd*<sub>2</sub> were selected for the central area of the bed of the main channel in Coogoon Valles, which correspond to Members 1 and 2, respectively (Figure 4.3.a). They are located contiguous to the *INtt*<sub>3</sub> area to evaluate the changes in age. The delta/fan surface dating was also assessed through an area named as *NACd*<sub>3</sub> (Figure 4.3.a).

#### 4.3.2 CRATER COUNT RESULTS

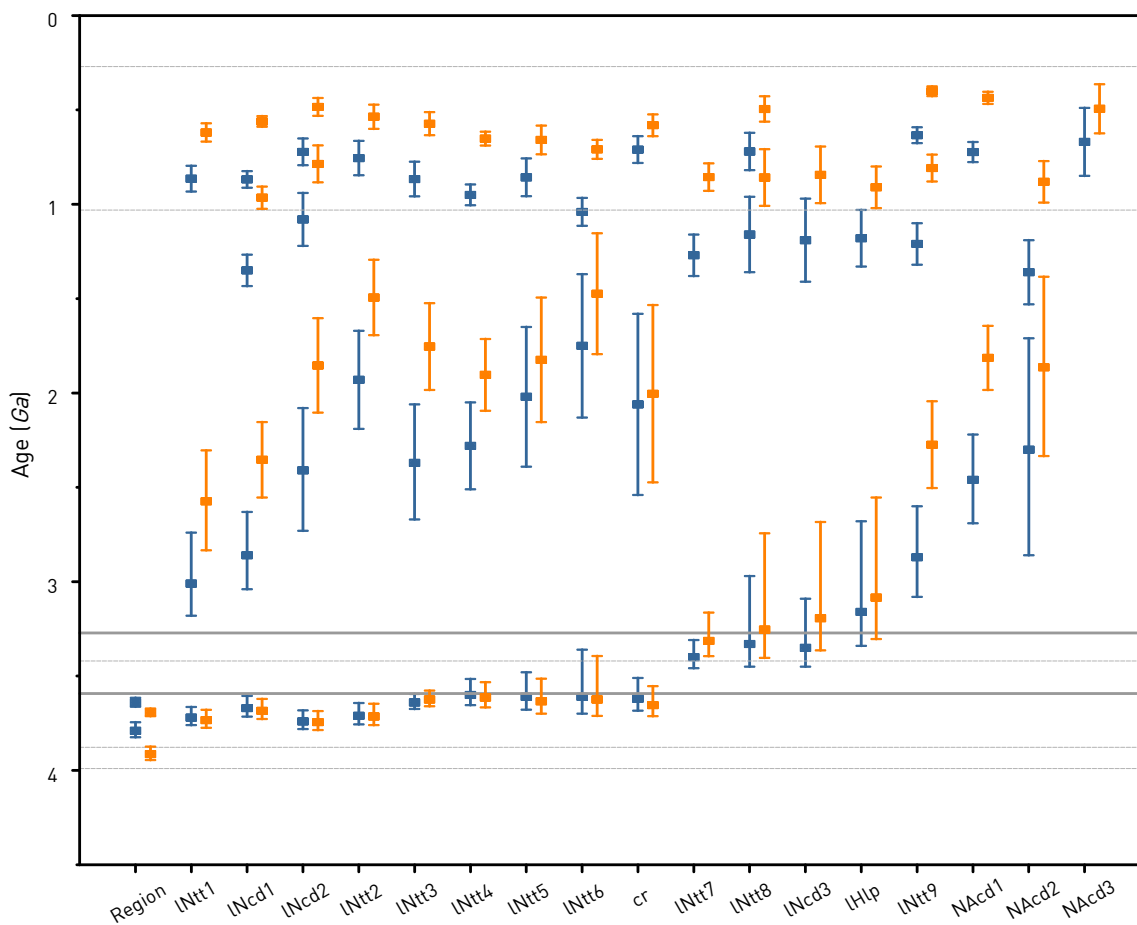
We analyzed the CSFD for the entire study area (Figure 4.3.b) where the resulting crater diameters were adjusted to two equilibrium functions. The results are very similar using differential and cumulative crater frequency, providing an age of formation of about  $3.8 \pm 0.1$  Ga by using the Hartmann 2004 iteration (Figure 4.3.b), as well as resurfacing age of  $3.6 \pm 0.0$  Ga. The randomness analysis reveals that the confidence level of the adjustment is adequate (Figure 4.3.b).



**Figure 4.3.b** Differential (left) and cumulative (right) CSFD for the full study area in Coogoon (Figure 4.3.b), obtained as explained in Subpart 2.2.4ii. Randomness analysis results are displayed at the top of the figure.

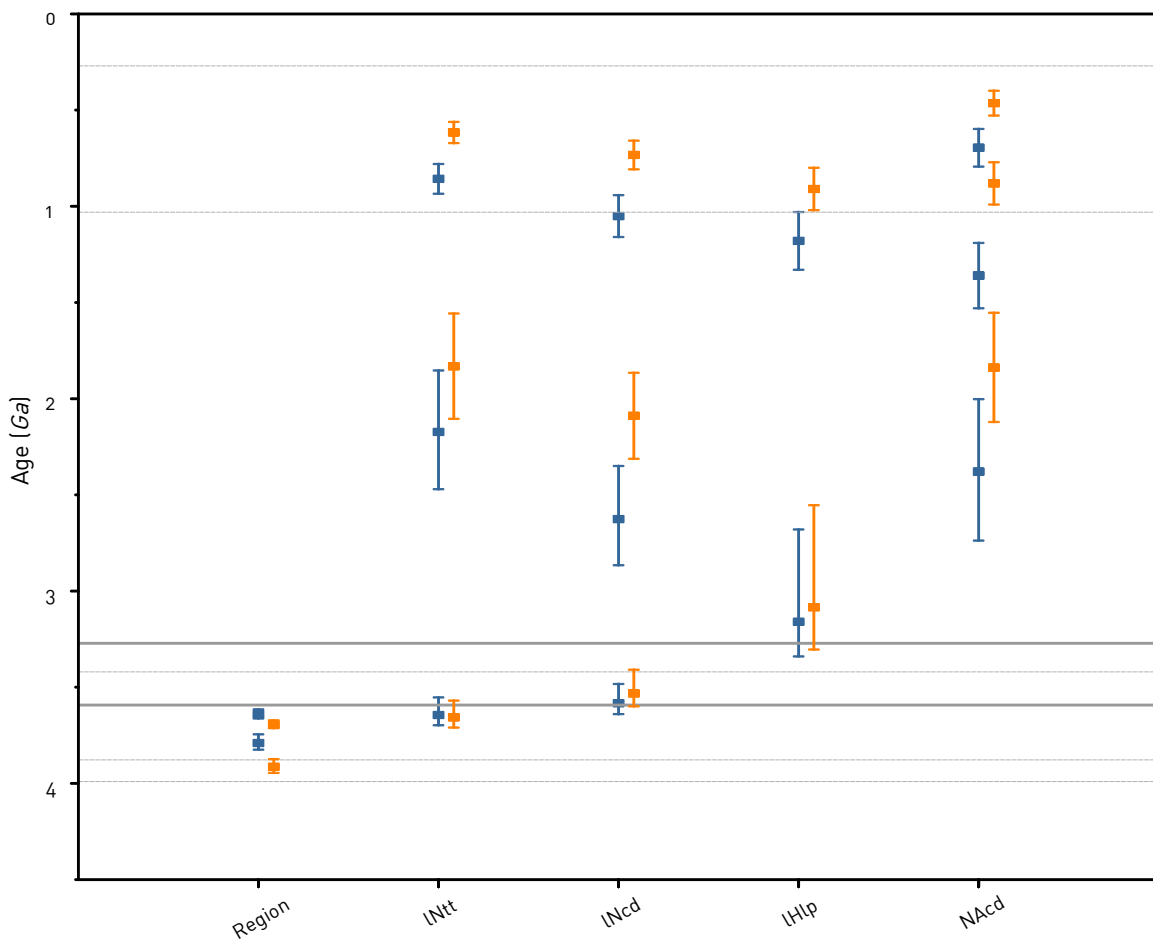


To contrast the age of some terrains and units, a similar analysis was made for the partial areas (Figure 4.3.c, plots can be found in Appendix 8.2). Most of the forming ages (i.e. the oldest equilibrium function that can be fitted to the impact crater distributions) of the areas where *INtt* and *INcd* occur are well constrained during the Late Noachian or close to the Noachian-Hesperian transition. The upper layer of *INcd* (*INcd*<sub>1</sub> and *INcd*<sub>2</sub>) and the *INtt* areas from 1 to 6 can be adjusted to an average age of  $3.5 \pm 0.1$  Ga and  $3.6 \pm 0.1$  Ga, respectively (Figure 4.3.d). The areas corresponding to *INtt* number 7 and 8, as well as the *INcd*<sub>3</sub> have younger formation ages that are closer to the Hesperian-Amazonian transition, which is quite similar to the *IHlp* age ( $3.2 \pm 0.2$  Ga with Hartmann, Figure 4.3.d). The *INtt*<sub>9</sub> area displays a younger formation age that fits  $2.9 \pm 0.3$  Ga ( $3.2 \pm 0.2$  Ga with Hartmann, Figure 4.3.d). The age calculations show much younger records for both *NAcd*<sub>1</sub> and *NAcd*<sub>2</sub> areas, which are  $2.5 \pm 0.2$  Ga and  $2.3 \pm 0.6$  Ga, respectively (with Hartmann, Figure 4.3.c).



**Figure 4.3.c** Adjusted ages for the different crater counting areas of Coogoon, obtained with the Hartmann (**blue**) and Neukum-Ivanov (**orange**) chronology systems (Subpart 2.2.4ii). Hartman derived transition ages are displayed as horizontal lines. The CSFD plots can be found in Appendix 8.2

The surface of the studied areas does not fit a unique equilibrium function. In the same way as the complete study area, the distribution of the crater diameters versus their frequency shows steps that can also be fitted to other functions. As it has been discussed in the methodology section (Subpart 2.2.4ii), the ages corresponding to such functions are interpreted as resurfacing events [Michael, 2013] that have modified the crater distribution to suppress the larger craters. Some of those resurfacing ages are consistent between the different areas, indicating that the resurfacing events that affected the various surfaces can be the same.



**Figure 4.3.d** Average ages for each studied unit, resulting of crater size-frequency distribution (Figure 4.3.c) that were calculated for some specific sampling areas (Figure 4.3.b), The chronology systems used were Hartmann (blue) and Neukum-Ivanov (orange) (Subpart 2.2.4ii), where Hartmann derived transition ages [Michael, 2013] are displayed as horizontal lines.

In this regard, some particular patterns can be recognized, as the case of the resurfacing episode that took place synchronously in INtt<sub>1</sub> and INcd<sub>1</sub>, and which correspond to the oldest age obtained from IHlp (around 3 Ga). Close the formation

of the *NAd* surfaces, there is also a common event recorded in most of the areas, excepting those areas occurring to the NW, as IHlp. In fact, they show a matching event at  $1.2 \pm 0.2$  Ga (Figure 4.3.d). This event (also observable in INcd<sub>1</sub>) is slightly younger than their equivalents in the other areas, which could happen around the transition between the Early and the Middle Amazonian. However, the resurfacing event involved in the partial age reset may be the same considering the high uncertainties associated the surface age determination in the studied areas, or, on the contrary, such an event might have lasted longer in some zones than in others.

## 4.4 SPECTRAL ANALYSIS

### 4.4.1 VISIBLE NEAR INFRARED CRISM DATA

Different spectroscopic studies of the bright-tone materials forming the *INcd* unit have shown that they occur discontinuously along an extensive squared area of more than 1,000 x 1,000 km going from Mawrth Vallis to West Arabia Terra [e.g., Poulet *et al.*, 2005; Michalski and Noe Dobrea, 2007; Noe Dobrea *et al.*, 2010]. However, in Coogoon only 5 CRISM cubes were available for the study area by the time that this work was conducted (Table 4.4.a). They are concentrated west of the study area (Figure 4.4.a) overlapping some fluvial morphologies in Oxia Planum (1 and 2) and light-toned outcrops of the *eNcd* unit (from 3 to 5). The hyperspectral images were analyzed in detail as described in Subpart 2.2.4iii.

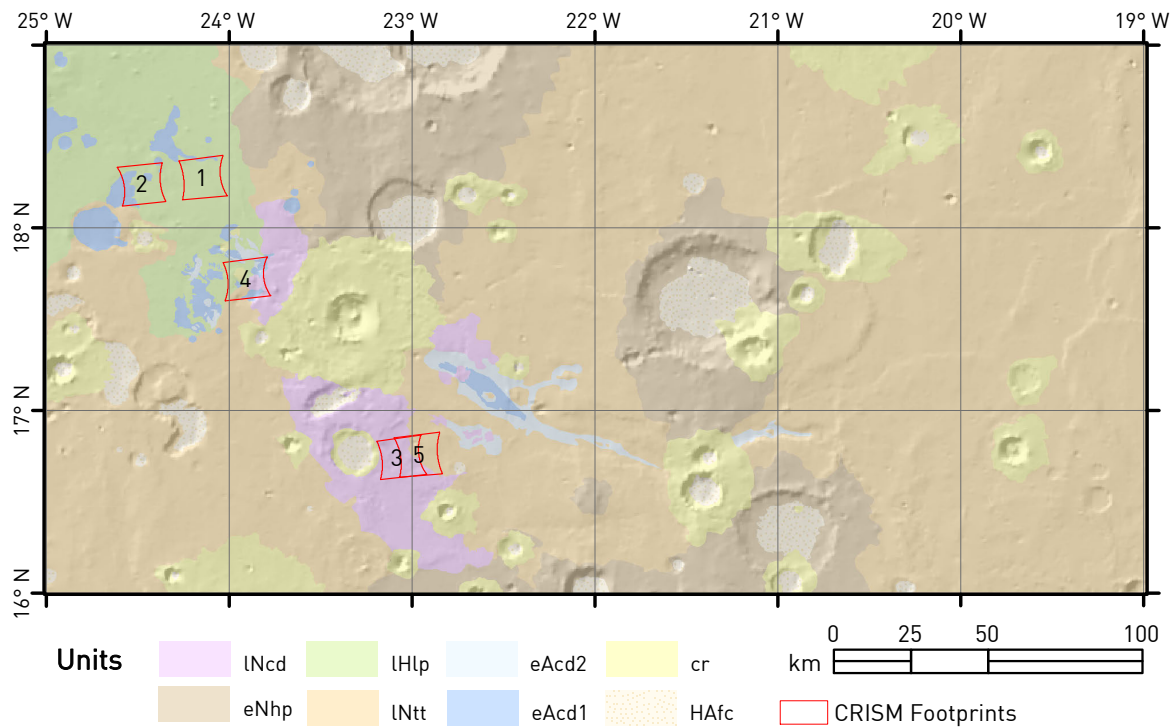
**Table 4.4.a** List of CRISM cubes in the Coogoon study area (Figure 4.4.a), where image labels refer to *FRT000XXXXX*. The table includes acquisition information, center coordinates and the number of ROIs couples (spectra of interest and nearby neutral spectra, used for spectral ratios). The highlighted row corresponds to the cube outline and spectral data shown in Figure 4.4.b and Figure 4.4.c, respectively.

#ID	LABEL	ACQUISITION		COORDINATES	
		DATE	TIME	LAT	LON
1	04686	22/02/07	8:56	18.28	-24.15
2	0810D	06/10/07	10:10	18.24	-24.48
3	08438	17/10/07	17:17	16.75	-23.06
4	09A16	25/01/08	9:25	17.72	-23.90
5	10FE9	11/02/09	15:29	16.76	-22.96

While several indexes were applied by using spectral data of CRISM cubes in order to identify mineral composition and distribution, only the phyllosilicate index (PHY) [Viviano-Beck *et al.*, 2014] produces conclusive results. The PHY index provide information of hydroxylated minerals, including phyllosilicates. As a result, hydrated Fe/Mg-OH bearing minerals (e.g., Fe/Mg-phyllosilicates) are shown red, whereas hydrated Al/Si-OH bearing minerals (e.g., Al-phyllosilicates or hydrated silica) appear as green, or cyan. On the other hand, blue colors are indicative of other hydrated minerals (such as sulfates, hydrated silica, carbonate or water ice). In this section, we have focused on the cube identified as 3 (FRT0008438; Table 4.4.a and

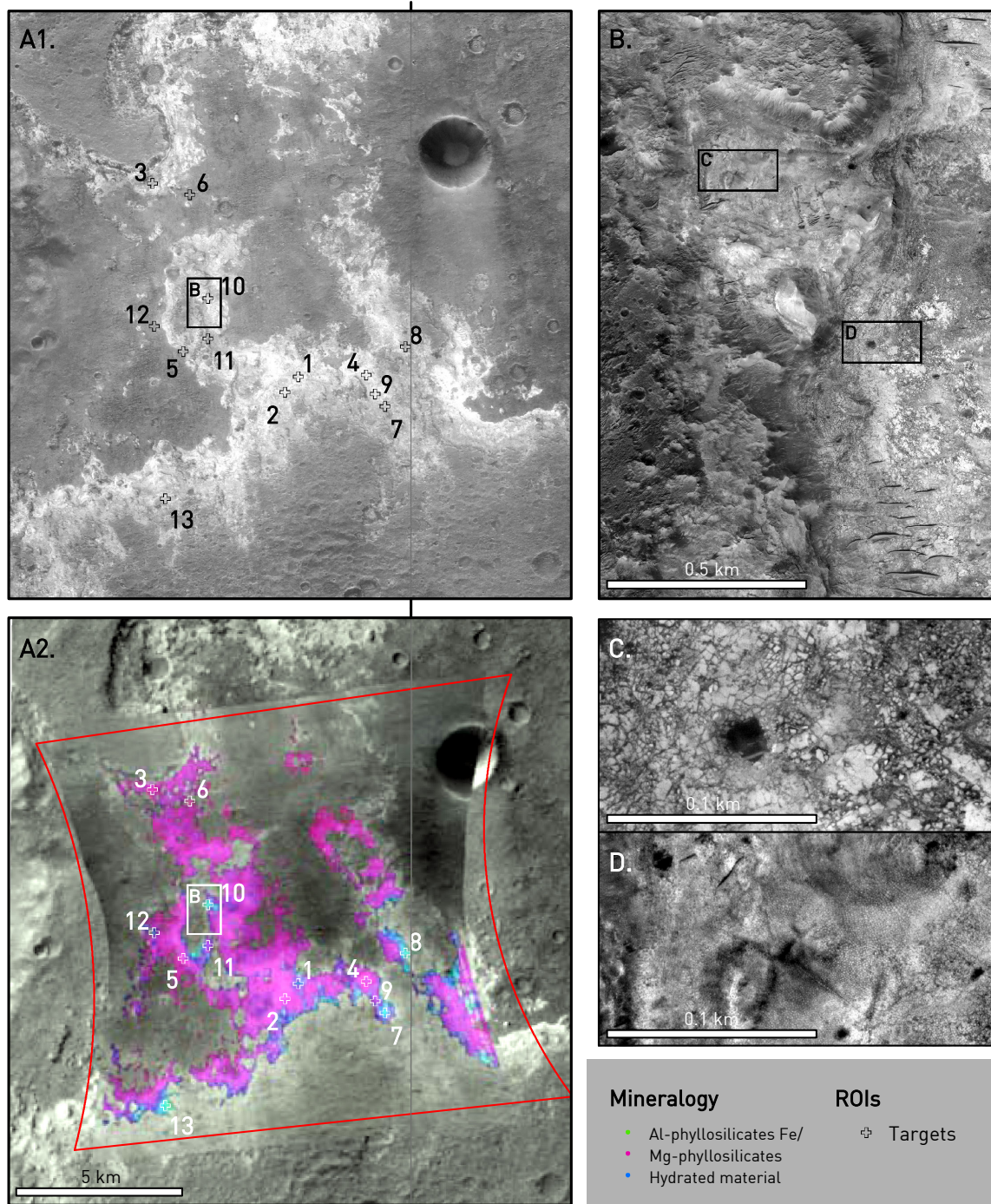


Figure 4.4.a), where the sequence of materials described in Subchapter 4.2 is clearly identifiable in HiRISE images. Indeed, we characterize the spectral manifestation of the HiRISE textural variation by using the CRISM cube data analyzing the spatial distribution inferred of the phyllosilicate index (Figure 4.4.b), and the spectral signatures obtained for selected profiles (Figure 4.4.c).



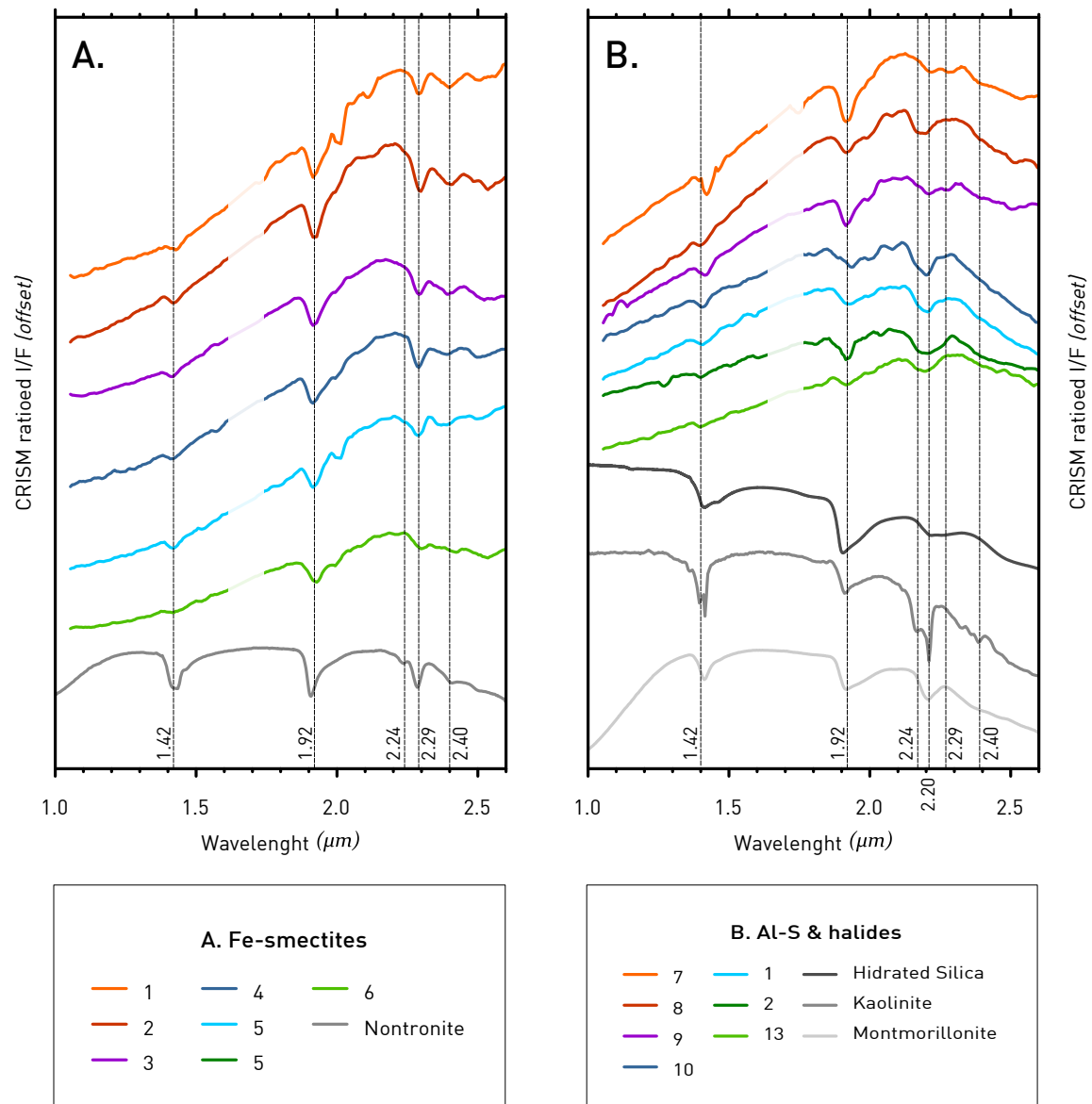
**Figure 4.4.a** CRISM cube footprints and identification number (#ID) described in Table 4.4.a. The background is MOLA shaded relief and the geologic units described in Subchapter 4.2.

In Figure 4.4.b-A1, an example of the denuded surface of the *INcd* unit (Subchapter 4.2) can be observed. Two high-standing mesas covered with a dark mantling material (Member C) remain south and northwest of the area. In cliffs and highly eroded relict reliefs, a light-toned material (Member A and B) outcrops underneath the dark materials. Those locations match with a strong signal for hydroxylated minerals (Figure 4.4.b-A2). However, other surfaces are spectrally flat in the CRISM spectral range, not presenting absorptions in the 1 – 2.6  $\mu\text{m}$  region. A closer look in the CTX image (Figure 4.4.b-B) reveals that the Fe/Mg-clays (Member B, reddish-purple in Figure 4.4.b-A2) are widespread. Meanwhile, the Al-phyllosilicates (Member B, greenish/blueish in Figure 4.4.b-A2) are restricted to the brinks of some cliffs.



**Figure 4.4.b** ROIs (hollow crosses) where spectra profiles were extracted from the CRISM FRT0008438 cube (Table 4.4.a) to calculate the ratioed spectra shown in Figure 4.4.c. CRISM cube is outlined as a red polygon which location in Coogoon is shown in Figure 4.4.a. The background (A1) is a CTX image mosaic and (A2) the result of calculating the phyllosilicate index (R: D2300; G: BD2200; B: BD1900R; [Viviano-Beck *et al.*, 2014]) that overlaps an enhanced visible color image (R: 2.53  $\mu\text{m}$ ; G: 1.51  $\mu\text{m}$ ; B: 1.08  $\mu\text{m}$ ) from CRISM. High resolution images (HiRISE PSP\_005740\_1970) of some specific outcrops (C to D) are also displayed to correlate texture and composition of the geological units in the area.

Regions of interest (ROIs) were selected where the signal was strongest (Figure 4.4.b-A2). Each one of the spectra was ratioed with a near neutral ROI located in the same data column, as described in Subpart 2.2.4iii. About thirteen spectra profiles were obtained in this process and then classified by their absorption bands and general shape. The resulting spectral signatures were finally classified by comparison with analog laboratory samples (Figure 4.4.c).



**Figure 4.4.c** CRISM (color) and lab (grays) spectra of (A) Mg-smectite, (B) Al-smectite and halides, and (C) sulfate-bearing materials in Coogoon. The spectra are obtained as the average of a 3 x 3 pixel ROIs ratioed by a nearby spectrally neutral region of the same size. Labels refer to the image id (*FRT0000XXXX*) followed by the ROI id. The lab spectrum sources are specified in Appendix 8.4. Major spectral absorptions indicated as vertical lines.



Phyllosilicates and some other hydrated compounds include a water absorption band at 1.91  $\mu\text{m}$ , which is produced by the combination of stretching and bending vibrations of water in the crystalline lattice, as well as the occurrence of a shoulder at 1.95  $\mu\text{m}$  as a result of water absorption itself. To this regard, the occurrence of Fe/Mg smectites as part of the mineral association in the region has been demonstrated by several distinctive spectroscopic features that are shown as a succession of different features between 2.29 – 2.31  $\mu\text{m}$ , which correspond to vibrations of the OH-anion in octahedral positions. Alternatively, some other spectral signs occurring in the range 2.17 – 2.21  $\mu\text{m}$  as a result of the combining vibrations of OH<sup>-</sup> with Al<sup>3+</sup> or Si<sup>4+</sup> are diagnostic when occurring as singlets or doublets in Al-clays and hydrated silica.

Although both Fe and Mg endmembers of the smectite series are detected in Coogoon Valles ([Figure 4.4.c-A](#)), their occurrence show a complementary distribution along the study area. Nontronite concentration (Fe-smectite, ideal formula  $\text{Na}_{0.3}\text{Fe}_2^{3+}(\text{Si}, \text{Al})_4\text{O}_{10}(\text{OH})_2 \cdot n\text{H}_2\text{O}$ ) is higher in the southern CRISM cubes (3 and 5, [Figure 4.4.a](#)), meanwhile saponite (Mg-smectite, ideal formula  $(\text{Ca}/2, \text{Na})_{0.3}(\text{Mg}, \text{Fe}^{2+})_3(\text{Si}, \text{Al})_4\text{O}_{10}(\text{OH}_2) \cdot 4(\text{H}_2\text{O})$ ) is more abundant in the CRISM cube to the north (4, [Figure 4.4.a](#)). Nontronite is characterized by both a strong absorption band at 1.91 – 1.92  $\mu\text{m}$ , and a weak feature at 1.42 – 1.43  $\mu\text{m}$  plus the commonly discriminating bands at 2.29  $\mu\text{m}$  and 2.39 – 2.40  $\mu\text{m}$  (see [Figure 4.4.c](#)). Additionally, it displays a spectral feature at 2.24  $\mu\text{m}$  that only occurs in specific locations (possibly in profiles 2 and 6, [Figure 4.4.c](#)). This feature has been attributed to serpentine in other places of Arabia Terra [*Ehlmann et al.*, 2010; *Noe Dobrea et al.*, 2010]. In the range from 1 to 2  $\mu\text{m}$ , the spectral slope is positive at those sites located mostly in topographic low areas, which is owed to the accumulation of the Fe-bearing minerals. On the other hand, saponite shows an asymmetric feature at 1.91  $\mu\text{m}$ , which occasionally spread to 1.94  $\mu\text{m}$ . The weak 1.38 – 1.39  $\mu\text{m}$  absorption feature is shifted to 1.41  $\mu\text{m}$ , as well as present absorptions at 2.31  $\mu\text{m}$  and 2.39 – 2.40  $\mu\text{m}$  as a result of the OH-Mg bonding [*Bishop et al.*, 2008; *McKeown et al.*, 2009].

Other spectra obtained in the Coogoon area with strong absorptions at ~1.9  $\mu\text{m}$ , have the 2.31  $\mu\text{m}$  feature shifted to ~2.21  $\mu\text{m}$  instead ([Figure 4.4.c-B](#)). This spectral



signature is attributed to the occurrence of endmembers or mixtures of the kaolinite and the montmorillonite-beidellite series minerals (Al-smectites). On the first hand, the presence of kaolinite (ideal formula  $\text{Al}_2\text{Si}_2\text{O}_5(\text{OH})_4$ ) is evidenced by the detection of absorption doublets sourced on the OH-Al vibrations at both the previously mentioned  $\sim 2.21 \mu\text{m}$  and  $\sim 2.16 \mu\text{m}$ , together with the occurrence of the water band at  $\sim 1.41 \mu\text{m}$  [Clark *et al.*, 1990]. At the highest stratigraphic position, the  $1.91 \mu\text{m}$  band is not manifest, which is typical of kaolinites that are close to their stoichiometric composition (e.g., profile 13 in [Figure 4.4.c-B](#)).

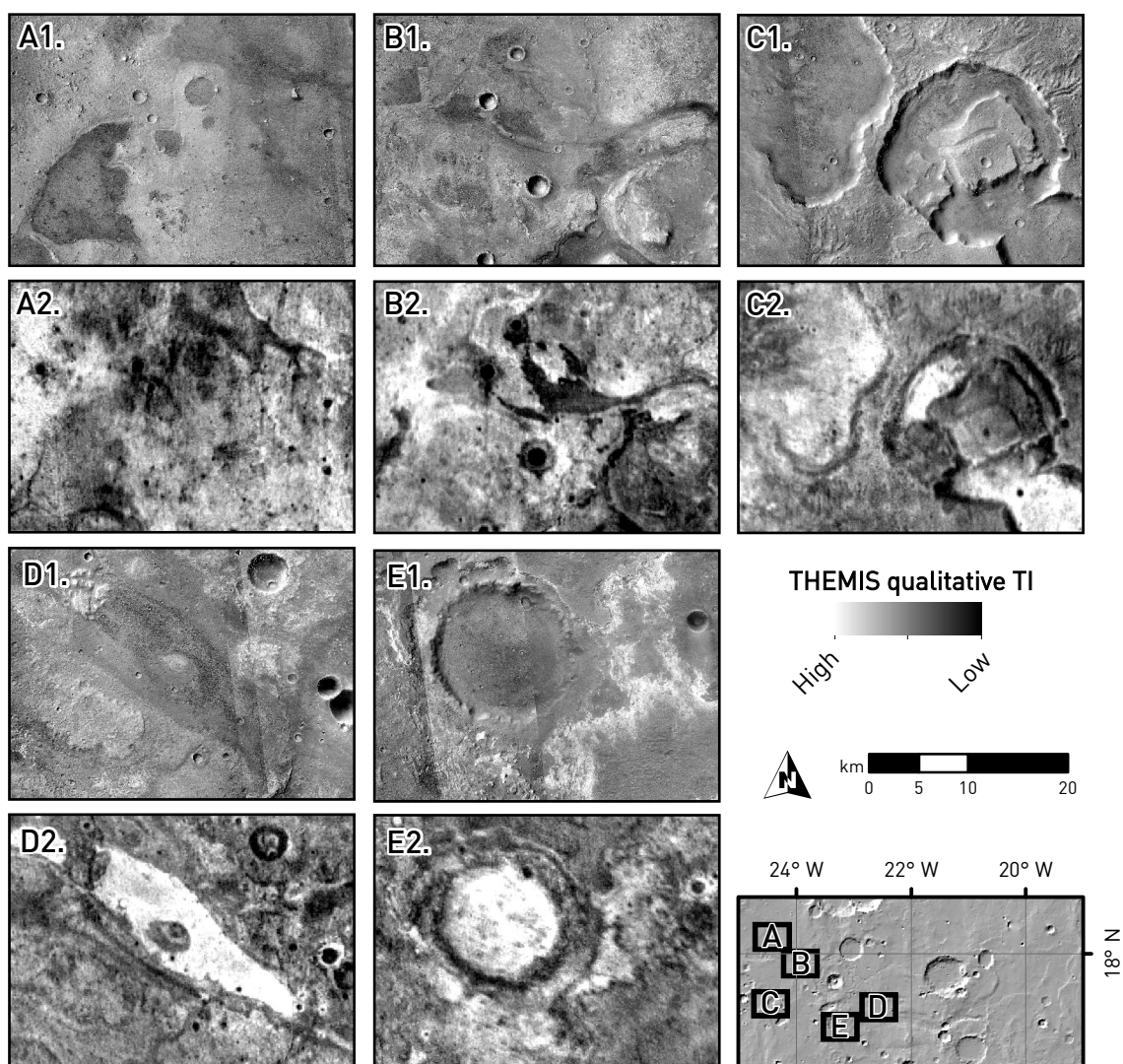
The detection of absorption bands at  $1.92 \mu\text{m}$  and  $1.42 \mu\text{m}$ , and the occurrence of one feature at  $2.20 \mu\text{m}$  suggest the presence of montmorillonite (ideal formula  $(\text{Na}, \text{Ca})_{0.3}(\text{Al}, \text{Mg})_2\text{Si}_4\text{O}_{10}(\text{OH})_2 \cdot n(\text{H}_2\text{O})$ ). This fact is supported by the presence of a shoulder at  $2.16 \mu\text{m}$ , which is characteristic in mixtures of kaolinite and montmorillonite (e.g., profile 10, [Figure 4.4.c-B](#)). In addition, it should be expected a contribution of hydrated silica (ideal formula  $\text{SiO}_2 \cdot n\text{H}_2\text{O}$ ) as the  $2.20 \mu\text{m}$  absorption is broad (e.g., profile 7, [Figure 4.4.c-B](#)), due to Si-OH combination tones,  $2.26 \mu\text{m}$  due to H-bound Si-OH,  $1.91 \mu\text{m}$  due to structural  $\text{H}_2\text{O}$ , and  $1.4 \mu\text{m}$  due to structural  $\text{H}_2\text{O}$  and OH [Stolper, 1982]. That the  $1.91 \mu\text{m}$  band is shifted to  $1.92 - 1.95 \mu\text{m}$  is an indicator of the presence of these hydrated amorphous phases.

#### 4.4.2 INFRARED THEMIS DATA AND DERIVED THERMAL INERTIA

As mentioned above, the TI of Mars surface can provide information about distribution of exposed materials, based on its composition and consolidation degree. The [Figure 4.4.d](#) shows some examples of the identification of features and materials in Coogoon area by their appearance trough visible (directly related to albedo variation) and TI derived from IR data.

Thermal images usually provide a better observation of surface materials which are difficult to observe on visible imagery, while in certain cases the distinction among materials is easier through visible imaging. That is the case of the fan/delta deposits in [Figure 4.4.d-A2](#), where the relatively high TI of the *lHlp* unit (Subpart 4.2.2iv) do not show a high contrast with the lower TI of the fan/delta materials, much

sharper in visible images (Figure 4.4.d-A1). The uncertain boundary between units in TI images may indicate that the original extension of the inverted fans is higher than we can observe directly in visible images, where parts of the fan lithological features may be buried. The TI image shown in Figure 4.4.d-B2 provides a higher contrast for *NACd2* (Subpart 4.2.2vi), but lower for *NACd1* (Subpart 4.2.2v). Accordingly, the combination of both visible and thermal images allows to observe the complete distribution of the overlaying materials in the multi-lobate structure. Such differences in contrast in TI images can be interpreted as variable particle size, composition, and degree of cementation (Mellon et al., 2000; Putzig and Mellon, 2007).



**Figure 4.4.d** A to E CTX visible images (labeled as number 1) and its correlative THEMIS thermal inertia mosaics (labeled as 2) as shown by Christensen et al. [2013] in selected locations of interest in the Coogoon Valles. The fan/delta deposits (A and B) show the lowest values, while the interior of the craters (C and E) and the main channel (D) show the highest thermal inertia.

The *HAfc* materials (Subpart 4.2.2vii) infilling craters display the highest TI values (Figure 4.4.d-C and E). The crater interior to the west of Coogoon area (Figure 4.4.d-C) shows the ejecta deposits from a more recent impact as a low TI blanket. We can recognize in Figure 4.4.d-C that in the depression of uncertain origin (see Subpart 4.2.3ii), the materials in their interior, have similar TI values than to the materials in the external surrounding area. This fact supports the hypothesis that it is not a typical impact crater. The infilling deposits occurring in the central zone of the main channel display also some of the highest TI in Coogoon, which contrast with their very low albedo, as it is found in the infilling deposits of craters. Similar TI records are also found in bedrock, coarse sands, and cemented soils.

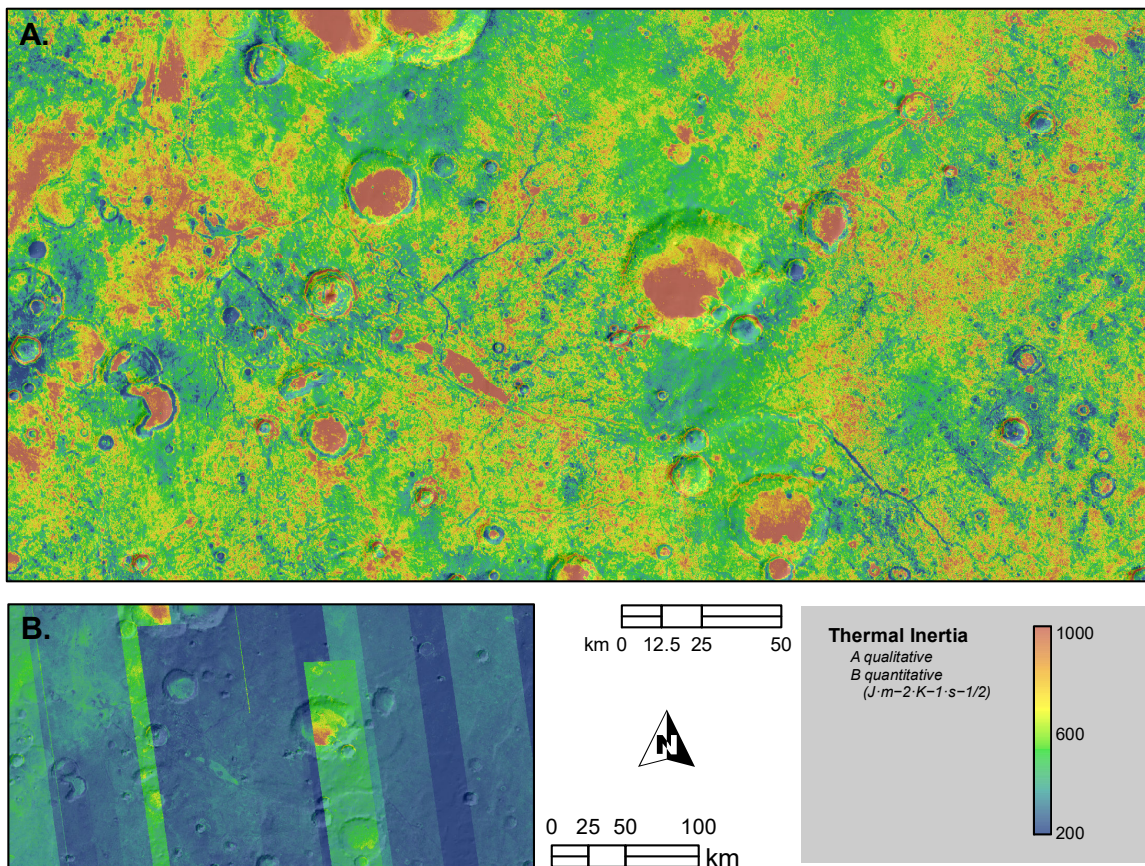
The *NAcd1* materials in the channel interior (Subpart 4.2.2v) shows a very different TI from the *NAcd1* materials identified in the fan/delta deposits to the west (Figure 4.4.e). However, since in the visible part of the spectrum they look similar, different TI records can result from different particle size (where coarser grain size occurs in the channel and the finer would be emplaced in the lowlands), compaction rate (channel materials were possibly buried and exposed to higher pressures), or, in addition, a higher ice content occurring in the channel interior *NAcd1* materials. The Figure 4.4.d-E image show that the phyllosilicate-bearing materials (*INcd*, Subpart 4.2.2ii) display a very diverse TI since texture and compaction are more relevant to the thermal properties of materials than composition. However, although the *INcd* materials show a varying TI, they usually record high TI values.

The qualitative and quantitative THEMIS IR thermal inertia mosaic for the entire Coogoon study area (Figure 4.4.e) allow to compare TI of geological units and observe regional trends. While qualitative data do not provide quantitative thermophysical or compositional information of surface, they are extremely useful as explorative tools, especially in areas where materials exhibit a broad range of thermophysical characteristics. In this regard, the *IHp* unit in lowlands displays high-TI patches that are disrupted by crater rims, inverted channels and the lobes of fan/delta deposits where *NAcd2* is present. The relatively lowest TI records are found related to channel, ridge, and crater slopes, as an artifact caused by the topography.



As mentioned above, the crater infillings (*AHfc*) and *NACd1* in the central zone of the channel bed show the highest IT values. In this regard, the quantitative record is around 600 tiu (**Figure 4.4.e-B**) which is consistent with the existence of a duricrust (**Table 3.4.b**).

For most of the *INtt* surface a similar rugged texture can be observed in the TI qualitative image mosaic (**Figure 4.4.e-A**). The highest patches of TI values may be related with the outcrop of the relict phyllosilicate-bearing material, obscured by the diverse mass wasting, aeolian and fluvial deposits (see Subpart 4.2.2iii).



**Figure 4.4.e** Qualitative (A) and quantitative (B) THEMIS IR derived thermal inertia image mosaics [Christensen *et al.*, 2013] for Coogoon overlapping a MOLA shaded relief. Thermal inertia is expressed in tiu ( $J \cdot m^{-2} \cdot K^{-1} \cdot s^{-1/2}$ ).



## 4.5 PHYSICAL ANALYSIS

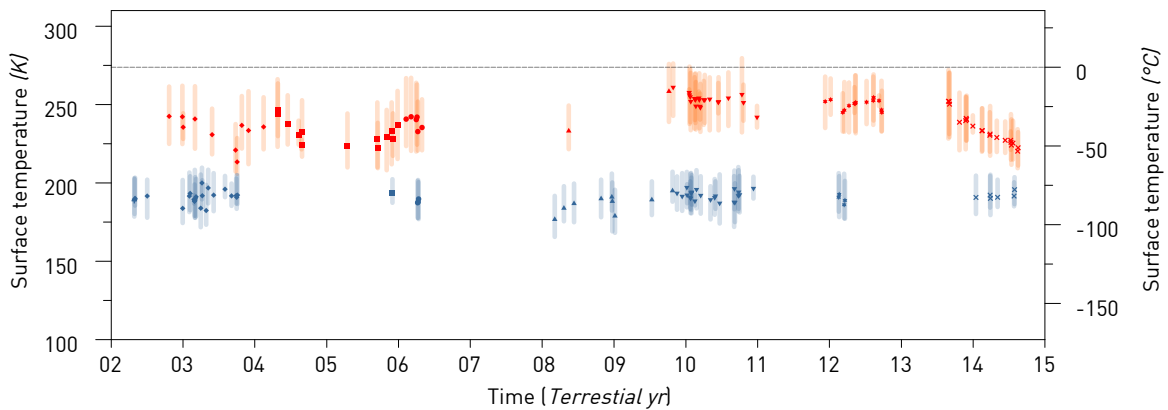
### 4.5.1 TEMPERATURE

The temporal coverage of daytime THEMIS consisting of images that were taken each 14 to 16 hour in local time in the Coogoon area is sparse. They are lacking at the beginning of 2002, from mid-2006 to the end of 2009, as well as from years 2011 and 2013. The situation is similar for nighttime images that are taken each 4 to 6 hour in local time. There is not data for years ranging from 2004 to 2008, some few at the beginning of 2006; neither years going from 2011 to 2014, but only few records at the beginning of 2012. The THEMIS coverage is summarized in [Table 4.5.a](#).

**Table 4.5.a** Statistics of the THEMIS BTR images obtained and processed for the area from 2002 to 2015.

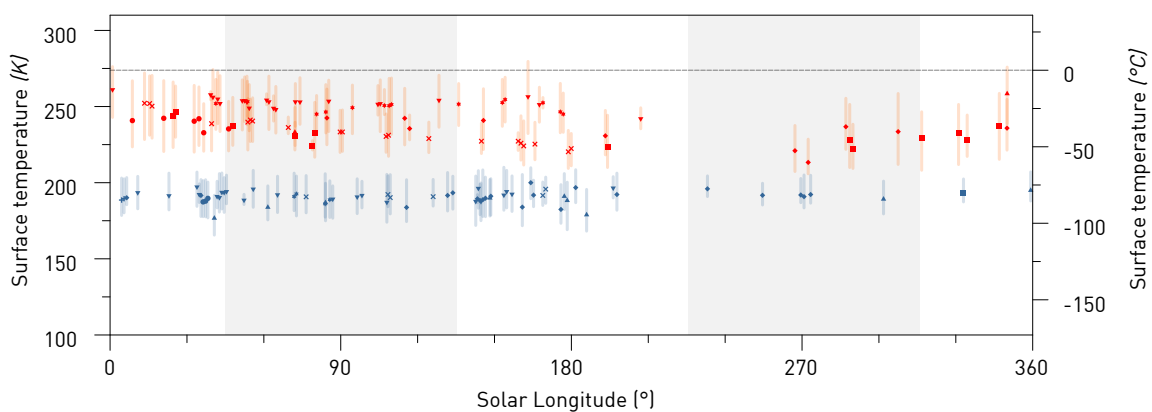
	Number of images	Surface temperature ( <i>K</i> )		
		Mean	Minimum	Maximum
<b>Daytime</b> (14 to 16 h)	87	241.2	227.0	257.0
<b>Nighttime</b> (4 to 6 h)	69	180.8	203.0	190.5

A plot of mean surface temperatures obtained from each image against acquisition time is shown in [Figure 4.5.a](#). For a surface with a thin atmosphere and insignificant humidity, the specific heat results very low. Under these thermal conditions, the direct insolation is the main factor for varying surface temperatures. Consequently, the range of daily temperatures is larger than 50 temperature degrees. However, as the temperature sampling of Coogoon surface is scarce, the annual temperature cycle is not easily recognizable. Winter and summer solstices (each two terrestrial years) usually match the minimum and maximum Mars surface temperatures, respectively. It is only observed in year 2005 a lowering in the daytime surficial temperatures in, which becomes more gradual during the year 2014 to reach -50 °C. On the other hand, nighttime temperatures are even more regular ranging between -75 and -50 °C.



**Figure 4.5.a** Daytime (**orange circles**, 14 to 16 h) and nighttime (**blue circles**, 4 to 6 h) mean surface temperatures for each image against acquisition time (in Earth dates).

Scatter diagram in [Figure 3.5.b](#) plots all available data in Coogoon versus the Ls, overlaying the records from the different years, in order to study the season effect. The result displays that there are much fewer records for the second part of the year. The scatter pattern suggests that the variation in surface temperature is not strongly associated to the planet orbital cycle as usually occurs on the Martian surface. This behavior is likely because Coogoon is located close to the Equator and the seasonal differences are less accentuated. As a consequence, the TI that is calculated from different images is more reliable, and will lead to a more uniform and accurate mosaic as was already observed in the Part 4.4.2.

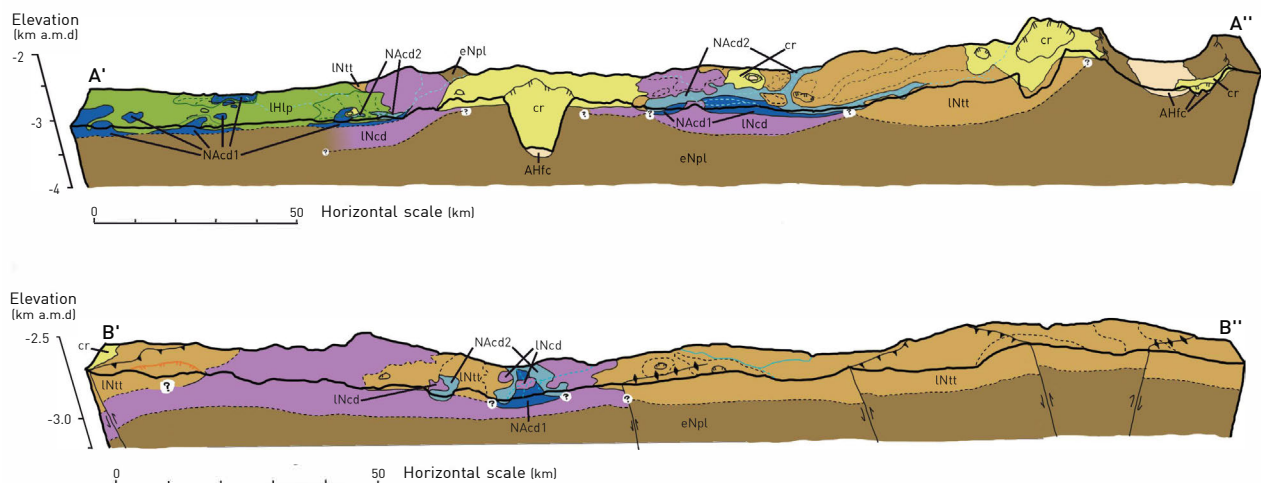


**Figure 4.5.b** Daytime mean surface temperature (**orange circles** each 14 to 16 h, and nighttime mean surface temperature (**blue circles**) recorded each 4 to 6 h against acquisition time (in Martian solar longitude, ° Ls) for all available image.

## 4.6 GEOLOGICAL HISTORY OF COOGOON

In this work, we have conducted an extensive geological survey of Coogoon Valles and its surroundings [Molina *et al.*, 2017]. The area was mapped (Subchapter 4.2) and analyzed through multi- and hyper-spectral data sets in order to better understand the materials of the surface (Subchapter 4.4). Selected areas of this surface were dated in order to infer their age and the possible resurfacing events that may have affected them (Subchapter 4.2). All the recovered information allows us to construct a hypothesized regional stratigraphic sequence and cross sections. Furthermore, we will use such chronostratigraphic framework to discuss the geological history of the area and, therefore, assessing the nature and possible origin of the landscape that we observe in Coogoon at present.

In this regard, [Figure 4.6.a](#) shows two block diagrams that summarize our interpretation of the geology of the area. The diagrams are based on MOLA elevation of the geologic map described in Subchapter 4.2, and the profiles have been constructed by establishing the stratigraphical framework, the geometry of the contacts between units, and the estimation of absolute model ages through crater counting dating.



**Figure 4.6.a** Two block diagrams resulting from the combination of the geological map of the area ([Figure 4.2.a](#)) and interpretative geological cross section sections (A' - A'' and B' - B'' transects shown in [Figure 4.2.a](#)) in Coogoon Valles [Molina *et al.*, 2017].

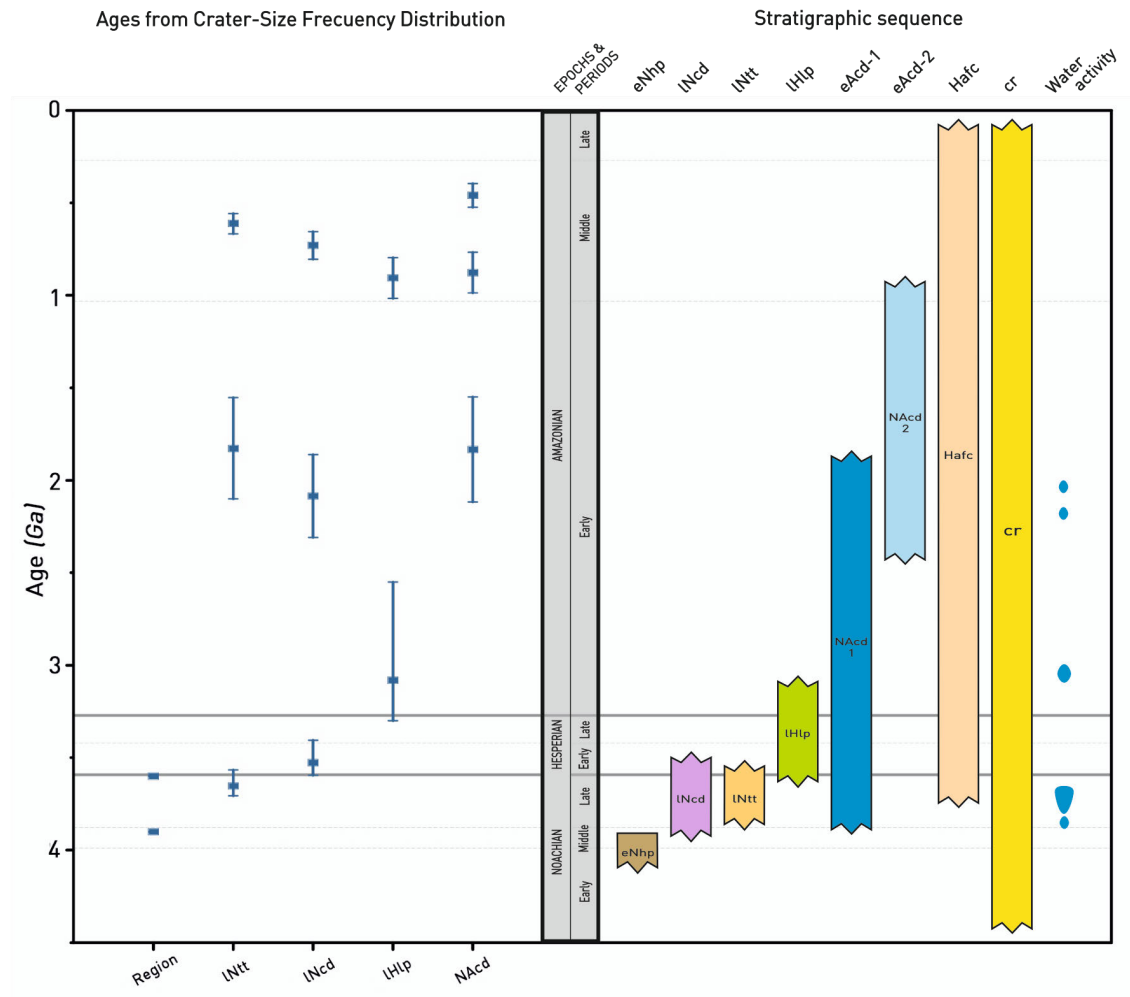
Combining the geologic profiles and the results of the age determination of the different surface units, we can provide model ages for each unit and their resurfacing processes (Figure 4.6.b). The unit surface age is considered as the age range for the end of the creation or resurfacing in that unit. The Early Noachian highlands plains (*eNhp*) unit constitutes the basement and oldest surface in our mapping area, underlying all the other units. It dates from about 3.8 – 4.0 Ga (Figure 4.6.b) that agrees previous studies where the basement age has been aged as Early Noachian [Scott and Tanaka, 1986; Tanaka et al., 2014] or Middle Noachian to Early Hesperian [Tanaka et al., 2005]. As most of the highlands materials, it shows a relatively flat spectrum in CRISM images highly eroded surfaces that are mostly formed by large impact crater structures.

The study area is also located close to the global Mars' dichotomy that, while having an uncertain origin, is claimed to date from the boundary between Early Noachian and 'pre-Noachian' time at around 4.13 Ga [Frey, 2006]. It means that the topography low predates the channel. In addition, the dichotomy may have been lately modified until reaching its current stage, and the series of events involving the lateral crustal flow and the subsequent erosion processes around the dichotomy [Nimmo, 2005] were decisive to the geologic evolution of the area.

As discussed in the regional settings of Coogoon (Part 4.1.1), the highly-altered surface of Arabia Terra difficult to establish a consistent geologic history. However, its history can be partly unlocked from the results obtained through the geological survey performed in this work. In this context, the phyllosilicate-bearing deposits of the *INcd* unit must have been deposited or resulted of weathering that was triggered by hydrological and/or volcanic processes during the Noachian. As the capping unit surface was aged as old as 3.5 Ga (Figure 4.6.b), the underlying materials are younger than the Noachian-Hesperian transition. Based in the recorded geomorphology (Part 3.2.3), we suggest that the primordial Coogoon main channel should have carved the Noachian materials before the Noachian-Hesperian transition. The fluvial erosion formed a wide and deep channel similar to Mawrth Vallis that was carved by groundwater flow or precipitation-sourced runoff. The fluvial activity deposited the



*NAcd1* unit consisting of phyllosilicate-rich materials in the bed and termination of the channel that resulted in the southern fan/delta (Subpart 4.2.3iv) when flowed to the hypothetical ocean or lake occupying the lowlands [e.g., *Fairén et al., 2003a*].



**Figure 4.6.b** (Left) Age determination (blue squares) and error ranges (blue lines) obtained from the different units of the study area of Coogoon. Horizontal lines represent boundaries between the different geologic periods of Mars, whereas dashed lines mark boundaries between epochs [Michael, 2013]. (Right) Stratigraphic sequence of Coogoon inferred from age determinations and spatial relations between units determined by geological mapping; where, the blue ellipses show the duration of valley networks and the outflow channel activity on Mars [Tanaka, 1997; Fassett and Head, 2008].

A complex geologic sequence of events formed the third Noachian surface *INtt* unit (Subpart 4.2.2iii) that was created simultaneously or slightly later to the early Coogoon main channel (Figure 4.6.b). We suggest that part of that material consist of airborne dust that deposited over the entire region as a mantling deposit. The

hypothesized supervolcanoes (see Part 4.2.3) that may have erupted around this time could have been the source of tuff that formed the pyroclastic deposits. The planetary cooling [Watters, 1993] may have promoted active faulting during late Noachian and early Hesperian as well. In this regard, the lateral crustal flow may have triggered the volcanic event and additionally caused the crest set system (Figure 4.6.a) that predate *NACd2*, postdate *NACd1* and *INtt*, and which asymmetric profile (Figure 4.2.h) fits better with a contractional stage.

The multilayered ejecta (MLE) and central pit in the crater at the terminus of Coogoon (Figure 4.2.j), together with the sapping morphologies found in the fluvial network (Part 4.2.3), strongly suggest that the hydrological systems in the area were long-lasting. The morphology and preservation stage of the ejecta is similar to the equatorial MLE craters of Amazonian age. Such an age meets our results (Subchapter 4.3), which suggest that the ejecta formed at around  $2.0 \pm 0.5$  Ga overlaying the materials of 3.5 Ga (*INcd*, *INtt*) (Figure 4.6.b). Mars Odyssey Gamma-Ray Spectrometer confirm a high enrichment in hydrogen in the region [Boynton *et al.*, 2004], which indicates near-surface water abundance. Besides, Arabia Terra is one of the few Noachian exposed surfaces that sustained the existence of a long-lived aquifer on the planet [Andrews-Hanna *et al.*, 2010]. The regional groundwater may contribute to the alteration of the transitional terrain and favor the development of the most recent sapping fluvial network that we observe today. If such aquifer was confined, the impact may have been the source of a new fluvial episode that could have reshaped the surrounding area, more particularly downstream of the western sector of Coogoon. The reactivation of the fluvial network seems to have occurred at around 2 Ga that likely matched the impact (Figure 4.6.b). In addition, it exposed or relocated the *NACd1* fine-grained materials that led the formation of some other lobate features in the lowlands.

Later on, the persistent denudation process that came to follow, exposed both the *INcd* and *NACd1* materials that were buried during most of the Hesperian. Mass wasting occurred and dissection in the highland boundary during the early Hesperian [e.g., Hynek and Phillips, 2001] formed the *INtt* landscape (Figure 4.2.e). Such a process

transported and deposited large amounts of material to the lowlands, and was associated to the formation of the surface affecting the *IHlp* unit that it is currently recognized. The periglacial reworking of plain deposits and spring discharges from northern plains may have deposited the *NACd2* fine grain size materials that were sourced on weathering and erosion during the Amazonian ([Figure 4.6.b](#)).

In summary, the Coogoon Valles area shows an odd assemblage of characteristics that makes difficult to obtain a conclusive geological history. In any case, we hypothesized a feasible explanation for the geologic activity that led to the formation of materials and features that we observe in Coogoon today. During the Noachian, a region characterized to be a transitional area between the lowlands and highlands (*eNhp*) was carved by a broad outflow channel. The water eroded and remobilized the phyllosilicate-rich materials (*INcd*) formed in the region, which were remobilized in the channel bed and the lowlands. Volcanic activity that was triggered by the evolution of the dichotomy –likely occurring during the Hesperian–proliferated in the area. In this context, supervolcanoes that may have been related to the formation of the phyllosilicates in their early stages covered the region including the channel structure with a pyroclastic blanket. During this time, contractional tectonics that emerged from planetary cooling or lateral crustal flow deformed the highlands surface. Tectonics was associated to the formation of a new channel system and a new episode of mass wasting led the surface denudation that reshaped the highlands (*INtt*) and remobilized the phyllosilicate materials to form a new set of deposits in the lowlands (*IHlp*). Finally, during the Amazonian, a large crater may have reactivated the hydrology in the region by subsurface inflow and water runoff that obscured the termination of the channel. Several other episodes may have exhumed the old channel bed materials (*NACd1*), and reshaped the lowlands (*IHlp*) during the Amazonian to its current state. Weathering and erosion during the Amazonian, likely driven by fluvial and periglacial processes, deposited fine deposits in the channel bed and termination of the channel (*NACd2*).





## 5 DISCUSSION

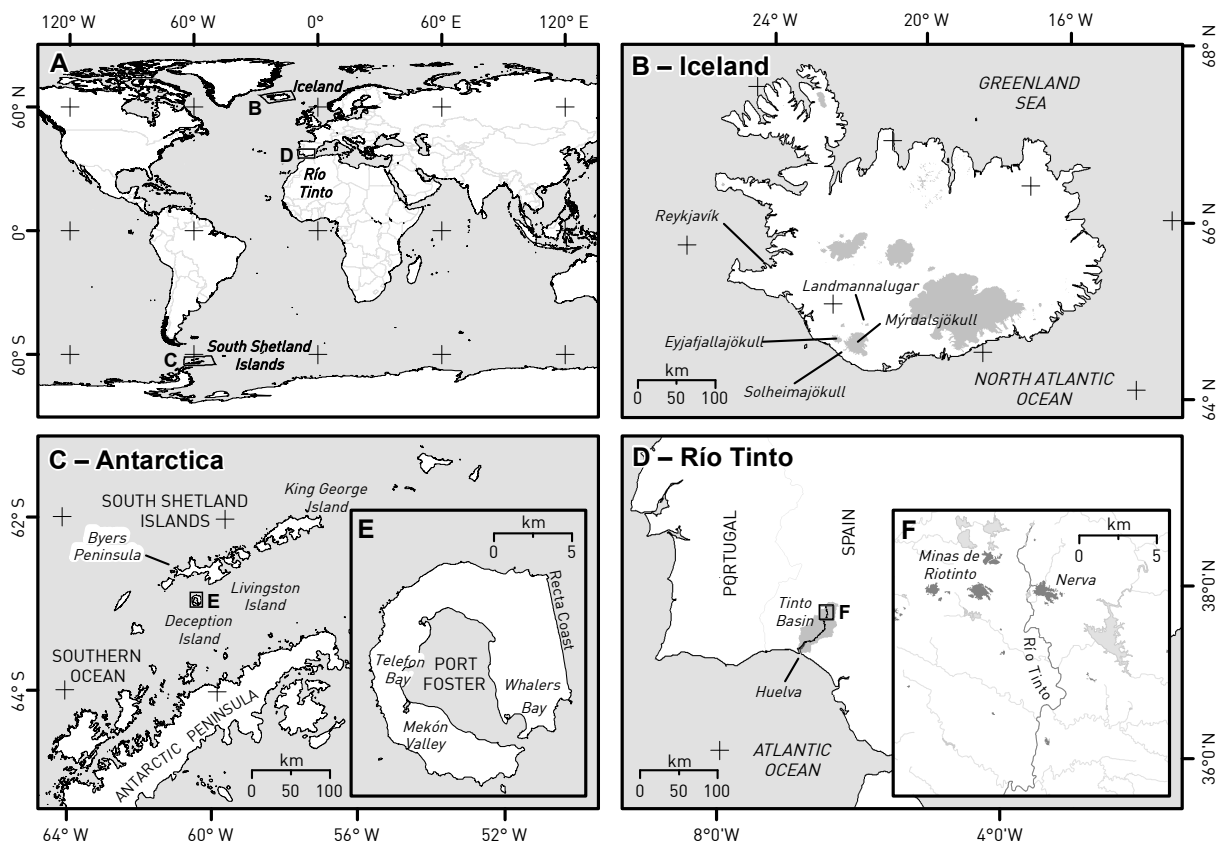
### 5.1 TERRESTRIAL ANALOGS

#### 5.1.1 UNDERSTANDING THE EARTH TO UNDERSTAND MARS

The study of geological process occurring in terrestrial analogs play a major role in understanding the origin of the geological features observed on Mars [*Robbins and Hynek, 2012*]. All science needs the use of analogy, what means ‘similarity between like features of two otherwise different things’ [*Baker, 2014*]. In planetary analog studies, the landforms found in other planets are compared either with features that were experimentally produced/modeled, or resembling features on Earth that have a well-known origin. That is the most effective resource for developing working hypotheses, follow their implications, and then, test those consequences [*Baker, 2014*]. To evaluate those assumptions, researchers visit and study these analog areas on Earth to determine characteristics that provide evidence for the origin of surfaces when compared with the detected by instruments in ongoing and future missions to Mars [*Greeley, 2013*]. Such terrestrial analog studies are necessarily based on our knowledge of processes occurring on Earth; especially on Mars, which surface is the most alike to our planet in the Solar System.

Usually, geology cannot be controlled through experimentation, unlike other sciences as physics or chemistry. Geologic studies cannot be restricted to simplified aspects of natural phenomena owing to the complexities of the natural world. An alternative to corroborate hypotheses generated by analogy is by adopting those assumptions and then by exploring their consequences [*Baker, 2014*]. A common way to achieve this is through the regional planetary geological mapping process, which involves a continuous assessment of hypotheses for a feature by checking the observed relationships [*Wilhelms, 1990*]. That is one of the main reasons why we have performed the geological mapping for the two study areas in this work: Ariadnes basin (Subchapter 3.2) and Coogoon Valles (Subchapter 4.2).

To achieve the assessment of the working hypothesis properly, the author has performed field work in recognized martian analog sites (among other locations) during the development of this work. In this chapter, it will be briefly highlighted the most relevant characteristics of those sites (Figure 5.1.a), and the application to the studied areas. In addition, the knowledge acquired through these processes together with an extensive bibliographic survey, helped to constrain the possible origin of some of the most interesting features identified in Ariadnes and Coogoon. That discussion is included below (Subchapter 5.2).



**Figure 5.1.a** (A) Location map of the terrestrial analog sites described in this chapter: (B) Iceland, where gray shapes are glaciers; (C) South Shetland Islands in Antarctica; and (D) Río Tinto in Spain, where a gray shape is the river basin. Two closer views of (E) Deception Island and (F) the Tinto River headwaters. Dark gray shapes are populated areas, while light gray shapes are water bodies in F.

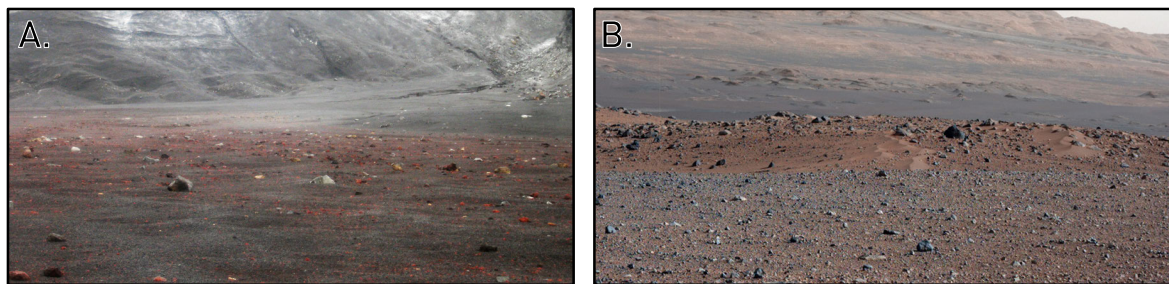
### 5.1.2 DECEPTION ISLAND, AN UNUSUAL ANTARCTIC ANALOG

Antarctica is considered one of the most suitable terrestrial analog for martian surface processes [Anderson *et al.*, 1972]. Specifically, the best-known are the Antarctic Dry Valleys, close to the McMurdo American base, which are in a hyper-arid polar desert and among the coldest (mean annual air temperatures are lower than  $-20\text{ }^{\circ}\text{C}$ ) and driest (less than 10 cm of precipitation per year) places on Earth [Heldmann *et al.*, 2013; and references therein]. The chemical composition and geology of their surfaces are also similar to the ones found on Mars. Thus, Dry Valleys is one of the key location where martian-like geomorphologic features, periglacial and soil formation processes can be studied in situ. Other places in Antarctica, however, also can be used to investigate the characteristics of other planets.

Deception Island ( $62^{\circ}, 57' \text{ S}$ ;  $60^{\circ}, 37' \text{ W}$ ), located in the South Shetland Archipelago at the northwest of the Antarctic Peninsula (Figure 5.1.a-C), is one of the few and more active volcanoes in the Antarctic region. This young ( $< 780 \text{ Ka}$ ) stratovolcano [Baraldo and Rinaldi, 2000], which have erupted lastly during the early seventeens [Baker and McReath, 1971], is a suitable Mars analog in many respects. Unusual ice-magma interaction processes have created a specific combination of conditions, materials, and landscapes, which some scientists have already investigated as other planet analogies [e.g., Hernandez de Pablo *et al.*, 2009; Gilichinsky *et al.*, 2010; Gilichinsky, 2011; Garcia-Descalzo *et al.*, 2012; Prieto-Ballesteros *et al.*, 2012; Centeno *et al.*, 2013]. Even, the logistic privilege setup of the island, close to the King George Island airfield (Figure 5.1.a-C) and holding two Antarctic Research Station, has led to its use as a testing area for few planetary sensors [Estepan *et al.*, 2009; Prieto-Ballesteros *et al.*, 2010; Ramos *et al.*, 2012]. Although the most highlighted aspects of previous studies have been the ones related to physics and biology, we have focus in the no less significant geomorphologic analogies [Molina *et al.*, 2013c, 2014a].

The island is characterized by a horseshoe-shaped morphology in plan, formed by an inner caldera that was flooded by the sea (Port Foster, Figure 5.1.a-E). Mounds, hills, and small plateaus, with lava flows, and volcanic craters are broadly distributed landforms in its surface. Additionally, the irregular landscape of Deception Island

made possible the presence of a wide variety of slope features related to both erosion and sedimentation as slumps, landslides, or rolling boulders. The general appearance of the ice-free areas is very similar to some of the landscapes we were able to observe on the surface of Mars ([Figure 5.1.b](#)). Both the fresh lava flows, and the ash loose deposits (which alteration turned them into black, reddish, brown and yellowish) are likely comparable to martian materials. As usually happens on Mars, the intense tectonic activity is a clear determinant of the landscape. That is the case of Recta Coast ([Figure 5.1.a-E](#)), the northwest outer coast is perfectly straight, caused by an undersea fault [*Fernández-Ibáñez et al., 2005*].

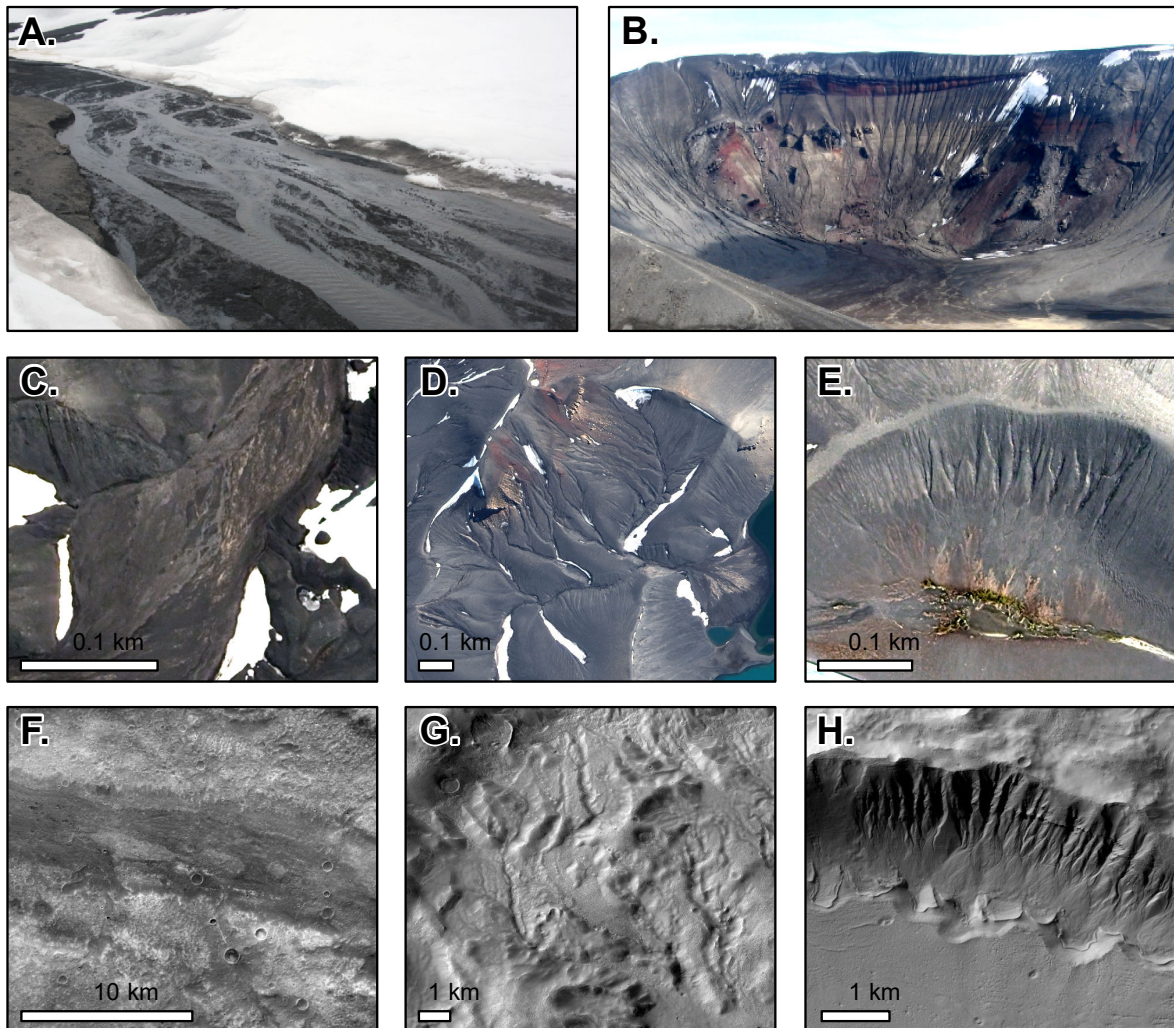


**Figure 5.1.b** (A) Plateau close to Whalers Bay ([Figure 5.1.a-E](#)) in Deception Island [*Source: A. Molina*], compared with (B) a true color image of Gale Crater as photographed by the NASA MSL Curiosity rover [*Source: NASA/JPL-Caltech/MSSS*].

Glacial and periglacial activity have later modified the volcanic landscape of this island. Glaciers cover a significant portion of the island, and due to the recent eruptions, they are partially covered by pyroclastic materials, hiding the ice beneath the surface, what could be the case of the possible glaciers described on Mars [*Head et al., 2005*]. Ice and ash-fall deposits' layering on them are also similar to the layering on the Martian ice deposits [*Guallini and Nerozzi, 2014*]. Melting process of this ice reservoirs during the warm season mobilizes relevant amounts of liquid water in short time lapses in Deception, what lead to the formation of fast floods and mud-flows-like events. This water activity carves gullies, sapping channels, and wide flatbed valleys ([Figure 5.1.c](#)). The remobilized pyroclasts form beaches, bed streams, alluvial and colluvial fans. The Mekón Valley ([Figure 5.1.a-E](#)) shows morphologies that resembles to the outflow channels on Mars, as Central Coogoon ([Figure 5.1.c-A, C and F](#)), but also the melt of snow patches in the summits of the volcanic crater rims, cause



the formation of the typical gullies on martian craters (Figure 5.1.c-B, E and H). On the other hand, permafrost is also well distributed beneath the island surface (except on thermal hotspots). Its structure in its upper part controlled by weather and snow at the short time period and by the ash-fall deposits at the long-time period, and the high geothermal activity of the active volcano in the lower part.

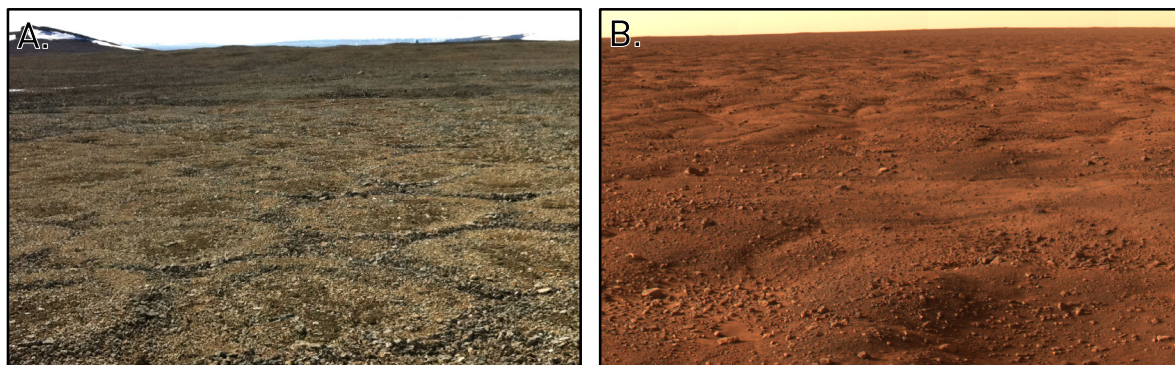


**Figure 5.1.c** Photographs from (A) Mekón Valley and (B) a rim close to Telefon Bay in Deception Island [Source: A. Molina and M.A de Pablo]. Image satellite from different types of fluvial features in Deception Island (C to E) and Coogoon (F) and Ariadnes (G and H).

Besides to the identification of Mars-like features on the field and satellite imagery in Deception, the direct participation of the author during three Antarctic Campaigns (within PERMAPLANET and ANTARPERMA research projects of the University of Alcalá) helped to understand other geologic processes. For example, we

worked in Byers Peninsula, Livingston Island (Figure 5.1.a-C), the largest ice-free area in Maritime Antarctica and considered a reference study site for natural processes at landscape scale [Quesada *et al.*, 2009].

The incipient degree of chemical weathering in the region made the soil attributes similar to the parent material, i.e. basaltic lava and volcanic tuffs sourced from Deception Volcano [Crame *et al.*, 1993]. Compositionally, they show chlorite, smectite, illite, quartz, hematite and other compounds [e.g., Moura *et al.*, 2012] similar to the described in Mars and found in Ariadnes and Coogoon. In addition, thermal contraction cracking in the ice-rich permafrost produce periglacial morphologies as patterned grounds (Figure 5.1.c). Such features have also been observed in the martian subpolar regions, where ice is shallower, from the orbit [Mellon *et al.*, 2008] and the ground (Figure 5.1.d). Thus, the author performed a soil survey with representative sample distributed along Deception and Livingston Islands, analyzing their particle size distribution and mineralogy [Molina *et al.*, 2013a], whose results are not directly related to the aim of this work and will not be included.



**Figure 5.1.d** (A) Patterned ground in Byers Peninsula, Livingston Island [Source: A. Molina] and (B) similar morphologies found in the NASA Phoenix landing site [Source: [NASA/JPL-Caltech/University of Arizona/Texas A&M University](#)].

### 5.1.3 ICELAND, THE ICE-LAVA INTERACTION HOT SPOT

Iceland is in the convergence of the Mid-Atlantic spreading ridge and a large mantle plume (i.e., hot spot). Due to a subpolar location (Figure 5.1.a-B) the island surface is also extensively affected by glacial and periglacial processes. The resulting unusual geologic interaction between ice and magma is easily observable owing to

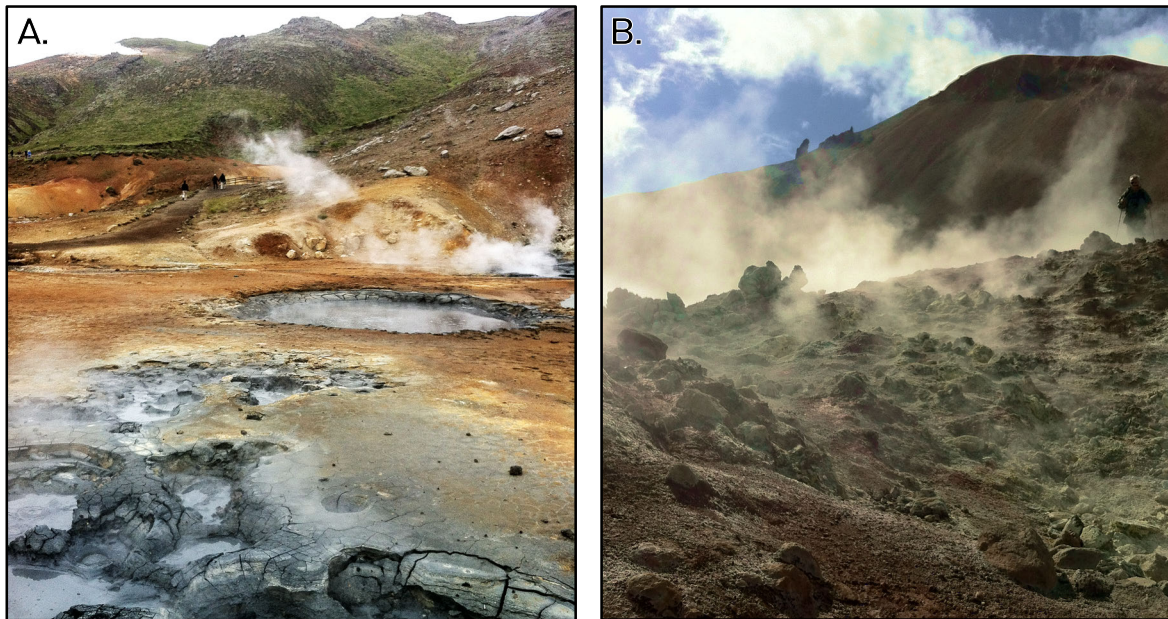
manageable access, poorly formed soils, and sparse vegetation, what made of Iceland a suitable location for researchers. Consequently, it has long been suggested as an analog for Mars in volcanology, petrology, glacial, and surface alteration processes [e.g., *Bishop et al.*, 2002; *Keszthelyi et al.*, 2004; *Ehlmann et al.*, 2012].

The petrology of the island is very homogeneous, comprised mostly by extrusive basaltic lava flows, emplaced over the last 16 Ma, but also a minor fraction of rhyolites. Interestingly, Icelandic basalts show a high Fe content [*Peate et al.*, 2008] similar to the displayed by the martian basaltic rocks. Several sites in Iceland provides analogies for eruptive rock alteration under acid, neutral, and alkaline conditions. This diversity provides the opportunity to determine the geochemical and mineralogical signatures of these processes in the field [*Gerard et al.*, 2014], constraining the formation conditions of materials with similar spectral signatures found on Mars [*Ehlmann et al.*, 2012].

In a similar way, as in Deception Island glaciers (Subchapter 5.1.2), some Icelandic ice caps shows tephra deposits that intercalate with ice layers, as in Solheimajökull glacier. An outburst flood took place in this glacier as the result of subglacial volcanism during 1999. This process is known with the Icelandic word 'jökulhlaups' [*Russell et al.*, 2010]. Similar ice-lava interaction was supposed to be significant on Mars, where the cryosphere and magma may have frequently interacted to produce catastrophic floods and carve outflow channels that we can observe today.

The shallow magma and a porous and water-rich media in Iceland occasion the presence of an active and intense hydrothermal activity. Mud and steam springs are abundant in the surface, which pH range from acidic (pH 2 – 5 in Krýsuvík; [Figure 5.1.e-A](#)) to alkaline (some springs with pH ~8 in Landmannalaugar; [Figure 5.1.e-B](#)). Those geothermal systems are studied since hold rich microbial ecosystems with relevant astrobiological importance [*Gerard et al.*, 2014].





**Figure 5.1.e** Geothermal springs and fumaroles in (A) Krýsuvík, Reykjanes peninsula, and (B) Landmannalaugar, Iceland. Locations in [Figure 5.1.a](#) [Source: A. Molina].

The author has visited some of the best-known places for their geologic interest in Southwestern Iceland ([Figure 5.1.a-B](#)) during the Nordic-NASA Summer School ‘Water, Ice and the Origin of Life in the Universe’ of 2012. For two-weeks of lectures and field trips, it was possible to study various environments and features in Iceland that represent well the geologic settings of this unique island and perform some in-situ measurements. This research was focused on the astrobiological characterization of an old and other young lava fields and glaciers. The older Laugahraun field was formed in a 1477 eruption while the younger one, Goðahraun field in Fimmvörðuháls, was created by an eruption of the Eyjafjallajökull volcano in 2010 ([Figure 5.1.a-B](#)) [[Amador et al., 2015](#)]. The recognition of the mineralogy and landforms associated with different eruption types and degrees of alteration helped the author to understand better volcanic and geothermal processes, being both hypothesized to happen in Ariadnes and Coogoon.



#### 5.1.4 RIO TINTO, A MARTIAN RIVER IN SPAIN

Río Tinto holds a highly diverse microbial ecosystem, despite its extremely acidic environment (pH 2.3) and high concentration of heavy metals. The river springs in the core of the Iberian Pyrite Belt in Southern Spain and flows south for about 100 km to the Atlantic Ocean (**Figure 5.1.a-D**). The Iberian Pyrite Belt is a volcanic-sedimentary complex with massive bodies of iron and copper sulfides concentrated by hydrothermalism, considered one of the largest sulfidic deposits on Earth [Amils *et al.*, 2014].

The characteristic bright red color of the Rio Tinto headwaters (**Figure 5.1.f**) originates with the release of groundwater rich in protons, sulfate, and iron percolate from the iron sulfide ores [Fernández-Remolar and Knoll, 2008]. The strong buffer capacity of ferric iron produces that their waters are always acid despite the income of neutral water from tributaries, and diverse microorganisms are adapted to grow in such acidic and strongly oxidizing environment [Amils *et al.*, 2014 and references therein]. The easy access (**Figure 5.1.a-F**) and unique characteristics of this environment made Río Tinto an excellent model for the study of the microbial ecology of extreme acidic environments and has been extensively studied as martian analog.



**Figure 5.1.f** Images of (A) origin and (B) downstream Río Tinto during a dry period, when sulfate salts precipitate on the river shores [Source: A. Molina].

In the past, it was generally accepted that the Río Tinto conditions were the result of the last 5,000 years mining activities in the area. However, recent geological, geophysical and hydrogeological studies support that the oxidation of subsurface sulfidic bodies and metabolism of chemolithotrophic microorganisms are the primary source of the acidic fluids [Gómez-Ortiz *et al.*, 2014]. Iron oxidizing microorganisms' activity produce the solubilization of sulfidic minerals and high concentrations of iron, sulfate, and protons. Sedimentary record in ancient Río Tinto terrace deposits, which predate the oldest mining activity in the area (2.1 – 6 Ma), evidence the generation of acidic water naturally.

Volcanic, hydrothermal, weathering and sedimentary processes formed phyllosilicates as chlorite, illite, montmorillonite and kaolinite along the Río Tinto basin [Fernández-Remolar *et al.*, 2011]. The weathering and sedimentary materials in Ariadnes and Coogoon show geochemical trends that might be the result of active weathering of a primary basaltic source rock, as in Río Tinto where some similar phases are considered products of tuffs of a volcano-sedimentary complex weathering.

Interestingly, hot and dry summers typical of the Mediterranean weather reduce the river volume of water, forming a fluvial-evaporative system where sulfate minerals are produced in acidic evaporative pools and river shores (Figure 5.1.f). Sulfate minerals on some locations on Mars suggest a past aqueous, acidic, sulfate-rich environment, similarly to the Tinto basin, where the chemical weathering of basalts form sulfate-rich sediments [Fernández-Remolar and Knoll, 2008]. This river is used as a model for the formation of sulfates on Mars by evaporation of acidic waters, and would help to understand the process that may have formed the sulfate-bearing sediments in the Ariadnes basin.

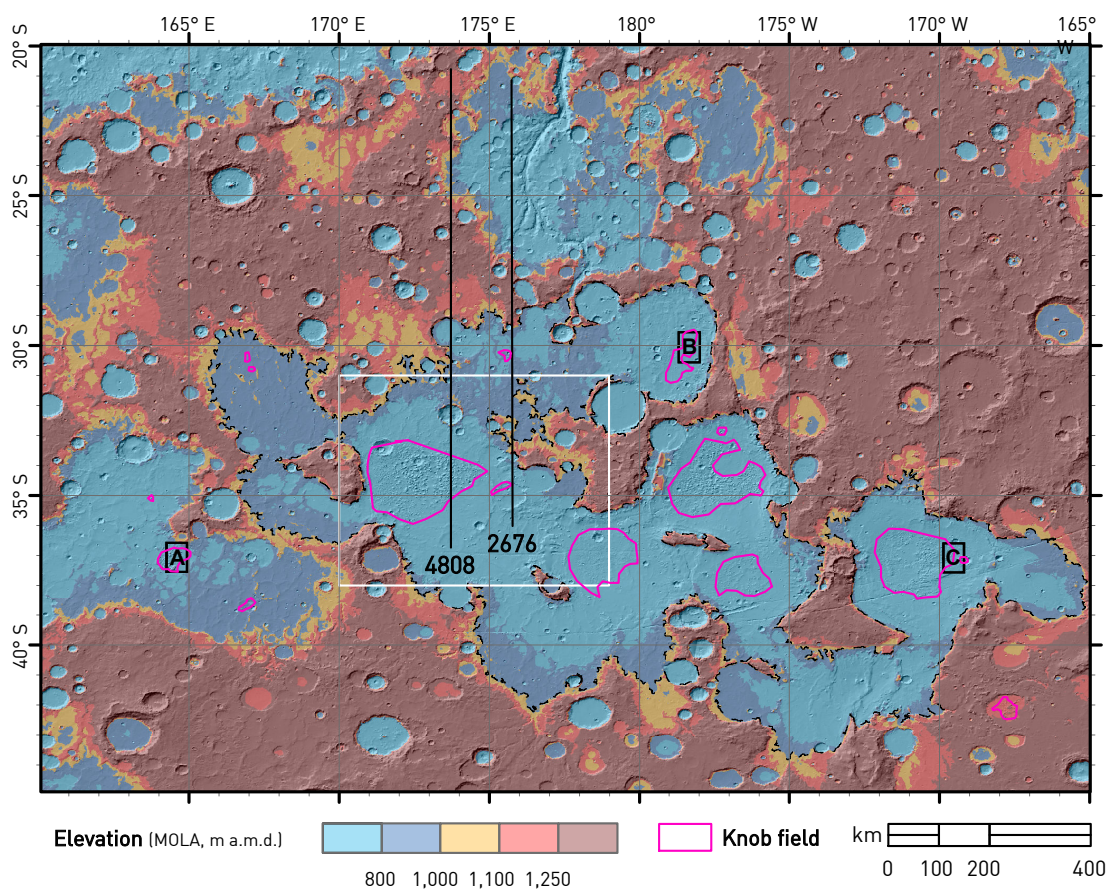
To sum up, the investigation of surficial aqueous processes on early Mars is a major focus of Mars studies, since such environmental conditions may have supported exobiological life or prebiotic chemistry. We found sedimentary deposits that record ancient physical, chemical and biological characteristics in Río Tinto, and

martian fluvial sediments should have a similar potential. In this work, following the experience acquired by the author drilling and sampling in the field during a three-months campaign within the Iberian Pyritic Belt Subsurface Life Detection (IPBSL) research project of the National Institute of Aerospace Technology (INTA), it is performed an interpretation of the Coogoon and Ariadnes records to characterize the environmental conditions during the Noachian-Hesperian transition. Additionally, the unique ecosystem of Río Tinto stands as evidence of the capability of martian systems to support subsurface life, even considering the unfavorable surface conditions.

## 5.2 GENETIC HYPOTHESIS

### 5.2.1 ERIDANIA SYSTEM

The Eridania System is composed of a suite of six ancient and highly degraded basins of 180 – 240 km in diameter, which are topographically connected and present concave floors (Part 3.1.1). The depressions are defined by the 1,100 and 1,250 m contours (Figure 5.2.a) and represent several of the lowest points in the cratered highlands. They enclose five large knob fields, including Ariadnes and Caralis Colles, and other minor knob aggregates.

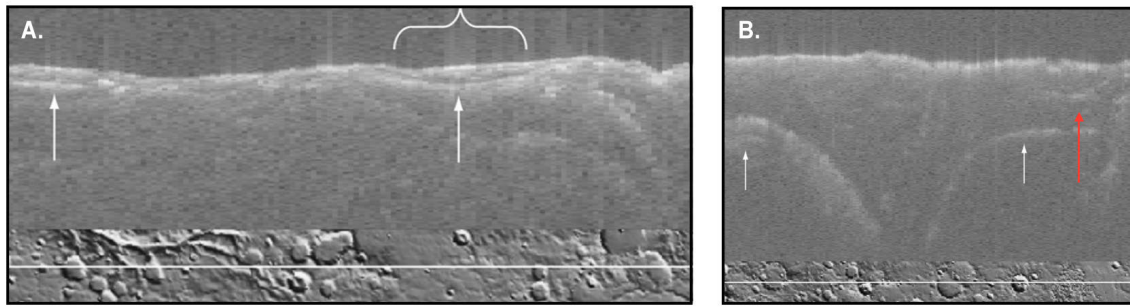


**Figure 5.2.a** Reclassified elevation of the Eridania System region, showing height ranges of the Eridania rims and the different levels of the hypothesized paleolake, where black dashed line shows the 1 km a.m.d. paleoshoreline [Irwin *et al.*, 2002, 2004b]. Pink-outlined polygons indicate the extension of the knob aggregations found in the region. The vertical black lines show the MARSIS orbits referred in Figure 5.2.b. White square displays the Ariadnes study area and black squares the extent of the images in Figure 5.2.d.



The depressed topographic terrains of Eridania System have been considered as been shaped by the erosional integration of several primary sub-basins formed by a series of impact events [e.g., *Howard and Moore, 2004*]. However, the Eridania sub-basins show: **1)** rounded but not circular outlines, **2)** concave bowl-shaped internal relief, and **3)** relatively steep, inward-declining slopes (generally about  $0.5 - 1.5^\circ$ ); which are rather unusual for impact basins of this size on Mars [*Craddock and Howard, 2002; Irwin et al., 2004a*]. Impact crater larger than 60 km in diameter on Mars are usually circular oval, their rim is lowered, and their interior is filled with advanced degradation [*Forsberg-Taylor, 2004*]. Gorgonum and Atlantis exhibit the greatest internal relief (more than 1 km) and Ariadnes and Caralis basins display up to 500 m (see Part 3.5.2), when basins with diameters of 150 km infrequently have an internal relief higher than 500 m [*Howard, 2000*]. This set of peculiar characteristics, together with their clustered distribution, points to unique local conditions and deserve to discuss alternative hypothesis for their formation or a later modification.

Interestingly enough, [*White et al., 2009*] described the north of Ariadnes as one of the few places on Mars where exist numerous MARSIS (an orbital sounding radar) [*Picardi et al., 2005*] reflections clustered in one location. The orbits 2676 and 4808 cross the north of the study area in longitudinal profiles, and the 4808 overlaps the Ariadnes knob field itself (**Figure 5.2.a**). These irregular in shape and distribution reflections (white arrows in **Figure 5.2.b**) are likely caused by a potential subsurface interface that could represent the base of the Eridania System. The estimated interface depth is 710 m [*White et al., 2009*], which in the case of icy or porous rock would result in a greater inferred depth [*Zhang et al., 2008*]. The radargram from the orbit 2676 (**Figure 5.2.b-B**) also displays two additional horizontal tenuous reflections at its southern end with higher time delays, which White et al. [2009] consider that may be explained by ionospheric distortion of MARSIS signals. However, this work does not even mention an observed reflection that perfectly fits with the extension of the knob field in the orbit 4808 radargram (red arrow in **Figure 5.2.b-A**). In this regard, such reflection could be another shallower interface related with the knob field itself.



**Figure 5.2.b** Radargrams in the north of Ariadnes area, displaying the variety of echoes seen with MARSIS from orbits 2676 (A) and 4808 (B). Arrows highlight relevant reflections. Ground tracks are shown on a shaded relief map of the surface below (horizontal white lines) and on Figure 5.2.a [Source: Adapted from White *et al.*, 2009].

The location of those reflections roughly corresponds to a ~400 km in diameter ‘Quasi-Circular Depression’ (QCD) [Frey *et al.*, 2002; Edgar, 2014]. The QCDs often have a bowl-like shape, softened profiles, and subdued relief [Frey *et al.*, 2002] with slightly lower topography than its surroundings. Those depressions are sometimes only visible in high-resolution topography with no visual correspondence on the surface [Edgar, 2014] and are usually interpreted to be ancient eroded impact basins [Irwin *et al.*, 2002].

If these basins are indeed degraded impact basins, they must have formed or extensively modified by erosion (by aeolian, fluvial, glacial, or any other weathering processes), burial/accumulation (by mass wasting, sedimentation, or lava infill) or a combination of both [Potter, 2014]. The redistribution of sediment within the basin margins instead of concentration within the deepest portions of their interiors during infilling might be a marker of the predominant/key processes. There are two main explanations for this morphology: 1) flooding of the basin interiors by lava; and/or 2) the basins contained shallow ephemeral or perennial lakes that through wave action redistributed sediment [Howard, 2000]. In this regard, Irwin *et al.* [2004a] asseverate that this morphology reveals that the sediment transport processes must have been relatively inefficient within the basins, consistently with standing body of water. Several shreds of evidence support that paleolake existence, and since below ~800 m a.m.d. any water in the basins would be confined and only would be released into a transient lake or the groundwater system [Golder, 2013]. At its highest water level, the lake would have had a volume 562,000 km<sup>3</sup>, creating one of the largest lake systems

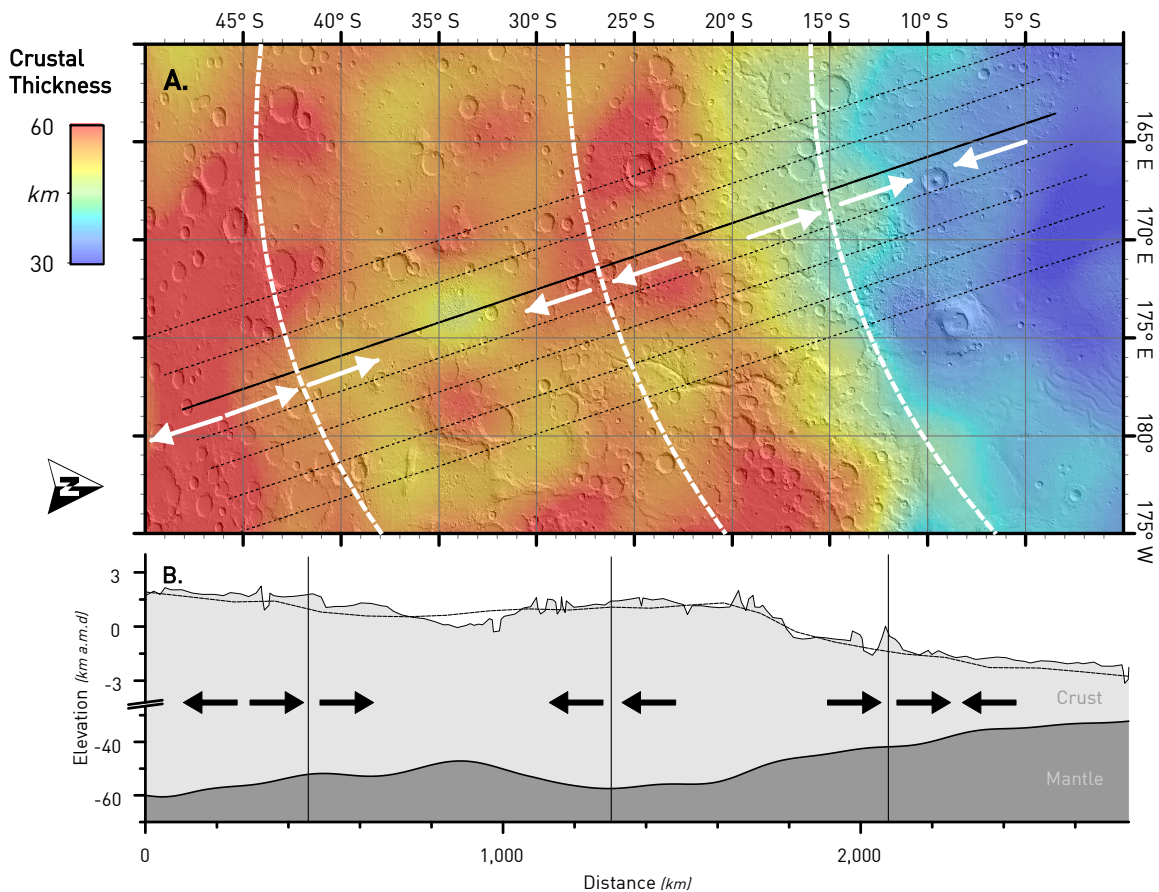
in early Mars [Baker and Head, 2012a], being able to mantle efficiently any large basin hence. However, Irwin *et al.* [2004a] also indicate as most of the sub-basins have wide gaps in their original crater rims, what in their opinion indicate erosive processes rather than simple mantling.

Some of the basins floors are outlined by concentric ridges (Subparts 3.2.2iv and 3.2.3i) that may be indicative of subsidence events, which would explain the unusual bowl-shaped profiles of the depressions [Baker and Head, 2009]. However, as those stresses are part of a regional tectonic system [Capitan and Van De Wiel, 2011], they might be indicative of a tectonic formation (or modification) of the depressions rather than an origin directly related to impact excavation [Wendt *et al.*, 2012].

As it was discussed in Subpart 3.2.3i, several tectonic pulses might affect the areas that were involved in the formation of the Tharsis, Elysium, Hadriaca, Tyrrhena and other volcano-tectonic regions [Watters, 1993; Schultz and Tanaka, 1994; Lias *et al.*, 1999]. In addition, extensional surface stresses around the dichotomy boundary [Nimmo, 2005] could explain the differences in crustal thickness between the northern lowlands and the southern highlands (Figure 5.2.c-A). Lateral flow of lower crustal material results in compression and a reduction in height on the thick-crust side and vice versa on the thin-crust side (Figure 5.2.c). The modeled topographic profile resulting from such process [Figure 3.B in Nimmo, 2005] fits well with the elevation of the region, where a small depression on the thicker side of the dichotomy is followed by a rise, developing an elevated bench below the subsequent dichotomy scarp. The topographic lows may correspond to the chain of depressions along the 180° meridian in the region between Aeolis, Memnonia, Eridania and Phaetontis quadrangles, while the latter could be the steep scarp of 100 – 200 km wide to the north (Figure 5.2.c-B).

Despite the fact that the origin of the dichotomy remains uncertain, the lateral crustal flow may have modified those terrains after the dichotomy development, which anyhow is dated as older as 4.1 Ga [Frey, 2004]. In addition, later thermal events would also generate episodes of enhanced crustal flow [Nimmo, 2005]. Thus, the

volcanic activity related to the formation of the AHRp and/or the lowland terrains during the Hesperian [Head *et al.*, 2002] could cause a series of lower-crustal flow events that resulted in some of the tectonic features observed in the area. Interestingly, the predominant direction of ridges ( $\sim 170^\circ$ ; see Subpart 3.2.3i) is similar to the expected for the crust deformation.



**Figure 5.2.c** (A) Regional map of crustal thickness [Zuber *et al.*, 2000]. (B) Surface topography (average as dotted lines and Ariadnes cross-cutting section as straight line) and crustal profile (not at the same vertical scale). Arrows denote approximate locations of compressional and ex-tensional regions.

There is another possible process that might have caused the deformation of the Eridania basins. Michalski and Bleacher [2013] suggested that some of the most ancient basins Mars, commonly assumed to have formed by impact, are in fact a type of volcanic construct that they named as plains-style caldera complexes, an ancient type of supervulcano formed through mafic explosive volcanism on Mars. The authors themselves consider that the distinction between an impact versus volcanic origin for many ancient Martian basins is complicated [Michalski *et al.*, 2013a].



Differently than the large shield and highland volcano calderas (i.e., 'pateras') the plains-style caldera complexes, are characterized by the presence of collapse features, lower topographic relief, and association with plains-style lavas and friable layered deposits. The latter fine-grained, layered, and clay-bearing sediments described by *Michalski and Bleacher* [2013] resemble to the knobs fields inside Ariadnes and Caralis basins. Although those formations will be discussed in detail in the following section, this is an additional support to this formation in the area. In addition, a thinner crust agrees with the sub-basins shape ([Figure 5.2.c](#)), what would favor magma migration and the subsequent volcanic eruption.

Some volcanic edifices (Noachian highland edifices, Nhe) have been described in the region over the relict reliefs between sub-basins ([Figure 3.1.c](#)) [*Tanaka*, 2000; *Tanaka et al.*, 2014]. There are also similar features to the east of the study area that we have classified as the *eNhp* unit (or *eHed*, when covered with a thin blanket) in the geological map of the area ([Figure 3.2.a](#)). However, none of these structures individually contains enough shreds of evidence to clearly point to volcanism. The region has been extensively modified through a series of more recent processes (Subchapter 3.6), that may have erased most of the features that would evidence an ancient volcanic event. The possible subsidence of the region originated by thermokarst activity is the less feasible theory. The features related to permafrost (or ice lenses) melting registered on Mars are orders of magnitude smaller (below 10 km in diameter), and while volcano-ice interaction could have been involved in the modification of basins, it could hardly explain the origin of the large depressions [*Michalski and Bleacher*, 2013; and references therein].

Conclusively, it is not possible to asseverate which could be the origin of such an intriguing feature as the Eridania System, a set of ancient sub-basins widely modified. Nevertheless, we discussed here a group of alternative hypotheses other than the most accepted of being formed as a cluster of modified impact craters ([Table 5.2.a](#)). Impact craters are ubiquitous on Mars, and they were even larger and more frequent during the Late Heavy Bombardment (4.1 to 3.8 Ga). Therefore, impact theory is broadly accepted. However, although it could not be discarded, the lack of

surrounding ejecta, clustered distribution, and different profile from the expected for an impact degraded basin; the Eridania System must be either formed or modified through another mechanism. It is inarguable that the lower-crustal flow operated in the area, but is not easy to establish on what scale. There are not enough pieces of evidence to evaluate the possibility of the sub-basins as ancient supervulcano calderas, though most of their characteristics are compatible with that hypothesis.

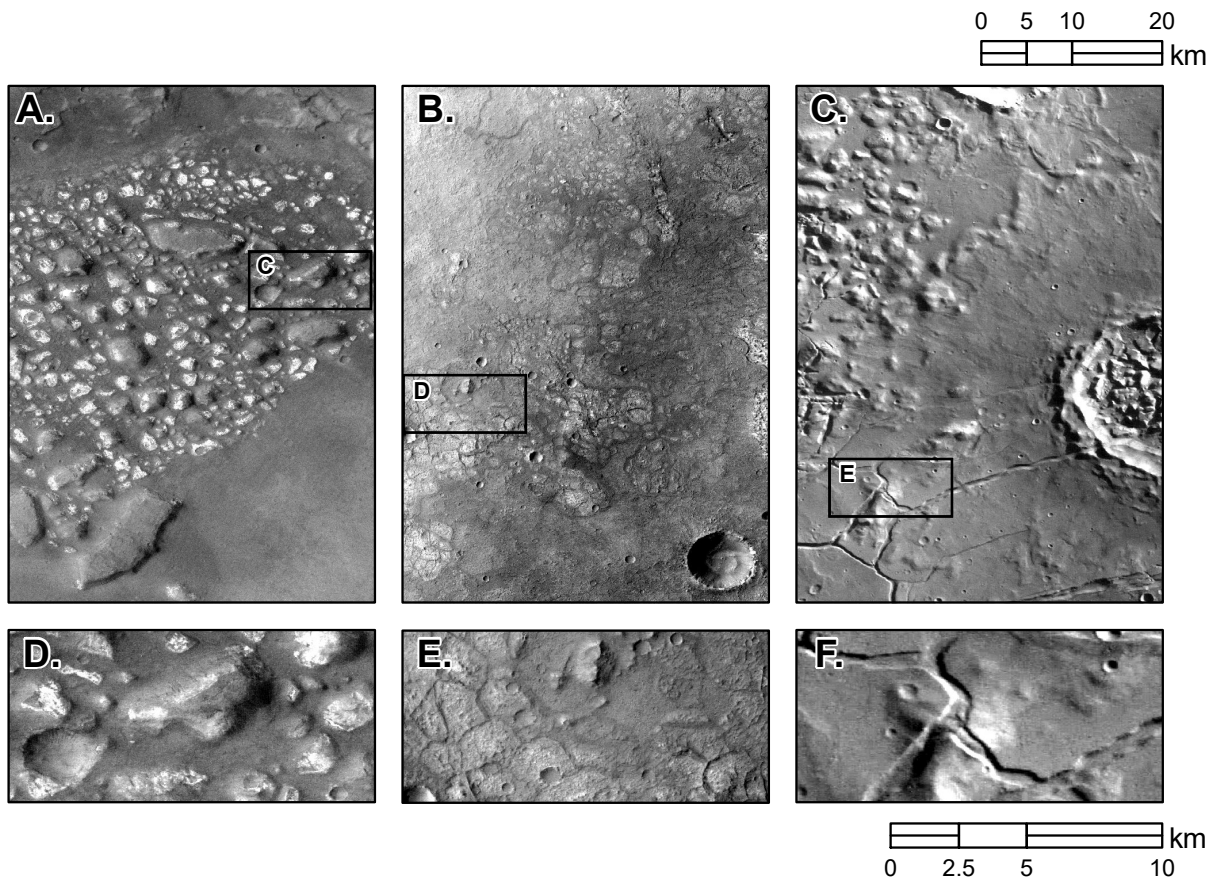
The result of the Eridania System depression as a combination of the processes occurring during the martian history is within reason. In early Noachian (or even Pre-Noachian), an impactor may have crashed in the already attenuated crust via regional stresses. This sub-basin could be Gorgonum, since its unique morphologies [e.g., *Capitan and Van De Wiel, 2011*]. The impact could have triggered a volcanic event causing a rapid ascent of magma. This volcanic process would have extended to a larger area favored by crustal thinning. Furthermore, it would enhance as a feedback process the lower-crustal flow, enlarging the depressions. Such an ancient supervulcano would produce enough volcanic materials to be remobilized later as the *eHed* (and *HNkf*) deposits and the thermal activity would release volatiles, leading to the water-rich episode that formed the paleolake in the Eridania System.

**Table 5.2.a** Different mechanisms that could have potentially formed the Eridania System depressions.

Observed morphology	Possible formation process			
	Impact excavation	Lower-crustal flow	Plains-style caldera complex	Thermokarst subsidence
Regional settings	Yes	Yes	Yes	Maybe
Extent	Maybe	Yes	Yes	No
Elevation	Maybe	Yes	Maybe	Maybe
Internal relief	Unlike	Maybe	Yes	Maybe
Rounded shape	Unlike	Maybe	Yes	No
Steep slopes	Unlike	Maybe	Yes	Yes
Tectonic features	–	Yes	Yes	Yes
Subsurface interface	Yes	Maybe	Maybe	Yes
Crustal thickness	–	Yes	Yes	–
Composition	Maybe	Yes	Yes	Maybe

## 5.2.2 ARIADNES AND CARALIS LIGHT-TONED DEPOSITS

Several groups of light-toned degraded knobs and stepped angular mesas (mapped as *HNkf* unit in this work, Subpart 3.2.2ii) appears in the lowest elevation points of the Eridania System sub-basins (Figure 5.2.a), showing a meter-sized polygonal texture and cross-cutting lineaments on their surface (Figure 3.2.c-F to H). A dark smooth material (similar to *AHrp* and *eAsp*) fills the space between them which, when not present, is replaced by channel-like groove surface (Figure 3.2.c-B). Additionally, a darker capping layer in angular unconformity lies at the top of the mesa-like mounds (Figure 3.2.c-A). Small channels and gullies carve the knobs flanks and the space between the knobs, exposing bedding morphologies that suggest internal layering (Figure 3.2.c).



**Figure 5.2.d** CTX imagery showing the diversity of the knob fields in the Eridania System outside of the study area in two different scales. See Figure 5.2.a for A to C images context. Images A to C show the extension of D to F images. The scale in the upper position corresponds to A to C, whereas the scale below corresponds to D to F.

There are two main questions to be addressed related to this knob fields: 1) what is the source and deposition process of the layered clay-bearing and sulfate-bearing materials (Subchapter 3.4), and 2) how they were shaped as the knobby and mesa-like features that we can observe today. We will only focus in the first question in this section, analyzing the second aspect in the following (Part 5.2.3). The relatively uniform albedo, texture, and morphometry of the knobs, developing fields elsewhere in the region (Figure 5.2.a), strongly suggest that they once formed a continuous layer extending along the whole Eridania System [Wendt *et al.*, 2013]. Furthermore, a fine-grained deposit forming mesas in the sub-basins margins (*eHed* unit, Subpart 3.2.2iii), displays light-toned patches on its surface and similar morphologies than the mesa-like knobs. This so-called Electris deposit may have a common geologic history (in either formation or later alteration), even though Electris deposit shows other morphologic and spectral differences [Noe Dobrea *et al.*, 2008; Grant *et al.*, 2010]. Concerning the latter, it is noteworthy that the strong absorption bands are only observed in the fresh knob surfaces, exposed by erosion.

The location of these layered deposits inside the crater-like Eridania depressions, not always centered, resembles to the central mounds found in craters of varying sizes occurring across the martian surface [Malin and Edgett, 2000] that may be later modified. The processes responsible for those mound formation and subsequent modification are still uncertain, and it is also debated if their original extension once filled the entire craters and were later eroded [Malin and Edgett, 2000; Bennett and Bell III, 2016] or if the sediment never went forward the crater walls [Kite *et al.*, 2013]. The geologic agents that contributed to the primary deposition of the mounds sediment is controversial and include alluvial, deltaic, lacustrine, submarine, ice related, aeolian, explosive volcanic and impact processes [Bennett and Bell III, 2016; and references therein].

The dominating constituent in the knob materials are Fe- and Mg-smectites, which presence seems uniform along the exposed surfaces in the region. Specifically, we found signatures consistent with saponite and talc-saponite mixed layering in CRISM spectra (Part 3.4.1), which is in line with deep-water sediments and



subaqueous hydrothermal deposits. Those materials are overlain by a thinner layer of Al-rich clays. This weathering sequences of basaltic rocks can be explained due to surficial leaching (i.e., ion remobilization) with the preferential removal of Mg and Fe, while the less mobile Al cations remain inside the clay minerals. Interestingly, this dissolution restricted to the upper parts of the sequences similar to terrestrial abiotic pedogenesis is characteristic of very high rainfalls climatic regimes [Carter *et al.*, 2015]. However, the same stratigraphic distribution could be the result of hydrochemical changes over time (from less acidic to more acidic weathering fluids) or a climatic change from dryer to wetter conditions [Fernández-Remolar *et al.*, 2011], that would increase the leaching rates to produce cation-depleted clays.

In contrast, the overlying *AHrp* materials contain strong signals for olivine [Michalski *et al.*, 2015], which is typically related to Hesperian igneous processes [Mustard *et al.*, 2005; Ehlmann and Edwards, 2014] that is in agreement with the hypothesized formation of the unit. Finally, the sulfate-rich deposits have been reported at the bottom of the stratigraphic sequence [Gilmore *et al.*, 2011; Pajola *et al.*, 2016]. Such smectite-sulfate assemblages were probably formed when interstitial brines resulting from the phyllosilicate formation that deposited and accumulated underground [Zolotov and Mironenko, 2014], while the sulfates could also precipitate from acidic standing bodies of water. In this context, the chloride-bearing *eAed* may have formed through evaporative pumping (i.e., evapotranspiration) or, less likely considering their estimated age, may have been resulted from the intersection of the water table with the surface.

Based on the composition and the location of the knobs, we can conclude that the most feasible genetic process was the sediment deposition in a lake or aquifer (Table 5.2.b) in a Noachian event following the formation of the depressions [e.g., Howard and Moore, 2004]. The knobs are smaller towards the sub-basins rims, indicating a thinner peripheral thickness, which in combination with their horizontal layering and the unusual shape of the sub-basins floors are indicative of a deposition of sediment in standing water. However, it could be the case that the deposited

material was pre-existing clay. In spite of the lack of subaqueous morphologies does not support this, we cannot discard this possibility.

The martian highlands shows evidence of many palaeolakes, whose end of formation appears to be constrained at the Late Noachian–Early Hesperian boundary [Fassett and Head, 2008]. Indeed, previous studies backed up the existence of a paleolake in Eridania System [e.g., Irwin *et al.*, 2002, 2004a; Fassett and Head, 2008; Noe Dobrea *et al.*, 2008; Baker and Head, 2012b; Golder, 2013]. That is supported by 1) the elevation of Ma’adim Vallis’ head (~1,200 m a.m.d.; Figure 3.1.a), 2) the termination of valley networks between 950 and 1,100 m a.m.d. (Figure 3.1.b), 3) the slope transition in the sub-basin floors, 4) the regional valley network and Ma’adim Vallis flow modeling [Irwin *et al.*, 2004b], and 5) crater-count estimated ages (Section 3.3.3). A long-lasting but fluctuating water table fed from multiple sources may have reached its maximum level prior to the overspill event that formed Ma’adim Vallis. Variations in the groundwater system, fluvial activity, and direct surface evaporation caused the bed layering. In addition, the Eridania System is one of the few locations in the highlands where groundwater upwelling may occur, which together with its low elevation and volume/watershed area ratio, show that that Eridania paleolake was preferentially sourced from groundwater income during most of his history [Fassett and Head, 2008].

Several properties of these deposits might also be consistent with volcanic lava flows (Table 5.2.b). Although lava flows are typically lobate, a high-volume flux that inhibits the formation of a crust during emplacement may produce a continuous body of liquid lava across the entire width of the flow (i.e., ‘flood lavas’) [Keszthelyi *et al.*, 2000]. Interestingly, some lava flows show surface morphology as ridges, plates, and smooth surfaces that are broken into polygons and grooves (i.e., ‘platy-ridged’) [Keszthelyi *et al.*, 2000, 2004] similar to the observed morphologies in the deposits. The cross-cutting lineaments along the surface of the knobs (Figure 3.2.c) can be explained as a consequence of tectonic activity (e.g., faulting), but also may be related to volcanism or hydrothermal activity (e.g., dikes). Tanaka [2000] noted a significant number of small-scale volcanic features in the region. Although flood lavas can

explain the absence of evident flow features and composition can fit when they are weathered; the patterns of erosion in the knobs rims indicate a much more easily eroded material than the typical volcanic rocks, but also the extent and scale of the bedding, and the lack of a clear source makes this an unlikely origin.

Light-layered deposits in subaqueous basins can also be intruded by rapid and extensive mud volcanism, produced by fluidized sediments that rise along faults and fractures triggered by events that enhance overpressure [Kopf, 2002]. Such as lateral tectonic compression may have been produced by the lower-crustal flow acting in the area (Part 5.2.1). Upward mobility can also be facilitated when the confining pressure is reduced through uplift and unloading due to the removal of an overburden [Kopf, 2002], as could be the case of the previously mentioned Eridania paleolake overspill [Irwin *et al.*, 2004a].

Several of the deposits which initially were assumed as lava flows released from fissures or fractures on Mars have been reconsidered as mud flow deposits [Wilson and Mouginis-Mark, 2014]. The mud eruption origin was proposed for deposits on various locations on Mars [e.g., Franchi *et al.*, 2014; Pondrelli *et al.*, 2011; Oehler and Allen, 2010; Komatsu *et al.*, 2016], especially cones-like mounds and lobate formations. However, mud volcanoes on Earth display a variety of morphologies, that range from those steep-sided cones to broad domes and caldera-like depressions [Hargitai, 2014] that resembles to the ones found in the area. However, they are generally poorly-sorted compared with the lacustrine deposits, forming what is known as ‘mud breccia’ [Pondrelli *et al.*, 2011]. Furthermore, the formation of ancient deep clays (younger than early Hesperian, the formation age of the *HArp* overlying materials) still needs to be constrained. So Ariadnes and Caralis knob material may have been created by an eruption of mud with characteristics are still not described on Mars; but does not fit well with the currently known as martian mud flows by the same reasons than with lava-related volcanism (Table 5.2.b): the absence of pits, vents or flowing morphologies, and the observed structure of the bedding.

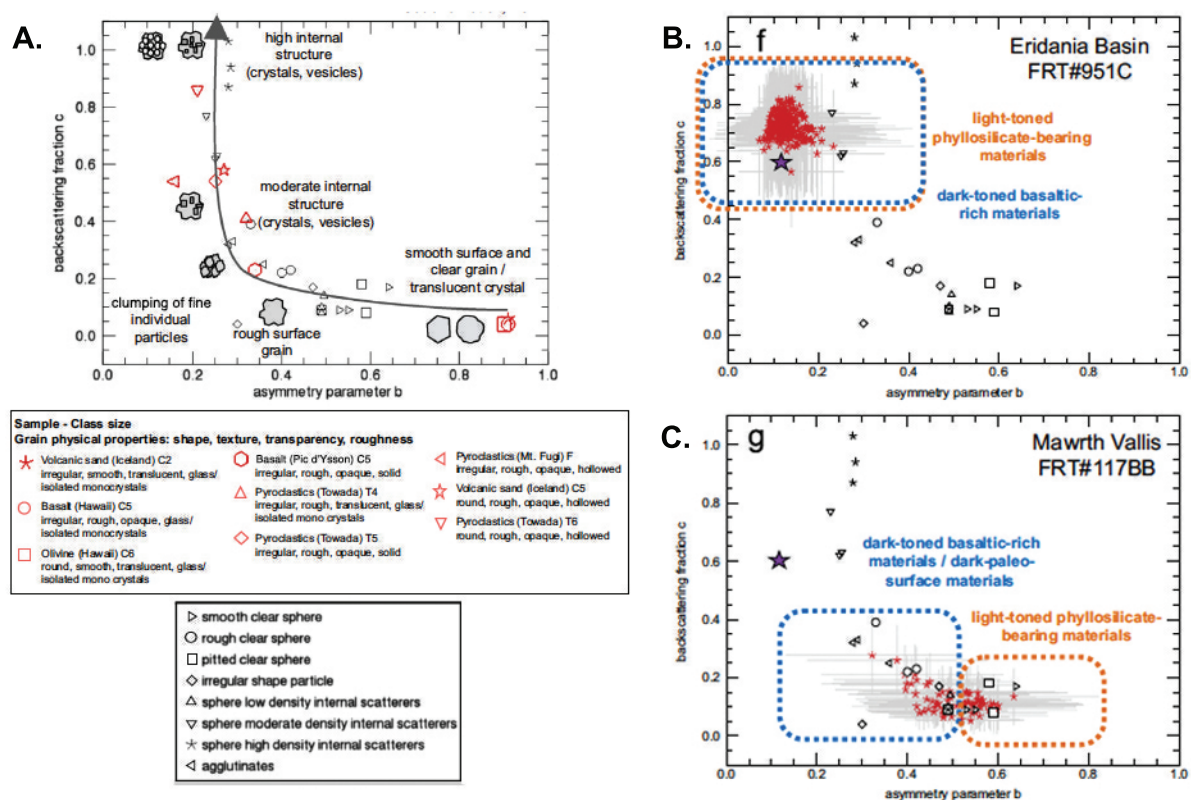
However, an airfall origin can produce deposits which deposition shows vertical distribution, thickness, and scale consistent with the observations (Table 5.2.b). Airfall deposition can include accumulation of layered dust and ice [Schultz and Lutz, 1988; Tanaka, 2000], pyroclastic material [Moore and Howard, 2005], or windblown fine-grained materials as loess [Grant *et al.*, 2010]. These deposits typically show low relief, lack of flow features, high albedo and fine-grained texture as the characteristic of the constituting material of the knobs. Such a composition indeed suggests basaltic weathering or hydrothermal alteration products, consistent with pyroclastic materials [Kerber *et al.*, 2012] that would be compatible with pyroclastic fall by suspension, but also subaqueous pyroclastic deposits and aeolian loess of a primary volcanic airfall ash [Filiberto, 2014].

The surface micro-textural information (i.e., surface grain parameters as grain size and morphology) is a useful resource to identify geological processes. Magmas cooling velocity produce a range between amorphous glasses to finely crystallized micro-lithic texture. Rough grains indicate recent erosion, while smooth and smaller grains are typical of later aeolian and aqueous transport processes. [Fernando *et al.*, 2016; and references therein] proposed the use of CRISM multi-angular derived photometric measurements to study the surface micro-texture, through light scattering by the surface materials in the VNIR (Figure 5.2.e-A). They studied an image in Sigmud Colles (Figure 5.2.e-B) that shows the outcrops of topographically flat smooth light-toned materials that are covered by a dark thin material [Adeli *et al.*, 2015]. The observed scattering pattern [Fernando *et al.*, 2016] of the Noachian-Hesperian phyllosilicate-bearing materials [Adeli *et al.*, 2015] may suggest in-situ alteration of highly microtextured primitive basaltic materials (Figure 5.2.e-B), like in altered serpentized peridotite on Earth. It can also be produced after a very short transportation. Since those deposits are quite similar to those in Ariadnes and Caralis, we can assume that they may have a comparable formation.

The genetic process that produced and deposited the clay- and sulfate-bearing friable deposits that comprise the light-toned knob field at the bottom of Ariadnes and Caralis basins is not easy to verify. As well as with the formation of the



depressions itself, the origin is obscured by subsequent processes; and there is a wide range of suitable possibilities (Table 5.2.b). Present data are insufficient to choose conclusively among the various possibilities, but observations support a lacustrine and/or pyroclastic related deposition, which may be linked to the higher Electris deposits. Besides the different location and morphologies of the Electris and the knob deposits, the materials forming the knobs seems to be more cemented, exposed and present dike-like features. This might be indicative of a different origin, but also a later modification process that only affected the lowest part.



**Figure 5.2.e** (A) Plot that shows the relation between the backscattering fraction and the asymmetry parameter, which is related to internal heterogeneity and the surface roughness, as experimental studies on artificial (**black symbols**) and natural samples (**red symbols**) having varied physical properties as grain shape, roughness, internal structure [Fernando *et al.*, 2016; and references therein]. Those results are compared to the obtained with two CRISM images in (B) Eridania Basin (FRT000951C), and (C) Mawrth Vallis (FRT000117BB). Purple stars are the mean Mars values. [Adapted from: Fernando *et al.*, 2016].

We propose an alternative hypothesis to the broadly accepted formation by lacustrine deposition [e.g., *Irwin et al.*, 2002], which otherwise fits well the observations. Basaltic ashfall may have fallen around all Eridania System sourced from the volcanic edifices in the area or a near volcano. Airfall pyroclasts deposited in the Eridania paleolake and formed a distinctive tephra layer, which was reworked along the evolution of the water table. The material was indurated, fractured and enriched in sulfates from processes related to groundwater brine upwelling and tectonic stresses. Later pedogenesis produced the differentiation of the clay sequences in height. The knob field morphology provides additional information to constrain this origin and will be discussed in the next section.

**Table 5.2.b** Evaluation of the different geological processes that could be involved in the formation of the light-toned deposits in Eridania System.

Observed morphology	Possible formation process			
	Lacustrine sediment	Lava flow	Mud volcanism	Pyroclastic deposit
Regional settings	Yes	Maybe	Maybe	Maybe
Extent	Yes	Yes	Maybe	Yes
Elevation settings	Yes	Maybe	Maybe	Maybe
Thickness distribution	Yes	Unlike	Unlike	Yes
High albedo	Yes	Unlike	Unlike	Yes
Texture	Yes	No	No	Yes
Bedding layering	Yes	Maybe	Maybe	Yes
Surficial alignments	No	Yes	Maybe	No
Composition	Yes	Maybe	Yes	Yes
Micro-texture	Maybe	Yes	Maybe	Yes

### 5.2.3 ARIADNES AND CARALIS KNOB FIELDS

Gorgonum, Atlantis, and Caralis were named as chaoses, which is certainly defined as the accumulation of angular mesas and knobs separated by fractures [*Sharp*, 1973]. Chaotic terrains on Mars are commonly found at the heads of Hesperian outflow channels to the east of the Tharsis region and are not so common in this part of the planet. The martian chaoses actually have been interpreted as the result of the subsurface collapse of a confined aquifer, typically associated with a large outflow

channel system [Carr, 1979]. Ariadnes Colles knob field could be linked to Ma'adim Vallis indeed, but the other knob fields in the Eridania System (Figure 5.2.a) are not directly related to any outflow features. Furthermore, the material that comprises these features displays a significant higher albedo than the surroundings and show an enigmatic morphology. Consequently, we consider that the denomination of knob field for this features instead of chaos is more adequate, and it has been used in the most recent articles [Wendt *et al.*, 2013; Adeli *et al.*, 2015; Pajola *et al.*, 2016].

Knob field formation seems to have occurred fast and regionally, triggered at the same time across the sub-basins. The observed concentric ridges in the area also appear regionally, encircling the other sub-basins, and may be indicative of common subsidence events [Baker and Head, 2009]. Interestingly, the observed knob fields have experienced several degrees of incision and erosion, displaying different morphologies (Figure 5.2.d). Since some are quite similar to the knobs found in Ariadnes (e.g., Figure 5.2.d-A and D), some others are much different. For example, in Figure 5.2.d-B and E) the relief seems inverted (as a flat light-toned surface divided by lifted dark crests) but otherwise have a similar pattern. This can show either an early stage of knob field evolution or a later modification. In other sub-basins, as in Gorgonum (e.g., Figure 5.2.d-C and G), knobs look rounder and are apparently not affected by some surficial faults and impacts. In Figure 5.2.d-C, the crater appears filled with a knob field with similar morphologies than the surroundings, which are covered by the crater ejecta blanket. That implies that the mound formation predated the impact but were not affected by it, most likely because a water table present at the time could have absorbed the impact.

Several genetic hypotheses were proposed for the features found at the bottom of the Eridania sub-basins [Howard and Moore, 2004; Baker and Head, 2009; Wendt *et al.*, 2013; Adeli *et al.*, 2015; Pajola *et al.*, 2016], although there is not an explanation that meets all the observation in a suitable way. Based on our work we would constraint the most likely formation mechanisms associated with the chaotic terrain [Hiesinger and Head, 2000] within Eridania, with particular attention to the Ariadnes and Caralis knob fields (Table 5.2.c).

Polygonal terrains with similar dimensions to Ariadnes knob fields was described on Mars caused by regional tectonic activity [Pechmann, 1980]. As it was analyzed in Part 3.5.2, the knobs show an NS trend similar to the preferred direction of the ridges (Figure 3.2.i). Since the buried topography may influence the superimposed sediments [Cooke *et al.*, 2011], if a tectonic process (as lower-crustal flow, Part 5.2.1) formed the Eridania depressions, a cracked surface would be overprinted by a later deposited layer of sediments (Part 5.2.2). The same applies to other basin formation mechanism that would yield to a polygonal pattern. Alternatively, cooling of lava flows may produce polygons as the response to tension [Hiesinger and Head, 2000], and as it was mentioned in the previous section, flood lavas may show platy-ridged morphology [Keszthelyi *et al.*, 2000, 2004].

Moreover, the aquifer genetic model hypothesizes a chaos to be formed when the cryosphere that confines an aquifer cracks by a build-up of pore spaces pressure, releasing the groundwater catastrophically [Carr, 1979; Meresse *et al.*, 2008]. This discharge carves an outflow channel and causes the collapse of the surrounding terrain. The breakup pattern observable in the fields suggests that such a collapse may have occurred, causing fractures and loss of lithostatic support, and further weathering would shape the current features [Carr, 1979]. The recharge zone of Tharsis rise [Russell and Head, 2007] might have caused enough pressure for sustaining a knob-forming process and build up pressure of hydraulic head due to multiple charge/discharge events [Andrews-Hanna, 2014]. The cracking of the confining permafrost could also be triggered by an impact, volcanism or tectonic stresses. The Sirenum Fossae is much younger than the knob formations [Anderson and Dohm, 2011b; Kneissl *et al.*, 2015], but other tectonic influences as the related to the lower-crustal flow are within reason.

Another possible theory is a volcanic heating that would release water from hydrated minerals either from the surface or the subsurface [Miller, 2003; Montgomery and Gillespie, 2005; Kargel *et al.*, 2007]. The emplacement of AHrp volcanic material (Subpart 3.2.2iv) may have triggered the catastrophic release of fluids (releasing up to 75 % of their water content) when the lake was already dry in



anomalously weak porous zones [Montgomery and Gillespie, 2005]. That would cause the subsequent surface disruption that would form chaotic terrains at the same stratigraphic interval across all the sub-basins. The subsidence may be due to crustal cooling and volume reduction, where the loading was produced by *AHrp* materials deposition, or both [Watters, 1993]. The presence of limited dehydrated mineral phases in Ariadnes (e.g., sulfates and less-hydrated smectites, Part 3.4.1) supports this interpretation.

There is another possibility that considers a sediment layer was covering a preexisting ice sheet. That would increase pressure and temperature until reaching the melting point of the ice [Zegers *et al.*, 2010]. The continuous melting would cause a collapse, forcing high-pressure expulsion of the confined waters. This model is uniquely optimal in a drying paleolake that would provide the required ice lens [de Pablo and Fairén, 2004]. Due to the similarities in the area, depth and, of course, climate owing to their proximity, they might have dried simultaneously forming the knob fields at a close time range. The melting of the ice sheet or destabilization of the aquifer could also be produced by the intrusion of a volcanic dike and a concordant intrusive sheet system below the surface [Golder, 2013].

Related to the previous hypothesis, it may be that the groups of light-toned mounds are ice-wedge polygon fields [French, 2013; Hargitai and Soare, 2014]. Wedges formed by thermal contraction fissures are enlarged by ice thaw-freeze cycles. Those wedges expansion lead to consolidated networks of polygons. Ice-wedged polygons usually have a dozen of meters in diameter, but larger than 100 m have been observed in Eastern Siberia [Hargitai and Soare, 2014] and landforms often show greater magnitudes on Mars. When active and mature (Figure 5.2.f-A), the polygons are low in the center showing high rims at the margins, as the observed in Figure 5.2.d-E; but degraded polygons (Figure 5.2.f-B) have a distinctively high-centered appearance owing to deflation [Black, 1976; Mackay, 1999], similar to the Ariadnes mounds.



**Figure 5.2.f** Ice-wedge polygon fields in Northern Alaska displaying (A) an active state with raised margins, and (B) a degraded state with elevated centers [Source: *Permafrost Laboratory of the University of Alaska Fairbanks*].

Additionally, seasonal subsurface temperature variations (quite severe in the area for current conditions, Part 3.5.1) can produce thermal contraction polygons owing to horizontal stress in ice-rich permafrost on Mars [e.g., *Mellon, 1997*]. Those patterns, however, are much smaller than Ariadnes knob field (10 – 100 m), but could explain the small-scale crack pattern in the top of the knobs.

Any of the previous mechanism would be also influenced by further surficial deflation (i.e., abrasion by wind transported loose material) and erosion of the materials, shaping them to their current appearance. Dry lake beds and floodplains like the ones hypothesized in Eridania System are a suitable source of particles for deflation, and the possible analogous friable deposits known as central mounds were also hypothesized to be shaped by the same agent [*Kite et al., 2013; Bennett and Bell III, 2016*]. This also could be also an alternative hypothesis for the breakup a continuous deposit into a jumbled mesa field with troughs separating the knobs [*Wendt et al., 2013*].

To recap; there is not enough evidence to know which of the described methods caused the Ariadnes and Caralis knob fields formation. The existence of similar knobs along the Eridania System at higher elevations suggests localized subsidence ([Figure 5.2.a](#)). The knob fields do not seem to be interconnected but are always enclosed to a depression suggesting that the paleolake has already retreated to the individual sub-basins. By then, any water activity would be restricted to each isolated depression,

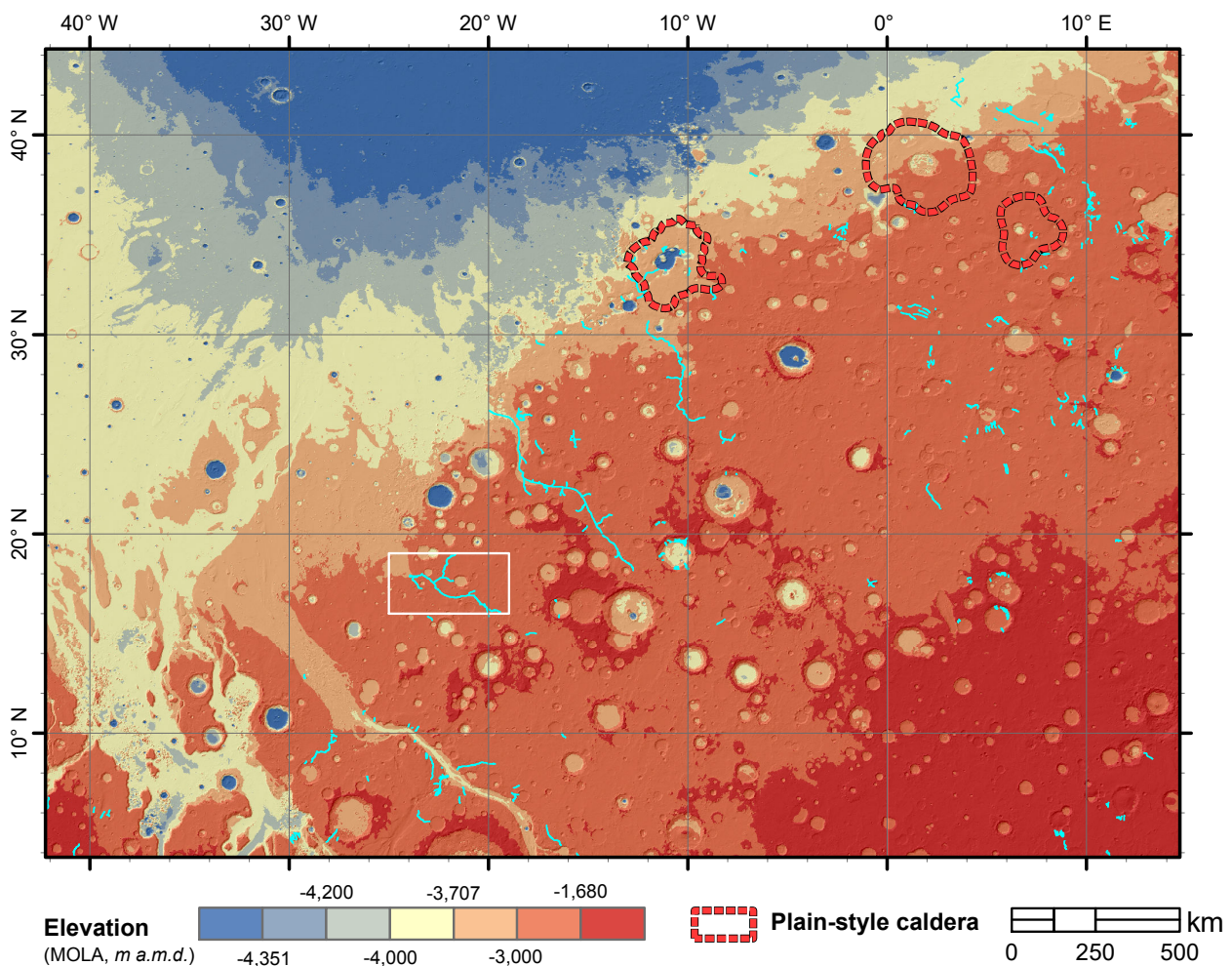
and the water would be lost by percolation to the aquifer or direct evaporation (favored by dewatering of minerals). Also, volcanic activity seems confined to the Eridania System interior without an apparent external source area, that together with compressional ridge pattern that is concentric to the knob fields, indicate that they may have formed from direct extrusion into the basins. In addition, the knob shapes seem intimately related to tectonics, with a broke characteristic pattern. Thus, we favor a process which involves either volcanic and/or water release related collapse, which breakup process is influenced by flaws in the sediment layer mediated by tectonic stresses operating in the region (Table 5.2.c).

**Table 5.2.c** Possible origins of Ariadnes and Carolis knob fields a based on the observed morphologic characteristics.

<b>Observed morphology</b>	<b>Possible process</b>						
	Tectonic stresses	Platy-ridge lava	Aquifer release	Volcanic heating	Buried ice sheet	Ice wedges	Thermal stresses
<b>Regional settings</b>	Yes	Maybe	Yes	Maybe	Maybe	Maybe	Yes
<b>Polygon size</b>	Yes	No	Yes	Yes	Maybe	Unlike	Unlike
<b>Thickness</b>	Yes	No	Yes	Yes	Yes	Unlike	Unlike
<b>Polygon shape</b>	Yes	Maybe	Yes	Yes	Yes	Yes	Yes

### 5.2.4 WESTERN ARABIA TERRA

The Arabia Terra region comprises the northernmost portion of the martian highlands and one of the oldest terrains on the planet. As it was introduced in Part 4.1.1, this region is also the most gradual transition between the both sides of the Mars' dichotomy, with a regional slope of around  $0.06^\circ$  in the western sector (about 3 km in elevation over 3,000 km; [Figure 5.2.g](#)). It remains unclear if the region is part of the northern plains basement that was uplifted [[Zuber, 2001](#)] or the southern highlands that were extensively denuded by through fluvial activity fed by rainwater [[Hynek and Phillips, 2001](#)].

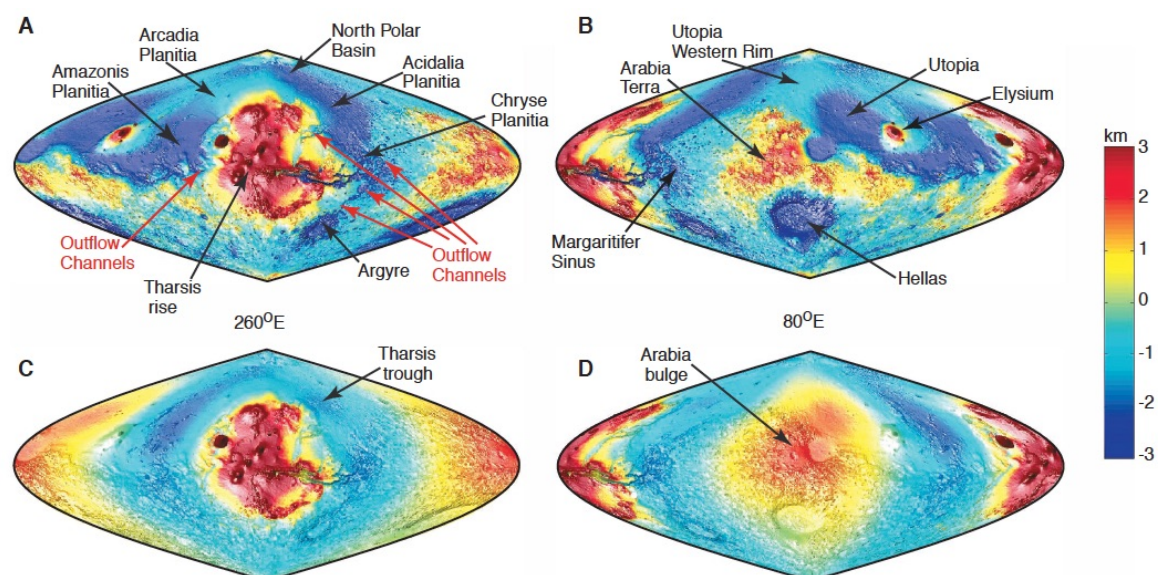


**Figure 5.2.g** Reclassified elevation of Western Arabia Terra region showing the mean elevation of some of the hypothesized paleoshorelines [[Head et al., 1999](#); [Webb, 2004](#)]. The -3,000 m a.m.d. contour line is very approximate to the Arabia shoreline height in the region. The red dash outlined polygons to the NE indicate the possible plain-style caldera found in the region [[Michalski and Bleacher, 2013](#)] and in light blue the channels of [[Hynek et al., 2010](#)]. The white square displays the Coogoon study area (Chapter 4).



Alternatively, it has been hypothesized that the full region could be a water-filled basin created by a 3.95 Ga old massive impact [Dohm *et al.*, 2007]. On the other hand, it could be the Borealis basin outer ring, a hypothetical impact that may have formed the dichotomy itself [Andrews-Hanna *et al.*, 2008]. Certainly, there were found many Quasi-Circular Depressions (QCD) formed about 4 Ga by large impacts in the Chryse Planitia basin [Frey, 2006] to the west of the study area (Figure 5.2.h-A).

The dichotomy origin remains unclear today, but it has been dated around 4.13 Ga, between the pre-Noachian and Early Noachian ages [Frey, 2006]. The Tharsis load must have existed shortly before that, in the Late Noachian, and its loading antipodal compensation response was found to the east of Arabia Terra and named as the Arabia bulge [Phillips *et al.*, 2001]. That crustal thickening is supported by a large long-wavelength gravity field anomaly detected from the Mars Global Surveyor spacecraft data [Smith *et al.*, 1999b]. This rise together with a systematic variation of crustal thickness with latitude [Smith *et al.*, 1999a], which formation is also dated earliest in Martian history [Phillips *et al.*, 2001], suggest that the topographic gradient was already present at the time when most of the fluvial features found in the region formed, including the Coogoon channel.

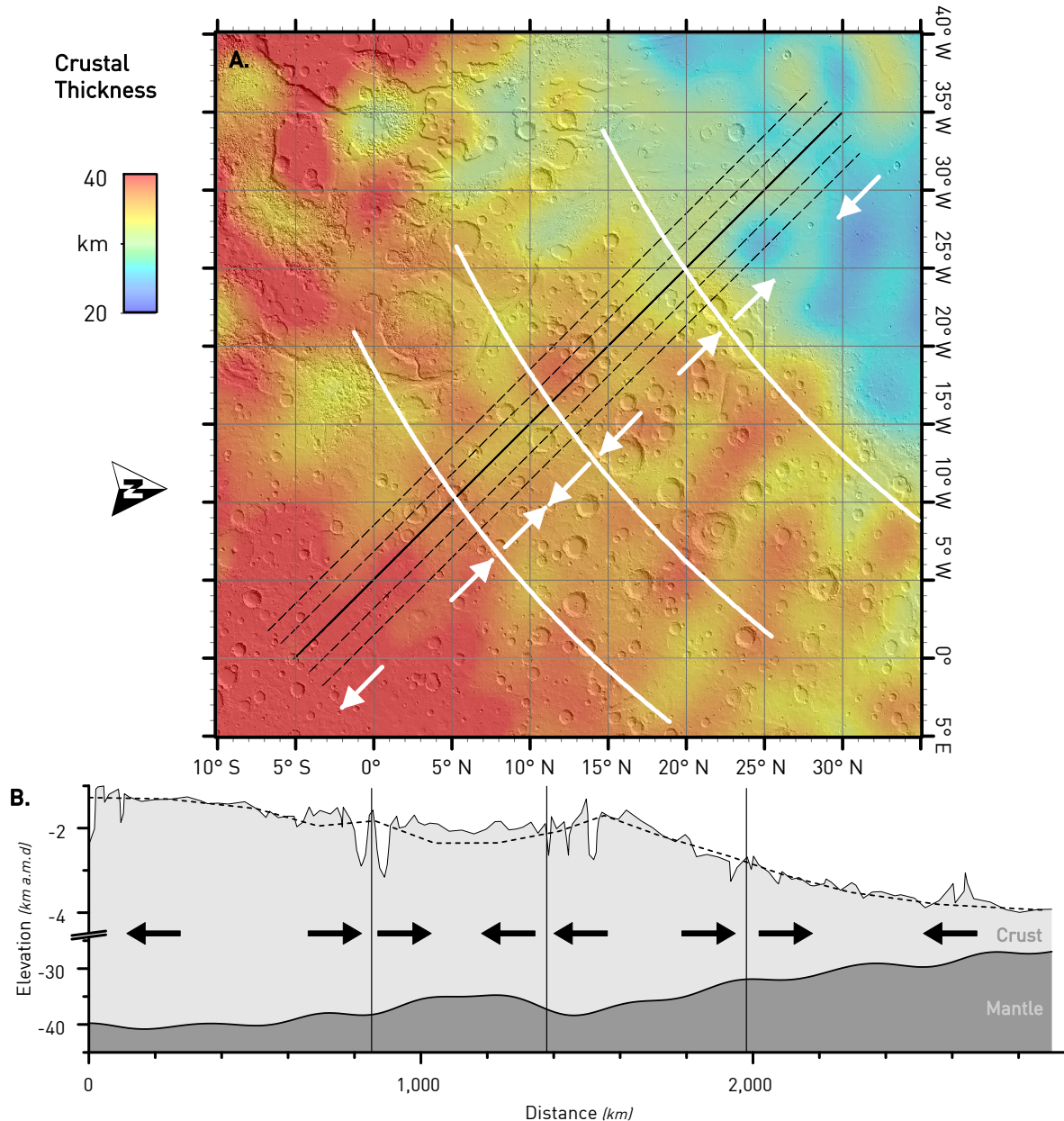


**Figure 5.2.h** Observed topography for (A) the Tharsis and (B) anti-Tharsis hemispheres compared with the modeled topography for the same hemispheres (C and D, respectively), all of them overlapping a shaded relief. [Source: Phillips *et al.*, 2001]

The surface deformation explains quite well the observed valley network orientations in the region, pointing to a formation after they were in place [Phillips *et al.*, 2001]. However, the differences in crustal thickness probably induced to extensional surface stresses caused by the lateral flow of lower crustal material [Nimmo, 2005]. When lower crustal flow occurs, it modifies drainage patterns by local changes in slope. We observed some topographic distortion on the Coogoon main channel, but the large impacts in its termination and middle course prevent to evaluate of the main causes that were involved in the channel morphology (see Part 4.2.3). As in the Eridania System (Part 5.2.1), we found that the topography and crustal thickness pattern in the profiles parallel to Coogoon Valles and across Western Arabia Terra (Figure 5.2.i) are consistent with the expected compressional and extensional regions caused in a moderate lower-crustal flow scenario [Nimmo, 2005].

Another unusual characteristic of Arabia Terra is its low valley network density (Figure 5.2.g). Fluvial morphologies are very common in the southern highlands, but they are truncated upon entering in the region. It is possible that more fluvial morphologies have formed in the region but have been buried and eroded, or they did not form here at all. A recent study claims that Arabia Terra shows evidence for extensive networks of inverted fluvial channels [Davis *et al.*, 2016], and we found buried fluvial landforms in our study area. The region has a heavily degraded landscape with many high-standing mesas (Subpart 4.2.3iii) compared to the smooth, lightly cratered, and topographically lower adjacent lowlands (Subpart 4.2.2iv). Those landforms are consistent with a large glacial, fluvial, aeolian, or atmospheric deposition followed by a subsequent period of considerable erosion. In this way, Arabia Terra could have been evenly blanketed by deposit, similar to the Electris deposits in the Eridania region (see Subpart 3.2.2iii). It is not clear whether these deposits consist of a widely deposited unit or several different deposits emplaced at different times by various processes [Tanaka, 2000]. To the west of Arabia Terra, they form mesas and outcrops with even and continuous layering. The airborne particles that covered the region in a large deposit could have been a cemented mixture of dust and ice, pyroclastic tuff [Moore, 1990], or even paleopolar deposits [Schultz and Lutz, 1988]. The origin of this material is unknown, despite the fact that that most

observations favor a pyroclastic origin for the mantling deposit, which are able to cover a large area evenly [Moore, 1990; Michalski and Bleacher, 2013]. Those tuffs may come from a close volcano, including Olympus, Ascræus, Pavonis and Arsia Montes, Alba Mons, and Syrtis Major, but none of those are considered a convincing volcanic source [Kerber *et al.*, 2012]. The absence of a nearby clear source may suggest that these deposits could have an alternative origin, but the recently hypothesized supervolcanoes [Michalski and Bleacher, 2013] may solve this discrepancy.



**Figure 5.2.i** (A) Regional map of crustal thickness [Zuber *et al.*, 2000]. (B) Surface topography (average as dotted lines and Coogoon cross-cutting section as a straight line) and crustal profile (not at the same vertical scale). Arrows denote approximate locations of compressional and extensional regions.

The regional extension combined with the thermal erosion of the lower part of the crust caused an anomalously thin crust favor the ascent of magma and promoting eruption [Michalski and Bleacher, 2013]. The volcanic edifices proposed in that work are indeed close to Coogoon Valles area (Figure 5.2.g). In addition, the presence of collapse features with low topographic relief in the area (the intriguing topographic depressions in Subpart 4.2.3ii) and their association with plains-style lavas (the multiple dark capping units found in the area) and friable layered deposits matches well with the plain-style caldera complexes in that work.

Regardless of their origin (further discussed in the next Part 5.2.5), the unconformable layered deposits were eroded and relocated. The eroded materials by fluvial activity were likely not redeposited in the surroundings, but have been washed out to cover the northern plains [Hynek and Phillips, 2001], flowing towards those water bodies occurring downslope. The existence of a martian ocean is broadly accepted [e.g., Fairén et al., 2003b; Webb, 2004], but the timing of its emplacement is poorly understood. Several possible shorelines have been mapped representing multiple flooding events or distinct high-standing bodies of water that has been interpreted as different contacts of at least two flooding episodes separated on time [Webb, 2004; and references therein]. The martian oceanic shorelines vary in elevation by hundreds of meters (Figure 5.2.g), as the so-called Arabia shoreline that ranges from about -1 to -4 km. Multiple processes may have produced the observed long-wavelength deformation in the shorelines, from the isostasy compensation after the water removal [Webb, 2004] to the true polar wander [Perron et al., 2007], which is the reorientation of the planet relative to its rotation pole. In addition, the lateral crustal flow may have altered their original shape and elevation in the region. In any case, it is broadly accepted that water episodically covered the northern plains, which was most extensive during the Late Noachian and Late Hesperian [Head et al., 1999; Fairén et al., 2003b].

A recent study compares the crater morphologies and distribution in Arabia Terra with the southern highlands and northern lowlands [Brugman et al., 2015], using the crater database of Robbins and Hynek [2012] and the QCD in Frey et al.



[2002]. The results support that Arabia Terra is a modified part of the southern highlands. The crater cumulative size-frequency distribution (see Subpart 2.2.4ii) is nearly identical to that of the southern highlands but with a lower spatial density [Brugman *et al.*, 2015]. The analysis of the obtained curves provided a young age (3.75 Ga) and similar crater population for Arabia Terra, with also similar rim-floor depths to the southern highlands. Those results are consistent with a denudation process [Hynek and Phillips, 2001], but it should have ended early (3.90 – 3.70 Ga) and the eroded material should have been deposited in the northern plains [Brugman *et al.*, 2015].

Therefore, West Arabia Terra is likely an ancient part of the southern highlands (Table 5.2.d). The region is certainly a transitional area, being on the border of many global processes that take place during the early history of Mars. The terrain was affected by the unknown process that formed the dichotomy, but also by the Arabia bulge raise to the east, and the possible Borealis oceans to the west (that may even cover the study area in one of their highest levels). That intermediate position stressed the surface tectonically, in compensation to the crustal thickness differences and the changes in the water load after ocean level fluctuations, which ultimately favored the volcanic activity. Volcanic materials may have covered this area, but the topographic slope (produced early in its history), always favored the transport over the deposition, washing those materials to the next and depressed Northern lowlands and shaping Arabia Terra to its current characteristic denuded surface.

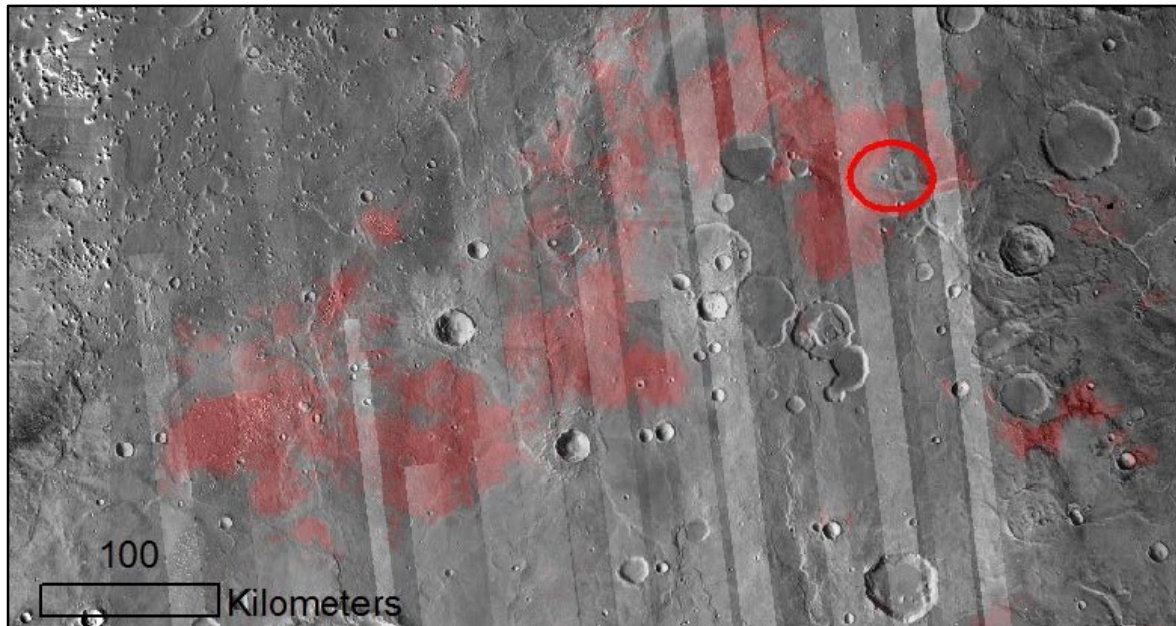
**Table 5.2.d** Hypotheses on the possible origin of the Western Arabia Terra terrains based on the observed characteristics.

Observed morphology	Possible origin hypotheses			
	Uplifted northern plains	Eroded southern highlands	Ancient crater basin	Borealis basin outer ring
Regional settings	Yes	Yes	Maybe	Yes
Extent	Yes	Yes	Maybe	Maybe
Elevation settings	Yes	Yes	Maybe	Maybe
Crustal thickness	No	Yes	Maybe	No
Fluvial landforms	Maybe	Yes	No	Yes
Crater distribution	No	Yes	Maybe	No
Crater shape	Maybe	Maybe	No	Maybe

### 5.2.5 COOGOON PHYLLOSILICATE-BEARING DEPOSITS

We observed unconformable light-toned layered materials outcrops forming mounds and covered with a dark thin capping material in the area of Coogoon, with certain similarities to the Eridania knob fields materials (Part 5.2.2). Thus, a similar analysis on the possible formation processes is relevant here. Those occurrences outcrop in the denuded terminus of Coogoon Valles, flanking the channel morphologies (mapped as the *INcd* unit, see Subpart 4.2.2ii). There is even a similar material to the Electris deposits in the area, as mesas of bright friable deposits mantling most of the study extension (*INtt* unit, Subpart 4.2.2iii). An extensive phyllosilicate signal was described over Oxia Planum as well (unit *IHp*, Subpart 4.2.2iv; [Figure 5.2.j](#)); and although the channel deposits (*NAcd1* and *NAcd2*) do not have hyperspectral coverage, the hi-resolution images ([Figure 4.2.g](#)) reveal that these materials show similar polygonal textures, locally covered with dark capping layers. Those patterns together with the thermal inertia results (Part 4.4.2) suggest that those outcrops may correspond to phyllosilicate-bearing deposits.

Phyllosilicates are abundant in the Coogoon study area and the entire Arabia Terra region, considering Mawrth Vallis as the largest exposure of this kind of mineralogy on Mars [e.g., *Noe Dobrea et al.*, 2010]. The sequence there ranges from 150 to 300 m thick and shows a vertical stratigraphic profile composed of Al-rich phyllosilicates overlying Fe/Mg-phyllosilicates and silica, what favors a post-deposition weathering like in-situ leaching of basaltic rock [e.g., *Loizeau et al.*, 2010; *Noe Dobrea et al.*, 2010; *Carter et al.*, 2015], as has been previously discussed in this thesis dissertation (Part 5.2.2). For such wide profile as found in Mawrth, the alteration may have occurred in syndeposition, i.e. simultaneously with the materials deposition [*Loizeau et al.*, 2010]. The fact that a similar sedimentation sequence matches the observations for the *INcd* materials (see Part 4.4.1) points to a possible genetic relationship. That possibility implies a formation condition with enough water availability to produce the leaching. Again, hydrochemical changes or climatic changes are also a possible explanation for that stratigraphy [*Fernández-Remolar et al.*, 2011].



**Figure 5.2.j** Mg/Fe phyllosilicate detections (**red colors**) to the west of Coogoon study area, obtained with 3.2  $\mu\text{m}$  band from OMEGA and CRISM MultiSpectral Polar (MSP) images, overlapping a THEMIS daytime IR mosaic. The red outlined circle points to the delta-like structure in the outlet of Coogoon Valles. [Source: Westall *et al.*, 2014].

The observed deposit diversity in the Coogoon Valles and the nearby Mawrth Vallis [Loizeau *et al.*, 2015] point to several distinct environments occurring along their history. The sedimentary and geomorphic framework supports a long-lasting history of hydrological activity that either may have formed or later remobilized the sediment to the different occurrences found in the area. The MLE craters are proposed as indicators of the existence of liquid reservoirs [Barlow and Bradley, 1990], or volatile-rich substrates, and as a consequence of an impact affecting multiple layers of ice or a subsurface layer saturated with water [Barlow and Perez, 2003]. Also, Arabia Terra is one of the few Noachian exposed surfaces which sustained the existence of a long-lived aquifer on the planet [Andrews-Hanna *et al.*, 2010]. In this context, Mars Odyssey's Gamma-Ray Spectrometer data that have provided a high enrichment in hydrogen in the region [Boynton *et al.*, 2004], which ultimately indicates near-surface water abundance. Those facts, together with the possibility of an ancient ocean covering (or adjacent to) Coogoon and the multiple reactivation events observed in the fluvial network, entail sustained water activity along the geologic history of the area.

Therefore, it is possible that at least some of the layered deposits found in the Coogoon area come from fluvio-lacustrine sedimentation. We already introduced two hypotheses that provide a compatible environment for this type of deposition in Part 5.2.4: The full region could have been a water-filled basin [Dohm *et al.*, 2007], or an ancient ocean may have covered the area. However, we have discarded both as very reliable hypotheses already (Table 5.2.d). The phyllosilicate-bearing *INcd* unit is the result of aqueous weathering, sedimentary and/or volcanic processes occurring during the Noachian. The geological settings do not allow to estimate either the extension nor the thickness of the *INcd* deposits, which seems to be the older and a primary deposit of clays in the area. What we do know is that the layering deposits are at least 200 m-in-thick and their formation must be prior the early Hesperian. It is possible then that the outcropped clays are seafloor sediments, although few shreds of evidence are pointing to such a high level of Borealis ocean for a substantial time.

Besides kaolinite, we spotted from the analysis of the spectrometric data of Coogoon another Al-bearing smectite as montmorillonite (Part 4.4.1). The most common origin of montmorillonites is the in-situ alteration of volcanic ash or tuff deposits in alkaline conditions with low drainage [Clark *et al.*, 2007]. The composition, therefore, enforces the possibility that the sediments have a volcanic origin. Besides, the regular layering of fine materials and the narrow forward scattering behavior at Mawrth Vallis [Fernando *et al.*, 2016] suggest a calm environment where the sediment deposition take place under after a great transportation, which is in contradiction with it has been reported for Eridania deposits (Part 5.2.2). According to Fernando *et al.* [2016], wind and water driven transportation lead to the homogenous medium of less textured grains consequent to the observed backward scattering behavior. This fact, again, points to lithified airborne tuffs, that also fits well with the distribution and observed characteristics of the *INtt* material.

We interpret the several ridges in *INtt* surface as blind thrust faults (Subpart 4.2.3i). Although these landforms could be the result of several different types of processes, they are typically observed in Early Hesperian and interpreted as low-



viscosity lava flows [Scott and Tanaka, 1986]. However, we cannot discard other possibilities as the region stress compensation derived from under crustal flow may have promoted the formation of the crest set system in the area. As a result, this regional event records the planetary cooling process, which was accompanied by active faulting [Watters, 1993]. Either they are weathered lavas or lithified aeolian deposits, their diagenesis into the observed sediments in surface or near-surface conditions would have required sustained water activity. A possible scenario could be the deposition of tuffs sourced from the nearby volcanic edifices (see Part 5.2.4) that may have deposited in an open water table. The fact that Arabia Terra is one of the few locations where groundwater upwelling may occur on Mars [Fassett and Head, 2008] reinforces this hypothesis.

The deposits may have resulted from the underground chemical weathering, and ancient volcanic material may have altered by groundwater or even hydrothermal fluids. Variations in the groundwater system, fluvial activity, and direct surface evaporation could have caused the observed bed layering. We favor an aeolian deposition over lava (or mud) flows, considering the deposit extension and thickness. The continuity and similarities between *INcd* and *INtt* materials together with the lack of phyllosilicate-bearing signal and polygonal texture on the latter, allow us to hypothesize that both were airborne deposits from the same source and only *INcd* material was altered enough for clays to be formed. That possibility is enforced by the proximity to open water (Oceanus Borealis could be to the NW, Figure 5.2.g) and the uncertain origin depressions, that may indicate the existence of a hotspot in the area that could have induced geothermal activity. If the clays diagenesis took place underground, the phyllosilicate-bearing layer (*INcd*) may extend below the *INtt* unit materials (see Figure 4.6.a).

The flowing landforms in the *NACd* unit suggest that they result from the remobilization of the *INcd* materials, deposited in the topographically lower areas of the Coogoon channel along different episodes of geological reactivation. It is also possible that *NACd* are lava flows that ended in those depressed areas and were later altered into clays, but their Amazonian estimated age (Figure 4.6.b) is not consistent

with that interpretation. However, our analyses support that they were buried and later exhumed (see Part 5.2.6), enabling a later underground diagenesis of those possible lavas. In this context, the Coogoon outflow channel carved, transported, and deposited the phyllosilicate-rich materials along the channel to the northwest. The denudation process deposited a large amount of material to the lowlands, in Oxia Planum, which was the base for forming the surface of the *IHlp* unit. That analysis is supported by the large phyllosilicate signal along this flat and relatively young unit (Figure 5.2.j), which seems to be partially formed by the amalgamation of several alluvial fan/delta deposits. In this case, the clays are most likely not formed in situ, i.e. the *IHlp* would be clay secondary deposits.

So according to our observations, the phyllosilicate-bearing light-toned layered materials in the Coogoon study area are probably formed from airborne transported volcanic tuffs (or ashes) that covered an extensive area during the late Noachian. Part of those aeolian deposits was cemented and altered into clays from interaction with water. That interaction could have happened near the surface, but most likely underground combined with hydrothermal activity. The long-lasting water activity in the area remobilized the clays and emplaced them in different types of deposits along the valley network. The resulting denudation process also unburied some of those underground deposits, transporting large amounts of material to the lowlands.

**Table 5.2.e** Potential origins of the *INcd* phyllosilicate-bearing deposits in Coogoon Valles area.

Observed characteristics	Possible emplacement process			
	Lacustrine/fluvial sediment	Lava flow	Mud volcanism	Pyroclastic dep. + groundwater
Regional settings	Maybe	Maybe	Maybe	Yes
Extent	Maybe	No	No	Yes
Elevation settings	Maybe	Maybe	Maybe	Yes
Thickness distribution	Maybe	Unlike	Unlike	Yes
High albedo	Yes	Maybe	No	Yes
Texture	Yes	No	Maybe	Yes
Stratigraphy	Maybe	Unlike	No	Yes
Synposition	Yes	Unlike	Maybe	Maybe
Composition	Maybe	Maybe	Maybe	Yes

### 5.2.6 COOGOON MAIN CHANNEL

Coogoon Valles has characteristics of both outflow channels and valley networks, similar to Mawrth Vallis [Carr, 1996]. The main and older channel in Coogoon, at its center (Subpart 4.2.3iii), displays a broadening morphology that resembles the Martian outflow channels ending at the northern lowlands (e.g., Ares Vallis) [Rodriguez et al., 2015; and references therein]. This section is more than 100 km long, experiences notable changes in width (~4 – 12 km) and shows several similarities with Mawrth Vallis, carving both Noachian materials unlike most of the outflow channels (as Ares) that were dated as Hesperian [Carr and Head, 2010]. The outflow channels occur mainly in the young surfaces in the northern lowlands, while the valley networks occur throughout the older heavily cratered terrains of the Noachian and Hesperian periods. Here we study the different characteristics of this intriguing section of Coogoon Valles and how they fit the various channel types found on Mars.

The central Coogoon Valles carves the *INcd* and *INtt* units materials (Figure 4.2.a) that are also locally found as relict relief ‘islands’ inside the channel and that are later covered by younger fluvial deposits of the *NACd* unit. The fluvial pattern suggests that these ‘islands’ may form local anabranches dividing the main stream section, typical from catastrophic outflow channels. The age determination of the outer channel materials and the fluvial infillings in central Coogoon suggests that the ~3.6 Ga Noachian unit (*INcd*) was affected by one or several ~2.4 Ga fluvial events that also meet the age estimated for the *NACd<sub>1</sub>* surface (Subchapter 4.3). The channel shows evidence of reactivation, however, such as the possible terracing levels on the channel banks, and ~2.4 Ga may correspond to the end of the denudation process that also exhumed the *INcd* materials providing a scenario where *NACd<sub>1</sub>* materials can be much older. A second fluvial event was associated with the deposition (or redeposition) of the *NACd<sub>2</sub>* unit that may occur at approximately  $1.4 \pm 0.2$  Ga, followed by a late resurfacing episode (~700 Ma). This last resurfacing age becomes evident all around the Coogoon Valles area in crater size-frequency distributions (Figure 4.3.d) and agrees with a major inundation episode in the northern plains [Rodriguez et al., 2015].

The evolution of Coogoon channel system consisted of a complex sequence of geological events, and a younger network overlaps the original channel, with narrower channels that postdate and modify the main central section. This network is formed by channels ending in steep theater headwalls, with almost constant widths, low drainage density, flat-floored, and lacking in tributaries, which are interpreted to be produced by groundwater sapping [Sharp and Malin, 1975; Harrison and Grimm, 2005]. Although, those characteristics must be interpreted with caution, as erosion may have destroyed the small headwater tributaries. In addition, theater-headed valleys can also be created in layered materials, and *INtt* shows a clear layering. The presence of a regional aquifer, supports also this interpretation [Lamb *et al.*, 2006; Luo and Howard, 2008], which is also compatible with the *INcd* formation process (Part 5.2.5).

Arabia Terra is one of the few areas on Mars where groundwater is predicted to reach the surface [Andrews-Hanna *et al.*, 2008] and the channels may be fed by groundwater and/or snow melting during the Hesperian-Amazonian. Because this mechanism of valley formation would not require warm conditions, coming from snow/ice melting, the sapping channels may have operated during the Hesperian to Amazonian periods, which is in agreement with our age determinations (Subchapter 4.3). However, the extensive denudation that occurred regionally obscures the exact nature of these other (or series of) fluvial events.

The relation of the fluvial structure with the N-trending ridges (Subpart 4.2.3i) of regional extent in Arabia Terra provides another temporal marker to constrain the relative formation of the Coogoon main channel. The ridges deform the infillings in this section, and because the formation of regional wrinkle ridges in the Martian highlands appears to have globally reached a maximum in the Hesperian [Golombek and Phillips, 2009], it can be inferred that the central section of the channel predates the deformation structures. In addition, because the channel structures in the eastern Coogoon Valles postdated the ridges, the central part of Coogoon Valles obviously predates the channel activity in the eastern area of Coogoon.



The deposits that filled the main channel display a zoned arrangement showing a variation in appearance and texture from the center to the margins of the channel. This zonation can only be fully recognized in the northwest area of the channel where it is well preserved (Figure 4.2.g). These differences are very clear in TI derived from the THEMIS data (Part 4.4.2). The differences may result from different reasons such as the exposure of rock fragments/bedrock, the presence of duricrust, and the induration of older materials [Ferguson *et al.*, 2006]. In the central part of the channel, the NAc<sub>d</sub> unit postdates the materials preserved as “islands” in the channel (IN<sub>tt</sub> and IN<sub>cd</sub> units). Furthermore, the fact that there is a topographically depression in the area in the center of the channel, instead of having a decreasing altitude towards its terminus reveals that either the channel was buried or deformed downstream or there was an open-basin lake [Fassett and Head, 2008].

The last prevalent denudation episode exposed the materials of both the IN<sub>cd</sub> and NAc<sub>d1</sub> units, which may have been buried during most of the Hesperian. This process was driven by mass wasting and fluvial dissection that affected the highland boundary during the early Hesperian [Hynek and Phillips, 2001] to produce the unit landscape that is defined as IN<sub>tt</sub>. These processes transported and deposited a large amount of material to the lowlands, which was the base for forming the surface of the IH<sub>lp</sub> unit. The presence of inverted craters inside the amphitheater-like valleys indicates that they have been covered and subsequently exhumed by erosive agents operating in Coogoon. The last episode could have been dominated by reworking of plain deposits and spring discharges that were sourced in the northern plains, and both were involved in the fine particles formation or remobilization of the NAc<sub>d2</sub> materials during the Amazonian (Subchapter 4.3).

Our geological mapping shows that one the alluvial fan / delta at the Coogoon termination is emplaced following an ideal line that is prolonged from the main direction of the outflow channel in the central Coogoon Valles (Figure 4.2.a). In addition, the channel and the alluvial fan are both located at the same altitude, which is higher than the rest of the sedimentary structures of Oxia Planum. These observations and the lack of a geographic connection with the younger sapping

channels in the central and western Coogoon Valles suggest that this sedimentary structure was formed before this younger channel system. Consequently, we suggest that the channel of the central Coogoon Valles and the alluvial fan / delta could be genetically related, predating the formation of most of the channel systems and sedimentary structures observed in Oxia Planum. However, the combined effect of late fluvial activity and MLE produced by an impact crater, which eroded and covered the area between the main channel of the central Coogoon Valles and the alluvial fan, make a direct relation between them unclear.

According to our results, Coogoon main channel is either Noachian or early Hesperian. Most outflow channels thought to be Hesperian in age [Kreslavsky and Head, 2002], but some outflow channels could be much younger [Rodriguez *et al.*, 2015] or older [Carr and Head, 2010]. This type of channels are tens of kilometers wide, hundreds of kilometers long, may show an anastomosing pattern, inner 'islands', and rarely have tributaries [Kereszturi and Hargitai, 2014]. Formed by catastrophic floods resulted from the catastrophic release of water from subsurface aquifers by a series of several to hundreds of individual flood events [Andrews-Hanna and Phillips, 2007]. The proposed formation mechanisms include 1) subsurface melting of ground ice by geothermal heat, 2) breach of enclosed basins, 3) dike intrusion or extensional faulting, 4) dewatering of hydrated sediments, 5) dissociation of methane hydrate, 6) high lake breakouts, and 7) snowpack melting around volcanic rises [Kereszturi and Hargitai, 2014; and references therein]. Hence, outflows usually start abruptly, related with different landforms. However, in Coogoon, the original channel lack of an obvious source, similarly to Mawrth, that may be buried. Our guess is that their origin may be related with the Tharsis and Arabia bulge [Phillips *et al.*, 2001], which rise is as old as the estimated for the channel (see Part 1.1.3).

The alternative to outflow channels are the runoff channel, or as they are more recently referred, valley networks [Hargitai and Kereszturi, 2014]. These hierarchical systems of quasi-dendritic depressions on Mars have widths and lengths that range widely and their terminations are associated with sedimentary fans or deltas. The proposed formation mechanisms of the surface runoff are fed by 1) precipitation, 2)

ice melting fed, 3) near-surface melting by subsurface heat, and 4) subsurface aquifers by sapping [Fassett *et al.*, 2014; and references therein]. The latter may show amphitheater-headed canyons, and both U- and V-shaped profiles [Harrison and Grimm, 2005]. So, unlike the outflow channels, valley networks activity produced mostly during the Noachian with an abrupt rather than gradual cessation around the Noachian/Hesperian boundary (see Part 1.1.3). Interestingly, these networks commonly include inlet and outlet valleys of Noachian-aged basins [Fassett and Head, 2008].

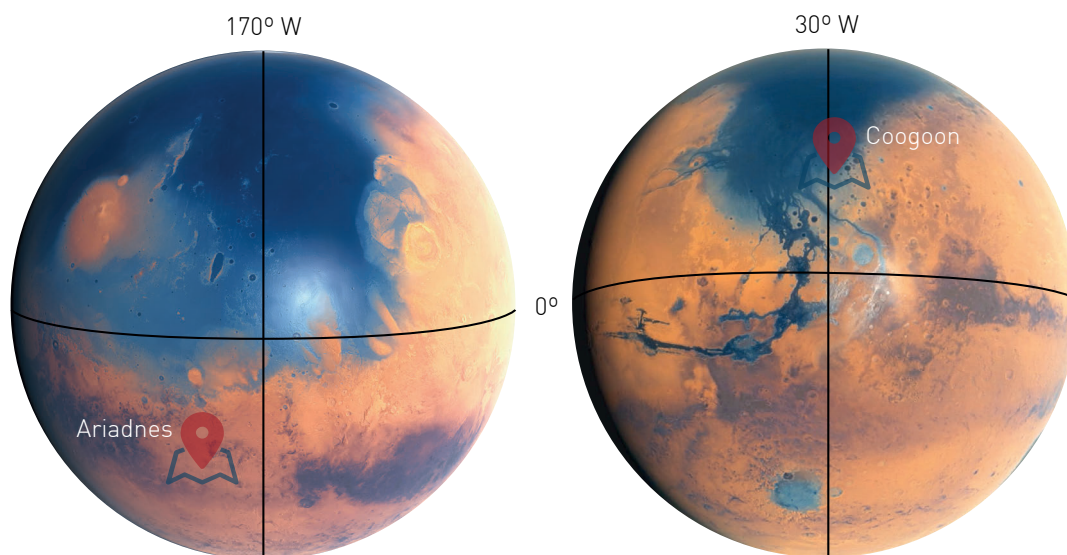
The martian channels undergo modifications by mass wasting, gravity sliding of ice-rich material, impact cratering, dust blanketing, among others processes [Ansan and Mangold, 2006] that veil their original characteristics. Some valleys may be even buried and then later exhumed [e.g., Williams and Edgett, 2005]. Since Coogoon Valles has characteristics of both outflow channels and valley networks, we hypothesized that it was formed in different phases; initially by a series of outflow events, later by surface runoff, and subsequently by headward extending sapping, which reactivated the valleys. Therefore, the primordial Coogoon Valles channel (i.e., the wide channel in the central Coogoon Valles, Subpart 4.2.3iii) should have eroded the Noachian deposits before the Hesperian, based on geomorphological constraints, and followed a similar evolution as the Mawrth Vallis outflow channel [Loizeau *et al.*, 2012]. Consequently, we consider that the central part of Coogoon Valles could be the exposed remain of a late Noachian outflow channel in the western Arabia Terra.

**Table 5.2.f** Comparative of how the observed characteristic in Coogoon main channel (i.e., central section) fits the types of channels on Mars.

Observed characteristics	Possible channel type	
	outflow	runoff
Broad	Yes	Maybe
Stepped walls	Yes	Maybe
Noachian age	Maybe	Yes
Lack of source	Maybe	Maybe
No tributaries	Yes	Maybe
Anastomosing pattern	Yes	No
Delta / fan	Unlike	Maybe

### 5.3 NOACHIAN-HESPERIAN GLOBAL PROCESSES

During the Noachian period (see Part 1.1.3) impact cratering, volcanism, and erosion were vigorous [e.g., *Carr and Head, 2010*]. River valley networks carved the surfaces that were already eroded and altered by water activity in a much wetter environment (**Figure 5.3.a**). The Hesperian period continued with extensive volcanism and erosion, but the valley network formation slowed dramatically (**Figure 1.1.c**). Still, a significant number of catastrophic floods occurred, even forming episodic lakes or seas. This decreasing abundance of stable liquid water over time is tied to a gradual loss of much of the early Noachian atmosphere to space [*Lammer et al., 2013*], restricting the aqueous alteration of materials to more localized surfaces. The planet's interior cooled, and the magnetic field diminished, enabling the input of charged particles from the solar wind. The decrease in global temperatures and atmospheric thickness made liquid water more vulnerable to freezing and evaporation. This change was not only linear in time, the Mars extreme obliquity cycles [*Laskar et al., 2004*] have also existed for all of the planet's history, causing a significant variation in the latitudinal distribution of insolation and the stability of volatiles, as carbon dioxide and water.



**Figure 5.3.a** Ariadnes and Coogoon antipodal locations over an artist's impression which shows how Mars may have looked about 4 Ga ago. Early Mars would have an ocean occupying almost half of Mars's northern hemisphere, and in some regions reaching depths greater than 1.6 km [Source: *ESO/M. Kornmesser/N. Risinger*].



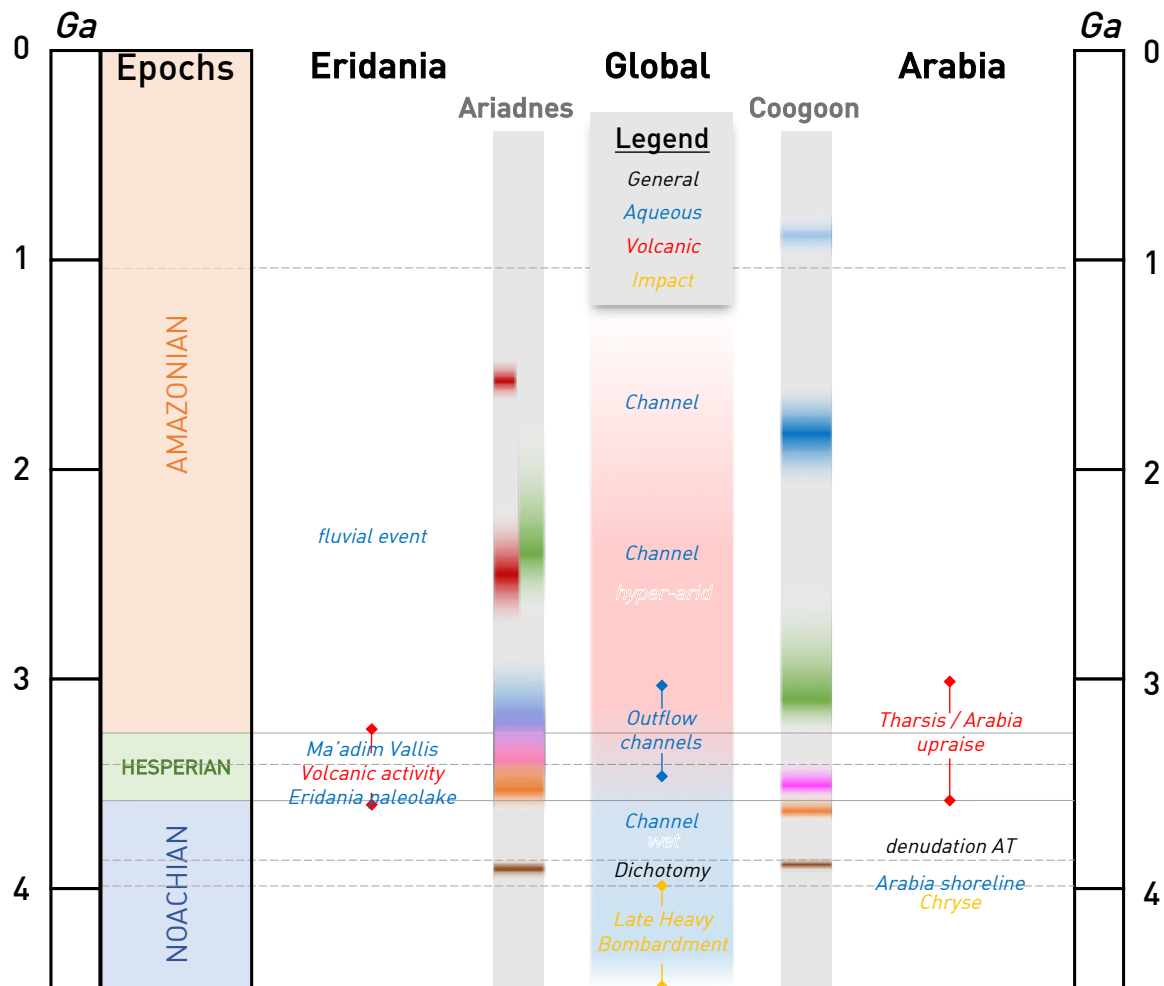
Martian climate and water history, however, is still subject to debate [Jaumann *et al.*, 2014]. The widespread water-related landforms and their associated assemblages of hydrated materials led the researchers to hypothesize that the Martian climate was warmer and wetter during the Noachian times [e.g., Malin and Edgett, 2003; Irwin *et al.*, 2005a; Poulet *et al.*, 2005]. However, alternative studies put this assumption into question showing that the aqueous altered clay minerals do not only form under humid conditions, since groundwater or subsurface hydrothermal processes can lead to similar materials under cold and dry environments [Ehlmann *et al.*, 2011; Fairén *et al.*, 2011; Ehlmann *et al.*, 2013; Fairén *et al.*, 2014]. This alternative scenario supports that the Martian oceans and long-lasting aquifers were likely low in temperature, with only temporary heat coming from volcanic or impact related activity, even during Noachian times. Mineral composition and stratigraphic relationships of phyllosilicates suggest neutral to an alkaline environment and a subarid climate during the Noachian Epoch indeed, but the multiple alteration products found indicate various alteration, erosion and aqueous episodes that provided diversity in water chemistry and environments with at least short-lived liquid water [Jaumann *et al.*, 2014]. The timing of all of these clays and fluvial / lacustrine deposits is similar despite the challenging correlation of sediments: Late-Noachian to Early-Hesperian.

In this research, we used morphological and mineralogical analysis to determine the environment of this sediments deposition and to identify the agents of their exposure (see Subchapter 5.2). The timeline of the main events recorded in both Eridania and Arabia regions and the dates obtained from the different units found in our areas of study are summarized in [Figure 5.3.b](#). Both Ariadnes and Coogoon basement formation age are quite similar (~3.8 Ga), and their topographic settings made them a sink for sediments and fluids during the Noachian-Hesperian boundary [Milliken and Bish, 2010]. Our findings lend support to the claim that in both areas were strongly influenced by volcanic activity in their early history, partially by the dichotomy induced lateral flow of lower crustal material [Nimmo, 2005] and the evolution of the Tharsis (and its Arabia counterpart) rising [Anderson *et al.*, 2001; Phillips *et al.*, 2001]. Those were complex global processes, displaying a multi-stage

behavior during most of the martian history. Our data appears to suggest that Eridania may be a plain-style caldera complex triggered by an impactor (Part 5.2.1) that supports the hypothesis of the Western Arabia Terra supervolcanoes (Part 5.2.4). This substantial volcanic activity leads to the airborne tuffs that covered both areas as thick deposits (orange color in [Figure 5.3.b](#), *eHed* in Ariadnes and *INtt* in Coogoon) as well as enhancing hydrological activity. In Ariadnes, paleolakes formed in interconnected basins [*Kuzmin et al.*, 2000; *Irwin et al.*, 2004a]. Coogoon area held a large aquifer [*Andrews-Hanna et al.*, 2010], which release probably formed an outflow channel flowing to the lowlands (Part 5.2.6).

Clay minerals forms at low temperatures and near-neutral pH on Earth. That could be the case in both of our study areas. We found two clay-rich deposits with close relative formation ages (pink colors in [Figure 5.3.b](#), *HNkf* in Ariadnes and *INcd* in Coogoon) and those very different morphologies but similar composition. The small differences between them, however, are the key to reconstructing their origin. The knob field in Ariadnes and Caralis are likely an indurated and fractured tephra layer, weathered in a close basin during several lacustrine episodes and groundwater brine upwelling. The identification of Fe- and Mg-smectites together with a talc-saponite mixed layering supports they are subaqueous hydrothermal deposits (Part 5.2.2). The Al-rich clays found in the upper strata were the result of a later pedogenesis [*Carter et al.*, 2015], and smectite-sulfate assemblages may come from interstitial brines deposited and accumulated underground [*Zolotov and Mironenko*, 2014]. However, those materials could be also the result of hydrochemical changes over time. Acidic standing bodies of water favor the precipitation of cation depleted clays (Al-clays) [*Fernández-Remolar and Knoll*, 2008; *Baldrige et al.*, 2009] and sulfates [*Ehlmann and Edwards*, 2014]. Unfortunately, these deposits have been extensively modified (Part 5.2.3), which prevents to evaluate the most likely scenario from the available orbital data. We also found Al-smectites in the highest levels of the deposits in Coogoon, but one of them that has montmorillonite, may have been formed from the in situ alkaline alteration of volcanic deposits under low flowing regimen [*Clark et al.*, 2007]. According to our findings, these deposits were also cemented and altered airfall volcanic deposits, but the clay formation takes place

most likely underground combined with hydrothermal activity (Part 5.2.5). The phyllosilicates in Coogoon were also subsequently buried and degraded, but still West Arabia Terra is still one of the largest outcrops in the planet [Loizeau *et al.*, 2015; Thomas *et al.*, 2017; and references therein].



**Figure 5.3.b** Timeline of the main geological events identified globally on Mars (center) and Eridania and Arabia regions (both sides). The end of formation date range for the different units defined in the studied areas (Ariadnes and Coogoon) is also displayed. Horizontal lines show the epoch (straight) and periods (stripped) boundaries.

The apparently parallel geologic evolution in Ariadnes and Coogoon diverges from this point (Figure 5.3.b). The Eridania water-rich activity seems to stop after the deposition of lavas (probably fissural) filling the system of basins, in a volcanic event that might be intimately related to the water release, which likely caused the chaos pattern visible today (Part 5.2.3) and the outflow to Ma'adim Vallis. We found also evidence of isolated activity that postdates this event. The chloride deposition [Osterloo *et al.*, 2010] in high-standing lakes surrounding the major depressions (*eAed*

unit, Subpart 3.2.2vi). Also much more recent channels [Adeli *et al.*, 2016] are found in the area carving the younger lavas inside Ariadnes basin (*eAsp* unit, Subpart 3.2.2v).

There is a regional set of ridges, troughs, and fractures in Coogoon similar to the structures that are found in Ariadnes, but which are not related to Hesperian lavas (Subpart 4.2.3i). During the Hesperian-Amazonian epochs, there was a series of reactivation of the channel network that denuded (probably together with aeolian erosion) part of the surface, exposing the Noachian materials and features, and remobilizing large amounts of material to the lowlands (*IHlp* unit, Subpart 4.2.2iv), creating new fluvial deposits (*NACd* unit, Subparts 4.2.2v and 4.2.2vi). Some of these events was most likely triggered by impact craters (Subpart 4.2.3ii).

The observation of the same geological processes occurring in both antipodal sides of the planet, Ariadnes and Coogoon, supports a global Noachian environment with high rates of volcanic activity and rich in relatively neutral pH water. The materials and landforms, however, do not need maintained warm environmental conditions to be formed, and in some cases, the water-derived alteration seems to take place underground. The existence of fluvial features and thick layered sediments support the occurrence of frequent episodes of (surface and/or subsurface) flowing liquid water before the end of the Hesperian. We found evidence of a change to drier and more acidic conditions, but even though multiple episodic recent and localized aqueous events must happen during the recent martian history. It is hard to asseverate the exact source and nature of the different reactivation events, but what appears to be certain is that they were more frequent and widespread in the past.



## 5.4 ARIADNES AND COOGOON AS LANDING SITES

### 5.4.1 LANDING MISSIONS

Before any human landing on Mars, the research into the geological processes operating on the planet rely on the interpretation of images and other data returned by unmanned orbiters and landers [Greeley, 2013]. In this regard, during the last decades, several missions have gathered orbital information from most of the planetary surface. However, to understand the geology of the planet and the nature of some of its key geological processes fully require a detailed investigation, which can only be provided by landing missions. Those landers or rovers (i.e., vehicles) are very limited and only able to reach a small portion of the planet surface. Thus, the selection of these ‘landing sites’ is crucial and needs a detailed and thoughtful selection process.

Although every mission has different scopes and objectives, in all cases the guideline for choosing between the multiple candidates can be resumed in technical constraints and scientific criteria. The first group of characteristics, depending on the landing orbit and operational environmental conditions of the vehicle, are easy to evaluate since they are basically security restrictions. To make a comparative assessment of the scientific relevance of different sites is far more complicated. The author was part of the Working Group that presented Coogoon Valles as a landing candidate for the ESA and Roscosmos ExoMars mission [Gómez *et al.*, 2014]. Besides, sites close to both Coogoon Valles [Quantin *et al.*, 2015, 2016] and Ariadnes basin [Pajola *et al.*, 2014, 2016] study areas are proposed as high-interest places for ExoMars and the upcoming NASA Mars2020. In this section, there will be discussed the interest and suitability of the studied places as a target for upcoming missions.

### 5.4.2 TECHNICAL CONSTRAINTS

The available technology today restricts the capability of a robotic mission to land on the surface of a planet. There is a series of engineering constraints (Table 5.4.a) that a site on the surface of Mars needs to address to be considered suitable for a mission. In case they are not satisfied, a candidate landing site can result in being

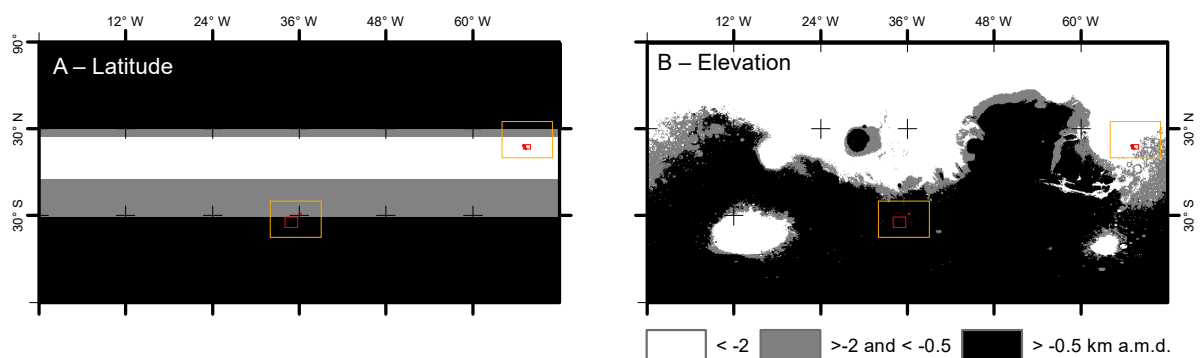
judged unfeasible for the mission and therefore rejected. Those constraints are defined in order to maximize the rover performance and asseverate safe Entry-Descent-Landing (EDL) and surface operations.

**Table 5.4.a** Basic technical constraints for ExoMars and Mars2020 missions and the approximate value of those variables (range or average  $\pm$  SD) in Ariadnes and Coogoon study areas and the proposed landing sites close to them.

Parameter	Missions		Study areas and landing sites			
	ExoMars	Mars2020	Ariadnes basin	[Pajola et al., 2016]	Coogoon Valles	[Quantin et al., 2016]
<b>Latitude</b>	5° S to 25° N	30° N to 30° S	31° S to 38° S	28° 20' S to 28° 53' S	16° S to 19° S	18° 80' N to 17° 85' N
<b>Elevation</b> ( <i>m a.m.d.</i> )	$\leq -2$	$\leq -0.5$	3.681 to -1.211	0.316 to 0.514	-1.853 to -4.068	-2.830 to -3.150
<b>Slopes</b>	$\leq 8.6^\circ$	$\leq 25 - 30^\circ$	$1.29 \pm 2.65^\circ$	$\leq 5.71^\circ$	$1.68 \pm 2.56^\circ$	$\leq 8.5^\circ$
<b>Rock abundance</b> (%)	$\leq 7$	$\leq 7$	$7.46 \pm 5.88$	$\leq 7$	$8.89 \pm 3.98$	No Data
<b>Thermal Inertia</b> ( $J \cdot m^{-2} \cdot s^{-0.5} \cdot K^{-1}$ )	$\geq 150$	$\geq 150$	$278 \pm 538$	259 to 354	$289 \pm 55$	257 to 483
<b>Albedo</b>	$\geq 0.1 / \leq 0.26$	$\leq 0.25$	0.11 to 0.16	0.13 to 0.16	0.19 to 0.06	0.18 to 0.22

The Entry-Descent-Landing (EDL) is the process of safely bring a vehicle from approach conditions to contact with the surface of a celestial body, and it will determine the limitations and precision of the ‘landing ellipse’ (i.e., the area where the spacecraft is probable to land). The need of a minimum atmospheric pressure to ensure the decrease in velocity of the spacecraft limit the elevation and latitude for a secure landing. Also, the further from the equator, the most difficult is the landing, as the polar orbits are energy-cost. Also, the days (or sols) are shorter and owing to the axis tilt of the planet (similar to the Earth’s one) there are large differences in day length and temperature range among seasons. The nights are cold, and the lack of light may be a logistic constraint for the mission operations (e.g., image acquisition, solar panels), so a landing site with high latitude is less recommendable than an equatorial place with similar scientific interest.

ExoMars and Mars2020 have a significant latitude restriction (Table 5.4.a and Figure 5.4.a-A), leaving as only possible landing area a narrow strip around the planet equator. Coogoon area is within the allowed range, while the Ariadnes area is barely outside the limit for the Mars2020 mission. The proposed landing site to the NE of Ariadnes basin [Pajola *et al.*, 2016] is in an acceptable latitude for Mars2020 constraints but lies still above the defined limit. Similarly, altitude is out of range for both missions in Ariadnes, but not in Coogoon (Table 5.4.a and Figure 5.4.a-B).

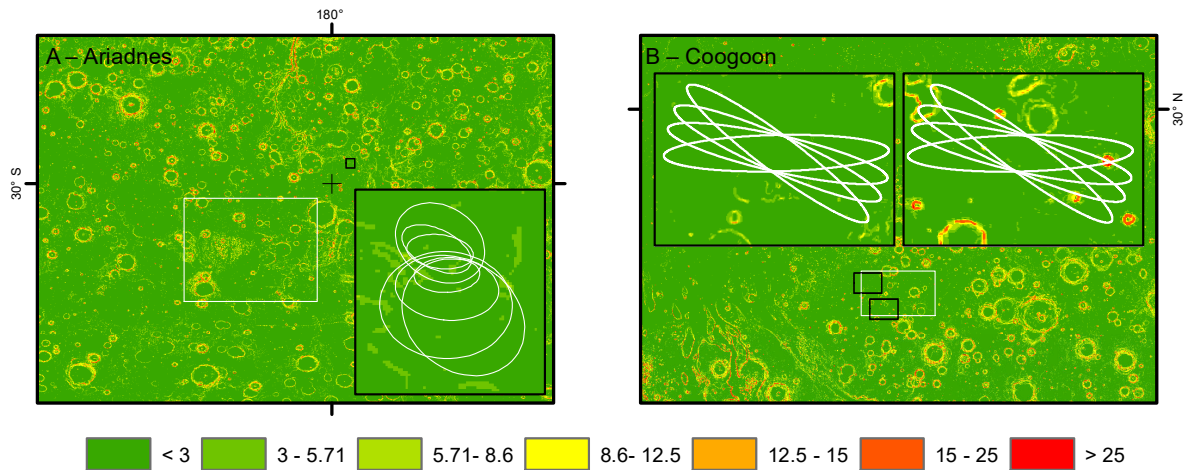


**Figure 5.4.a** Latitude (A) and Elevation (B) constraints for the ExoMars (**grey**) and Mars2020 (**black**) missions. Ariadnes and Coogoon regions (**orange**) and study areas and proposed landing sites (**red**) extensions.

The atmospheric and climate conditions is another important factor to take into account. Strong winds, elevated temperature ranges, or extremely low temperatures for long time periods are unadvised since they may affect to operational conditions of the rover and its instruments. The winds may mobilize dust covering the sensor and reducing their precision, and larger particles may damage the integrity of the spacecraft. Low temperatures reduce the available energy that needs to be spent on warming up the systems which usually operate with much higher temperatures than the surface of Mars. Additionally, the effect of winds would reduce the efficiency of the warming.

Generally, and especially with rovers, the landing terrain must be plain without important reliefs (Table 5.4.a). Low slopes at large scales are requested to ensure a slant and incidence compatible with radar that uses multiple beams to measure the vertical and horizontal components of the descent velocity vector during the EDL. High slopes at lower scales (Figure 5.4.b) may endanger the landing with severe

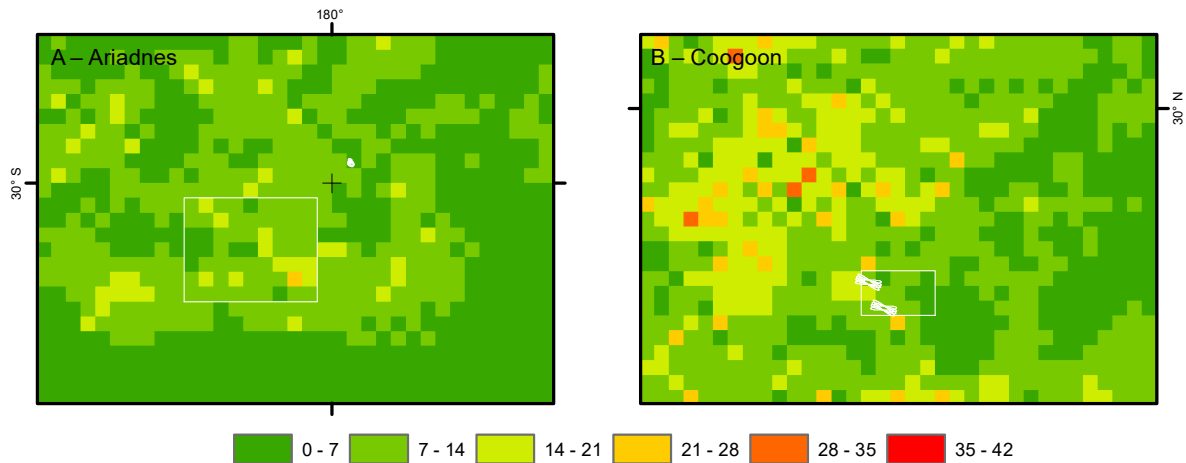
consequences on fuel consumption, control authority, and landing conditions. They can also difficult the transit of the vehicle, but also cause instabilities in its track (i.e., trafficability and stability of the rover).



**Figure 5.4.b** Slopes ( $^{\circ}$ ) obtained from MOLA data (at about 330-m length scale) in Ariadnes (A) and Coogoon (B) regions (extension in [Figure 5.4.a](#)). Study areas and landing ellipses are white lined, and black boxes are the close-up areas for the latter.

Both areas and proposed ellipses have low average slopes at MOLA scale ( $\sim 330$  m; [Table 5.4.a](#) and [Figure 5.4.b](#)). Some of the ellipses proposed in Coogoon [[Gómez et al., 2014](#)] display higher slopes associated with crater rims. Also, the Eridania study area shows steep slopes associated with the basin and knobs rims, being the adequate landing sites in the plains related to hydrated materials (e.g., *eAed*; Subpart 3.2.2vi), as the proposed in [[Pajola et al., 2016](#)].

The density of rocks is another important factor ([Table 5.4.a](#) and [Figure 5.4.c](#)) to ensure an appropriate rover traverse performance and to decrease probability of encountering a rock during landing. The parameter value is very depending on the rover settings and capabilities. In the case of the Mars2020 rover, for example, the request is a probability lower than the 0.5 % of finding a rock as large as the area of the belly pan in a randomly sampled area as large as the area out to the inside of the wheels. This constraint is evaluated through the rock abundance ([Table 5.4.a](#)), which is calculated trough the analysis of the TI.

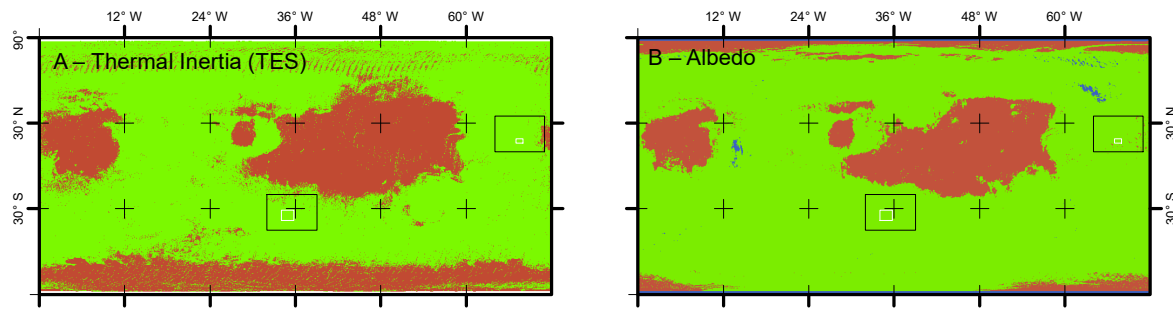


**Figure 5.4.c** Rock abundance (%) from Viking Infrared Thermal Mapper (IRTM) in Ariadnes (A) and Coogoon (B) regions (extension in [Figure 5.4.a](#)). Study areas and landing ellipses are white lined.

The IRTM data on both study areas ([Table 5.4.a](#) and [Figure 5.4.c](#)) display higher values of rock density than the allowed for both missions in a significant portion of their surfaces. The ellipse proposed by [[Pajola et al., 2016](#)] displays an acceptable range in this data for all its surface, although both in Coogoon are mostly above the allowed boundary. However, because of the low spatial resolution of this information, usually the final value considered is derived from HiRISE image (Subpart 2.1.2iii) boulder counting.

The TI and albedo are also considered in landing site characterization ([Figure 5.4.d](#)). As it can be observed, there is a clear relation between TI and albedo, as low TI and high albedo are interpreted as loose dust (red areas in [Figure 5.4.d](#)). Both parameters limit the rover thermal design constraints, and the TI correlates with the existence of a load-bearing surface. Both regions fulfill the requirements in TI and albedo from TES (Mars Global Surveyor's Thermal Emission Spectrometer) data ([Figure 5.4.d](#)). Most thoughtful analyses on TI with THEMIS data is available in Parts 3.4.2 and 4.4.2 for Ariadnes and Coogoon respectively. Other measurable physics properties of the surface are required to be within an operative range, as the radar reflectivity, that indicate the mechanical properties of the surface.





**Figure 5.4.d** Thermal Inertia (A) and Albedo (B) constraints for the ExoMars and Mars2020 missions. The green color is within the acceptable range, and red and dark blue are outside the permitted range (Table 5.4.a). Ariadnes and Coogoon regions (black box) and study areas and proposed landing sites (white lined) extensions.

Finally, the autonomy of the vehicle restricts the capability of a mission to reach the scientific targets in the landing area. The relevant features, therefore, should be either widespread or easily reachable and/or inside the landing ellipse.

### 5.4.3 SCIENTIFIC RELEVANCE

The relative scientific interest among the landing sites candidates for a landing mission is used to be evaluated through a long process that involves dozens of participants from the science community and instrument science teams during a series of workshops. The discussion of the science merits of the sites provides a community ranking based on their current knowledge and the suitability to achieve the mission's goals. Those goals are quite variable and a site well fitted for one mission could not be as good for another. For example, both ExoMars and Mars2020 seek signs of past life on Mars finding a geologically diverse and ancient site interpreted to have strong potential for past habitability, but with very different perspectives. ExoMars focus on the physical and chemical signs of life and organic matter (including abiotic/prebiotic organics) in the surface and the shallow subsurface [Westall *et al.*, 2014], reachable through a 2-meter drill. However, Mars2020 focus on the store of a compelling suite of samples in a returnable cache, and demonstrate technology for future robotic and human exploration of Mars [Mustard *et al.*, 2013].

Therefore, without going into much detail, ExoMars evaluates the following scientific criteria [Westall *et al.*, 2014]. They favor an ancient depositional age of the terrain (i.e., older than 3.6 Ga and possibly extending into the Hesperian), with

potential for preservation of organics. To ensure the identification of biosignatures, they seek materials with reduced radiation accumulation in the subsurface, as fine-grained sediments which are more resistant to the penetration of biologically-damaging agents than coarse materials. Recent exposure age is desirable, aiming for sites with high erosion rates or young craters that can provide the means to access deeper sediments. Those outcrops must be available for the drilling and well-distributed to ensure reachability. Also, favorable life conditions are hypothesized to be found in areas with morphological and mineralogical evidence for long-duration and low-energy transport aqueous activity. It is also essential to avoid loose dust deposits distributed by aeolian transport since dust is not an interesting target as any biomarker would be deteriorated by the oxidants and UV and ionizing radiation in the atmosphere and on the surface of Mars. Besides, dunes can endanger the trafficability and the drilling.

Oxia Planum and Coogoon landing sites are broadly consistent with the scientific objectives and engineering constraints of the ExoMars mission [Westall *et al.*, 2014]. Both exhibits one of the widest Mg/Fe phyllosilicates exposures associated with a regionally extended Noachian sedimentary unit, with a similar potential for biosignature preservation. These materials are ubiquitous across the Oxia landing ellipse, ensuring immediate accessibility to sites of scientific interest. Sinuous valleys, inverted channels, craters with fluidized ejecta patterns, a palaeobasin, and a fan, indicate a sustained aqueous depositional environment in the area. Although, Oxia lack of precise information regarding the geologic context and origin of the clay-bearing unit, Coogoon deposit seems to be more similar to the Mawrth materials. However, owing to engineering constraints, Coogoon landing site was discarded, and Oxia Planum was chosen as the primary candidate for ExoMars mission [Quantin *et al.*, 2016].

Mars2020 mission also seeks an ancient habitable environment with with high potential of biosignature preservation, but empathizing the presence of a characterizable geologic setting and history [Mustard *et al.*, 2013]. The main reason for that is that they seek to ensure the astrobiological and petrological quality of

returned samples. The average of the votes considering these criteria during the second Mars 2020 Landing Site Workshop (held in Monrovia, California; from August 4-6, 2015) were 2.6 (mode 3) for Eridania [Pajola *et al.*, 2016] and 2.2 (mode 2.2) for Oxia, in a 5-scale. Both, although selected within the 21 candidates, were ranked in the lowest positions (17 and 19, respectively).

In the 2<sup>nd</sup> Landing Site Workshop, Eridania landing site was claimed to provide the unique possibility to complete the measurements obtained by NASA Spirit rover in Gusev crater. The site is located in the Ma'adim Vallis mouth, the sources of one of the biggest outflow channel present on Mars, and an ancient paleolake. So, many samples of aqueous minerals could be traversed and analyzed in the landing ellipse. The in-situ exploration of the pedogenetic sequences in the area would provide key observations regarding early martian times (> 3.8 Ga). However, the participants were skeptic about the quality of the returned samples in Eridania landing site, but also in Oxia. The primary candidate for ExoMars obtained even a lower rank in the workshop, being both not in further consideration as landing site candidates for the Mars2020 mission.

## 6 CONCLUSIONS

- The multidisciplinary and intensive analysis of the orbital data is a valuable tool to obtain information of the planetary geologic history. However, there are still some questions that needs from data collected in-situ (i.e., by landers, rovers, or even a manned mission) to be addressed. The use of an integral GIS (Part 2.2.1) has proved to be an effective way not only for manage the data but also for mapping and data analysis.
- The 1:1,000,000 geologic maps produced as part of this Ph.D. research (Subchapters 3.2 and 4.2) show unprecedented detail for two under-examined areas of study (by the time of the research beginning at least): Ariadnes and Coogoon. The mapping technique used differentiate geologic material and geomorphic features and allows a differentiated analysis and age determination.
- The two areas of study are some of the few that hold geologic record from the Noachian to the Amazonian (as it was evidenced in Subchapters 3.3 and 4.3), with evident signals of water-related activity. Also, several landforms resemble volcanic and impact-related features; and tectonics played a major role in their development.
- Despite the scarce coverage, the visible near infrared spectral analysis of the CRISM data (Parts 3.4.1 and 4.4.1) provided valuable information on the different clays present in both areas, and the indexes allow to place them spatially. This permit to identify geologic process, as leaching, and supply a way to narrow their formation.
- Our observations support that both Ariadnes and Coogoon phyllosilicate-rich deposits were deposited as airborne tuffs, but while in Ariadnes the materials come from the weathering of a lacustrine bed that was subsequently deformed by tectonism, (aquifer release), in Coogoon they were formed by the interaction with groundwater, partially denuded, and later transported across the channel during different episodes.

- The infrared-derived products from THEMIS were very versatile. They allowed a better distinction of materials and landforms from the IR mosaics, enable the thermophysical characterization of the surfaces through the TI mosaics, and provide surficial temperatures. The latter was helpful to constrain the conditions that would identify a potential mission in the near future.
- The evaluation of the study areas as potential landing candidates (Subchapter 5.4) showed that despite their geologic interest, they do not suit the engineering constraint for the upcoming missions today. However, both were landing candidates and Oxia, at the termination of Coogoon, is still the primary candidate landing site for the ExoMars mission.
- Eridania and Western Arabia Terra were strongly influenced by volcanic activity in their early history, driven in part by the dichotomy induced lateral flow of lower crustal material and the evolution of the Tharsis. Volcanic activity (as Plains-style caldera complexes) lead to an extensive amount of airborne ashes and tuffs that covered both areas. Water activity (paleolakes in Ariadnes and a large aquifer in Coogoon) formed and altered those deposits forming the different clay-rich deposits. Water was released catastrophically during the Noachian-Hesperian forming outflow channels.
- The talc-saponite mixed layering found in Ariadnes supports that they are subaqueous hydrothermal deposits, and the montmorillonite located in Coogoon suggest underground hydrothermal alteration; both in alkaline conditions. Later pedogenesis may cause the Al-rich clays found in the upper strata in Ariadnes and Coogoon and sulfates in Ariadnes, but also acidic standing bodies of water.
- Our results coming from almost antipodal locations of the planet shows an apparently similar environmental evolution during the earliest times, that diverges with time. Our findings, however, are in concordance with a Noachian with more frequent and lasting wet episodes, and increasingly acidic conditions. Materials and landforms could have been formed in a not maintained warm environment though, but it is required a series of aqueous events to lead to the described geologic settings.



## 7 REFERENCES

- Adeli, S., L. Le Deit, E. Hauber, A. Molina, and R. Jaumann (2012a), Phyllosilicate-rich Knobs in the Atlantis Chaos Basin, Terra Sirenum, *EPSC Abstracts.*, vol. 7, p. 291.
- Adeli, S., E. Hauber, L. Le Deit, and R. Jaumann (2012b), Sedimentary Evolution of the Eridania Paleolake in the Atlantis Chaos Basin, Terra Sirenum, *LPI Contrib. No. 1680*, p. 7047.
- Adeli, S., E. Hauber, L. Le Deit, and R. Jaumann (2015), Geologic evolution of the eastern Eridania basin: Implications for aqueous processes in the southern highlands of Mars, *J. Geophys. Res. Planets*, 120(11), 1774–1799, doi:10.1002/2015JE004898.
- Adeli, S., E. Hauber, M. Kleinhans, L. L. Deit, T. Platz, P. Fawdon, and R. Jaumann (2016), Amazonian-aged fluvial system and associated ice-related features in Terra Cimmeria, Mars, *Icarus*, doi:10.1016/j.icarus.2016.05.020.
- Albee, A. L., R. E. Arvidson, F. Palluconi, and T. Thorpe (2001), Overview of the Mars Global Surveyor mission, *J. Geophys. Res. Planets*, 106(E10), 23291–23316, doi:10.1029/2000JE001306.
- Almeida, M. P., E. J. R. Parteli, J. S. Andrade, and H. J. Herrmann (2008), Giant saltation on Mars, *Proc. Natl. Acad. Sci.*, 105(17), 6222–6226, doi:10.1073/pnas.0800202105.
- Amador, E. S. et al. (2015), Synchronous in-field application of life-detection techniques in planetary analog missions, *Planet. Space Sci.*, 106, 1–10, doi:10.1016/j.pss.2014.11.006.
- Amils, R., D. Fernández-Remolar, and the IPBSL Team (2014), Río Tinto: A Geochemical and Mineralogical Terrestrial Analogue of Mars, *Life*, 4(3), 511–534, doi:10.3390/life4030511.
- Anderson, D., F. Ugolini, and L. Gatto (1972), Antarctic Analog of Martian Permafrost Terrain, *Antarct. J. U. S.*, 7(4), 114.
- Anderson, R. C., and J. M. Dohm (2011a), Understanding the Spatial and Temporal Histories of Faulting for the Terra Sirenum Region, Mars, *AGU Fall Meet. Abstr.*, #P43C-1690.
- Anderson, R. C., and J. M. Dohm (2011b), Unraveling the Complex History of Faulting for the Terra Sirenum Region; Mars, *LPI Contrib. No. 1608*, p. 2221.
- Anderson, R. C., J. M. Dohm, M. P. Golombek, A. F. C. Haldemann, B. J. Franklin, K. L. Tanaka, J. Lias, and B. Peer (2001), Primary centers and secondary concentrations of tectonic activity through time in the western hemisphere of Mars, *J. Geophys. Res. Planets*, 106(E9), 20563–20585, doi:10.1029/2000JE001278.
- Anderson, R. C., J. M. Dohm, S. Robbins, B. Hynek, and J. Andrews-Hanna (2012), Terra Sirenum: Window into Pre-Tharsis and Tharsis Phases of Mars Evolution, *LPI Contrib. No. 1659*, p. 2803.
- Anderson, R. S., and S. P. Anderson (2010), *Geomorphology: The Mechanics and Chemistry of Landscapes*, Cambridge University Press.
- Andrews-Hanna, J. C. (2014), Lowland (Mars), in *Encyclopedia of Planetary Landforms*, pp. 1–8, Springer New York.
- Andrews-Hanna, J. C., and R. J. Phillips (2007), Hydrological modeling of outflow channels and chaos regions on Mars, *J. Geophys. Res.*, 112(E8), doi:10.1029/2006JE002881.

- Andrews-Hanna, J. C., M. T. Zuber, and W. B. Banerdt (2008), The Borealis basin and the origin of the martian crustal dichotomy, *Nature*, 453(7199), 1212–1215, doi:10.1038/nature07011.
- Andrews-Hanna, J. C., M. T. Zuber, R. E. Arvidson, and S. M. Wiseman (2010), Early Mars hydrology: Meridiani playa deposits and the sedimentary record of Arabia Terra, *J. Geophys. Res. Planets*, 115(E6), E06002, doi:10.1029/2009JE003485.
- Ansan, V., and N. Mangold (2006), New observations of Warrego Valles, Mars: Evidence for precipitation and surface runoff, *Planet. Space Sci.*, 54, 219–242, doi:10.1016/j.pss.2005.12.009.
- Baker, D. M., and J. W. Head (2009), The Origin of Eridania Lake and Ma'adim Vallis: An Investigation of Closed Chaos Basins, Hesperian Ridged Plains, and Tectonic Constructs on the Floor of a Large Hypothesized Paleolake on Mars, *LPI Contrib. No. 1468*, p. 1835.
- Baker, D. M. H., and J. W. Head (2012a), Geology and Chronology of the Ma'adim Vallis-Eridania Basin Region, Mars: Implications for the Noachian-Hesperian Hydrologic Cycle, *LPI Contrib. No. 1659*, p. 1252.
- Baker, D. M. H., and J. W. Head (2012b), The Noachian to Hesperian Hydrologic Evolution of the Ma'adim Vallis-Eridania Basin Region, Mars, *LPI Contrib. No. 1680*, p. 7058.
- Baker, P. E., and I. McReath (1971), 1970 Volcanic Eruption at Deception Island, *Nature*, 231(18), 5–9, doi:10.1038/10.1038/physci231005a0.
- Baker, V. R. (2014), Terrestrial analogs, planetary geology, and the nature of geological reasoning, *Planet. Space Sci.*, 95, 5–10, doi:10.1016/j.pss.2012.10.008.
- Baker, V. R., R. G. Strom, V. C. Gulick, J. S. Kargel, G. Komatsu, and V. S. Kale (1991), Ancient oceans, ice sheets and the hydrological cycle on Mars, *Nature*, 352(6336), 589–594, doi:10.1038/352589a0.
- Baldrige, A. M., S. J. Hook, J. K. Crowley, G. M. Marion, J. S. Kargel, J. L. Michalski, B. J. Thomson, F. C. R. de Souza, N. T. Bridges, and A. J. Brown (2009), Contemporaneous deposition of phyllosilicates and sulfates: Using Australian acidic saline lake deposits to describe geochemical variability on Mars, *Geophys. Res. Lett.*, 36(19), doi:10.1029/2009GL040069.
- Bandfield, J. L., and W. C. Feldman (2008), Martian high latitude permafrost depth and surface cover thermal inertia distributions, *J. Geophys. Res. Planets*, 113(E8), E08001, doi:10.1029/2007JE003007.
- Baraldo, A., and C. . Rinaldi (2000), Stratigraphy and structure of Deception Island, South Shetland Islands, Antarctica, *J. South Am. Earth Sci.*, 13(8), 785–796, doi:10.1016/S0895-9811(00)00060-2.
- Barlow, N. G. (2006), Impact craters in the northern hemisphere of Mars: Layered ejecta and central pit characteristics, *Meteorit. Planet. Sci. Arch.*, 41(10), 1425–1436.
- Barlow, N. G., and T. L. Bradley (1990), Martian impact craters - Correlations of ejecta and interior morphologies with diameter, latitude, and terrain, *Icarus*, 87, 156–179, doi:10.1016/0019-1035(90)90026-6.
- Barlow, N. G., and C. B. Perez (2003), Martian impact crater ejecta morphologies as indicators of the distribution of subsurface volatiles, *J. Geophys. Res. Planets*, 108(E8), 5085, doi:10.1029/2002JE002036.
- Barlow, N. G., and S. Robbins (2014), Layered Ejecta, in *Encyclopedia of Planetary Landforms*, pp. 1–8, Springer New York.

- Barlow, N. G., J. D. Stopar, and H. Hargitai (2014), Ejecta (Impact), in *Encyclopedia of Planetary Landforms*, pp. 1–8, Springer New York.
- Bennett, K. A., and J. F. Bell III (2016), A global survey of martian central mounds: Central mounds as remnants of previously more extensive large-scale sedimentary deposits, *Icarus*, 264, 331–341, doi:10.1016/j.icarus.2015.09.041.
- Berger, G., A. Meunier, and D. Beaufort (2014), Clay mineral formation on Mars: Chemical constraints and possible contribution of basalt out-gassing, *Planet. Space Sci.*, 95, 25–32, doi:10.1016/j.pss.2013.05.024.
- Bibring, J.-P. et al. (2005), Mars Surface Diversity as Revealed by the OMEGA/Mars Express Observations, *Science*, 307(5715), 1576–1581, doi:10.1126/science.1108806.
- Bibring, J.-P. et al. (2006), Global Mineralogical and Aqueous Mars History Derived from OMEGA/Mars Express Data, *Science*, 312(5772), 400–404, doi:10.1126/science.1122659.
- Bishop, J. L., P. Schiffman, and R. Southard (2002), Geochemical and mineralogical analyses of palagonitic tuffs and altered rinds of pillow basalts in Iceland and applications to Mars, *Geol. Soc. Lond. Spec. Publ.*, 202(1), 371–392, doi:10.1144/GSL.SP.2002.202.01.19.
- Bishop, J. L., M. D. Lane, M. D. Dyar, and A. J. Brown (2008), Reflectance and emission spectroscopy study of four groups of phyllosilicates: smectites, kaolinite-serpentines, chlorites and micas, *Clay Miner.*, 43(1), 35–54, doi:10.1180/claymin.2008.043.1.03.
- Black, R. F. (1976), Periglacial features indicative of permafrost: Ice and soil wedges, *Quat. Res.*, 6, 3–26, doi:10.1016/0033-5894(76)90037-5.
- Boynton, W. V. et al. (2004), The Mars Odyssey Gamma-Ray Spectrometer Instrument Suite, in *2001 Mars Odyssey*, edited by C. T. Russell, pp. 37–83, Springer Netherlands, Dordrecht.
- Brugman, K. K., B. M. Hynek, and S. J. Robbins (2015), Crater-Based Tests Unlock the Mystery of the Origin and Evolution of Arabia Terra, Mars, *LPI Contrib. No. 1832*, p. 2359.
- Burrough, P. A., R. McDonnell, R. A. McDonnell, and C. D. Lloyd (2015), *Principles of Geographical Information Systems*, OUP Oxford.
- Capitan, R. D., and M. Van De Wiel (2011), Landform hierarchy and evolution in Gorgonum and Atlantis basins, Mars, *Icarus*, 211(1), 366–388, doi:10.1016/j.icarus.2010.08.006.
- Carr, M. H. (1979), Formation of Martian flood features by release of water from confined aquifers, *J. Geophys. Res.*, 84(B6), 2995, doi:10.1029/JBo84iBo6p02995.
- Carr, M. H. (1996), *Water on Mars*, Oxford University Press, New York.
- Carr, M. H. (2007), *The Surface of Mars*, Cambridge Planetary Science, Cambridge University Press, New York.
- Carr, M. H., and J. W. Head (2003), Oceans on Mars: An assessment of the observational evidence and possible fate, *J. Geophys. Res. Planets*, 108(E5), 5042, doi:10.1029/2002JE001963.
- Carr, M. H., and J. W. Head (2010), Geologic history of Mars, *Earth Planet. Sci. Lett.*, 294(3–4), 185–203, doi:10.1016/j.epsl.2009.06.042.
- Carter, J., D. Loizeau, N. Mangold, F. Poulet, and J.-P. Bibring (2015), Widespread surface weathering on early Mars: A case for a warmer and wetter climate, *Icarus*, 248, 373–382, doi:10.1016/j.icarus.2014.11.011.

- Centeno, J. D., M. A. de Pablo, A. Molina, and M. Ramos (2013), Glaciers on Deception Island, Antarctica: Analogue of the Debris-Covered Glaciers on the Hecates Tholus Volcano of Mars, *LPI Contrib. No. 1719*, p. 1495.
- Christensen, P. R. et al. (2004), The Thermal Emission Imaging System (THEMIS) for the Mars 2001 Odyssey Mission, *Space Sci. Rev.*, *110*, 85–130, doi:10.1023/B:SPAC.0000021008.16305.94.
- Christensen, P. R., R. L. Fergason, C. S. Edwards, and J. Hill (2013), THEMIS-Derived Thermal Inertia Mosaic of Mars: Product Description and Science Results, *LPI Contrib. No. 1719*, p. 2822.
- Clark, B. C. et al. (2007), Evidence for montmorillonite or its compositional equivalent in Columbia Hills, Mars, *J. Geophys. Res. Planets*, *112*(E6), E06S01, doi:10.1029/2006JE002756.
- Clark, R. N., T. V. V. King, M. Klejwa, G. A. Swayze, and N. Vergo (1990), High spectral resolution reflectance spectroscopy of minerals, *J. Geophys. Res. Solid Earth*, *95*(B8), 12653–12680, doi:10.1029/JB095iB08p12653.
- Clifford, S. M., and T. J. Parker (2001), The Evolution of the Martian Hydrosphere: Implications for the Fate of a Primordial Ocean and the Current State of the Northern Plains, *Icarus*, *154*, 40–79, doi:10.1006/icar.2001.6671.
- Cloutis, E. A. et al. (2006), Detection and discrimination of sulfate minerals using reflectance spectroscopy, *Icarus*, *184*(1), 121–157, doi:10.1016/j.icarus.2006.04.003.
- Cooke, M., F. Islam, and G. McGill (2011), Basement controls on the scale of giant polygons in Utopia Planitia, Mars, *J. Geophys. Res.*, *116*(E9), doi:10.1029/2011JE003812.
- Craddock, R. A., and A. D. Howard (2002), The case for rainfall on a warm, wet early Mars, *J. Geophys. Res. Planets*, *107*(E11), 21-1-21-36, doi:10.1029/2001JE001505.
- Craddock, R. A., and T. A. Maxwell (1993), Geomorphic evolution of the Martian highlands through ancient fluvial processes, *J. Geophys. Res. Planets*, *98*(E2), 3453–3468, doi:10.1029/92JE02508.
- Craddock, R. A., T. A. Maxwell, and A. D. Howard (1997), Crater morphometry and modification in the Sinus Sabaeus and Margaritifer Sinus regions of Mars, *J. Geophys. Res. Planets*, *102*(E6), 13321–13340, doi:10.1029/97JE01084.
- Crame, J. A., D. Pirrie, J. S. Crampton, and A. M. Duane (1993), Stratigraphy and regional significance of the Upper Jurassic-Lower Cretaceous Byers Group, Livingston Island, Antarctica, *J. Geol. Soc.*, *150*(6), 1075–1087, doi:10.1144/gsjgs.150.6.1075.
- Cuadros, J., J. R. Michalski, V. Dekov, J. Bishop, S. Fiore, and M. D. Dyar (2013), Crystal-chemistry of interstratified Mg/Fe-clay minerals from seafloor hydrothermal sites, *Chem. Geol.*, *360–361*, 142–158, doi:10.1016/j.chemgeo.2013.10.016.
- Davis, J. M., M. Balme, P. M. Grindrod, R. M. E. Williams, and S. Gupta (2016), Extensive Noachian fluvial systems in Arabia Terra: Implications for early Martian climate, *Geology*, *G38247.1*, doi:10.1130/G38247.1.
- De Hon, R. A. (1977), Geologic map of the Eridania Quadrangle of Mars, *USGS Numbered Series*, IMAF 1008. Scale 1:46,000.
- Dekov, V. M., J. Cuadros, W. C. Shanks, and R. A. Koski (2008), Deposition of talc — kerolite–smectite — smectite at seafloor hydrothermal vent fields: Evidence from mineralogical, geochemical and oxygen isotope studies, *Chem. Geol.*, *247*(1–2), 171–194, doi:10.1016/j.chemgeo.2007.10.022.

- Di Achille, G., and B. M. Hynek (2010), Ancient ocean on Mars supported by global distribution of deltas and valleys, *Nat. Geosci.*, 3(7), 459–463, doi:10.1038/ngeo891.
- Dohm, J. M. et al. (2007), Possible ancient giant basin and related water enrichment in the Arabia Terra province, Mars, *Icarus*, 190, 74–92, doi:10.1016/j.icarus.2007.03.006.
- Edgar, L. (2014), Quasi-Circular Depression, in *Encyclopedia of Planetary Landforms*, pp. 1–4, Springer New York.
- Edwards, C. S., K. J. Nowicki, P. R. Christensen, J. Hill, N. Gorelick, and K. Murray (2011), Mosaicking of global planetary image datasets: 1. Techniques and data processing for Thermal Emission Imaging System (THEMIS) multi-spectral data, *J. Geophys. Res.*, 116(E10), doi:10.1029/2010JE003755.
- Ehlmann, B. L., and C. S. Edwards (2014), Mineralogy of the Martian Surface, *Annu. Rev. Earth Planet. Sci.*, 42(1), 291–315, doi:10.1146/annurev-earth-060313-055024.
- Ehlmann, B. L. et al. (2009), Identification of hydrated silicate minerals on Mars using MRO-CRISM: Geologic context near Nili Fossae and implications for aqueous alteration, *J. Geophys. Res. Planets*, 114(E2), E00D08, doi:10.1029/2009JE003339.
- Ehlmann, B. L., J. F. Mustard, and S. L. Murchie (2010), Geologic setting of serpentine deposits on Mars, *Geophys. Res. Lett.*, 37(6), L06201, doi:10.1029/2010GL042596.
- Ehlmann, B. L., J. F. Mustard, S. L. Murchie, J.-P. Bibring, A. Meunier, A. A. Fraeman, and Y. Langevin (2011), Subsurface water and clay mineral formation during the early history of Mars, *Nature*, 479(7371), 53–60, doi:10.1038/nature10582.
- Ehlmann, B. L., D. L. Bish, S. W. Ruff, and J. F. Mustard (2012), Mineralogy and chemistry of altered Icelandic basalts: Application to clay mineral detection and understanding aqueous environments on Mars: clay mineral detection, icelandic basalt, *J. Geophys. Res. Planets*, 117(E11), n/a-n/a, doi:10.1029/2012JE004156.
- Ehlmann, B. L., G. Berger, N. Mangold, J. R. Michalski, D. C. Catling, S. W. Ruff, E. Chassefière, P. B. Niles, V. Chevrier, and F. Poulet (2013), Geochemical Consequences of Widespread Clay Mineral Formation in Mars' Ancient Crust, *Space Sci. Rev.*, 174(1–4), 329–364, doi:10.1007/s11214-012-9930-0.
- El-Maarry, M. R., G. Erkeling, Á. Kereszturi, and H. Hargitai (2014a), Crater Lake, in *Encyclopedia of Planetary Landforms*, pp. 1–7, Springer New York.
- El-Maarry, M. R., R. Soare, and Á. Kereszturi (2014b), Crater-Floor Polygons (Mars), in *Encyclopedia of Planetary Landforms*, pp. 1–6, Springer New York.
- Esteban, B., M. Ramos, E. Sebastián, C. Armiens, J. Gómez-Elvira, W. Cabos, and M. A. de Pablo (2009), The Antarctic permafrost as a testbed for REMS (Rover Environmental Monitoring Station-Mars Science Laboratory), *Geophysical Research Abstracts*, Vol. 11, EGU2009-562-1.
- Fairén, A., J. Dohm, and V. Baker (2003a), Major water-related episodes on the lowlands of Mars, *EGS-AGU-EUG Joint Assembly Contrib.*, p. 3282.
- Fairén, A. G., J. M. Dohm, V. R. Baker, M. A. de Pablo, J. Ruiz, J. C. Ferris, and R. C. Anderson (2003b), Episodic flood inundations of the northern plains of Mars, *Icarus*, 165(1), 53–67, doi:10.1016/S0019-1035(03)00144-1.
- Fairén, A. G., A. F. Davila, L. Gago-Duport, J. D. Haqq-Misra, C. Gil, C. P. McKay, and J. F. Kasting (2011), Cold glacial oceans would have inhibited phyllosilicate sedimentation on early Mars, *Nat. Geosci.*, 4(10), 667–670, doi:10.1038/ngeo1243.
- Fairén, A. G. et al. (2014), A cold hydrological system in Gale crater, Mars, *Planet. Space Sci.*, 93–94, 101–118, doi:10.1016/j.pss.2014.03.002.



- Farrand, W. H., J. F. Bell, J. R. Johnson, S. W. Squyres, J. Soderblom, and D. W. Ming (2006), Spectral variability among rocks in visible and near-infrared multispectral Pancam data collected at Gusev crater: Examinations using spectral mixture analysis and related techniques, *J. Geophys. Res. Planets*, *111*(E2), E02S15, doi:10.1029/2005JE002495.
- Fassett, C., R. Williams, Á. Kereszturi, and R. A. Parsons (2014), Valley Network (Mars), in *Encyclopedia of Planetary Landforms*, pp. 1–10, Springer New York.
- Fassett, C. I., and J. W. Head (2008), Valley network-fed, open-basin lakes on Mars: Distribution and implications for Noachian surface and subsurface hydrology, *Icarus*, *198*, 37–56, doi:10.1016/j.icarus.2008.06.016.
- Ferguson, R. L., P. R. Christensen, and H. H. Kieffer (2006a), High-resolution thermal inertia derived from the Thermal Emission Imaging System (THEMIS): Thermal model and applications, *J. Geophys. Res. Planets*, *111*, E12004, doi:10.1029/2006JE002735.
- Ferguson, R. L., P. R. Christensen, J. F. Bell, M. P. Golombek, K. E. Herkenhoff, and H. H. Kieffer (2006b), Physical properties of the Mars Exploration Rover landing sites as inferred from Mini-TES-derived thermal inertia, *J. Geophys. Res.*, *111*(E2), doi:10.1029/2005JE002583.
- Fernández-Ibáñez, F., R. Pérez-López, J. J. Martínez-Díaz, C. Paredes, J. L. Giner-Robles, A. T. Caselli, and J. M. Ibáñez (2005), Costa Recta beach, Deception Island, West Antarctica: a retreated scarp of a submarine fault?, *Antarct. Sci.*, *17*(3), 418–426, doi:10.1017/S0954102005002841.
- Fernández-Remolar, D. C., and A. H. Knoll (2008), Fossilization potential of iron-bearing minerals in acidic environments of Rio Tinto, Spain: Implications for Mars exploration, *Icarus*, *194*(1), 72–85, doi:10.1016/j.icarus.2007.10.009.
- Fernández-Remolar, D. C., O. Prieto-Ballesteros, D. Gómez-Ortiz, M. Fernández-Sampedro, P. Sarrazin, M. Gailhanou, and R. Amils (2011), Río Tinto sedimentary mineral assemblages: A terrestrial perspective that suggests some formation pathways of phyllosilicates on Mars, *Icarus*, *211*(1), 114–138, doi:10.1016/j.icarus.2010.09.008.
- Fernando, J., F. Schmidt, and S. Douté (2016), Martian surface microtexture from orbital CRISM multi-angular observations: A new perspective for the characterization of the geological processes, *Planet. Space Sci.*, *128*, 30–51, doi:10.1016/j.pss.2016.05.005.
- FGDC (2006), FGDC Digital Cartographic Standard for Geologic Map Symbolization: USGS Techniques and Methods 11-A2 (<http://pubs.usgs.gov/tm/2006/11A02/>).
- Filiberto, J. (2014), Pyroclastic Deposits, in *Encyclopedia of Planetary Landforms*, pp. 1–11, Springer New York.
- Forget, F., R. M. Haberle, F. Montmessin, B. Levrard, and J. W. Head (2006), Formation of Glaciers on Mars by Atmospheric Precipitation at High Obliquity, *Science*, *311*(5759), 368–371, doi:10.1126/science.1120335.
- Forsberg-Taylor, N. K. (2004), Crater degradation in the Martian highlands: Morphometric analysis of the Sinus Sabaeus region and simulation modeling suggest fluvial processes, *J. Geophys. Res.*, *109*(E5), doi:10.1029/2004JE002242.
- Franchi, F., A. P. Rossi, M. Pondrelli, and B. Cavalazzi (2014), Geometry, stratigraphy and evidences for fluid expulsion within Crommelin crater deposits, Arabia Terra, Mars, *Planet. Space Sci.*, *92*, 34–48, doi:10.1016/j.pss.2013.12.013.
- French, H. M. (2013), *The Periglacial Environment*, John Wiley & Sons.

- Frey, H. V. (2003), Buried Impact Basins and the Earliest History of Mars, *LPI Contribution No. 1164*, p. 3104.
- Frey, H. V. (2004), Impact Constraints on the Age and Origin of the Crustal Dichotomy on Mars, *LPI Contrib No. 1213*, p. 19.
- Frey, H. V. (2006), Impact constraints on the age and origin of the lowlands of Mars, *Geophys. Res. Lett.*, 33(8), L08S02, doi:10.1029/2005GL024484.
- Frey, H. V., J. H. Roark, K. M. Shockey, E. L. Frey, and S. E. H. Sakimoto (2002), Ancient lowlands on Mars, *Geophys. Res. Lett.*, 29(10), 22-1-22-4, doi:10.1029/2001GL013832.
- Gaffey, S. J. (1985), Reflectance spectroscopy in the visible and near-infrared (0.35–2.55  $\mu\text{m}$ ): Applications in carbonate petrology, *Geology*, 13(4), 270–273, doi:10.1130/0091-7613(1985)13<270:RSITVA>2.0.CO;2.
- Garcia-Descalzo, L., E. García-López, A. Maria Moreno, A. Alcazar, F. Baquero, and C. Cid (2012), Mass spectrometry for direct identification of biosignatures and microorganisms in Earth analogs of Mars, *Planet. Space Sci.*, 72(1), 138–145, doi:10.1016/j.pss.2012.08.009.
- Gazetteer, I. (2015), *Gazetteer of planetary nomenclature. International Astronomical Union (IAU) Working Group for Planetary System Nomenclature (WGPSN)* (<https://planetarynames.wr.usgs.gov>).
- Gendrin, A. et al. (2005), Sulfates in Martian Layered Terrains: The OMEGA/Mars Express View, *Science*, 307(5715), 1587–1591, doi:10.1126/science.1109087.
- Gerard, T. L., L. J. McHenry, G. L. Carson, and B. I. Cameron (2014), Mineralogy and Geochemistry of an Icelandic Fumarole: Analog to Mars Hydrothermal Alteration, *LPI Contrib. No. 1777*, p. 2815.
- Gilichinsky, D. (2011), Terrestrial Permafrost Models of Martian Habitats and Inhabitants, *AGU Fall Meet. Abstr. #C54A-05*.
- Gilichinsky, D., E. Rivkina, T. Vishnivetskaya, G. Felipe, V. Mironov, J. Blamey, M. Ramos, M. Ángel de Pablo, M. Castro, and F. Boehmwald (2010), Habitability of Mars: hyperthermophiles in permafrost, *COSPAR Scientific Assembly. Contrib.*, vol. 38, p. 11.
- Gillespie, A. R., A. B. Kahle, and R. E. Walker (1986), Color enhancement of highly correlated images. I. Decorrelation and HSI contrast stretches, *Remote Sens. Environ.*, 20(3), 209–235, doi:10.1016/0034-4257(86)90044-1.
- Gilmore, M. S., D. R. Thompson, L. J. Anderson, N. Karamzadeh, L. Mandrake, and R. Castaño (2011), Superpixel segmentation for analysis of hyperspectral data sets, with application to Compact Reconnaissance Imaging Spectrometer for Mars data, Moon Mineralogy Mapper data, and Ariadnes Chaos, Mars, *J. Geophys. Res. Planets*, 116(E7), E07001, doi:10.1029/2010JE003763.
- Glotch, T. D., J. L. Bandfield, L. L. Tornabene, H. B. Jensen, and F. P. Seelos (2010), Distribution and formation of chlorides and phyllosilicates in Terra Sirenum, Mars, *Geophys. Res. Lett.*, 37(16), L16202, doi:10.1029/2010GL044557.
- Goetting, H. R., and R. J. P. Lyon (1986), A knowledge-based software environment for the analysis of spectroradiometer data, *Proceedings of the 5<sup>th</sup> Thematic Conf. Remote Sensing for Exploration Geology*, pp. 513–520.
- Golder, K. (2013), Geomorphology of Eridania Basin, Mars: A Study of the Evolution of Chaotic Terrain and a Paleolake, *Masters Theses*.
- Golombek, M. P., F. S. Anderson, and M. T. Zuber (2001), Martian wrinkle ridge topography: Evidence for subsurface faults from MOLA, *J. Geophys. Res. Planets*, 106(E10), 23811–23821, doi:10.1029/2000JE001308.

- Golombek, M. P. et al. (2006), Erosion rates at the Mars Exploration Rover landing sites and long-term climate change on Mars, *J. Geophys. Res. Planets*, *111*(E12), E12S10, doi:10.1029/2006JE002754.
- Gómez, F. et al. (2014), ExoMars 2018 Landing Site Proposal: Coogoon Valles, *LPI Contrib. No. 1791*, p. 1491.
- Gómez-Ortiz, D., D. C. Fernández-Remolar, Á. Granda, C. Quesada, T. Granda, O. Prieto-Ballesteros, A. Molina, and R. Amils (2014), Identification of the subsurface sulfide bodies responsible for acidity in Río Tinto source water, Spain, *Earth Planet. Sci. Lett.*, *391*, 36–41, doi:10.1016/j.epsl.2014.01.022.
- Grant, J. A., and P. H. Schultz (1990), Gradational epochs on Mars: Evidence from West-Northwest of Isidis Basin and Electris, *Icarus*, *84*(1), 166–195, doi:10.1016/0019-1035(90)90164-5.
- Grant, J. A., S. A. Wilson, E. Noe Dobrea, R. L. Fergason, J. L. Griffes, J. M. Moore, and A. D. Howard (2010), HiRISE views enigmatic deposits in the Sirenum Fossae region of Mars, *Icarus*, *205*(1), 53–63, doi:10.1016/j.icarus.2009.04.009.
- Greeley, R. (2013), *Introduction to Planetary Geomorphology*. Cambridge University Press. ISBN: 9780521867115
- Greeley, R., and J. Guest (1987), Geologic map of the eastern equatorial region of Mars. USGS Numbered Series, IMAP 1802-B. Scale 1: 5,000,000.
- Guallini, L., and S. Nerozzi (2014), Polar Layered Deposits, in *Encyclopedia of Planetary Landforms*, pp. 1–14, Springer New York.
- Gwinner, K. et al. (2016), The High Resolution Stereo Camera (HRSC) of Mars Express and its approach to science analysis and mapping for Mars and its satellites, *Planet. Space Sci.*, *126*, 93–138, doi:10.1016/j.pss.2016.02.014.
- Halliday, A. N., H. Wänke, J.-L. Birck, and R. N. Clayton (2001), The Accretion, Composition and Early Differentiation of Mars, *Space Sci. Rev.*, *96*(1–4), 197–230, doi:10.1023/A:1011997206080.
- Hamilton, V. E., M. M. Osterloo, and B. S. McGrane (2007), THEMIS decorrelation stretched infrared mosaics for compositional evaluation of candidate 2009 Mars Science Laboratory landing sites, *LPI Contrib. No. 1338*, p. 1725.
- Hansen, V. L. (2000), Geologic mapping of tectonic planets, *Earth Planet. Sci. Lett.*, *176*(3–4), 527–542, doi:10.1016/S0012-821X(00)00017-0.
- Hargitai, H. (2014), Mud Volcano, in *Encyclopedia of Planetary Landforms*, pp. 1–7, Springer New York.
- Hargitai, H., and Á. Kereszturi (2014), Runoff Channel (Mars), in *Encyclopedia of Planetary Landforms*, pp. 1–2, Springer New York.
- Hargitai, H., and R. Soare (2014), Ice Wedge Polygon, in *Encyclopedia of Planetary Landforms*, pp. 1–4, Springer New York.
- Harrison, K. P., and R. E. Grimm (2005), Groundwater-controlled valley networks and the decline of surface runoff on early Mars, *J. Geophys. Res. Planets*, *110*, E12S16, doi:10.1029/2005JE002455.
- Hartmann, W. K. (2005), Martian cratering 8: Isochron refinement and the chronology of Mars, *Icarus*, *174*(2), 294–320, doi:10.1016/j.icarus.2004.11.023.
- Hartmann, W. K., and G. Neukum (2001a), Cratering Chronology and the Evolution of Mars, in *Chronology and Evolution of Mars*, edited by R. Kallenbach, J. Geiss, and W. K. Hartmann, pp. 165–194, Springer Netherlands.

- Hartmann, W. K., and G. Neukum (2001b), Cratering Chronology and the Evolution of Mars, *Space Sci. Rev.*, 96(1–4), 165–194, doi:10.1023/A:1011945222010.
- Head, J. W., H. Hiesinger, M. A. Ivanov, M. A. Kreslavsky, S. Pratt, and B. J. Thomson (1999), Possible Ancient Oceans on Mars: Evidence from Mars Orbiter Laser Altimeter Data, *Science*, 286(5447), 2134–2137, doi:10.1126/science.286.5447.2134.
- Head, J. W., M. A. Kreslavsky, and S. Pratt (2002), Northern lowlands of Mars: Evidence for widespread volcanic flooding and tectonic deformation in the Hesperian Period, *J. Geophys. Res. Planets*, 107(E1), 3–1, doi:10.1029/2000JE001445.
- Head, J. W. et al. (2005), Tropical to mid-latitude snow and ice accumulation, flow and glaciation on Mars, *Nature*, 434(7031), 346–351, doi:10.1038/nature03359.
- Head, J. W., L. Wilson, J. Dickson, and G. Neukum (2006), The Huygens-Hellas giant dike system on Mars: Implications for Late Noachian–Early Hesperian volcanic resurfacing and climatic evolution, *Geology*, 34(4), 285–288, doi:10.1130/G22163.1.
- Heldmann, J. L., W. Pollard, C. P. McKay, M. M. Marinova, A. Davila, K. E. Williams, D. Lacelle, and D. T. Andersen (2013), The high elevation Dry Valleys in Antarctica as analog sites for subsurface ice on Mars, *Planet. Space Sci.*, 85, 53–58, doi:10.1016/j.pss.2013.05.019.
- Hernandez de Pablo, M., M. Ramos, G. Vieira, D. Gilichinsky, F. Gómez, A. Molina, and R. Segovia (2009), Deception island, Antarctica: a terrestrial analogue for the study and understanding of the martian permafrost and subsurface glaciers, *Geophysical Research Abstracts*, Vol. 11, EGU2009-1292.
- Herrick, R. R. (2014a), Butterfly Ejecta, in *Encyclopedia of Planetary Landforms*, pp. 1–6, Springer New York.
- Herrick, R. R. (2014b), Elliptical Crater (Oblique Impact), in *Encyclopedia of Planetary Landforms*, pp. 1–6, Springer New York.
- Herrick, R. R., and K. K. Hessen (2006), The planforms of low-angle impact craters in the northern hemisphere of Mars, *Meteorit. Planet. Sci.*, 41(10), 1483–1495, doi:10.1111/j.1945-5100.2006.tb00431.x.
- Heywood, I., S. Cornelius, and S. Carver (2006), *An introduction to Geographical Information Systems*, 3rd ed., Pearson Education, Spain.
- Hiesinger, H., and J. W. Head (2000), Characteristics and origin of polygonal terrain in southern Utopia Planitia, Mars: Results from Mars Orbiter Laser Altimeter and Mars Orbiter Camera data, *J. Geophys. Res. Planets*, 105(E5), 11999–12022, doi:10.1029/1999JE001193.
- Howard, A. D. (2000), Ancient Crater Basins: A Triad of Morphologies, in *Eos Transactions AGU*, vol. 81, p. P62C–06, San Francisco, California, USA.
- Howard, A. D., and J. M. Moore (2004), Scarp-bounded benches in Gorgonum Chaos, Mars: Formed beneath an ice-covered lake?, *Geophys. Res. Lett.*, 31(1), L01702, doi:10.1029/2003GL018925.
- Howard, A. D., and J. M. Moore (2011), Late Hesperian to early Amazonian midlatitude Martian valleys: Evidence from Newton and Gorgonum basins, *J. Geophys. Res. Planets*, 116(E5), E05003, doi:10.1029/2010JE003782.
- Hynek, B. M., and R. J. Phillips (2001), Evidence for extensive denudation of the Martian highlands, *Geology*, 29(5), 407–410, doi:10.1130/0091-7613(2001)029<0407:EFEDOT>2.0.CO;2.
- Hynek, B. M., M. Beach, and M. R. T. Hoke (2010), Updated global map of Martian valley networks and implications for climate and hydrologic processes, *J. Geophys. Res. Planets*, 115(E9), E09008, doi:10.1029/2009JE003548.

- Irwin, R. P., T. A. Maxwell, A. D. Howard, R. A. Craddock, and D. W. Leverington (2002), A Large Paleolake Basin at the Head of Ma'adim Vallis, Mars, *Science*, 296(5576), 2209–2212, doi:10.1126/science.1071143.
- Irwin, R. P., A. D. Howard, and T. A. Maxwell (2004a), Geomorphology of Ma'adim Vallis, Mars, and associated paleolake basins, *J. Geophys. Res. Planets*, 109(E12), E12009, doi:10.1029/2004JE002287.
- Irwin, R. P., T. R. Watters, A. D. Howard, and J. R. Zimbelman (2004b), Sedimentary resurfacing and fretted terrain development along the crustal dichotomy boundary, Aeolis Mensae, Mars, *J. Geophys. Res. Planets*, 109(E9), E09011, doi:10.1029/2004JE002248.
- Irwin, R. P., A. D. Howard, R. A. Craddock, and J. M. Moore (2005a), An intense terminal epoch of widespread fluvial activity on early Mars: 2. Increased runoff and paleolake development, *J. Geophys. Res. Planets*, 110, E12S15, doi:10.1029/2005JE002460.
- Irwin, R. P., R. A. Craddock, and A. D. Howard (2005b), Interior channels in Martian valley networks: Discharge and runoff production, *Geology*, 33(6), 489–492, doi:10.1130/G21333.1.
- Ivanov, B. A. (2001), Mars/Moon Cratering Rate Ratio Estimates, *Space Sci. Rev.*, 96(1–4), 87–104, doi:10.1023/A:1011941121102.
- Jakosky, B. M. (1986), On the thermal properties of Martian fines, *Icarus*, 66(1), 117–124, doi:10.1016/0019-1035(86)90011-4.
- Jakosky, B. M., and P. R. Christensen (1986), Global duricrust on Mars: Analysis of remote-sensing data, *J. Geophys. Res.*, 91(B3), 3547, doi:10.1029/JB091iB03p03547.
- Jaumann, R. et al. (2007), The high-resolution stereo camera (HRSC) experiment on Mars Express: Instrument aspects and experiment conduct from interplanetary cruise through the nominal mission, *Planet. Space Sci.*, 55(7–8), 928–952, doi:10.1016/j.pss.2006.12.003.
- Jaumann, R., D. Tirsch, E. Hauber, G. Erkeling, H. Hiesinger, L. Le Deit, M. Sowe, S. Adeli, A. Petau, and D. Reiss (2014), Water and Martian habitability: Results of an integrative study of water related processes on Mars in context with an interdisciplinary Helmholtz research alliance “Planetary Evolution and Life,” *Planet. Space Sci.*, 98, 128–145, doi:10.1016/j.pss.2014.02.013.
- Jones, E., G. Caprarelli, F. P. Mills, B. Doran, and J. Clarke (2014), An Alternative Approach to Mapping Thermophysical Units from Martian Thermal Inertia and Albedo Data Using a Combination of Unsupervised Classification Techniques, *Remote Sens.*, 6(6), 5184–5237, doi:10.3390/rs6065184.
- Kahle, A. B., A. R. Gillespie, and A. F. H. Goetz (1976), Thermal inertia imaging: A new geologic mapping tool, *Geophys. Res. Lett.*, 3(1), 26–28, doi:10.1029/GL0031001p00026.
- Kargel, J. S., R. Furfaro, O. Prieto-Ballesteros, J. A. P. Rodriguez, D. R. Montgomery, A. R. Gillespie, G. M. Marion, and S. E. Wood (2007), Martian hydrogeology sustained by thermally insulating gas and salt hydrates, *Geology*, 35, 975, doi:10.1130/G23783A.1.
- Kerber, L., J. W. Head, J.-B. Madeleine, F. Forget, and L. Wilson (2012), The dispersal of pyroclasts from ancient explosive volcanoes on Mars: Implications for the friable layered deposits, *Icarus*, 219(1), 358–381, doi:10.1016/j.icarus.2012.03.016.
- Kereszturi, Á., and H. Hargitai (2014), Outflow Channel (Mars), in *Encyclopedia of Planetary Landforms*, pp. 1–11, Springer New York.



- Keszthelyi, L., A. S. McEwen, and T. Thordarson (2000), Terrestrial analogs and thermal models for Martian flood lavas, *J. Geophys. Res. Planets*, 105(E6), 15027–15049, doi:10.1029/1999JE001191.
- Keszthelyi, L., T. Thordarson, A. McEwen, H. Haack, M.-N. Guilbaud, S. Self, and M. J. Rossi (2004), Icelandic analogs to Martian flood lavas, *Geochem. Geophys. Geosystems*, 5(11), n/a-n/a, doi:10.1029/2004GC000758.
- Kieffer, H. H., T. Z. Martin, A. R. Peterfreund, B. M. Jakosky, E. D. Miner, and F. D. Palluconi (1977), Thermal and albedo mapping of Mars during the Viking primary mission, *J. Geophys. Res.*, 82, 4249–4291, doi:10.1029/JSo82i028p04249.
- Kite, E. S., I. Halevy, M. A. Kahre, M. J. Wolff, and M. Manga (2013), Seasonal melting and the formation of sedimentary rocks on Mars, with predictions for the Gale Crater mound, *Icarus*, 223(1), 181–210, doi:10.1016/j.icarus.2012.11.034.
- Kneissl, T., G. G. Michael, T. Platz, and S. H. G. Walter (2015), Age determination of linear surface features using the Buffered Crater Counting approach - Case studies of the Sirenum and Fortuna Fossae graben systems on Mars, *Icarus*, 250, 384–394, doi:10.1016/j.icarus.2014.12.008.
- Komatsu, G., C. H. Okubo, J. J. Wray, L. Ojha, M. Cardinale, A. Murana, R. Orosei, M. A. Chan, J. Ormö, and R. Gallagher (2016), Small edifice features in Chryse Planitia, Mars: Assessment of a mud volcano hypothesis, *Icarus*, 268, 56–75, doi:10.1016/j.icarus.2015.12.032.
- Kopf, A. J. (2002), Significance of Mud Volcanism, *Rev. Geophys.*, 40(2), 1005, doi:10.1029/2000RG000093.
- Korteniemi, J., and H. Hargitai (2014), Chaotic Crater Floor (Mars), in *Encyclopedia of Planetary Landforms*, pp. 1–6, Springer New York.
- Korteniemi, J., L. S. Walsh, and S. S. Hughes (2014), Wrinkle Ridge, in *Encyclopedia of Planetary Landforms*, pp. 1–10, Springer New York.
- Kreslavsky, M. A., and J. W. Head (2002), Fate of outflow channel effluents in the northern lowlands of Mars: The Vastitas Borealis Formation as a sublimation residue from frozen ponded bodies of water, *J. Geophys. Res. Planets*, 107(E12), 4-1-4-25, doi:10.1029/2001JE001831.
- Kuzmin, R., R. Greeley, R. Landheim, N. Cabrol, and J. Farmer (2000), Geologic mapping of the Ma'adim Vallis-Gusev crater region of Mars, *US Geol Surv Misc Inv Ser MTM*, 2256–2257.
- Lamb, M. P., A. D. Howard, J. Johnson, K. X. Whipple, W. E. Dietrich, and J. T. Perron (2006), Can springs cut canyons into rock?, *J. Geophys. Res. Planets*, 111(E7), E07002, doi:10.1029/2005JE002663.
- Lammer, H. et al. (2013), Outgassing History and Escape of the Martian Atmosphere and Water Inventory, *Space Sci. Rev.*, 174(1–4), 113–154, doi:10.1007/s11214-012-9943-8.
- Laskar, J., B. Levrard, and J. F. Mustard (2002), Orbital forcing of the martian polar layered deposits, *Nature*, 419(6905), 375–377, doi:10.1038/nature01066.
- Laskar, J., A. C. M. Correia, M. Gastineau, F. Joutel, B. Levrard, and P. Robutel (2004), Long term evolution and chaotic diffusion of the insolation quantities of Mars, *Icarus*, 170(2), 343–364, doi:10.1016/j.icarus.2004.04.005.
- Lemoine, F. G., D. E. Smith, D. D. Rowlands, M. T. Zuber, G. A. Neumann, D. S. Chinn, and D. E. Pavlis (2001), An improved solution of the gravity field of Mars (GMM-2B) from Mars Global Surveyor, *J. Geophys. Res. Planets*, 106(E10), 23359–23376, doi:10.1029/2000JE001426.

- Levrard, B., F. Forget, F. Montmessin, and J. Laskar (2004), Recent ice-rich deposits formed at high latitudes on Mars by sublimation of unstable equatorial ice during low obliquity, *Nature*, 431(7012), 1072–1075, doi:10.1038/nature03055.
- Lias, J. H., K. L. Tanaka, and T. M. Hare (1999), Geologic, Tectonic, and Fluvial Histories of the Eridania Region of Mars, *LPI Contrib. No. 964*, p. 1074.
- Loizeau, D., N. Mangold, F. Poulet, V. Ansan, E. Hauber, J.-P. Bibring, B. Gondet, Y. Langevin, P. Masson, and G. Neukum (2010), Stratigraphy in the Mawrth Vallis region through OMEGA, HRSC color imagery and DTM, *Icarus*, 205(2), 396–418, doi:10.1016/j.icarus.2009.04.018.
- Loizeau, D., S. C. Werner, N. Mangold, J.-P. Bibring, and J. L. Vago (2012), Chronology of deposition and alteration in the Mawrth Vallis region, Mars, *Planet. Space Sci.*, 72(1), 31–43, doi:10.1016/j.pss.2012.06.023.
- Loizeau, D., N. Mangold, F. Poulet, J.-P. Bibring, J. L. Bishop, J. Michalski, and C. Quantin (2015), History of the clay-rich unit at Mawrth Vallis, Mars: High-resolution mapping of a candidate landing site, *J. Geophys. Res. Planets*, 120, 1820–1846, doi:10.1002/2015JE004894.
- Lucchitta, B. K., H. M. Ferguson, and C. Summers (1986), Sedimentary deposits in the Northern Lowland Plains, Mars, *J. Geophys. Res. Solid Earth*, 91(B13), E166–E174, doi:10.1029/JB091iB13p0E166.
- Lucchitta, B. K., N. K. Isbell, and A. Howington-Kraus (1994), Topography of Valles Marineris: Implications for erosional and structural history, *J. Geophys. Res. Planets*, 99(E2), 3783–3798, doi:10.1029/93JE03095.
- Luo, W., and A. D. Howard (2008), Computer simulation of the role of groundwater seepage in forming Martian valley networks, *J. Geophys. Res. Planets*, 113(E5), E05002, doi:10.1029/2007JE002981.
- Mackay, J. R. (1999), Periglacial features developed on the exposed lake bottoms of seven lakes that drained rapidly after 1950, Tuktoyaktuk Peninsula area, western Arctic coast, Canada, *Permafrost Periglacial Processes*, 10(1), 39–63, doi:10.1002/(SICI)1099-1530(199901/03)10:1<39::AID-PPP305>3.0.CO;2-R.
- MacKinnon, D. J., and K. L. Tanaka (1989), The impacted Martian crust: Structure, hydrology, and some geologic implications, *J. Geophys. Res. Solid Earth*, 94(B12), 17359–17370, doi:10.1029/JB094iB12p17359.
- Malin, M. C., and K. S. Edgett (2000), Sedimentary Rocks of Early Mars, *Science*, 290(5498), 1927–1937, doi:10.1126/science.290.5498.1927.
- Malin, M. C., and K. S. Edgett (2003), Evidence for Persistent Flow and Aqueous Sedimentation on Early Mars, *Science*, 302, 1931–1934, doi:10.1126/science.1090544.
- Malin, M. C. et al. (2007), Context Camera Investigation on board the Mars Reconnaissance Orbiter, *J. Geophys. Res. Planets*, 112(E5), E05S04, doi:10.1029/2006JE002808.
- Marquez, A., M. de Pablo, R. Oyarzun, and C. Viedma (2005), Evidence of gully formation by regional groundwater flow in the Gorgonum–Newton region (Mars), *Icarus*, 179(2), 398–414, doi:10.1016/j.icarus.2005.07.020.
- McEwen, A. S. et al. (2007), Mars Reconnaissance Orbiter’s High Resolution Imaging Science Experiment (HiRISE), *J. Geophys. Res. Planets*, 112, E05S02, doi:10.1029/2005JE002605.
- McKeown, N. K., J. L. Bishop, E. Z. Noe Dobrea, B. L. Ehlmann, M. Parente, J. F. Mustard, S. L. Murchie, G. A. Swayze, J.-P. Bibring, and E. A. Silver (2009), Characterization of phyllosilicates observed in the central Mawrth Vallis region,

- Mars, their potential formational processes, and implications for past climate, *J. Geophys. Res. E Planets*, 114(11), doi:10.1029/2008JE003301.
- McKeown, N. K., J. L. Bishop, and E. A. Silver (2013), Variability of rock texture and morphology correlated with the clay-bearing units at Mawrth Vallis, Mars, *J. Geophys. Res. Planets*, 118(6), 1245–1256, doi:10.1002/jgre.20096.
- Mellon, M. T. (1997), Thermal contraction cracks in Martian permafrost - Implications for small-scale polygonal features, *LPI Contrib. No. 1090*, p. 933.
- Mellon, M. T., B. M. Jakosky, H. H. Kieffer, and P. R. Christensen (2000), High-Resolution Thermal Inertia Mapping from the Mars Global Surveyor Thermal Emission Spectrometer, *Icarus*, 148(2), 437–455, doi:10.1006/icar.2000.6503.
- Mellon, M. T., R. E. Arvidson, J. J. Marlow, R. J. Phillips, E. Asphaug, M. L. Searls, S. Martinez-Alonso, and H. Team (2008), Polygonal Patterned Ground and Sorted Rocks on Mars as Seen by HiRISE: The Phoenix Landing Site, Northern Plains and Beyond, *LPI Contrib. No. 1391*, p. 1770.
- Meresse, S., F. Costard, N. Mangold, P. Masson, and G. Neukum (2008), Formation and evolution of the chaotic terrains by subsidence and magmatism: Hydraotes Chaos, Mars, *Icarus*, 194(2), 487–500, doi:10.1016/j.icarus.2007.10.023.
- Michael, G. G. (2013), Planetary surface dating from crater size–frequency distribution measurements: Multiple resurfacing episodes and differential isochron fitting, *Icarus*, 226(1), 885–890, doi:10.1016/j.icarus.2013.07.004.
- Michael, G. G., and G. Neukum (2010), Planetary surface dating from crater size–frequency distribution measurements: Partial resurfacing events and statistical age uncertainty, *Earth Planet. Sci. Lett.*, 294(3–4), 223–229, doi:10.1016/j.epsl.2009.12.041.
- Michael, G. G., T. Platz, T. Kneissl, and N. Schmedemann (2012), Planetary surface dating from crater size–frequency distribution measurements: Spatial randomness and clustering, *Icarus*, 218(1), 169–177, doi:10.1016/j.icarus.2011.11.033.
- Michael, G. G. et al. (2016), Systematic processing of Mars Express HRSC panchromatic and colour image mosaics: Image equalisation using an external brightness reference, *Planet. Space Sci.*, 121, 18–26, doi:10.1016/j.pss.2015.12.002.
- Michalski, J. R., and J. E. Bleacher (2013), Supervolcanoes within an ancient volcanic province in Arabia Terra, Mars, *Nature*, 502(7469), 47–52, doi:10.1038/nature12482.
- Michalski, J. R., and E. Z. Noe Dobrea (2007), Evidence for a sedimentary origin of clay minerals in the Mawrth Vallis region, Mars, *Geology*, 35(10), 951–954, doi:10.1130/G23854A.1.
- Michalski, J. R., J. E. Bleacher, and S. P. Wright (2013a), A Holey Conundrum: Distinguishing Between Ancient Calderas and Degraded Impact Craters on Mars, *LPI Contrib. No. 1737*, p. 3078.
- Michalski, J. R., J. Cuadros, P. B. Niles, J. Parnell, A. Deanne Rogers, and S. P. Wright (2013b), Groundwater activity on Mars and implications for a deep biosphere, *Nat. Geosci.*, 6(2), 133–138, doi:10.1038/ngeo1706.
- Michalski, J. R., E. Z. Noe Dobeia, and C. M. Weitz (2015), Mg-Rich Clays and Silica-Bearing Deposits in Eridania Basin: Possible Evidence for Ancient Sea Deposits on Mars, *LPI Contrib. No. 1832*, p. 2754.
- Miller, R. D. (2003), Redistribution of water in terrestrial soils at subfreezing temperatures: A review of processes and their potential relevance to Mars, *J. Geophys. Res.*, 108(E4), doi:10.1029/2002JE001873.

- Milliken, R. E., and D. L. Bish (2010), Sources and sinks of clay minerals on Mars, *Philos. Mag.*, 90(17–18), 2293–2308, doi:10.1080/14786430903575132.
- Molina, A., E. Hauber, L. Le Deit, S. Adeli, D. C. Fernández-Remolar, and M. A. de Pablo (2012), Geologic analysis of knob fields and sedimentary deposits in Ariadnes Colles, Terra Sirenum, Mars, *EPSC Abstracts.*, vol. 7, p. 213.
- Molina, A., M. A. de Pablo, T. Bardají, and M. Ramos (2013a), Caracterización granulométrica y mineralógica de los diferentes tipos de suelos presentes en las islas Livingston y Decepción (Shetland del Sur, Antártida), in *Avances, métodos y técnicas en el estudio del periglaciario*, p. 59.
- Molina, A., E. Hauber, L. L. Deit, S. Adeli, and D. F. Remolar (2013b), Cartografía geológica de la región de Ariadnes Colles, Terra Sirenum, Marte, in *Cuartas Jornadas de Jóvenes Investigadores de la Universidad de Alcalá: Ciencias*, edited by G. Ros, J. Aguado Molina, M. A. Hidalgo, A. Guerrero Ortega, pp. 167-174. ISBN 978-84-15834-15-1,
- Molina, A., M. A. de Pablo, and M. Ramos (2013c), Deception Island, Antarctica, an Earth-Mars Analogue, *LPI Contrib. No. 1719*, p. 1202.
- Molina, A., M. De Pablo, and M. Ramos (2014a), Deception Island (Antarctica) as an Earth-Mars geomorphological analogue, *EUCOP4 Abstracts*, p. 250.
- Molina, A., M. Á. de Pablo, E. Hauber, L. Le Deit, and D. (Carlos) Fernández-Remolar (2014b), Geology of the Ariadnes Basin, NE Eridania quadrangle, Mars – 1:1Million, *J. Maps*, 10(3), 487–499, doi:10.1080/17445647.2014.888018.
- Molina, A., I. López, O. Prieto-Ballesteros, D. Fernández-Remolar, M. Á. de Pablo, and F. Gómez (2017), Coogoon Valles, western Arabia Terra: Hydrological evolution of a complex Martian channel system, *Icarus*, 293, 27–44, doi:10.1016/j.icarus.2017.04.002.
- Montgomery, D. R., and A. Gillespie (2005), Formation of Martian outflow channels by catastrophic dewatering of evaporite deposits, *Geology*, 33, 625, doi:10.1130/G21270.1.
- Moore, J. M. (1990), Nature of the mantling deposit in the heavily cratered terrain of northeastern Arabia, Mars, *J. Geophys. Res. Solid Earth*, 95(B9), 14279–14289, doi:10.1029/JB095iB09p14279.
- Moore, J. M., and A. D. Howard (2005), Layered Deposits and Pitted Terrain in the Circum Hellas Region. *LPI Contrib. No. 1234*, p. 1512.
- Moura, P. A., M. R. Francelino, C. E. G. R. Schaefer, F. N. B. Simas, and B. A. F. de Mendonça (2012), Distribution and characterization of soils and landform relationships in Byers Peninsula, Livingston Island, Maritime Antarctica, *Geomorphology*, 155–156, 45–54, doi:10.1016/j.geomorph.2011.12.011.
- Murchie, S. et al. (2007), Compact Reconnaissance Imaging Spectrometer for Mars (CRISM) on Mars Reconnaissance Orbiter (MRO), *J. Geophys. Res. Planets*, 112(E5), E00D06, doi:10.1029/2006JE002682.
- Murchie, S. L. et al. (2009), A synthesis of Martian aqueous mineralogy after 1 Mars year of observations from the Mars Reconnaissance Orbiter, *J. Geophys. Res. Planets*, 114(E2), E00D06, doi:10.1029/2009JE003342.
- Mustard, J. et al. (2013), Report of the Mars 2020 science definition team, *Jet Propuls. Lab. Calif. Inst. Technol. Pasadena CA*.
- Mustard, J. F., F. Poulet, A. Gendrin, J.-P. Bibring, Y. Langevin, B. Gondet, N. Mangold, G. Bellucci, and F. Altieri (2005), Olivine and Pyroxene Diversity in the Crust of Mars, *Science*, 307(5715), 1594–1597, doi:10.1126/science.1109098.

- Neukum, G., and B. A. Ivanov (1994), Crater Size Distributions and Impact Probabilities on Earth from Lunar, Terrestrial-planet, and Asteroid Cratering Data, in *Hazards due to comets and asteroids*, edited by T. Gehrels, M. S. Matthews. and A. Schumann. University of Arizona Press, p. 359.
- Neukum, G., R. Jaumann, and HRSC Co-Investigator and Experiment Team (2004), HRSC: The high resolution stereo camera of Mars Express, *Eur. Space Agency Spec. Publ. ESA SP*, (1240), 17–35.
- Neumann, G. A. (2003), Two Mars years of clouds detected by the Mars Orbiter Laser Altimeter, *J. Geophys. Res.*, 108(E4), doi:10.1029/2002JE001849.
- Neumann, G. A., D. D. Rowlands, F. G. Lemoine, D. E. Smith, and M. T. Zuber (2001), Crossover analysis of Mars Orbiter Laser Altimeter data, *J. Geophys. Res. Planets*, 106(E10), 23753–23768, doi:10.1029/2000JE001381.
- Neumann, G. A., M. T. Zuber, M. A. Wieczorek, P. J. McGovern, F. G. Lemoine, and D. E. Smith (2004), Crustal structure of Mars from gravity and topography, *J. Geophys. Res. Planets*, 109(E8), E08002, doi:10.1029/2004JE002262.
- Nimmo, F. (2005), Tectonic consequences of Martian dichotomy modification by lower-crustal flow and erosion, *Geology*, 33(7), 533–536, doi:10.1130/G21342.1.
- Noe Dobrea, E. Z., J. Moore, A. Howard, D. Catling, and J. Grant (2008), Spectral and Geomorphic Evidence for a Past Inland Sea in Eridania Basin, Mars, *AGU Fall Meet. Abstr.*, #P32B-03.
- Noe Dobrea, E. Z. et al. (2010), Mineralogy and stratigraphy of phyllosilicate-bearing and dark mantling units in the greater Mawrth Vallis/west Arabia Terra area: Constraints on geological origin, *J. Geophys. Res. Planets*, 115(E7), E00D19, doi:10.1029/2009JE003351.
- Núñez, J. I., O. S. Barnouin, S. L. Murchie, F. P. Seelos, J. A. McGovern, K. D. Seelos, and D. L. Buczkowski (2016), New insights into gully formation on Mars: Constraints from composition as seen by MRO/CRISM, *Geophys. Res. Lett.*, 43(17), 2016GL068956, doi:10.1002/2016GL068956.
- Oehler, D. Z., and C. C. Allen (2010), Evidence for pervasive mud volcanism in Acidalia Planitia, Mars, *Icarus*, 208(2), 636–657, doi:10.1016/j.icarus.2010.03.031.
- Osinski, G. R. et al. (2013), Impact-generated hydrothermal systems on Earth and Mars, *Icarus*, 224(2), 347–363, doi:10.1016/j.icarus.2012.08.030.
- Osterloo, M. M., V. E. Hamilton, J. L. Bandfield, T. D. Glotch, A. M. Baldrige, P. R. Christensen, L. L. Tornabene, and F. S. Anderson (2008a), Chloride-Bearing Materials in the Southern Highlands of Mars, *Science*, 319(5870), 1651–1654, doi:10.1126/science.1150690.
- Osterloo, M. M., V. E. Hamilton, J. L. Bandfield, T. D. Glotch, A. M. Baldrige, P. R. Christensen, L. L. Tornabene, and F. S. Anderson (2008b), Chloride-Bearing Materials in the Southern Highlands of Mars, *Science*, 319(5870), 1651–1654, doi:10.1126/science.1150690.
- Osterloo, M. M., F. S. Anderson, V. E. Hamilton, and B. M. Hynek (2010), Geologic context of proposed chloride-bearing materials on Mars, *J. Geophys. Res. Planets*, 115(E10), E10012, doi:10.1029/2010JE003613.
- Oyarzun, R., C. Viedma, A. Márquez, and J. Lillo (2003), Freezing-resistant liquid water in porous media, a possible mechanism to account for the fluidized transport of sediments on Mars: an example from East Gorgonum crater: Fluidized sediment transport on Mars, *Terra Nova*, 15(4), 238–242, doi:10.1046/j.1365-3121.2003.00487.x.



- de Pablo, M. A., and J. D. C. Carrillo (2012), Geomorphological map of the lower NW flank of the Hecates Tholus volcano, Mars (scale 1:100,000), *J. Maps*, 8(3), 208–214, doi:10.1080/17445647.2012.703902.
- de Pablo, M. A., and A. G. Fairén (2004), Atlantis basin, Sirenum Terrae, Mars: geological setting and astrobiological implications, *Int. J. Astrobiol.*, 3(3), 257–263, doi:10.1017/S147355040400196X.
- Pajola, M., J. Carter, S. Rossato, E. Baratti, C. Mangili, K. S. McBride, and M. Coradini (2014), Eridania Paleolakes Basin Floor: A new Landing Site for the next Mars 2020 Rover, *LPI Contrib. No. 1791*, p. 1213.
- Pajola, M., S. Rossato, J. Carter, E. Baratti, R. Pozzobon, M. S. Erculiani, M. Coradini, and K. McBride (2016), Eridania Basin: An ancient paleolake floor as the next landing site for the Mars 2020 rover, *Icarus*, 275, 163–182, doi:10.1016/j.icarus.2016.03.029.
- Peate, D. W., J. A. Baker, S. P. Jakobsson, T. E. Waight, A. J. R. Kent, N. V. Grassineau, and A. C. Skovgaard (2008), Historic magmatism on the Reykjanes Peninsula, Iceland: a snap-shot of melt generation at a ridge segment, *Contrib. Mineral. Petrol.*, 157(3), 359, doi:10.1007/s00410-008-0339-4.
- Pechmann, J. C. (1980), The origin of polygonal troughs on the Northern Plains of Mars, *Icarus*, 42(2), 185–210, doi:10.1016/0019-1035(80)90071-8.
- Perron, J. T., J. X. Mitrovica, M. Manga, I. Matsuyama, and M. A. Richards (2007), Evidence for an ancient martian ocean in the topography of deformed shorelines, *Nature*, 447(7146), 840, doi:10.1038/nature05873.
- Phillips, R. J. et al. (2001), Ancient Geodynamics and Global-Scale Hydrology on Mars, *Science*, 291(5513), 2587–2591, doi:10.1126/science.1058701.
- Picardi, G. et al. (2005), Radar Soundings of the Subsurface of Mars, *Science*, 310(5756), 1925–1928, doi:10.1126/science.1122165.
- Pondrelli, M., A. P. Rossi, G. G. Ori, S. van Gasselt, D. Praeg, and S. Ceramicola (2011), Mud volcanoes in the geologic record of Mars: The case of Firsoff crater, *Earth Planet. Sci. Lett.*, 304(3–4), 511–519, doi:10.1016/j.epsl.2011.02.027.
- Potter, R. (2014), Degraded Basin, in *Encyclopedia of Planetary Landforms*, pp. 1–4, Springer New York.
- Poulet, F. et al. (2005), Phyllosilicates on Mars and implications for early martian climate, *Nature*, 438(7068), 623–627, doi:10.1038/nature04274.
- Prieto-Ballesteros, O., M. García-Villadangos, J. A. Rodríguez-Manfredi, F. Gómez, Y. Blanco, and V. Parro (2010), Antarctic permafrost studies for testing the Signs Of Life Detector (SOLID), *EPSC Abstracts*, vol. 5, p. 601.
- Prieto-Ballesteros, O., F. Gómez, M. Moreno, G. de Diego, M. Fernandez-Sampedro, M. P. Martín-Redondo, and V. Parro (2012), Underground warmed environments at cold regions. The case of Cerro Caliente in Deception island, Antarctica, *EPSC Abstracts*, vol. 7, p. 466.
- Putzig, N. E., and M. T. Mellon (2007), Apparent thermal inertia and the surface heterogeneity of Mars, *Icarus*, 191(1), 68–94, doi:10.1016/j.icarus.2007.05.013.
- Quantin, C. et al. (2015), Oxia Planum: a suitable landing site for ExoMars 2018 Rover, *EPSC Abstracts*, vol. 10, p. 704.
- Quantin, C. et al. (2016), Oxia Planum — The Landing Site for ExoMars 2018, *LPI Contrib. No. 1903*, p. 2863.

- Quesada, A., A. Camacho, C. Rochera, and D. Velázquez (2009), Byers Peninsula: A reference site for coastal, terrestrial and limnetic ecosystem studies in maritime Antarctica, *Polar Sci.*, 3(3), 181–187, doi:10.1016/j.polar.2009.05.003.
- Ramos, M., M. A. de Pablo, E. Sebastian, C. Armiens, and J. Gómez-Elvira (2012), Temperature gradient distribution in permafrost active layer, using a prototype of the ground temperature sensor (REMS-MSL) on deception island (Antarctica), *Cold Reg. Sci. Technol.*, 72, 23–32, doi:10.1016/j.coldregions.2011.10.012.
- Rice, M. S., E. A. Cloutis, J. F. Bell III, D. L. Bish, B. H. Horgan, S. A. Mertzman, M. A. Craig, R. W. Renaut, B. Gautason, and B. Mountain (2013), Reflectance spectra diversity of silica-rich materials: Sensitivity to environment and implications for detections on Mars, *Icarus*, 223(1), 499–533, doi:10.1016/j.icarus.2012.09.021.
- Robbins, S. J., and B. M. Hynek (2012), A new global database of Mars impact craters  $\geq 1$  km: 1. Database creation, properties, and parameters, *J. Geophys. Res. Planets*, 117(E5), E05004, doi:10.1029/2011JE003966.
- Rodriguez, J. A. P., T. Platz, V. Gulick, V. R. Baker, A. G. Fairén, J. Kargel, J. Yan, H. Miyamoto, and N. Glines (2015), Did the martian outflow channels mostly form during the Amazonian Period?, *Icarus*, 257, 387–395, doi:10.1016/j.icarus.2015.04.024.
- Russell, A. J., F. S. Tweed, M. J. Roberts, T. D. Harris, M. T. Gudmundsson, Ó. Knudsen, and P. M. Marren (2010), An unusual jökulhlaup resulting from subglacial volcanism, Sólheimajökull, Iceland, *Quat. Sci. Rev.*, 29(11–12), 1363–1381, doi:10.1016/j.quascirev.2010.02.023.
- Russell, P. S., and J. W. Head (2007), The Martian hydrologic system: Multiple recharge centers at large volcanic provinces and the contribution of snowmelt to outflow channel activity, *Planet. Space Sci.*, 55(3), 315–332, doi:10.1016/j.pss.2006.03.010.
- Salamunićcar, G., and S. Lončarić (2008), GT-57633 catalogue of Martian impact craters developed for evaluation of crater detection algorithms, *Planet. Space Sci.*, 56(15), 1992–2008, doi:10.1016/j.pss.2008.09.010.
- Salamunićcar, G., S. Lončarić, and E. Mazarico (2012), LU60645GT and MA132843GT catalogues of Lunar and Martian impact craters developed using a Crater Shape-based interpolation crater detection algorithm for topography data, *Planet. Space Sci.*, 60(1), 236–247, doi:10.1016/j.pss.2011.09.003.
- Scholten, F., K. Gwinner, T. Roatsch, K. –. Matz, M. Wählisch, B. Giese, J. Oberst, R. Jaumann, and G. Neukum (2005), Mars Express HRSC data processing - Methods and operational aspects., *Photogramm. Eng. Remote Sens.*, 1143–1152, doi:10.14358/PERS.71.10.1143.
- Schultz, P. H., and A. B. Lutz (1988), Polar wandering of Mars, *Icarus*, 73(1), 91–141, doi:10.1016/0019-1035(88)90087-5.
- Schultz, R. A. (1998), Multiple-process origin of Valles Marineris basins and troughs, Mars, *Planet. Space Sci.*, 46(6–7), 827–834, doi:10.1016/S0032-0633(98)00030-0.
- Schultz, R. A., and K. L. Tanaka (1994), Lithospheric-scale buckling and thrust structures on Mars: The Coprates rise and south Tharsis ridge belt, *J. Geophys. Res.*, 99(E4), 8371, doi:10.1029/94JE00277.
- Scott, D. H., and K. L. Tanaka (1986), Geologic map of the western equatorial region of Mars, *USGS Numbered Series*, IMAP 1802-A. Scale 1:500,000.
- Sharp, R. P. (1973), Mars: Fretted and chaotic terrains, *J. Geophys. Res.*, 78(20), 4073–4083, doi:10.1029/JB078i020p04073.

- Sharp, R. P. (1980), Geomorphological Processes on Terrestrial Planetary Surfaces, *Annu. Rev. Earth Planet. Sci.*, 8(1), 231–261, doi:10.1146/annurev.ea.08.050180.001311.
- Sharp, R. P., and M. C. Malin (1975), Channels on Mars, *Geol. Soc. Am. Bull.*, 86(5), 593–609, doi:10.1130/0016-7606(1975)86<593:COM>2.0.CO;2.
- Shean, D. E., J. Fahle, M. C. Malin, L. J. Edwards, and L. Posiolova (2011), MRO CTX Stereo Image Processing and Preliminary DEM Quality Assessment, *LPI Contrib. No. 1608*, p. 2646.
- Smith, D., G. Neumann, R. Arvidson, E. Guinness, and S. Slavney (2003), *Mars global surveyor laser altimeter mission experiment gridded data record. MGS-M-MOLA-5-MEGDR-L3-V1.0*, NASA Planetary Data System.
- Smith, D. E. et al. (1999a), The Global Topography of Mars and Implications for Surface Evolution, *Science*, 284(5419), 1495–1503, doi:10.1126/science.284.5419.1495.
- Smith, D. E., W. L. Sjogren, G. L. Tyler, G. Balmino, F. G. Lemoine, and A. S. Konopliv (1999b), The Gravity Field of Mars: Results from Mars Global Surveyor, *Science*, 286(5437), 94–97, doi:10.1126/science.286.5437.94.
- Smith, D. E. et al. (2001), Mars Orbiter Laser Altimeter: Experiment summary after the first year of global mapping of Mars, *J. Geophys. Res. Planets*, 106(E10), 23689–23722, doi:10.1029/2000JE001364.
- Smith, M. R., J. L. Bandfield, E. A. Cloutis, and M. S. Rice (2013), Hydrated silica on Mars: Combined analysis with near-infrared and thermal-infrared spectroscopy, *Icarus*, 223(2), 633–648, doi:10.1016/j.icarus.2013.01.024.
- Stolper, E. (1982), Water in silicate glasses: An infrared spectroscopic study, *Contrib. Mineral. Petrol.*, 81(1), 1–17, doi:10.1007/BF00371154.
- Tanaka, K. (2000), Dust and Ice Deposition in the Martian Geologic Record, *Icarus*, 144(2), 254–266, doi:10.1006/icar.1999.6297.
- Tanaka, K. L. (1997), Sedimentary history and mass flow structures of Chryse and Acidalia Planitiae, Mars, *J. Geophys. Res. Planets*, 102(E2), 4131–4149, doi:10.1029/96JE02862.
- Tanaka, K. L., N. K. Isbell, D. H. Scott, R. Greeley, and J. E. Guest (1988), The resurfacing history of Mars - A synthesis of digitized, viking-based geology, *LPI Contrib. No. 1585*, pp. 665–678.
- Tanaka, K. L., J. A. Skinner, and T. M. Hare (2005), Geologic map of the northern plains of Mars, *USGS Scientific Investigations Map 2888*. Scale 1:2,000,000.
- Tanaka, K. L., J. A. Skinner Jr, J. M. Dohm, R. P. Irwin III, E. J. Kolb, C. M. Fortezzo, T. Platz, G. G. Michael, and T. M. Hare (2014), Geologic map of Mars, *USGS Scientific Investigations Map 3292*. Scale 1:20,000,000.
- Thomas, R. J., B. M. Hynek, M. M. Osterloo, and K. S. Kierein-Young (2017), Widespread exposure of Noachian phyllosilicates in the Margaritifer region of Mars: Implications for paleohydrology and astrobiological detection, *J. Geophys. Res. Planets*, 2016JE005183, doi:10.1002/2016JE005183.
- Toon, O. B., J. B. Pollack, and C. Sagan (1977), Physical properties of the particles composing the Martian dust storm of 1971–1972, *Icarus*, 30(4), 663–696, doi:10.1016/0019-1035(77)90088-4.
- Torson, J. M., and K. J. Becker (1997), ISIS - A Software Architecture for Processing Planetary Images, *LPI Contrib. No. 1090*, p. 1443.
- USGS Astrogeology Team (1999), United States Geological Survey Integrated Software for Imaging Spectrometers (ISIS), <https://isis.astrogeology.usgs.gov>.

- Viviano-Beck, C. E. et al. (2014), Revised CRISM spectral parameters and summary products based on the currently detected mineral diversity on Mars, *J. Geophys. Res. Planets*, 119(6), 2014JE004627, doi:10.1002/2014JE004627.
- Wang, H., and M. I. Richardson (2015), The origin, evolution, and trajectory of large dust storms on Mars during Mars years 24–30 (1999–2011), *Icarus*, 251, 112–127, doi:10.1016/j.icarus.2013.10.033.
- Watters, T. R. (1993), Compressional tectonism on Mars, *J. Geophys. Res. Planets*, 98(E9), 17049–17060, doi:10.1029/93JE01138.
- Webb, V. E. (2004), Putative shorelines in northern Arabia Terra, Mars, *J. Geophys. Res. Planets*, 109(E9), E09010, doi:10.1029/2003JE002205.
- Wendt, L., J. L. Bishop, and G. Neukum (2012), Phyllosilicates in the Knob Fields around Ariadnes Colles on Mars: Stratigraphy, Mineralogy and Morphology, *Geophysical Research Abstracts*, vol. 14, EGU2012-9105.
- Wendt, L., J. L. Bishop, and G. Neukum (2013), Knob fields in the Terra Cimmeria/Terra Sirenum region of Mars: Stratigraphy, mineralogy and morphology, *Icarus*, 225(1), 200–215, doi:10.1016/j.icarus.2013.03.020.
- Wentworth, C. K. (1922), A Scale of Grade and Class Terms for Clastic Sediments, *J. Geol.*, 30, 377–392, doi:10.1086/622910.
- Werner, S. C. (2009), The global martian volcanic evolutionary history, *Icarus*, 201(1), 44–68, doi:10.1016/j.icarus.2008.12.019.
- Westall, F., H. G. Edwards, L. Whyte, A. G. Fairén, J.-P. Bibring, J. C. Bridges, E. Hauber, G.-G. Ori, and others (2014), Recommendation for the Narrowing of ExoMars 2018 Landing Sites, *Jet Propuls. Lab. Calif. Inst. Technol. Pasadena CA, EXM-SCI-LSS-ESA/IKI-004*.
- White, O. L., A. Safaeinili, J. J. Plaut, E. R. Stofan, S. M. Clifford, W. M. Farrell, E. Heggy, and G. Picardi (2009), MARSIS radar sounder observations in the vicinity of Ma'adim Vallis, Mars, *Icarus*, 201(2), 460–473, doi:10.1016/j.icarus.2009.01.015.
- Wilhelms, D. E. (1990), Geologic mapping, in *Planetary Mapping*, edited by R. Greeley and R. M. Batson, pp. 208–260, Cambridge University Press, NY.
- Williams, R. M. E., and K. S. Edgett (2005), Valleys in the Martian Rock Record, in *36th Annual Lunar and Planetary Science Conference*, vol. 36.
- Wilson, L., and J. W. Head (2002), Tharsis-radial graben systems as the surface manifestation of plume-related dike intrusion complexes: Models and implications, *J. Geophys. Res. Planets*, 107(E8), 1–1–1–24, doi:10.1029/2001JE001593.
- Wilson, L., and P. J. Mouginis-Mark (2014), Dynamics of a fluid flow on Mars: Lava or mud?, *Icarus*, 233, 268–280, doi:10.1016/j.icarus.2014.01.041.
- Wray, J. J., B. L. Ehlmann, S. W. Squyres, J. F. Mustard, and R. L. Kirk (2008), Compositional stratigraphy of clay-bearing layered deposits at Mawrth Vallis, Mars, *Geophys. Res. Lett.*, 35(12), L12202, doi:10.1029/2008GL034385.
- Wray, J. J., S. W. Squyres, L. H. Roach, J. L. Bishop, J. F. Mustard, and E. Z. Noe Dobrea (2010), Identification of the Ca-sulfate bassanite in Mawrth Vallis, Mars, *Icarus*, 209(2), 416–421, doi:10.1016/j.icarus.2010.06.001.
- Yamanaka, T. et al. (2013), Shallow submarine hydrothermal activity with significant contribution of magmatic water producing talc chimneys in the Wakamiko Crater of Kagoshima Bay, southern Kyushu, Japan, *J. Volcanol. Geotherm. Res.*, 258, 74–84, doi:10.1016/j.jvolgeores.2013.04.007.

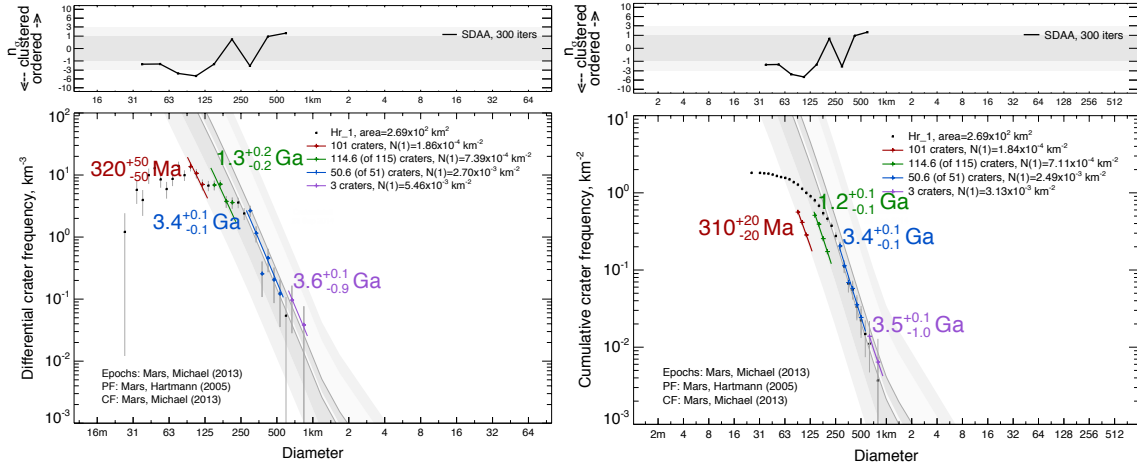
- Zegers, T. E., J. H. P. Oosthoek, A. P. Rossi, J. K. Blom, and S. Schumacher (2010), Melt and collapse of buried water ice: An alternative hypothesis for the formation of chaotic terrains on Mars, *Earth Planet. Sci. Lett.*, 297(3-4), 496-504, doi:10.1016/j.epsl.2010.06.049.
- Zhang, Z., T. Hagfors, E. Nielsen, G. Picardi, A. Mesdea, and J. J. Plaut (2008), Dielectric properties of the Martian south polar layered deposits: MARSIS data inversion using Bayesian inference and genetic algorithm, *J. Geophys. Res.*, 113(E5), doi:10.1029/2007JE002941.
- Zolotov, M. Y., and M. V. Mironenko (2014), Massive Sulfate Deposits on Mars Could be Remobilized Noachian Salts, *LPI Contrib. No. 1777*, p. 2876.
- Zuber, M. T. (2001), The crust and mantle of Mars, *Nature*, 412(6843), 220-227, doi:10.1038/35084163.
- Zuber, M. T., D. E. Smith, S. C. Solomon, D. O. Muhleman, J. W. Head, J. B. Garvin, J. B. Abshire, and J. L. Bufton (1992), The Mars Observer laser altimeter investigation, *J. Geophys. Res. Planets*, 97(E5), 7781-7797, doi:10.1029/92JE00341.
- Zuber, M. T. et al. (2000), Internal Structure and Early Thermal Evolution of Mars from Mars Global Surveyor Topography and Gravity, *Science*, 287(5459), 1788-1793, doi:10.1126/science.287.5459.1788.



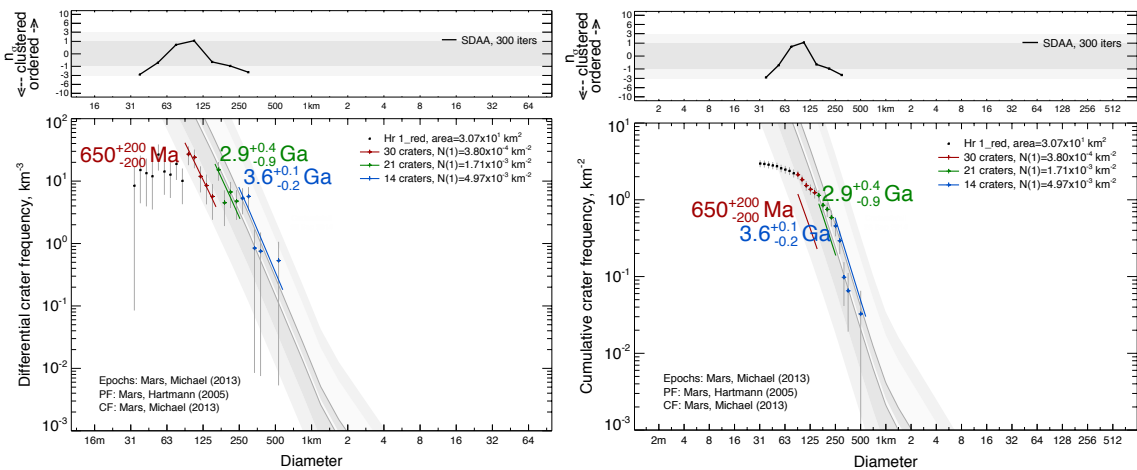
## 8 APPENDICES

### 8.1 CSFD PLOTS FOR ARIADNES AREAS

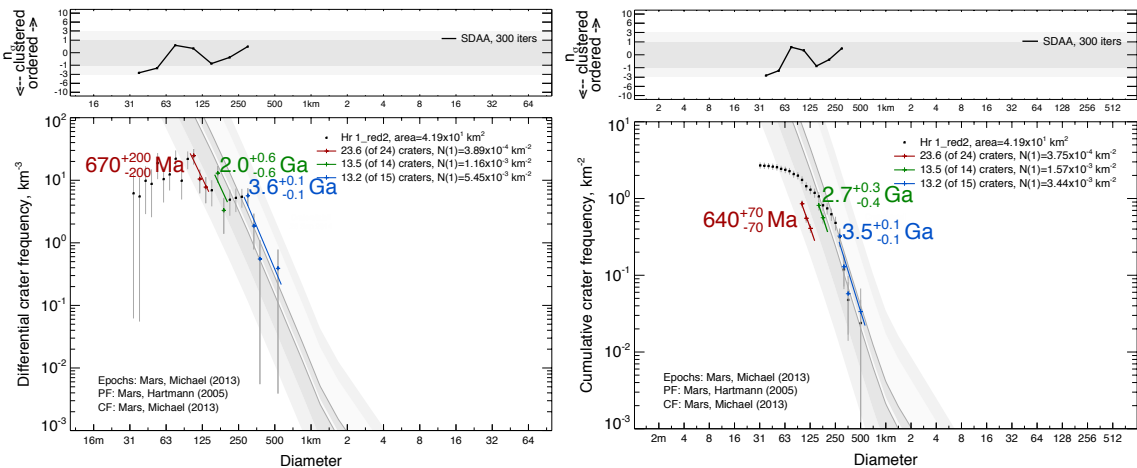
#### AHrp1



#### AHrp1R

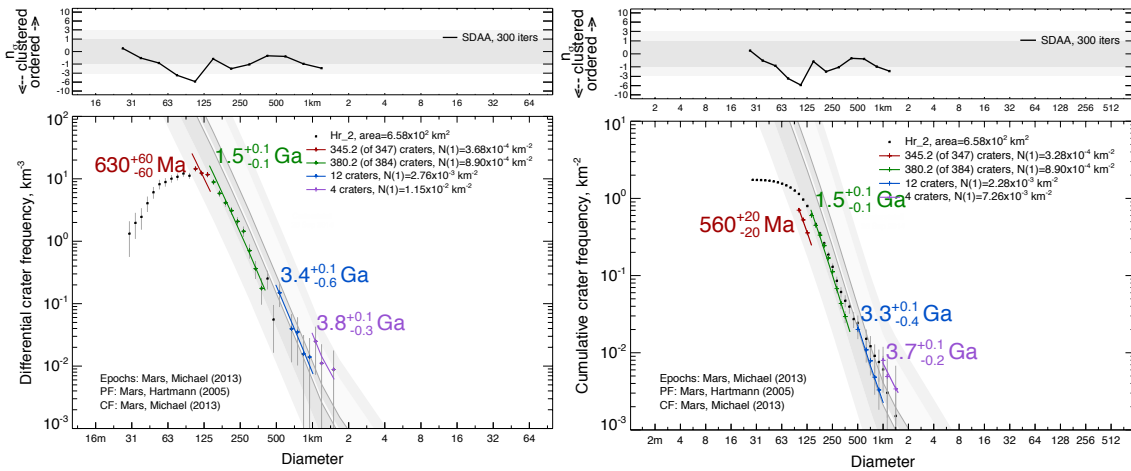


#### AHrp1R2

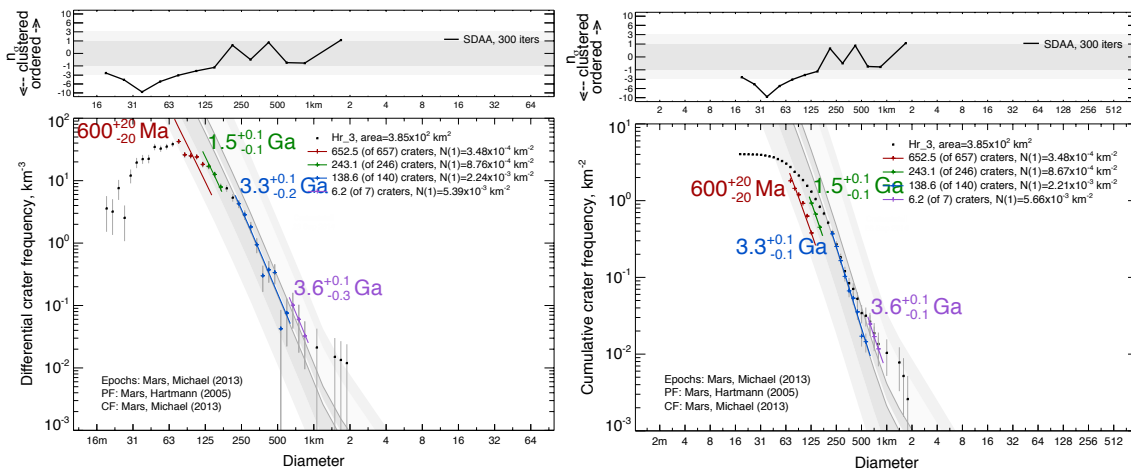


Paleoenvironmental Characterization of the Noachian-Hesperian Transition on Mars

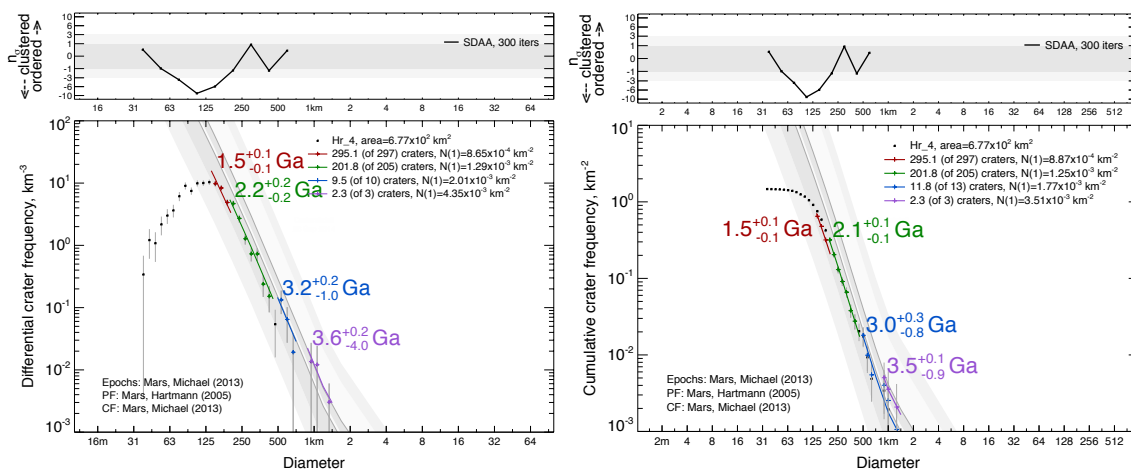
AHrp2

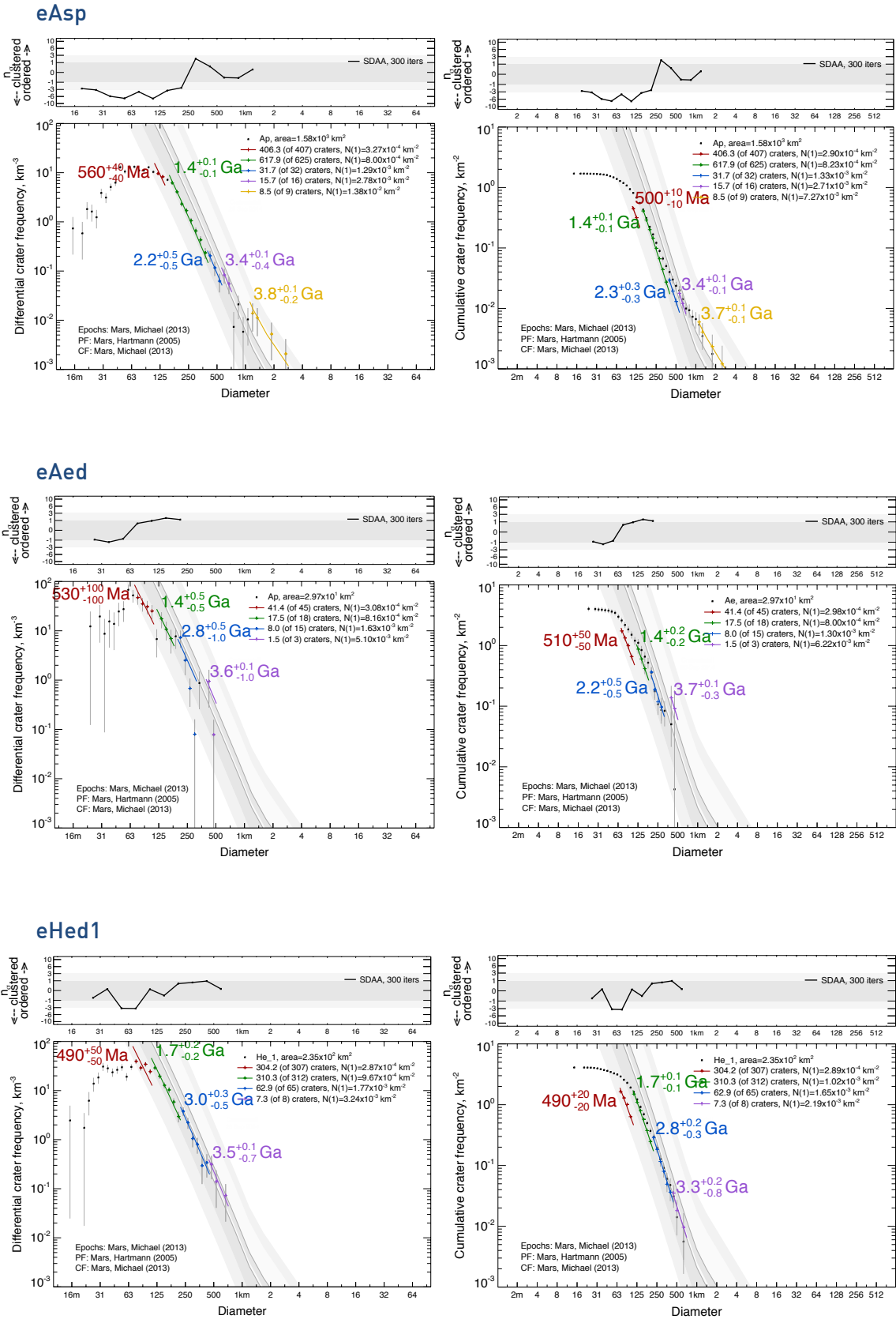


AHrp3

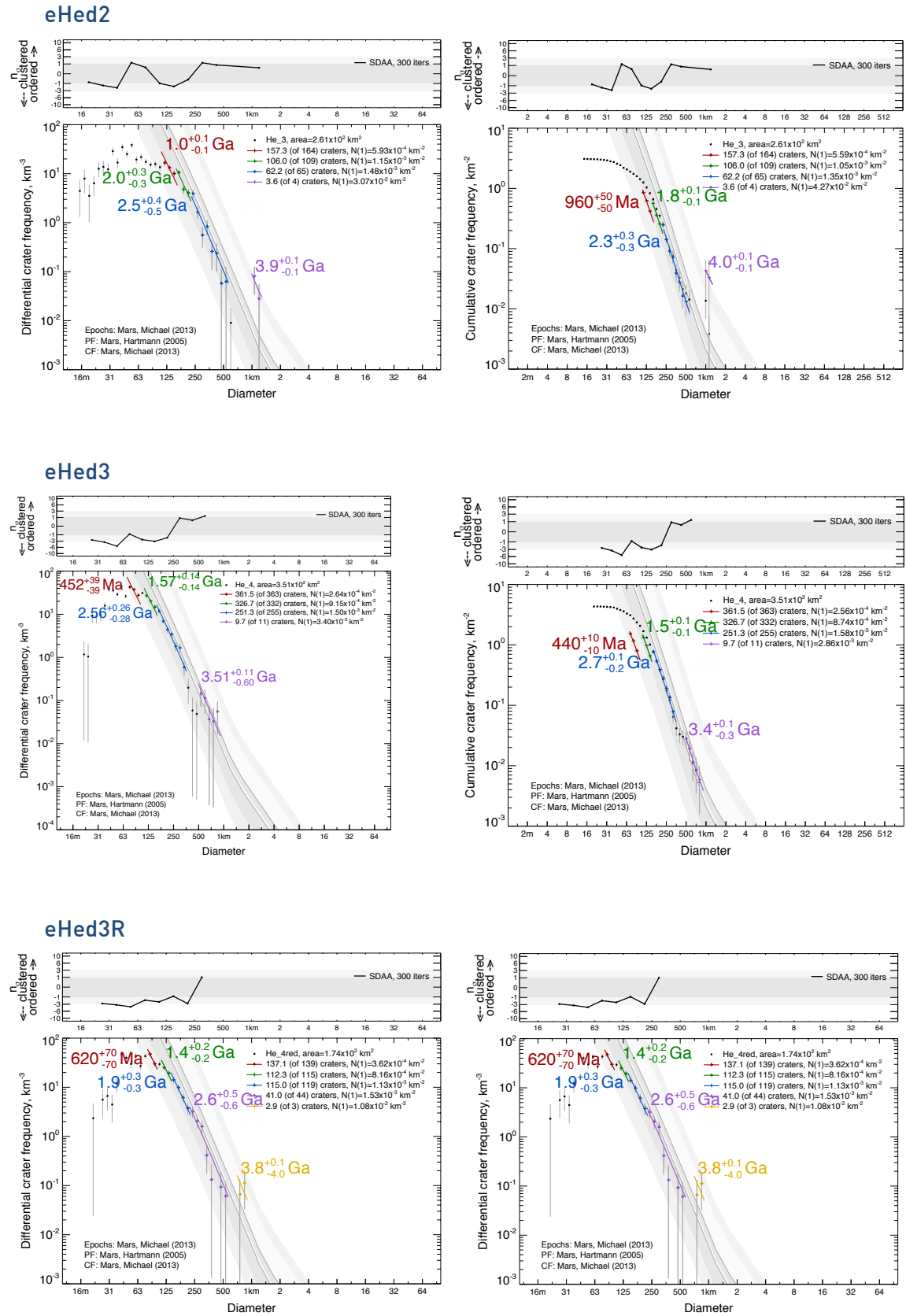


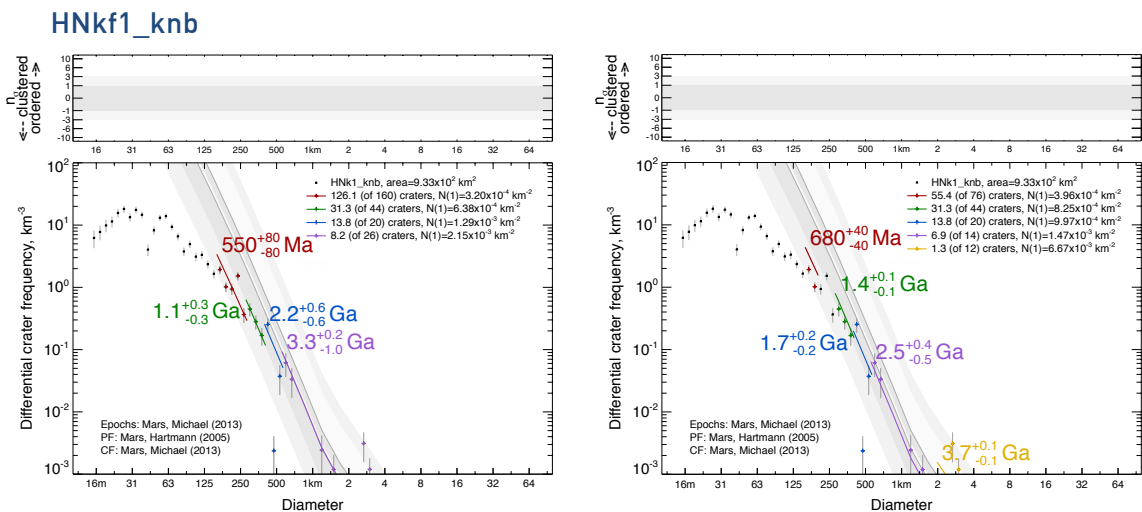
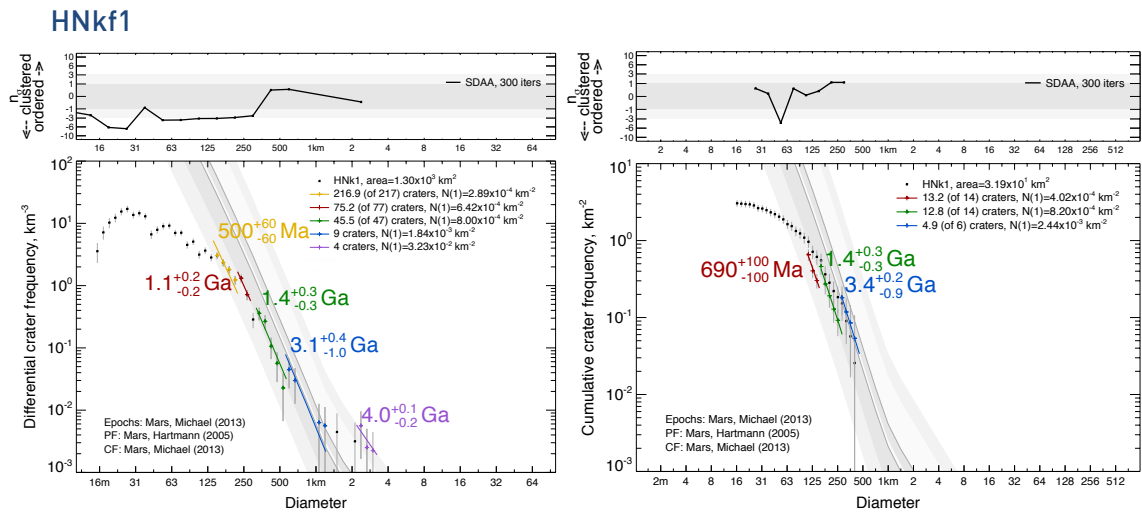
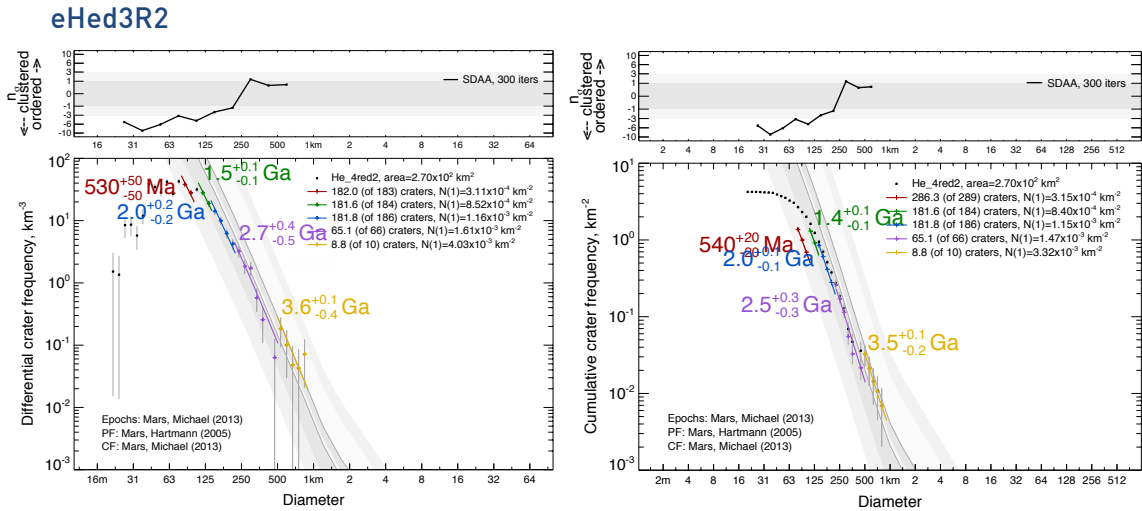
AHrp4





# Paleoenvironmental Characterization of the Noachian-Hesperian Transition on Mars

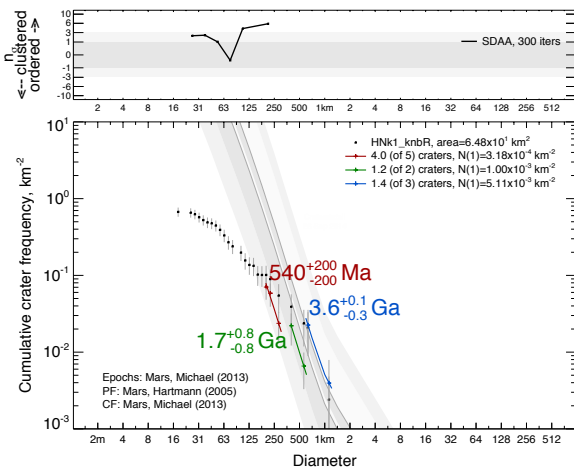
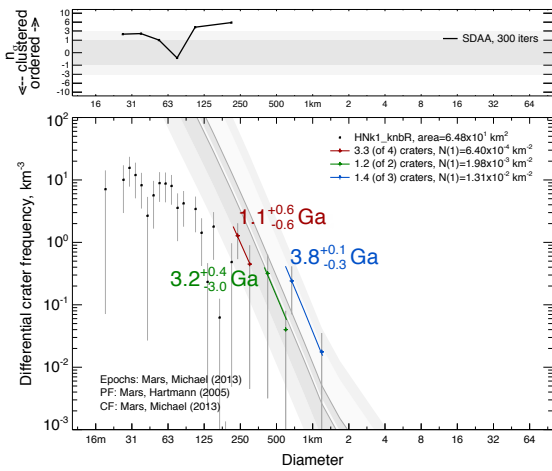




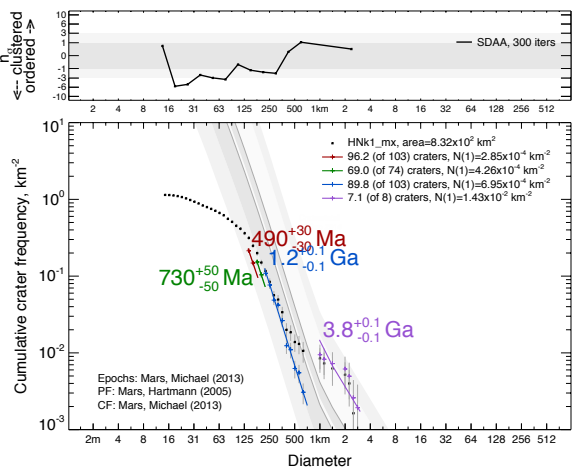
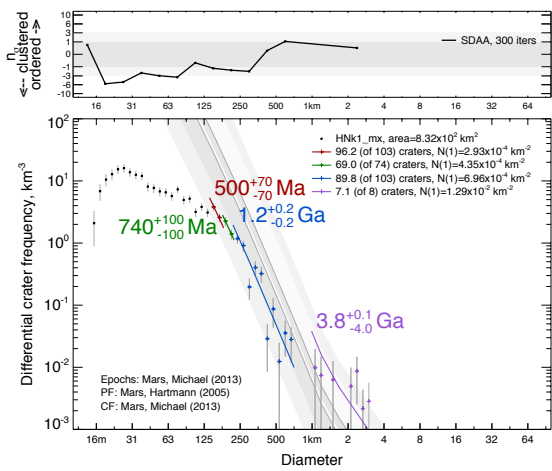


Paleoenvironmental Characterization of the Noachian-Hesperian Transition on Mars

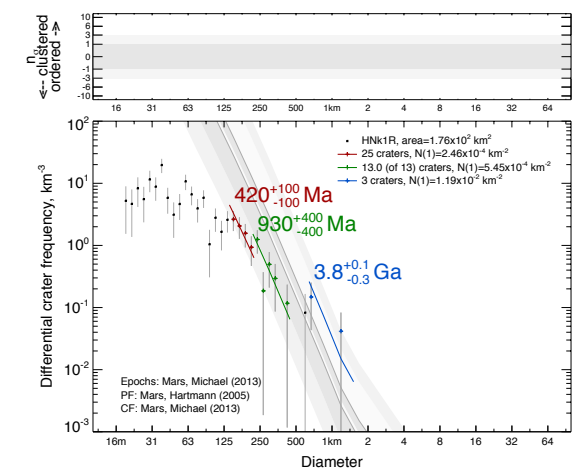
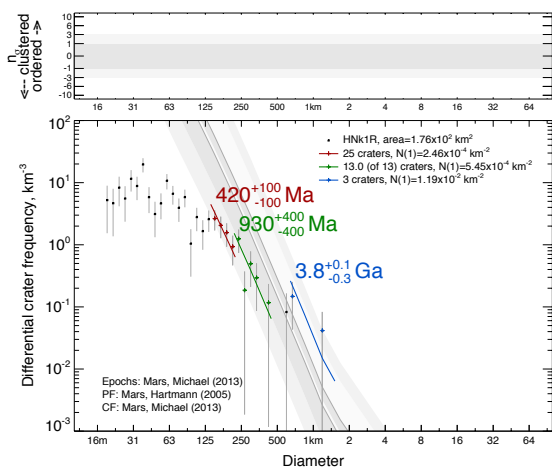
HNkf1\_knb2



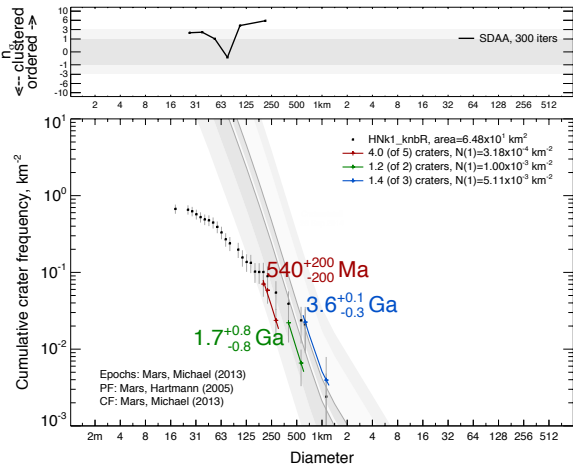
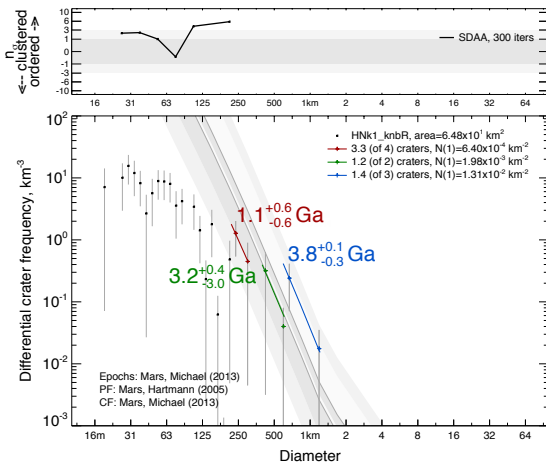
HNkf1\_mx



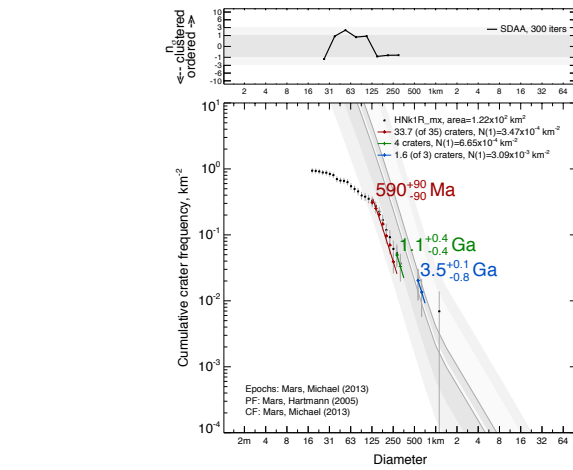
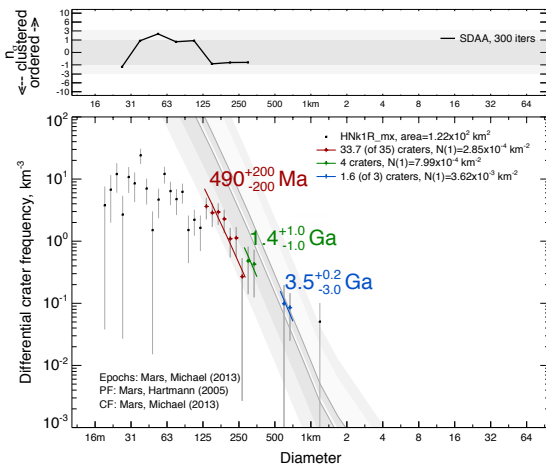
HNkf1R



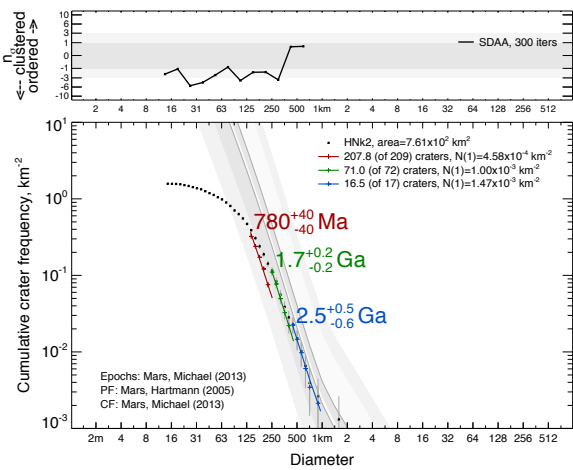
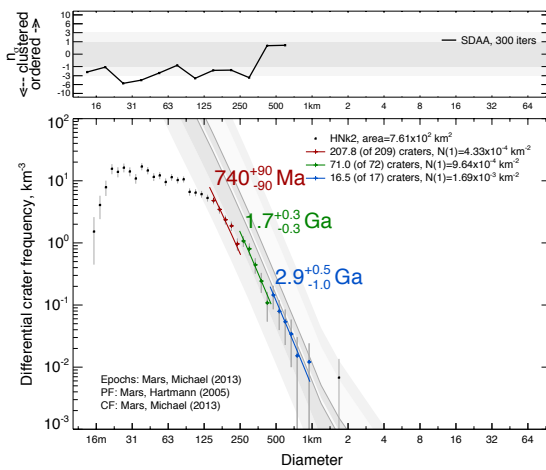
### HNkf1R\_knb



### HNkf1R\_mx

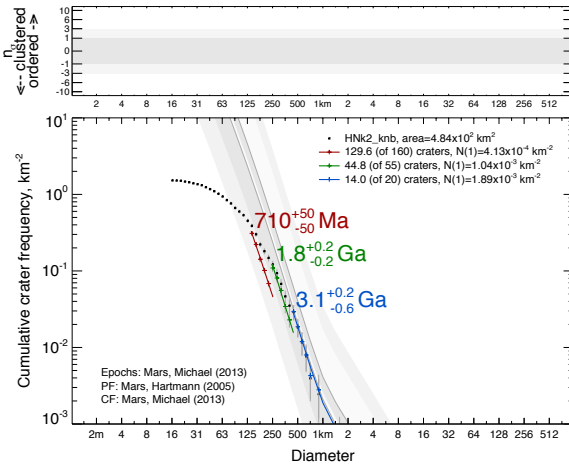
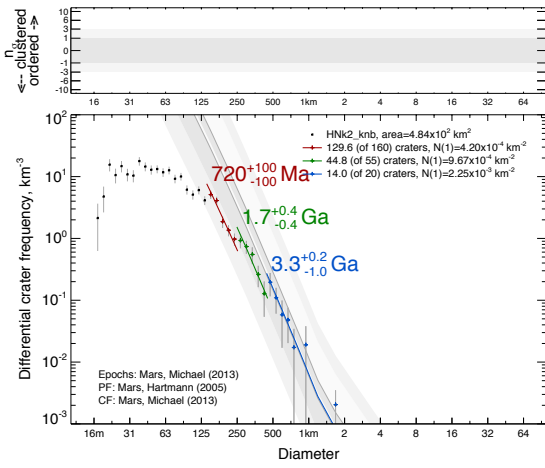


### HNkf2

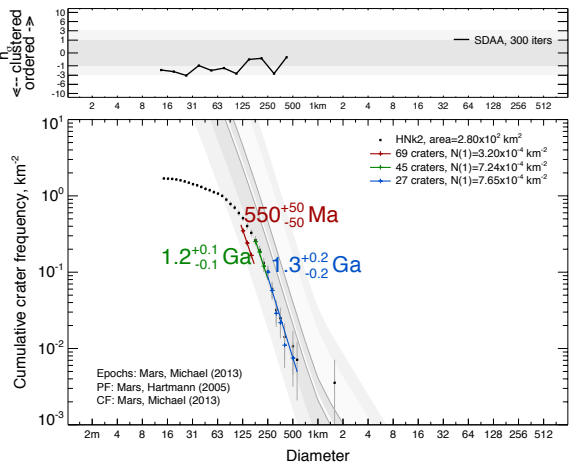
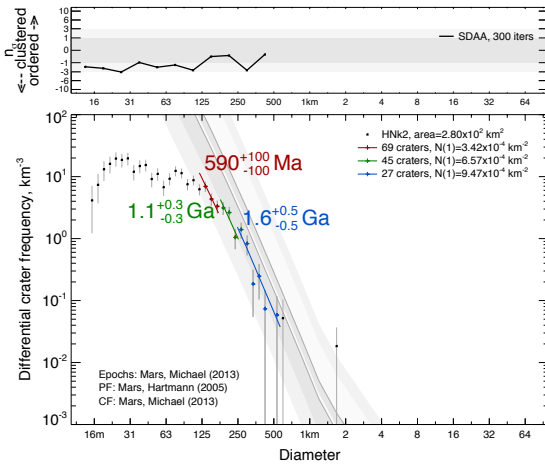


Paleoenvironmental Characterization of the Noachian-Hesperian Transition on Mars

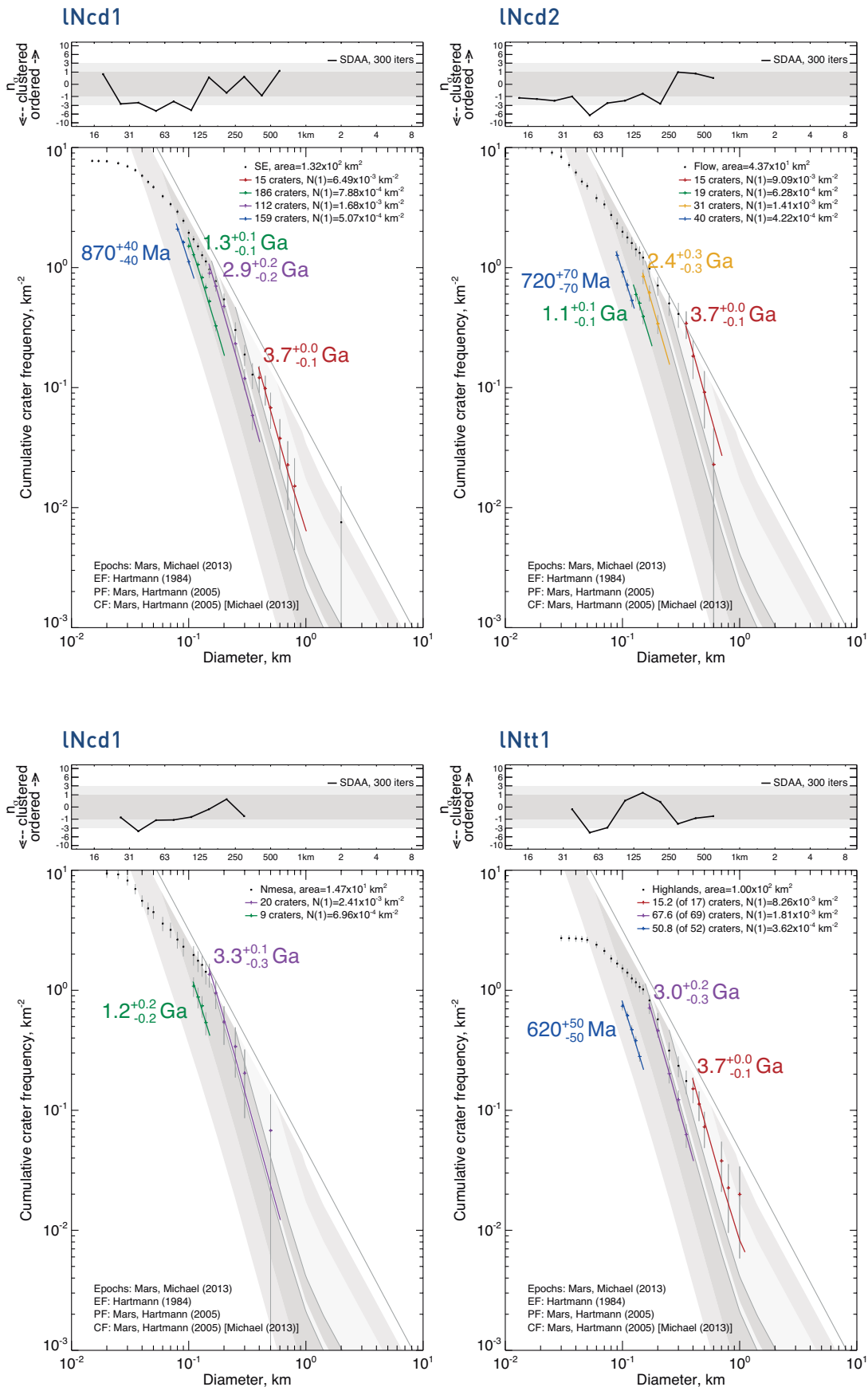
HNk2\_knb



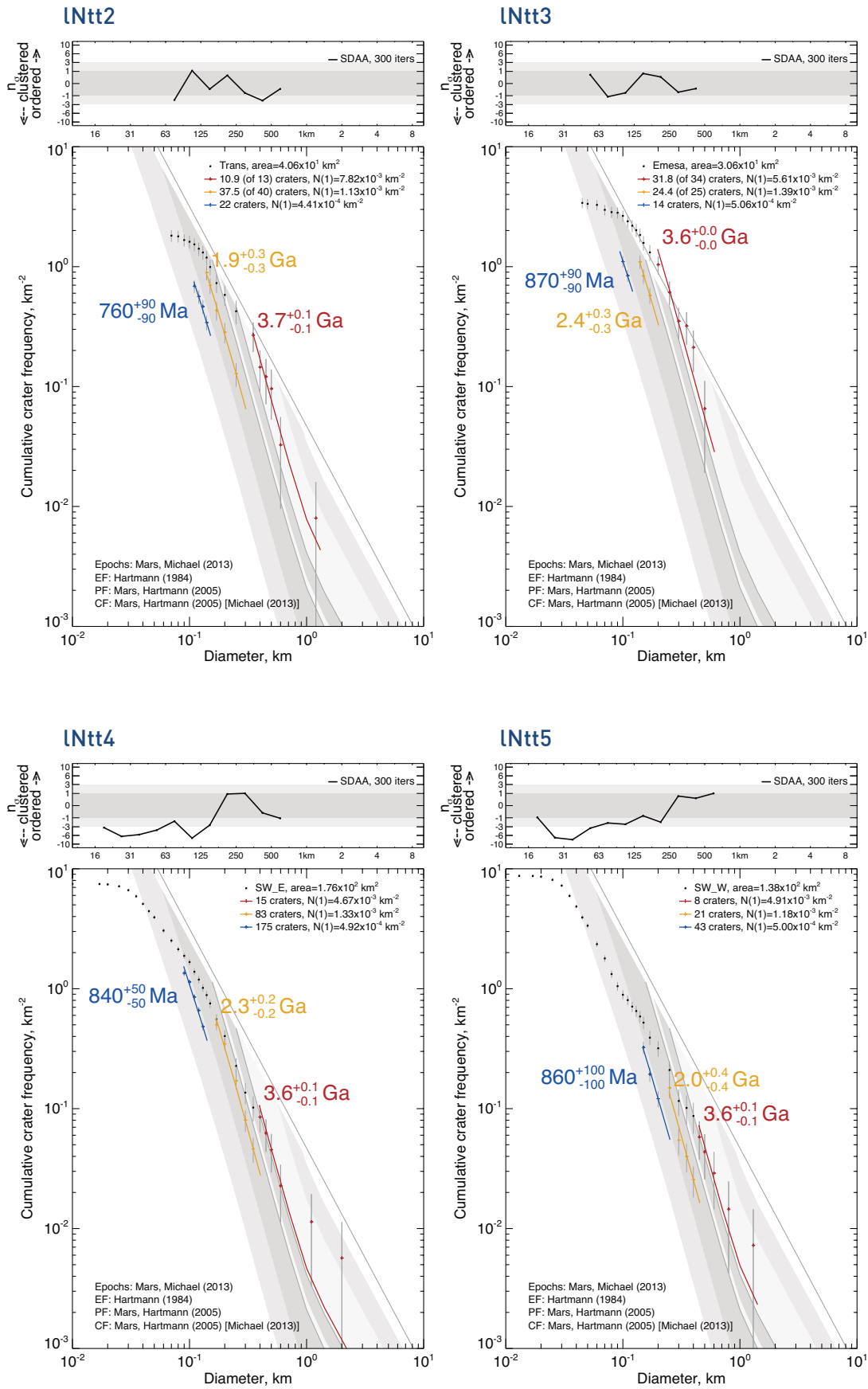
HNk2\_mx



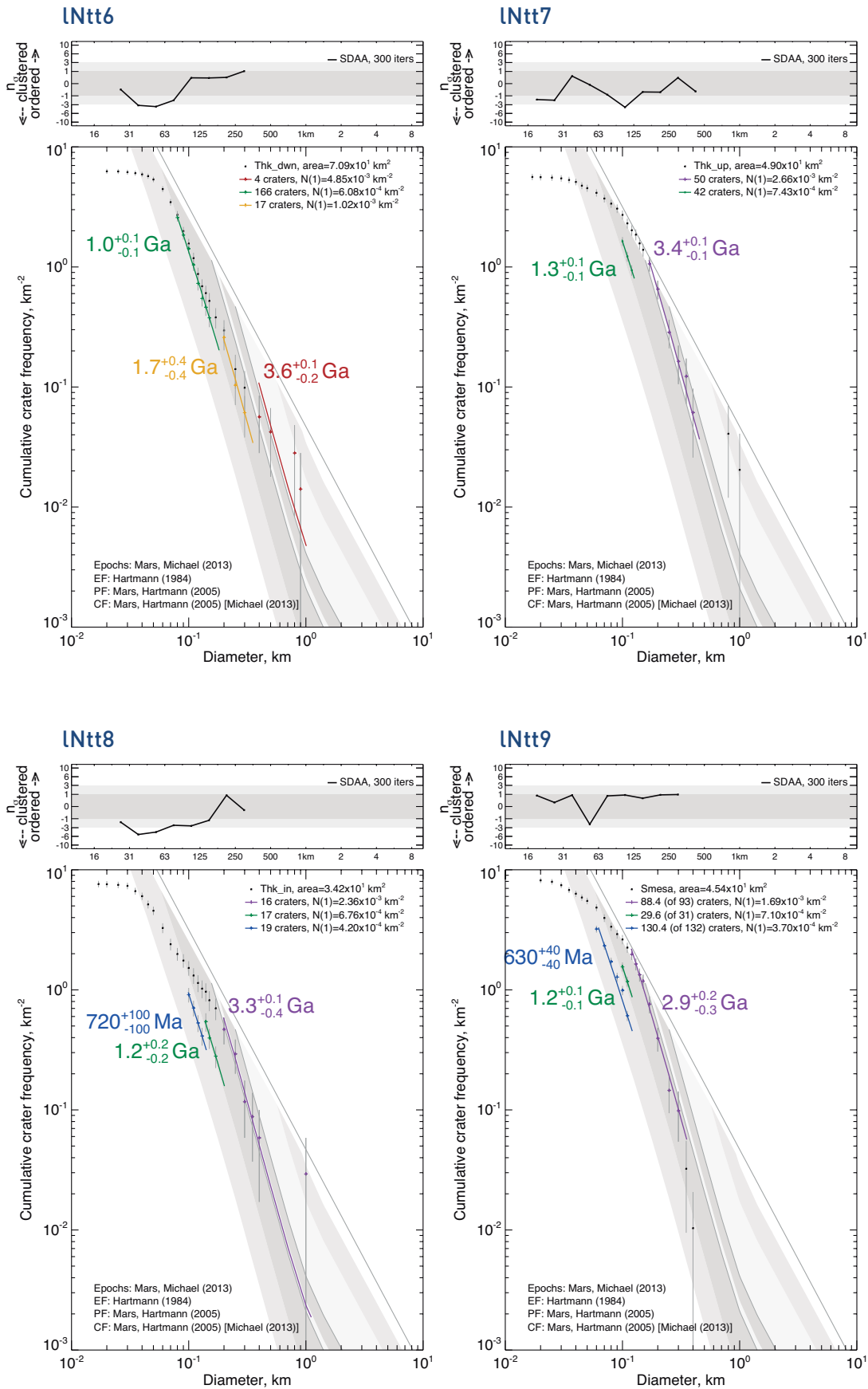
## 8.2 CSFD PLOTS FOR COOGOON AREAS



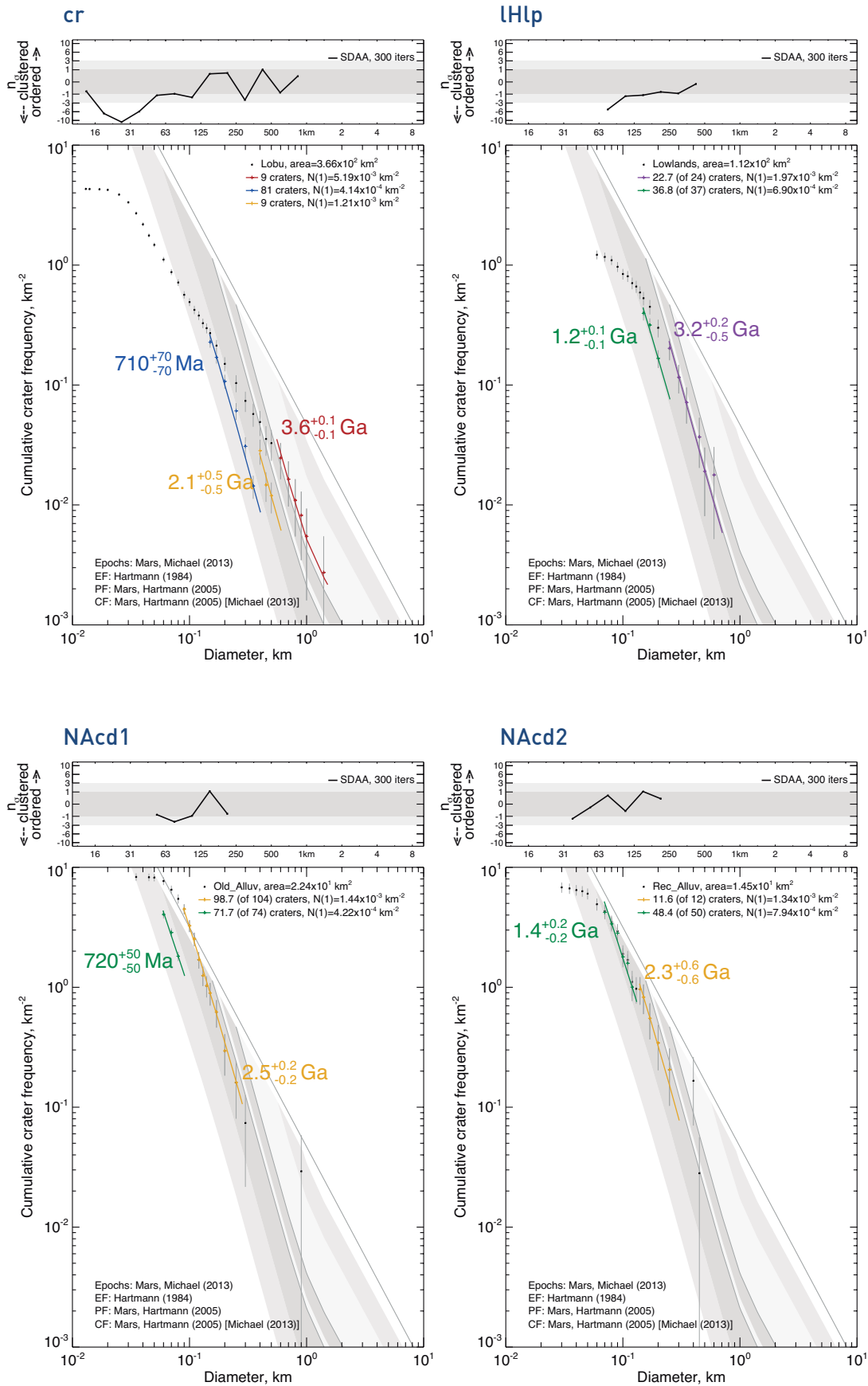
Paleoenvironmental Characterization of the Noachian-Hesperian Transition on Mars

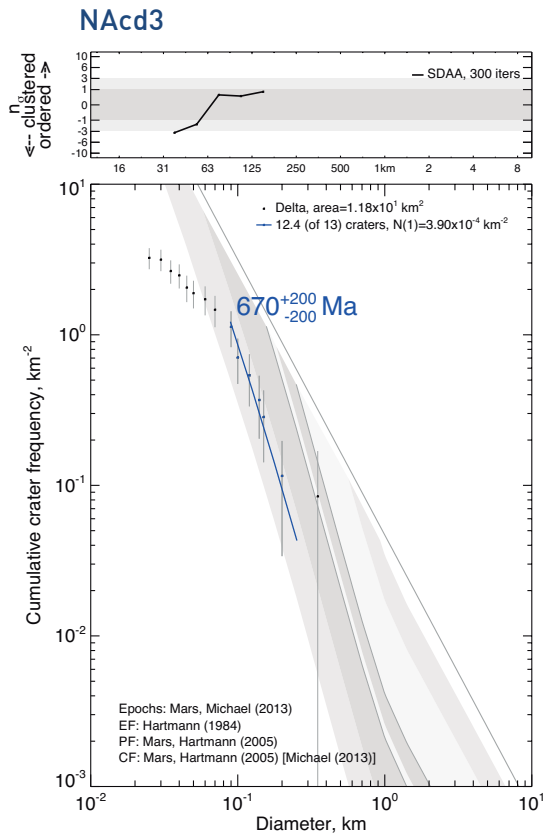






Paleoenvironmental Characterization of the Noachian-Hesperian Transition on Mars





### 8.3 MEASURED DIMENSIONS OF THE UNCERTAIN ORIGIN DEPRESSIONS

Dimension of the depressions located in Ariadnes and Coogoon plotted in [Figure 4.2.l](#).

FEATURE	LENGTH OF MAJOR AXIS (km)	LENGTH OF MINOR AXIS (km)
<b>ARIADNES</b>		
Ariadnes	250	180
Caralis	180	280
Atlantis	240	200
Gorgonum	260	230
Simois	180	170
Unnamed to the S	180	115
<b>COOGOON</b>		
4.2.k-A	19	18
4.2.k-C	16	16
To the West	23	17
To the East	19	16
4.2.k-C to the E	6	4
4.2.k-B	19	8
4.2.k-D	14	5

## 8.4 SPECTRAL SAMPLES

Source and sample ID of the laboratory analog material samples which spectral signature is displayed in [Figure 3.4.c](#) and [Figure 4.4.c](#). RELAB is the KECK/NASA Reflectance Experiment Laboratory ([Table 2.1.a](#)).

LABEL	SOURCE	SAMPLE ID
<b>A. Smectite</b>		
<b>Mg-smectite</b>	RELAB	Saponite LASA5
<b>Fe-smectite</b>	RELAB	Nontronite NCJB26
<b>Talc</b>	[Clark et al., 1990]	Talc GDS23
<b>B. Al-S &amp; Halides</b>		
<b>Hydrated Silica</b>	RELAB	Hydrated Si BKR1JB329C
<b>Kaolinite</b>	RELAB	Kaolinite LAKA04
<b>Al-smectite</b>	RELAB	Montmorillonite LAM002
<b>Illite</b>	RELAB	Illite LAIL02
<b>C. Sulfates</b>		
<b>Jarosite</b>	RELAB	Jarosite LASF21A
<b>Polyhydrated sulfate</b>	RELAB	Mg Sulfate 799F366
<b>Kaolinite</b>	RELAB	Kaolinite LAKA04
<b>Bassanite</b>	[Clark et al., 1990]	Bassanite GDS145
<b>Rozenite</b>	RELAB	Rozenite BKR1JB626B

## 8.5 ACADEMIC ACTIVITY DURING THE PH.D.

### 8.5.1 COURSES

*Training class in the development of SPICE-based applications supporting space science research*, 15/09/2016 (35 h) by NASA's Navigation and Ancillary Information Facility (NAIF).

*An Introduction to Interactive Programming in Python*, 03/06/2014 by Rice University (Coursera), certificate [coursera.org/verify/5K4WZEMVET](https://coursera.org/verify/5K4WZEMVET).

*Maps and the Geospatial Revolution* (with distinction), 01/09/2013 by The Pennsylvania State University (Coursera).

*Astrobiology and the Search for Extraterrestrial Life* (with distinction), 16/03/2013 by The University of Edinburgh (Coursera).

*Nordic-NASA Summer School "Water, Ice and the Origin of Life in the Universe"*, 15/07/2012 (120 h) by Nordic Network of Astrobiology and University of Hawai'i.

*ArcGIS Desktop II Tools and Functionality*, 12/04/2012 (16 h) by ESRI.

*Introduction to Astronomy and Astrophysics*, 29/03/2012 (24 h) by Madrid Planetarium.

*Immersion in the English language, Specialization: Life sciences and health (B2)*, 18/11/2011 (50 h) by Menéndez Pelayo International University.

*Navigation workshop in inflatable boats and maritime security in Antarctica*, 30/09/2011 (15 h) by Andalusian Centre for Marine Science and Technology.

*Preparation course for Antarctic research*, 23/09/2011 (10 h) by Spanish Polar Committee.

*International School of Astrobiology «Josep Comas i Solà». Mars Exploration: Unveiling an Habitable Planet*, 01/07/2011 (30 h) by Menéndez Pelayo International University, CAB, NASA, ESA, INTA and Science and Innovation Spanish Ministry.

### 8.5.2 TEACHING EXPERIENCE

Summer course 'Física y Astronomía Recreativas' (3 h) during 2015.

Workshop 'Explorando Marte desde el ordenador: Taller de análisis de imágenes' (6 h each) for the Semana de la Ciencia during the years 2010, 2011, 2012, and 2014.

### 8.5.3 PARTICIPATION IN R & D PROJECTS FUNDED IN PUBLIC CALLS

*Caracterización y evolución de la cubierta nival y su efecto en el régimen térmico del permafrost y la capa activa en las islas Livingston y Decepción (Antártida) (CTM2014-52021-R)*, 2015 to 2018 (3 yrs) funded by the Education and Science Ministry with Miguel Ángel de Pablo Hernández as Principal Researcher (P.I).

*Ciencia y tecnología de instrumentos espaciales para la caracterización del ambiente marciano en múltiples misiones de NASA: REMS, TWINS y MEDA (ESP2014-54256-C4-1-R)*, 2015 (1 yr) funded by the Economy and Competitiveness Ministry. Duration and with Jose Antonio Rodriguez Manfredi as Principal Researcher (P.I),

*Mantenimiento y actualización de las estaciones CALM y TSP en las Islas Livingston y Decepción, Antártida. ANTARPERMA (CTM2011-15565-E)*, 2011 to 2014 (3 yrs) funded by the Education and Science Ministry with Miguel Ángel de Pablo Hernández as Principal Researcher (P.I).



Science and technology development for in situ detection and characterization of subsurface life on the Iberian Pyritic Belt, IPBSL (**ERC-2009-AdG-250350**), 2010 to 2015 (5 yrs) funded by the European Union and the ERC with Ricardo Amils Pibernat as Principal Researcher (P.I)

Modelización y seguimiento de la capa activa y el permafrost en Livingston y Decepción. Antártida. PERMAPLANET (**CTM009-10165**), 2009 to 2012 (3 yrs) funded by the Education and Science Ministry with Miguel Ramos Sainz as Principal Researcher (P.I).

#### 8.5.4 PUBLICATIONS AND OTHER SCIENTIFIC-TECHNICAL DOCUMENTS

Ramos, M., G. Vieira, M. A. de Pablo, **A. Molina**, A. Abramov, and G. Goyanes (2017), Recent shallowing of the thaw depth at Crater Lake, Deception Island, Antarctica (2006–2014), *CATENA*, 149, Part 2, 519–528, doi:10.1016/j.catena.2016.07.019.

**Molina, A.**, I. López, O. Prieto-Ballesteros, D. Fernández-Remolar, M. Á. de Pablo, and F. Gómez (2017), Coogoon Valles, western Arabia Terra: Hydrological evolution of a complex Martian channel system, *Icarus*, 293, 27–44, doi:10.1016/j.icarus.2017.04.002.

de Pablo, M. A., M. Ramos, and **A. Molina** (2017), Snow cover evolution, on 2009–2014, at the Limnopolar Lake CALM-S site on Byers Peninsula, Livingston Island, Antarctica., *CATENA*, 149, Part 2, 538–547, doi:10.1016/j.catena.2016.06.002.

de Pablo, M.A.; **A. Molina**; C Recio; M. Ramos; G. Goyanes; M. A. Roperro, M.A. (2016). Análisis del estado de la capa activa en el emplazamiento de la base antártica española Gabriel de Castilla, Isla Decepción, Antártida. *Boletín Geológico y Minero*, 128 (1): 69–92 ISSN: 0366-0176, doi:10.21701/bolgeomin.128.1.004.

de Pablo, M. A., M. Ramos, and **A. Molina** et al. (2016), Frozen ground and snow cover monitoring in the South Shetland Islands, Antarctica: Instrumentation, effects on ground thermal behaviour and future research, *Cuadernos de Investigación Geográfica*, 42(2), doi:10.18172/cig.2917.

**Molina, A.**, M. A. De Pablo, M. Ramos, V. E. Hamilton, L. Le Deit, E. Hauber, and D. Fernández-Remolar (2015), Analysis of the surface temperatures of Ariadnes Colles (Mars) by MO-THEMIS BTR data, in *Avances, métodos y técnicas en el estudio del periglaciarismo*, edited by A. G. Ortiz, F. S. Franch, M. O. Franganillo, and M. S. Catarineu, pp. 287–300, Edicions Universitat Barcelona.

**Molina, A.**, M. A. De Pablo, T. Bardají, and M. Ramos (2015), Grain size distribution analysis of representative deposits in Livingston and Deception Island (South Shetland Archipelago, Antarctica), in *Avances, métodos y técnicas en el estudio del periglaciarismo*, edited by A. G. Ortiz, F. S. Franch, M. O. Franganillo, and M. S. Catarineu, pp. 287–300, Edicions Universitat Barcelona.

Jiménez, J. J., M. Ramos, M. A. De Pablo, G. Vieira, and **A. Molina** (2015), Active layer thermal variability, snow thickness coupled, in the vicinity of the Spanish Antarctic Station Juan Carlos I, in *Avances, métodos y técnicas en el estudio del periglaciarismo*, edited by A. G. Ortiz, F. S. Franch, M. O. Franganillo, and M. S. Catarineu, pp. 287–300, Edicions Universitat Barcelona.

**Molina, A.**, M. Á. de Pablo, E. Hauber, L. Le Deit, and D. Fernández-Remolar (2014), Geology of the Ariadnes Basin, NE Eridania quadrangle, Mars – 1:1Million, *Journal of Maps*, 10(3), 487–499, doi:10.1080/17445647.2014.888018.

Hamilton, V. E. et al. (16<sup>th</sup> **A. Molina**) (2014), Observations and preliminary science results from the first 100 sols of MSL Rover Environmental Monitoring Station

- ground temperature sensor measurements at Gale Crater, *J. Geophys. Res. Planets*, 119(4), 2013JE004520, doi:10.1002/2013JE004520.
- Gómez-Ortiz, D., D. C. Fernández-Remolar, Á. Granda, C. Quesada, T. Granda, O. Prieto-Ballesteros, **A. Molina**, and R. Amils (2014), Identification of the subsurface sulfide bodies responsible for acidity in Río Tinto source water, Spain, *Earth and Planetary Science Letters*, 391, 36–41, doi:10.1016/j.epsl.2014.01.022.
- de Pablo, M. A., M. Ramos, and **A. Molina** (2014), Thermal characterization of the active layer at the Limnopolar Lake CALM-S site on Byers Peninsula (Livingston Island), Antarctica, *Solid Earth*, 5(2), 721–739, doi:10.5194/se-5-721-2014.
- Molina, A.**, E. Hauber, L. L. Deit, S. Adeli, and D. F. Remolar (2013), Cartografía geológica de la región de Ariadnes Colles, Terra Sirenum, Marte, *Cuartas Jornadas de Jóvenes Investigadores de la Universidad de Alcalá: Ciencias / Germán Ros, Jesús Aguado Molina, Miguel Angel Hidalgo, Antonio Guerrero Ortega*, pp. 167–174. ISBN 978-84-15834-15-1
- de Pablo, M. a., J. j. Blanco, **A. Molina**, M. Ramos, A. Quesada, and G. Vieira (2013), Interannual active layer variability at the Limnopolar Lake CALM site on Byers Peninsula, Livingston Island, Antarctica, *Antarctic Science*, 25(Special Issue 02), 167–180, doi:10.1017/S0954102012000818.
- Molina, A.**, and M. Á. de Pablo (2012), HydraMars: una sencilla herramienta visual para realizar cálculos hídricos de canales abiertos (en la Tierra y Marte), in *Jornadas sobre investigación y didáctica en ESO y Bachillerato.*, vol. 22, pp. 17 – 22.
- Molina, A.**, and M. A. de Pablo Hernández (2011), La estructura de la atmósfera de Marte, *Investigación y didáctica para las aulas del siglo XXI: experiencias docentes y estrategias de innovación educativa para la enseñanza de la biología y la geología: Actas del I Congreso de docentes de Ciencias de la Naturaleza / Marisa González Montero de Espinosa, Luis Alfredo Baratas Díaz*, pp. 183-189. ISBN 978-84-680-0377-1.
- de Pablo M.A., M. Ramos, G. Vieira and **A. Molina** (2012) Revealing the secrets of permafrost. *Science in school*. 22, 17-22.
- Molina, A.**, M. A. D. Pablo, and M. Ramos (2011), Caracterización climática de la región de Nili Fossae, Marte, *M+A. Revista Electrónica de Medioambiente*, 0(10), 40–62, doi:10.5209/rev\_MARE.2011.n10.15857.
- de Pablo Hernández, M. A., and **A. Molina** (2011), Actividades sobre los cráteres de impacto de la Tierra, *Investigación y didáctica para las aulas del siglo XXI: experiencias docentes y estrategias de innovación educativa para la enseñanza de la biología y la geología: Actas del I Congreso de docentes de Ciencias de la Naturaleza / Marisa González Montero de Espinosa, Luis Alfredo Baratas Díaz*, pp. 191–199. ISBN 978-84-680-0377-1.
- Campanario, J. M., J. Carretero, V. Marangon, **A. Molina**, and G. Ros (2011), Effect on the journal impact factor of the number and document type of citing records: a wide-scale study, *Scientometrics*, 87(1), 75–84, doi:10.1007/s11192-010-0333-2.
- Molina, A.**, M. A. de Pablo Hernández, and M. Ramos (2010), Studying Martian permafrost from surface temperature data of Mini-TES, Spirit MER mission, *Ambientes periglaciares, permafrost y variabilidad climatic. Blanco, JJ, de Pablo, MA, Ramos, M. UAH Obras colectivas, Ciencias*, 197–204.

(And all the publications signed by MSL team, as more than 10 publications in Science).

### 8.5.5 STAYS IN FOREIGN CENTERS

University of Lisbon, Instituto Superior Técnico. Lisbon, Portugal.

20/10/2013 to 22/12/2013 (2 months)

German Aerospace Center (DLR), Institut für Planetenforschung. Berlin, Germany.

01/04/2012 to 01/07/2012 (3 months)

Antarctic Spanish Station “Juan Carlos I”, UTM/CSIC. Livingston Island, South Shetland Archipelago, Antarctica

09/01/2013 (20 days); 01/01/2012 (32 days); 31/12/2010 (24 days)

Antarctic Spanish Station “Gabriel de Castilla”, Spanish Army. Deception Island, South Shetland Archipelago, Antarctica

24/12/2012 (16 days); 05/02/2012 (9 days); 02/02/2011 (10 days)

Oceanographic Research Vessel “Las Palmas”, Spanish Navy. From the Southern Cone to West Antarctic Peninsula, several landings.

01/01/2012 (7 days); 27/12/2010 (26 days)

Oceanographic Research Vessel “Hespérides”, Spanish Navy and CSIC-UTM. From Southern Cone to West Antarctic Peninsula, several landings.

17/12/2012 (7 days)

### 8.5.6 GRANTS AND SCHOLARSHIPS OBTAINED

Permafrost Young Researchers Workshop travel grant. 01/06/2014

Attend to the International Permafrost Conference by the Bolin Centre for Climate Research

Nordic NASA-Hawai'i Summer School grant. 20/04/2012 (7 days)

This scholarship is awarded to students who have brilliant academic record for attending to the Summer School by the Nordic Network of Astrobiology.

Immersion in the English language grant. 22/07/2011 (7 days)

Attend to a intensive English course by Menéndez Pelayo International University.

Full Santander (UIMP) grant. 22/06/2011 (7 days)

This scholarship is awarded to students who have brilliant academic record for attending to the Summer School by Menéndez Pelayo International University.

JAE-Predoc 2010. 23/06/2010 (4 years)

To provide economic support to students as they work in their Ph.D. thesis by the Spanish National Research Council (CSIC)

### 8.5.7 CONTRIBUTIONS TO CONFERENCES

**A. Molina**, I. López, O. Prieto-Ballesteros, D. Fernández-Remolar, M.A. de Pablo and F. Gómez. *Coogoon Valles, a complex martian channel system*.

Lecture in V Reunión de Ciencias Planetarias y Exploración del Sistema Solar (CPSS5). Madrid, Spain. 06/06/2017 (TBC).

M.A. de Pablo; M. Ramos; **A. Molina**. *Air temperature and snow cover effect on ground surface temperatures in Byers Peninsula, Antarctica*.

TBD in the VI Congreso Ibérico de la International Permafrost Association. Mieres, España, 23/06/2017 (TBC)

M. Ramos; M. A. de Pablo; J.J. Jiménez; **A. Molina**; G. Vieira; Permasnow team. *Estudio comparativo del estado térmico del permafrost en dos sondeos con cobertura superficial diferenciada*.

TBD in VI Congreso Ibérico de la International Permafrost Association. Mieres, España, 23/06/2017 (TBC)

M. Ramos; J. J. Jiménez; M.A. de Pablo; **A. Molina**; G. Vieira; Permasnow team. *Ground surface enthalpy balance and snow layer isolation effect from bedrock temperatures (Livingston Island, Maritime Antarctic)*

TBD in the VI Congreso Ibérico de la International Permafrost Association. Mieres, España, 23/06/2017 (TBC)

**A. Molina**; E. Sebastián; J. Pérez Izquierdo; A. Bravo Cuesta; R. Ferrándiz; M. Ramos; M. A. de Pablo; G. Martínez; J. A. Rodríguez-Manfredi. *TIRS: El próximo sensor térmico y de radiación neta en Marte*.

Lecture in the 9<sup>th</sup> Asamblea Hispano-Portuguesa de Geodesia y Geofísica. Madrid, Spain 30/06/2016, see the Actas de la Asamblea 9AHPGG

J. J. Jimenez; C. Mora; M. Ramos; **A. Molina**; M. A. De Pablo; G. Vieira. *Estudios de la cobertura nival en entornos criosféricos deglaciados (Antártida Marítima) mediante técnicas activas de teledetección por microondas*.

Lecture in the 9<sup>th</sup> Asamblea Hispano-Portuguesa de Geodesia y Geofísica. Madrid, Spain 30/06/2016, see the Actas de la Asamblea 9AHPGG

M. A. de Pablo; M. Ramos; **A. Molina**; G. Vieira; M.A. Hidalgo; M. Prieto; J.J. Jiménez; S. Fernández; C. Recondo; J.F. Calleja; J.J. Peon; C. Mora; K. Laska; Z. Engel; F. Hrbáček. *Evolución de la cubierta de nieve y su efecto en el estado térmico del permafrost y la capa activa en las islas Livingston y Decepción, Antártida: el proyecto PERMASNOW*.

Lecture in the 9<sup>th</sup> Asamblea Hispano-Portuguesa de Geodesia y Geofísica. Madrid, Spain 30/06/2016, see the Actas de la Asamblea 9AHPGG

- M. Ramos; M. A. de Pablo; J. J. Jiménez; **A. Molina**; G. Vieira; G. Goyanes; A. Ferreira. *Variación local del régimen termo-mecánico de la capa activa y su correspondencia regional. Islas Livingston y Decepción (Shetland del Sur. Antártida)*.  
Lecture in the 9<sup>th</sup> Asamblea Hispano-Portuguesa de Geodesia y Geofísica. Madrid, Spain 30/06/2016, see the Actas de la Asamblea 9AHPGG
- A. Molina**; M. A. de Pablo; I. López; O. Prieto-Ballesteros; D. Fernandez-Remolar; M. Ramos. *Surface temperatures and thermal inertia in Coogoon Valles Mars*.  
Poster in XI International Conference on Permafrost. Potsdam, Germany 24/06/2016, see the [ICOP 2016 Book of Abstracts](#), pp. 546.
- A. Molina**; M.A. de Pablo; M. Ramos; C. Blitz; M.A. Roperó; G. Goyanes; M. Prieto. *Effects in the active layer and permafrost of the spanish antarctic station "Gabriel De Castilla" (Deception Island)*  
Poster in XI International Conference on Permafrost. Potsdam, Germany 24/06/2016, see the [ICOP 2016 Book of Abstracts](#), pp. 1140.
- A. Pisabarro; N. Campos; M. Gómez-Lende; **A. Molina**; R. Pellitero; M. González-García; A. Merino; D. Gallinar; J. Ruiz-Fernández; C. García-Hernández; J. Hall-Riaza; P. Carrera; J. M. Fernández; A. Nieuwendam; G. Goyanes; A. S. David; I. Girao; M. Cardoso; A. Ferreira; J. Branco; L. Bandeira; M. Lousada. *Permafrost research collaboration between PYRN Iberian members (Spain and Portugal)*  
Poster in XI International Conference on Permafrost. Potsdam, Germany 24/06/2016, see the [ICOP 2016 Book of Abstracts](#), pp. 82
- M.A. de Pablo; M. Ramos; **A. Molina**; J.J. Jiménez; M.á. Hidalgo; M. Prieto; S. Fernández; C. Recondo; J.F. Calleja; J.J. Peón; G. Vieira; C. Mora; K. Láska; F. Hrbáček; Z. Engel, D. Nyvlt. *PERMASNOW: Snow cover characterization and its effects on the thermal regime of permafrost and active layer in Deception and Livingston Islands, Antarctica*.  
Poster in XI International Conference on Permafrost. Potsdam, Germany 24/06/2016, see the [ICOP 2016 Book of Abstracts](#), pp. 119.
- M.A. de Pablo; M. Ramos; **A. Molina**; G. Vieira; M.A. Hidalgo; M. Prieto; J.J. Jiménez. *Snow cover evolution at Livingston and Deception Islands, Antarctica, from 2006 to 2015*.  
Poster in XI International Conference on Permafrost. Potsdam, Germany 24/06/2016, see the [ICOP 2016 Book of Abstracts](#), pp. 121.
- M. Ramos; M. A. de Pablo; J. J. Jimenez; **A. Molina**; G. Vieira. *Coupling in situ permafrost and active layer observations with Global Surface Temperatures from GISS: South Shetlands, Antarctica*.  
Poster in XI International Conference on Permafrost. Potsdam, Germany 24/06/2016, see the [ICOP 2016 Book of Abstracts](#), pp. 141.



- M. Ramos; J. J. Jimenez; M. A. de Pablo; **A. Molina**; G. Vieira. *Enthalpy method comparison between two different boreholes sites in Hurd Peninsula (Livingston Island)*.  
Poster in XI International Conference on Permafrost. Potsdam, Germany 24/06/2016, see the [ICOP 2016 Book of Abstracts](#), pp. 142.
- M.A de Pablo; M. Ramos; **A. Molina**; C. Recio. *Snow cover evolution at the Limnopolar lake CALM-S site (Byers Peninsula, Livingston Island, Antarctica) on 2009-2014 period*.  
Lecture in V Congreso Ibérico International Permafrost Association. Valladolid, España 26/06/2015, see the [V Congreso Ibérico IPA programa de sesiones y cuaderno de resúmenes](#), pp. 51.
- M. Ramos; M. A. de Pablo; **A. Molina**; G. Martinez; E. Sebastian; J. Gomez-Elvira; REMS and MSL team. *New method to determine the heat flux into the Mars soil surface. Applied to crater Gale (Mars) from MSL-REMS measures*.  
Lecture in V Congreso Ibérico International Permafrost Association. Valladolid, España 26/06/2015, see the [V Congreso Ibérico IPA programa de sesiones y cuaderno de resúmenes](#), pp. 30.
- M. Ramos; G. Vieira; M.A. de Pablo; A. Molina. *Evolución de la capa activa y su dependencia con el factor nival en la experiencia CALM-S "Crater Lake". Isla Decepción (Antartica)*.  
Lecture in V Congreso Ibérico International Permafrost Association. Valladolid, España 26/06/2015, see the [V Congreso Ibérico IPA programa de sesiones y cuaderno de resúmenes](#), pp. 14.
- M. Ramos; M. A. de Pablo; **A. Molina**. *Interannual active layer thermal and dynamics evolution at the crater Lake CALM site, Deception Island (Antarctica)*.  
Poster in the EGU General Assembly. Vienna, Austria 17/04/2015, see the Geophysical Research Abstracts, Vol. 17, EGU2015-11313-1.
- C. Recio; M. A. de Pablo; M. Ramos; **A. Molina**. *The state of permafrost surrounding Gabriel de Castilla Spanish Antarctic Station (Deception Island, Antarctica): Studying the possible degradation due to the infrastructures heating effect*.  
Poster in the EGU General Assembly. Vienna, Austria 17/04/2015, see the Geophysical Research Abstracts, Vol. 17, EGU2015-420.
- A. Molina**; L. Bandeira; P. Pina; M.A. de Pablo; M. Ramos; G. Vieira. *Automatic image-based grain size distribution classification: Mars and Antarctica*.  
Poster in 4th European Conference on Permafrost. Évora, Alentejo, Portugal 18/06/2014, see the Book of Abstracts of EUCOP4, pp. 249

**A. Molina;** M.A. de Pablo; M. Ramos. *Deception Island (Antarctica) as an Earth-Mars geomorphological analogue.*

Poster in 4th European Conference on Permafrost. Évora, Alentejo, Portugal 18/06/2014, see the Book of Abstracts of EUCOP4, pp. 250

J.J. Jiménez; M. Ramos; M.A. de Pablo; G. Vieira; **A. Molina.** *Enthalpic method and microclimatic variability in Livingston Island. A decade of experimental monitoring in the vicinity of SAS Juan Carlos I (Antarctica).*

Lecture in 4th European Conference on Permafrost. Évora, Alentejo, Portugal 18/06/2014, see the Book of Abstracts of EUCOP4, pp. 158

M. Ramos; **A. Molina;** E. Sebastian; C. Armiens; A. Lepinette; I. Carrasco; M. Genzer; F. Gómez; J. Gómez-Elvira; R. M. Haberle; V. E. Hamilton; A.-M. Harri; H. Kahanpää; O. Kempainen; J. Martín Soler; J. Martín-Torres; J. Martínez-Frías; M. Mischna; L. Mora; S. Navarro; C. Newman; M. A. de Pablo; J. Pla; V. Peinado; J. Polkko; S.C.R. Rafkin; N.O. Rennó; M. Richardson; J.A. Rodríguez-Manfredi; J.J. Romeral Planelló; M. de la Torre Juárez; J. Torres; R. Urqui; P. Valentín-Serrano; A. R. Vasavada; M.-P. Zorzano. *Heat flux into the soil surface on Crater Gale (Mars) from ground (GTS) and air (ATS) temperatures measures. First 100 mission MSL-REMS sols*

Lecture in the 4th European Conference on Permafrost. Évora, Alentejo, Portugal 18/06/2014, see the Book of Abstracts of EUCOP4, pp. 247 – 248

M. Ramos; M.A. de Pablo; G. Vieira; **A. Molina;** A.Abramov. *Interannual thermal evolution of the permafrost and active layer at the Crater Lake CALM Site, Deception Island, Antarctica.*

Poster in the 4th European Conference on Permafrost. Évora, Alentejo, Portugal 18/06/2014, see the Book of Abstracts of EUCOP4, pp. 439

F. Gomez; **A. Molina;** I. Lopez; O. Prieto-Ballesteros; A. Sansano; J.A. Rodriguez-Manfredi; M.A. de Pablo; D. Fernandez-Remolar; F. Rull; V. Parro; F. Tornos; S. Navarro; J. Gomez-Elvira. *Exomars 2018 Landing Site proposal: Coogoon Valles.*

Print only in the 8<sup>th</sup> International Conference on Mars. Pasadena, California, USA 14/06/2014, see the Eighth International Conference on Mars proceedings, pp. 1491

**A. Molina;** L. Bandeira; P. Pina; M.A. de Pablo; M. Ramos; G. Vieira. *Comparative of physical and optical surficial grain size analyses in representative soils of South Shetland Islands, Antarctica.*

Poster in the 5<sup>a</sup> Conf. Portuguesa de Ciências Polares. Faro, Algarve, Portugal 01/11/2013, see the 5<sup>a</sup> Conferência Portuguesa de Ciências Polares proc.

**A. Molina;** M.A. de Pablo; G. Vieira; M. Ramos. *Snow deposition patterns in relation with active layer evolution in Deception Island CALM site, Antarctica.*

Poster in the 5<sup>a</sup> Conf. Portuguesa de Ciências Polares. Faro, Algarve, Portugal 01/11/2013, see the 5<sup>a</sup> Conferência Portuguesa de Ciências Polares proc.

- M.A. de Pablo; M. Ramos; **A. Molina**. *Active layer thickness evolution on 2009-2013 period, at the limnopolare lake CALM site on Byers Peninsula (Livingston Island, Antarctica)*.  
Lecture in the IV Congreso Ibérico de la IPA. Val del Nuria, Catalonia, Spain 26/06/2013, see the [Avances, métodos y técnicas en el estudio del periglaciario](#).
- A. Molina**; M.A. de Pablo; M. Ramos, V.E. Hamilton; E. Hauber; L. Le Deit. *Analysis of the surface temperatures of Ariadnes Colles (Mars) by MO-THEMIS BTR data*.  
Lecture in the IV Congreso Ibérico de la IPA. Val del Nuria, Catalonia, Spain 26/06/2013, see the [Avances, métodos y técnicas en el estudio del periglaciario](#).
- M. Ramos; M.A. de Pablo; G. Vieira; A. Correia; **A. Molina**; A. Trinidad. *Análisis del estado térmico del permafrost en las Islas Livingston y Decepción (Antártida)*.  
Lecture in the IV Congreso Ibérico de la IPA. Val del Nuria, Catalonia, Spain 26/06/2013, see the [Avances, métodos y técnicas en el estudio del periglaciario](#).
- M. Ramos; M. A. de Pablo; V. E. Hamilton; M. de la Torre; **A. Molina**; E. Sebastian; A. Lepinette; C. Armiens; J. Gómez-Elvira; Equipo REMS y MSL. *Análisis preliminar del estado térmico del suelo en cráter Gale (Marte) y análogos terrestres. Instrumento REMS de la misión MSL*.  
Lecture in the IV Congreso Ibérico de la IPA. Val del Nuria, Catalonia, Spain 26/06/2013, see the [Avances, métodos y técnicas en el estudio del periglaciario](#).
- A. Molina**; M.A. de Pablo; M. Ramos, T. Bardají Azcárate; M. Fernandez Sampedro. *Caracterización granulométrica y mineralógica de los diferentes tipos de suelos presentes en las islas Livingston y Decepción (Shetland del Sur, Antártida)*.  
Poster in the IV Congreso Ibérico de la IPA. Val del Nuria, Catalonia, Spain 26/06/2013, see the [Avances, métodos y técnicas en el estudio del periglaciario](#).
- J.J. Jiménez; M. Ramos; M.A. de Pablo; G. Vieira; **A. Molina**. *Variabilidad térmica de la capa activa, acoplada al espesor nival, en las proximidades de la BAE Juan Carlos I (Antártida)*.  
Lecture in the IV Congreso Ibérico de la IPA. Val del Nuria, Catalonia, Spain 26/06/2013, see the [Avances, métodos y técnicas en el estudio del periglaciario](#).
- A. Molina**; M.A. de Pablo; M. Ramos. *Isla Decepción (Antártida) como análogo de Marte*.  
Lecture in the III Encuentro sobre Ciencias Planetarias y Exploración del Sistema Solar. Madrid, Spain 19/06/2013, see the [volumen de resúmenes](#), pp. 3 – 4.
- A. Molina**; E. Hauber; L. Le Deit; S. Adeli; D. Fernández Remolar; M.A. de Pablo. *Geologic analysis of knob fields and sedimentary deposits in Ariadnes Colles, Terra Sirenum, Mars*.  
Poster in the III Encuentro sobre Ciencias Planetarias y Exploración del Sistema Solar. Madrid, Spain 19/06/2013, see the [volumen de resúmenes](#), pp. 115 – 116.

M. de la Torre Juárez; M. Ramos; E. Sebastian; C. Armiens; J. Gómez-Elvira; A. Lepinette; I. Carrasco; R.M. Haberle; V.E. Hamilton; **A. Molina**; A. Lepinette; J. Martín Torres; J. Martínez Frías; M. Mischna; L. Mora; M.A. de Pablo; V. Peinado; J.A. Rodríguez Manfredi; R. Urqui O'Callahan; A.R. Vasavada; M.-P. Zorzano Mier; *MSL Science Team. Preliminary analyses of the REMS Ground temperature data in Gale: exploring thermodynamic processes behind the diurnal variability.*

Lecture in the EGU General Assembly. Vienna, Austria 12/04/2013, see the Geophysical Research Abstracts, Vol. 15, EGU2013-6733

**A. Molina**; M.A. de Pablo; M. Ramos. *Deception Island, Antarctica, an Earth-Mars analogue.*

Print-only in the 44<sup>th</sup> Lunar and Planetary Science Conference. Huston, Texas, USA 18/03/2013, see the abstracts of the 44th LPSC, Abstract #1202.

J.D. Centeno; M.A. de Pablo; **A. Molina**; M. Ramos. *Glaciers on Deception Island, Antarctica: Analogue of the Debris-Covered Glaciers on the Hecates Tholus Volcano of Mars.*

Print-only in the 44<sup>th</sup> Lunar and Planetary Science Conference. Huston, Texas, USA 18/03/2013, see the abstracts of the 44th LPSC, Abstract #1495.

M. de la Torre Juárez; M. Ramos; E. Sebastian; C. Armiens; J. Gómez-Elvira; A. Lepinette; I. Carrasco; R.M. Haberle; V.E. Hamilton; **A. Molina**; A. Lepinette; J. Martín Torres; J. Martínez Frías; M. Mischna; L. Mora; M.A. de Pablo; V. Peinado; J.A. Rodríguez Manfredi; R. Urqui O'Callahan; A.R. Vasavada; M.-P. Zorzano Mier; *MSL Science Team. Preliminary Interpretation of the REMS Ground Temperature Sensor in Gale: Exploring the Thermodynamic Processes Behind the Thermal Wave.*

Print-only in the 44<sup>th</sup> Lunar and Planetary Science Conference. Huston, Texas, USA 18/03/2013, see the abstracts of the 44th LPSC, Abstract #2553.

**A. Molina**; E. Hauber; L. Le Deit; S. Adeli; D. Fernández Remolar; M.A. de Pablo. *Cartografía geológica de la región de Ariadnes Colles, Terra Sirenum, Marte.*

Lecture in the IV Jornadas de Jóvenes Investigadores de la Universidad de Alcalá. Alcalá de Henares, Madrid, Spain 30/11/2012, see the Cuartas Jornadas de Jóvenes Investigadores de la Universidad de Alcalá: Ciencias.

**A. Molina**; E. Hauber; L. Le Deit; S. Adeli; D. Fernández Remolar; M.A. de Pablo. *Geologic analysis and habitability potential of Ariadnes Colles, Terra Sirenum, Mars.*

Lecture in the European Planetary Science Congress 2012. Madrid, Spain 23/09/2012, see the EPSC Abstracts Vol. 7, EPSC2012-213.

S. Adeli; L. Le Deit; E. Hauber; **A. Molina**; R. Jaumann. *Phyllosilicate-rich Knobs in the Atlantis Chaos Basin, Terra Sirenum.*

Lecture in the European Planetary Science Congress 2012. Madrid, Spain 23/09/2012, see the EPSC Abstracts Vol. 7, EPSC2012-291-2.

- A. Molina**; E. Hauber; L. Le Deit; S. Adeli; D. Fernández Remolar; M.A. de Pablo. *Geologic analysis of knob fields and sedimentary deposits in Ariadnes Colles, Terra Sirenum, Mars.*  
Poster in the Nordic-Hawai'i Summer School "Water, Ice and the Origin of Life in the Universe". Reykjavik, Iceland 02/07/2012, see the Water, Ice and the Origin of Life in the Universe Abstracts.
- M.A. de Pablo; **A. Molina**; M. Ramos. *Active Layer Monitoring in Limnopol Lake CALM Site in Byers Peninsula, Livingston Island, Antarctica.*  
Lecture in the 10<sup>th</sup> International Conference on Permafrost (TICOP). Salekhard, Yamal-Nenets, Russia 25/06/2012, see the Proceedings of Tenth International Conference on Permafrost.
- M. Ramos; M.A. de Pablo; **A. Molina**; G. Vieira; A. Trinidad; A. Correia. *Análisis de los ciclos de congelación y descongelación en la capa activa en el entorno de la BAE JCI. Periodo 2000-2011.*  
Lecture in the 7<sup>th</sup> Asamblea Hispano-Portuguesa de Geodesia y Geofísica. Donostia, País Vasco, Spain 23/06/2012, see the Actas de la Asamblea 7AHPGG, S09-723 -726
- M. Ramos; M.A. de Pablo; **A. Molina**; G. Vieira; A. Trinidad. *Progresión del frente de hielo en la capa activa de la experiencia CALM-S "Crater Lake" (Isla Decepción, Antártida).*  
Lecture in the 7<sup>th</sup> Asamblea Hispano-Portuguesa de Geodesia y Geofísica. Donostia, País Vasco, Spain 23/06/2012, see the Actas de la Asamblea 7AHPGG, S09-727 - 730
- M. Ramos; M.A. de Pablo; **A. Molina**; G. Vieira; A. Trinidad. *Evolución térmica del permafrost en dos entornos diferenciados Islas Shetland del Sur.*  
Poster in the 7<sup>th</sup> Asamblea Hispano-Portuguesa de Geodesia y Geofísica. Donostia, País Vasco, Spain 23/06/2012, see the Actas de la Asamblea 7AHPGG, S09-727 - 730, S09
- A. Molina**, M García-Villadangos, D. Gómez-Ortíz, O. Prieto Ballesteros, M. Sánchez-Román, D. Fernández-Remolar, D. Gleenson, N. Banerjee, N. Rodríguez, T. Barragán, R. Amils, P. Schmitt-Kopplin, G. Southam, M. Izawa, L. Loiselle, A. Granda, C. Quesada. *Searching for biosignatures in deep regions of the Rio Tinto aquifer: the Iberian Pyritic Belt Subsurface Life (IPBSL) Project.*  
Lecture in the Astrobiology Science Conference 2012. Exploring Life: Past and Present, Near and Far. Atlanta, Georgia, USA 18/04/2012, see the [Abscicon 2012 abstracts](#).



V. Parro; D. Fernández-Remolar; J.A. Rodríguez-Manfredi; F. López de Saro; M. Oggerin; M. Sánchez-Román; E. Omoregie; P. Fernández; M. García-Villadangos; N. Rodríguez; F. Puente-Sánchez; **A. Molina**; M.-P. Moreno; P. Cruz-Gil; C. Briones; F. Gómez; R. Amils; S. Arias-Rivas; K. Timmis; D. Gómez-Ortiz. *The Iberian Pyrite Belt Subsurface Life (IPBSL) drilling project*.

Lecture in the Astrobiology Science Conference 2012. Exploring Life: Past and Present, Near and Far. Atlanta, Georgia, USA 20/04/2012, see [Abscicon 2012 abstracts](#).

M.A. de Pablo; **A. Molina**; M. Ramos. *Estudio del espesor de la capa activa en las islas volcánicas Decepción y Penguin, Shetland del Sur, Antártida*.

Poster in the VIII Simposio de Estudios Polares. Palma de Mallorca, Balearic Islands, Spain 07/09/2011, see the [poster sessions](#) (PI-03)

**A. Molina**; M.A. de Pablo; M. Ramos; G. Vieira. *Estudio distribuido del efecto de la cobertura nival sobre los periodos de congelación/descongelación y evolución de la frontera libre en la capa activa en el entorno de la Base Antártica Española Juan Carlos I*.

Poster in the VIII Simposio de Estudios Polares. Palma de Mallorca, Balearic Islands, Spain 07/09/2011, see the [poster sessions](#) (PI-04)

M.A. de Pablo; M. Ramos; **A. Molina**. *Active Layer evolution (2009-2011) at Limnopolar Lake" CALM-S site on Byers Peninsula, Livingston Island (Antarctica)*.

Lecture in the III Congreso Ibérico de la International Permafrost Association. Piornedo de Cervantes, Galicia, Spain 21/06/2011, see the *Criosferas, Suelos Congelados y Cambio Climático: III Congreso Ibérico de la I.P.A. Libro de resúmenes*, pp. 75 – 78.

M.A. de Pablo; M. Ramos; G. Vieira; **A. Molina**. *Estado térmico del permafrost y evolución de la capa activa en la experiencia CALM-S (Crater Lake) (Isla Decepción)*.

Lecture in the III Congreso Ibérico de la International Permafrost Association. Piornedo de Cervantes, Galicia, Spain 21/06/2011, see the *Criosferas, Suelos Congelados y Cambio Climático: III Congreso Ibérico de la I.P.A. Libro de resúmenes*, pp. 95 – 99

**A. Molina**; M.A. de Pablo; M. Ramos; G. Vieira. *Estudio del efecto de la cobertura nival sobre los periodos de congelación-descongelación en el entorno de la Base Antártica Española Juan Carlos I*.

Lecture in the III Congreso Ibérico de la International Permafrost Association. Piornedo de Cervantes, Galicia, Spain 21/06/2011, see the *Criosferas, Suelos Congelados y Cambio Climático: III Congreso Ibérico de la I.P.A. Libro de resúmenes*, pp. 87 – 91

- A. Molina;** M.A. de Pablo; M. Ramos. *Methodologies proposal for Mars' permafrost study through orbital and rover data.*  
Lecture in the III Congreso Ibérico de la International Permafrost Association. Piornedo de Cervantes, Galicia, Spain 21/06/2011, see the Criosferas, Suelos Congelados y Cambio Climático: III Congreso Ibérico de la I.P.A. Libro de resúmenes, pp. 157 – 160
- M. Ramos; M.A. de Pablo; G. Vieira; **A. Molina.** *Monitorización sistemática de la evolución térmica del permafrost en las proximidades de las bases antárticas españolas basada en los protocolos CALM-S y TSP.*  
Lecture in the III Congreso Ibérico de la International Permafrost Association. Piornedo de Cervantes, Galicia, Spain 21/06/2011, see the Criosferas, Suelos Congelados y Cambio Climático: III Congreso Ibérico de la I.P.A. Libro de resúmenes, pp. 101 – 104
- M.A. de Pablo; **A. Molina;** M. Ramos. *Transecto de medición sistemática del espesor de la Capa Activa en las proximidades de la Base Antártica Española Juan Carlos I, Isla Livingston, Antártida.*  
Poster in the III Congreso Ibérico de la International Permafrost Association. Piornedo de Cervantes, Galicia, Spain 21/06/2011, see the Criosferas, Suelos Congelados y Cambio Climático: III Congreso Ibérico de la I.P.A. Libro de resúmenes, pp. 119 – 122
- A. Molina;** M.A. de Pablo. *Estudio morfológico e hidráulico de canales de escorrentía en Marte.*  
Print-only in the II Encuentro de exploración del Sistema Solar. Bilbao, País Vasco, Spain 16/06/2011, see the II Encuentro de exploración del Sistema Solar. Programa general. pp. 116 – 118
- A. Molina;** D.C. Fernández Remolar; M.A. de Pablo. *The Noachian-Hesperian paleoenvironmental conditions studied in Ophir Chasma, Valles Marineris.*  
Print-only in the II Encuentro de exploración del Sistema Solar. Bilbao, País Vasco, Spain 16/06/2011, see the II Encuentro de exploración del Sistema Solar. Programa general. pp. 119 – 121
- A. Molina;** M.A. de Pablo. *Implications of MER Mini-TES surficial and atmospheric temperatures. Evolution during a year on Gusev Crater, Mars.*  
Print-only in the 42<sup>nd</sup> Lunar and Planetary Science Conference. The Woodlands, Texas, USA 07/03/2011, see the Abstracts of the 42th Lunar and Planetary Science Conference. Abstract#1116.



# DISSERTATION

## TESIS DOCTORAL

Antonio Molina Jurado

Licenciado Ciencias Ambientales

Master Hidrología y Gestión  
de los Recursos Hídricos

This Ph.D. thesis is based on the stratigraphic and geomorphologic recognition and mapping of the Ariadnes (Eridania) and Coogoon (Arabia Terra) areas on Mars, which have extensive records from the Noachian-Hesperian transition (3.71 Ga ago). The ultimate goal is to characterize the paleohabitats arising during a global change occurred at the end of the Noachian, which transformed the planet conditions from wet and neutral to much dryer and acidic.

Esta tesis doctoral se basa en el reconocimiento y la cartografía estratigráfica y geomorfológica de las zonas de Ariadnes (Eridania) y Coogoon (Arabia Terra) en Marte, con el fin último de caracterizar los paleohabitats que se dieron en el planeta durante la transición entre el Noéico y el Hespérico (hace 3.71 Ga). Ambas áreas de estudio contienen registros de este cambio global que tuvo lugar al final del Noéico y que transformó las condiciones ambientales del planeta, de húmedas y con pH neutro a mucho más secas y ácidas.

